U.S. DEPARTMENT OF ENERGY | Energy Efficiency & Renewable Energy

2014

VEHICLE TECHNOLOGIES OFFICE

FY 2014 Annual Progress Report -
Lightweight Materials R&D

Contents

List of Figures

List of Tables

Acronyms and Abbreviations

β	dynamic collision angle
ºC	degrees Celsius
⁰C/s	degrees Centigrade per second
⁰K	degrees Kelvin
ΔTS	change in entropy in a mathematical equation
ΔZPE	the zero point energy in a mathematical equation
ε	symbol associated with hexagonal close-packed martensitic transformation
μ	microns
μA	microamps
μA/cm^2	microamps per square centimeter (current density)
μC/cm^2	microcoulomb per square centimeter (charge density)
μF	microfarad(s)
μm	micrometer(s)
μm^2	micrometer(s) square
μs	microsecond(s)
ν	Poisson's ratio
Ω−cm	ohm-centimeter (measure of electrical resistivity)
2D	two-dimensional
2T	two-layer
3D	three-dimensional
3T	three layer
3GAHSS	third generation advanced high strength steel
3M	company formerly known as the Minnesota Mining and Manufacturing Company
5xxx	series designation of aluminum alloyed with magnesium
6xxx	series designation for aluminum alloyed with *magnesium* and *silicon*, are easy to machine, and can be precipitation hardened, but not to the high strengths that 2000 and 7000
7xxx	series designation for aluminum alloyed with *zinc*, and can be precipitation hardened to the highest strengths of any aluminum alloy

A

A11, A22, etc.	fiber orientation tensor components
AA	aluminum alloy
AA5182	wrought aluminum alloy in the 5000 series

ABAQUS	a software suite for finite element analysis and computer-aided engineering
ab initio	from the beginning
ACBS	aluminum coated boron steel
ACC	Automotive Composites Consortium
ACC45tO60	a value in modeling software for the time (in seconds) for a vehicle to accelerate from 45 to 60 miles per hour
Acura CL	a coupé manufactured by Honda's from 1996 to 1999 and from 2001 to 2003.
AET	American Engineering Testing, Inc.
AET Integration	a research, development, and testing firm specializing in advanced material joining/welding technologies and related materials engineering services
AFM	atomic force microscope (or microscopy)
Ag	silver
AgCl	silver chloride
AHSS	advanced high-strength steel
AIW	adaptable insert welding
AK Steel	a producer of flat-rolled carbon, stainless and electrical steel products, primarily for automotive, infrastructure and manufacturing, construction and electrical power generation and distribution markets
Al	aluminum
Al:CuO	aluminum:copper(II) oxide
Al:Cu$_2$O	aluminum:copper(I) oxide
AlMn	aluminum-manganese
Al:NiO	aluminum:nickel(II) oxide
Al$_2$O$_3$	aluminum oxide
AlumiPlate®	The developer and provider of unique electroplating processes (electrodeposited aluminum), equipment and expertise for applying high purity aluminum
AM	aluminum-magnesium
AM60	aluminum-magnesium 60
AMO	Advanced Manufacturing Office
ANSI	American National Standards Institute
APS	advanced photo source
Ar	argon
ARD	anisotropic rotary diffusion
AS	advancing side (of welding tool motion)
ASMI	Autodesk® Simulation Moldflow® Insight
A/SP	Auto/Steel Partnership
ASTM	American Society for Testing and Materials

ASU	Arizona State University
atm	atmosphere (unit of pressure)
at%	atomic percent
AWD	all-wheel drive
AZ91	magnesium alloy with nine percent by weight aluminum and one percent by weight zinc

B

$b_{i(i=1,2,3,4)}$	a scalar constant used in calculation of tensor values
bal	balance
BASF	one of the largest chemical companies in the world headquartered in Ludwigshafen, Germany. BASF originally stood for Badisch Anilin und Soda-Fabrik (English translation: Baden Analin and Soda Factory)
bcc	body-centered cubic
BER	Biological and Environmental Research (a DOE user facility at PNNL)
BETAMATE™ 73305	a one-part, high-performance, heat-curing epoxy adhesive capable of bonding oily galvanized steel, col-rolled steel, and aluminum without primer and with corrosion resistance manufactured by Dow Chemical Corporation.
BETAMATE™ 73326	an air-cured structural adhesive that replaces body welding with bonding and bonds dissimilar metals or composite materials in lightweight designs manufactured by Dow Chemical Corporation
BIW	body-in-white (a car body's sheet metal components that have been welded together
$BMImBF_4$	1-butyl-3-methylimidazolium tetrafluoroborate
BOM	bill of materials – list of materials
BOP	bill of process – comprised of detailed plans explaining the manufacturing processes for a particular product including in-depth information on machinery, plant resources, equipment layout, configurations, tools, and instructions.
BP	batched prepared (polymers)
BSE	backscattered electron
BU	Brown University

C

C	capacitance (when referring to an electrical property)
C	fiber-interaction tensor (when referring to a mechanical property of a fiber)
C_b	shear rate constant
C/mol	coulomb per mole

Ca	calcium
CAD	computer-aided design
CAE	computer-aided engineering
Cameca SX-100	an electron probe micro analyzer for materials and geosciences made by Cameca
CANMET	Canada Center for Mineral and Energy Technology
CANMET MTL	Canadian federal laboratory in the energy sector with a focus on research in metals and materials in automotive, energy distribution, and power generation
CAVS	Center for Advanced Vehicular Systems, Mississippi State University
CBTN	carboxyl-terminated butadiene acrylonitrile
cc	cubic centimeter
CCB	cross-car beam
CCD	charge-coupled device
CC:urea	choline-chloride:urea
CF	carbon fiber
CFD	computational fluid dynamica
CFPC	carbon fiber polymer composites
CI	cyber infrastructure
cm	centimeter
CO_2	carbon dioxide
Cp	specific heat in joules per kilogram times degree Centigrade
CPM	crystal plasticity model
CRADA	cooperative research and development model
CSM	Colorado School of Mines
CT	computerized thermography (when referring to materials analysis)
CT	cross tension (when referring to material design)
CT	cornering and traction (when referring to tire testing)
CTC	compression-tension-compression
CTE	coefficient of thermal expansion
CU	Clemson University
CUV	crossover utility vehicle
CV	cyclic voltammetry (when referring to a type of potentiodynamic electrochemical measurement)
CV	coefficient of variation (when referring to statistical analysis)

D

D	diffusivity

D_g	drag coefficient
DADMs	dual-anneal diffusion multiples
dB	decibel
DEFORM 3D	DEFORM is an engineering software that enables designers to analyze metal forming, heat treatment, machining and mechanical joining processes on the computer rather than the shop floor using trial and error
DFT	density functional theory
DIC	digital image correlation
Digimat®	a nonlinear, multi-scale material and structure modeling platform by MSC Software
D-LFT	direct-injection long-fiber technology molding process, Pushtrusion™, is a PlastiComp, Inc. exclusive, patented and proprietary in-line manufacturing technology for injection and compression molding that eliminates pre-compounding
DMA	dynamic mechanical analysis
DOE	U.S. Department of Energy
DOI	distinctness of image
DOT	Department of Transportation
DP	dual phase
DSC	differential scanning calorimeter(y)
DTEM	dynamic transmission electron microscope (or microscopy)

E

E	Young's modulus (when referring to mechanical properties of materials)
E	enthalpy (when referring to heat transfer)
EAM	embedded atom method
EBSD	electron backscatter diffraction
EC2™	Alodine® EC2™, an electroceramic coating provided by Henkel Corporation
EC-AFM	electrochemical atomic force microscope (or microscopy)
e-coating	electrostatic coating
EDAG	Engineering + Design AG, Inc.
EDFA	erbium-doped fiber amplifier
EDS or EDX	energy dispersive x-ray spectroscope (or spectroscopy)
e.g.	for example
EG	electro-galvanized
EH(P)	electrohydraulic (pulse)
EHPW	electrohydraulic pulse welding
EM(P)	electromagnetic (pulse)

EMSL	Environmental Molecular Sciences Laboratory
Engg	contraction for "engineering"
ENR	engine noise reduction
EPA	Environmental Protection Agency
EPMA	electron probe micro-analysis
EPSC	elastic plastic self-consistent
ESC	electronic stability control
ESI	Engineered Solutions, Inc.
eV	electron volts
EVS	experimentally validated simulations
EX-EX	extrusion to extrusion
exp.	experimental
EX-SH	extrusion to sheet
ex situ	off site
EXW	explosive welding

F

F	deformation gradient in a mathematical equation
F	Faraday constant equal to 96,485.34 coulomb per mole
FARS	Fatality Analysis Reporting System
FBCC	front bumper crash can
FBG	Fiber Brag Grating (sensors) – record within the core of a single mode optical fiber only 9 microns in diameter
FCA US LLC	Fiat Chrysler Automobiles, U.S. LLC formerly Chrysler Group LLC
fcc	face-centered cubic
Fe	iron
FE	finite element
FEM	finite element model
FEG	field emission gun
FIB	focus ion beam
FLD	fiber length distribution (when referring to composite materials)
FLD	forming limit diagrams (when referring to modeling of metal structures)
FMC	Ford Motor Company
FMVSS	Federal Motor Vehicle Safety Standards
FOA	Funding Opportunity Announcement
FOOTPRINT	value for the vehicle footprint (in square feet) in crash models
F/R	front/rear
FRP	fiber reinforced polymer

FSW	friction stir welding
FSLW	friction stir linear welding
ft	foot or feet
FY	fiscal year

G

g	gram(s)
Ga	gallium
GFRP	glass-fiber reinforced plastic (composite)
GGA	generalized gradient approximation
GM	General Motors
Gleeble®	registered trademark by Dynamic Systems, Inc. for a fully integrated digital closed loop control thermal and mechanical testing system
GnP	graphene nanoplatelets
GPa	gigapascals

H

H	hydrogen
HAZ	heat-affected zone
H_2O	water
hcp	hexagonal close-packed
HEXRD	high energy x-ray diffraction
HIP	hot isostatically pressed or hot isostatic pressing
HPDC	high-pressure die casting
hr	hour
HSBS	hot-stamped boron steel
HSLA	high-strength, low alloy (steel)
HSS	high-strength steel
Hz	hertz (also cycles per second)

I

I3	inline three-cylinder (style of automotive engine)
ICME	integrated computational materials engineering
IIHS	Insurance Institute for Highway Safety
ILSS	interlaminar shear strength
ImageJ	ImageJ is an open source image processing program designed for scientific multidimensional images
IMC(s)	intermetallic compound(s)
in situ	on site or in place
in/min	inches per minute

IP	intellectual property (when referring to an idea, invention, or process that derives from the wok of the mind or intellect)
IP	instrument panel (when referring to automobile part or configuration)
Ir	iridium
IR	infrared
ISV	internal state variable
IVD	ion state variable
Izod	an ASTM standard method of determining the impact resistance of materials

J

JAC	Japanese Iron and Steel Federation Standard (JFS) A3011 material designation for hot-dip galvannealed steel sheet and strip products, grade from commercial quality to deep drawing quality, which can be used in various applications such as automobiles because of their deforming properties
J/m	joules per meter
J/m^2	joules per square meter
$J/mole^0K$	joules per mole degree Kelvin

K

K	thousand (when used with a number preceding the K)
Keyence	a digital microscope designed to overcome many of the limitations of conventional optical microscopes by combining the capabilities of multiple imaging and measurement systems in three dimensions
kg	kilogram
kJ	kilojoules
kMC	kinetic Monte Carlo
km/s	kilometer per second
kN	kilonewton
Ksi/ksi/kpsi	kilopound per square inch
KSOME	Kinetic simulation of microstructure evolution
kv	kilovolt
KWN	Kampmann-Wagner numerical (model)
kWH/kg	kilowatt hours per kilogram

L

lbs	pound(s)

LBS100	value for 100 pounds of weight reduction in crash models
LCA	life cycle assessment
LCCF	low-cost carbon fiber
LCF	long carbon fiber
LDV	laser doppler velocimeter
LGF	lattice green function
Li	lithium
LiClO$_4$	lithium perchlorate
LINCAP	Lateral Impact New Car Assessment Program
LLC	Limited Liability Company
LPP	lignin pilot plant
LSD	low speed damageability
LS-DYNA	an advanced general-purpose multi-physics simulation software package developed by the Livermore Software Technology Corporation
LS-OPT	a standalone design optimization and probabilistic analysis package with interface to LS-DYNA
LSTC	Livermore Software Technology Corporation
LVDT	linear variable differential transformer

M

M	molarity (moles of solute per liter of solution)
MA	martensite and austenite
MAGMASOFT®	modular simulation software supplied by MAGMA, a developer and supplier of software for casting process simulation
MANEUVER	value for the maximum speed (in miles per hour) a vehicle obtained on the avoidance maneuver test
Mathematica	software by Wolfram that provides a single integrated, continually expanding system covering the breadth and depth of technical computing
MATLAB®	MATLAB® (matrix laboratory) is a multi-paradigm numerical computing environment and fourth-generation programming language developed by MathWorks® that allows matrix manipulations, plotting of functions and data, implementation of algorithms, creation of user interfaces, and interfacing with programs written in other languages, including C, C++, Java, Fortran and Python.
MD	molecular dynamics
MEAM	modified embedded atom method
MFERD	Magnesium Front End Research and Development
Mg	magnesium
Mg(OH)$_2$	magnesium hydroxide

Mg$_2$Sn	magnesium hydroxide
MGI	Materials Genome Initiative
min	minute(s)
mj	millijoules
M-K method	Marciniak and Kuczynski method
ml	milliliter
mm	millimeter
MMLV	Multi-Material Lightweight Vehicle
mN	millinewtons
Mn	manganese
MnAl$_3$	manganese aluminide
mol/m^{3}s	moles per cubic meter-second
MPa	megapascals
mph	miles per hour
MPW	magnetic pulsed welding
MTS	MTS Systems Corporation
MSI or Msi	million pounds per square inch
MSU	Mississippi State University (report specific)
MSU	Michigan State University (report specific)
mV/s	millivolts per second
MW	megawatt (when referring to a unit of power)
M/W	microwave
MY	model year (referring to year of automobile manufacture)

N

n	sample number when referring to statistical results
nA	nanoamps
NaCl	sodium chloride
NanoBond®	Indium Corporation's patented process for bonding components utilizing NanoFoil®
NCAP	New Car Assessment Program
NDE	nondestructive evaluation
Nd:YAG	neodymium-doped yttrium aluminum garnet, a crystal that is used as a lasing medium for solid-state lasers
NETL	National Energy Testing Laboratory
nH	nanohenries
NHTSA	National Highway Traffic Safety Administration
NIST	National Institute of Standards and Technology
nm	nanometer
N/mm	newtons per millimeter
ns	nanoseconds
NVH	noise, vibration, and harshness
NWU	Northwestern University

O

OCP	open-circuit potential
octa.	octahedral
ODB	offset deformable barrier
OEM	original equipment manufacturer
OH	hydroxide
OPF	oxidized polyacrylonitirle fiber
ORNL	Oak Ridge National Laboratory
OSU	Ohio State University
OVEDRWT00	value for the mass reduction in heavier-than-average cars

P

PA	polyamide
PA66	polyamide 6,6 made from hexamethylenediamine and adipic acid
PAM-CRASH	A general purpose explicit finite element computer program for nonlinear dynamic analysis of structures in three dimensions
PAN	polyacrylonitirle
Pandat™	an integrated computational tool from CompuTherm LLC for multi-component phase diagram calculation and materials property simulation
Pa-s	pascal-seconds
PB	peak baseline
PC	polycarbonate
pctile	percentile
PDV	photonic Doppler velocimeter
PE	predictive engineering (when referring to a modeling tool)
PE	polyethylene (when referring to a material)
pH	negative logarithm of the effective hydrogen-ion concentration
PHS	press hardened steel
Pi joint	material joint shaped like an upside-down Greek letter "pi" (π)
PI	principal investigator
PJ	pulse joining
PNNL	Pacific Northwest National Laboratory
POD	proper orthogonal decomposition
PP	polypropylene
PPG	PPG Industries, originally Pittsburg Plate Glass
prepreg	a term for "pre-impregnated" composite fibers
PRISMS	predictive integrated structural materials science

Pt	platinum
PTFE	polytetrafluoroethylene
PU	polyurethane
PUs	pickups (term for trucks)
PVT	pressure-volume-temperature
PW	pulsed welding

Q

QI	quasi-isotropic
QMC, Inc.	Quality Measurement Control, Inc.
QP	quench and partitioned (for processing steel)

R

R	the gas constant equal to 8.314 joules per mole-degree Kelvin
R&D	research and development
RADIOSS	A multidisciplinary finite element solver developed by Altair Engineering
rad/sec	radian(s) per second
RAVF	retained austenite volume fraction
RE	rare earth
redox	reduction-oxidation
RIMIC™	a noise adsorption material produced by Autoneum having partial micro-perforation combined with single-walled heat shields made of aluminum
RIVTAC®	a joining technology supplied by Bollhoff for joining materials such as aluminum, steel, plastics, non-ferrous metals as well as mixed joints, multiple-layer joints and hybrid joints of these materials
RMX	company formerly ReMaxCo Technologies
ROM	reduced order modeling
RPM or rpm	rotations (revolutions) per minute
RR	right rear
RS	retreating side (of welding tool motion)
RSC	reduced strain closure
RSW	resistance spot weld
RUC	representative unit cell
RVE	representative volume element
RXN	reaction

S

S	probability profile control factor
s^{-1}	per second
SAE	Society of Automotive Engineers

SC-15®	a converter type two-phase epoxy cycloaliphatic amine resin supplied by Applied Poleramic Inc. used in applications such as ballistic panels
Scheil Model	The Scheil model assumes that diffusion rates are infinite in the liquid and zero in the solid; that local equilibrium is maintained at the advancing solidification interface, and the ratio of the liquidus composition to the solidus composition remains constant; and that there is negligible undercooling due to curvature or kinetics. The Scheil model can be used to describe the microsegregation present in primary phase dendritic growth and directional solidification.
Scotch-Brite	a line of abrasive cleaning pads produced by 3m
SD	standard deviation
SDAS	secondary dendrite arm spacing
SEA	statistical energy analysis
SECM	scanning electro-chemical microscope (or microscopy)
SEM	scanning electron microscope (or microscopy)
SENT	single edge notched tensile
SHM	structural health monitor
Si	silicon
SiC	silicon carbide
Si_3N_4	silicon nitride
SMC	sheet molding compound
Sn	tin
SPAC	self-pierce and clinch (referring to a type of rivet)
SpectroMax	an emission spectroscope with a very high accuracy and repeatability of results used to perform analyses of qualitative and quantitative chemical composition of metals
SPR	self-pierce riveting or self-piercing rivets
Sr	strontium
ST	shear tension (when referring to a property of a material)
ST	solution treated (when referring to a process for conditioning metals)
STEM	scanning transmission electron microscope (or microscopy)
SUV	sports utility vehicle
SVDC	super vacuum die casting
SVM	state variable model

T

T joint	material joint shaped like the letter "T"
T4	temper designation for solution heat-treated and naturally aged to a substantially stable condition. This designation applies to products which are not cold worked after solution heat-treatment, or in which the effect of cold work in flattening or straightening does not affect mechanical properties.
T5	temper designation for cooled from hot working and artificially aged (at elevated temperature)
T6	temper designation for solution heat treated and artificially aged aluminum alloy
TARDEC	U.S. Army Tank Automotive Research Development and Engineering Center
TCT	tension-compression-tension
TEM	transmission electron microscope (or microscopy)
tetra	tetrahedral
TGA	thermogravimetric analysis
ThermoCalc	ThermoCalc software magnesium-based alloy database version 2.0
Theta-Fiber™	a unique semi-structural felt material produced by Autoneum that has excellent acoustic and thermal properties including high heat resistance, low weight, excellent acoustics and integrated thermal insulation used for engine-mounted applications
Ti	titaniium
TP	thermoplastic
T PAN	textile polyacrylonitrile
TPNR	tire patch noise reduction
TRIP	transformation induced plasticity (for processing steel)
T.S.	tensile strength
TS	thermoset
TWB	tailor-welded blanks

U

U	the equilibrium potential or electric potential energy in a mathematical equation
UCR	upset cast riveting
UD	unidirectional
UHF	ultra-high frequency
UHSS	ultra-high strength steel
UIUC	University of Illinois at Urbana-Champaign

Ultra-LIght™	lightweight acoustic product produced by Autoneum that replaces insulation with absorption to significantly reduce part weight while optimizing acoustic performance.
UM	University of Michigan
UMAT	user material (programming subroutine)
UNDRWT00	value for the mass reduction in lighter-than-average cars
UPD	under potential deposition
UPJ	upset protrusion joining
USAMP	United States Automotive Materials Partnership
USCAR	United States Council for Automotive Research
UTS	universal testing system (when referring to a test methodology)
UTS	ultimate tensile strength (when referring to properties of materials)
UVW	uploaded vehicle weight

V

V	volt, voltage, or electrical potential (when referring to an electrical property)
V	velocity (when referring to a dynamic property)
VASP-PW91	Vienna ab-initio simulation package – Perdew-Wang 91
VDC	volts direct current
VE	vinyl ester
VFA	vaporizing foil actuator
VFAW	vaporizing foil actuator welding
viz.	synonym for "namely", "that is to say" , and "as follows"
VMM	validation of materials and models
VMT	vehicle miles of travel
VPI	Virginia Polytechnic Institute

VTO	Vehicle Technology Office

W

wCF	woven carbon fiber composite
WDS	wavelength-dispersive spectrometer (or spectrometry)
WIRS	weight-interval ranking sort (method)
WSU	Wayne State University
wt%	weight by percent

X

xpCF	cross-ply carbon fiber composite
XRD	x-ray diffraction

Y

YS	yield strength

Z

ZE20	an alloy melt containing, by weight, 2 percent zinc and 0.2 percent cerium and the balance magnesium cast into a round cylindrical billet for in-line extrusion
ZEK100	a novel magnesium alloy with reduced content of rare earth metals with a composition of Mg plus 1.0 wt% zinc, 0.1 wt%, rare earth metals, and 0.1 wt% zirconium
z/h	normalized thickness
Zn	zinc

I Introduction

As part of the U.S. Department of Energy's Vehicle Technologies Office the Lightweight Materials activity focuses on the development and validation of advanced materials and manufacturing technologies to significantly reduce light and heavy duty vehicle weight without compromising other attributes such as safety, performance, recyclability, and cost. Because it takes less energy to accelerate a lighter object, replacing cast iron and traditional steel components with lightweight materials such as high-strength steel, magnesium, aluminum, and polymer composites can directly reduce a vehicle's fuel consumption. For example, a 10% reduction in vehicle weight can result in a 6%–8% fuel economy improvement. Reducing vehicle weight has other benefits such as allowing cars to carry advanced emissions control equipment, safety devices, and integrated electronic systems without becoming heavier. Lightweight materials are especially important for improving the efficiency and range of hybrid electric, plug-in hybrid electric and electric vehicles because they offset the weight of power systems such as batteries and electric motors.

In the short term, vehicle weight reduction is possible through the application of materials such as advanced high strength steels and aluminum alloys; automotive alloys and processes within these material families already exist however further improvement is necessary to enable greater weight reduction while also addressing implementation technology gaps in joining, modeling, and recycling. In the longer term, even greater weight savings are possible though the use of magnesium alloys and carbon fiber composites. However, more extensive research and development is needed to address implementation barriers, improve the performance of these materials, and reduce their costs.

Research and development work conducted within the Lightweight Materials activity is broken down into three categories: Properties and Manufacturing, Multi-Material Enabling, and Modeling and Computational Materials Science. Work within Properties and Manufacturing aims to improve properties (such as strength, stiffness, or ductility) and manufacturability (such as material cost or production rate) of a variety of metal and polymer composite materials. Integrating components into a vehicle system while avoiding joining, corrosion, and other compatibility issues presents a significant challenge to the introduction of new lightweight materials. Work within Multi-Material Enabling targets novel processes, designs, materials, and technologies that enable assembly of disparate material systems into lightweight structures. Computational Materials Science and Integrated Computational Materials Engineering (ICME) continue to mature as important disciplines for lightweight materials development and deployment. Work within Modeling and Computational Materials Science engages broadly on topics ranging from model development and validation to framework deployment and ICME-driven development of new materials. In support of the President's Materials Genome Initiativei and the Vehicle Technologies Office objectives, much of this work emphasizes application on integrated computational and experimental techniques towards more rapid development and deployment of lightweight automotive materials.

Carbon Fiber and Polymer Composites

Carbon fiber reinforced polymer composites have the potential to reduce component weight by more than 60% however there are significant technical and cost barriers to their widespread introduction onto vehicles. The cost of input material (precursor) and the carbonization process contribute significantly to the total cost of carbon fiber hence significant focus has been provided to these areas. Focus on low cost carbon for both the precursor (polyacrylonitrile/lignin) and the advanced processing (plasma oxidation) show progress in both lower cost precursors as well as in lower cost oxidation of the precursor and conversion of the oxidized precursor to carbon fiber The process improvements continue to enable validation of successfully converting larger volumes (tows) of precursor to carbon at faster rates. ICME focused project include validation of models for long carbon fiber injection molding processing of a complex three dimensional part. In addition, the U.S. Automotive Materials Partnership's work on validation of crash models for carbon fiber composites show preliminary materials data for inputting in crash models. The analysis of crash data on vehicles at Lawrence Berkeley National Laboratory continues to provide insight into the impact of size and weight on crashes.

Magnesium Alloys

Magnesium alloys, with the lowest density of all structural metals, have the potential to reduce component weight by greater than 60%. However, significant technical barriers limit the use of Mg to approximately 1% of the average vehicle by weight. These barriers include high raw material cost and price volatility, relatively low specific stiffness, difficulty in forming sheet at low temperatures, low ductility of finished components, and a limited alloy set, among others. In addition, using Mg in multi-material systems introduces joining, corrosion, repair, and recycling issues that must be addressed. This year's report features results from several projects addressing key magnesium technology gaps.

Aluminum Alloys

Aluminum alloys represent a middle-ground in the structural light metals spectrum. Years of development within the aerospace, construction, and automotive industries have led to a well-developed and reasonably well understood alloy and processing set. Applications of aluminum within automotive design include hoods and panels, power train components, and even entire vehicle body-in-

white structures. There are several of barriers to the increased use of aluminum in vehicle weight reduction applications such as material cost, room temperature formability, and limitations within the existing manufacturing infrastructure. As with magnesium, the addition of significant amounts of aluminum to the automotive manufacturing stream presents added multi-material challenges in joining, corrosion, paint and coatings, repair, and recycling.

Advanced High Strength Steel (AHSS)

Conventional iron and steel alloys are prominent in existing vehicle architectures, making up about 45% of the weight of a vehicle. Despite the relatively high density of iron based materials, the exceptional strength and ductility of advanced steels offers the potential for efficient structural designs and reduced weight. Application of a new generation of advanced high strength steels has the potential to reduce component weight by up to 25%, particularly in strength limited designs. Steel components are also generally compatible with existing manufacturing infrastructure and vehicle materials, making them a likely candidate for near-term weight reduction. Steel development and research in the LM activity is focused on introducing the so-called "3rd generation AHSS." As shown in Figure X3ii, 3rd generation AHSS are targeted to properties in between 1st and 2nd generation AHSS with high strength, improved ductility, and low cost.
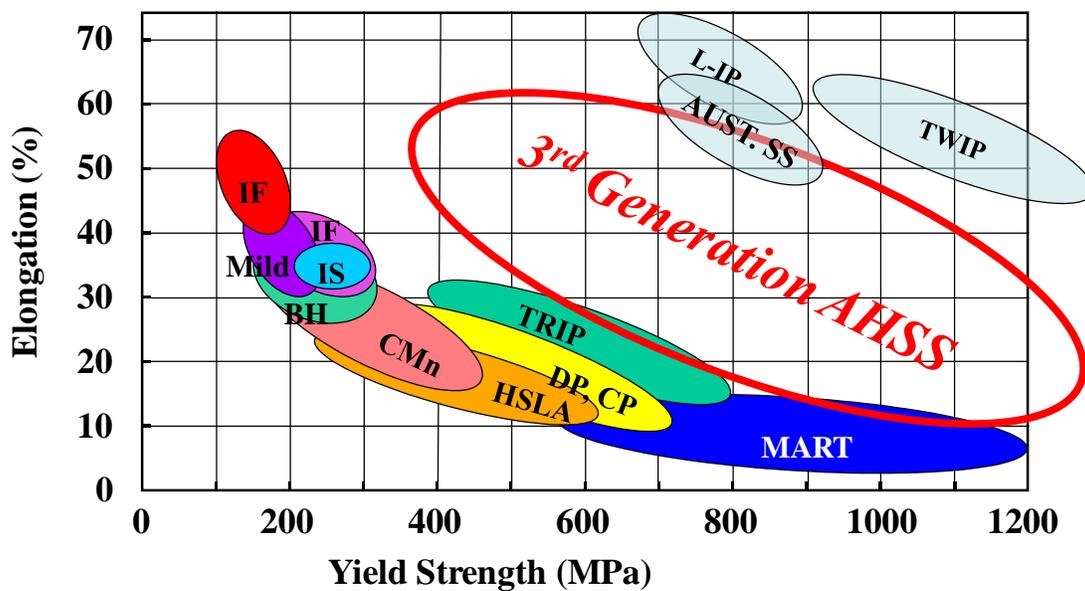
Figure I-1: Yield Strength versus Uniform Elongation for a variety of steel types[2]

Multi-Material Lightweight Vehicle (MMLV)

The MMLV demonstration project has made significant progress in demonstrating weight reduction potential for the midsize 2013 Ford Fusion baseline while maintaining safety and performance. This year six prototype vehicles of the Mach I design were built for testing. Current work demonstrates weight reduction for all systems of the vehicle. Preliminary crash test data as well as the challenges in achieving a 50% weight reduction for their Mach II design are presented in this year's report.

Looking Forward

The following reports provide a detailed description of the activities and technical accomplishments of the Lightweight Materials activity during the 2014 Fiscal Year. The work shown in this report has produced technologies that make today's vehicles more efficient, safe, and affordable. In collaboration with industry, universities, and national laboratories, the Vehicle Technologies Office continues to develop the next generation of lightweight components. These efforts are building the foundation of technologies—and technology manufacturers—that tomorrow's vehicles need to achieve ultra-high efficiency and resulting reductions in petroleum use and greenhouse gas emissions.

[1] http://www.whitehouse.gov/mgi

[2] Auto/Steel Partnership, www.autosteel.org

II FY 2014 Accomplishments

Significant progress was made in lightweight materials research during FY 2014 to further the use of these materials in automotive design and construction.

Below is a brief discussion of the accomplishments in FY 2014 for the various project areas discussed in detail later in the report.

II.1   Automotive Metals

- A superior extrusion speed was demonstrated for an experimental billet of an alloy melt containing, by weight, 2 percent zinc and 0.2 percent cerium and the balance magnesium. Adaptable insert welding was demonstrated as a novel means of joining dissimilar metals such as steel to magnesium. Studies of joining durability and corrosion were completed for the magnesium alloys and technologies.

- Two steel processing paths to produce third generation advanced high strength steel sheet with properties between the baseline QP980 steel and the two Department of Energy target third generation advanced high strength steel mechanical properties were identified. Full characterization of the tensile behavior of QP980 under different temperatures, quasi-static rates and sheet orientations was completed along with the evolution of strain fields obtained from digital image correlation. The first complete set of flow curves for QP980 at very high rates, greater than 400 cycles per second, were generated. A three dimensional phase-field model for martensitic transformations in elastic material was implemented. An elastic plastic self-consistent model for calculating the stress and strain partitions among different phases during deformation was developed.

- An apparatus was designed and operated that can test six zirconia compositions simultaneously As part of an effort to provide an industrial scale-up of low-cost, zero-emissions magnesium production using solid zirconia electrolysis. Development of high-quality zirconia tubes will increase tube lifetime and ultimately magnesium manufacturing uptime.

- Steels with improved quenching and partitioning parameters that met third generation advanced high-strength steels performance requirements of 1500MPa and 20% ultimate elongation were produced.

- The room-temperature formability, tensile behavior and aging response of aluminum alloy AA7075 were determined for different combinations of tempers and strain-rates. The formability of AA7075 in T6 and W tempers was found to be enhanced by pulse-pressure forming relative to the respective formability under quasi-static forming. Additional heat-treatment (and the associated added expense) of post-formed samples may not be necessary for pulse-pressure forming; thus, starting with W temper blanks, it may be economically feasible to obtain sufficient formability and achieve near-T6 strength in AA7075.

- To improve the overall formability of aluminum, more than 50% enhancement on tensile stretchability was achieved for large trimming clearances. With a previously developed integrated computational framework on edge stretchability prediction, the tensile stretching formability of trimmed parts was successfully predicted in terms of ductility. These simulation results correlate very well with experimental observations. An advanced trimming process was demonstrated and validated and has been prototyped with results showing that at least 50% improvement of stretching ductility can be achieved at room-temperature.

- A novel energy-efficient extrusion system was developed to produce fine-grained magnesium alloys. A magnesium alloy containing no rare earth elements was developed using a low-cost, high-shear extrusion process and shown to absorb energy similar to 6061 aluminum but with a 20 percent mass savings over 6061 aluminum.

- During research of aerodynamic lightweight cab structure components, mechanical testing on as-fabricated and paint-baked A-pillar covers was completed with the results that a paint-bake yield strength of ~132 megapascals was achieved which, although lower than the target 180 megapascals, is acceptable for the proposed application. The paint-bake failure strain was determined to be >23% (engineering) and exceeded the target strain of 15%.

- Synthetic microstructure-based three-dimensional/two-dimensional extrinsic modeling was performed to develop a computationally efficient two-dimensional modeling method for prediction of the ductility of thin-walled magnesium castings. The methodology developed can provide a basis for establishing possible a two-dimensional/three-dimensional fracture strain correlation curve for other complex loading conditions.

- A custom induction heater was developed and integrated into a full-scale self-piercing riveting system that successfully made induction-heated magnesium-magnesium joints at both room temperature and elevated temperature.

- Technologies were transferred to an industrial supplier facility that provided a capability for high-speed joining (greater than six meters per minute) of similar aluminum alloys with dissimilar thicknesses employing tailor-welded blanks in friction stir welding equipment. This capability produced aluminum welded panels for 70 door stampings at

both original equipment manufacturer and supplier facilities. These door panel prototypes were showcased to participants and members of the U.S. House of Representatives attending the Clean Energy Manufacturing Initiative, American Energy and Manufacturing Competitiveness Summit sponsored by the U.S. Department of Energy, Office of Energy Efficiency and Renewable Energy in 2014.

- To better understand protective film formation by magnesium alloys in automotive applications, an isotopic tracer study of an aqueous film formation growth mechanism in commercial magnesium alloys relative to ultrahigh purity magnesium was successfully completed. This is the first isotopic tracer study of magnesium corrosion ever reported. A new analytical tool called small angle neutron scattering was found to be sensitive to the formation of nanoporous, filamentous magnesium hydroxide resulting from the accelerated corrosion of magnesium alloys in salt solutions which has implications for understanding film growth and breakdown. An advanced transmission electron microscopy characterization study was successfully completed of ambient immersed aqueous film formation as a function of exposure time and alloy type that revealed nanoscale film segregation tendencies for addition of aluminum, rare earth, zinc, and zirconium alloy.

- A new prototype system of online weld nondestructive evaluation with infrared thermography was developed that integrated novel hardware and data analysis algorithms. The prototype system was successfully evaluated in the laboratory using a large sampling of weld coupons that were made from different advanced high-strength steels, thicknesses, coatings, and stack-up configurations. An evaluation of the online system was initiated in the assembly production environment at a Tier One automotive-body component manufacturer with promising initial testing results for both real-time and post-weld nondestructive evaluation inspections. Technology transfer and licensing with two private companies was initiated.

- High-energy synchrotron measurement was employed to confirm substantial reductions of residual stresses in advanced high-strength steel welds in the region near the low transformation temperature thereby providing the technical basis for drastically improved weld fatigue life.

- An effort for modeling, prototype development, novel infrared heat treatments of bimetallic joints, and residual stress and mechanical property characterizations improved the state-of-the-art for overcast joining technology. The results are applicable to multiple joints throughout current and other vehicle architectures. Numerous Tier I automotive suppliers will benefit from this research.

- The first development and successful use of electro-hydraulic pulse welding of high strength aluminum to dual-phase high-strength steel for body-in-white components was demonstrated that exceeded weld base metal strength targets. Welds did not fail but rather the tube base metal

failed at a value of 21 kilonewtons. The weld interface morphology resulting from the use of electromagnetic pulse welding was modeled based on both shape and length scales and validated against actual metallographic measurements.

- To further the investigation of dealloying, microstructure and corrosion protection of cast magnesium alloys, an electrochemical aluminum assay protocol using lithium underpotential deposition was developed and utilized to observe aluminum enrichment on magnesium-aluminum alloys under full-immersion, potentiostatic corrosion in a non-aqueous deep eutectic solvent.

- Using a systematic multi-scale modeling and experimental approach to protecting grain boundaries in magnesium alloys from corrosion, the preferred adsorption configuration and energetics of molecules relevant to hydrogen evolution, i.e., water, hydroxide and hydrogen, on pure and doped magnesium surfaces were identified after performing geometry optimization computations within the framework of density functional theory. The findings point out changes in the potential dependent reaction rates due to the dopant presence on the surface. A physically-based internal state variable model was developed to capture the fundamental mechanisms of corrosion through kinematics, thermodynamics, and kinetics. The model will fit into the cradle-to-grave integrated computational materials engineering design system.

- The anodic surface film formed on a pure magnesium ingot was investigated and characterized which is important and essential knowledge for understanding the corrosion resistance and passivity of metastable magnesium alloys.

- For the high-throughput study of diffusion and phase transformation kinetics of magnesium-based systems, a precipitation model for magnesium-aluminum-zinc, magnesium-tin, and magnesium-aluminum-tin alloys was developed to simulate the precipitation kinetics during aging treatment. The predicted microstructure evolution for the first two alloys was in agreement with the experimental data.

- During the in situ investigation of microstructural evolution during solidification and heat-treatment in a die-cast magnesium alloy, sputtering techniques were developed to reproducibly fabricate thin (~80 nanometer) and electron transparent magnesium-aluminum films on a support membrane. These films are ideal for in situ melting-solidification experiments using dynamic transmission electron microscopy.

- Using a high pressure super vacuum die casting technique, ternary magnesium-aluminum alloy plates were produced to establish reliable and consistent electron probe micro-analysis and metallographic procedures that facilitated development of a Monte Carlo simulation of micro-segregation behavior and investigation of transformation kinetics.

II.2   Carbon Fiber and Polymer Composites

- Pilot scale technical efforts for a novel low-cost carbon fiber evaluated a broad range of polyacrylonitrile polymer molecular weights, co-monomer ratios, and spinning conditions to produce the best precursor morphologies obtained to date for polymer blends ranging from 25% to 45% lignin. Commercial scale carbon fibers were tested and properties exceeded project targets. Improved air flow uniformity within a prototype oxidation oven and lower energy consumption per unit of output was confirmed following changes based on computational fluid dynamics studies. Longer effective oven heated length offers the potential for higher process speed and further cost reduction.

- Construction and optimization of a one ton/year plasma oxidation oven was completed. The oven processed two tows of commodity-grade, 24,000-filament precursor fiber in 30 minutes, reducing the oxidation time from the 80–120 minutes conventional process. All properties for carbonized fiber produced by this process exceeded Department of Energy thresholds of 250 kilopounds per square inch tensile strength, 25 million pounds per square inch tensile modulus, and 1% strain to failure. Based on these results, an industrial partnership was established with a major carbon fiber manufacturer to further commercialize the plasma oxidation technology.

- Operations at the Carbon Fiber Technology Facility primarily focused on converting carbon fibers in a variety of formats. Approximately 1275 kilograms were produced during the period from a variety of traditional polyacrylonitrile precursor and textile acrylic fiber precursor materials in small tow (12,000), medium tow (24,000 and 48,000) and large tow (610,000) formats. Progress was made in the development of the conversion protocol for the textile acrylic fibers. Tests of production runs showed that tensile strength and tensile modulus values were improving, reaching up to 511 kilopounds per square inch and 33.6 million pounds per square inch, respectively. These results indicated that this material might be a good candidate for full-scale production of lower-cost carbon fibers. During the second year of operation, the Carbon Fiber Technology Facility exhibited a perfect record of safety and environmental compliance.

- Research to further the development of predictive engineering tools for injection-molded long carbon fiber thermoplastic composites was completed by teams at two National Laboratories. Pacific Northwest National Laboratory completed material characterization for the rheological, thermal, and mechanical properties for 30-wt% and 50-wt% combinations of long carbon fiber/polypropylene and long carbon fiber/polyamide. A new fiber length distribution model was implemented based on an unbreakable length assumption with reduced order modeling by the proper orthogonal decomposition approach in the mid-plane, dual-domain, and three-dimensional Autodesk® Simulation Moldflow® Insight solvers to provide more accurate fiber orientation predictions. At Oak Ridge National Laboratory, fiber length measurement results from experimental trials showed the ability of the molders to retain long fiber length in injection-molded carbon fiber-filled thermoplastics. Materials for all molding trials and molded plaques were produced and used for establishing model parameters. Initial simulations of a complex part have revealed a significant number of potential weld lines that will have to be avoided during sampling

- The United States Automotive Materials Partnership made considerable progress to complete the majority of baseline steel front bumper and crash can crash testing with detailed analysis of crash responses that support predictive modeling for all four commercial codes (PAM-CRASH, LS-DYNA, ABAQUS and RADIOSS). Definitions of equivalency were developed that can be incorporated in crash models to help drive the design of innovative composite structures that leverage the strength and lightweighting potential of carbon fiber product forms.

II.3   Crosscutting Research

- Multi-Material Lightweight Vehicle Mach I prototype subsystems and component parts were manufactured and integrated with baseline vehicles to begin full vehicle testing. Much of the design for Mach-II lightweight systems has been completed and the remaining efforts will complete the 50% weight reduction, perhaps through reduction in vehicle content and features.

- Extensive thermo-mechanical material characterization, modeling/simulation and physical experimentation was used to optimize process parameters for round boss joints using upset protrusion joining techniques for joining dissimilar metals (aluminum-magnesium and aluminum-zinc). A full test matrix of over 200 self-piercing rivet joints ed evaluated for mechanical/structural performance and subjected to accelerated corrosion exposure to serve as a benchmark for upset protrusion joining design and process development.

- Heavily diluted novel composite reactive foils whose reaction products can be utilized to braze dissimilar metals together were fabricated. Initial testing found that added dilution decreases the amount of gas generated by the reaction; however, more dilution can be achieved by further refining the average reactant spacing within the foils. With enhanced reactivity, more diluent can be added to the foil to increase the quantity of braze available for joining.

- Considerable progress was made to develop an active, tailorable adhesive technology for multi-material jointing, repair and reassembly of lightweight structures. Experimental characterization of an adhesive modified with electrically conductive graphene nanoplatelets demonstrated improvement in tensile and flexural modulus of lap-joints formed with aluminum, steel and composite materials. Results show great promise in use of adhesives reinforced with graphene nanoplatelets as 'active' adhesives for dissimilar material joining. Incorporation of novel non-destructive evaluation tools in experimental characterization and use accurate measurements in numerical simulations provided an excellent tool for 'rational' development of design tools and elimination of a 'trial-and-error' approach.

- Effective laser-assisted ablation of carbon fiber composite and aluminum components was demonstrated. Carbon fibers were directly exposed on both the top surface and on the side surfaces, creating an ideal bonding surface for adhesives. A dramatic increase in the lap shear strength compared to baseline data was observed for the laser-processed specimens, demonstrating the proof of concept for the use of laser structuring and/or ablation technology for surface preparation of both carbon fiber polymer composites and aluminum coupons prior to adhesive joining.

- Successful collision welding of dissimilar materials using vaporizing foil actuator technology was accomplished with almost all the material combinations subjected to flat target welding. Automotive grade aluminum was effectively welded to high strength steel, as well as galvannealed steel. Welds were stronger in lap shear mode than in peel mode. Aluminum/steel welds were generally strong in peel mode, and during testing of some of the combinations, failure even occurred in base metal. With aluminum/magnesium samples, maximum peel strengths as high as 32.5 newtons per millimeter were obtained. Processes were also developed for creating lap and spot welds, which will enable faster industrial adaptation of the vaporizing foil actuator welding technique.

- A comprehensive compilation of industry knowledge of vehicle mass reduction techniques and approaches was completed using a literature review; interviews with researchers, vehicle manufacturers, and supplier engineers/designers; published vehicle specification data; commercial databases; and previous cost analyses. A technical cost model was developed to analytically evaluate the weight reduction performance and cost effectiveness of four weight reduction scenarios down to the component level. Technology paths for reaching the vehicle weight reduction targets of 40% and 45% were determined. The cost-effectiveness of various options was determined and technology gaps for realistically meeting these goals were defined. A significant amount of advanced lightweighting would be required for 40% mass reduction. Mass reduction of 45% or more will require not only extensive use of lightweight materials, such as carbon fiber and magnesium, but also next-generation electrical and interior systems.

- Several safety data analyses were conducted to better understand the relationship between decreasing vehicle weight or footprint and increasing crash frequency. From these analyses, the estimated effect of mass reduction on societal fatality risk per vehicle miles traveled was determined to not consistently decrease as vehicle weight increased. When the weight "flexpoint" was optimized to reduce fatality risk, a large, statistically-significant increase in risk from mass reduction in lighter cars, and a similar decrease in risk from mass reduction in heavier cars was obtained; however, the flexpoint necessary to achieve this statistical result was at the 90th percentile weight for cars, and would dramatically reduce the sample size of "heavy" cars if used.

III Automotive Metals

III.1 Development and Demonstration of a Magnesium-Intensive Vehicle Front-End Substructure – United States Automotive Materials Partnership (USAMP) LLC

James F. Quinn, Principle Investigator
General Motors Research & Development Center
30500 Mound Road
Warren, MI 48090-9055,
Phone: (586) 596-439; Fax: (586) 986-9204
E-mail: james.f.quinn@gm.com

Joy H. Forsmark, Principle Investigator
Ford Motor Company
Ford Research and Innovation Center
2101 Village Road
Dearborn, MI 48124
Phone: (313) 845-3056
E-mail: jforsma5@ford.com

Stephen D. Logan, Principle Investigator
FCA US LLC
800 Chrysler Drive
Auburn Hills, MI, 48326-2757
Phone: (248) 512-9485; Fax: (248) 576-7490
E-mail: sl16@chrysler.com

Aaron Yocum, Project Manager
National Energy Technology Laboratory
3610 Collins Ferry Road
Morgantown, WV, 26505
Phone: (304) 285-4852
E-mail: aaron.yocum@netl.doe.gov

William Joost, Technology Area Development Manager
U.S. Department of Energy
1000 Independence Avenue, S.W.
Washington, DC 20585
Phone: (202) 287-6020; Fax: (202) 856-2476
E-mail: william.joost@ee.doe.gov

Contractor: United States Automotive Materials Partnership LLC
Contract No.: DE-EE0005660

Abstract/Executive Summary

The goal of this project is the design, manufacture and performance evaluation of magnesium (Mg)-intensive "demonstration" vehicle front end substructures, enabled through the incorporation of Mg alloys, advanced materials processing, joining, finishing and use of computer-aided engineering. The "demonstration" structure concept provides a common geometric platform adaptable to investigation of alternative materials and processes, whereby computer aided design (CAD) renderings and fixtures for processing and testing are virtually the same. The structures designed for this project employ a central, super-vacuum die cast (SVDC) AM60B Mg "shock tower" component to which upper and lower rail pieces are joined, reminiscent of structural archetypes seen in typical unibody passenger vehicle front-end construction. A focal point of this work is the development and subsequent study of mixed-metal structures including galvanized steel and wrought aluminum (Al) to demonstrate multi-material joining and finishing techniques as well as durability performance (including fatigue and corrosion). The project includes efforts in the Integrated Computational Materials Engineering (ICME) of die-cast and wrought Mg alloys and components fabricated from them. The awardee participates in an international collaboration with Canada and The People's Republic of China to further advance Mg technology aimed at similar automotive applications.

Accomplishments

- Acquired all component parts for two families of demonstration structures (i.e. high-strength, low alloy (HSLA) steel and Al upper rail versions), including high-vacuum die-cast AM60B Mg shock tower castings.
- Validated joining and finishing processes that will be employed in manufacture of the demonstration structures.
- Demonstrated superior extrusion speed for ZE20 experimental billet stock using the lower rail profile and extrusion capabilities of supplier Mag Specialties, Inc.
- Completed coating and experimental corrosion measurements for an extensive array of mixed-metal coupons, surface treatments and joining methods as anticipated for use in the project, employing two industry standard corrosion test protocols.
- Compared two aluminizing technologies for corrosion prevention coating of hardened steel self-piercing rivets and measured influences on galvanic corrosion when coupled to AM60B Mg.
- Provided improvements to the LS-DYNA MAT_233 MAGNESIUM material properties card for shell elements as may be employed for analysis of thin-walled castings of AM60B Mg, and introduced a version of this material card

for 3-D elements anticipated for analysis of thick-walled castings.

- Conducted coupon fatigue studies of dissimilar metal (Al 6022 T4 – Mg AM60B) friction-stir welds in various configurations for use in development of "structural stress" models for use in predicting fatigue life of such joints in the actual demonstration structures being fabricated.
- Developed improved "structural stress" formalisms for the joining methods (friction-stir welding and adaptable inserts) that are used in the demonstration structures and collected coupon level data for confirmation.
- Demonstrated capabilities for "Adaptable Insert Welding" as a novel means of joining dissimilar metals such as steel to Mg. Developed a large test matrix of such joints on coupon pieces to evaluate strength, durability (fatigue) and corrosion performance. Developed computer aided engineering (CAE) model for fatigue prediction using the "structural stress" approach.

Future Directions

- Complete construction of the demonstration structures as designed.
- Complete all durability and corrosion testing of the demonstration structures and document findings.
- Conclude ICME, durability and corrosion studies of advanced Mg alloy ZE20.

Technology Assessment

- Target: **Design**. Create a design for a Mg plus dissimilar metal demonstration structure to evaluate candidate joining methods, durability and corrosion mitigation strategies while accommodating an improved Mg shock tower design. Design such demonstration structure for robust fixturing for durability testing.
- Status: All design work is complete.
- Target: **Crashworthiness**. Analytically predict peak load and displacement at peak load within 5% (or within test scatter band) of average of physical tests for a selected Mg AM60B SVDC component.
- Gap: Lack of accurate material property input cards for LS-DYNA® to permit finite element calculation of deformations at high strain rates for wrought Mg alloys exhibiting both tension/compression yield asymmetry and texture.
- Status: A 2D shell element model for die-cast AM60B was completed and implemented into the LS-DYNA software. A 3D version is presently undergoing validation.
- Target: **Durability (Fatigue).** Achieve capability for CAE prediction of fatigue life of similar and dissimilar metal joints (incorporating Mg) within a factor of two with respect to experimentally obtained values.
- Gaps: Lack of reliable mechanistic models that permit transference of laboratory coupon load/cycles-to-failure data into structural stress failure susceptibility at similar joints in actual assemblies with complex geometries.

Validation of fatigue life predictions with experimental data for joints of interest in the demonstration structures.

- Status: A number of FEA formalisms have been developed in this project for the principal joining techniques used in the demonstration structures including self-piercing rivets (SPRs), friction stir welding (FSW) and adaptable inserts.
- Target: **Corrosion**. Achieve zero or minimal galvanic corrosion associated with coated, hardened steel SPRs in Mg.
- Gap: Paucity of both coating technologies that achieve galvanic isolation between steel and Mg, as well as analytical methods to assess the efficacy of isolation approaches that are available. Historically, coating technologies have been aimed at reducing self-corrosion of steel fasteners as opposed to inhibiting galvanic corrosion with adjacent Mg.
- Status: Several techniques have been advanced in this project to measure the degree of galvanic coupling with adjacent Mg for particular rivet coatings. Coating systems have been identified which greatly minimize galvanic coupling.
- Target: **Extrusion.** Mg extruded alloy with improved ductility, resistance to recrystallization and grain growth, and limited imposed texturing during forming in order to enhance performance in high strain-rate deformation (e.g. crash) and extrusion speed (manufacturing).
- Gap: Need for improved material models that can be used in deformation codes for the extrusion process (e.g. DEFORM® 3D) as well as predictive codes for component deformation during crash (e.g. LS-DYNA®).
- Status: ZE20 Mg alloy was selected as a promising candidate and an extrusion/billet supplier was enlisted; materials and lower-rail extrusions were acquired and various characterization studies initiated.
- Target: **Casting.** Comprehensive assessment of the value of SVDC in improving the tensile and fatigue properties of die cast AM60B alloy. To date, a controlled, statistically-designed study has not been completed to quantify any potential benefits, beyond improvements in weldability and resistance to blistering during heat treatment.
- Gap: Lack of suppliers (of Mg alloy die castings with vacuum capability) to conduct such a study.
- Status: SVDC die cast shock towers were acquired for demonstration builds; no further USAMP activity is planned.
- Target: **Joining.** Identification and demonstration of joining technologies compatible with the dissimilar material combinations included in the present generation of demonstration structures. Assembly of approximately 200 'demonstration' structures for use by the project.
- Gap: Paucity of robust, validated, mass- production joining technologies for Mg to galvanized steel and Al.
- Status: Candidate methods (SPR, FSW and adaptable insert welding (AIW)) identified, prototype processes developed and assembly of demonstration structures launched.

✧   ✧   ✧   ✧   ✧

Introduction

This project builds upon developments from several prior, interrelated USAMP Magnesium Front End R&D (MFERD) projects. The overarching goal is the development of robust, enabling technologies permitting greater utilization of Mg alloys in light-vehicle body structures, of which the "demonstration" front end substructure is exemplary [1,2]. The precursor projects included design, manufacture and evaluation of all-Mg demonstration structures employing FSW and SPRs as the principal joining methods, with commercially-available surface pretreatments and cathodic electrocoat as the protective finish. SPRs, while offering substantial joint strength, had disadvantages of a) requires preheating of the Mg alloys used and b) susceptibility to galvanic corrosion attack in regions adjacent to the rivets. FSW of similar and dissimilar alloys of Mg was found to be generally acceptable for creating joints in all-Mg structures.

The current project, while employing a structure design envelope nearly identical to that of the prior "all-Mg" assemblies, utilizes "mixed" metal construction, specifically, HSLA 350 electrogalvanized steel and wrought Al (6022-T4) in the form of sheet-fabricated upper rail components and high-strength extrusions (Al 6082-T4) for the lower rails. This approach addresses concerns from the earlier phases, wherein commercially-available wrought grades of Mg used in "crush-sensitive" applications were more prone to early

fracture, particularly in high-strain rate (i.e. crash) loadings. Integration of large Mg structural castings in predominantly steel or Al body-in-white structures is perhaps a more likely scenario in the near term and suggests greater study of joining, finishing and durability of such mixed metal assemblies. The project maintains an effort to improve and understand Mg alloys and their processing at a fundamental level with the aims of reducing production cost and improving mechanical properties to be more competitive with current lightweighting materials such as Al and advanced high-strength steels. The project also maintains a longstanding (since 2007) international (U.S., Canada and China) cooperative effort aimed at advancing the knowledge base and technologies required for greater use of Mg alloys in automotive structures.

Approach

This project is organized similarly to the prior USAMP 'MFERD' efforts, principally by the technical specialties shown in Table III-1. A similar organizational structure is also employed by the three-country collaborative effort, wherein the technical task titles refer to the working groups for each country. Note: USAMP is not conducting noise, vibration, and harshness (NVH) research in this particular project, although some work is being done internationally.

Table III-1: Project subject matter and team organization.

Task	Title	Description
1	Project Administration	Maintains project financials, purchasing, reporting and project management.
2	Design, Build and Logistics	Develops and maintains CAD data for demonstration structures and builds; arranges logistics.
3	Crashworthiness and NVH	Develops improved material models for high strain-rate deformation of magnesium alloys of interest in structures.
4	Durability and Fatigue	Develops CAE models for structural durability of joints; arranges and conducts durability testing of structures.
5	Corrosion and Surface Treatment	Conducts corrosion testing of demonstration structures; analyzes strategies to mitigate galvanic corrosion.
6	Extrusion	Assesses performance of advanced Mg alloys for extrusion. Contributes to ICME of Extruded Mg.
7	Low-cost Sheet and Forming	Provides aluminum and steel sheet-formed parts for multi-material structures.
8	Casting	Provides super-vacuum die-cast AM60B magnesium shock towers for demonstration structures.
9	Joining	Provides joining technologies for mixed metal demonstration structures; arranges final assembly of demonstration structures.
10	Integrated Computational Materials Engineering (ICME)	Continue development of computational tools for the processing-structure-properties behaviors of ZE20 and AZ91D magnesium alloys.

During the project it has become apparent that the original "linear" layout of project tasks by technical specialty overlooks important synergies that have emerged in the meantime. The first of these technology 'clusters' centers around the technologies of assembly and testing of the subject "demonstration" structures, incorporating both similar and dissimilar-metal joining of Mg alloys, galvanic and general corrosion, and durability (e.g. fatigue of joints) as the subtopics . A decision made in one technical area influences the others, such that outcomes are interdependent. For example, the decision to use SPRs in construction then drives both the engineering for galvanic corrosion around such features, as well as the capability of particular CAE models for both forming and durability of this joint. Specific strength requirements of a particular joint may dictate required technologies to achieve the same, with corresponding ramifications for corrosion and surface treatments.

A second cluster focuses on examining issues associated with the use of Mg at the component level through ICME and CAE approaches to ultimately predict crash performance. Both a traditional cast Mg alloy (AM60) and a novel extruded Mg alloy (ZE20) are being employed in this exercise. In the case of AM60, advanced testing techniques and modeling approaches have been utilized to develop the material behavior inputs for the CAE prediction (in the LS-DYNA® commercial software package) of the AM60 shock tower. This new material 'card' will be implemented within the LS-DYNA® code for future use. In the case of ZE20, the elements of ICME and crashworthiness will be combined. This particular clustering of technical areas is unique in that it brings together the fundamentals of the forming technology for a novel material (in this instance ZE20), the processing, structure, and properties modeling for extrusion (viz. ICME), and ultimately the prediction of component performance. This project team is fortunate in having access to all the essential elements of a complete ICME system beginning with the as-cast Mg billet, tooling and design of a particular component, and extending capabilities for developing unique material parameters for deformation simulations in end use, e.g. LS-DYNA®. The 'system' in this case incorporates all of the critical technologies including the supply base for materials, academic institutions, federal laboratories, and OEM end users, working collaboratively.

In contrast to prior reporting, the Project leadership has elected to arrange this report primarily around the clusters so identified. The original project tasks remain recognizable, where appropriate, and there is no fundamental change to project management, budget or recording. Although this layout may appear different, the clustering of task areas and focus on their interdependence is believed to be reasonable.

Results and Discussion

The following tasks (2, 7 and 8) are effectively complete.

Design (Task 2). During the past year this team has provided all essential CAD data for the two versions of the demonstration structures (i.e. one with steel and the other with Al upper rails), including details as needed for modification and development of fixtures for use in durability testing and other assembly details such as placement location for fasteners, weldment and adhesives. The Design Team has also organized the project timing grid and participated in the logistics aspects of parts delivery, storage and queuing for assembly of the various structures. Continuing contributions will be on an "as-needed" basis.

Sheet and Forming (Task 7). The goal for this Task Team had been the design and procurement of sheet-metal components (Al 6022-T4 and HSLA 350 electro-galvanized (EG) steel) as the upper rails for the demonstration structures. Additionally, the team monitors technical developments for the more-formable ZEK100 sheet alloy. All work by this team is effectively complete**.**

Casting (Task 8). The goal for this Task has been the design and procurement of the SVDC AM60B Mg shock tower castings for the demonstration structures. The CANMET Materials Division of Natural Resources Canada (NRC-CAN) (the Canadian partner organization) provided a sufficient number of sound castings for completion of the project during May 2014. Although some minor casting defects in particular areas are still encountered on occasion, there are enough sound castings to provide to the Durability Team to meet its testing agenda. Castings with minor defects are quite usable for joining development studies, corrosion and display purposes. Work of this team is effectively complete.

Cluster I – Joining (Task 9), Durability (Task 4) and Corrosion (Task 5)

Figure III-1 illustrates the synergy between the Joining, Durability and Corrosion tasks. Not all areas of overlap illustrated are encompassed by this Project (notably environmentally-assisted fracture of Mg and corrosion/fatigue of joints). Linkages have been formed between the Joining and Durability tasks, for example, where the CAE formalism for prediction of fatigue in mixed-metal structures is critically dependent upon "localized stress" analysis of coupon joint samples fabricated using the materials and technology of interest. Manufacture of specific specimen geometries at the coupon level then permits a complex 'structural stress' vs cycles-to-failure predictive relationship to be generated.
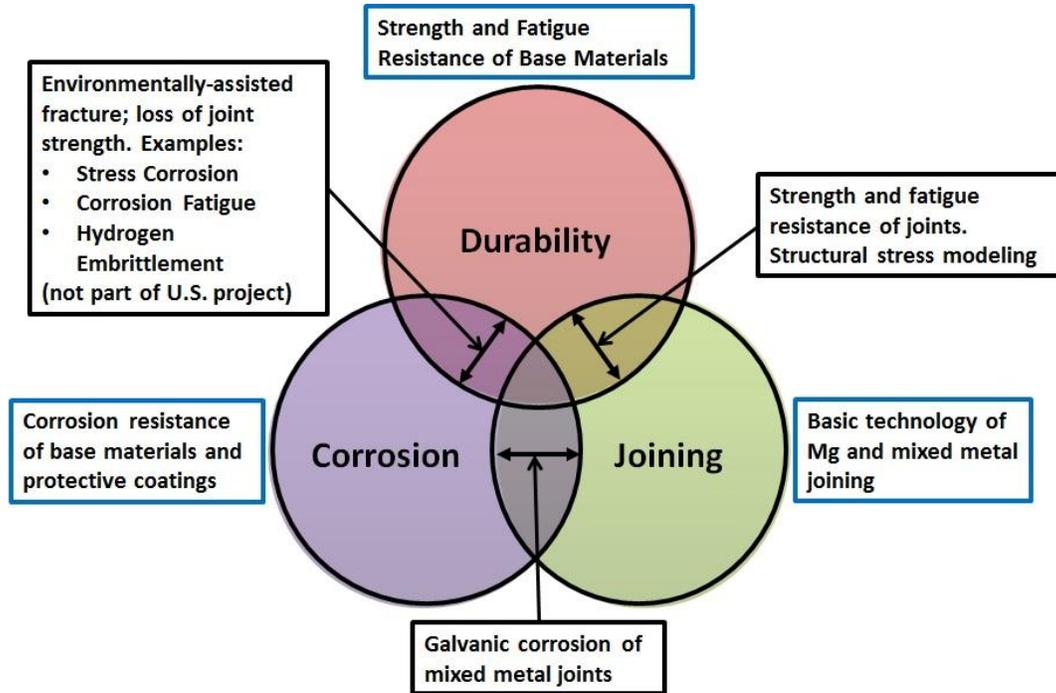
Figure III-1: Interrelationships for the "Joining and Assembly" cluster of MFERD technical tasks.

Joining (Task 9). The goal of this task is to identify and demonstrate joining technologies compatible with the material combinations of the demonstration structures, with strength, durability (i.e. fatigue resistance) and corrosion behavior that meet or exceed established criteria for such structural applications. The technical focus of the Task Team during the last year has been on continued development and implementation of the specific joining technologies selected for the demonstration structures. A common material and joint structure for both the steel (upper rail) and Al versions of the demonstration assemblies is the lower rail (extruded 6082-T4 Al) attachment to the AM60B Mg die-cast shock tower, employing coated steel SPR for the joints. Early in this project, it was found that by placing the Mg as the 'top' or pierced member of the SPR joint, the requirement for preheating the Mg, (which was necessary in Phase II) was eliminated, along with the associated manufacturing encumbrance. Efforts for this technology were then directed to the improvement of rivet coatings for minimizing the galvanic coupling of the base steel to Mg, and are reported through Task 5 (Corrosion).

Adaptable Insert Welding (AIW)

The AIW joining process which employs an adaptable insert welded to a similar base material through a hole in the dissimilar material to capture the dissimilar material, as shown in Figure III-2 was described in more detail in the FY13 annual progress report [3]. Development of processing parameters

and options for demonstration structure assembly were completed during this year. This included production of over 300 similar metal (Mg–Mg and steel-steel) resistance spot weld (RSW) joints and over 400 dissimilar Mg/steel AIW joints, in six unique coating/adhesive configurations during development of optimized electrode designs and process parameters for joining steel to Mg. For purposes of the demonstration structures, the electrocoated (and therefore electrically isolated) steel upper rail half will be secured to the Mg shock tower using pretreated AZ31 Mg inserts. Corrosion studies of the fully-coated assemblies will be conducted during the final year of the project.

Mechanical testing of adaptable insert joints employing the Mg insert has shown quasi-static lap-shear strengths ranging from approximately 4-6 kilonewton (kN), which is within the range of joint strengths observed by the project for a variety of joining technologies used with Mg. Lap-shear strengths may approach 11 kN when supplemental adhesive is used in the joint. The limitations of lap-shear-only strength testing should be understood in the context of eventual use of 'structural stress' in durability analysis of entire structures. In general, lap-shear values tend to be more optimistic, since loading conditions often include tensile components, for which the same joints, usually result in lower strengths.
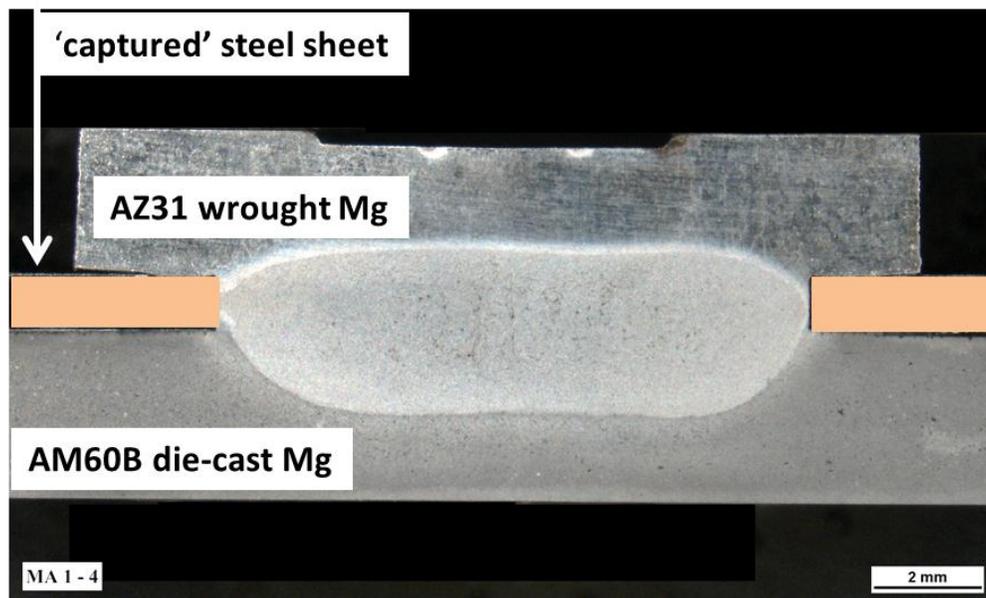
Figure III-2: Cross-sectional image of adaptable insert resistance weld joint between Mg and galvanized steel (colorized to highlight the location of the captured steel sheet member).

Friction-stir Linear Welding (FSLW)

The Al upper-rail version of the demonstration structure will employ FSLW as the primary joining technology, with provision for optional inclusion of structural adhesive. Subawardee Hitachi America (implementer of this technology) produced various geometries and types of FSLW samples (e.g. lap-shear and coach-peel, 2-plate and 3-plate overlay geometries, with and without adhesive) for coupon-level testing in corrosion and durability. A fixture used for producing the FSLW upper joints of the Phase II demonstration structure was acquired from General Motors and found to be partially usable for the current project. Figure III-3 illustrates the coach-peel FSW between press-formed Al 6022 sheet and AM60B Mg die casting and fixture required to produce this joint. The team employed a previously-designed 'top hat' die casting to achieve the right-angle bend required for the 'coach-peel' sample geometry. The Al member was excised from existing upper rail halves formed in 6022-T4. Acquiring coach-peel strength data is highly desirable for deriving the most accurate prediction capability using the 'structural stress' approach in finite-element analysis of entire structures. This type of loading is also more closely matched to the geometry of the upper-rail/shock-tower joint.

A hybrid joining process employing both FSLW and adhesive bonding was investigated this year, establishing that: 1) the presence of adhesive at the faying surface does not adversely affect the friction welding process and only minimal amounts of adhesive are left in the weld, 2) the maximum lap-shear load of these hybrid joints is substantially greater than the FSLW-only joints (typical values being 6.3 kN vs. 3.1 kN – FSLW only), and 3) adhesive, acting as a thermal insulator, increases the joint temperature and consequently affects material flow, requiring careful monitoring of the temperature. Further investigations are underway for this aspect as to how temperature can be controlled to improve process robustness.

Fatigue performance and metallographic analyses of various FSLW specimens by the University of Alabama indicated micro-voids in the weld zone leading to lower fatigue strengths. These studies have indicated the need to both monitor the weld temperature more accurately and to be more precise in controlling the penetration depth of the welds. Accordingly, Hitachi will use a miniature, 'in-tool' thermocouple and an infrared camera, to monitor the stir-zone and sheet temperatures, respectively, as well as excising and testing lap-shear specimens from actual demonstration structures to confirm weld quality.

Additional Joining Studies for Dissimilar Metals

In addition to development of the principle joining technologies indicated above, the team continued to investigate novel approaches to dissimilar metal joining. Studies included production of a 'self-pierce and clinch i.e. SPAC' rivet using high-strength Al, and the investigation of so-called 'stamp rivets' also employing a high-strength grade of Al that both pierces and then joins Mg and Al sheets mechanically. Al rivets are advantageous insofar as typically not inducing galvanic corrosion in adjacent Mg and avoiding complications of coatings for steel rivets or fasteners. Both SPAC and 'stamp' rivet technologies yielded lap-shear strengths for the Mg-Al couple that was within the observed range for other technologies considered. Exploration of these methods is continuing at the coupon level; however, these technologies will not be employed in demonstration structures.
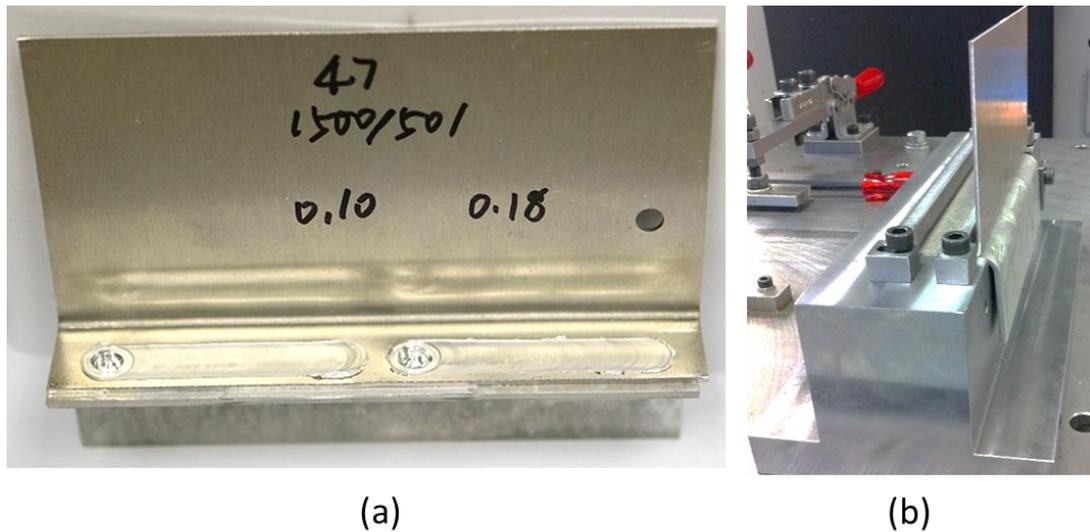
Figure III-3: (a) Example of the FSW "coach peel" joint between 6022-T4 Al and the AM60B Mg "top hat" casting wall portion and (b) fixture required to produce this joint.

Durability and Fatigue (Task 4). The objectives of this task are a) to develop fatigue characteristics for monolithic samples of novel Mg alloys (e.g. ZE20), b) to acquire fatigue data from coupon samples of novel joining methods for Mg and dissimilar metals, c) to advance CAE methodologies for improved prediction of fatigue at joint locations in complex structures, and .) to provide for fatigue testing of the project's demonstration structures, with emphasis on failure at the joint areas. During this year, the Team contracted with Exova, Ltd., Warren, MI, to conduct durability testing of demonstration structures, and provided necessary materials and CAD information for development of proper fixtures and test schedules.

Fatigue Modeling Capability Development (University of Michigan-Dearborn)

Fatigue data from coupon studies of SPRs, and FSWs were acquired through subawardees AET Integration, Inc., Troy, MI, and the University of Alabama. Coupon-level data is being developed into parametric "structural stress" vs life equations by subawardee University of Michigan-Dearborn. Figure III-4 illustrates the information flow for acquiring data and developing formalisms for fatigue life prediction in structures employing the advanced joining techniques developed by the project.

In addition to the ongoing development of finite-element modeling capabilities for prediction of fatigue life in complex structures utilizing the dissimilar materials joints developed by the project, this subawardee had also provided near-term guidance on structural details (e.g. fastener placement) which then affect the fatigue lifetimes the Durability Team seeks to determine experimentally. Detailed fatigue studies of all-Mg (i.e. Phase II) demonstration structures were completed and data analysis undertaken.

Fatigue Lifetime Determination for Friction-stir Weld Joints (University of Alabama)

Subawardee University of Alabama performed mechanical testing and microstructure characterization of FSLW Al-Mg joints, in order to quantify the joint performance anticipated for the demonstration structures. Microstructural characterization of these joints revealed intermetallic compound (IMC) formations in the stir zone, not encountered in similar-metal (e.g. Mg-Mg) joints. IMC formation is an ongoing concern in FSW of Mg-Al since it may lead to brittle joint behavior. Fatigue testing showed that in the presence of welding defects (primarily voids and possibly the FSW tooling keyhole), the joints fractured through the IMCs. Fracture through the IMCs was typically associated with lower strength and cycles to failure. Further observations showed that defect-free joints were more likely to produce fractures away from the weld zone, in either the Mg die casting or Al sheet.

Since the FSLW joints in the demonstration structure will experience loading beyond pure shear modes, Al-Mg coupons were created to test the strength in 'coach-peel' mechanical loading. Testing under static and fatigue loading on the coach-peel coupons revealed that the FSLW joint is particularly vulnerable to peeling forces. Minor voids that had minimal effect on the joint under shear loading appeared to be more detrimental to mechanical performance under peeling loads. Images of through-weld fractures for acceptable and poor welds in both lap-shear and coach peel geometries are compared in Figure III-5, along with schematization of the fracture paths. The worst case is a brittle weld zone that has no fracture path including base metal. The Joining team is pursuing process controls to refine the structural integrity of the FSLW in order to achieve acceptable shear and peeling loads.

Friction-stir weld lap-shear coupon

Fabricate and test joints under defined fatigue conditions

Define the modeling techniques –e.g. contact definitions

Assess data for quality and reproducibility

Establish joint fatigue behavior under 'local' loading conditions

Create FEA models for the coupon specimens tested, and recover forces and moments from the finite element analysis.

Calculate structural stresses for coupon assemblies

Define the structural stress equation for the joint selected

Demo structure assembly with multiple joint technologies

Establish structural stress vs. life curve

Determine the parameters required for fatigue analysis of target structure

Use structural stress vs life curve for fatigue life analysis of complex structures

Figure III-4: Model development and data flow chart for development of the "structural stress" formalism for prediction of fatigue lifetimes for joint areas in complex structures such as the "demonstration".

Figure III-5: Comparison of friction weld zone appearances for examples of good and poor welds in both lap-shear and coach peel geometries. AS= 'advancing side', RS='retreating side' of tool motion.

Task 5 – Corrosion and Surface Treatment

The principal accomplishment for this task in the past year was the completion of an extensive test matrix (over 600 joined two-metal (Mg-Al) and three-metal (Al-Mg-steel) panels) combining the base materials of construction, candidate pretreatment processes, joining methods, top coatings and testing protocols. Table III-2 details the variables in this statistically-designed experiment layout. This study is a novel approach to exploring the range of material processing options for the particular mixed-metal constructions envisioned. This type of data (for mixed-metal construction) is extremely valuable to coatings providers attempting to devise metal treating and coating systems. Analysis of the *post mortem* corrosion test assemblies is ongoing, however, a number of salient findings with implications for the structure builds and general mixed-metal construction have emerged. Foremost among these are:

a) The relatively poor performance of virtually all coating systems tested for the AM60B Mg as measured by 'scribe creep,' (which was selected by the Task Team as the most suitable metric when gauging coating systems performance for this application). Although not all OEMs have a scribe-creep performance specification for coatings on Mg alloys, based on typical limits for Al, no acceptable coating systems for the Mg alloy were identified in the study.

b) Ion Vapor Deposited (IVD) Al coatings for the baseline 10B37 hardened steel SPRs did not result in greater reduction of galvanically-enhanced corrosion of adjacent Mg in these joints compared to the baseline zinc-tin (Zn-Sn) barrel coatings. Highly engineered coatings employing electrolytic Al (viz. AlumiPlate®) with electrophoretic ceramic top coating (Henkel Corp. Electroceramic Coating (EC2™)) and sealant were, however, able to greatly reduce galvanic coupling between steel SPRs and Mg.

c) Cosmetic corrosion of joints using SPRs is extremely difficult to inhibit, for either the baseline Zn-Sn coating or the IVD Al. Greater polymer topcoat thicknesses appear to extend the time to onset of cosmetic corrosion adjacent to the rive heads. Remaining work will cover the use of specially-applied sealants for this purpose, as well as potential coating thickness effects.

d) An observation of substantial retained lap-shear joint strength for SPR joints incorporating Mg and Al, following extensive galvanic corrosion.

e) A capability for exuded adhesive (where employed) at joint edges to inhibit corrosion in these areas.

f) A sensitivity to fluid collection and increased corrosion at the "keyhole" void for FSW.

Figure III-6 illustrates an example of comparisons possible from the test matrix – in this case the effect of alternate top coating (i.e. powder epoxy vs electrocoat) – on cosmetic corrosion for one of the metal pretreatments considered. Scribing through the coating over the rivet resulted in underlying corrosion regardless of the polymer topcoat, although performance of individual pretreatments varied.

Cluster II - Extrusion (Task 6), Crashworthiness (Task 3) and Integrated Computational Materials Engineering – ICME (Task 10)

Figure III-7 illustrates the synergy between the Extrusion (Task 6), ICME (Task 10) and Crashworthiness (Task 3) activities, in this instance to enable the prediction of the behavior of the lower rail and shock tower components in high-speed crush testing. The primary limitation on the use of conventional wrought grades of Mg such as AZ31 in such crush applications, as identified by testing in MFERD Phase 2, is the relatively poor performance of the alloy under such loading, possibly due to the combined effects of mechanical properties asymmetry for Mg (e.g. yield and ultimate strength values that are different in tension versus compression loading) and localized texture and microstructure variation. Further, limitations in the predictive capability of existing CAE material inputs to the performance simulation were also identified in Phase 2. To that end, a novel Mg alloy was sought that would have a more uniform microstructure and the program embarked on research activities that would fully characterize the material microstructure and properties from billet stock to final component.

Table III-2: Variable values for designed experiment testing of joined and coated corrosion test panels.

Substrates	Pretreatments	Joining Methods	Topcoats	Corrosion Test
AM60B die-cast Mg plate Al 6082-T4 sheet HSLA 350 EG70 steel	Alodine® 5200 (Henkel) Tectalis (Henkel) ZircoBond 4200 (PPG Industries) Interlox 5705 (Atotech)	Self-piercing rivets (Zn-Sn coated) Self-piercing rivets (IVD Al coated) Friction-stir linear welding (FSLW) Break-stem rivets (steel and Al)	Powercron 590-534 cathodic epoxy electrocoat (PPG Industries) Protech ES542N49 epoxy powder coat (Almond Products)	ASTM B-117 500h exposure SAE J-2334 120 cycles.
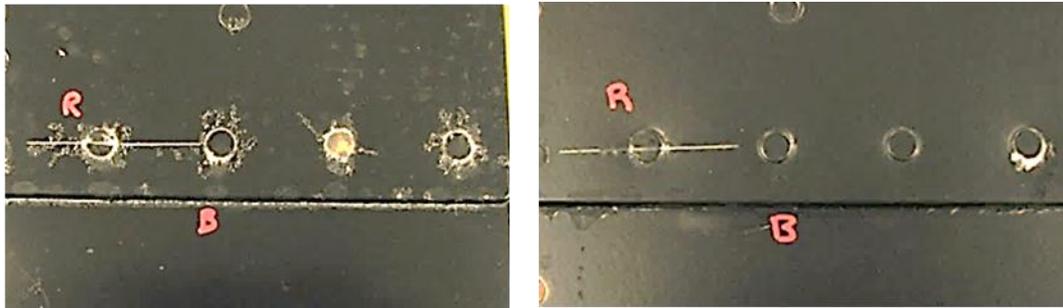
Electrocoat   **Powder coat**

Figure III-6: Example coupon studies showing the lesser cosmetic corrosion for powder coating for similarly-coated (Zn-Sn) rivets joining AM60B Mg to 6082-T4 Al with identical pretreatments. The scribe through the coating (designated 'R' in the photos) initiates corrosion in either case. 'B' indicates the location of the overlap or 'bond' joint between panels. The Mg panel is at the top in these pictures.
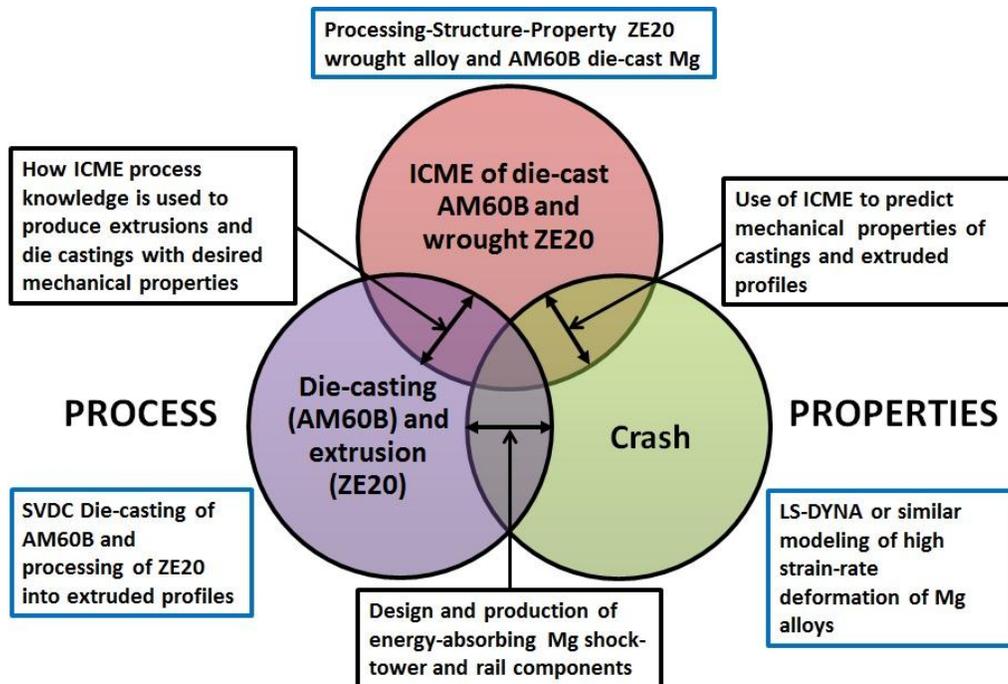
Figure III-7: Interrelationships for the ICME "cluster" of technologies.

During this year, a more collective approach was taken to the development of extrusion processing for one advanced grade of wrought Mg (ZE20) and determination of processing and property characteristics. This was undertaken, in part, due to the exceptional capabilities and cooperation of extrusion supplier Mag Specialties Inc., Denver, CO, to obtain as-cast alloy billet stock, provide sample sections, and engage in careful measurements and manufacturing control to provide operational parameters useful in modeling of the material behavior. The information and experimentation flows are illustrated in Figure III-8, which then represents, in greater detail, the synergy between processing, property determination and performance. The University of Michigan conducted detailed studies of microstructure development and recrystallization kinetics. Ohio State University conducted Gleeble® (i.e. elevated temperature deformation) testing of as-received billet stock. Mississippi State University conducted microstructural and texture determination on extruded pieces. Lehigh University began converting such deformation and recrystallization data into parameters than can be used in the extrusion simulation program DEFORM® 3D. Pacific Northwest National Laboratory (PNNL) was enlisted to

conduct carefully-controlled and measured extrusion tests of ZE20 on shape profiles prescribed by Lehigh to permit ready validation of the DEFORM® model predictions for an actual profile shape (e.g. 'I' beam). The Crashworthiness Team (Task 3) has arranged for generation of high-strain rate testing of the extruded ZE20 profile sections by the University of Dayton Research Institute for generation of deformation characteristics of the extruded component. Provided the metallurgical behavior of ZE20 indeed defuses texturing and recrystallization in the extrusion, incorporation of a material card for LS-DYNA® similar to that used for more randomly-textured die castings may be possible.

In addition to the collective efforts portrayed in Figure III-7 and Figure III-8, the task teams conducted the works outlined below.

Extrusion (Task 6). This team provided the Al 6082-T4 alloy extruded lower rail components for the demonstration structure builds via contract with Kaiser Al, and relevant suppliers of surface treatments as required.

Crashworthiness (Task 3). This team has continued development of material models for the LS-DYNA® deformation simulation program, and this year provided both refinements to the previously-developed MAT_233 MAGNESIUM material card for die-cast AM60B Mg employing shell elements, as well as introducing a comparable material card for 3D (solid) elements as may be used in modeling of

thick-walled castings. The team has further conducted validation (crash) experiments for the SVDC AM60B shock tower components in the current design configuration (i.e. including design improvements implemented after Phase II MFERD to permit more durable structures), for comparison to the predictions from LS-DYNA® using the MAT_233 MAGNESIUM material card. Although initial crash determinations indicated a need for greater control of component constraints evidenced by an unexpected shift in temporal location of the peak load, maximum forces, failure locations and loading characteristics were generally in good agreement. Testing with the improved constraining fixture is underway.

Integrated Computational Materials Engineering (Task 10). In addition to the contributions to the extrusion modeling efforts for ZE20 by Ohio State University, University of Michigan, and Mississippi State University, this team also continued study of microstructural development and strengthening mechanisms for the AZ91D Mg version of the SVDC die-cast shock tower. In this case, efforts at the University of Michigan and Mississippi State are directed to study of β-phase precipitation accompanying heat treatment as a strengthening feature (University of Michigan) and modeling of the fatigue process for these structures using various microstructural damage models (Mississippi State University).
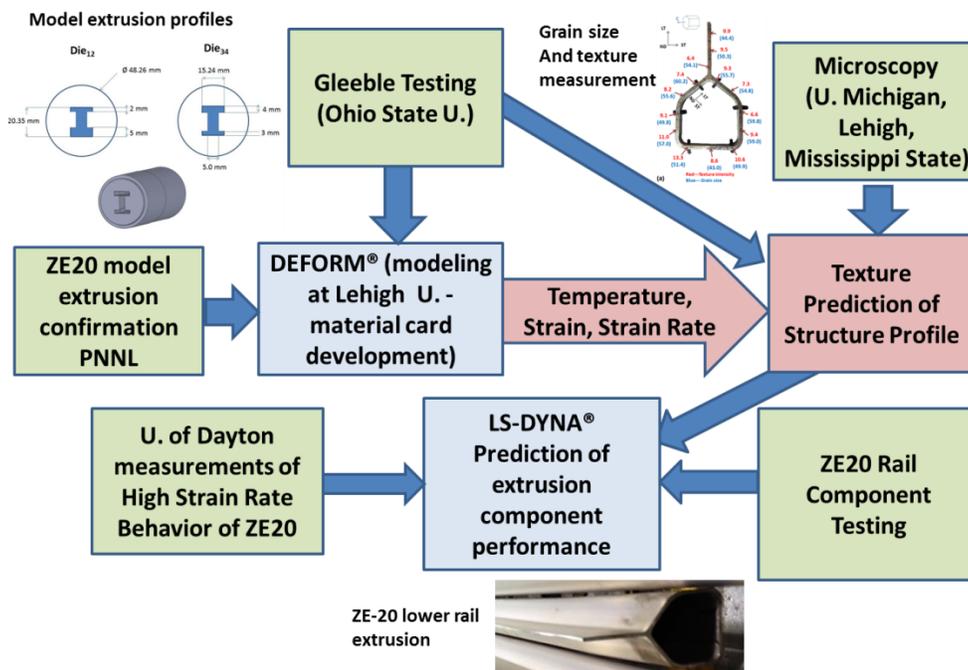
Figure III-8: Experimental and simulation information flows for the ZE20 extrusion modeling.

Technology Transfer Path

Increased use of Mg as a lightweighting material alternative in automotive structural design is fraught with both economic and technical challenges including material cost, perceived durability concerns, a receding supplier base in North America, and manufacturing concerns such as joining and surface treatment. Although massive incorporation of Mg components into articulated subassemblies such as the originally-envisioned 'front end' appears unlikely in the near term, Mg will continue to have a role in vehicle lightweighting, predicated on its attractive features of low density, high specific stiffness and amenability to thin-wall die casting and component integration. In this case, efforts devoted to improve strength and durability (fatigue) of castings, joining to dissimilar metals and finishing alternatives will remain quite relevant. Comments regarding the constituent stakeholders are as follows:

OEMs. Improved material properties models for specific grades of Mg (e.g. AM60B, ZE20) will be of value in various design simulations including crashworthiness. Developments in the physical metallurgy of advanced grades of Mg (e.g. ZE20, ZEK100) may eventually permit utilization of lightweight components in load-sensitive applications where more isotropic behavior of the metal is desirable. Knowledge gained with regard to corrosion protection systems and scope of applicability – particularly for novel, multi-material pretreatments – is expected to be of value. Additionally, novel joining methods and parameters such as rivet coatings are of interest. Durability modeling of joining technologies is of general value, as are novel approaches for joining dissimilar metals.

Suppliers. USAMP has enlisted over 30 distinct suppliers of materials, technologies and services relating to the design, production and incorporation of Mg components in automotive structures over the course of the several MFERD projects. Through technical committees and web-based tools suppliers are both engaged in discussion of Mg technologies as well as in providing often unique adaptations of existing technologies for deployment with Mg. Suppliers are thus engaged in understanding the particular technical challenges and building their capabilities to meet expanded use of Mg alloys in vehicle lightweighting.

Universities. A long-range goal of the MFERD initiative, originally set forth by its architects, has been the fostering of greater Mg technology education and innovation through the university system. To this end, 11 universities have been engaged in the overall project with nine in the current embodiment, focusing on physical metallurgy, ICME, durability, metal deformation and corrosion. Such sponsored university research was intended to instill a greater interest in Mg science and technology among students, as well as

providing a means for linking knowledgeable graduating students with possible opportunities in supplier or OEM organizations.

Conclusion

At the end of its second full fiscal year, the project team has received all component parts and begun construction of "demonstration" structures using the joining and finishing technologies evaluated and developed – including FSW, AIW and SPR. Subsidiary studies of joining durability and corrosion have been completed or are underway for the materials and technologies being employed. A concerted effort to produce, characterize and simulate extrusion processing of the advanced Mg alloy ZE20 was undertaken this year.

Presentations/Publications/Patents

1. Castano, C.; O'Keefe, M.; Fahrenholtz, W. 'Microstructural evolution of cerium-based coatings on AZ31 magnesium alloys." *Surface and Coatings Tech*nology, (*246),2014, pp.*77-84.

2. Castano, C.; O'Keefe, M.; Fahrenholtz, W. "Characterization of cerium-based nano materials for photocatalytic applications." Presented at the TMS 2014 Annual Conference, San Diego, CA on Feb 16 - 20, 2014.

3. Forsmark, J.H. "Adventures in Incorporating Lightweight Metals in Vehicles – a USAMP Story." Presented at the ECOAT14 Conference, Orlando, FL on April 22, 2014

References

1. Luo, A. A.; Quinn, J.F.; Wang, Y.-M.; Lee, T.M.; Verma, R.; Wagner, D.A.; Forsmark, J.H.; Su, X.; Zindel, J.; Li, M.; Logan, S.D.; Bilkhu, S.; McCune, R.C. (April 2012) "The USAMP Magnesium Front End Research and Development Project." *Light Metal Age*, pp. 54-58.

2. Forsmark, J.H.; Li, M.; Wagner, D. A.; Zindel, J.W.; Luo, A. A.; Quinn, J. F.; Verma, R.; Wang, Y.-M.; Logan, S. D.; Bilkhu, S.; McCune, R.C. (2014) "The USAMP Magnesium Front End Research and Development Project – Results of the Magnesium 'Demonstration' Structure." *Magnesium Technologies*, pp. 517-524.

3. "Lightweight Materials R&D Program, DOE/EE 1039." (2013). U.S. Department of Energy Vehicle Technologies Office. Accessed December 2, 2014: http://energy.gov/sites/prod/files/2014/04/f15/2013_lightweight_materials_apr.pdf

III.2 Integrated Computational Materials Engineering Approach to Development of Lightweight 3GAHSS Vehicle Assembly (ICME 3GAHSS)

Dr. Louis Hector, Jr., Principal Investigator
General Motors R&D Center
Mail Code 480-106-RL1
30500 Mound Road
Warren, MI 48090-9055
Phone: (586) 651-2628
E-mail: Louis.hector@gm.com

Ron Krupitzer, Principal Investigator
American Iron and Steel Institute (AISI)
Vice President Automotive Applications
2000 Town Center, Suite 320
Southfield, MI 48075
Phone: (248) 945-4761
E-mail: rkrupitzer@steel.org

David Ollett, Technology Project Officer
National Energy Technology Laboratory (NETL)
DOE/NETL/PMC/VTP Division
626 Cochrans Mill Road
Pittsburgh, PA 15236-0940
Phone: (412) 386-7339
E-mail: david.ollett@netl.doe.gov

Will Joost, Technology Development Manager
U.S. Department of Energy
1000 Independence Avenue, S.W.
Washington, DC 20585
Phone: (202) 287-6020
E-mail: william.joost@ee.doe.gov

Contractor: United States Automotive Materials Partnership
Contract No.: DOE DE-EE0005976

Abstract/Executive Summary

The goal of the program is to successfully demonstrate the applicability of Integrated Computational Materials Engineering (ICME) for the development and deployment of third generation advanced high strength steels (3GAHSS) for immediate weight reduction in passenger vehicles. The ICME approach will integrate results from well-established computational and experimental methodologies to develop a suite of material constitutive models (deformation and failure), manufacturing process and performance simulation modules, as well as the computational environment linking them together for both performance prediction and material optimization. The project officially started on February 1, 2013.

In the prior annual report, Colorado School of Mines (CSM) proposed two steel processing recipes; a quench and partitioned (QP) recipe and a transformation induced plasticity (TRIP) recipe that could possibly achieve the mechanical properties for the DOE proposed exceptional strength, high ductility steel and high strength, exceptional ductility steel, respectively. During this period of performance, the project used these recipes to make heats of steel at both AK Steel and the Canada Center for Mineral and Energy Technology (CANMET). The purpose of the AK Steel heats is to validate the CSM's process recipes whereas the CANMET heats are to enable the production of larger samples in sufficient volumes for comprehensive testing.

The heats at CANMET were produced but processing held pending further process refinements at AK Steel. In May, AK Steel produced some cold rolled strip from both heats for material characterization and mechanical property testing. The QP cold rolled sheet achieved the tensile strength target of 1500 megapascals (MPa) but with 10% tensile elongation. This reflects the difficulty in scaling up laboratory based processing recipes using industrial intent production equipment, but the mechanical properties were an improvement over the baseline QP980 steel and within the 3GAHSS mechanical properties space. The team concluded that the QP chemistry was acceptable but some process refinement was necessary to improve the ductility.

The TRIP recipe initially did not achieve the projected properties but was later found to have picked up nitrogen during annealing which formed brittle surface layers that adversely affected the material tensile strength and ductility. Once these layers were removed by hand grinding, the steel exhibited mechanical properties (1166 MPa tensile strength / 37% tensile elongation), which are better than projected and close to that of the DOE proposed high strength, exceptional ductility steel. The team is currently evaluating a means of adapting the annealing process to produce the TRIP steel without forming brittle surface layers. In the meantime, the limited volumes of this steel are being used in the Task 2 experimental components to generate baseline data for the Task 2 computational components aimed at microstructure-based constitutive model development.

The objective of the steel heats is to produce samples for measurement of phase flow properties at Brown University (BU), macroscale flow properties and transformation kinetics at Clemson University (CU), and validation of Michigan State University's (MSU) Crystal Plasticity Model (CPM) and Pacific Northwest National Laboratories' (PNNL) State Variable Model

III.2. Integrated Computational Materials Engineering Approach to
Development of Lightweight 3GAHSS Vehicle Assembly (ICME 3GAHSS)

Hector–GM; Krupitzer AISI

(SVM). MSU and PNNL collaborated on developing a test matrix for 3GAHSS steels to produce the needed information for material model development. Due to the types of testing and sample sizes listed in the test matrix, the project team confirmed the need to source 3GAHSS sheet from CANMET, which can produce larger width strip in greater amounts and will be useful for generating forming limit diagrams and for forming simulation trials.

Once the sample materials are provided, the MSU/PNNL test matrix will be executed by CU and BU, which are nearing completion for conventional testing of the baseline QP980 steel. While waiting for samples, both universities have been evaluating novel experimental methods to achieve some elusive material information, such as quantifying austenitic transformation with strain, which is not well understood, and lacks agreed upon test methods for measuring the transformation, but could improve model predictive accuracy if better understood.

In January 2014, the Task 5 team defined the baseline side-structure sub-assembly and completed the baseline technical cost model. In June the team completed the sub-assembly baseline performance assessment by applying eight separate load cases to the vehicle body assembly. With the baseline sub-assembly completely defined, the team is preparing for design optimization, which starts with a sensitivity analysis to define what components contribute the most to the performance of the assembly and are most susceptible to changes in stiffness. To conduct this analysis the team is collecting 3GAHSS material cards.

Livermore Software Technology Corporation (LSTC) adapted the SVM from an ABAQUS user material (UMAT) to LS-Dyna. Additionally, LSTC has been working to align the input and output variables from both models in LS-OPT in preparation to assemble these in a pre-ICME model and to meet Milestone #2: Meso-scale Computational Prediction, which will provide initial predictions of 3GAHSS mechanical properties based on microstructural constituents. The current SVM model uses solid finite element modeling (FEM) elements and PNNL and LSTC are working to include the ability of the SVM to use shell elements for improved performance modeling.

The project accomplishments during this period of performance have been significant and the interdependency between tasks is evident. The ability of the project to meet its deliverables underscores the importance of intercommunication within and between tasks; between modelers, experimentalists, steel makers and designers. Integration is important to the success of this project and the flow of information between tasks is encouraging. The project is on track to meet all deliverables for the second project year and the remaining two years.

Accomplishments (2014 FY)

- Engineering + Design AG Corporation (EDAG) and the Task 5 team completed project Milestone #7: "Baseline Assembly Design Defined" by providing a bill of materials of the donor vehicle side-structure sub-assembly complete with a technical cost model, component alloy identification and mechanical properties.

- EDAG completed the National Energy Testing Laboratory (NETL) Milestone #2: "Baseline Assessment Complete" by applying eight load cases to the baseline vehicle body assembly.

- The Steel Expert Team completed project Milestone #1: "Plan to manufacture 3GAHSS coupons for model validation" by identifying two steel processing paths to produce 3GAHSS sheet with properties between the baseline QP980 steel and the two U.S. Department of Energy (DOE) target 3GAHSS steel mechanical properties.

- AK Steel produced a QP heat and a TRIP heat based on the processing recipes provided by CSM. AK Steel then produced limited amounts of 3GAHSS sheet from both heats for analysis at CSM and for generation of baseline data for the Task 2 computational components.

- PNNL and LSTC adapted the SVM from ABAQUS UMAT to LS-DYNA.

- Full characterization of the tensile behavior of QP980 under different temperatures, quasi-static rates and sheet orientations was completed along with the evolution of strain fields obtained from digital image correlation (DIC).

- Completed several sets of mechanical formability tests on QP980 and generated the first complete forming limit curves for the material at a selected strain rate (for different sheet orientations and punch geometries) using existing necking-initiation DIC-based algorithms.

- Completed several sets of high rate testing on QP980 at the National Institute for Standards and Technology (NIST) and generated the first complete set of flow curves at very high rates (>400 cycles per second (s^{-1})) including DIC analysis of material deformation.

- Progressed with retained austenite volume fraction (RAVF) measurements using Neutron Diffraction at NIST. Several sets of deformed material samples, under different loading paths, have been generated and sent for analysis at NIST. Initial curves of RAVF measurements have been constructed for both the uniaxial and plane strain loading cases.

- Continued integration of efforts with MSU to feed needed experimental data and compare experimental results with crystal plasticity model predictions. Initial model predictions match well with the experimentally obtained quasi-static tensile behavior.

- Continued integration of efforts with PNNL and General Motors (GM) in regards to RAVF measurements, and comparison of data based on Neutron Diffraction (CU and NIST) and High Energy X-Ray Diffraction (PNNL and Argonne National Laboratories).

- Developed, built and calibrated a new tension/compression testing instrumentation to enable characterization of material flow behavior under complex loading paths. Initial systematic testing of QP980 has started, and preliminary data for compression until

buckling, multi-loop tension-compression-tension (TCT) and compression-tension-compression (CTC) testing cycles has been generated.

- University of Illinois at Urbana-Champaign (UIUC) completed the background calculations necessary for modeling screw dislocations in body-centered cubic (bcc) iron (Fe), and has begun density functional theory (DFT)/ lattice green function (LGF) flexible boundary condition calculations for optimizing the bcc screw dislocation core-geometry.

- UIUC implemented a three dimensional (3D) phase-field model for martensitic transformations in elastic material, and has initiated work on extending the phase-field code to include plastic strain deformation.

- UIUC investigated ordered magnetic structures as viable approximations for the paramagnetic structure of austenite, and has performed many of the calculations to quantify the sensitivity of solute effects to magnetism in this phase.

- MSU and LSTC incorporated the CPM into LS-OPT, installed sub-optimization loops and successfully produced an optimized CPM based on baseline QP980 steel properties.

- MSU simulated 1) the behavior of ferrite and martensite phases of QP980, 2) austenite to martensite transformation, and 3) integrated different phase models, and predicted the macroscopic stress-strain curve of QP980 under uniaxial tension, with crystal plasticity model.

- MSU developed a QP980 3D representative volume element (RVE) for future simulation of the behavior of QP980 under complex loadings.

- PNNL performed in-situ High Energy X-Ray Diffraction (HEXRD) test on QP980 and developed an elastic plastic self-consistent (EPSC) model in post-processing the experimentally measured lattice strains in calculating the stress and strain partitions among different phases during deformation.

- PNNL developed a single state-variable based constitutive model for QP980 using the HEXRD-obtained phase properties, and developed the associated ABAQUS user material subroutine. LSTC has converted the ABAQUS UMAT into LS-Dyna for further implementation and testing in forming simulations at GM.

- PNNL developed a martensite and austenite (MA) constituent model to quantify the effects of volume fraction, morphology and stability of the austenite laths on the overall anisotropic behaviors of the MA constituent. The MA model will be incorporated into the overall microstructure-based finite element model to predict the overall QP980 deformation behaviors under different loading paths.

- PNNL facilitated atom probe tomography at the Environmental Molecular Sciences Laboratory (EMSL), a DOE Biological and Environmental Research (BER) User Facility housed at PNNL, to measure chemical compositions in each of the three phases in QP980.

Future Directions

- The Steel Expert Team, CSM and AK Steel will continue to modify and validate the QP and TRIP process recipes to produce 3GAHSS coupons with desired interim mechanical properties.

- Contract with CANMET to produce 3GAHSS coupons in sufficient amounts to enable comprehensive mechanical properties and formability testing.

- Characterize 3GAHSS materials at CU and BU using the MSU/PNNL test matrix for further CPM and SVM model development.

- Build a T-Component die for forming evaluation of the CANMET material and validation of the PNNL SVM and for developing and validating forming and fracture models.

- Assemble the CPM and SVM into a pre-ICME model capable of providing meso-scale computational predictions for 3GAHSS microstructures and mechanical properties (Project Milestone #2).

- Perform a design sensitivity analysis to enable the identification of 1) those components that contribute the most to the side structure's performance, 2) components that could benefit the most from 3GAHSS substitution, and 3) opportunities for further lightweighting through design optimization.

- Develop and apply forming and fracture simulation 3GAHSS optimized components and assembly designs (Project Milestones #4 and #3 respectively).

Evaluate the potential weight savings that can be achieved by substituting 3GAHSS and applying gauge optimization. Once actual 3GAHSS materials are devised conduct full design optimization, including shape optimization, of the baseline assembly to determine the cost impact and weight savings of using 3GAHSS on automotive structural assemblies.

Integrate material length scale models with the forming model and fracture model with design optimization. Provide a user manual for the ICME model.

Technology Assessment

- Target: Model elements must be within 15% of experimental results and the optimized 3GAHSS assembly must achieve 35% weight savings at no more than $3.18 cost per pound of weight savings.

- Gap: There is no existing ICME framework that ties together all length scale computer models with forming simulation, fracture modeling and design optimization, especially with low and high level optimization loops. Although a linear input/output connectivity can be achieved between the length scale material models, optimization loops will require significant coding that may be complicated by disparate codes used in the individual models.

- Gap: Boundary conditions have been applied to model elements to facilitate assembly and integration within the project four year duration. For example, the number of

solutes to be evaluated has been limited, inclusions and precipitates are largely ignored, and dislocation dynamics are superficially treated. These are all opportunities for future work and model improvement but these boundary conditions may adversely affect model accuracy.

- Gap: The weight savings targets are aggressive and it is not known if these targets can be achieved with the selected sub-assembly using the two proposed 3GAHSS grades as defined in the Funding Opportunity Announcement (FOA). An optimized joining strategy of spot welding with adhesive bonding was selected for the baseline and 3GAHSS design optimization studies. The project will first assess the potential weight savings through material substitution and gauge optimization using the two proposed 3GAHSS grades. Once 3GAHSS coupons are made available, full design optimization, including shape optimization, will be performed to determine if optimized 3GAHSS designs can achieve the desired weight savings while meeting strength requirements.

- Gap: Shape optimization may propose component designs that meet the weight savings target but are difficult and costly to manufacture. The project will evaluate the formability of optimized component designs through forming simulation and within the context of available manufacturing technologies.

- Target: Two different 3GAHSS are defined by the FOA, exceptional strength and high ductility (>1500 MPa ultimate tensile strength (UTS), >1200 MPa yield strength (YS), >25% elongation) and high strength and exceptional ductility (>1200 MPa UTS, >800 MPa YS, >30% elongation).

- Gap: The ICME model will predict the necessary chemistry and steel microstructure needed to meet the target mechanical properties but process development (melting, rolling, intermediate heat treatments, finishing, etc.) may be needed to produce sheet steel with the predicted microstructure. The project will leverage the expertise of steel industry participants to guide process development using laboratory size heats to develop a process that can achieve the predicted microstructure.

✧   ✧   ✧   ✧   ✧

Introduction

The goal of the program is to successfully demonstrate the applicability ICME for the development and deployment of 3GAHSS for immediate weight reduction in passenger vehicles. The ICME approach used in this project will accelerate the development and widespread deployment of 3GAHSS through modeling of multi-scale metallurgical, thermal and mechanical processes in coil sheet development to automotive part and assembly manufacturing and ultimately in vehicle performance. By integrating a suite of comprehensive, science-based computational models at different length scales in the ICME environment, this project

will demonstrate to end users in both the automotive and steel industries that immediate cost-effective weight savings can be achieved with 3GAHSS, and that the ICME framework will support a reduced development to deployment lead time in all lightweight materials systems. The product of this proposed effort will be a simulation toolset and computational infrastructure composed of material models and associated validation data at different length scales together with the software and application programming interfaces developed by the project team.

The project faces three distinct challenges, 1) to develop an ICME model, 2) to develop viable 3GAHSS sheet and 3) to optimize an automotive design concept for a material that does not yet exist. Figure III-9 illustrates the relative values for the QP980 steel and the two DOE targets for 3GAHSS. Although the manufacturing of 3GAHSS is not a deliverable of this program, the DOE proposed two 3GAHSS grades with mechanical properties listed in Table III-3 as targets for the program. The project began the task of adapting existing material models for steel by selecting an advanced high strength steel (AHSS) grade, QP980, which has mechanical properties on the cusp of the 3GAHSS envelope. In the absence of the 3GAHSS, the QP980 with its mixed martensite and retained austenite microstructure will 1) facilitate the identification of relevant constitutive parameters for each length scale material model 2) provide a means to validate these models and 3) help define the microstructural elements that will be needed for a 3GAHSS.

A baseline sub-assembly from a 2008 model year (MY) Original Equipment Manufacturer (OEM) production vehicle has been identified to demonstrate the potential benefits of the 3GAHSS in reducing automotive component and assembly weight. The baseline assembly will be fully characterized in terms of the weight, cost and performance criteria. An iterative design optimization process of gauge and shape optimization will be applied to the baseline assembly substituting 3GAHSS for AHSS and developing a 3GAHSS design that can meet the proposed weight savings target listed in Table III-4. Coupled with design optimization are forming modeling and simulation, fracture modeling and simulation and technical cost modeling to assess the manufacturability, performance and cost of the different design iterations with the goal of achieving the cost targets listed in Table III-4 without compromising component and assembly performance.

Work to integrate the material, forming, fracture, and cost models with design optimization will span the entire length of the program. The primary project deliverable includes an ICME model and user guide to enable users to run the model. The objective is to create an ICME model capable of predicting part and assembly properties from the sheet properties and the process history within 15% accuracy at all length scales that will enable the baseline structure to meet the specified weight and cost targets.
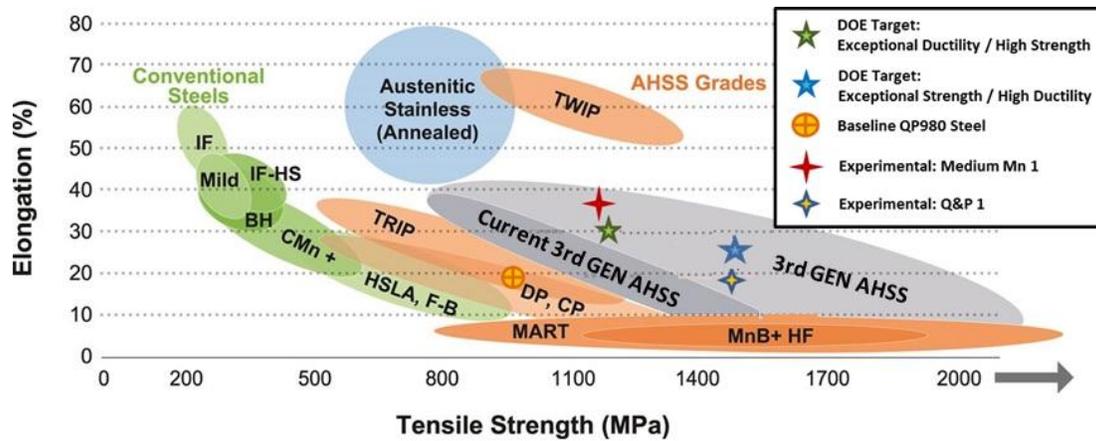
Figure III-9: 3GAHSS mechanical properties.

Table III-3: 3GAHSS types specified in FOA.

Ferrous Sheet Metal Type	Yield Strength (MPa)	Tensile Strength (MPa)	Total Elongation (Uniaxial Strain to Failure)	Uniform Elongation
High Strength, Exceptional Ductility	≥800	≥1200	≥30%	≥20%
Exceptional Strength, High Ductility	≥1200	≥1500	≥25%	≥8%

Table III-4: DOE FOA weight and cost targets

Vehicle System	System Definition	Weight Reduction Target	Cost per Pound of Weight Saved ($/lb. saved)
Body	Body-In-White, Closures, Windows, Fenders, and Bumpers	≥35%	≤3.18/lb.

Table III-5: Project participants.

Universities/National Labs	Industry
Brown University	Chrysler Group LLC
Clemson University	Ford Motor Company
Colorado School of Mines	General Motors Company
Michigan State University	AK Steel Corporation
Pacific Northwest National Lab	ArcelorMittal
University of Illinois	Nucor Steel Corporation
	U. S. Steel
Consortiums	EDAG, Inc.
Auto/Steel Partnership	Livermore Software Technology Corporation
United States Automotive Materials Partnership	

The challenges of this program require significant academic and cross-industry expertise, and regular communication and collaboration between these parties to make the integration component of the project successful. The project is highly leveraged with expertise from the participants shown in Table III-5 supporting the entire life cycle of material, process and product development. Prior collaboration between these project participants through the United States Automotive Materials Partnership (USAMP) and the Auto/Steel Partnership (A/SP) provides a unique and successful foundation for addressing the technical challenges of this program.

Approach

The project has been structured with seven tasks as follows:

- Task 1: Project Management and Planning
- Task 2: Model Development and Model-Level Validation
- Task 3: Forming: Component-Scale Performance Prediction and Validation
- Task 4: Assembly
- Task 5: Design Optimization
- Task 6: Integration
- Task 7: Technical Cost Modeling

Project Year 1:

The first year of the program developed the framework to assemble the length scale material models, identified the steel pathways, chemistries and processing recipes for making 3GAHSS sheet to the DOE mechanical property targets, and coordinated the testing needed to further develop material and forming models and prepare for the validation phase in subsequent years.

QP980 steel was identified as the baseline material for initial 3GAHSS model development. Under Task 2, the experimentalist at BU and CU began characterizing the QP980 steel and provided test results to the modelers at UIUC, MSU and PNNL. A key accomplishment during this period was the development of three dimensional representative volume elements (3D RVEs), which should improve the accuracy of the CPM as 3D RVEs can better account for material anisotropy than 2D RVEs.

Additional steels were needed for further model development in year two. Using prior literature studies, CSM identified two pathways, a QP process and TRIP process, which may be able to produce 3GAHSS with the mechanical properties of the DOE proposed steels (See Table III-3 previously). CSM proposed steel chemistries and processing recipes, which were approved by the Steel Expert Team as reported in Project Milestone #1. The team then began evaluating laboratories to produce 3GAHSS sheet using the approved recipes.

In Task 4, the A/SP outlined the process for assembling the material models and integrating these models with forming simulation, fracture simulation, design optimization and technical cost modeling. LSTC, which began work toward the end of the first project year, started preparing an ICME user interface using LS-OPT, a software system capable of integrating computer models. Concurrently, LSTC worked with MSU and PNNL to identify the input and output variables for both the CPM and SVM in preparation for assembly into an ICME model.

Under Task 5, EDAG and the A/SP identified the 2008 MY side-structure sub-assembly from a production OEM donor vehicle as the baseline assembly for which to demonstrate the potential of 3GAHSS materials to lightweight automotive components and assemblies without compromising vehicle performance. (Project Milestone #7). To eliminate joining as a variable in design optimization, the team decided to apply spot welding with adhesive bonding for all joints in the baseline and optimized designs, which, if unchanged by the end of the program, will satisfy Project Milestone #6. A technical cost model was created and applied to the baseline assembly and will be applied to optimized design for cost comparison when complete (Project Milestone #11).

Project Year 2:

This year, the project team produced interim 3GAHSS sheet product from the CSM supplied recipes for QP and TRIP chemistries and processes, began the process of adapting and linking material models into the ICME framework, fully characterized the baseline sub-assembly with respect to materials and performance, and identified a component based forming model and simulation for design and SVM validation.

Under Task 2, the experimentalists completed conventional characterization of the baseline QP980 steel. Using the chemistries and process recipes provided by CSM, AK Steel and CANMET both produced QP and TRIP ingots. Taking sections from their ingots, AK Steel produced some limited amounts of cold rolled strip with the intention of validating the QP and TRIP process recipes (See Figure III-10). Analysis of the QP and TRIP cold rolled material indicated that further process refinement was needed for both recipes, but the TRIP steel could be used immediately by the modelers once sufficient sample amounts were produced for testing. The QP process requires some additional investigative work to determine how the elongation can be improved from the measured 10% to the targeted 25%. Once the process recipes are fully validated, the project intends to contract with CANMET, who can supply greater quantities of cold rolled 3GAHSS in larger coupons sizes.

In a joint Task 2 / Task 4 meeting, the A/SP, LSTC and PNNL agreed to build upon PNNL's QP980 model, which was developed in an earlier program, is a fairly simplistic material model and would require less adaption for this program especially considering that QP980 is the baseline material for this program. Under Task 4, LSTC adapted the SVM from ABAQUS based UMATs into LS-DYNA. The SVM is a FEM-based model and was originally constructed for solid elements. To enable the model's use in performance modeling, the team instructed LSTC to adapt the model for shell elements, which is expected to be complete at the end of the second year.

While working with MSU and PNNL to adapt the models into LS-DYNA, LSTC began to define the ICME user interface in LS-OPT in preparation to link the CPM and SVM. The linked models should have the ability to predict 3GAHSS mechanical properties from defined steel microstructural constituents, which would satisfy Milestone #2: Meso-Scale Computational Predictions, due at the end of the second year.
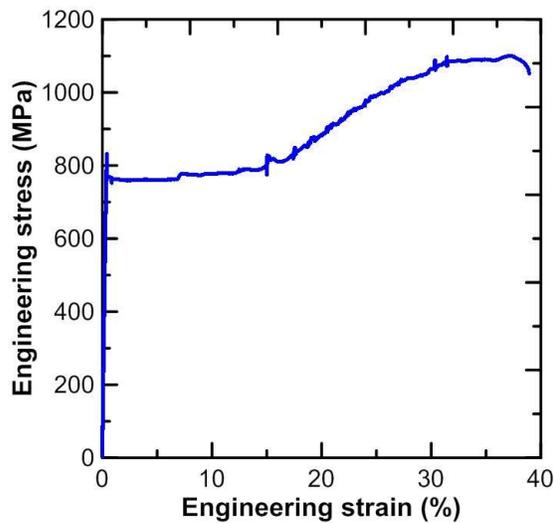
Fe-10Mn-0.15C-1.5Al-0.2Si (TRIP Steel)

4. Yield strength = 770 MPa
5. Ultimate tensile strength = 1100 MPa
6. Uniform elongation = 37.2%
7. Total elongation = 38.9%
8. thickness =1.5mm
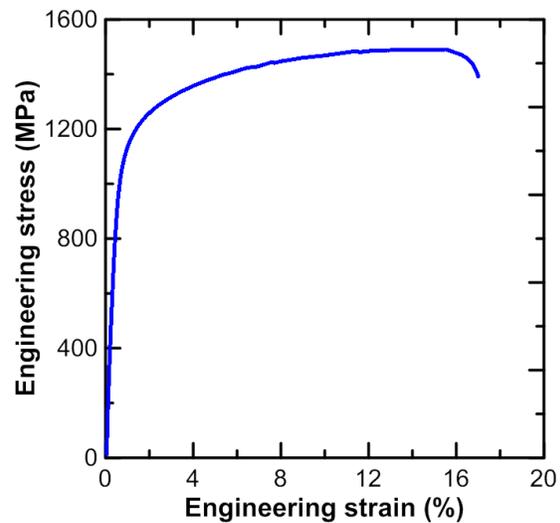
Fe-0.3C-3Mn-1.6Si (QP Steel)

9. Yield strength = 1055 MPa
10. Ultimate tensile strength = 1492 MPa
11. Uniform elongation = 15%
12. Total elongation = 17%
13. thickness=1mm

Figure III-10: Tensile curves from ak steel experimental heats.

Task 3 began at the onset of the second year. After reviewing several forming simulations, the team selected a component based forming simulation, called a T-Component, which will be used to validate PNNL's SVM and any component design concepts proposed by Task 5. A T-Component die will be built toward the end of the second year, and will begin forming trials using the baseline QP980 steel. The T-Component simulation and die will be applied to 3GAHSS sheet when sufficient material becomes available and the results will be useful in validating the optimized design when complete.

During this year, the Task 5 team fully characterized the side structure with respect to materials, cost and performance, the latter of which was reported in NETL Milestone #2: Baseline Assessment Complete. The team began preparations for design optimization by beginning a sensitivity analysis, which will enable the team to identify the following: 1) those components that contribute the most to the side structure's performance, 2) components that could benefit the most from 3GAHSS substitution, and 3) opportunities for further lightweighting through design optimization.

Project Year 3:

Year three will focus on completing model development and begin validating material and forming models. In Task 2, the project team will work to validate the preliminary ICME model by comparing model predictions against the interim steel microstructures and mechanical properties. Key to the

validation stage is the ability to manufacture 3GAHSS sheet at CANMET in sufficient amounts for comprehensive testing. The A/SP Steel Expert Team will coordinate the supply of 3GAHSS material to Task 2 and Task 3 experimentalists and testing to be performed based on the needs of the modelers. In the interim, sample material produced at AK Steel can be used to provide limited, but useful, material property data. BU will conduct micropillar testing, CU micro-tensile testing and GM/PNNL will evaluate austenite to martensite transformation as a function of strain using Synchrotron testing at Argonne National Laboratories.

By the end of the third year, the Task 3 team will provide a T-Component forming simulation, which will be validated through forming trials and will satisfy (Project Milestone #4). The team will apply the T-Component forming simulation to QP980 and compare results against forming limit diagrams (FLDs) generated by CU. Later, when sufficiently sized 3GAHSS coupons are provided, the team will test 3GAHSS sheet and compare the results with 3GAHSS FLDs generated by CU. Assuming general agreement, the validated forming model can then be applied to proposed component designs for the side-structure sub-assembly.

During this period the material models will continue to evolve requiring adjustments in the model assembly. LSTC will adapt the models assembly and refine the user interface accordingly. However, the emphasis of Task 4 work will shift to integrating these models with forming, fracture, and performance models. By the close of the budget period the

project is expected to have a rudimentary ICME model (Project Milestone #3).

The Task 5 team is expected to complete its sensitivity analysis, which will highlight candidate components for 3GAHSS substitution and design optimization. Preliminary design optimization will begin during this year as the team seeks opportunities to lightweight components through gauge reduction and design optimization.

Project Year 4:

Integration will be the project focus during the fourth year as the material, forming and fracture models reach maturity. At the end of the year, the project will deliver a 3GAHSS forming model (Project Milestone #5), an optimized design that meets the stated weight and cost targets (Project Milestone #8), a 3GAHSS ICME model with user guide and data model (Project Milestone #9 and 10) and a technical cost model (Project Milestone #11). Task 3 will be the nucleus of the integration efforts where the output of the assembled material models and the optimized design are validated through forming simulations.

Results and Discussion

Utilizing 3GAHSS chemistries and process recipes provided by CSM, AK Steel cast 3GAHSS heats, one heat was a QP steel and the other a TRIP steel, and processed both heats into hot band strips. AK then processed partial amounts of the hot band strips into cold rolled strips, which was tested and analyzed by CSM. The TRIP heat was found to have picked up nitrogen during annealing forming brittle surface layers. These layers were removed and the TRIP steel retested. Table III-6 compares the mechanical properties of the QP and TRIP steels against the CSM projected properties and the two DOE proposed 3GASS steels; the High Strength, Exceptional Ductility; and the Exceptional Strength, High Ductility steels.

The objective of the heats was to provide steels within the 3GAHSS space sufficient for 3GAHSS material model development. As shown in Table III-6 and depicted in Figure III-9, both heats met this objective and the mechanical

properties are sufficient for further material characterization and subsequent model development. The TRIP heat achieved mechanical properties close to the High Strength, Exceptional Ductility targets. The QP heat achieved the tensile strength but lacked the yield strength and ductility of the Exceptional Strength, High Ductility steel.

UIUC has completed size and chemical misfit calculations for aluminum (Al), manganese (Mn), silicon (Si), carbon (C), and nitrogen (N) in bcc Fe to quantify the effect of solutes on strength, and has completed much of the work required for optimizing the core structure of screw dislocations in bcc Fe. UIUC has also completed many of the calculations to determine the sensitivity to magnetism of solute misfits in face centered cubic (fcc) Fe. In addition to quantifying strengthening effects, solute size-misfits also determine the role of solutes in changing the lattice parameters of Fe phases. UIUC has also initiated phase-field modeling to study martensitic phase transformation kinetics in steel. A 3D phase-field microstructure evolution model for elastic material has been implemented, and it produces martensite growth and nucleation under appropriate simulation conditions. Current efforts include testing a parallel version of the phase-field code, and implementing plastic strain evolution to predict the amount of martensite formed as a function of plastic strain.

BU has characterized the flow properties of ferrite and martensite in the QP980 steel using micropillar testing and determined using electron backscatter diffraction (EBSD) that the austenite in the alloy does transform to martensite during tensile deformation and that the transformation is easier in the larger particles of austenite (See Figure III-11).

The flow properties of austenite in the QP980 steel could not be measured using micropillar testing due to the fine submicron size of the austenite lath grains within the QP980 steel. As an alternative, BU has used a 201LN stainless steel which is essentially austenitic in the as-received sheet form to measure the flow properties of austenite and characterize the deformation induced transformation of austenite to martensite (See Figure III-12 and Table III-7).

Table III-6: AK produced 3GAHSS sheet mechanical properties.

Mechanical Properties Summary Table	YS (MPa)	UTS (MPa)	Tensile Elongation	Uniform Elongation
High Strength, Exceptional Ductility	≥ 800	≥ 1200	≥ 30%	≥ 20%
TRIP - Projected Properties	779	1088	45.9	44.8
TRIP - Actual Properties (Average after surface layer removal)	750	1166	37	34
Exceptional Strength, High Ductilty	≥ 1200	≥ 1500	≥ 25%	≥ 8%
QP - Projected Properties	1100	1500		17%
QP - Actual	830	1520		10%
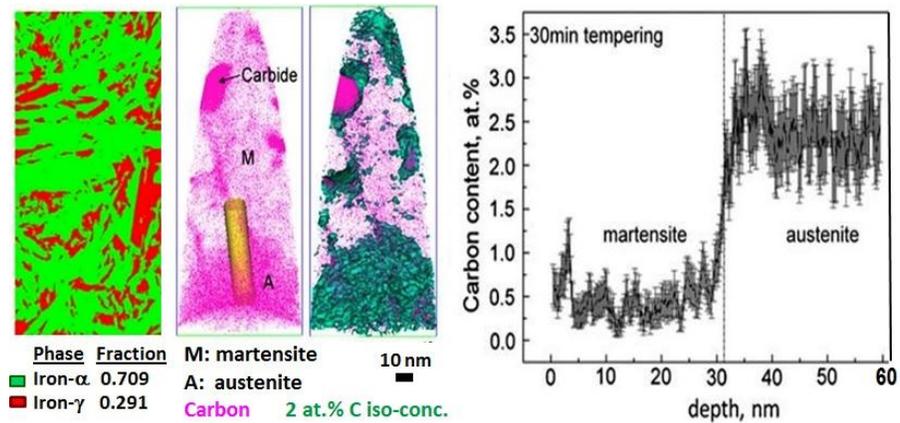
Figure III-11: Macroscopic stress-strain response of the Max Planck Fe-13.6Cr-0.44C steel as a function of tempering times at 400°C (from Yuan et al., Acta Materialia, 60 (2012) 2790-2804). The macroscopic stress-strain response for this steel after tempering for 30 minutes at 400°C is shown in Figure III-10 above and was obtained from L. Yuan, D. Ponge, J. Wittig, P. Choi, J.A. Jienez, D. Raabe, Acta Materialia, 60 (2012) 2790-2804. The yield strength is around 1.25 GPa, the UTS is ~1.75 GPa and an elongation to fracture of ~23 percent. The austenite volume fraction in this heat treatment was reported to be ~0.4.
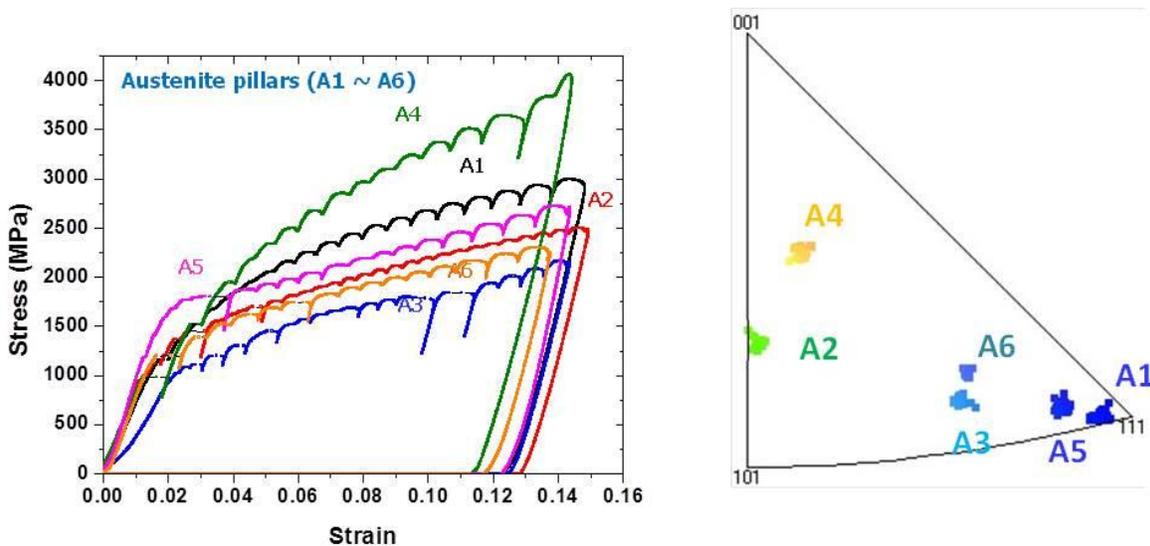
Figure III-12: Compressive micropillar stress-strain curves for the various single crystal orientations of austenite and the standard triangle showing the specific orientations for specimens A1-A6.

Table III-7: Estimated compressive yield stress for the different micropillar specimens with the loading axis orientation for each of the specimens.

Specimen	Orientation	Compressive Yield Stress (MPa)
A1	(111), (566)	1160
A2	(023), (035)	950
A3	(356), (245)	1020
A4	(316), (102)	980
A5	(656), (545), (546), (434)	1180
A6	(234)	1200

The martensite to austenite transformation occurs and is thought to be strain induced, with austenite first transforming to ε martensite (hexagonal close-packed (hcp)), the process primarily started at stacking fault intersections, and subsequently, at larger strains, the ε' martensite forms and co-exists with α' martensite. The transformation route that will be representative of the austenite to martensite transformation in QP980 is unknown at this time. Over the next year, BU will examine a chromium (Cr)-rich steel with TRIP characteristics and provided by the Max Planck Institute where the austenite is claimed to be larger in size as a consequence of certain

heat treatments. BU will also test the AK Steel TRIP steel with its brittle layers removed using micropillar analysis.

CU has fully characterized the fundamental mechanical behavior of the QP980 starting material under all nominal quasi-static conditions, and generated all the data needed to feed into the crystal plasticity modelling effort at MSU. The compiled results encompass all desired quasi-static rates, temperatures and sheet orientations, with complete analysis of digital image correlation data and the results are all uploaded on the PNNL SharePoint site. In addition, significant progress has been made with regards to high rate tensile testing, sheet formability testing, phase transformation kinetics and material deformation under complex loading paths. While these tests are not complete, initial data sets have been generated to support the ongoing crystal plasticity modelling effort at MSU, and also help start the phenomenological modeling at MSU and fracture modeling at BU efforts. Initial forming limit curves, high rate flow curves, quasi-static retained austenite volume fraction curves in tension and plane strain, TCT and CTC loops have been all generated for QP980.

MSU worked on the crystal plasticity modeling of QP980 multi-phase AHSS. The goal was to develop separate models for each individual phase of QP980, and later integrate them into one crystal plasticity model to simulate the macroscopic behavior of the material under proportional and non-proportional loading conditions. The most challenging aspect of the work was to develop and verify the accuracy and effectiveness of the austenite to martensite phase transformation model. A constitutive phase transformation model was developed and its predictions were verified with experimental results obtained from the uniaxial tensile testing of QP980. Overall, the MSU team feels that their crystal plasticity model is capable of predicting the complex behavior of multi-phase AHSS. Additional verification work is currently under way in order to identify the areas that need additional development or refinement. The MSU CPM has been imported into LS-OPT and sub-optimization loops have been provided.

PNNL performed in-situ HEXRD test at Advanced Photo Source (APS) on the QP980 steel. Subsequently, PNNL developed an EPSC model in post-processing the experimentally measured lattice strains for QP980 and derived the stress and strain partitions during deformation among different phases. The EPSC developed phase properties are provided to MSU for the development and verification of the crystal plasticity model. The EPSC-quantified phase properties together with the measured retained austenite transformation kinetics are used in the development of a single state-variable based constitutive model for QP980 at PNNL. A material user subroutine in ABAQUS/explicit for QP980 was developed and tested in simple tensile deformation as well as in hat-section forming simulations with ABAQUS. The developed UMAT has been provided to LSTC to be converted into LS-Dyna for further implementation and testing in forming simulations at GM.

PNNL also developed a martensite and austenite (MA) constituent model to quantify the effects of volume fraction, morphology and stability of the austenite laths on the overall anisotropic behaviors of the MA constituent. Various model/loading conditions were simulated in order to obtain/analyze the macro response of MA constituent under different loading conditions. Since the inter-lamellar spacing may be an important parameter controlling the yield stress and/or flow stress for QP steels with lamellar (or layered)-type microstructure, an hierarchical upscaling scheme, is envisioned for the QP980 steel where the predicted stress-strain curves for the MA constituent under different loading conditions will be incorporated into the microstructure-based finite element model to predict the overall QP980 deformation behaviors under different loading paths.

Task 3 started in February 2014 and began evaluating available component based forming simulations to be used in validating PNNL's SVM and for 3GAHSS concept component designs. A T-Component simulation (see Figure III-13) was selected as this component design would enable linear forming, non-linear forming and perhaps fracture simulation. Furthermore, component trials could be performed to validate the simulations. The team completed the component design and corresponding die design. By the end of the second budget period a die will be built. Initial work will use forming limit diagrams produced by CU for the baseline QP980 steel and compare the predictions against forming trials using the same material (see Figure III-9).
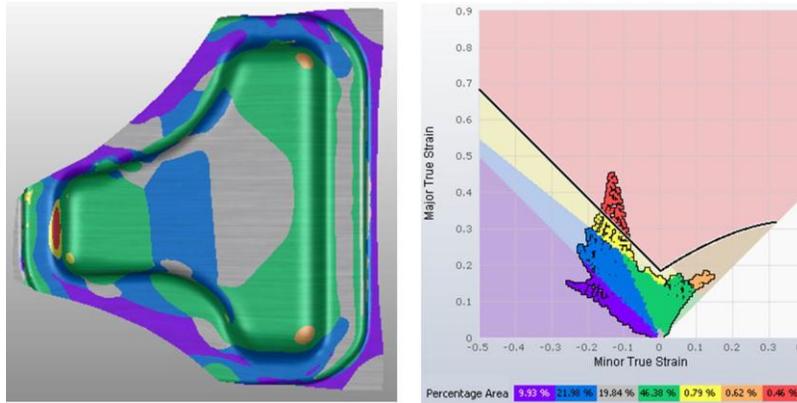
Figure III-13: Example showing T-Component formability simulation Linear Strain Path - 16mm draw home (courtesy of AK Steel).
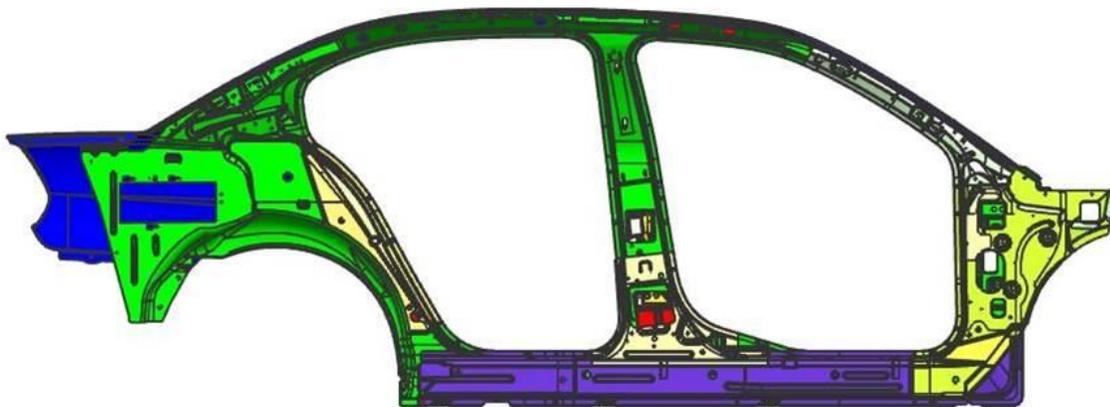
Figure III-14: Baseline body structure assembly.

Last year, the team identified a side-structure from a 2008 MY production vehicle as the baseline assembly (See Figure III-14). During this period of performance, the side structure was fully characterized in terms of materials, cost and performance. A specific performance criterion does not exist for the side structure; instead, there are vehicle performance requirements in which the side structure provides significant contributions. To isolate the side structure performance, load cases had to be identified and applied to the side structure where the simulated response to the load cases essentially became the performance criterion. The team identified eight load cases; 1. Side barrier impact, 2. Pole impact, 3. Roof crush, 4. Front Impact, 5. Rear Impact, 6. Seat belt anchorage strength, 7. Body torsion and bending stiffness, and 8. Body normal modes of vibration. The response to these load cases was simulated by EDAG, which completed the baseline assessment, NETL Milestone #2. The baseline assembly design will eventually be compared to the optimized 3GAHSS design and will enable the weight savings, cost and performance benefits of 3GAHSS to be assessed.

Technology Transfer Path

The primary deliverable of this program is an integrated computer model with a user guide. The software will include a high level description of the integrated models along with a description of input variables, output variables, state variables, and relational databases implemented within the final software deliverable. The user's manual will provide an overall description of the user implementation approach for the software.

During the development of the ICME model, the project will be developing test methodologies for evaluating and characterizing 3GAHSS such as nano-hardness testing, micro-pillar, bulge testing, sheet tension-compression, measurement of austenite-to-martensite transformation with strain, etc. If the results from these tests can be correlated to macroscopic bulk materials properties testing then these tests are expected to be adopted for future work and, potentially, for industry standardization.

Additionally, if the individual length scale material models show a high degree of accuracy then these models will be adopted by industry and academia for expansion and refinement to cover additional steel processing paths. Primary

III.2. Integrated Computational Materials Engineering Approach to
Development of Lightweight 3GAHSS Vehicle Assembly (ICME 3GAHSS)

Hector–GM; Krupitzer AISI

users of the technology are the partners that are engaged in this project which is expected to speed the implementation of results and lessons learned.

Conclusion

The project has demonstrated a significant degree of communication and collaboration between project participants, which is exemplified in the creation of 3D RVEs (MSU/BU), a joint devised test matrix for CPM and SVM development (MSU/PNNL), an outline for model assembly and integration (A/SP/PNNL/LSTC), forming simulation (A/SP/CU), a PNNL SharePoint data repository for all project participants and the 3GAHSS alloy development (A/SP/CSM). Project Quarterly Review Meetings and monthly Project Integration and Communication Meetings have facilitated the flow of communication between task participants as well as between tasks.

The project is currently on schedule to meet all project milestones and deliverables. The greatest challenge for the remainder of this year and the next will be coordinating the manufacturing of 3GAHSS, the distribution of 3GAHSS samples to project sub-recipients, and prioritizing the testing based on available 3GAHSS material sufficient to keep model development on schedule. However, the initial success in producing 3GAHSS with properties near those of the proposed DOE steels is encouraging and will enable further model development and will improve the ability of the ICME model to accurately predict 3GAHSS properties.

The project has completed the baseline metrics, with conventional testing of the QP980, characterization of the sub-assembly, and the adaption of the state variable model into LS-DYNA. Assembly of the CPM and SVM models will occur in the later part of the second year, which will provide predictive capability and can be compared against experimental results. Work in the next project year will consist of interim 3GAHSS coupon production, characterization of 3GAHSS materials, model development to include 3GAHSS experimental results, further adaption of the assembled material models and assessment of the baseline design for 3GAHSS substitution, down gauging and preliminary shape optimization.

Presentations/Publications/Patents

1. Choi, K.S.; Hu, X; Sun, X.; Taylor, M.; De Moor, E.; Speer, J.; Matlock, D. (April 2014) "Effects of constituent properties on performance improvement of a Quenching and partitioning steel." Society of Automotive Engineers (SAE) Technical paper 2014-01-0812. Presented at SAE 2014 World Congress, Detroit, Michigan, April 8 – 10, 2014.

2. Hector, Jr., Lou. "Integrated Computational Materials Engineering (ICME) in the Automotive Industry: Successes and Opportunities." Presented at the 2014 SAE World Congress, Detroit, Michigan, April 8 – 10, 2014.

3. Hector, Jr., Lou. "The Next Generation of Advanced High Strength Steels – Computation, Product Design and Performance, First Year Progress Update on the DOE ICME 3GAHSS Project." Presented at the 2014 Great Designs in Steel, Livonia, Michigan, May 13, 2014.

4. Hector, Jr., Lou. "Integrated Computational Materials Engineering Approach to Development of Lightweight 3GAHSS Vehicle Assembly." Presented at the DOE Annual Merit Review, Washington, DC, June 16 – 20, 2014.

5. Hector, Jr., Lou. "Integrated Computational Materials Engineering (ICME) Approach to Development of Lightweight 3GAHSS Vehicle Assembly - Third Generation Advanced High Strength Steels." Presented at the Materials Genome Initiative - Data Workshop, Wright Brothers Institute, TechEdge, Dayton, OH, July 15 – 16, 2014

6. Hector, Jr., Lou. "Integrated Computational Materials Engineering (ICME) Approach to Development of Lightweight 3GAHSS Vehicle Assembly - Third Generation Advanced High Strength Steels." Presented to the Fundamental and Computational Sciences Directorate, PNNL, Richland, WA, September 2014.

7. Choi, K.S.; Sun, X.; De Moor, E.; Taylor, M.D.; Speer, J.; Matlock, D.K. (2014). "Effects of Constituent Properties on Performance Improvement of a Quenching and Partitioning Steel." *SAE paper* 2014-01-0812.

8. Taylor, M.D.; Choi, K.S.; Sun, X.; Matlock, D.K.; Packard, C.E.; Xu, L.; Barlat, F. (2013). "Relationship between Micro- and Macro- Properties for Eight Commercial DP980 Steels." Submitted to *Materials Science and Engineering A*.

9. Taylor, M.D.; Choi, K.S.; Sun, X.; Matlock, D.K.; Packard, C.E.; Xu, L.; Barlat, F. (2014) "Correlations between nanoindentation hardness and macroscopic mechanical properties in DP980 steels." In press at *Materials Science and Engineering A*.

10. Rana, R.; Gibbs, P.J.; De Moor, E.; Speer, J.G.; Matlock, D.K. "A Composite Modeling Analysis of the Deformation Behavior of Medium Manganese Steels." Plenary presentation at the 2nd International Conference on High Manganese Steels, Aachen, Germany, August – September 2014.

11. Srivastava, A.; Ghassemi-Armaki, H.; Sung, H.; Chen, P.; Kumar, S.; Bower, A.F. (2014) "Micromechanics of plastic deformation and phase transformation in a three-phase TRIP-assisted advanced high strength steel: Experiments and Modeling." Manuscript submitted to *Journal of Mechanics and Physics of Solids.*

12. Wang, Y.Y.; Sun, X.; Wang, Y.D.; Hu, X.H.; Zbib, H.M. (2014) "A Mechanism-based Model for Deformation Twinning in Polycrystalline FCC Steel." In press at Materials Science & Engineering A.

13.   *First-Principles Solution Strengthening Model for Iron*. (2014) Presented at the TMS Annual Meeting, San Diego, CA, February 15 – 20, 2014.

14.   "Modeling of Deformation of Ferrite and Martensite Micro-pillars in a Dual Phase Steel." Presented at the U.S. National Congress on Theoretical & Applied Mechanics (USNCTAM).East Lansing, MI, June 15 – 20, 2014.

15.   "A Constitutive Model for Martensitic Phase Transformation Plasticity in Advanced High Strength Steels." Presented at the U.S. National Congress on Theoretical & Applied Mechanics (USNCTAM), East Lansing, MI, June 15 – 20, 2014.

III.3 Industrial Scale-Up of Low-Cost Zero-Emissions Magnesium by Electrolysis: INFINIUM, Inc.

Adam C. Powell, IV, Principle Investigator
INFINIUM, Inc.
3 Huron Drive
Natick, MA 01760
Phone: (781) 898-3430
E-mail: apowell@infiniummetals.com

Aaron Yocum, Project Officer
National Energy Technology Laboratory
3610 Collins Ferry Road
Morgantown, WV 26507
Phone: (304) 285-4852
E-mail: Aaron.Yocum@netl.doe.gov

Will Joost, Technology Area Development Manager
U.S. Department of Energy
1000 Independence Avenue, S.W.
Washington, DC 20585
Phone: (202) 687-6020
E-mail: william.joost@ee.doe.gov

Contractor: INFINIUM, Inc.
Contract No.: DE-EE0005547

Abstract/Executive Summary

Direct electrolysis of magnesium oxide (MgO) has been a dream of the magnesium (Mg) industry for decades. MgO is typically made from brines or sea water by reaction of dissolved magnesium chloride ($MgCl_2$) with sodium hydroxide (NaOH) producing sodium chloride (NaCl) and insoluble magnesium hydroxide $Mg(OH)_2$, which is removable by filtration. Heating the hydroxide then drives off its water to produce MgO. Today's chloride electrolysis plants must then use carbochlorination or hydrochlorination with chloride dehydration to produce pure anhydrous $MgCl_2$, and electrolyze that to produce Mg metal and Cl_2 gas [1]. Direct MgO electrolysis would save this $MgCl_2$ production step, which is energy and capital intensive and can produce harmful dioxin and furan emissions. MgO electrolysis would also eliminate the need to contain chlorine which often escapes as a pollutant, and would use less energy also due to the lower formation enthalpy of MgO vs. $MgCl_2$.

The INFINIUM MagGen™ system performs this direct MgO electrolysis. This process dissolves MgO in a molten salt, then applies a direct current (DC) potential across the salt, producing magnesium at the cathode and oxygen gas at the solid electrolyte-sheathed anode. The solid electrolyte

separates the magnesium and oxygen products, preventing back-reaction between them. The anode is also protected from the harsh molten salt environment, enabling the use of a variety of inert anode materials such as oxide conductors used as solid fuel cell cathodes, and liquid metals. Zirconia is a very selective solid electrolyte, such that the oxygen by-product is much more pure than that produced by conventional inert anodes without zirconia protection, such as nickel ferrite.

The overarching objective of this project is to bring INFINIUM's MagGen™ primary magnesium production system from large laboratory demonstration to the threshold of industrial production. This efficient zero-emissions process makes high-purity magnesium directly from abundant domestically-produced industrial magnesia in a single step, with a high-purity oxygen by-product, and with condenser heat available for other uses.

Success of this project will prepare the technology for industrial implementation of this process, reducing the costs, energy use, and emissions associated with magnesium production, and helping vehicle manufacturers to realize their goals of reduced weight and increased vehicle efficiency. Improved vehicle recyclability may also result by increasing the value of post-consumer automotive scrap metal.

Toward those ends, this project's tasks during this period were as follows:

1. *Project Management and Reporting*
2. *Design, Build and Test Prototypes* Produce fully-featured prototypes designed to demonstrate all aspects of the process, one with a focus on maximum possible run time and the other at increasing scale
3. *Anode Optimization and Manufacturing* Optimize zirconia tube composition and structure for this novel application, and develop other components including low-cost charge transfer material and current collector.
4. *Make and Test Parts from the Recipient Mg* Manufacture representative automotive parts from the alloyed magnesium product.
5. *Mg Plant Cost, Energy, Greenhouse Gas (GHG) and Other Emissions Modeling* Characterize these aspects of the process relative to current practices in automotive materials and magnesium competitors.

Accomplishments

- Conducted a scoping study on Mg primary production approaches and potential products.
- Upgraded Alpha prototype furnace to operate at low pressure, including metal gas lines and seals, pressure control system, replaceable salt crucible, and

III.3. Industrial Scale-Up of Low-Cost Zero-Emissions Magnesium by
Electrolysis: INFINIUM, Inc.

Powell–INFINIUM

programmable logic controller. Ran for 4536 hours, including 2568 hours continuous uptime as of September 30, 2014.

- Successfully tested new method for removing dissolved metal in the molten salt and increasing current efficiency.
- Acquired and installed a programmable logic controller (PLC) for Alpha and Beta prototypes.
- Developed mixed metal-oxide current collector assembly to operate in pure oxygen environment and modified it for higher-current lower-resistance operation.
- Conducted multiple successful electrolysis runs with metal-oxide current collector as a new standard for electrolysis operation.
- Developed capability to "hot swap" the current collector, without having to swap out the entire anode assembly.
- Designed, built and operated apparatus for testing six zirconia compositions simultaneously.
- Completed installation and began operation of large zirconia tube sintering furnace for firing tubes at a rate sufficient to meet all prototype operation and production needs.
- Cast, sintered and inspected 32 zirconia tubes with 100% yield.
- Adjusted salt composition for improved zirconia lifetime, and conducted electrolysis in Alpha prototype with nearly twice the maximum single-anode lifetime performance of FY 2013.
- Maintained tube inventory from four different compositions and three different stabilizer mole percentages to meet prototyping needs.
- Designed a device to reduce the cost and improve heat and mass transfer in the liquid metal anode.
- Conducted detailed multi-physics Finite Element Analysis (FEA) models of electric current, heat transfer and fluid flow in a single anode-cathode assembly.
- Completed a ground-up preliminary plant cost model based on the detailed plant design narrative of FY 2013; labor cost estimate is within 5-10% of two fused salt electrolysis industry benchmarks.
- Completed a new energy balance model integrated into the techno-economic cost model. It shares variables with the cost model, such that when anode dimensions change, the model calculates changes to anode resistance and impact on energy cost, as well as cost of the anode itself.
- Submitted one provisional patent application and one non-provisional utility patent application.

Future Directions

- Plan the remainder of the project based on the scoping study on primary production approaches.
- Run a large prototype at high current to produce sufficient magnesium to cast automotive test parts using new tooling at subcontractor site.
- Incorporate FEA anode model results into new energy balance model framework.

- Complete life-cycle model of Mg production costs, energy use, and emissions using this technology.

Technology Assessment

- Target: Production of sufficient magnesium for automotive test part casting by the end of 2015.
- Gap: Need to improve electrolysis cell productivity.
- Target: Achieve profitable economics of Mg production in initial pilot scale facility in order to fund growth.
- Gap: Profitability at small scale likely requires a higher-value product.
- Target: Down-select final methods for producing anode assembly components.
- Gap: Need to finalize materials and anode design.

✧   ✧   ✧   ✧   ✧

Introduction

The primary objective of this project is to bring INFINIUM's Mg production technology from large laboratory demonstration to the threshold of industrial production. This energy-efficient process makes high-purity Mg from domestic industrial magnesia in a single step. By-products include high-purity oxygen gas and condenser heat, both available for other uses.

A secondary objective is to explore the application of this technology to direct production of Mg alloys. To do so can open up higher-value product options in order to enable short-term profitability of Mg production.

Approach

INFINIUM has taken a three-pronged approach to technology scale-up. First, techno-economic modeling identifies key areas of cost, energy consumption, and emissions, and potential for their reduction. Second, two electrolysis cell prototypes ran Mg production experiments using existing zirconia solid electrolyte technology. Third, new solid electrolytes are developed to improve current density, lifetime, and other key parameters identified by techno-economic modeling.

The Alpha prototype shown in Figure III-15 is designed to run for as long as possible. The goal is to identify and ameliorate as many failure modes as possible at a small scale, then apply those lessons to other prototypes in order to maximize uptime and productivity in full scale production. The main system components to refine include the furnace, gas connections, crucible, insulation, cathode, zirconia tube, anode, current collector, and condenser. The Beta prototype, with at least 10 times the production capacity of the Alpha, will test subsystems at larger scale and produce Mg metal and/or alloys for tensile testing and part die-casting, and will have all required process features for a full industrial-scale unit.

III.3. Industrial Scale-Up of Low-Cost Zero-Emissions Magnesium by
Electrolysis: INFINIUM, Inc.

Powell–INFINIUM

Results and Discussion

Significant improvements were made to the anode-cathode assembly and current collector assembly. Re-engineering the alpha furnace in November-December 2013 (shown in Figure III-15) enabled it to operate continuously for almost all of FY 2014, with just one planned downtime in May and June. Additionally, a new method successfully demonstrated very rapid *in situ* removal of Mg metal dissolved in molten salt, enabling dramatic reduction in electronic conductivity and improvement in current efficiency.

INFINIUM continued to make high-quality zirconia tubes from several different compositions in order to increase tube lifetime and ultimately Mg manufacturing uptime. One new composition in particular has established a new benchmark for both static corrosion performance and robustness under electrolysis conditions. Figure III-16 shows a set of finished zirconia tubes.

Figure III-15: Alpha prototype furnace (left) with gas panel (center) and control computer (right).

Figure III-16: Fired zirconia tubes for electrolysis tests.

III.3. Industrial Scale-Up of Low-Cost Zero-Emissions Magnesium by
Electrolysis: INFINIUM, Inc.

Powell–INFINIUM

Mg use in the automotive industry will reap significant fuel and energy savings. Techno-economic modeling and calculations determined annual fuel savings from significantly expanded Mg use at 5.79×10^9 gallons of gasoline, equivalent to 724 trillion British Thermal Units (TBTU), and reducing U. S. transportation emissions by 51.6 million metric tons of Carbon dioxide equivalent (MMT CO_2e). Annual energy savings from magnesium production ranges from 84-340 TBTU/year, reducing industrial emissions by 4.3-45 MMT CO_2e, depending on elasticity of Mg demand.

Technology Transfer Path

INFINIUM is exploring commercialization by direct production of Mg alloys using our technology. This can result in significant value added relative to commodity Mg production, and may lead to profitable operation at a small scale. As production grows, we can produce new alloys, and continue to improve production economics until large-scale production of commodity Mg directly from MgO raw material is profitable.

Conclusions

The achievements described above have put in place a strong technological foundation for significant near-term growth in Mg production scale using this technology. INFINIUM plans to operate a new electrolysis cell design in the beta prototype furnace to produce enough metal in the next year for testing of a large automotive prototype component. Beyond that, we will be well positioned to execute on the technology transfer path outlined above, and build a strong industry for primary Mg production directly from abundant domestic MgO raw material.

Presentations/Publications/Patents

1. Powell, A.; Earlam, M. and Barriga, S. "Pure Oxygen Anodes™ for Low- or Zero-Carbon Energy Efficient Metal Oxide Reduction," Presented at the *TMS Annual Meeting,* Symposium on Energy and Carbon in Metal Production, San Diego, CA on February 18, 2014, DOI: 10.1002/9781118888735.ch16.

2. X. Guan, X.; Pal, U.; S. Gopalan, S.; Powell, A. "Electrochemical Characterization and Modeling of a Solid Oxide Membrane-based Electrolyzer for Production of Magnesium and Oxygen," Presented at the *TMS Annual Meeting,* Celebrating the Megascale Symposium on Pyrometallurgy in Honor of David G.C. Robertson, California, CA on February 20, 2014, DOI: 10.1002/9781118889657.ch40.

3. Powell, A.; Earlam, M.; Barriga, S. "Pure Oxygen Anodes™ for Efficient Clean Production of Reactive

Metals," Presented at the Reactive Metal Workshop, Pasadena, CA on February 21, 2014.

4. Guan, X.; Pal, U.; Gopalan, S.; Powell, A. "Electrochemical Characterization and Modeling of a Solid Oxide Membrane-based Electrolyzer for Production of Magnesium and Oxygen," in P. Mackey, E. Grimsey, R. Jones and G. Brooks, eds., *Celebrating the Megascale: Proceedings of the Extraction and Processing Division Symposium on Pyrometallurgy in Honor of David G.C. Robertson,* DOI: 10.1002/9781118889657.ch40 2014.

5. Powell, A.; Earlam, M.; Barriga, S. "Pure Oxygen Anodes™ for Low- or Zero-Carbon Energy Efficient Metal Oxide Reduction," in Cong Wang ed., *Energy Technology 2014: Carbon Dioxide Management and Other Technologies,* DOI: 10.1002/9781118888735.ch16 2014.

6. Guan, X.; Pal, U. B.; Powell, A.C. "Energy-Efficient and Environmentally Friendly Solid Oxide Membrane Electrolysis Process for Magnesium Oxide Reduction: Experiment and Modeling," *Metall. Mater. Trans. E* 2 (1E:2) *2014,* pp. 132-144. DOI: 10.1007/s40553-014-0013-x

7. E.S. Gratz, E.S.; Guan, X.; Milshtein, J. D.; Pal, U.B.; Powell, A.C. "Mitigating Electronic Current in Molten Flux for the Magnesium SOM Process," *Metall. Mater. Trans. B* (45B:4), *2014,* pp. 1325-1336. DOI: 10.1007/s11663-014-0060-9

8. Guan, X.; Su, S.; Pal, U. B.; Powell, A. C. "Periodic Shorting of SOM Cell to Remove Soluble Magnesium in Molten Flux and Improve Faradaic Efficiency," *Metall. Mater. Trans.* B (45B), 2014. DOI: 10.1007/s11663-014-0142-8

9. Pal, Uday; Guan, Xiaofei; Powell, Adam C. "Method to Remove Soluble Metal in the Flux (molten salt electrolysis), Increase Electrolysis Process Efficiency and Prevent Membrane Degradation," U.S. Provisional Patent Application 61/899,013 filed November 1, 2013.

10. Powell, Adam; Strauss, John; Tucker, R. Steve; Voellinger, J Brodie. "Improved Liquid Metal Electrodes for Gas Separation," PCT Patent Application PCT/US14/42163 filed June 12, 2014.

References

1. Kippouros, G; Sadoway, D. "A thermochemical analysis of the production of anhydrous $MgCl_2$." *J. Light Metals* (*1),* 2001; pp 111–117, DOI: 10.1016/51471-5317(01)00004-9.

III.4 Processing and Manufacturability – Pacific Northwest National Laboratory

Yuri Hovanski, Field Technical Monitor
Pacific Northwest National Laboratory
902 Battelle Boulevard
Richland, WA 99352
Phone: (509)375-3940
E-mail: yuri.hovanski@pnnl.gov

William Joost, Technology Area Development Manager
U.S. Department of Energy
1000 Independence Avenue, SW
Washington, DC 20585
Phone: (202) 287-6020
E-mail: William.joost@ee.doe.gov

Contractor: Pacific Northwest National Laboratory
Contract No.: DE-AC05-00OR22725 & DE-AC06-76RL01830

Abstract/Executive Summary

The Processing and Manufacturability project consists of five tasks focused on research and development activities advancing the basic mechanical properties, manufacturability, and cost of lightweight materials towards the levels needed for increased implementation in automotive applications. These tasks include the following:

- Microstructure and Deformation Fundamentals in Advanced Lightweight Materials
- Enhanced Room-Temperature Formability in High-Strength Aluminum Alloys Through Pulse Pressure Forming
- Aluminum Formability Extension Through Superior Blanking Process
- Non-Rare Earth High-Performance Wrought Magnesium (Mg) Alloys
- Aerodynamic Lightweight Cab Structures

The following sections outline specific task work conducted at PNNL in the area of processing and manufacturability of lightweight metals. Each task supports one or more goals within the Processing & Manufacturability Agreement as outlined below.

III.5 Microstructure Deformation Fundamentals in Advanced Lightweight Materials

Xin Sun, Principal Investigator
Pacific Northwest National Laboratory
Phone: (509) 372-6489; Fax: (509) 372-6099
E-mail: Xin.Sun@pnl.gov

David K. Matlock and John Speer, Principal Investigators
Phone: (303) 273-3775; Fax: (303) 273-3016
E-mail: dmatlock@mines.eduAdvanced Steel
Phone: (303) 273-3897; Fax: (303) 273-3016
E-mail: jspeer@mines.edu
Processing and Products Research Center
Colorado School of Mines
1500 Illinois Street
Golden, CO 80401

Accomplishments

- Developed an elasto-plastic self-consistent (EPSC) model to determine the mechanical properties (i.e., phase stress-strain curves) of the constituent phases. (FY 2014)
- Performed nano secondary ion mass spectrometry (nano-SIMS) test on a quenching and partitioning (Q&P) steel to quantify the carbon distribution between the retained austenite and the matrix phases. (FY 2014)
- Performed the analyses and further experiments with the 2nd heat Q&P steels to develop new heat-treatment parameters for the 3rd heat steels. (FY 2014)
- Produced the final heat (i.e., 3rd heat) Q&P steels with improved Q&P parameters for 3rd generation advanced high-strength steels (AHSS) properties of 1500MPa and 20% ultimate elongation (FY 2014)
- Performed nano-indentation test with the Q&P steels selected from different heats to quantify the hardness difference for different phases and to examine their influence on the overall performance. (FY 2014)

Technology Assessment

- Target: Develop a 3rd generation AHSS product with 1200 MPa ultimate tensile strength (UTS) and 30% total elongation (TE).
- Gap: Reduced alloying and lower cost are important considerations for the development of 3rd generation AHSS. In addition, automotive steel industry still lacks and

overall understandings on key material parameters controlling the mechanical properties of AHSS.

✧　　✧　　✧　　✧　　✧

Introduction

AHSS represent an important class of materials in efforts to reduce vehicle weight for improved fuel-efficiency and occupant safety. These steels have evolved with new alloying and processing strategies to tailor microstructures containing various mixtures of ferrite, martensite, bainite, and retained austenite. Following previous development of 1st and 2nd generation AHSS, 3rd generation AHSS concepts are being pursued to identify lower alloy steels that achieve ultra-high-strength properties in combination with formability sufficient for implementation in automotive production. Relative to the 2nd generation steels, reduced alloying and lower cost are the focus of these steels.

This project is focused on multi-modal experiments and microstructural-based modeling analyses designed to improve the overall understanding of the variables which control austenite stability against straining, and thus mechanical properties of new AHSS products. The proposed effort is also focused on improved understanding of the relationship between AHSS microstructural features and the effects of microstructure on global and local deformation mechanisms. Thus, 3rd generation AHSS developed in this effort can possess good localized deformation capacity for automotive forming and trimming operations. It is envisioned that steels with 1200MPa UTS and 30% TE is the property goal, along with a consideration of cost target of this class of material anticipated by the global automotive and steel industry. The results of these analyses can be used to accelerate the development of 3rd generation AHSS products.

Approach

As the Q&P process has been identified as a potential process to generate 3rd generation AHSS properties [1], the material development in this study was focused on Q&P steels. In FY12~13, in-situ High Energy X-ray Diffraction (HEXRD) tests under a uniaxial tensile condition have been performed with the Q&P steels selected from the 1st and 2nd heats to obtain the volume fraction evolution of the austenite phase during the deformation process as well as to determine the mechanical properties for the constituent phases. In FY14,

an EPSC model was developed in order to obtain more accurate properties of the constituent phases based on the HEXRD test results. The EPSC model is able to account for the deformation heterogeneity of the grains with different crystal orientations. The obtained results from EPSC model is expected to be used as inputs for the microstructure-based modeling approach for bulk property prediction of multi-phase steels.

As carbon partitioning from martensite to austenite is a primary mechanism for stabilizing austenite and retaining increased austenite fractions at room-temperature, nano-SIMS with a spatial resolution of 100nm was also implemented in FY14 for a Q&P steel to determine the carbon levels within the martensite/austenite microstructures. The obtained information on the carbon content level/distribution within the Q&P microstructure may be used in quantifying the effectiveness of the partitioning process and in estimating the austenite stability in the microstructure-based models by considering variable stability within austenite grains.

In FY12, the 1st heat Q&P tensile samples (i.e., MAT1~4) which may be in 3rd generation AHSS property range were produced based on two different chemical compositions (i.e., 0.3C-3Mn-1.6Si, 0.2C-3Mn-1.6Si) with different heat-treating parameters, and investigated experimentally and computationally. Based on the information from the microstructure-based modeling approaches with the 1st heat Q&P steels, the 2nd heat samples (i.e., MAT5~8) were then produced in FY13 using the same chemical compositions of MAT1 (i.e., 0.3C-3Mn-1.6Si), exhibiting the best TE of ~19% among the 1st heat samples. The heat-treatment parameters for the 2nd heat samples were mainly focused on increasing the volume fraction and stability of austenite phase. Among the 2nd heat samples, MAT5 and MAT8 showed the increase in both UTS and TE, compared to MAT1, and their properties are over 1500MPa UTS and 20% TE (see Table III-8).

In FY14, further experiments and analyses, such as on the tempering effects on the hardness of Q&P steels, were performed with the 2nd heat samples. With the intention of

further improving the TE even with some possible reduction in UTS, the 3rd heat samples (i.e., MAT9~11) were then produced based on the modification of the heat-treating parameters of MAT8 showing the best TE of ~22% among the 2nd heat samples. Nano-indentation tests were also performed with the Q&P steels (i.e., MAT1, MAT8, MAT10) selected from the three different heats to measure hardness numbers of their constituent phases. It is expected that a possible correlation can be found between the nano-indentation test results of these samples and the computational observations from virtual material design process.

Results and Discussion

Figure III-17(a) shows the experimental setup for the in-situ HEXRD tests under uniaxial tensile condition. Figure III-17(b) and Figure III-17(c), respectively, show the integrated intensity of diffraction rings vs. 2θ angles and the calculated austenite volume fraction evolution vs. macro strain for MAT1. As shown in Figure III-17(c), the austenite phase transforms gradually with the deformation process, which helps to enhance the ductility of the Q&P steels. Figure III-17(d) shows the phase stress-strain curves of MAT1, determined based on the developed EPSC model. As the heterogeneous deformation between the grains in multi-phase materials is considered in the self-consistent model, the stress versus strain curves shown in Figure III-17(d) are expected to be more accurate than the phase stress-macrostrain curves previously reported, which was based on uniform deformation assumption. It is generally accepted that the EPSC model can reasonably capture the strain variations for various phases during tensile loading with the appropriate selection of constitutive models and parameters for the slip systems of the various phases. Incorporation of grain orientation updates and martensitic transformation may be needed for further improvement of the EPSC model.

Table III-8: Heat-treating parameters and some test results for the selected Q&P steels (0.3C-3Mn-1.6Si).

Heat No.	Material Name	Annealing (°C/sec)	Quenching (°C/sec)	Partitioning (°C/sec)	Retained Austenite (%)	Carbon Content (wt%)	UTS (MPa)	TE (%)
1st	MAT1	820/120	180/10	400/100	21.4	1.13	~1530	~19
2nd	MAT5	820/120	180/10	425/100	-	1.35	1578	20.74
2nd	MAT8	820/120	160/10	400/100	14.6	1.28	1598	21.80
3rd	MAT9	820/120	160/10	400/100 with 150°C /10hr tempering	20.4	1.20	1542	21.57
3rd	MAT10	820/120	160/10	400/300	21.1	1.28	1518	20.79

(a)   (b)

(c)   (d)
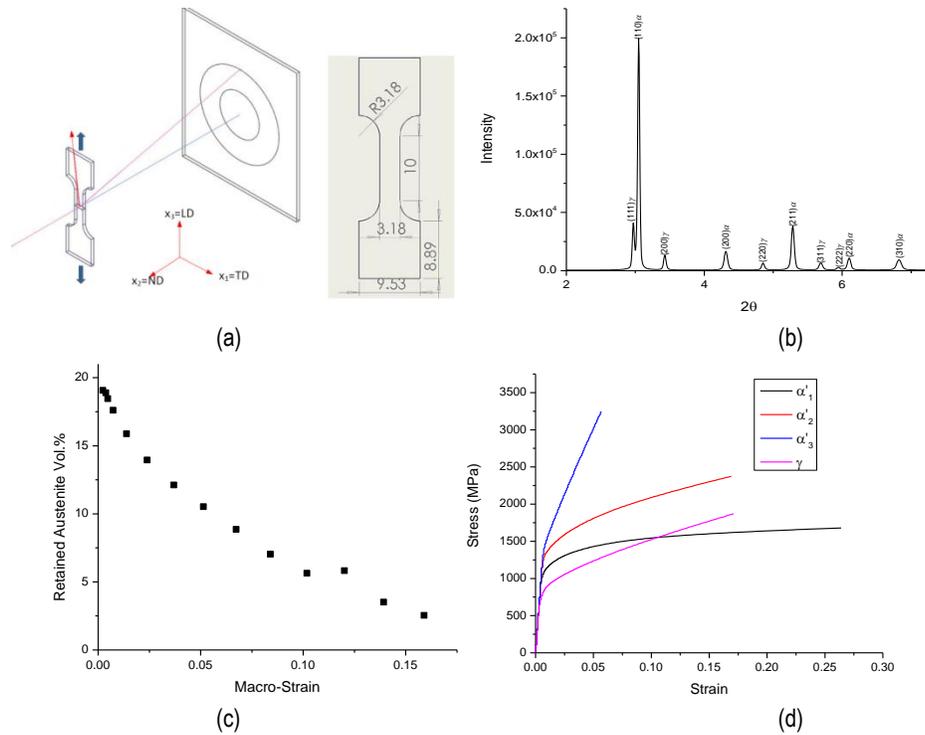
Figure III-17: (a) Schematic of experimental setup for in-situ HEXRD tests under uniaxial tension, (b) intensity vs. 2θ profile integrated from diffraction rings, (c) austenite volume fraction evolution and (d) phase stress-strain curves estimated from EPSC model for MAT1.

(a)   (b)   (c)   (d)
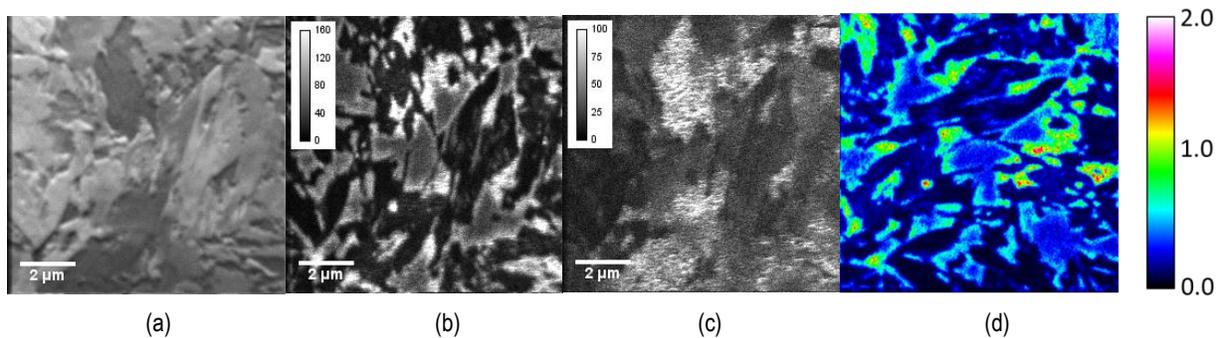
Figure III-18: Nano-SIMS test results of MAT1. (a) Ion-induced SEM, (b) carbon counts, (c) silicon count and (d) color coded carbon distribution in wt%.

Figure III-18 shows the results obtained from nano-SIMS scans with MAT1. Figure III-18(a) shows the ion-induced scanning electron microscopy (SEM) and Figure III-18(b) and Figure III-18(c) show the carbon and silicon counts in gray scale, respectively. In Figure III-18, the carbon and silicon distributions are not necessarily consistent with each other. Figure III-18(d) show the color coded carbon distribution in wt%, which was converted from Figure III-18(b) by assuming the average carbon count from the image is consistent with the carbon content in bulk material (i.e., 0.3wt%). In order to identify the high carbon content regions in Figure III-18(b) and Figure III-18(c), the Electron Backscatter Diffraction (EBSD) scan was performed on the same location. Figure III-19(a) shows the overlay of nano-SIMS image and EBSD phase map

image, which indicates that the high carbon content regions are mostly the retained austenite phases. Line scans were performed on some locations as shown in Figure III-19(a) and the resulting carbon profiles are shown in Figure III-19(b) and Figure III-19(c). The line scans presented in Figure III-19 clearly confirm the enrichment of austenite with carbon and depletion of the martensitic regions compared to the bulk carbon content of the alloy and show more depletion apparent away from martensite/austenite boundary. Although its resolution does not allow for distinction of transition carbide and accurate carbon profile across grain boundary, nano-SIMS appears to be a relatively simple and good experimental method for the investigation of the carbon content levels and distributions within the complicated Q&P microstructures.
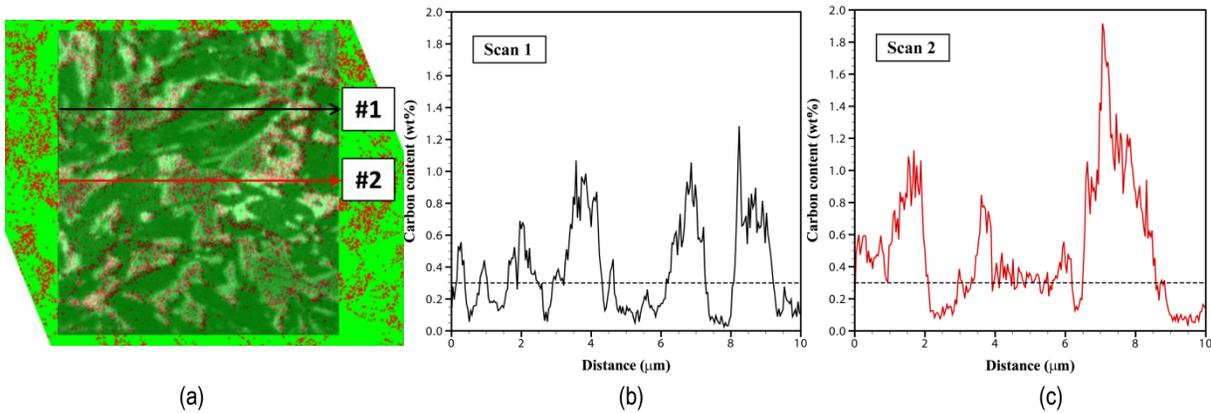
Figure III-19: (a) Overlay of carbon count image from nano-SIMS on EBSD phase map, (b) and (c) carbon distributons along the two lines.
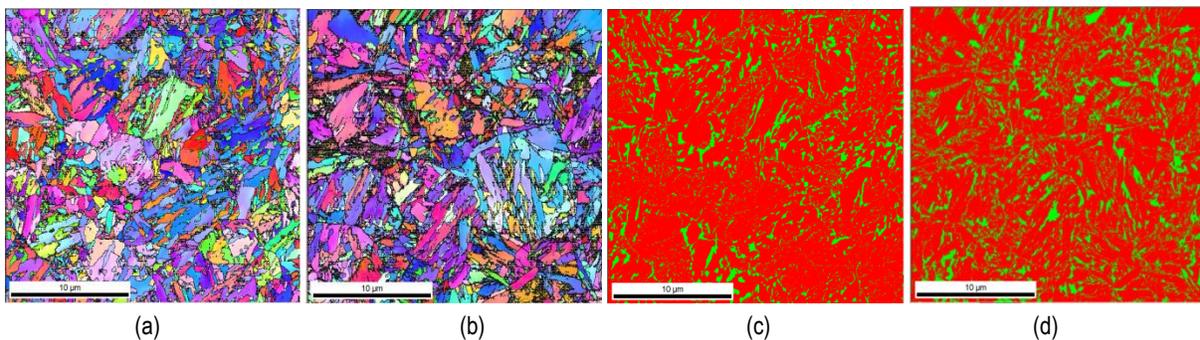
Figure III-20: Microstructure comparison between MAT8 and MAT9. Grain orientation maps of (a) MAT8 and (b) MAT9 and phase maps of (c) MAT8 and (d) MAT9.

The 3rd heat samples (i.e., MAT9~11) were produced based on modifying the heat-treating parameters of MAT8 by applying additional tempering process (MAT9) or longer partitioning time (MAT10). These heat-treating parameters were devised to increase the ductility with the decrease of strength as well as to further increase the austenite stability, compared to MAT8. However, both MAT9 and MAT10 only showed similar TE to that of MAT8 with some decrease in UTS (see Table III-8). Figure III-20 compares the microstructures of MAT8 and MAT9 as an example. It appears that slightly finer grain size and more austenite volume fraction of MAT9, as shown Figure III-20(b) and Figure III-20(d), do not improve its ductility. From the observations on the results of the 3rd heat samples, ~21% may be the maximum level of TE that could be achieved with the chemistry of 0.3C-3Mn-1.6Si.

With these results, it is concluded that heat-treatment alone with a specific Q&P chemistry may not be sufficient to achieve as significant performance improvement as those achieved in the computational works performed in FY13. This is possibly because the material parameter adjustment suggested from computational works may not be thermodynamically consistent hence may not be physically achievable through heat-treatment. Different sets of chemical compositions, not only the carbon content but also other alloying elements, may need to be considered for further performance improvements. Since the

Q&P samples in this study were provided as in-kind contributions from Advanced Steel Processing and Products Review Center's industrial partners, optimizing and controlling initial chemical compositions are considered beyond the scope of our current work. The properties achieved in both the 2nd and the 3rd heat of the0.3C-3Mn-1.6Si steel do meet the alternative 3rd generation AHSS requirement of excellent strength (>1500MPa) with good ductility (>20%). From this perspective, the project has demonstrated the process of using computational tools in progressively enhancing the Q&P steel properties to meet the 3rd generation AHSS performance requirement (see Figure III-21).

In order to validate the computational observations on the effects of constituent properties on the overall material performance, which were obtained from the virtual material design process, additional nano-indentation tests were performed with MAT8 and MAT10 to measure the hardnesses of their constituent phases. Figure III-22 shows some example results obtained from the nano-indentation tests with the two materials. The nano-indentation test results for MAT1, MAT8 and MAT10 are under analysis to possibly estimate the stress-strain curves of constituent phases. The estimated phase stress-strain curves are expected to be used to validate the computational observations against the actual material performance obtained from the tests (i.e., UTS, UE, TE).

(a)   (b)
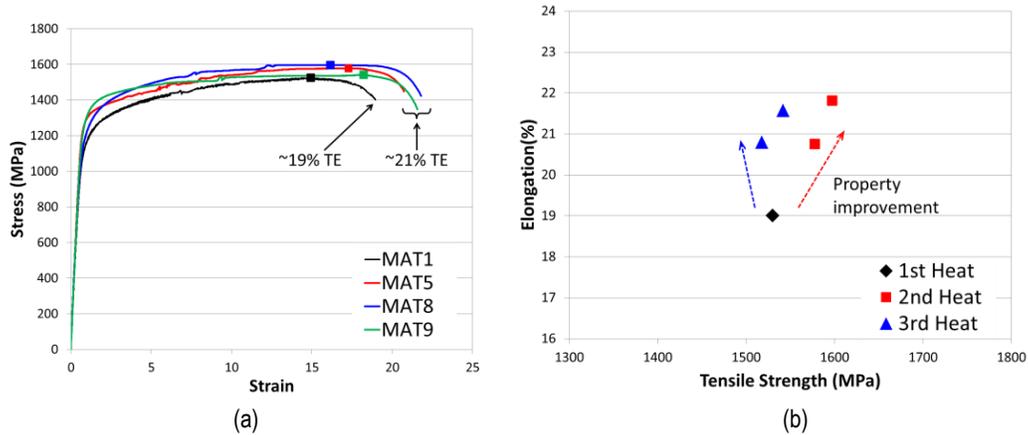
Figure III-21: (a) Representative stress-strain curves for different Q&P steels and (b) property improvement between different heats on the tensile strength vs. TE map.

(a)   (b)   (c)
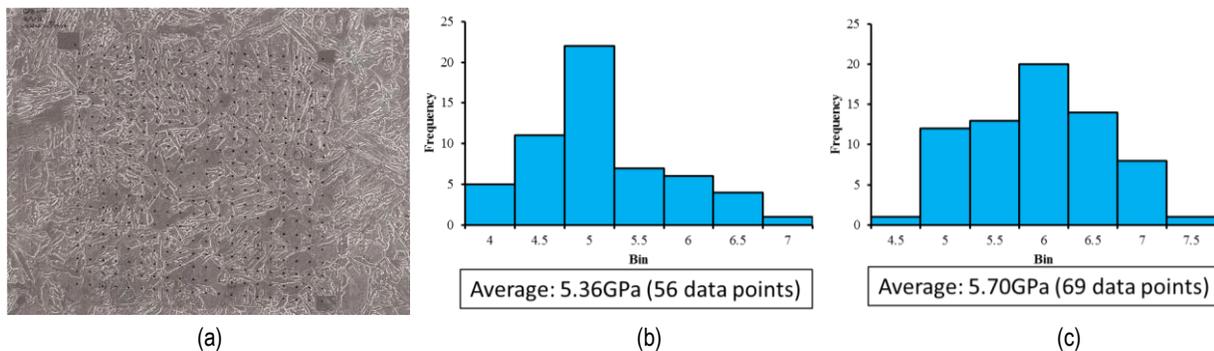
Figure III-22: (a) Nano-indentation test with MAT8, and some hardness results for tempered martensite in (b) MAT8 and (c) MAT10.

Technology Transfer Path

The deliverables of this projects will be transferred to the original equipment manufacturer (OEM) participants and steel producers through the industry/university cooperative research center-Advanced Steel Processing and Products Research Center at Colorado School of Mines, during regularly scheduled semi-annual review meetings.

Conclusions

Q&P steel was selected as the model steel for the development of 3rd generation AHSS. The 1st heat samples were produced with different chemistry and heat-treating parameters. After possible directions for property improvement were identified based on an integrated experimental and computational approach, the 2nd heat and subsequently the 3rd heat samples were produced. Some samples from the 2nd and 3rd heats showed the enhanced UTS and TE, compared to the 1st heat samples, and did meet the performance requirement of the 3rd generation AHSS. It is also found that different sets of chemical compositions may need to be considered for further performance improvement. In summary, the integrated experimental and simulation framework has been established to achieve the 3rd generation property requirement with multiphase Q&P steels, which is to be validated with nano-indentation test results.

III.6 Enhanced Room-Temperature Formability in High-Strength Aluminum Alloys through Pulse-Pressure Forming (PPF)

Aashish Rohatgi, Principal Investigator
Pacific Northwest National Laboratory
Phone: (509) 372-6047; Fax: (509) 375-4448
E-mail: aashish.rohatgi@pnnl.gov

Richard W. Davies, Principal Investigator
Pacific Northwest National Laboratory
Phone: (509) 375-6474; Fax: (509) 375-6844
E-mail: rich.davies@pnnl.gov

Accomplishments

- Determined the room-temperature formability of AA7075 in different tempers and at different strain-rates and developed guidance for selecting the temper/strain-rate combinations to achieve desired formability under given processing constraints. (FY 2014)
- Determined the mechanical behavior of AA7075 under quasi-static and high-strain-rates to enable development of a constitutive equation that incorporates variable strain-rate sensitivity. (FY 2014)
- Determined the influence of natural aging and strain on the aging hardness curves of AA7075. (FY 2014)

Future Directions

- Develop constitutive equations to describe the deformation behavior and formability of AA7075 in different tempers and under high strain-rates.
- Fabricate a prototypical automotive component in 5xxx, 6xxx or 7xxx Al alloy using PPF.
- Conduct a finite element model analysis to quantify the mass savings with the use of AA7075 in a candidate automotive part.

Technology Assessment

- Target: Achieve 70 percent improvement in the room-temperature formability (near plane-strain) in 7xxx Al alloys.
- Gap: The room-temperature formability of Al alloys (e.g., 5xxx and 6xxx) in plane-strain typically does not exceed 25 percent while high-strength 7xxx alloys have almost no formability. An improvement of 70 percent or more can help make the formability of some Al alloys comparable to the formability of deep-drawing-quality steels, which possess plane-strain formability of ~45 percent. However, such formability enhancements in Al alloys are generally not possible unless forming is done at elevated temperatures.
- Target: Determine the strain, strain-rate, velocity, and strain-path of AA7075 as a function of time during PPF.

- Gap: The strain-rates during PPF of sheet metals typically exceed 1000/s and the constitutive behavior of Al alloys can be quite different at strain-rates exceeding 1000/s, relative to their behavior at quasi-static rates. Further, PPF strain-rates can vary significantly during the course of deformation as a function of time and location on the workpiece. However, literature regarding strain-rates and strain-path during high-rate forming is generally lacking, which has hindered development of accurate and validated numerical models of high-rate forming processes.

✧   ✧   ✧   ✧   ✧

Introduction

The goal of this project is to extend the room-temperature formability of high-strength aluminum alloys (e.g., 6xxx and 7xxx) to enable their use in structural automotive components conventionally made of steel. Such structural members are not typically fabricated in 6xxx and 7xxx Al alloys owing to the limited formability of these alloys under conventional room-temperature stamping conditions. In a prior project [2], Pacific Northwest National Laboratory (PNNL) demonstrated that high-strain-rate forming (without a die) of AA5182-O Al alloy at room-temperature can achieve safe strains ~2.5x times greater than those achievable under room-temperature quasi-static forming. Further, enhancement in safe strains can be as high as ~6x times when the forming process is performed inside a die. Similar formability enhancements were envisioned in heat-treatable, high-strength 6xxx and 7xxx alloys, enabling lightweight alternatives to steel structural members in automotive applications. However, further understanding is needed of the practical forming limits in PPF processes and their dependence upon process parameters and design. This project will quantify the deformation behavior of 6xxx and 7xxx Al alloys under PPF and develop validated constitutive relations to enhance understanding of high-rate forming processes and the resulting sheet metal formability. Over the course of this project, the focus has been narrowed down to AA7075 alloy on account of its high-strength (~600 MPa) in T6 temper and the consequent potential for significant mass savings if 7075-T6 could replace mild steel in structural components such as B-pillar.

Approach

The work scope of this project was developed in conjunction with General Motors (GM) and Alcoa. Two Alcoa Al alloys, AA6022-T4E32 (1.2 mm) and AA7075-T6 (1 mm), were identified as representative high-strength, heat-treatable

Al sheet alloys that, if sufficiently formable at room-temperature, would be attractive candidates for automotive structural applications. Accordingly, in FY 2012 PNNL demonstrated an approximately 78 percent increase in the safe major strain at a minor strain of approximately -5 percent for AA6022 through PPF as compared to the safe strain at quasi-static strain-rate [3]. Therefore, the aim in FY 2013 was to determine if formability improvements could be obtained in AA7075 analogous to the improvements observed in AA6022. Accordingly, we demonstrated in FY 2013 that it is indeed possible to enhance the room-temperature formability of AA7075 by ~100% through PPF at strain-rates between 2000-4000 /s. More importantly, such formability enhancements are possible in the strongest temper (i.e. T6) and without any need for elevated-temperature forming. It is recognized that despite a *relative* increase of 100% in formability in 7075-T6 at high strain-rates, the *absolute* values of formability are in a range (10-20% engineering strain) that is still significantly lower than that of mild steel. Therefore, the possibility of forming AA7075 in W temper was explored. Initial experiments were encouraging as they indicated the possibility of achieving formability enhancements at somewhat lower strain-rates, than those needed for the T6 temper, if AA7075 was formed in W temper.

Thus, the goal in FY 2014 was to develop baseline room-temperature formability data for AA7075 in W tempers at quasi-static and high strain-rates. The W-temper sheets were prepared by subjecting the T6 temper sheets to solutionizing, quenching, and natural aging (1 day or 6 days). Quasi-static forming data was obtained using the conventional limiting dome height (LDH) method and strain-grid technique. High-rate forming data was obtained by using PNNL's high-speed imaging + digital image correlation (DIC) system [4], [5], [6]. Strains were quantified by the DIC method and corroborated by the conventional strain-grid technique. Uniaxial tensile tests at quasi-static and high-strain-rates were performed to develop constitutive equations for AA7075. Finally, aging curves were determined for W temper sheets as a function of prior natural aging, aging temperature and plastic strain.

Results and Discussion

Figure III-23 shows an example of a series of room-temperature tested LDH samples (W temper) where the initial dimensions of the rectangular blank were varied to get strain states lying between equi-biaxial and plane-strain. Failure in these samples is in the form of a crack running across the sample and away from the dome apex

Figure III-24 shows an example of room-temperature PPF-tested W temper AA7075 (1-day aged and 6-days aged) samples. Failure in these samples is in the form of a crack

running across the gauge region and perpendicular to the rolling direction.

Figure III-25a shows the forming limit data measured in the PPF-tested W temper samples while Figure III-25b shows the corresponding data under quasi-static LDH testing. Figure III-26 shows the forming limit diagram (FLD) for the quasi-statically bulge tested and PPF formed domes in T6 tempers. The data in Figure III-25a shows that safe major strains (near plane-strain) in PPF-tested W temper specimens are similar order of magnitude and as high as ~0.27 (engineering). These plane-strain formability values are ~2.7x (i.e. ~170% greater) than the safe major strains of ~10% (engineering) measured in quasi-statically tested 7075-T6 samples, as shown by the FLC in Figure III-25b. Further, the safe major strains in PPF-tested W temper samples (Figure III-25a) are ~35% greater than the safe major strains (~0.2 engineering) in their quasi-static tested counterparts, as shown by the quasi-static FLCs in Figure III-25b. Finally, Figure III-26 shows that the room-temperature high-rate formability of AA7075 in T6 temper is enhanced by ~100% through PPF at strain-rates between 2000-4000 /s. In summary, the room-temperature formability of AA7075 in all the three tempers tested increases at high-strain-rates, relative to their formability at quasi-static rates, with the magnitude of formability enhancement being a function of the temper. Based on the data in Figure III-25 and Figure III-26, the strain-rate/temper combinations can be qualitatively arranged in the order of decreasing formability as follows:

PPF, W tempers ≳ PPF, T6 ≳ Quasi-static W tempers >> Quasi-static T6

Thus, one can consider two possible approaches to **room-temperature** forming of AA7075 (and perhaps, other high-strength 7xxx alloys by analogy):

1. **If T6 is the preferred temper for forming, then high-strain-rate forming is necessary** in order to achieve reasonable formability. However, one is likely to run into supply-chain issues associated with high-rate forming techniques. These supply-chain issues are currently being investigated with the project team and potential suppliers.

2. **If quasi-static forming (e.g., stamping) is the preferred path, then W temper is required** to achieve reasonable formability. However, this approach will add costs on account of (a) heat-treatment to produce W temper, and (b) scheduling controls to ensure the correct W temper during forming.
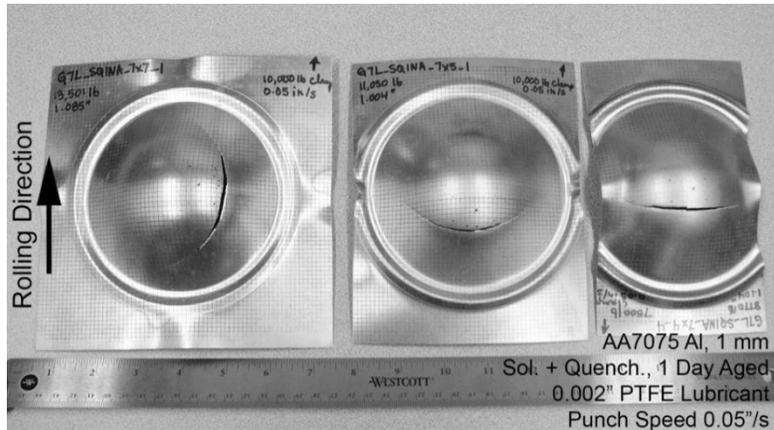
Figure III-23: Pictures of tested AA7075 specimens (solutionized + quenched +1 day natural aged) used to determine the corresponding forming limit curve (FLC) using the LDH tests.
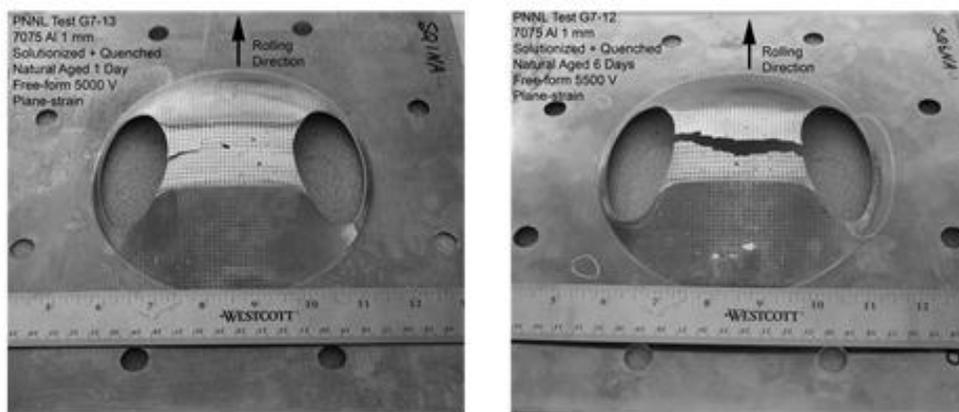
Figure III-24: Pictures of the pulse-pressure free-formed samples of AA7075 in W temper, 1-day (left) and 6-days (right) natural aged.

(a)

(b)
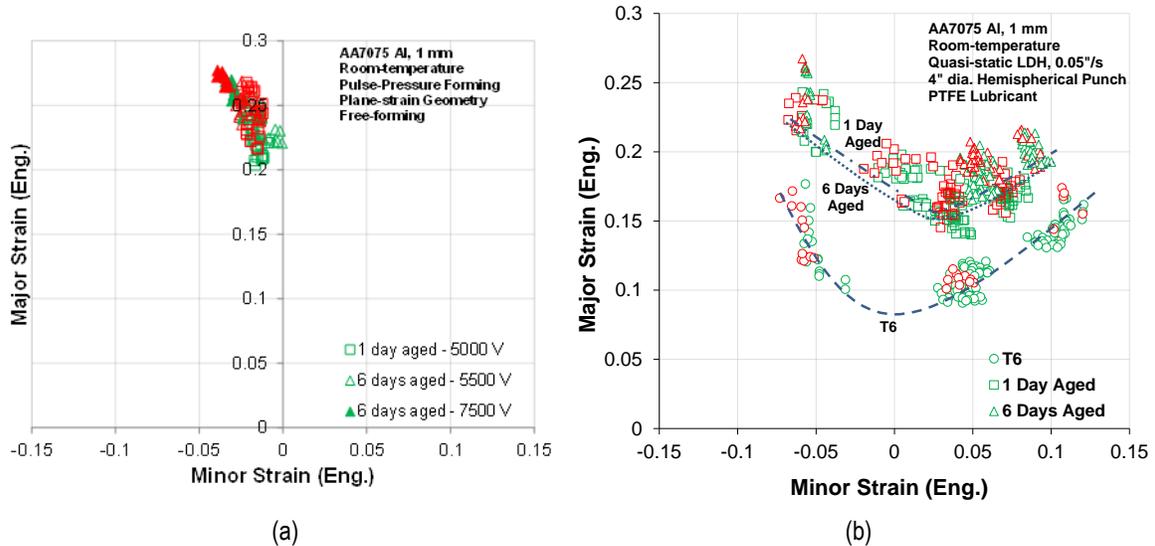
Figure III-25: (a) FLD of PPF AA7075 in W tempers. (b) Quasi-static FLC of AA7075 obtained by LDH tests. The dashed lines are meant to guide the eye and not indicative of any model or best fit. Green symbols signify safe strains while red symbols signify unsafe strains.
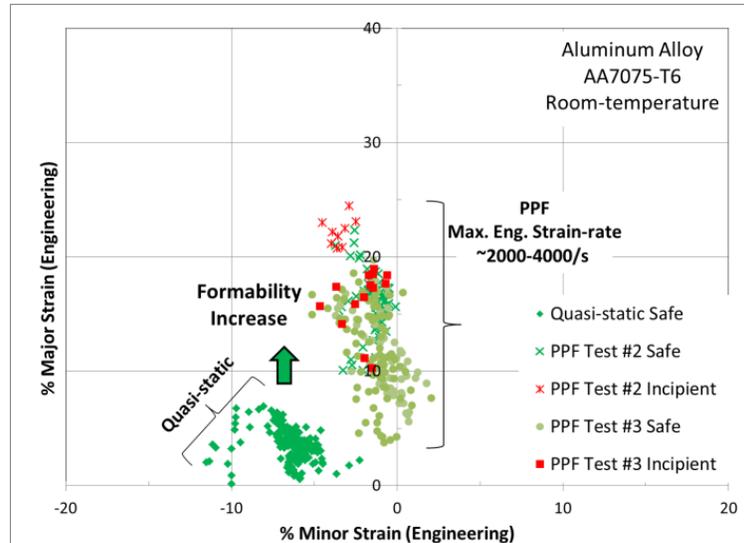
Figure III-26: FLD of AA7075-T6 under PPF and quasi-static bulge forming. Green symbols signify safe strains while red symbols signify unsafe strains.

Figure III-27 shows the room-temperature quasi-static and high-rate tensile stress-strain curves for AA7075-T6. The data shows a high positive strain-rate sensitivity in the strain-rate range of 0.005/s – 500/s, i.e. a significant increase in flow stress as the strain-rate increases from 0.005/s to 500/s. However, further increase in strain-rate does not seem to produce any additional strengthening. Similar experiments were conducted in W temper 7075 and the data is being analyzed to develop temper-appropriate constitutive equations. It is believed that such positive strain-rate sensitivity is responsible for enhancing the formability of AA7075, as shown for the T6 temper in Figure III-26.

Figure III-28 shows the strain distribution in the W temper plane-strain geometry samples that were PPF formed. After forming, both samples were further natural aged for ~6 months and their microhardness measured in the high-rate formed region. The data in Figure III-28 shows that the Vickers microhardness for both the samples is in the range of 170-180 HV which is within 5-10% of the T6 hardness of ~189 HV. In other words, **if 7075 is formed in W temper by PPF, the combination of work hardening and natural aging alone may be sufficient to bring its hardness (or strength) within 5-10% of the T6 value**. The above results do *not* imply that post-formed parts need to be aged 6 months to achieve near-T6 hardness. Instead, preliminary experiments have shown that natural aging followed by deformation (and without any additional natural aging) can be sufficient to increase the hardness to within 10% of T6 hardness. Experiments to determine the effect of paint-bake heat-treatment on hardness in high-rate formed samples are on-going,

Technology Transfer Path

PNNL will identify commercial vendor(s) with the capability to implement high-rate forming in industrial settings. A prototype component and Al alloy (5xxx, 6xxx or 7xxx) will be identified in discussions with the project partners. PNNL will provide the results of the formability investigation and the constitutive equations for the selected alloy to help evaluate which structural component features, currently not formable via cold-stamping, would be best candidates for high strain-rate forming.

Figure III-27: Room-temperature uniaxial tensile stress-strain data for AA7075-T6 at quasi-static and high-strain-rates.

(a)   (b)
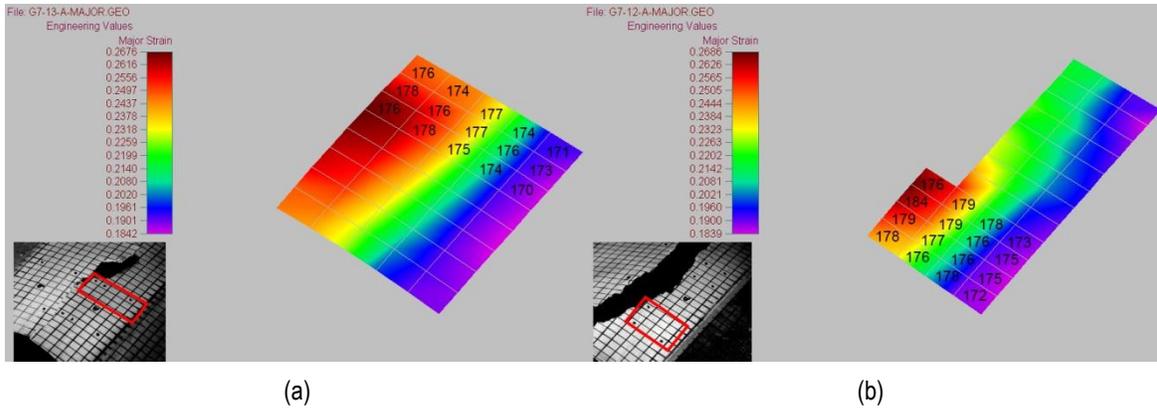
Figure III-28: Strain contour maps of PPF formed W temper samples i.e. the blanks were natural aged at room-temperature for (a) 1 day and (b) 6 days. After forming, both samples were further natural aged ~6 months and their hardness measured as shown. The strain contour maps are superimposed with the average Vickers microhardness (HV) values at the locations identified. The inset shows the image of the strain gridded PPF specimen, and the area analyzed by microhardness is enclosed by the red-outlined box.

Conclusions

The room-temperature formability, tensile behavior and aging response of AA7075 were determined for different combinations of tempers and strain-rates. Under the experimental conditions employed in this work, the following conclusions can be drawn:

The room-temperature formability of AA7075 in T6 and W tempers and under plane-strain conditions was found to be enhanced by PPF relative to the respective formability under quasi-static forming. The strain-rate/temper combinations can be qualitatively arranged in the order of decreasing formability as: PPF, W tempers ≳ PPF, T6 ≳ Quasi-static W tempers >> Quasi-static T6

The data shows a high positive strain-rate sensitivity in the strain-rate range of 0.005/s – 500/s, i.e. a significant increase in flow stress as the test strain-rate increases from 0.005 /s to 500/s. It is believed that such positive strain-rate sensitivity is responsible for enhancing the formability of AA7075, as shown for the T6 temper in Figure III-26.

If 7075 is formed in W temper by PPF, the combination of work hardening (due to plastic deformation) and natural aging alone may be sufficient to bring its hardness (or strength) within 5-10% of the T6 value. In other words, additional heat-treatment (and the associated added expense) of post-formed samples may not be necessary for PPF formed W temper samples. Thus, starting with W temper blanks, it may be economically feasible to obtain sufficient formability *and* achieve near-T6 strength in AA7075 through PPF.

III.7 Aluminum Formability Extension through Superior Blanking Process

Xin Sun and Richard W. Davies, Principal Investigators
Pacific Northwest National Laboratory
Phone: (509) 372-6489; Fax: (509) 372-6099
E-mail: xin.sun@pnnl.gov
Phone: (509) 375-6474; Fax: (509) 375-4448
E-mail: rich.davies@pnnl.gov

Sergey Golovashchenko, Principal Investigator
Oakland University
2200 N Squirrel Road
Rochester, MI 48309
Phone: (313) 337-3738; Fax: (313) 390-0514
E-mail: golovash@oakland.edu

Accomplishments

- With the previously developed integrated framework, the tensile stretchability for edges prepared with advanced trimming methods (with scrap support and dull punch) has been predicted and validated: more than 50% enhancement on tensile stretchability has been achieved for large trimming clearances.
- Advanced trimming process has been prototyped and demonstrated at Ford Motor Company.
- Performed hole piercing experiments on AA6111-T4 aluminum sheets with different clearances and corresponding cross-sectional metallography examinations of the pierced hole edges.
- Performed hole expansion experiments on AA6111-T4 aluminum sheets with previously pierced holes, measured variation of the critical hole expansion ratio with hole piercing clearances.
- Performed accumulate rolling and tension test identify flow curve at large strains.
- Performed 2D hole piercing simulations with the use of new flow curve: the predicted results of burr formation shows very good agreement with experiments. With the integrated framework developed from last fiscal year, the 3D hole expansion simulations were performed using the shearing zone information calculated from the hole piercing model. The calculated critical hole expansion ratios show very good agreement with experiments.

Future Directions

- A new aluminum alloy sheet other than AA6111T4, such as AA6022, will be examined to determine the influence of hole piercing on the subsequent hole expansion ratio.

Flow curves and damage parameters will be determined for this alloy.
- Hole punching and hole expansion tests with the additional aluminum alloy sheets.
- Simulations of hole expansion ratios on the new aluminum alloy with different punched hole edge conditions using the integrated modeling framework to determine the effects or edge conditions on the final hole expansion ratio.

Technology Assessment

- Target: Achieve 90 percent accuracy of the blanking simulations with experiments in terms of cut edge geometry.
- Gap: The simulations results of cut edge geometry are very close to experimental observations. For more precise prediction, more accurate damage parameters and plastic model at large strains are necessary.

✧ ✧ ✧ ✧ ✧

Introduction

The automotive OEMs and their Tier 1 suppliers have an extraordinary high capital investment into their sheet metal forming facilities, equipment, and associated infrastructure. The ability to redirect these capitally-intensive facilities from steel to aluminum component manufacturing would dramatically increase the wide-spread commercialization of aluminum sheet into vehicles. This project aims to enhance the overall formability of aluminum using the existing OEM capital infrastructure by developing enhanced processes for the blanking, piercing, and trimming operations to extend aluminum formability in the subsequent forming operations. The formability of the aluminum sheet in conventional automotive stamping is typically limited by the processes that prepare the blank for the stamping operation, i.e., blanking, piercing, and trimming. The overall formability and subsequent quality of the part is often limited by the height of burrs on a sheared surface, the microstructural damage imparted on the sheet, and the dimensional accuracy and the absence of splitting [7] [8].

Approach

In this project, we will further develop and mature a superior blanking process to enhance the room-temperature formability of aluminum sheets with improvements on existing trimming infrastructures. Our proposed approach is based on a new trimming method previously developed [7], [8], [9] with

various mechanisms of scrap/offal support, as well as extensions of the technology using other new and unique techniques. The goal of this work is to use a combined experimental and numerical approach to develop processing windows and parameters for preparation of stamping blanks that achieve robust, extended ductility compared to conventionally trimmed blanks. Our activities in FY14 focused on developing the experimental validated modeling framework for accelerating the development and subsequent implementation of the superior blanking process.

Results and Discussion

First, experimental studies were carried out to determine the flow behavior at large strains for AA61111-T4 sheets by the use of accumulated rolling and tension approach [10] by Oakland University and Ford. The previously determined three-section Ludwik parameters provide a flow curve rather close to the new data obtained through accumulated rolling and tensile test results. A better fit for the accumulated rolling and tension test data can be seen Figure III-29.

Based on the experiments at Ford and finite element (FE) analyses utilizing the integrated computational framework from trimming to stretchability simulations, it has been proposed that adding scrap support with the combination of a dull punch during the trimming process can improve the subsequent edge stretchability during tensile deformation, especially for the case of large trimming clearances. The simulation has demonstrated that fracture initiation location and propagation path have been altered during the trimming process, so that the burr and large deformation zone can be shifted to the scrap side. The facts of no burr and much smoother fracture surface leads to much less variation of later tensile stretchability (Figure III-30). The tensile ductility is greatly improved, especially for cases of large clearances. The predicted results have been validates with experimental

measurements, and very good agreements have been achieved under various trimming clearances.

In addition to the use of scrap support, the computational framework has also been used to examine various other factors in improving the edge stretchability. This is because trimming operation inevitably introduces cutting edge geometric features and large plastic deformations along the trimmed edge. Since the ultimate damage and fracture in aluminum alloys are controlled mostly by the excessive plastic deformation, we have examined the possibility of improving edge stretchability by removing the trimming-induced initial plastic strains (IPS). For those models traditionally trimmed, the FE simulations with IPS removed show that almost all models exhibit shear-type failure, while the tensile elongations are greatly improved (Figure III-31). Computational results in Figure III-31 indicate that edge annealing (i.e., removing the IPS at the trimmed edges) can significantly improve the edge stretchability during subsequent tensile deformation [11].
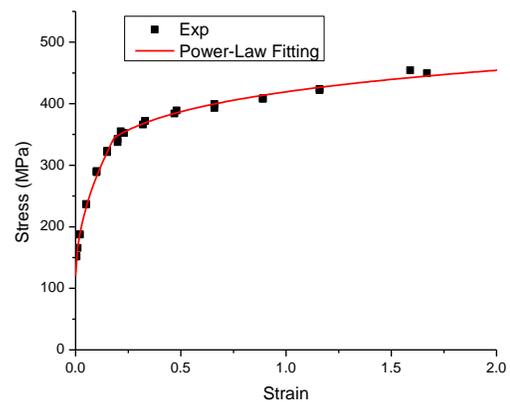
Figure III-29: The experimental and fitted flow curves for the AA6111 T4 alloy.

(a)   (b)
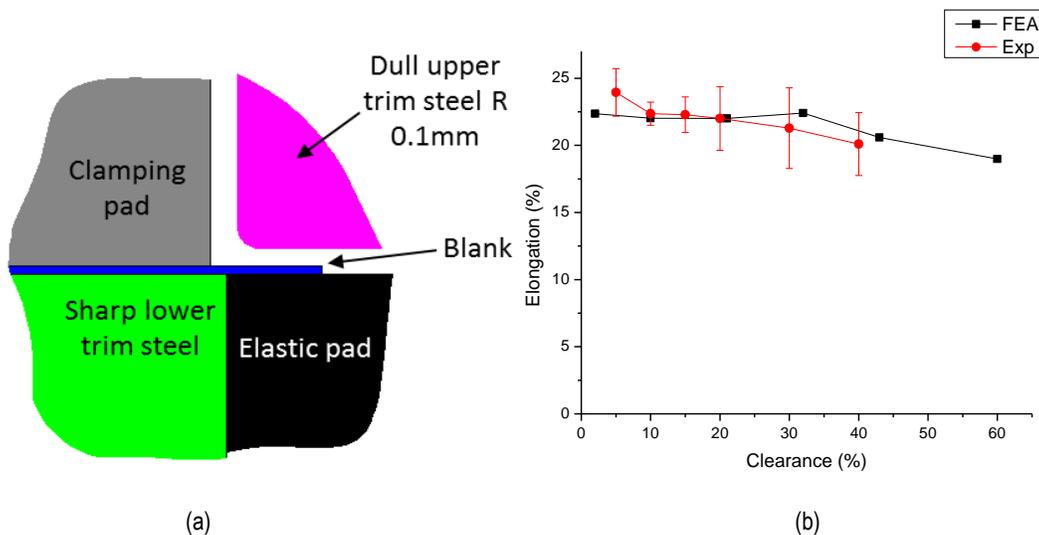
Figure III-30: (a) The advanced trimming geometry, (b) the tensile elongations predicted for advanced trimming with dull punch and scrap support in comparison with experimentally measured results.
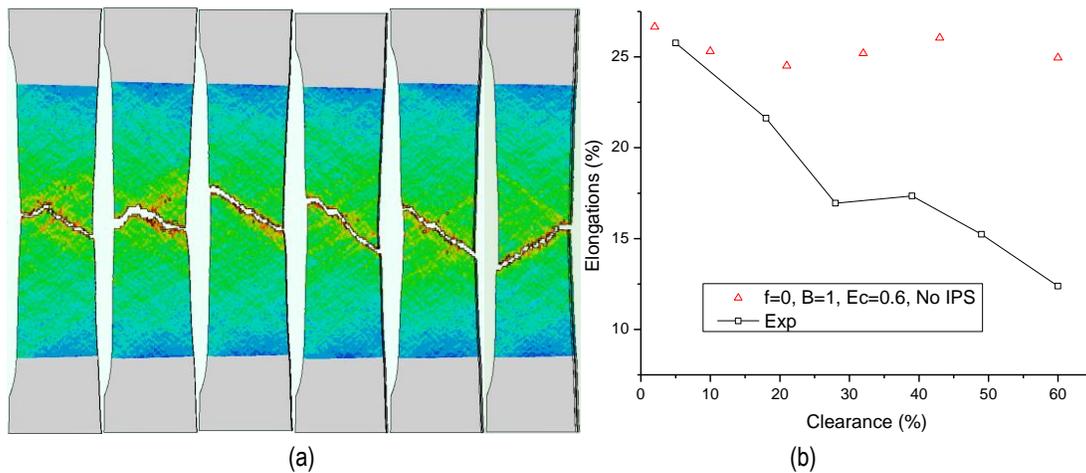
Figure III-31: Results of FE models of different cutting clearances from 2%–60%, where the IPS and damage are set to zero: (a) the equivalent plastic strain contours of the fractured samples and (b) the elongations in comparison with experiments without IPS removal.

The advanced trimming processes with scrap support and dull punch has been prototyped and demonstrated at Ford with the overall formability substantially improved (Figure III-32). This process slightly modifies the traditional trimming process by adding a scrap support under the aluminum sheet at the scrap side and utilizing a dull punch to facilitate a cracking process with a single crack initiated at the corner of the sharp lower trim steel and essentially eliminated the burr and leave the large indentation part with large deformation in the scrap side. The fracture surface of trimmed edge is also much smoother. The combined effects of all these improvements on trimming quality lead to a consistent stretching formability with small variation with cutting clearances and the safe strain has doubled those of conventional trimming process at clearances 30% and higher.
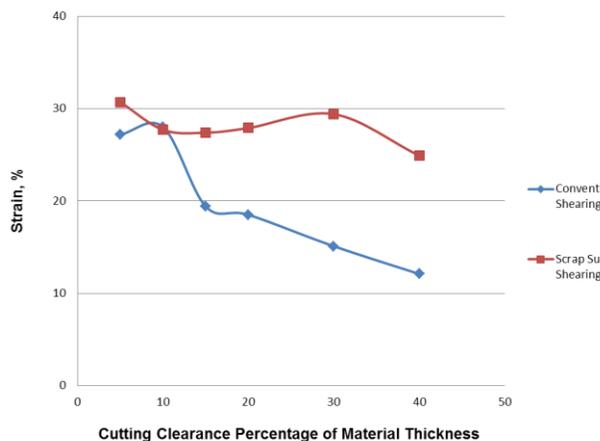
Figure III-32: Improved edge stretchability with scrap support.

Hole piercing – hole expansion and subsequent hole expansion experiments on AA6111 T4 sheets have also been performed in FY14 [12]. The hole piercing and expansion tests are based on the ISO16630-2009 hole expansion standard. Experimental hole piercing is far from ideal. As described in the trimming operations (Hu et al. 2014b), tool stiffness is one problem that can result in cutting clearance variations as the hole piercing process progresses. Another issue is that the punch cylinder may be off-center from the upper and lower cylindrical clamp tools, resulting in variable clearances along the edge of the hole. Cross-sections can be cut at different locations around the pierced hole. The actual clearances of these locations can be calibrated based on the method described by Hu [13]. Experimental results show that no burr is formed for nominal clearances less than 25%. For 30% clearance or larger, burrs are apparent.

Correspondingly, 2-D axis-symmetric hole piercing simulations using a ϕ10 mm hole were performed for six cutting clearances (δ): 5%, 10%, 15%, 20%, 30%, and 40%. The results of simulation in terms of equivalent plastic strain contour and demonstrates that almost no burrs formed at the part side of the sheet after hole piercing for clearances between 5% and 25%. On the contrary, burrs are observed at larger clearances, 30% and 40%. This corresponds quite well with experimental hole piercing results. The predicted hole piercing results on burr formation and variation both correspond well with experimental measurements.

The integrated framework developed previously is extended to incorporate the hole piercing results into the subsequent 3-D hole expansion simulations. The simulation results show more uniform deformation is experienced in the sheets pierced with less than 25% the hole punching clearances. For larger punching clearances of 30-40%, edge deformation during hole expansion is more concentrated at

the edge with very little deformation in the region away from the hole edges. The critical hole expansion ratio (HER) reflects this as well in the sense that the HERs change very little for the cases with clearances less than 20%, but then suddenly decrease significantly for clearances larger than 30%. The predicted HER trend with respect to increasing punching clearance corresponds well with experimental results.

Technology Transfer Path

Technology transfer of this project will be directly through Ford Motor Company and its Tier 1 suppliers. The broader commercialization of the technology through the Tier 1 suppliers will reach the entire automotive OEM industry.

Conclusions

In FY 2014, Ford and Oakland University continued their efforts on determining the stress-strain curves at large strains for AA6111-T4. New trimming experiments on AA6111-T4 aluminum sheets with scrap support (advanced trimming) have also been performed and the results are used as model validation. With the previously developed integrated computational framework on edge stretchability prediction, the

tensile stretching formability of previously trimmed part was successfully predicted in terms of ductility. These simulation results correlate very well with experimental observations. Experimental characterizations on sheared edge stretchability, edge crack initiation and propagation have also been conducted and used as model validation.

More sensitivity studies using this framework indicate that edge IPS removal processes (e.g., annealing) can significantly improve the stretch formability of previously trimmed edges in tensile deformation. The advanced trimming process demonstrated and validate above has been prototyped at Ford, and the results show that at least 50% improvement of stretching ductility can be achieved at room-temperature.

Hole piercing and subsequent hole expansion tests on AA6111-T4 have been performed at Ford and Oakland University. The corresponding piercing and hole expansion ratio predictions with the integrated modeling framework have been performed at PNNL, and the simulation results in terms of hole edge geometry and hole expansion ratio show good agreements with experimental results.

FY15 activities include hole punching with various clearances and subsequent hole expansion experiments with different aluminum alloys and simulations with the newly developed framework.

Curt A. Lavendar, Principal Investigator
Pacific Northwest National Laboratory
Phone: (509) 372-6770; Fax: (509) 444-4568
E-mail: curt.lavendar@pnnl.gov

Tim Skszek, Principal Investigator
Magna Cosma International
1807 East Maple Road
Troy, MI 48083
Phone: (248) 689-5512
E-mail: tim.skszek@cosmaeng.com

Accomplishments

- A novel extrusion system has been developed to produce fine-grained magnesium alloys.
  - The process is energy efficient
  - A Patent for the process has been filed with the USPTO
- A series of magnesium (Mg) alloys were cast and extruded to produce high-performance Mg alloys with fine grain sizes.
  - Grain sizes appear to be less than 5 μm.
  - Dispersions near 15 nm interact with dislocations.
- A Mg alloy containing no rare earth elements that was processed for fine grain size using a low-cost, high-shear extrusion process was shown to absorb energy similar to 6061 aluminum (Al)
  - This is a 20 percent mass savings over 6061.
  - The mode of failure is different.
- Microstructural modeling has been initiated to help understand the behavior and predict energy absorption.
- A new model for strength in Mg has been implemented using the phi theory.
  - Fracture of a hard second phase particle during high-shear processing has been modeled.

Future Directions

- Establish commercial goals for tubular Mg alloy extrusions and demonstrate high-strength in prototypic-size components
- Build an extrusion system to develop prototype

Technology Assessment

- Target: Develop high energy–absorption Mg alloys that do not contain rare earth elements and that can replace Al extrusions at a mass savings of 20 percent (based on density).

- Target: Use inverse process modeling to develop a low cost process to produce microstructures required for high-performance at a low cost, making Mg extrusion viable for automotive applications.
- Gap: Currently produced Mg alloys that possess high-strength and ductility (energy absorption) use rare earth elements, which increase cost and are of limited supply, resulting in reluctance of the automotive industry to use Mg extrusions.
- Gap: The cost to produce high-performance Mg extrusion has prevented use in automotive applications.

✧   ✧   ✧   ✧   ✧

Introduction

It has been demonstrated that the application of magnesium alloys in bumper beams, crush tips and intrusion beams would result in significant vehicle weight savings [14]. However, to increase the structural use of Mg alloys, development of cost-effective bulk metal forming methods are necessary. In this regard, extrusion technique, which is typically used to produce cylindrical bars or hollow tubes or even with complex cross-sections at a fairly rapid speed, is an important metal forming method to investigate. Several researchers have studied the role of different process variables during extrusion of Mg alloys It is to be noted that in all the above mentioned studies, extrusion experiments were conducted at elevated temperatures, since Mg alloys suffer from limited room-temperature ductility due to limited slip systems. In order to control the grain size of the extruded material the feed rates are kept to a low value or need to be followed by severe plastic deformation processes to refine the grain size. The purpose of this project is to develop and demonstrate low cost wrought Mg alloys that do not rely on rare earth alloying elements for their strength, ductility, and energy absorption properties. A novel low-cost processing method, in conjunction with Mg alloys containing rare earth substitutes, will be developed to produce the microstructure and properties needed for the automotive applications in a cost-effective manner.

Approach

The project is being performed in three phases. In the first phase, the project team produced high-performance alloys using rare earth additions to develop high-energy–absorbing microstructures that were used as model systems for non-rare earth alloys. The second phase of the project was to develop the microstructure found in Phase 1 to produce high-performance alloys without rare earth additions. During the second phase, at least one alloy will be selected and

processed for evaluation by Magna Cosma International for use in automotive applications that require additional formability such as bending or hydroforming. The third phase of the project will use an inverse process modeling method to develop a cost-effective processing approach to produce the alloy with the energy absorbing properties.

The following technical steps were planned and executed over the past two years along with steps forward:

- Produced rare earth-Mg alloy extrusions and performed mechanical tests comparing quasi-static tension and compression results to the Al alloy 6061 and the conventional Mg alloy AZ31.
- Evaluated energy absorption capability of the rare earth-Mg alloy via impact tests and compared to 6061 and AZ31.
- Evaluate—experimentally—the deformation mechanisms of the rare earth alloys using interrupted strain tests in tension and compression at room-temperature.
- Develop a continuum-level model to predict microstructure evolution and mechanical deformation behavior of Mg alloys during processing. Validate using experimental data.
- Select up to three alloys from the previous task, consolidate the materials by extrusion, and evaluate the non-rare earth alloys for strength and energy absorption characterization, at both quasi-static and elevated strain-rate tension tests.
- Produce sufficient material to provide partner Magna Cosma International with tubular extrusions that can be formed into shapes such as crush tips, roof structural support beams, etc., for testing and comparison to conventional materials.
- Develop the "Model Alloy" by implementing a statistical continuum mechanics model embedded with crystal plasticity. Use the model to predict grain size, dispersion, and textural effects.
- Use experimental data, crystal plasticity, inverse process path modeling, and laboratory trials to develop the necessary process to create the desired microstructure using an optimum low-cost, high-shear processing route.
- Prototype and demonstrate a small system that will produce extruded shapes by fracturing the coarse intermetallics and developing the strain needed for the fine grain size (as predicted by the inverse modeling) and provide the driving force for the subsequent extrusion.
- Magna Cosma International will evaluate extrusions produced by the system for formability. Billets produced by the process will be extruded at PNNL and subjected to formability tests using warm gas-pressure forming.

Results and Discussion

1. Modeling: Defining the Grain Size and Mechanical Properties using ICME

1.1 Effect of grain size on the mechanical properties and Compression tension yield asymmetry:

Strengthening of magnesium alloys is usually performed by grain refinement or by alloying additions. The current authors [15] and others [16] [17] have also demonstrated that the yield asymmetry i.e. the ratio of compressive yield stress and tensile yield stress (CYS/TYS) is drastically improved as the grain size decreases (Figure III-33). It was demonstrated using polycrystalline viscoplasticity model that as the grain size is decreased, the twinning in Mg is suppressed and compressive yield strengths are increased. Conventionally processed Mg alloys have a compressive strength normally 70 percent that of the tensile strength, resulting in buckling during bending and compression. In addition, a significant increase in ductility can be expected when the grain size decreases. Therefore the fine-grained alloy should be expected to absorb more energy, which is critical to the current applications under consideration.
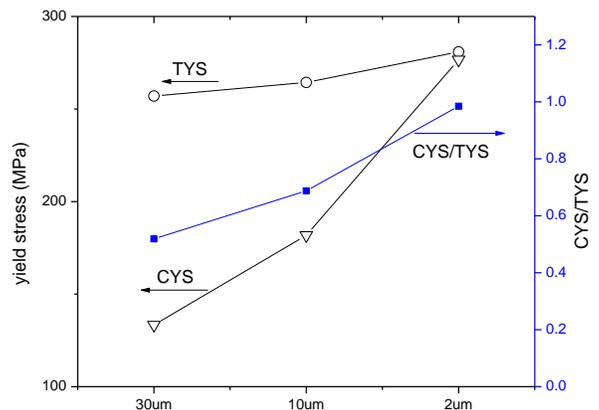
Figure III-33: Tension and compression yield stress and CYS/TYS along rolling direction for rolled AZ31 sheets with different grain sizes of 30 μm, 10 μm and 2 μm, respectively[1].

1.2 Effect of precipitate size and volume fraction on the mechanical properties and Compression tension yield asymmetry:

In order to understand the effect of precipitate size on the grain size and the mechanical properties; the simulation was performed quantitatively by coupling a stochastic second phase grain refinement model and a modified polycrystalline crystal viscoplasticity φ-model. The models were developed assuming dispersion of hard intermetallics having aspect ratio 1:2 in an unalloyed magnesium matrix. The details of which can be found elsewhere [18], however significant results will be discussed here. Using the stochastic second phase grain

refinement model, grain size was quantitatively determined from the precipitate size and volume fraction as shown in Figure III-34. It was determined that if the precipitate shape and size are kept constant, grain size decreases with increasing precipitate volume fraction. If the precipitate volume fraction was kept constant, grain size decreases with decreasing precipitate size during precipitate refinement. The stochastic effect with length scale was also studied. The grain size variance was large when the precipitate volume fraction was low and the precipitate size was large. Yield strength in different directions (yield asymmetry), and deformation behavior are calculated from the modified φ-model and the results are shown in Figure III-35a and Figure III-35b. The mechanical behavior of magnesium alloys was also improved by precipitate refinement. Yield strengths and asymmetry increase with decreasing grain size and contributions from increasing precipitate volume fraction or decreasing precipitate size. The evolution of yield strengths and asymmetry with precipitate volume fraction and size has been quantitatively simulated by coupling the stochastic grain refinement model and modified φ-model. This provides guidance for second phase strengthening via precipitate engineering, both for precipitate content control and precipitate refinement.

With these tools in hand selection of alloys was primarily decided based on the secondary precipitate form, shape and highest plausible strength attainable. Strengthening using second phase particle currently is being employed using rare earth elements. Despite the advantages the cost of these alloys is disruptive and thus alternatives are being sought [19]. Aluminum Zinc (AZ), Zinc-zirconium (ZK) based magnesium

alloys and magnesium silicon (Mg-Si) alloys do provide alternatives to the current alloy system. These alloys used in extruded or cast conditions usually have large grain sizes or in the case of Mg-Si alloys have large brittle Chinese script or blocky Mg_2Si precipitates. These large grains and phases are usually associated with lowering of the strength and causing anisotropy in the material. In order to combat this fine dispersion of precipitates would eliminate the anisotropy and refine the grain size.
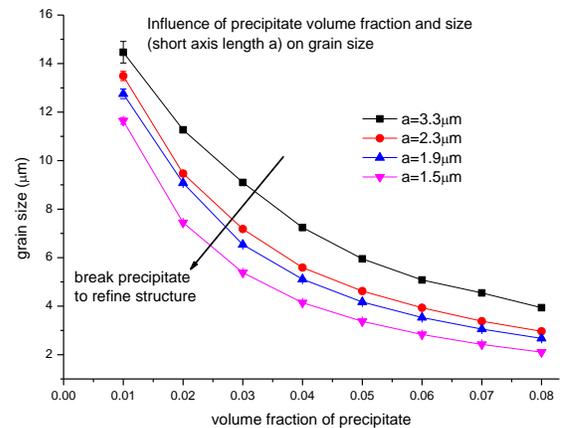
Figure III-34: Evolution of grain size with precipitate volume fraction and size.
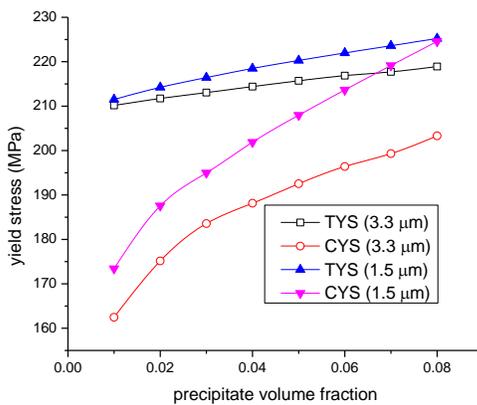
(a)
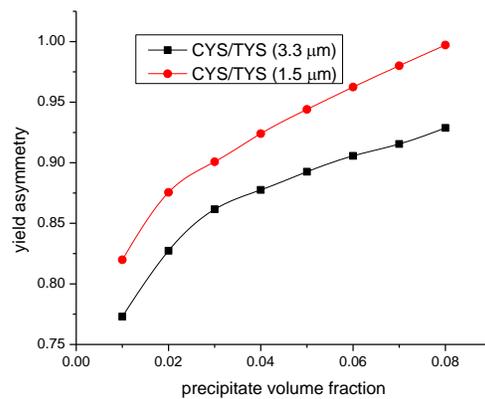
(b)

Figure III-35: Evolution of (a) yield strengths and (b) yield asymmetry with precipitate volume fraction when the precipitate size is kept constant.
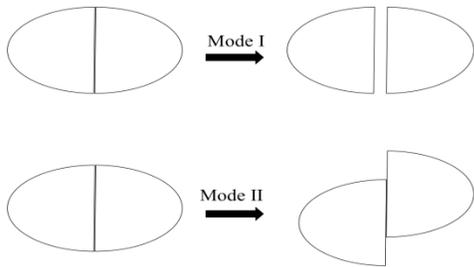
Figure III-36: Schematic illustration of the 2D version of Griffith's brittle failure criterion.

1.3 Modeling the Precipitate Refinement in Mg Alloy in High temperature deformation

By taking advantage of a recently developed analytical model, the stress field inside a single elliptical α-Mg17Al12 precipitates embedded in a rate dependent inelastic AZ31 Mg alloy was determined in two different loading conditions. The effects of fracture of the precipitates as a function of aspect ratio and their orientation were studied using Griffith Criteria (Figure III-36). In plane-strain compression, mode-I failure, which is an extensional mode, always fragments the precipitates. The strain rate at which the precipitate fails strongly depends on the orientation of the precipitate with respect to direction of loading. When the major semi-axis of the precipitate is oriented along global x-axis, a strain rate of 1180 (s^{-1}) splits the precipitate while if the orientation is 45°, precipitate failure occurs at strain rates in the order of 10^{-3} s^{-1}. Refinement happens in circular precipitates (unity aspect ratio) at ultra-high rates, in the order of 10^4 s^{-1}. In pure shear loading, in addition to mode-I of precipitate failure, mode-II which is a shear mode, may get activated depending on the orientation of the precipitate (Figure III-37).

2. Process Development

The current technique of torsional shear assisted indirect extrusion process (SAIE) uses a rotating ram as opposed to the axially fed ram used in the conventional indirect extrusion process. The ram face contains scroll features in a spiral manner. When the rotating ram face comes in contact with the solid billet underneath and a forging load is applied, significant heating occurs due to friction, thus softening the underlying billet material. The combined action of the forging load together with the rotating action of the ram face, force the underlying material to flow plastically. The scroll features on the ram face are believed to help in the material flow. The ram is turned in such a way that scroll features rotate towards the center of the ram, and, thus material is fed continuously to the central hollow inside the ram. The deformation process adds additional heat to the process. Significantly low ram load has been noted in this process compared to conventional extrusion process, which is possibly related to the rotational motion of the ram. The mandrel in the center of the ram helps in forming of the tubes.

Figure III-39 shows the plots of ram plunge depth as a function of load and spindle torque respectively. It was observed that as the ram plunges into the puck, a breakthrough pressure and torque is required to achieve steady state conditions similar to direct extrusion. The response in vertical load build-up as a function of plunge depth during this process is similar to that observed during plunging stage of the Friction Stir Welding (FSW) process. The initially cold billet material offers resistance to flow, and hence high load is noted. As the material heats up due to friction/deformation at the ram/billet interface, it starts flowing, thus lowering the process load considerably. It is interesting to note the presence of two peaks in the load-depth plot. It is likely that the first peak corresponds to initial resistance of the cold billet, while the second one corresponds to frictional resistance at the ram throat as the extrudate tries to move up through the gap between mandrel and the inner ram wall. However, it should be noted that the process load required for current technique is considerably lower than the conventional indirect extrusion technique. The peak pressure in this case was approximately 90% less whereas the operating pressure was approximately 95% less than the one required in indirect extrusion of the similar material.
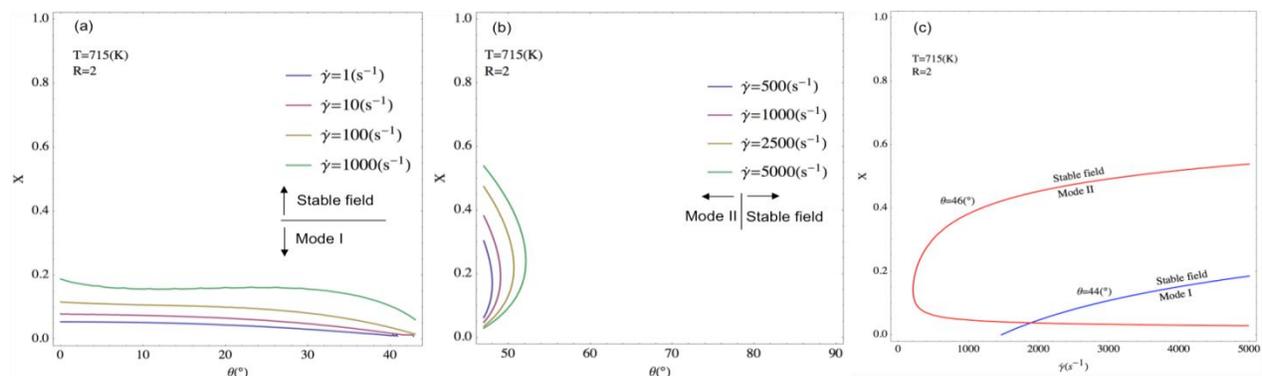
Figure III-37: Failure maps in pure shear; (a) in the situations that mode-I governs and (b) in situations that mode-II governs. (c) shows the failure map close to mode-I/II transition.
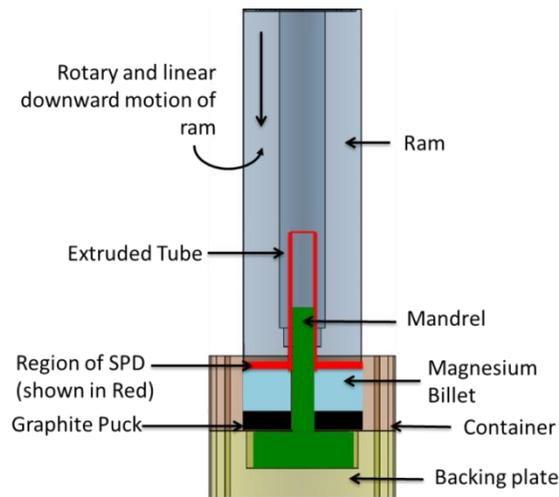
(a)

(b)

(c)

Figure III-38: (a) Diagram of the SAIE process and (b,c) shows the scrolls on the face of the ram which assists in heating and flow of material.
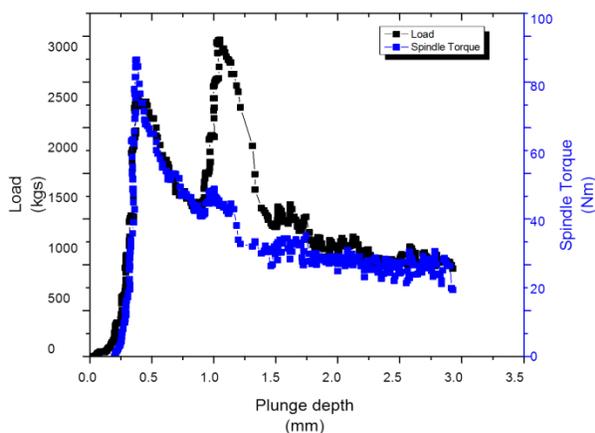
Figure III-39: Extrusion load and torque on the ram during the extrusion of ZK60 as a function of ram plunge depth.

The formed tubes and a cross-sectional image (only half section) of the billet and the extruded tube is shown in Figure III-40. We were able to extrude 5" tall tube at the end of this process. The tube was homogenous with no porosity and had a uniform cross-section with an outer diameter (OD) of 7.45 ± 0.02 mm and an ID of 5.84 ± 0.03 mm. The flow behavior in the underlying billet is shown in Figure III-40b. Formation of a basin shaped region near the top surface of the billet can be clearly noted in this micrograph. A closer observation reveals that the original column-like grain structure of the as-received material has ceased to exist in this basin shaped region. Further examination of the micrograph showed the presence of a flow pattern, as indicated by the white and the red arrows. It is likely that the material present on the top layer softened as the billet heated up. Under the combined action of ram rotation and the extrusion pressure, this softened layer of material tried to flow downwards and towards the center of the ram. As it reaches the central region,

it is forced to move upwards since the material at bottom layer of the billet is relatively cooler, and hence stronger. Finally, the softened material extrudes through the gap between the inner ram wall and the mandrel. Presence of scroll features on the ram face facilitated in this material movement.

The cross-sectional analysis of the extruded tube revealed the grains to be oriented ~ 30° to the extrusion axis, indicating a spiral flow pattern. Figure III-41 depicts the microstructures of the extruded ZK-60 sample, near the billet, approximately 2" from the billet and approximately 4.5" from the billet respectively. The grain size was the finest near the ram face/billet interface and had a grain size of ~ 2-5 μm. The grain structure was uniform from the outer diameter to the inner diameter. The grain size is noted have increased by almost 50% along the length of the extrudate (Figure III-41). The grain size at the outer edge was slightly smaller than the inner edge indicating recrystallization and differential cooling rates. It was observed that the basal planes were oriented 45° to the extrusion axis (Figure III-41c) and the scroll profiles were responsible for the same.

(a)   (b)
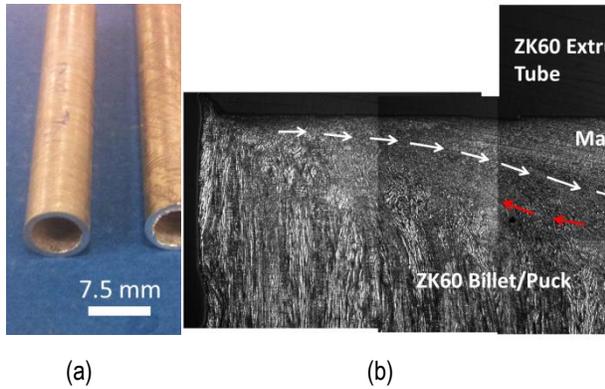
Figure III-40: (a) Formed tube, showing the uniform cross-section and defect free surface and (b) montage showing the possible material flow pattern in the puck/billet during the formation of the tube.

(a)

(b)

(c)
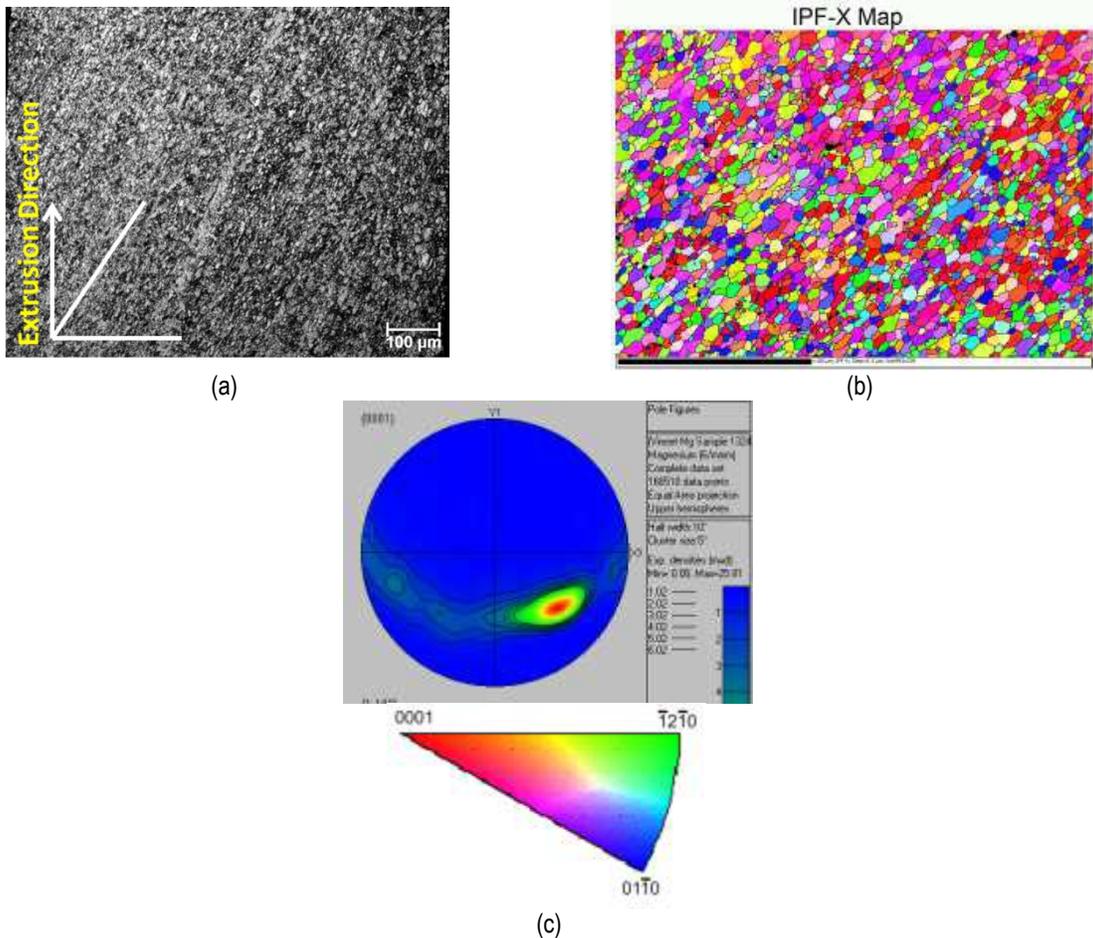
Figure III-41: (a) Optical image showing the ZK60 tube longitudinal cross-section at the central region of formed tube and (b) Inverse pole figure (IPF) of the same region and (c) texture analysis of the same.

The current process demonstrated pressures significantly lower than the ones used currently to process magnesium alloys. Preheating of the billets may not be needed. The scroll pattern is responsible to directly change the orientation of the grain alignment and hence the texture (not shown here). All this provides significant opportunities towards cost reduction of the end product without compromising the properties and at the same time tailoring the microstructure to the desired properties.

Technology Transfer Path

The technology transfer for this project will occur late in Phase 2 and during Phase 3. The initial phase will be focused on laboratory development and understanding the Mg alloys from a mechanistic standpoint. After the alloy is understood, the technology transfer will occur in two ways: 1) produce and deliver tubes to Magna Cosma for evaluation; and 2) transfer process knowledge to Transmet, Inc., and Magnesium Electron North America (MENA). MENA has already contributed alloy feedstock for the high-shear extrusion processing and has played an active role in alloy selection.

Magna Cosma and MENA are cost-sharing partners in the project, and Georgia Institute of Technology and Transmet are subcontractors and were engaged in the project during the appropriate phases.

Conclusions

A novel method for high-shear extrusion of tubular shapes was developed and demonstrated; a formal patent is to be filed.

A fine-grained Mg alloy containing no rare earth elements, ZK60A, was shown to absorb energy similar to Al alloy 6061 when processed using a commercially viable alloy and the novel high-shear extrusion process.

A new method called the phi model was developed to predict strength in magnesium alloys. Initial modeling results will be used as a guide for extrusion process development to produce desired grain size and texture for high energy absorption. Initial results indicate that the Mg_2Si alloy may be absorbing energy due to a texture that is favorable for compression, whereas ZK60A appears to have an inherently more isotropic microstructure.

A method to predict the fracture of particles in combined stresses under hydrostatic stress was developed. The method is used as a guide to select process conditions for extrusion and control the morphology of the eutectic constituent particles in the as-cast structure.

III.9   Aerodynamic Lightweight Cab Structure Components

Aashish Rohatgi, Principal Investigator
Pacific Northwest National Laboratory
Phone: (509) 372-6047; Fax: (509) 375-4448
E-mail: aashish.rohatgi@pnnl.gov

Mark T. Smith, Principal Investigator
Pacific Northwest National Laboratory
Phone: (509) 375-6905; Fax: (509) 375-4448
E-mail: mark.smith@pnnl.gov

Nona Larson, Industrial Partner
PACCAR Technical Center
12479 Farm To Market Road
Mount Vernon WA 98273
Phone: (360) 757-5365
E-mail: nona.larson@paccar.com

Accomplishments

- Completed fabrication of 25 left- and right-hand A-pillar covers at Magna Stronach Centre for Innovation (SCFI), a Tier-1 supplier for PACCAR. (FY 2014)
- Completed mechanical testing on the as-fabricated and paint-baked A-pillar covers. The paint-bake yield strength was ~132 MPa which, although lower than the target 180 MPa, is acceptable for the proposed application. The paint-bake failure strain was >23% (engineering) and exceeded the target strain of 15%. (FY 2014)

Future Directions

- Evaluate the E-coat response of the A-pillar covers using PACCAR's production E-coating procedures.
- Install A-pillar covers on PACCAR's test cabs and perform cab shake-tests.
- Investigate the microstructural evolution and the hardening mechanisms in the X608 Al alloy used for fabricating the A-pillar covers.

Technology Assessment

- Target: Develop an elevated-temperature hot-forming process, combined with a cold-finish forming process that can increase the useable elongation and formability to the equivalent of over 40 percent for a 6000-series Al sheet alloy.
- Target: Demonstrate the feasibility of hot-forming complex Al sheet components requiring overall formability levels of up to 40 percent equivalent tensile elongation, while meeting mechanical property and finish requirements for exterior cab component applications.
- Gap: Current 6000-series Al sheet alloys have desirable strength levels and surface finish characteristics, but lack sufficient formability (>18-20 percent tensile elongation) to allow their use in the manufacture of many aerodynamic cab components and structures.
- Gap: Existing Al hot-forming processes typically result in formed sheet tensile properties below 100 MPa yield strength. This limits the use of hot-formed Al sheet in applications that require higher strengths (150 MPa) for long-term fatigue and dent resistance.
- Gap: Room-temperature Al forming processes result in mechanical properties with insufficient final-formed ductility. This limits its use in applications where residual ductility is required for riveting and hemming assembly operations.

✧   ✧   ✧   ✧   ✧

Introduction

The objective of this project is to demonstrate lightweight materials manufacturing methods that will increase the efficiency of Class 8 trucks by enabling more wide-spread use of mass-saving Al and enabling aerodynamic styling through the use of a new approach to Al sheet forming. The project will develop forming technology that will enable Al sheet to replace steel sheet and molded fiberglass reinforced composite panels and components, providing individual panel and component weight savings of approximately 40 percent.

Approach

The project will use a combination of elevated-temperature and room-temperature forming process, which has been developed at PNNL, to demonstrate enhanced formability in 6000-series Al alloy sheet. The high ductility forming process will enable PACCAR member companies to design prototype cab components with aerodynamic features that would otherwise not be feasible to manufacture. PNNL will develop and optimize a hot-forming plus cold-forming process using sheet tensile specimens and PACCAR will evaluate surface conditions and corrosion behavior of formed specimens. Based on the selected process parameters, PNNL and PACCAR will design and build a prototype component for laboratory testing. The technology for the process developed at PNNL will be transferred to a Tier-1 supplier and project partner, Magna SCFI, who will build full-scale prototype components. PACCAR will then finish the parts and perform durability testing (e.g., fatigue and corrosion testing). Planned technical steps and milestones include conducting elevated-temperature tensile tests at various strain-rates on the alloy provided by PACCAR to develop a constitutive materials relation for use in forming analysis. This data will provide a basis for selection of the temperature and strain-rates for subsequent forming trials.

The alloy selected for this work is a Novelis X608 Al alloy. Based on the forming trials in the previous reporting period (FY 2013), the optimum thermo-mechanical processing conditions were determined to fabricate a full-scale prototype of an A-pillar cover. A schematic of the A-pillar cover is shown in Figure III-42a. The forming process comprised an initial solutionizing treatment at ~525°C followed by water quenching. The quenched sheet was then partially formed in a die at room-temperature. The preform was then re-solutionized and quenched as in the first step. Finally, the quenched preform was finished in a restrike operation in a die at room-temperature to create the flanges. Thus, using the above mentioned procedure, Magna SCFI completed fabrication of 25 pairs of left- and right-hand A-pillar covers that were delivered to PNNL for subsequent analysis.

Several as-received A-pillar covers were chosen at random and subjected to a simulated paint-bake heat-treatment (180°C-20 minutes). Both as-received and paint-baked A-pillar covers were characterized by tensile testing, hardness testing and electrical conductivity measurements. A naming convention was established to identify each A-pillar cover (e.g., R33, L37, R30 and L7, in Figure III-42). The location within an A-pillar cover was identified by letters (e.g., A, B, C, D) or numbers (e.g., #1, #2, etc.). Tensile coupons were machined out of two as-received and two as-received + paint-baked covers (see Figure III-42b). Thus, a total of four coupons per cover, i.e. 8 coupons per heat-treat condition (as-received or as-received + paint-baked) were tensile tested quasi-statically at room-temperature. The hardness and electrical conductivity of the A-pillar covers were measured along their length. Rockwell H scale was used for hardness measurements while a 1/8" diameter, 60 kHz sensor was used for eddy current testing.

Results and Discussion

Figure III-43a and Figure III-43b show the tensile stress-strain curves of the coupons from the four pillar covers shown in Figure III-42b. The data in Figure III-43 shows that the average 0.2% yield strength of the as-received pillar covers was ~117 MPa while that of paint-baked covers was ~13% greater at ~132 MPa. The strain to failure for all the samples was >23%, thus, exceeding PACCAR's requirement of 15% elongation in the post-formed part. Considering that the elongation is 50% greater than the target, it might be possible to increase the strength to 150 MPa or more, at the expense of ductility, through varying the processing conditions (e.g., solutionizing temperature, hot/cold-forming schedule, etc.) while still meeting the 15% tensile elongation target. The value and feasibility of modifying the processing approach to meet /exceed 150 MPa-15% elongation targets will be determined in discussions with PACCAR and Magna. The data in Figure III-43 also shows, for any given pillar, a systematic increase in the strength (as high as ~11% increase) of the test coupons going from location #A to location #D. While the increase in average strength after paint-bake can be attributed to age-hardening, the strength variation within any given pillar is likely due to variation in the extent of solutionizing/aging caused by non-uniformity of the temperature along the cover's length during the fabrication process.

(a)   (b)
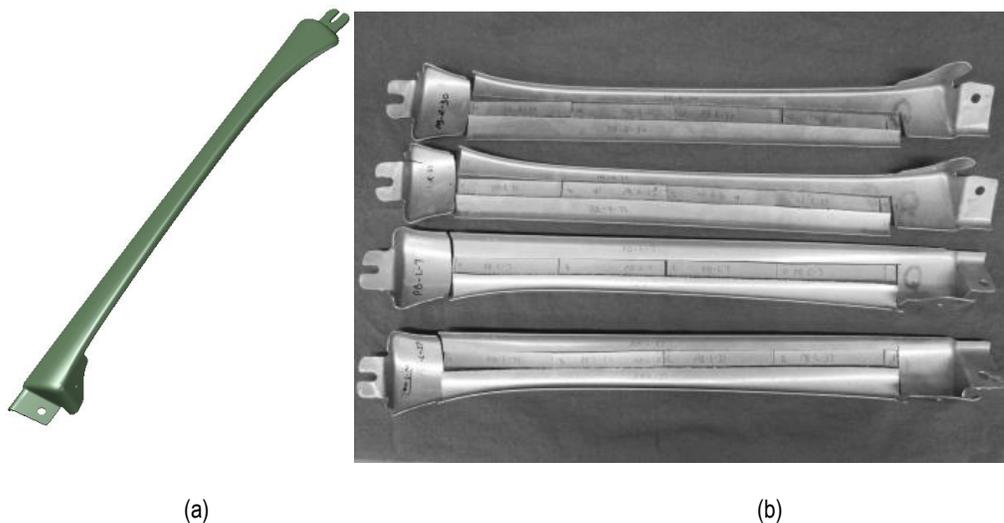
Figure III-42: (a) A schematic of the A-pillar cover. (b) Photograph of 4 A-pillar covers with cut sections showing the locations where the tensile coupons were obtained from along a cover's length.

(a)　　　　　　　　　　　　　　　　　　　　　(b)
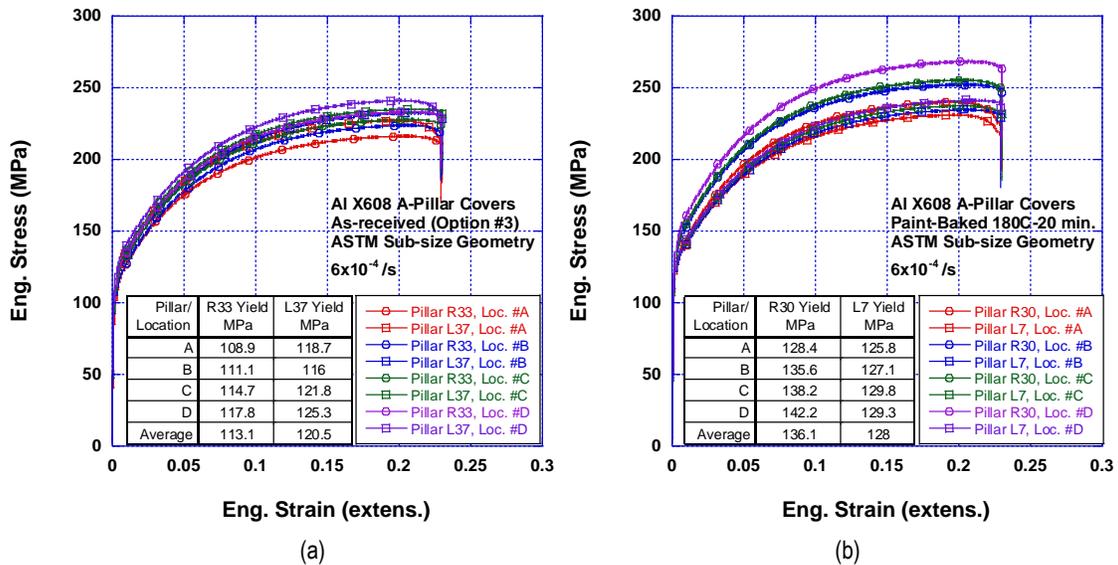
Figure III-43: Quasi-static stress-strain data of A-pillar covers in the (a) as-received and (b) paint-baked conditions. The specimens failed at an engineering (Eng.) strain somewhat greater than 23%. However, the failure strain exceeded the physical limits of the extensometer (extens.) and hence, extensometer strain >23% could not be recorded. As a result, the specimens "appear" to fail abruptly at 23% strain.

(a)　　　　　　　　　　　　　　　　　　　　　(b)
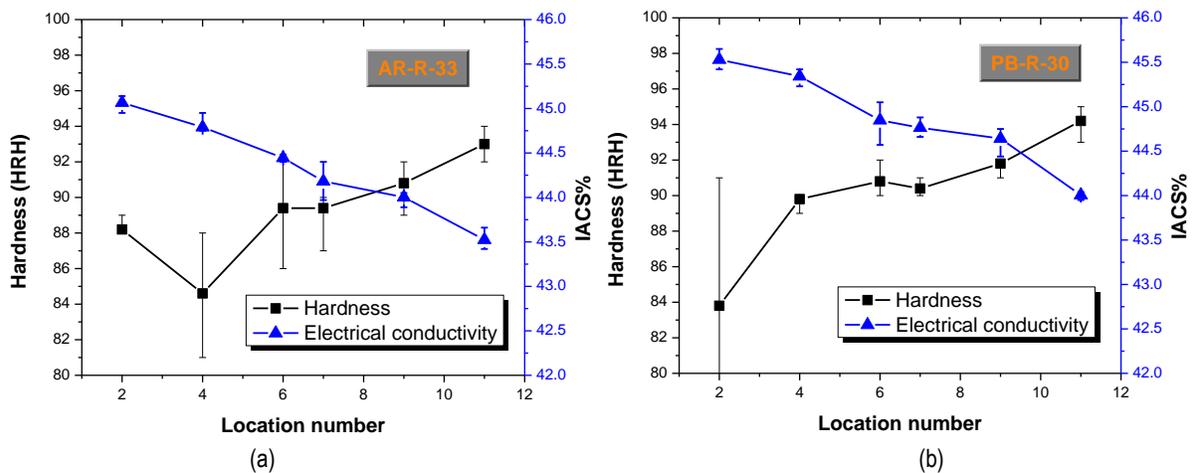
Figure III-44: Rockwell hardness and electrical conductivity in an (a) as-received and (b) paint-baked A-pillar cover. The x-axis (location number) refers to locations marked along the A-pillar cover's length. "AR" = as-received, "PB" = Paint-baked. Rockwell "H" scale, HRH: 1/8" dia. ball indenter with 10 kgf minor load and 60 kgf major load.

Figure III-44 shows the hardness and electrical conductivity variation along the length of an A-pillar cover. The data shows that the hardness increases along the length of the A-pillar cover (from location #2 to location #11). Since the Novelis X608 Al alloy used in this work is age-hardenable, hardness variation within a given A-pillar cover is believed to be related to non-uniform temperature distribution during solution heat-treatment in the pre-heat furnace. In other words, the sheet locations subjected to a higher temperature (e.g., #10, #11 and higher) were likely to have greater concentration of alloying elements in solution and result in greater precipitation hardening during aging than the locations heated to a lower temperature (e.g., #2, #3 etc.) that would show lower precipitation hardening response on account of

incomplete dissolution of solutes. It is also seen in Figure III-44 that the hardness in the selected as-received and as-received + paint-baked cover is quite similar. It is possible that the increase in hardness upon paint-bake may be of similar magnitude as the pillar-to-pillar scatter in the hardness.

The explanation for the trend in electrical conductivity observed in Figure III-44 requires additional work since hardness-conductivity trend for X608 Al alloy is not available in the literature. Further, existing literature on Al alloys suggests that hardness-conductivity trend is not linear and may be alloy specific as well. For example, Faisal et al. [20] observed an increase in both conductivity and hardness in AA2014 Al alloy, associated with GP zone formation and θ'

precipitation during artificial aging. On the other hand, Wu et al. [21] observed a decrease in conductivity and increase in hardness in AA7050 Al alloy associated with GP zone formation. Moreover, the conductivity-hardness trend changed with further progress of precipitation (Wu et al. 1996). Thus, an explanation of the hardness-conductivity trend observed in the A-pillar covers made from X608 requires additional work on this alloy with a focus on understanding the relationship between the precipitation sequence, hardness and electrical conductivity.

Technology Transfer Path

PACCAR and its Tier-1 supplier, Magna SCFI, are the key industrial partners that are helping to transfer the technology developed in this task to commercialization. PACCAR and its two truck companies have multiple applications in which high formability and good post-forming properties of the Al alloy sheet would allow them to replace low-strength glass-fiber composites in highly shaped aerodynamic panels and components. PNNL has developed the processing parameters for the Al alloy relevant to PACCAR and transitioned that knowledge to Magna SCFI and enabled them to fabricate a full-size prototype component. This component is now being evaluated at PACCAR for the feasibility of integrating it within their production vehicles.

Conclusions

In FY14, the project made significant progress, as demonstrated by the successful fabrication of 25 pairs of full-size A-pillar covers by Magna SCFI. This activity signifies a successful transition of laboratory-developed processing conditions to a Tier-1 supplier for fabricating a full-size prototype part. This activity also enabled the team to identify potential issues, e.g., size of heating furnaces and the temperature uniformity, that need to be considered if this component (or any other potential component) goes to full production in the future. PNNL has performed initial evaluation of the prototype components to verify if the strength and elongation targets were met. There is scope for improvement with regards to the post-formed strength but that is not expected to be a major concern. The components have been sent to PACCAR for evaluation with respect to dimensional fit, assembly, cab finishing process steps and durability testing.

Conclusions

The Processing & Manufacturability project is focused on research and development activities advancing the basic mechanical properties, manufacturability, and cost of lightweight materials towards the levels needed for increased implementation in automotive applications. This project includes five different tasks with unique scope and leadership that each addresses an aspect of the materials challenges limiting implementation of lightweight materials solutions in current or planned automotive applications. The following

highlights summarize the accomplishments of the tasks in this project:

- *Microstructure and Deformation Fundamentals in Lightweight metals:* During the 2014 fiscal year this task developed an elasto-plastic self-consistent model that allowed for mechanical properties of constituent phases to be determined. Measurements were made to determine the carbon distribution between retained austenite using nano-secondary ion mass spectrometry tests, which in conjunction with nano-indentation provided the material data necessary to develop new heat-treatment parameters to support third generation high strength steels. With the developed characterization and modeling tools, the 2nd and 3rd heats of the model steel have been processed, both with tensile strength >1500MPa and ultimate elongation >20%.

- *Enhanced Room-Temperature Formability in High-Strength Aluminum Alloys through Pulse-Pressure Forming* focused this year on quantitatively understanding the mechanical behavior of AA7075. This included determining the influence of natural aging and strain on the age hardening curves, as well as quantitatively evaluating the room-temperature formability of different tempers across a variety of strain-rates.

- *Aluminum Formability Extension Through Superior Blanking Process*: This year PNNL in collaboration with project partners utilized the previously developed integrated framework successfully predicted and validated more than a 50% enhancement of tensile stretchability for large trimming clearances. The process was prototyped and demonstrated at Ford Motor Company. Additionally, this task advanced beyond linear edge effects and performed hold piercing simulations and experimentation to support model development and validation.

- *Non-Rare Earth High-Performance Wrought Magnesium Alloys:* This task has focused on both the production and processing of Mg alloys without rare earth elements. In the 2014 fiscal year, we utilized a novel extrusion system to produce fine-grained magnesium alloys that had been cast with no rare earth elements. Mechanical evaluation of this material demonstrated energy absorption similar to AA6061, with a 20 percent mass savings over the same.

- *Aerodynamic Lightweight Cab Structures*: This fiscal year focused on working with suppliers to fabricate prototypical hardware (A-pillar covers) for evaluation at both PNNL and in service by PACCAR. Mechanical testing of these A-pillar covers demonstrated acceptable performance with mixed benefits.

Presentations/Publications/Patents

1. Choi, J.P.; Rohatgi, A.; Smith, M.T.; Lavender, C.T. (forthcoming). "Process Development for Stamping A-Pillar Covers with Aluminum." *TMS 2015 Conference Proceedings*.

2. Choi, K.S.; Hu, X.; Sun, X.; Taylor, M.; De Moor, E.; Speer, J.; Matlock D. (April 2014). "Effects of Constituent Properties on Performance Improvement of a Quenching

and Partitioning Steel." Prepared for SAE 2014 World Congress, April 8-10, 2014, Detroit, Michigan.

3. Choi, K.S.; Zhu, Z.; Sun, X.; De Moor, E.; Taylor, M.D.; Speer, J.; Matlock, D.K. (forthcoming). "Determination of Carbon Distribution in Quenched and Partitioning Microstructures Using Nano Secondary Ion." *Mass Spectroscopy*.

4. Rohatgi, A.; Davies, R.W.; Stephens, E.V. (April 2014). "An Experimental Investigation of Room-temperature Formability of AA7075 Aluminum". Prepared for SAE 2014 World Congress and Exhibition, April 8, 2014, Detroit, Michigan.

5. Hu, X.; Choi, K.S.; Sun, X.; Ren, Y.; Wang, Y.D. (forthcoming). "Determining Individual Phase Flow Properties in a Q&P Steel with In-situ High Energy X-ray Diffraction and Multi-Phase Elastic-Plastic Self-Consistent Method." *Metallurgical and Materials Transactions A.*

6. Joshi V.V.; Jana S.; Li, D.; Garmestani, H.; Nyberg, E.A.; Lavender, C.A. (2013). "High Shear Deformation to Produce High Strength and Energy Absorption in Mg Alloys." *Magnesium Technology 2014*. PNNL-SA-98774, Pacific Northwest National Laboratory, Richland, WA.

7. Lavender, C.A. et al. Provisional Patent Application No. Battelle IPID 30343-E PROV.

8. Li, D.S.; Ahzi, S.; Wen, W.; M'Guil, S.; Lavender, C.; Khaleel, M.A. (2014). "Modeling of Deformation Behavior and Texture Evolution in AZ31 Magnesium Alloy using the intermediate phi-model." *International Journal of Plasticity*, 52, pp. 77-94.

9. Li D.; Joshi, V.V.; Lavender, C.A.; Khaleel, M.A.; Ahzi, S. (2013). "Yield Asymmetry Design and Crashworthiness Improvement of Magnesium Alloys by Integrated Computational Materials Engineering." *Proceedings of The Minerals, Metals & Materials Society 2014 Conference*, San Diego, CA. PNNL-SA-97063.

10. Li D.; Joshi, V.; Lavender, C.A.; Khaleel, M.; Ahzi, S. (2013). "Yield Asymmetry Design of Magnesium Alloys by Integrated Computational Materials Engineering". *Computational Materials Science* 79, pp. 448-455. http://dx.doi.org/10.1016/j.commatsci.2013.06.045

11. Li, D.S.; Lavender, C. (forthcoming). "Strengthening and Improving Yield Asymmetry of Magnesium Alloys by Second Phase Particle Refinement under Guidance of Integrated Computational Materials Engineering." *Journal of Engineering Materials and Technology*.

12. Li, D; Lavender, C.A.; Nyberg, E.A; Sun, X.; Khaleel, M.A. (2011). "Modeling of Deformation Behavior of Multiphase Wrought Magnesium." *Proceedings of The Minerals, Metals & Materials Society 2013 Conference*, Orlando, FL. PNNL-SA-81747, Pacific Northwest National Laboratory, Richland, WA.

13. Pan, W.; Li, D; Tartakovsky, A.M.; Ahzi, S.; Khraisheh, M.; Khaleel, M.A. (2013). "A New Smoothed Particle Hydrodynamics Non-Newtonian Model for Friction Stir Welding: Process Modeling and Simulation of Microstructure Evolution in a Magnesium Alloy."

International Journal of Plasticity 48, pp. 189-204. doi:10.1016/j.ijplas.2013.02.013

14. Rohatgi, A.; Davies, R.W.; Stephens, E.V.; Soulami, A.; Smith, M.T. "An Experimental and Modeling Investigation on High-rate Formability of Aluminum." In Light Metals 2014, ed. J. Grandfield, *Proc. TMS 2014, 221-225,* San Diego, California.

15. Rohatgi, A.; Soulami, A.; Stephens, E.V.; Davies, R.W.; Smith, M.T. (2014). "An Investigation of Enhanced Formability in AA5182-O Al during High-rate Free-forming at Room-temperature: Quantification of Deformation History." *Journal of Materials Process Technology* 214 pp. 722-732.

16. Smith, M.T. "Aerodynamic Lightweight Cab Structure Components." (June 2014). Prepared for 2014 DOE Annual Merit Review, Washington, D.C.

17. Tabei A; Li, D.S.; Lavender, C.A.; Garmestani, H. (forthcoming). "Effects of Morphology and Geometry of Inclusions on Two Point Correlation Statistics in Two Phase Composites." *Computational Materials Science*.

18. Tabei, A.; Li, D.S.; Lavender, C.; Garmestani, H. (forthcoming). "Modeling of Precipitate Refinement in AZ31 Mg Alloy under Severe Plastic Deformation." *Computational Materials Science.*

19. Taylor, M.D.; Choi, K.S.; Sun, X.; Matlock, D.K.; Packard, C.E.; Xu, L.; Barlat, F. (2014). "Correlations between Nanoindentation Hardness and Macroscopic Mechanical Properties in DP980 Steels." *Materials Science and Engineering A,* 597, pp. 431-439.

20. Taylor, M.D.; Matlock D.K.; Speer J.G.; De Moor E. (March 2014). "Effect of Microstructure on the Fracture Response of AHSS." Prepared for Semi-Annual Review Meeting of Advanced Steel Processing and Products Research Center, March 17-19, 2014, Golden, Colorado.

21. Taylor, M.D.; Matlock D.K.; Speer J.G.; De Moor E. (September 2014). "Effect of Microstructure on the Fracture Response of AHSS." Prepared for Semi-Annual Review Meeting of Advanced Steel Processing and Products Research Center, September 15-17, 2014, Golden, Colorado.

References

1. De Moor, E.; Speer, J.G.; Matlock D.K.; Kwak J.-H.; Lee S.B. (2011). "Effect of Carbon and Manganese on the Quenching and Partitioning Response of CMnSi Steels." *ISIJ Intl.* 51, pp. 137-144.

2. DOE. (2011). "Pulse Pressure Forming of Lightweight Materials", U.S. DOE FY 2011 Annual Report.

3. DOE. (2012). "Enhanced Room-Temperature Formability in High-Strength Aluminum Alloys Through Pulse Pressure Forming", U.S. DOE FY 2012 Annual Report.

4. Rohatgi, A.; Soulami, A.; Stephens, E.V.; Davies, R.W.; Smith, M.T. (2014). "An Investigation of Enhanced Formability in AA5182-O Al during High-rate Free-forming at Room-temperature: Quantification of

Deformation History." Journal of Materials Process Technology 214 pp. 722-732.

5. Rohatgi, A.; Stephens, E.V.; Soulami, A.; Davies, R.W.; Smith, M.T. (2011). "Experimental characterization of sheet metal deformation during electro-hydraulic forming." J. Mater. Process. Technol. 211, pp. 1824-1833.

6. Rohatgi, A.; Stephens, E.V.; Davies, R.W.; Smith, M.T.; Soulami, A. (2012). "Electro-hydraulic Forming of Sheet Metals: Free-forming vs. Conical-die Forming." J. Mater. Process. Technol. 212, pp. 1070-1079.

7. Golovashchenko, S.F. (2006). International Journal of Mechanical Sciences, 48, pp. 1384.

8. Golovashchenko, S.F. (2008). Journal of Materials Engineering and Performance, 17, pp. 316.

9. Ilinich, A.M.; Golovashchenko, S.F.; Smith, L.M. (2011). Journal of Materials Processing Technology, 211, pp. 441.

10. Katykova, Y.; Golovashchenko, S.F. (forthcoming).

11. Hu, X.H.; Sun, X.; Golovashchenko, S.F. (2014). Computational Materials Science, 85, pp 409.

12. Le, Q.B.; deVries, J.A.; Golovashchenko, S.F.; Bonnen, J.J.F. (2014). Journal of Materials Processing Technology, 214, pp. 876.

13. Hu, X.H.; Choi, K.S.; Sun, X.; Golovashchenko, S.F. (2014) Journal of Manufacturing Science and Engineering, 136, pp. 021016.

14. Luo, A.; Nyberg, E.; Sadayappan, K.; Shi, W.; Magnesium front end research and development: a Canada-China-USA collaboration. Magnesium Technology, 2008: p. 3-10.

15. Li, D.; Joshi, V.; Lavender, C.; Khaleel, M.; Ahzi, S. (2013). Computational Materials Science, 79 pp. 448-455.

16. Graff, S.; Brocks, W.; Steglich, D. (2007). International Journal of Plasticity, 23 pp. 1957-1978.

17. Yin, S.M.; Wang, C.H.; Diao, Y.D.; Wu, S.D.; Li, S.X. (2011), Journal of Materials Science & Technology, 27, pp 29-34

18. Li, D.; Lavender, C. (2013). Submitted Metallurgical and Materials Transactions A.

19. Nie, J.-F. (2012). Metall and Mat Trans A, 43 pp. 3891-3939

20. Faisal, F.T.; Naz, N.; Baloch, R.A. (2012). "Characterization of Material Properties of 2xxx Series Al-Alloys by Non Destructive Testing Techniques". *J. Nondestruct. Eval.* 31 pp. 17-33.

21. Wu, X.J.; Koul, A.K.; Zhao, L. (1996). "A New Approach to Heat Damage Evaluation for 7xxx Aluminum Alloy" Canadian Aeronautics and Space Journal, 42 (2), pp. 93-101.

III.10 Mechanistic – Based Ductility Prediction For Complex Magnesium (Mg) Castings

Xin Sun, Principal Investigator
Pacific Northwest National Laboratory (PNNL)
902 Battelle Boulevard
P.O. Box 999
Richland, WA 99352
Phone: (509) 372-6489
E-mail: xin.sun@pnnl.gov

Mei Li, Industry Partner
Ford Motor Company (FMC)
1 American Road
P.O. Box 6248
Dearborn, Michigan 48126-2798
Phone: (313) 206-4219
E-mail: mli9@ford.com

John Allison, University Collaborator
University of Michigan (UM)
500 South State Street
Ann Arbor, MI 48109
Phone: (734) 615-5150; Fax: (734) 763-4788
e-mail: johnea@umich.edu

Yuri Hovanski, Field Technical Monitor
Pacific Northwest National Laboratory (PNNL)
Phone: (509) 375-2620
E-mail: yuri.hovanski@pnl.gov

William Joost, Technology Area Development Manager
U.S. Department of Energy (DOE)
1000 Independence Avenue, SW
Washington, DC 20585
Phone: (202) 287-6020; Fax: (202) 856-2476
E-mail: william.joost@ee.doe.gov

Contractor: Pacific Northwest National Laboratory (PNNL)
Contract No.: DE-AC05-00OR22725 & DE-AC06-76RLO1830

Abstract/Executive Summary

An integrated experimental and multi-physics modeling approach was adopted to develop the ductility prediction capability for complex Mg castings. The FY 2014 focus included 1) casting preparation with the subsequent location-dependent microstructure and ductility characterization (FMC and UM), 2) microstructure-based finite element modeling considering both intrinsic and extrinsic ductility limiting factors (PNNL).

Accomplishments

- Designed and cast round and flat high pressure die-cast (HPDC) AM60 tensile bars.
- Performed Computerized Tomography (CT) scans on 20 F3 as-cast flat tensile samples and 20 F1 machined sub-size tensile bars in the gauge region.
- Completed microstructure quantification, specifically characterized grain size and beta-phase fraction and distribution, for all as-cast conditions as well as solution treated and hot isostatically pressed (HIP) samples of selected conditions.
- Completed initial solution treatment and hot isostatic pressing (HIP) to dissolve β-$Mg_{17}Al_{12}$ and minimize porosity in the castings.
- Continued literature study assessing current models for yield strength and ductility in AM-series alloys.
- Expanded intrinsic modeling to include plastic localization as the failure mechanism to capture ductility limit.
- Performed nanoindentation on sample extracted from generic frame casting to explore viability of extracting material parameters and variations for intrinsic modeling input parameters.
- Performed synthetic microstructure-based three dimensional/two dimensional (3D/2D) extrinsic modeling works to develop a computationally efficient 2D modeling method for prediction of the ductility of thin-walled Mg castings.

Future Directions

- Quantify the influence of beta-phase and solidification-induced porosity on tensile properties via solution treatment dissolution and HIP studies.
- Develop weak link analytical model for ductility and strength in AM series alloys by quantifying the hierarchy of effects of aluminum (Al) content, porosity, beta phase, externally solidified crystals, thickness and skin.
- Develop a plate bulge test to extend the results from tensile testing to component-like conditions and eliminate edge effects. Validate the models developed.
- Complete nanoindentation experiments of as-cast and treated samples. Extract elastic and plastic properties and variations.
- Validate intrinsic modeling capability incorporating material parameters from nanoindentation.

- Validate the microstructure-based modeling method based on actual pore distribution data with the incorporation of intrinsic ductility.

Technology Assessment

- Target: Develop a mechanistic-based ductility prediction method for high-pressure die casting with potential for less than 5 percent error.
- Gap: Conventional computational techniques and most phenomenological approaches have little or no capability for predicting ductility.

✧   ✧   ✧   ✧   ✧

Introduction

Mg castings have found increasing applications in lightweight vehicles because Mg and its alloys are the lightest metallic structural material. However, limited ductility is a critical technical hurdle hindering wider application of Mg castings in vehicle applications. It is well established that microstructure features (e.g., properties and distributions of porosity, brittle eutectic phases, and grain size) can significantly influence the ductility of Mg castings. However, these microstructure features vary from alloy to alloy, with different casting processes, and in different locations on a single casting. [1] [2] Although some commercial casting software and material models [3] are available for research of Mg castings, their predictive capabilities typically stop short of predicting the location-dependent stress versus strain behavior, particularly ductility. The purpose of this project is to develop an empirical casting process simulation tool and a mechanistic-based ductility predictive capability to provide a modeling framework applicable to future alloy design and casting process optimizations.

Approach

In order to study the 'skin effects' in HPDC AM60 samples, a set of tensile bars was designed and cast by Ford as illustrated in Figure III-45. Each casting contained two flat tensile samples and a flat plate (2.5 millimeters (mm) thickness and of varying width) and four round tensile samples of varying diameter. Approximately 50 sound castings of AM60B were produced under controlled conditions. Samples were then cut apart and prepared for tensile testing. Samples F2, F3, R2, and R3 could be tested in the as-cast condition. Samples F1, R3, R4, and R5 produced tensile test samples where the "skin" was machined away.

Plates were cast by Ford in eight different conditions and characterized through metallographic preparation. Tensile testing was conducted on samples cut from the plates. Characterization was used to map the microstructure for all conditions and develop a weak link analytical model for ductility and strength in the AM series. In order to assess the

impact of different microstructural features on the tensile behavior, they were systematically evaluated through dissolution of the beta-phase by solution heat treatment and reduction of shrinkage-induced microporosity by HIP. These results will be extended to real world structures by using plate bulge testing to eliminate any edge effects and to validate the models developed in the project.
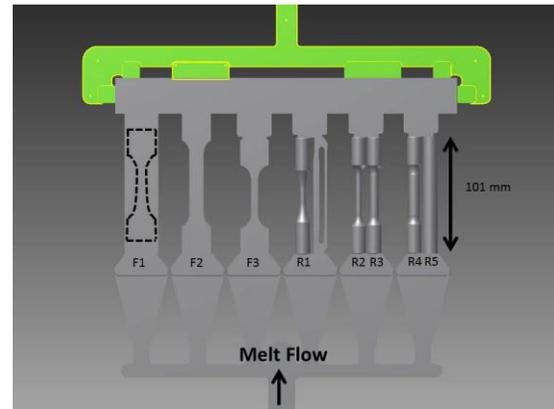
Figure III-45: Schematic diagram of tensile bar casting indicating sample locations. Dashed lines on F1 indicate the location of machined flat tensile bar.

For the task on ductility prediction with extrinsic factors (i.e., porosity), the feasibility of using 2D microstructure-based models was examined in predicting the ductility of thin-walled Mg castings. For this purpose, a series of 3D synthetic microstructure-based finite element models as well as the corresponding 2D models were generated with various porosity features. The ductility of 3D and 2D models were compared in order to obtain a 3D/2D ductility correlation curve. The validity of the obtained ductility correlation curve was then examined with actual sample microstructures.

Results and Discussion

MAGMASOFT® simulations were conducted by Ford to determine flow properties. Although the casting was designed to minimize differences between the samples, there were some differences observed for flow length and air entrapment. The simulation results suggested that, while possibly minor, there could be some differences between the samples due to processing effects that might influence the mechanical results as illustrated by Figure III-46. Ford also performed CT scans on 20 F3 as-cast flat tensile samples and 20 F1 machined sub-size tensile bars in the gauge region. Figure III-47 shows representative examples from each of the tensile bar sets. The F1 samples were observed to have more large pores and overall large pore volume than observed in the F3 "as-cast" samples. Selections of the CT scans were provided to PNNL for use in the porosity models.

(a)   (b)
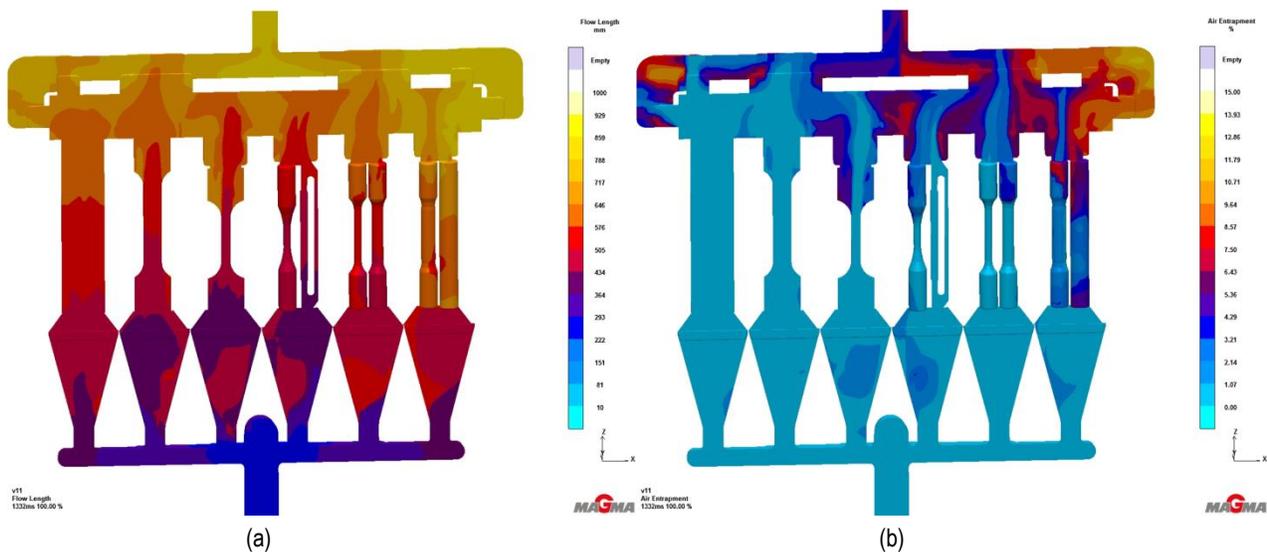
Figure III-46: MAGMASOFT® simulation results showing differences in (a) Flow Length and (b) Air Entrapment
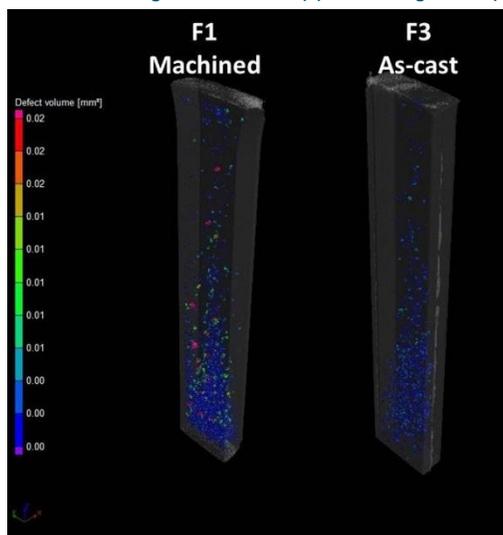
Figure III-47: CT scans of flat tensile bars indicating differences between porosity levels in machined and as-cast samples.

Metallography and tensile testing was completed for Super Vacuum Die Cast (SVDC) plates received from Ford in two thicknesses (2.5 and 5 mm) and four compositions (4, 5, 6, and 7 weight percent (wt.%) of Al). A significant increase in area fraction and connectedness in β-$Mg_{17}Al_{12}$ was observed with increasing aluminum content from 4 to 7 wt. %, which was quantified through image analysis of micrographs from a scanning electron microscope (SEM). β-$Mg_{17}Al_{12}$ content was lowest on the surface and in the center, with an increase just below the surface, as shown in Figure III-48.

The β-$Mg_{17}Al_{12}$ fraction was higher in the 2.5mm plates than in the 5mm plates. Sections from the plates were also prepared for X-ray diffraction (XRD) which was used to quantify phase fraction of β-$Mg_{17}Al_{12}$. Theoretical predictions

for the wt. % of β-$Mg_{17}Al_{12}$ formed under equilibrium conditions were determined using ThermoCalc (ThermoCalc Software Mg-based alloy Database, Version 2.0 (TCMG2)) for the AM alloys. Both the SEM area fraction and XRD measured values of β-$Mg_{17}Al_{12}$ were generally lower compared to that predicted by Scheil solidification models. Grain size was quantified for all as-cast conditions through electron backscatter diffraction (EBSD) for edge and center, as well as initial tests on solution treated and hot HIP samples, as shown in Figure III-49. The average grain diameter and distribution was larger for the center than for the edge, but were similar for all conditions in a given location. The microstructural quantification has been provided to PNNL for use in the micro-mechanics modeling of mechanical behavior.
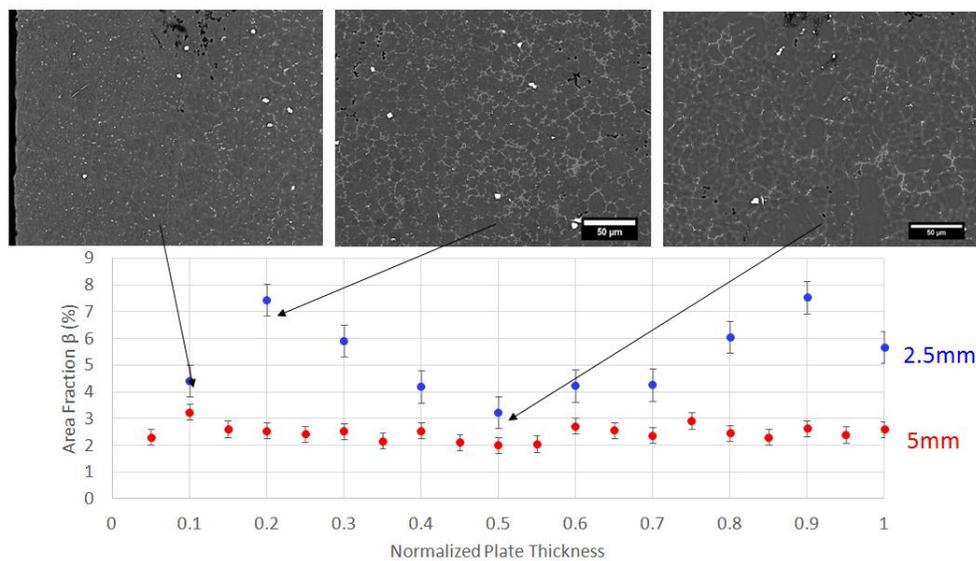
Figure III-48: A comparison of the distribution of β-Mg$_{17}$Al$_{12}$ in as-cast AM70 2.5 and 5 mm plates. The β-Mg$_{17}$Al$_{12}$ fraction is higher in the 2.5mm plate than the 5mm plate, and there is a peak just below the surface.
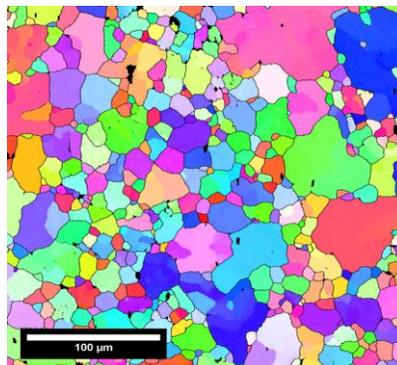
Figure III-49: An example of orientation imaging microscopy used to measure the grain size for each condition and location. This is the center of a HIP AM70 5mm plate. The black sections are Aluminum-Manganese (AlMn) intermetallics phases.

Tensile testing on each of the eight as-cast conditions was further analyzed. In the previous annual report, we noted that with increasing aluminum content, the ductility (elongation at failure) decreased, yield strength increased, fracture strength decreased, and Young's modulus increased. Initial tensile testing was done on AM60 2.5mm solution treated samples to begin to assess the impact of beta phase on the tensile properties. The results of this are shown in Figure III-50, where, compared with the as-cast condition, solution treated (ST) samples exhibited a slight decrease in yield strength and an increase in average elongation, or ductility. As shown in the microstructural insert, solution treatment completely dissolved the β-Mg$_{17}$Al$_{12}$.

Our previous intrinsic microstructure models utilized very low hardening values for the α phase to isolate the impact of the volume fraction and morphology of the β phase [4]

where the material parameters for the β phase have been extracted from first-principle calculations. [5] To utilize the intrinsic scale models to predict matrix properties including the initial yield, hardening parameter, and a ductility limit, accurate α phase hardening properties need to be established first. Exploratory work was conducted to extract α phase parameters and their variations from nanoindentation experiments. The indentation machine uses accepted algorithms to automatically calculate Young's modulus and hardness, see Figure III-51. Algorithms for determining yield stress and hardening parameters are less understood and poorly accepted in the materials community. Several algorithms are being investigated in conjunction with ongoing experimentation.
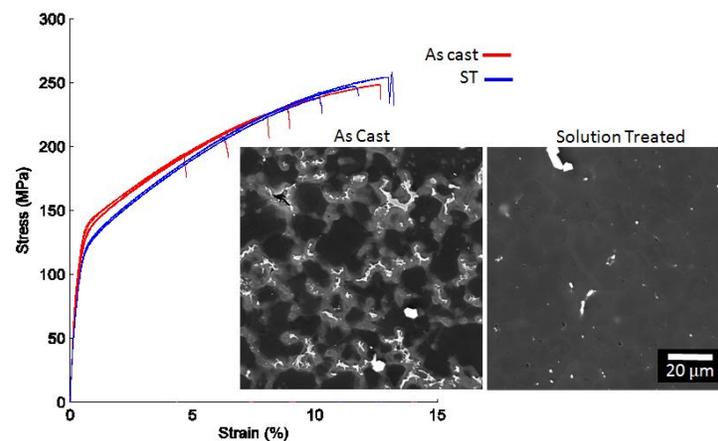
Figure III-50: Comparison between AM60 2.5mm as cast and solution treated samples.
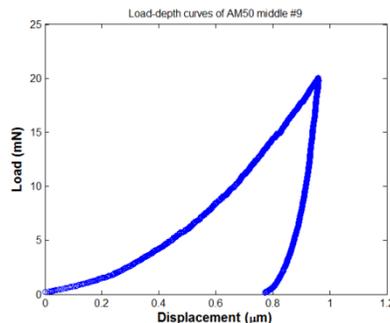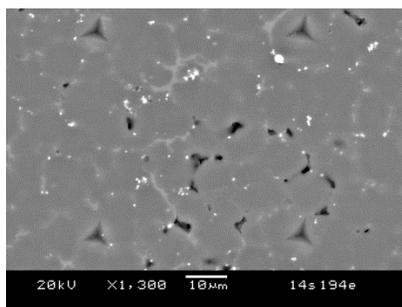
Max Load(mN): 20.03

Max Depth(nm): 958.83

Hardness(GPa): 1.0095

Elastic Modulus(GPa): 48.4191

(mN = millinewtons, nm = nanometers, GPa = gigapascals)

Figure III-51: Sample SEM image, loading-unloading curve, and machine output from nano-indentation experiment on AM50 as-cast sample.

After these parameters are identified, plastic localization will be used in the intrinsic model as failure mechanism to determine the matrix ductility limit. The predicted intrinsic properties will be used in the subsequent extrinsic scale models by explicitly considering the pore distributions in the castings.

In the modeling works on extrinsic factors, ductility correlation between 3D and 2D models was investigated. Figure III-52 illustrates the developed 2D modeling method and the resulted 3D/2D ductility correlation curve. Figure III-52(a) shows a 3D model with synthetic pore distribution and the corresponding 2D model generated by integrating the porosity in the sample thickness direction. The input properties for the higher porosity elements in 2D model were determined based on the Neuber's rule and the simulation of 3D cubic model with spherical void, see Figure III-52(b). Figure III-52(c) shows the obtained 3D/2D ductility correlation,

which shows a linear relation with the flatness of adopted fracture strain curve. [6] Figure III-53 shows the validation of obtained ductility correlation curve by using actual sample microstructures. [2] As shown in Figure III-53(c), the ductility estimated based on 2D model together with the ductility correlation curve agrees well with the ductility of 3D models.

Technology Transfer Path

The deliverables of this project will be transferred through Ford to the original equipment manufacturer participants and casting producers. Industry can use the modeling methodology and results to improve performance of materials and manufacturing processes and reduce the number of prototypes needed to validate a design, saving time and cost.

(a)

(b)

(c)
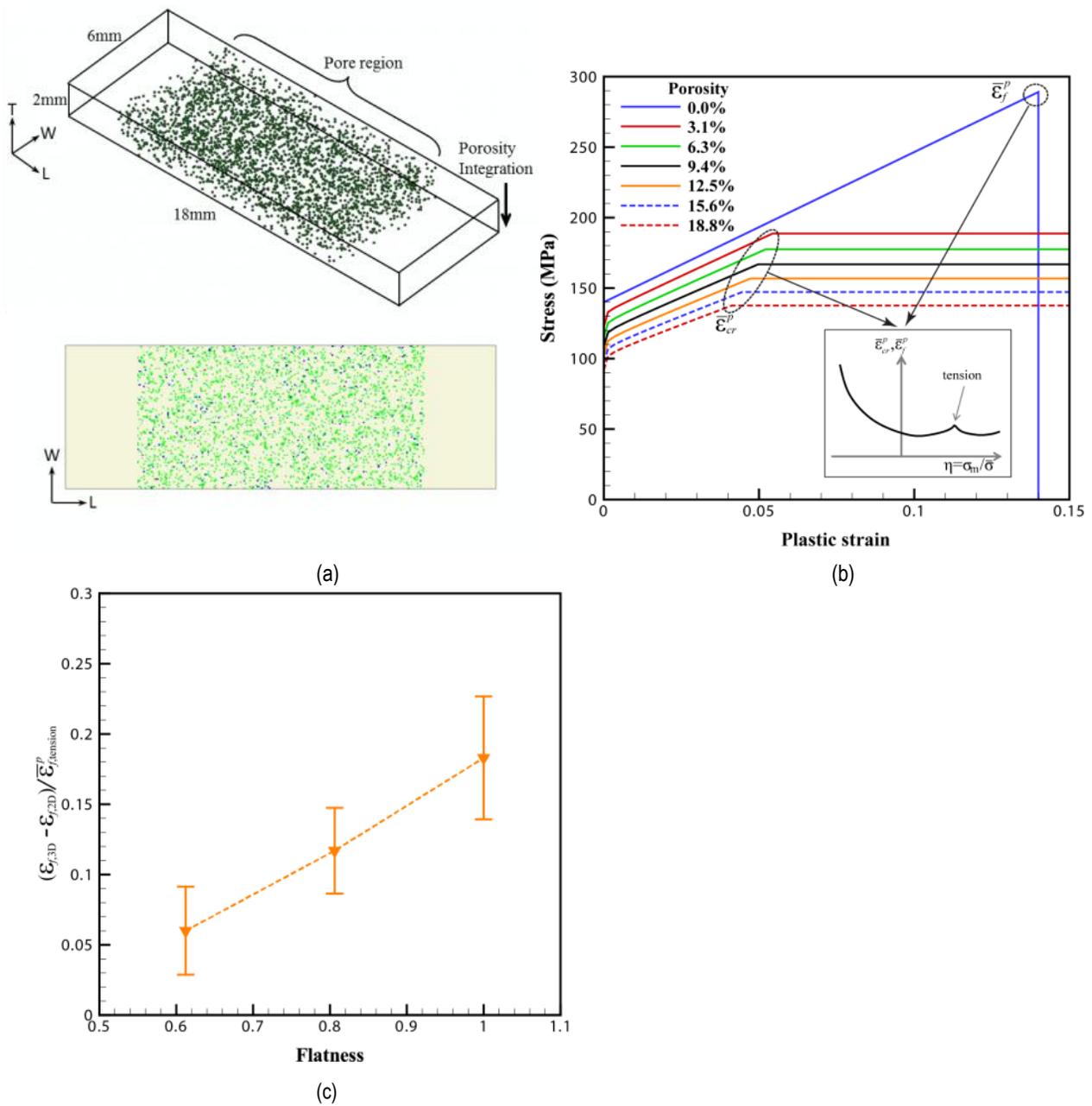
Figure III-52: (a) A 3D model with synthetic pore distribution (top) and the corresponding 2D model (bottom), (b) input properties for 3D and 2D model and (d) obtained 3D and 2D ductility correlation curve.

(a)

(b)

(c)
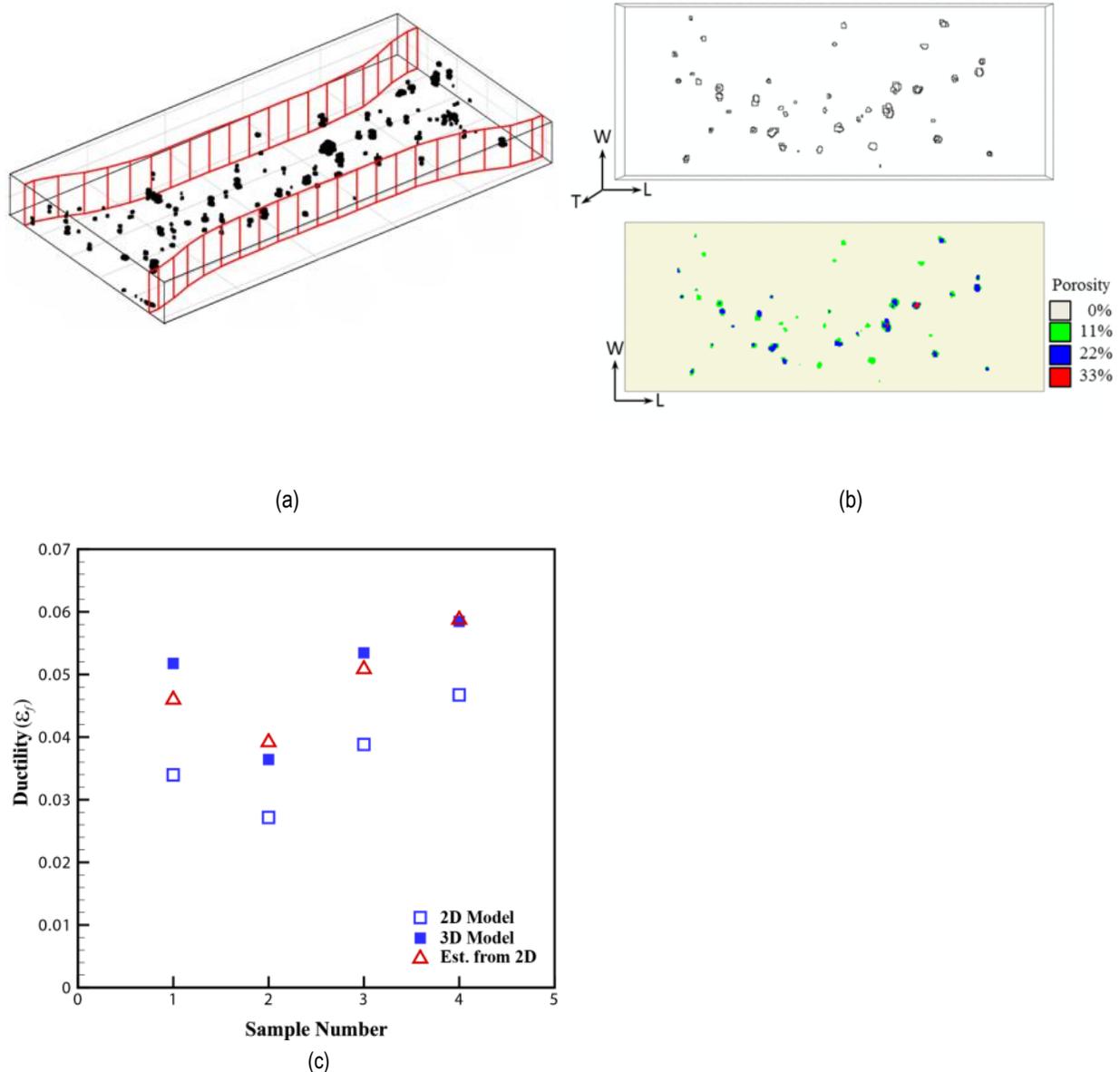
Figure III-53: Application of the developed 2D modeling methodolgy to actual pore distribution models. (a) An example of actual pore distribution (Song et al., 2009), (b) generated 3D model based on the actual pore distribtion (top) and the corresponding 2D model (bottom) and (c) comparison of ductility estimated from 2D model and those of 3D model.

Conclusion

Impressive progress has been made on all fronts of the project in FY 2014 by contributors from various institutions. Tensile testing for all conditions was completed for the as-cast conditions, and initial work completed on solution treated and HIP conditions. The fraction and distribution of β-$Mg_{17}Al_{12}$ was quantified across conditions, and was shown to be higher in the thinner samples. The grain diameter was also measured for all conditions, and was similar between Al contents for a given location. In general, with increasing Al content, the ductility decreased, yield strength increased, fracture strength decreased, strain hardening exponent decreased, and Young's modulus increased. The yield strength decreased and ductility increased slightly for solution treated samples.

Validated intrinsic models predicted yield stress and initial hardening slope with at least 90% accuracy. Bulk properties from intrinsic analyses utilizing plastic localization were demonstrated to be usable as matrix input parameters in extrinsic models. Work is ongoing to extract a phase parameters and variation from experiments for both skin and core regions of cast samples.

In modeling works on extrinsic factors, a computationally efficient 2D microstructure-based modeling method, together with a 3D/2D ductility correlation curve, was developed in order to predict the ductility of thin-walled Mg castings. The suggested methodology can provide a basis for establishing possible 3D/2D fracture strain correlation curve for other complex loading conditions.

Presentations/Publications/Patents

1. Barker, E.I., Choi, K.S., and Sun, X. (February 2014). "Microstructure Modeling to Ductility Prediction of Mg Alloys." Presentation at TMS 2014 143rd Annual Meeting and Exhibition, San Diego, California, February 16-20, 2014.

2. Han, L.H., Hu, H., Northwood, D.O. and Li, N.Y. "Microstructure and nano-scale mechanical behavior of Mg-Al and Mg-Al-Ca alloys." Mat. Sci. Eng. A 2008, 473, pp. 16-27.

3. Shan, Z.H. and Gokhale, A.M." Utility of micro-indentation technique for characterization of the constitutive behavior of skin and interior microstructure of die-cast magnesium alloys." Mat. Sci. Eng. A 2003, 361 pp 267-274.

References

1. Chadha, G., Allison, J.E. and Jones, J.W. The Role of Microstructure on Ductility of Die-Cast AM50 and AM60 Magnesium Alloys. *Metallurgical and Materials Transactions A*, 38, pp. 286–297, 2007.

2. Song, J., Xiong, S.M., Li, M. and Allison, J.E. The correlation between microstructure and mechanical properties of high-pressure die-cast AM50 alloy. Journal of Alloys and Compounds 2009, 447, pp. 863-869.

3. Weiler, J.P. and Wood, J.T. Modeling fracture properties in a die-cast AM60B magnesium alloy I —Analytical failure model. Materials Science and Engineering A 527 (2009) 25-31.

4. Barker, E.I., Choi, K.S., Sun, X., Allison, J., Li, M., Forsmark, J., Zindel, J. and Godlewski, L. (2014) "Microstructure-based Modeling of β Phase Influence on Mechanical Response of Cast AM Series Mg Alloys," Computational Materials Science, (92), pp. 353-361, 2014.

5. Wang, J.; Shang, S.-L.; Wang, Y.; Mei, Z.-G.; Liang, Y.-F.; Du, Y.; Liu, Z.-K., First-principles calculations of binary Al compounds: Enthalpies of formation and elastic properties. Calphad 2011, 35 (4), 562-573

6. Choi, K.S., Barker, E.I., Sun, X., Song, J. and Xiong, S.-M. An integrated two-dimensional modeling method for predicting ductility of thin-walled die cast magnesium, submitted for publication in International Journal of Fracture, 2014.

III.11 Multi-Material Enabling – Pacific Northwest National Laboratory

Yuri Hovanski, Field Technical Monitor
Pacific Northwest National Laboratory
902 Battelle Boulevard
Richland, WA 99352
Phone: (509) 375-3940
E-mail: yuri.hovanski@pnnl.gov

William Joost, Technology Area Development Manager
U.S. Department of Energy
1000 Independence Avenue, SW
Washington, DC 20585
Phone: (202) 287-6020
E-mail: William.joost@ee.doe.gov

Contractor: Pacific Northwest National Laboratory
Contract No.: DE-AC05-00OR22725 & DE-AC06-76RL01830

Abstract/Executive Summary

The Multi-Materials Enabling project consists of two tasks focused on research and development that can lead to greater implementation and manufacturing of multi-material lightweight components/systems in automotive applications. The tasks include the following: 1) self-pierce riveting (SPR) process simulation, analyses, and development for Magnesium (Mg) joints; and 2) high-speed joining of dissimilar alloy Al (Al) tailor-welded blanks (TWBs).

More energy efficient and environmentally friendly highway transportation is critical to reducing both the environmental impacts and energy consumption associated with transportation mobility. While transformational propulsion technologies and hybrid architectures show great promise in meeting such goals, these and other forthcoming solutions depend upon significant weight savings in passenger and commercial vehicles to fully capitalize on their potential to provide freedom of mobility without harmful emissions and dependence on foreign petroleum. Significant weight savings in the automotive fleet is likely to occur through the use of various advanced materials. While improvements in the properties, manufacturability, and cost of advanced materials are critical in achieving vehicle weight reduction, technologies that support the use of these materials in a multi-material system are equally important. Unlike a single material system, structures composed of different metals and polymer composites present significant challenges in areas such as joining, corrosion, recycling, and nondestructive evaluation. Work conducted in this agreement seeks to overcome these challenges by developing new techniques and preparing advanced technologies for a production environment.

The purpose of the SPR project is to provide a reliable mechanical joining technology for Mg joint applications and to enable the success of mechanical fastening of Mg by assisting the Mg SPR process development and cycle time through rivet process simulation and experimentation. This will be achieved by providing actual SPR joint performance data of Mg/Mg and Mg/dissimilar metal joints, so that more accurate data is applied to the overall structural design, and by developing process windows to provide design recommendations/guidelines for effective Mg SPR joining.

For the Al TWB project, the purpose is to develop the joining technology needed to demonstrate the fabrication of an Al tailor-welded component for an automotive door inner assembly that is currently made from steel, and demonstrate a greater than 40% mass savings. The project also aims to successfully transfer the production of TWBs into the automotive supply chain, thus enabling the rapid utilization of the technology in high-volume applications.

III.12 Self-Pierce Riveting Process Simulation, Analyses, and Development for Magnesium Joints

Elizabeth Stephens, Principal Investigator
Pacific Northwest National Laboratory
Phone: (509) 375-6836
E-mail: elizabeth.stephens@pnnl.gov

Xin Sun, Pacific, Co-Principal Investigator
Pacific Northwest National Laboratory
Phone: (509) 372-6489
E-mail: xin.sun@pnnl.gov

Eric Nyberg, Co-Principal Investigator
Pacific Northwest National Laboratory
Phone: (509) 375-2103
E-mail: eric.nyberg@pnnl.gov

Dr. Siva Ramasamy, Principal Investigator
Stanley Engineered Fastening
49201 Gratiot Avenue
Chesterfield, Michigan 48051
Phone: (586) 949-0550
E-mail: siva.ramasamy@sbdinc.com

Accomplishments

- The Pacific Northwest National Laboratory (PNNL) and Stanley Engineered Fastening (Stanley) have developed and integrated a custom induction heater into a full-scale SPR system at Stanley. (FY 2014)
- Successfully made induction-heated Mg-Mg SPR joints. (FY 2014)
- PNNL validated the FY 2013 modeling results experimentally by forming joints at both room temperature and elevated temperature using induction heating. (FY 2014)
- Assessed interlock of joints created. (FY 2014)
- Produced and implemented new die designs. (FY 2014)

Future Directions

- Complete the joint characterization and performance in terms of shear strength, fatigue, and corrosion.
- Explore alternate rivet materials and/or interlayers via the modeling tool.
- Develop the design guidelines and recommendations for successful Mg SPR joining.

Technology Assessment

- Target: Create Mg SPR joints of similar and dissimilar materials under the guidance of SPR modeling tools established by PNNL with no tail-side cracking.
- Target: Produce Mg SPR joints with a minimum target joint strength of 1.5 kN of lap shear strength per millimeter of substrate thickness.
- Gap: Mg alloys have low ductility at room temperature and when conventional SPR processing is used with magnesium, rivet tail end cracking occurs.
- Gap: Cracks in the SPR joint can be detrimental to the joint performance in terms of static and fatigue strength, as well as corrosion performance.

✧　　✧　　✧　　✧　　✧

Introduction

Because of increased pressure from government agencies and consumer advocate groups to produce safer, more durable, fuel-efficient vehicles, automotive original equipment manufacturers (OEMs) are investigating Mg for use in the major structural sections of vehicles. Mg components offer a potential weight reduction of approximately 50% when substituted for the higher-density or lower-strength steel materials conventionally deployed in vehicles. Historically, poor joining methods for Mg components have limited their applications in vehicles. Over the years, a variety of joining technologies have been introduced into the automotive industry to achieve lightweight vehicle goals. SPR is potentially a viable method for joining similar and dissimilar metals involving Mg. SPR is a low-energy consumption joining process with relatively low initial capital equipment cost. Because SPR is a mechanical joining process, the joint formation process involves large plastic deformation at the rivet tail end to ensure a mechanical interlock between the rivet material and the bottom sheet material. However, Mg alloys have low ductility at room temperature; thus, conventional SPR processing typically causes rivet tail end cracking. These cracks can be detrimental to the rivet performance in terms of static strength, fatigue strength, and corrosion performance.

Approach

This project is focused on developing and enabling the SPR process for joining Mg components in new vehicle applications to reduce vehicle weight through efforts established in a Cooperative Research and Development Agreement between PNNL and Stanley Engineered Fastening. This project aims to eliminate or substantially address key technical barriers in using SPRs in Mg-joining applications by using an integrated modeling and experimental approach. Barriers include tail-side cracking of Mg sheet or castings due to the lack of ductility at room temperature; lack of desired joint properties including corrosion at the joint; and lack of acceptable processing parameter windows. Further, the project will explore alternative/non-conventional rivet metals similar to the materials being joined to minimize the galvanic potential in the joint and an alternative joining method (i.e., adhesives) that may further promote joining of Mg. Initial work focused on the development of a numerical tool used to develop reliable Mg riveting process parameters through modeling and provide guidance in the development of joining process windows.

Phase 1 focused on experimental validation of the modeling tool previously developed for Mg SPR joining using conventional rivet materials and geometries. This phase experimentally validated the predicted results from the modeling tool to provide actual joint performance data (e.g., joint strength, fatigue strength, and corrosion performance) for the joint combinations evaluated. Phase 2 will focus on optimizing Mg SPR joints using the established modeling tool to investigate alternate rivet materials, including coatings or interlayers (e.g., adhesives). In addition, Phase 2 will address potential joint corrosion issues and optimize rivet geometry (i.e., shape and length) and die design to ensure joint integrity and performance.

Results and Discussion

In FY 2014, efforts centered on integrating the induction heating system into Stanley's SPR system, creating induction-heated Mg SPR joints, and validating and improving PNNL's modeling tool. MSI Automation, Wichita, KS, built a custom-designed induction heater system for PNNL. After completing functionality testing, PNNL sent the induction system to Stanley's research and development facility in Chesterfield, MI, where it was integrated into their SPR joining system (Figure III-54).

Preliminary heating and joining trials determined that the target temperature (~300°C) could be reached within 1 to 3 seconds, with overall cycle times of 3 to 5 seconds achieved (Figure III-55). These results are promising given Stanley's target total cycle time is 3 seconds. Select processing conditions were then performed on 2 mm to 2 mm Al-zinc (AZ)31B SPR lap shear coupons to assess the joint strengths of the induction-heated joints.
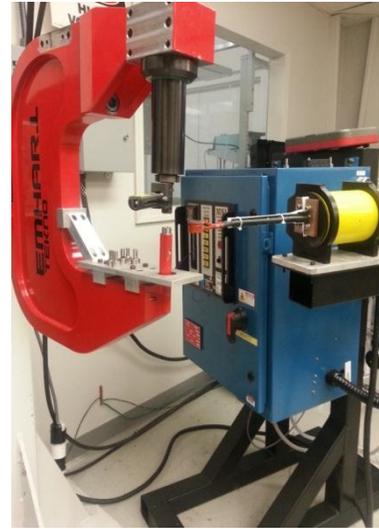
Figure III-54: PNNL's custom induction heating system integrated into Stanley's SPR system.

Figure III-55: Induction heating integrated into the Stanley Engineered Fastening SPR system for joining Mg sheet samples.

Figure III-56 illustrates the lap shear test results of the joints made at elevated temperature (~250 to 300°C) via the induction heat system using AZ31B alloy for the Mg sheets and carbon steel rivet. All specimens exceeded the target joint strength of 3.5 kN. The mean joint strength observed was 5.7 kN, with a maximum of 6.2 kN and a minimum of 4.8 kN observed. Variation of strengths observed is due to the varying rivets and die geometries selected for processing. Figure III-57 illustrates the joint interlocks achieved for select induction-heated SPR joints evaluated.

In FY 2014, modeling efforts focused on improving the previously developed SPR finite element model (FEM) through validation with the actual riveted joints. The team conducted simulations of the SPR process using Stanley's geometries with the thermo-mechanical FEM. Better selection of material properties at the various areas of the joining zone aided in improving the joint interlock, hence indicating a good joint.
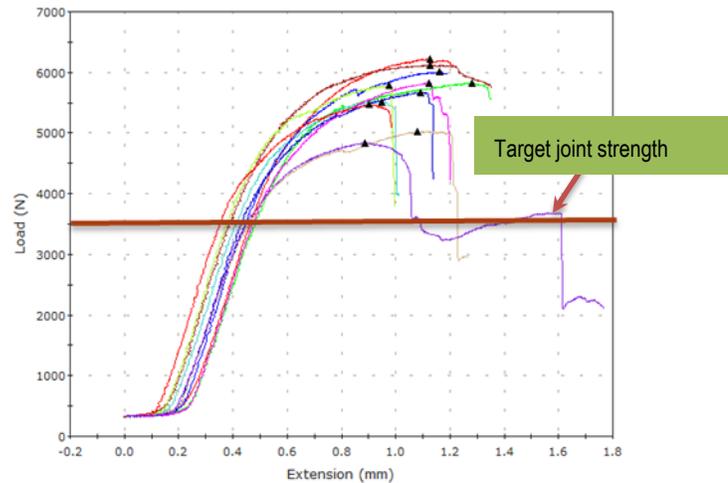
Figure III-56: Lap shear results of AZ31 Mg SPR joints created at elevated temperatures with an induction heat system.

(a)   (b)
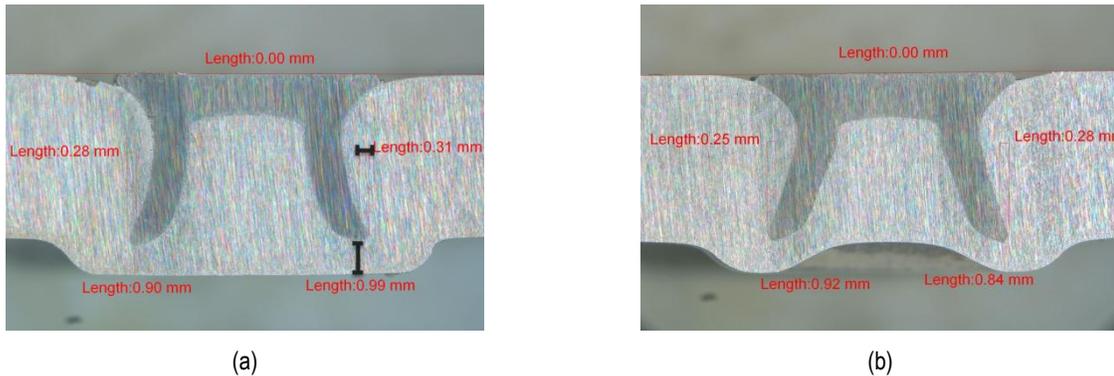
Figure III-57: Representative cross-section images of select 2 mm to 2 mm AZ31B SPR joints created at 300ºC via the induction heat system. Interlock measurements are shown for a (a) flat-bottom die and (b) pip die.

As a validation of the model, the team compared the predicted joint geometry, i.e. interlock shape, to an actual SPR joint created using the same die and rivet geometries to join the two AZ31B sheets (2 mm thick each). Previously, the model demonstrated that at room temperature, the localized plastic strain near the rivet tip and at the tail exceeds the AZ31B failure strain and therefore results in failure (element deletion in the simulations). The modeling effort, along with actual joints made at room temperature, agreed on the necessity to introduce a heat source to the SPR joining process for Mg sheets.

Figure III-58 shows a comparison between an actual joint and the simulation at a temperature (T) of 200ºC. Good agreement is shown between the experiment and the model (Figure III-58a). The equivalent plastic strain distribution of the tail sheet, before and after its contact with the die, is also shown (Figure III-58b). During piercing, the equivalent plastic

strain contours indicate that ductile failure was dominant, while after contact the tail is in compression.

Another validation parameter that will be used to further validate the model is the force versus rivet displacement during joining. Figure III-59 represents the simulated force versus rivet-head displacement curve. In FY 2015, experimental data during the joining process will be gathered to validate these simulated results.

Technology Transfer Path

Technology transfer will occur throughout the project via close collaboration between PNNL and Stanley Engineered Fastening. The technology transfer approach includes the development of process equipment and processing parameters necessary to achieve successful Mg SPR joints.
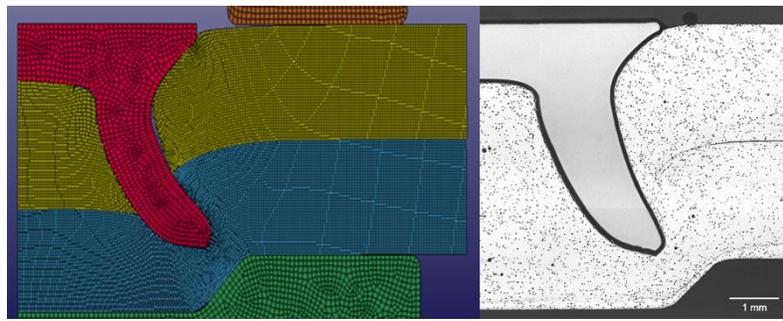
(a)
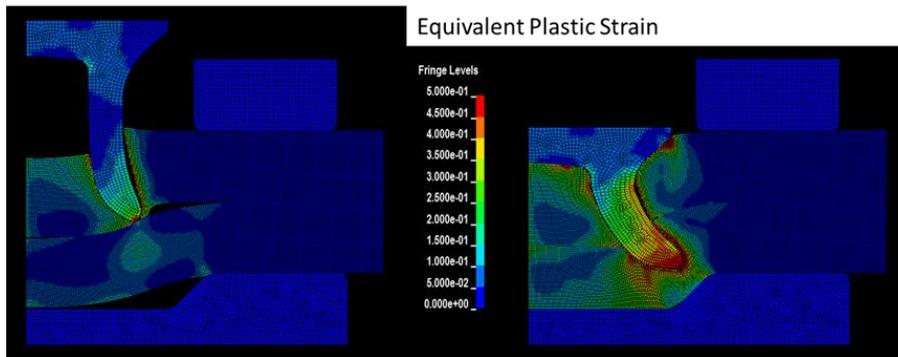
(b)

Figure III-58: FEM SPR results of 2 mm x 2 mm Mg sheets at 200º C showing a comparison of the (a) cross section of the model predicted shape and actual joint and the (b) predicted joint and strain contours.
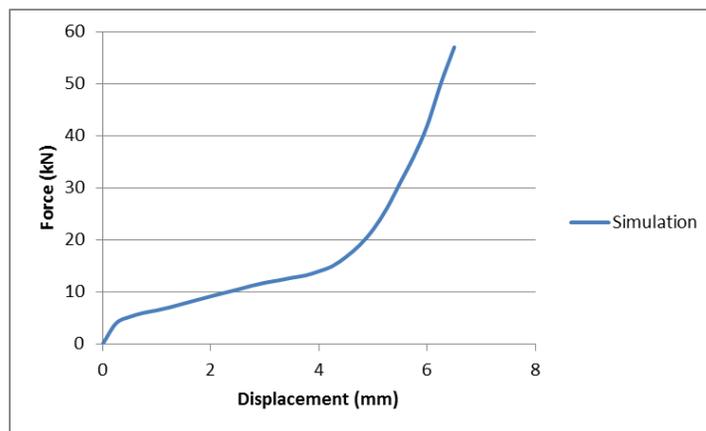
Figure III-59: The simulated force versus rivet-head displacement curve during SPR joining at elevated temperature.

Conclusions

In this reporting period, the project achieved successful integration of the induction heating system with Stanley's SPR system as well as successfully created AZ31B SPR joints via induction heating at elevated temperatures ranging from 250 to 300º C. When evaluating SPR joints created via induction heating, the technology assessment joint strength target was met. Under lap shear loading conditions, a mean joint strength of ~5.7kN was observed. In addition, continued improvement of the modeling tool is being performed through experimental validation. Good agreement between AZ31 SPR joints of 2 mm x 2 mm sheets were observed between predicted and experimental results.

III.13 High-Speed Joining of Dissimilar Alloy Aluminum (Al) Tailor-Welded Blanks (TWBs) – Pacific Northwest National Laboratory

Yuri Hovanski, Principal Investigator
Pacific Northwest National Laboratory
Phone: (509)375-3940
E-mail: yuri.hovanski@pnnl.gov

Accomplishments

- Supported technology transfer and facilitated high-speed welding development in newly installed friction stir welding (FSW) equipment at TWB Company (supplier). Provided optimized welding parameters, tooling, and setup for final component welding and demonstration. (FY 2014)
- Produced Al welded panels for 70 door stampings at General Motors (GM) and TWB Company, LLC. (FY 2014)
- Completed probabilistic formability limit evaluation of welded panel that served as input to formability limit model to predict component forming limit. (FY 2014)
- Validated component forming model with established probabilistic limit and experimentally measured weld properties. (FY 2014)
- Continued high-speed development (3 to 6 meters per minute (m/min)) and component production of the door inner welded blank at GM and TWB Company, LLC facilities. (FY 2014)
- Presented door panel prototype as a project showcase to members of Clean Energy Manufacturing Initiative,

American Energy and Manufacturing Competitiveness (AEMC), U.S. Department of Energy-Energy Efficiency and Renewable Energy (DOE-EERE) and members of the U.S. House of Representatives at the AEMC Summit on September 2014 (Figure III-60. (FY 2014)

Technology Assessment

- Target: Develop capability for high-speed FSW within the automotive supply chain by transferring high-speed FSW techniques to at least one supplier that is capable of producing high-volume quantities of welded blanks.
- Gap: FSW is currently performed by only a few niche companies, none of which has the capability to support high-volume production.
- Target: Full-size welded components that demonstrate modeled performance.
- Gap: Current modeling efforts do not accurately represent as-welded components; thus, the project needs to fully verify a modeling effort and conduct full-size component testing.

✧   ✧   ✧   ✧   ✧
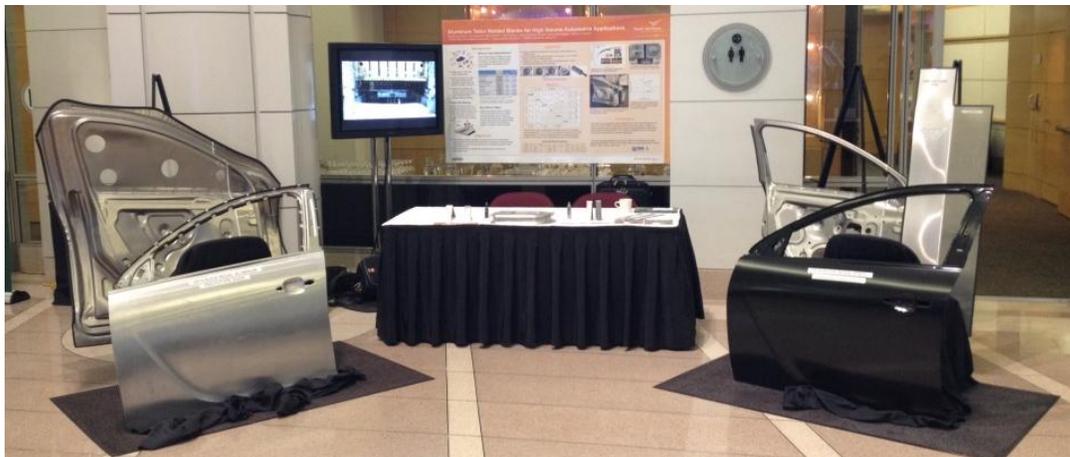
Figure III-60: Project showcase presented at AEMC summit in September 2014 showing door panels including FSW TWB door inner assembly. The project presented the associated poster and video feature to members of the Clean Energy Manufacturing Initiative, AEMC, DOE-EERE.

Introduction

Strategic research and development investments over the last few decades have moved tailor-welded products from concept to reality. Several companies now produce dissimilar thickness panels, tailor-welded coils, and tailor-welded tube sections in a variety of steel alloys for use in many applications (e.g., door inners, shock towers, and floor pans). Use of the tailor-welded technology is increasing with greater demand for lightweight structures that reduce part count and lower cost. While automotive OEMs would like to expand the usage of tailor-welded technologies into Al alloys, current joining technologies significantly reduce the formability of the as-welded materials. Al alloys have great potential for use in tailor-welded structures, and preliminary assessments show that the weight of numerous high-volume automotive components could be reduced by more than 40%.

While preliminary assessments demonstrate that tailor-welding technologies have the potential to reduce part count, cost, and weight, the joining technology needed to provide adequate formability of the as-welded blank is not sufficiently developed to transfer the technology to any supplier. While several groups have shown the preliminary potential for FSW 5083 Al blanks of similar thickness, no weld schedules exist that can be modified or adapted for very dissimilar thicknesses (2:1 thickness ratios and greater) in dissimilar Al alloy combinations (e.g., 5000 series to 6000 or 7000 series Al alloys). To achieve weight savings in excess of 40%, weld parameters must be developed that enable multiple alloys to be joined in very dissimilar thickness sheet combinations while maintaining the majority of their original formability.

As the majority of data related to FSW of Al TWBs is based on non-precipitation strengthened alloys—a material set that is very amenable to producing as-welded blanks with formability similar to the parent sheet—very little data has been produced relating the functional relationships between tool design, process parameters, fixturing, and alloy combinations. As joining of dissimilar Al alloys has proved much more problematic when considering the as-welded formability of TWBs, successful implementation depends upon a much greater understanding of the influence of each of these factors on the formability of the tailor-welded component. Thus, the project needs to further develop the FSW process in these form factors to provide a side-by-side comparison with other welding techniques.

Furthermore, previous pitfalls have hindered the progress of Al TWBs, as several groups have moved directly from welding to stamping without understanding the formability limits of the TWBs. This weld-and-stamp approach has proven problematic, as very little information on the as-welded component's usability comes from the stamped part. Whether the part forms or fails provides little data as to whether the blanks will ultimately work in another application and as such does not lead to a successful deployment path.

PNNL has previously developed and used predictive formability analysis to determine the probabilistic forming limit for a weld blank. This approach, in conjunction with stamping models, has the potential to determine the overall probabilistic

formability limits and provide an understanding of how they can be applied to numerous part geometries while avoiding the expense of the weld-and-stamp methodology.

This project proposes to develop the functional relationships of factors driving the weld formability of both dissimilar thickness of wrought Al alloy, AA5182, as well as dissimilar alloy combinations. Furthermore, we will then analyze the best-in-class parameter set for each to determine the probable forming limit, which we then will use to model the overall stamping process. PNNL will validate the process as the technology is transferred for actual part production, and provide the tools needed to further implement the process on other parts, geometries, and materials.

Approach

To develop the joining technology needed to enable Al TWBs for high-volume automotive components, the project divided the work scope into four main task areas. The first focuses on the initial weld development for formability, including quantifying the effects of tool design and process parameters on formability. The second compares the formability of Al welds produced via friction stir, laser, and laser-plasma welding. This task will ultimately lead to a decision gate that provides the information necessary to justify capital investments and product design using Al TWBs. The third task is divided into several areas that will emphasize preparing the process for commercialization. This includes pushing the process to higher linear weld speeds, tying probabilistic formability data into the component-forming models, and assisting the transfer of the weld process into a supplier's facility. That task will lead to the fourth and final task of producing actual production-ready coupons that will be stamped and tested by GM as a conclusion to the project efforts.

Having completed the first and the second tasks in the past two fiscal years, the project focused efforts in FY 2014 on technology transfer and enabling commercialization at the OEM and supplier. This effort also involved finalizing and communicating the component forming model that included probabilistic formability dataset to the OEM and supplier as a guideline for allowable forming limit of produced TWBs. Because of support in tooling, setup, and process parameters from PNNL, both the OEM and supplier are thus well positioned to start high-volume production of dissimilar thickness FSW blanks this fiscal year.

Results and Discussion

The project principal investigator was personally available for several days at both OEM and supplier sites to effectively facilitate technology transfer, including welding parameters, tooling, and setup, from the laboratory environment to industrial settings. The inevitable variations among FSW systems at different sites meant that the welding parameters had to be slightly altered for each specific FSW machine. Extensive research work at PNNL was valuable to address this need. Consequently, at the GM facility, numerous TWBs were made between dissimilar thicknesses AA5182 (2.0mm-1.1mm) at 3m/min of welding speed. TWB panels were also

successfully made between dissimilar thicknesses AA6022 (2.0mm- 1.0mm) at 3m/min and up to 6m/min. All the welds performed passed the tensile and bend test.

At TWB Company's facility, the newly procured and installed FSW system is in use, and tool drawings and their associated weld databases were established (see Figure III-61). Multiple combinations of more than 70 dissimilar thickness TWBs were successfully stamped into full-size door inner panels from FSW sheets made of AA5182 and AA6022 (see Figure III-62).

To provide guidelines for allowable forming limit in the produced TWB, PNNL developed and validated a computational model to simulate sheet deformation during stamping. The model was developed for a variety of thickness combinations and validated against several experimental data points obtained from sheet deformation performed at the supplier and OEM sites. A statistical probabilistic forming limit diagram of TWB was also tied into the computational model to better predict sheet deformation during stamping.
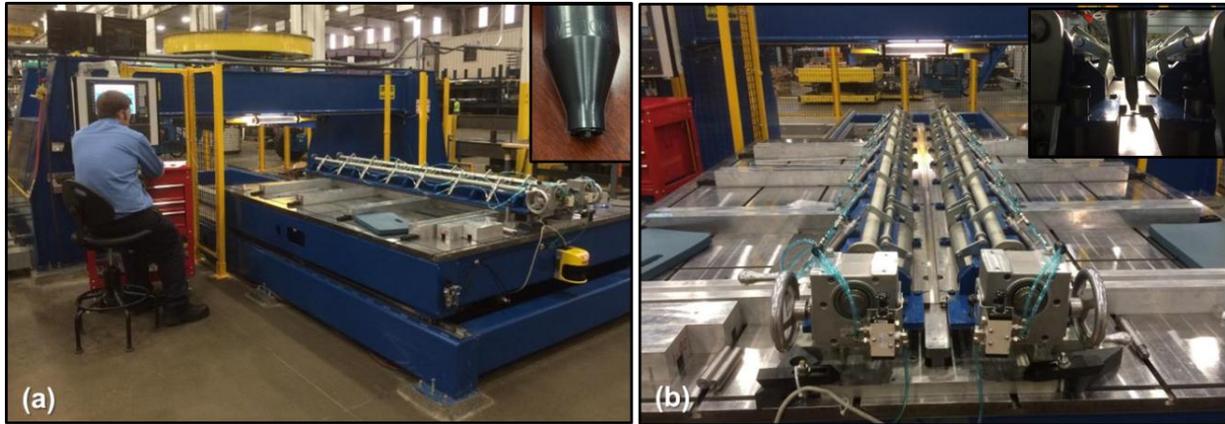
Figure III-61: High speed FSW equipment onsite at TWB Company, Monroe, MI. Machine and operator inside TWB plant with a typical tool used for welding is shown in the inset (a). Pneumatically controlled fixture for dissimilar thickness blanks. FSW tool attached to the machine head tilted to weld dissimilar thickness is shown in the inset (b).

Figure III-62: Dissimilar thickness blanks produced at TWB for stamping trials showing production chain: (a) Welded blanks as produced, (b)welded blanks after laser cutting at Quality Measurement Control, Inc. (QMC Inc.), (c) laser-cut panels loaded for stamping at TWB, and (d) dissimilar thickness door inner panels after stamping showing 2-mm AA5083 welded to 1.1-mm AA5083.

PNNL established the formability envelop for TWB that includes the effects of weld region (red line) using a combination of Marciniak and Kuczynski (M-K method) and experimentally measured localization strains in the weld material (Figure III-63). The M-K method hypothesizes that pre-existing geometric imperfections in sheet material are the site of eventual strain localization and failure during biaxial stretching. The region outside of the imperfection is assumed to be homogeneous. With this assumption, the forming limit diagram is calculated by numerically applying loads on the sheet and tracking strains in both imperfect and homogeneous regions. The failure occurs when the imperfect region accumulates strain at a much higher rate than the homogeneous region.

PNNL determined the imperfection levels for TWB populations from tensile tests performed in weld samples at both longitudinal and transverse orientation (30 samples each). We obtained major and minor strain prior to crack initiation from each sample using the digital image correlation technique. The M-K method was used to calculate the level of imperfection that corresponds to measured major and minor strain for each sample. We then assigned a statistically based level of imperfection to the TWB population assuming Weibull probability distribution.

Commercial finite element software Abacus was used to model sheet deformation behavior under a hemispherical die to simulate Limiting Dome Height (LDH) test. A 2D axisymmetric model was used to simulate Al sheet of various thickness combinations. Punch and die were modeled as analytical rigid surfaces, while the Al sheet was modeled of shell elements with a thickness offset from die direction. The

model was capable of predicting the dome height reasonable accuracy for a wide range of thickness ratios (see Figure III-64). The failure during the test occurred in thin sheet away from the weld seam. Since the welded joint has greater strength than the base metal the failure can be attributed to geometric discontinuity rather than the presence of the weld. The strain localization in the thin sheet outside of the weld region observed in the simulation (red region in Figure III-64 inset) accurately predicts the failure location.

Technology Transfer Path

Technology transfer into the high-volume automotive supply chain was a critical task for the planning of the entire project. PNNL designed the project to provide technological expertise from PNNL researchers who engage the entire supply chain, including the material provider, Alcoa; the high-volume automotive supplier, TWB, LLC; and the OEM, GM. With this team engaged from start to finish in the project, the technology will be developed and transferred using alloys and gauges already set for production quantities and quality sufficient to meet the demands of high-volume automotive production. A production line will be set up within the high-volume supplier's facility with quality and production standards in place, allowing full-size production components to be produced for testing by the automotive OEM. At the conclusion of the project, the entire supply chain should be staged and able to supply Al TWBs for high-volume production components. This path should effectively bridge the gap between development and utilization by intrinsically supporting industrial implementation.
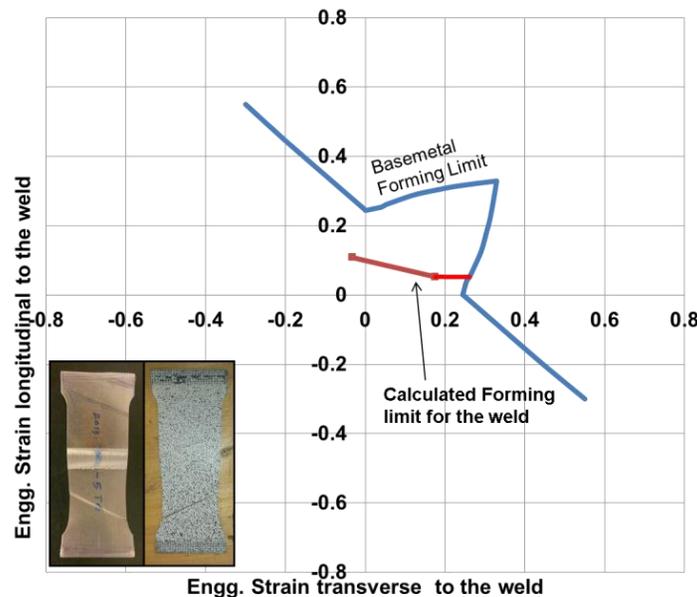
Figure III-63: Statistically calculated probabilistic formability limit diagram (red line) based on M-K method and experimental weld evaluation. Inset: A representative tensile sample showing typical failure in the thin sheet away from the weld line.
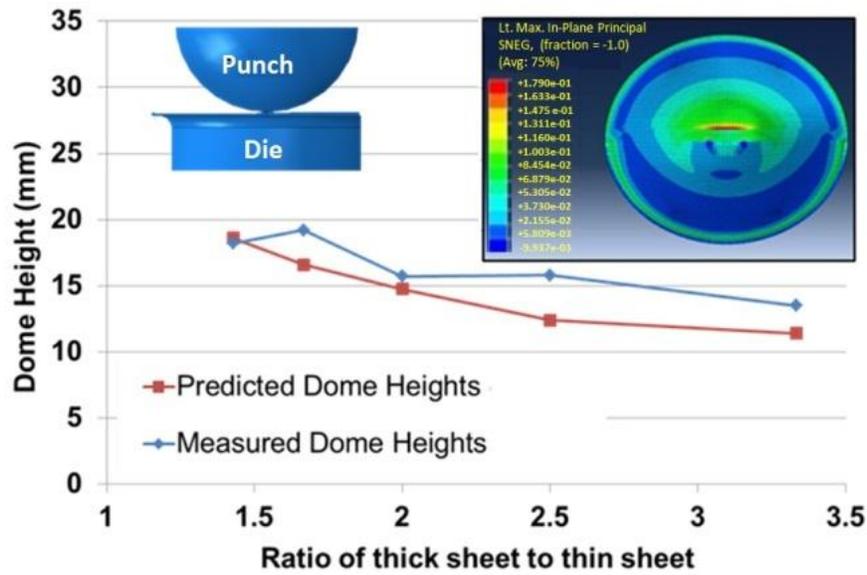
Figure III-64: Experimentally measured dome height and predicted dome height from computational model for various sheet thickness ratios. Inset: A representative strain map obtained from model showing strain localization outside of the weld line.

Conclusions

Having developed optimized welding parameters, tooling, and setup to produce tailor-welded blanks that meet industrial formability requirements, this project enabled high-volume supply chain for Al TWB. This capability led to successful technology transfer from the research environment at PNNL to industrial production settings at the automotive supplier. The project supported OEM and material provider to assure success, resulting in significant investments from project partners on the basis of measured and staged success.

Continued research and development at PNNL resulted in achieving significantly higher welding speeds of up to 6 m/min in similar material and dissimilar thickness for AA5182 and AA6022. Even higher speeds were demonstrated by the supplier for similar thickness case. Thus, PNNL has pushed the state of the art to facilitate high-volume production needs. The use of established probabilistic formability limit diagrams in the computational formability model is projected to enable accurate component formability and to increase confidence in the process for similar alloys in dissimilar thickness combinations. However, dissimilar alloy development remains a significant challenge.

A significant effort from the automotive supply chain provided interim evaluations of post-weld formability via stamping trials, which have prepared the work for moving to the final phase in component production. In combination with the modeling work that continues at PNNL, these data begin to bound the formability of each welded combination such that current modeling software may be adjusted to more accurately predict weld formability of Al welded blanks.

Conclusions

An induction heating system was successfully integrated with a SPR system and AZ31B SPR joints were created via induction heating at elevated temperatures ranging from 250 to 300o C. Good agreement was obtained between predicted and experimental results for AZ31 SPR joints of 2 mm x 2 mm sheets.

Welding speeds greater than 6 m/min in similar materials and dissimilar thicknesses for AA5182 and AA6022 were demonstrated with TWBs. This technology was successfully transitioned to industrial production settings at an automotive supplier. Dissimilar alloy development still presents challenges. Modeling efforts are providing weld formability limits that may be used to accurately predict weld formability of AL welded blanks.

Presentations/Publications/Patents

1. Hovanski, Y; Carsley, J; Carlson, B; Hartfield-Wunsch, S; Pilli, S. P. (2014). "Comparing Laser Welding Technologies with Friction Stir Welding for Production of Aluminum Tailor-Welded Blanks." *SAE International Journal of Materials and Manufacturing* (7:3); pp. 537-544. doi:10.4271/2014-01-0791.

2. Hovanski, Y.; Upadhyay, P.; Pilli, S. P.; Carlson, B.; Carsley, J.; Hartfield-Wunsch, S.; Eisenmenger, M. (2014) "Aluminum Tailor-Welded Blanks for High Volume Automotive Applications." In *Light Metals 2014: Aluminum Alloys: Development, Characterization and Applications, Proceedings for TMS Annual Meeting;* Feb. 2014, San Diego, CA.

3. Ramasamy, S.; Kenyon, B.; Belknap, R. (May 2014). "SPR Process Simulation, Analyses, & Development for Mg Joints Internal Program Review." Presented at the Stanley Engineered Fastening Global Technology Review.

4. Soulami A.; Stephens E.V.; Nyberg, E.A.; Sun, X. (December 2013). "SPR Process Simulation, Analyses, & Development for Mg Joints." Presented at THERMEC 2013.

5. Stephens, E.V.; Soulami, A.; Nyberg, E.A.; Sun, X. (April 2014). "SPR Process Simulation, Analyses, & Development for Mg Joints." Presented to the USCAR Materials Tech Team.

6. Stephens, E.V.; Soulami, A.; Nyberg, E.A.; Sun, X. (April 2014). "SPR Process Simulation, Analyses, & Development for Mg Joints." Presented at the Lightweight Materials Portfolio Review.

7. Stephens, .E.V.; Soulami, A.; Nyberg, E.A.; Sun, X. (June 2014). "2014 DOE Vehicle Technologies Office Review SPR Process Simulation, Analyses, & Development for Mg Joints." Presented at the DOE Vehicle Technologies Annual Merit Review.

III.14 Multi-Material Enabling—Oak Ridge National Laboratory

C. David Warren, Field Technical Monitor
Oak Ridge National Laboratory
1 Bethel Valley Road
Oak Ridge, TN 37831
Phone: (865) 574-9693; Fax: (865) 574-6098
E-mail: warrencd@ornl.gov

Will Joost, Technology Area Development Manager
US Department of Energy
1000 Independence Avenue, SW
Washington, DC 20585
Phone: (202) 287-6020; Fax: (202) 856-2476
E-mail: William.Joost@ee.doe.gov

Contractor: Oak Ridge National Laboratory (ORNL)
Contract No.: DE-AC05-00OR22725

Abstract/Executive Summary

Significant weight reduction in future vehicle structures will likely occur through the adoption of a variety of materials, including various combinations of light metals. Critical technologies are needed to enable the cost-effective performance necessary for application of these materials.

Those technologies include multi-material joining, corrosion prevention, and nondestructive evaluation (NDE).

Corrosion of alternative candidate automotive materials is a factor that could potentially limit their adoption. Research is needed on mitigating the corrosion of magnesium (Mg), aluminum (Al), and advanced high-strength steels (AHSSs) in an automotive environment. Corrosion issues are even more critical for dissimilar material joints, especially when the materials to be joined have a significant difference in electrochemical potentials. Corrosion mitigation strategies are being developed. The quality of material joints is critical to their application. Nondestructive inspection methods for verifying joint integrity and material quality are needed. Those methods need to be rapid, reliable, repeatable, and easily integrated into automotive production plants. Additionally, strategies for mitigating residual stresses are critical to joint integrity.

This project consists of four tasks critical for the welding, inspection, and development of lightweighting metal structures with dissimilar metals: (1) develop an understanding of film formation on Mg alloys, (2) develop a rapid, reliable spot weld inspection method for use in manufacturing plants, (3) improve the fatigue life of AHSS welds, and (4) design joints for Al-steel chassis structures.

III.15 Understanding Protective Film Formation by Magnesium Alloys in Automotive Applications

Michael P. Brady, Principal Investigator
Oak Ridge National Laboratory
Phone: (865) 574-5153; Fax: (865) 576-5413
E-mail: Bradymp@ornl.gov

Bruce Davis, Partner
Magnesium Elektron North America (MENA)
1001 College Street
PO Box 258
Madison, IL 62060,USA
Phone: (732) 657-6551
E-mail: Bruce.Davis@Magnesium-ElektronUSA.com

Accomplishments

- Successfully completed and published a $D_2^{16}O$ and $H_2^{18}O$ isotopic tracer study for aqueous film formation growth mechanism by commercial Mg alloys AZ31B and E717 relative to ultrahigh purity Mg. This is the first isotopic tracer study of Mg corrosion ever reported. (FY 2014)

- Demonstrated small angle neutron scattering (SANS) as a new tool to provide insights into Mg corrosion. SANS was found to be sensitive to the formation of nanoporous, filamentous magnesium hydroxide ($Mg(OH)_2$) resulting from the accelerated corrosion of Mg alloys in salt solutions. The SANS data indicated extremely high surface areas in the $Mg(OH)_2$ corrosion product, which has implications for understanding film growth and breakdown. (FY 2014)

- Successfully completed advanced transmission electron microscopy (TEM) characterization study of ambient immersed aqueous film formation as a function of exposure time (4-48 h) and alloy type (AZ31B, E717, and ultra-high purity (UHP) Mg) elucidating nanoscale film segregation tendencies of Al, rare earth, Zn, and Zr alloy additions (FY 2013).

- First successful demonstration of secondary ion mass spectrometry (SIMS)/D216O and H218O isotopic tracer studies for film formation by Mg alloys under immersed aqueous and air + steam exposure conditions providing new insights into film growth mechanism and relative penetration of H and O species. (FY 2013)

Future Directions

- Delineate the composition and/or microstructure aspects which enhance penetration of hydrogen species during

aqueous corrosion by isotopic tracer studies with cast model alloys based on the commercial Mg alloy E717.

- Attempt to expand tracer studies to aqueous environments containing corrosive salt species to better understand how the film growth mechanism is affected.

- Apply advanced characterization techniques to coating formation (conversion coatings ± e-coat) and stability on baseline AZ31B and E717 Mg alloys, with emphasis on how substrate alloying additions impact resulting surface coating formation.

Technology Assessment

- Target: Gain improved understanding of protective film formation by Mg alloys and conversion coatings as a function of alloy chemistry and impurities, microstructure, and exposure conditions.

- Target: Provide a fundamental basis to design and optimize new Mg alloys and/or conversion coating processes to improve corrosion resistance under automotive relevant conditions.

- Gap: The lack of corrosion prevention strategies is a key limiting factor to more widespread use of Mg alloys in automotive applications.

- Gap: Alloying has been shown to modify surface film performance; however, a detailed understanding of how and why is currently lacking. Such an understanding is needed to develop improved alloys and surface treatments/coatings to permit more widespread adoption of Mg alloys.

✧ ✧ ✧ ✧ ✧

Introduction

Mg alloys are of great interest to automotive manufacturers due to their attractive combination of low density, good strength, amenability to casting, ease of recycling, etc. A major obstacle to the widespread adoption of (Mg) alloys is susceptibility to corrosion [1–3]. Surface treatments and/or coatings are needed for many applications [3], which result in increased cost and can be a source of component durability issues. The inability of Mg alloys to establish a continuous and fully protective surface film under many exposure conditions is a key factor underlying their susceptibility to corrosive attack. Alloying and/or conversion coatings have been shown to modify surface film

performance; however, a detailed understanding of how and why is currently lacking. Such understanding is needed to develop improved alloys and surface treatments and/or coatings to permit more widespread adoption of Mg alloys.

The goal of this effort is to develop an improved understanding of how alloy composition, microstructure, and exposure conditions affect the establishment, continuity, nature, and growth of protective films on Mg alloys. To accomplish this goal, this project has employed advanced characterization techniques not previously widely applied to Mg surface film formation to provide new insights into film formation. The project is a systematic study of aqueous film formation and its evolution with time on two representative Mg alloy classes relative to UHP Mg as a control. Alloy AZ31B was studied as representative of the Mg-Al-Zn alloy class, and alloy Magnesium Elektron North America (MENA) 717 (also known as ZE10A, referred to as E717 for simplicity) as representative of the rare earth (RE) and Zirconium- (Zr-) alloyed class of Mg alloys. These results will then serve as baseline information for evaluation of more corrosive environments (e.g., salt species), modified alloy compositions, and conversion coatings. The study of both bare, untreated Mg alloy surfaces and conversion-coated surfaces is being pursued. The corrosion of Mg alloys has been the subject of intense research activity, with significant gains in mechanistic understanding in recent years for both pure Mg and Mg alloys. These studies have identified the inability of Mg alloys to establish a continuous and fully protective surface film under many exposure conditions as a key factor underlying their susceptibility to corrosive attack. Deliverables on this project are related to application, development, and suitability assessment of advanced characterization techniques to provide new insights into Mg alloy corrosion.

Approach

The ambient corrosion of Mg differs from many corrosion-resistant structural alloy classes in that the protective surface films can become quite thick, on the order of tens to hundreds of nanometers, rather than the few nanometers typically encountered in stainless steels [4–6]. As a result, corrosion resistance is influenced not only by classical thin film electrochemical passivity considerations but also by thermodynamic and kinetic considerations typically encountered in thick film, high temperature alloy oxidation phenomena.

The experimental approach adopted merges ambient and high temperature corrosion study approaches, leveraging extensive and unique expertise in these areas at MENA and ORNL. This approach takes advantage of the world-class characterization capabilities available at ORNL to more fully probe and understand the chemical, morphological, and structural features of the surface films formed on Mg alloys

and conversion coatings as a function of alloy composition, microstructure, and exposure condition.

A major goal of the project is to assess which advanced characterization techniques are most amenable to providing new insights into film formation on Mg alloys. This is a key activity as Mg alloys are notoriously difficult to work with. Sample procedure techniques are being developed, and not all proposed characterization approaches prove effective. Advanced characterization approaches to be investigated include (1) development of ex situ focused ion beam (FiB) sample preparation and TEM of film/surface layer cross sections, (2) SIMS $D_2^{16}O$ and $H_2^{18}O$ (^{18}O water) tracer studies of Mg alloys/coatings under immersion aqueous and gaseous vapor exposure conditions to gain insight into the growth aspects of the surface films, (3) ex situ neutron scattering techniques (small angle, inelastic, etc.) to characterize Mg alloy surface film nanoporosity and hydrogen species incorporation as a function of alloy composition and exposure condition, and (4) atom probe tomography (APT) techniques to provide 3D quantification of chemistry at the atomic scale in the bulk Mg alloy and the alloy in the vicinity of the alloy-surface layer interface to characterize corrosion-driven alloy clustering or precipitation phenomena.

Advanced TEM sample preparation techniques were successfully developed in FY 2012 and applied in FY 2013 and FY 2014 to Mg alloy aqueous film formation as a function of exposure time, alloying, and the absence or presence of salt. SIMS isotopic tracer techniques were successfully developed and demonstrated in FY 2013 and applied in FY 2014 for understanding the effects of alloying additions on the aqueous film formation growth mechanism of Mg. In FY 2014, SANS and TEM characterization were successfully applied to the formation of nonprotective, nanoporous $Mg(OH)_2$ corrosion products formed by Mg alloys in salt solutions. Initial attempts at applying APT techniques to Mg corrosion films were not successful due to sample preparation complications.

Results and Discussion

An isotopic tracer study of the film formation growth mechanism for UHP Mg, AZ31B, and E717 magnesium alloys in water at room temperature was performed [7]. A series of individual and sequential exposures were conducted in both $H_2^{18}O$ and $D_2^{16}O$, with isotopic tracer profiles obtained using SIMS: as polished control, 4 hours (h) D_2O, 4 h ^{18}O water, 4 h D_2O + 20 h ^{18}O water, 4 h ^{18}O water + 20 h D_2O. The water-formed films consisted primarily of partially hydrated MgO, with minor amounts of $Mg(OH)_2$ and $MgCO_3$ at the surface [7]. The SIMS sputter depth profiles (Figure III-65) indicated that H and D penetrated throughout the hydroxide/oxide film and into the underlying metal, particularly for the Zr- and Nd-containing E717 alloy.
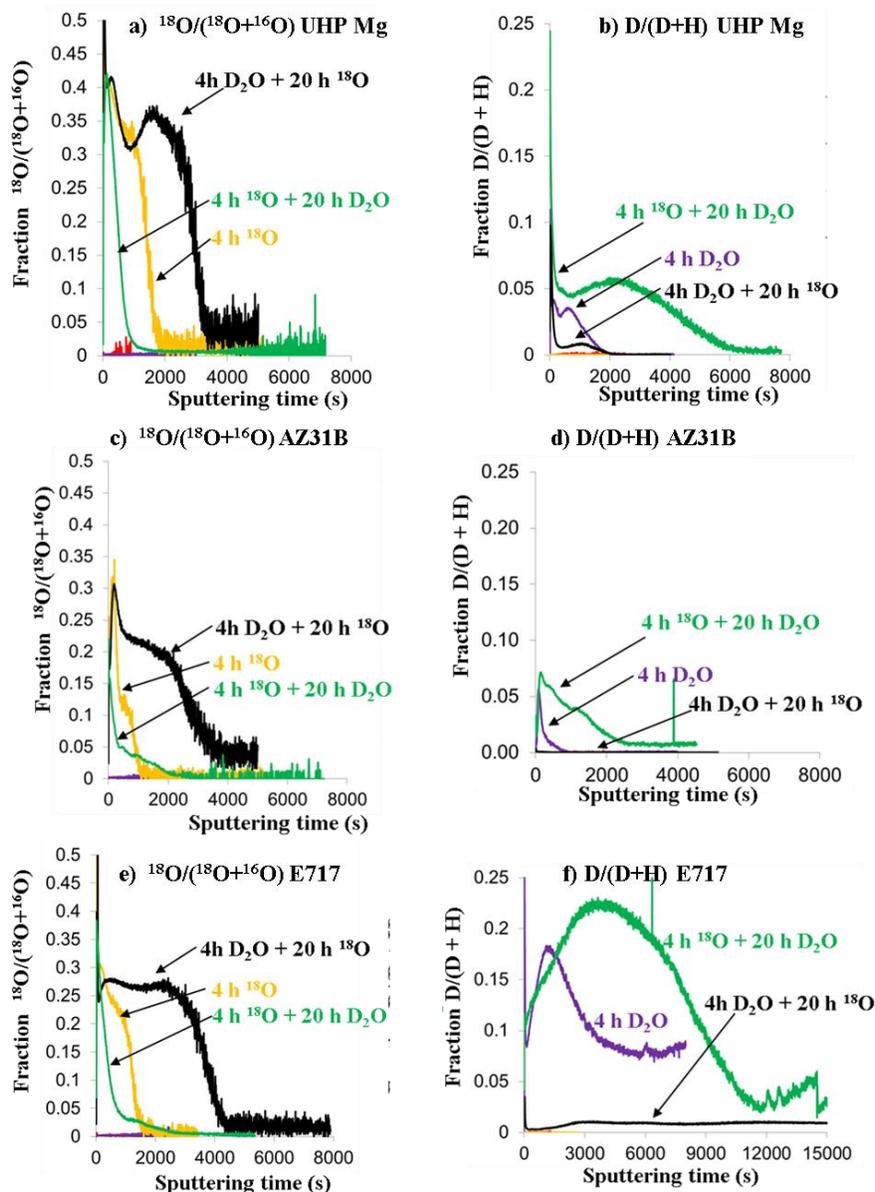
Figure III-65: Fraction $^{18}O/(^{18}O+^{16}O)$ (a, c, e) and Fraction D/(D+H) (b, d, f) master plots for UHP Mg, AZ31B, and E717. Conditions include as-polished (AP, red), 4 h D_2O (purple), 4 h ^{18}O water (orange), 4 h D_2O+ 20 h ^{18}O water (black), and 4 h ^{18}O water + 20 h D_2O (green). Zero sputtering time corresponds to the film surface (from reference 7).

The film growth mechanism for the UHP Mg involved aspects of both metal outward diffusion and oxygen/hydrogen inward diffusion processes ("dips" in profiles in Figure III-65a, b). In contrast, the film on the Al-containing AZ31B alloy grew primarily by inward oxygen and inward hydrogen diffusion (monotonically decreasing profile intensities with depth in Figure III-65c, d). The ^{18}O and D profiles for the film formed on E717 were the most complex (Figure III-65e, f), with the ^{18}O data most consistent with inward lattice oxygen diffusion, but the D data suggesting inward, short-circuit diffusion through the film (increase in D fraction with depth in Figure III-65f). This is the first isotopic tracer study of Mg corrosion ever

reported. The findings have significant implications not only for Mg corrosion, including stress corrosion cracking and embrittlement mechanisms, but also for Mg in hydrogen storage or production applications. The reasons for the extensive hydrogen penetration in E717 are not known. Tracer studies of a model alloy set based on the E717 composition will be studied in FY 2015 to isolate which alloying additions may be responsible for the enhanced hydrogen transport.

Studies of the accelerated corrosion of Mg alloys in salt solutions were also pursued in FY 2014. In short-term (4 to 48 h) immersion exposures in water, the sample mass uptake for UHP Mg, AZ31B, and E717 increased up to 2 orders of

magnitude in 1 to 5 wt % NaCl solutions, consistent with the well-established detrimental impact of salts on Mg corrosion. SANS studies were conducted on a matrix of AZ31B and E717 Mg alloys: as received metal, after 24 h immersion in H_2O and D_2O, and after 24 h immersion in H_2O + 5 wt % NaCl and D_2O + 5 wt % NaCl (Figure III-66). No scattering changes were detected for as-received metal and after 24 h in D_2O or H_2O for both AZ31B and E717, consistent with relatively dense and protective MgO-base film formation. However, significant scattering changes resulted for both alloys after immersion in 5 wt % NaCl solutions (Figure III-66). X-ray diffraction and metallographic analysis indicated that extensive Mg hydroxide formation occurred in the salt solutions. The SANS data intensity was greater in D_2O + 5 wt % NaCl than H_2O + 5 wt % NaCl, consistent with the greater scattering length density of D and uptake of D into the Mg hydroxide structure.

Scanning transmission electron microscopy (STEM) (high angle annular dark field, HAADF, and bright field, BF) images of the film cross-section formed on the AZ31B in D_2O + 5 wt % NaCl are shown in Figure III-67 [8]. The film was duplex, with a thin inner MgO layer (thickness of a few hundred nanometers (nm) to a few microns depending on location imaged) at the metal-film interface, and a thick, outer, filamentous and nanoporous Mg hydroxide region, extending many tens of microns. Similar structures were also observed for E717 in the 5 wt % NaCl solutions [8]. To gain insight into the hydroxide film nanoscale structure, modeling of the SANS data was pursued using a polydisperse hard sphere (PDHS) model which provides a quantitative representation of nanoscale porosity, and was developed to describe pore systems in coal, weathered rocks, and soils [discussed in reference 8]. The model is based on fitting scattering data by a

hard sphere model as a fractal assemblage of spheres to assess pore size distribution and surface roughness/surface area inside pores. For this analysis, the SANS scattering data from the as-received (unreacted) metal samples were subtracted from the 5 wt % NaCl solution metal sample scattering data (Figure III-66), yielding scattering curves representing only the corrosion films formed on the front and back surfaces of the test samples (Figure III-68). Assuming that all scattering resulted from nanoporous Mg hydroxide, the PDHS model indicated that the pore roughness/internal pore surface area was on the order of 100 m^2/cm^3 for both AZ31B and E717 in 5 wt % NaCl solutions. This value translates to ~43 m^2/g, a surprisingly high surface area for a film formed by a corrosion process, and approaches the surface area range exhibited by catalysts. Such high surface areas indicate that the outer Mg hydroxide layer provides no protection and permits continued access of the NaCl solution to the inner film regions. It also suggests that Mg hydroxide formation proceeds at least in part by a dissolution and precipitation mechanism.

A STEM cross section of AZ31B after 4 h in 1 wt % NaCl solution is shown in Figure III-69 [8]. The early transition from dense inner MgO-base film formation to outer filamentous and porous $Mg(OH)_2$ formation was captured in this section. As in pure water-formed films, Zn enrichment at the metal-film interface and Al enrichment in the inner film was observed. However, in NaCl solution, elemental mapping also showed the presence of chlorine (Cl) penetrating the inner MgO-base film regions. This suggests that film breakdown in NaCl solutions may be related to breakdown by Cl within the MgO-base inner film structure and at the MgO-$Mg(OH)_2$ interface.
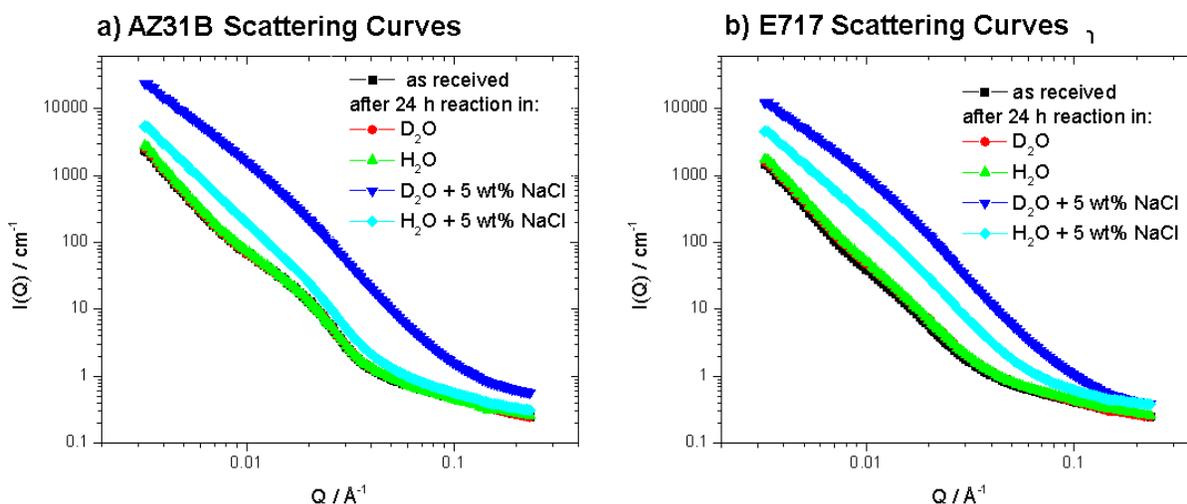
Figure III-66: SANS scattering curves (a, b) for AZ31B and E717 as received, after 24 h in D_2O or H_2O, and after 24 h in D_2O or H_2O with 5 wt % NaCl (from reference 8).

a) Overview of film-metal structure

b) Coarse outer film Mg(OH)₂

c) Fine inner film Mg(OH)₂

d) Fine inner film Mg(OH)₂
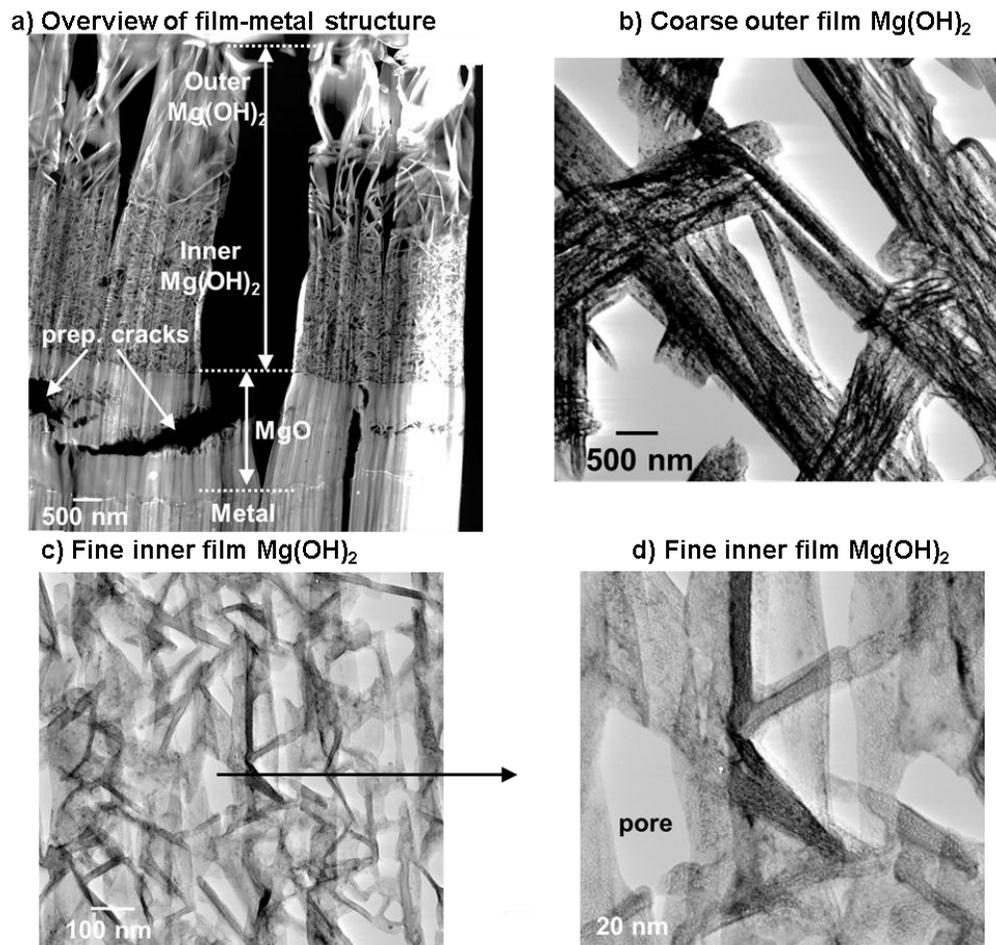
Figure III-67: AZ31B after 24 h in D₂O with 5 wt % NaCl: a) assemblage of multiple HAADF STEM images of film-metal structure; bright field (BF) STEM images of coarse outer (b) and finer inner (c, d) Mg(OH)₂ (from reference 8). Cracks in structure are attributed to sample preparation.
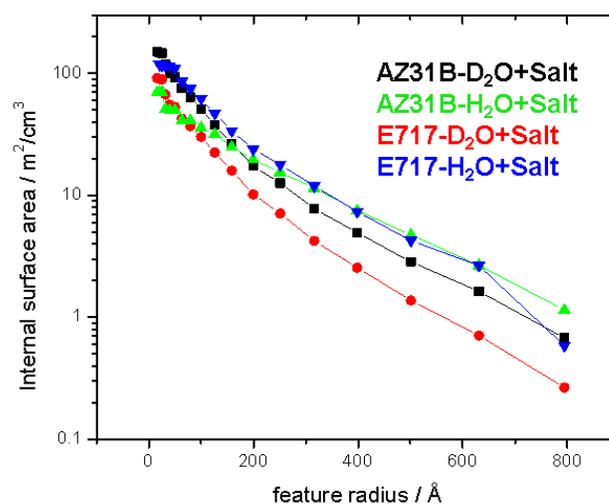
Figure III-68: Surface area distribution as a function of fitted feature radius size obtained from modeling the scattering data with a polydisperse hard sphere model (from reference 8).
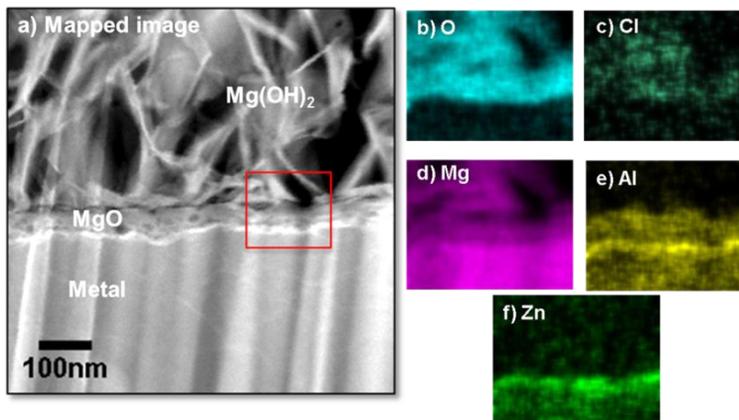
Figure III-69: Dark Field STEM of the film cross section (a) and corresponding energy dispersive spectrometry (EDS) elemental maps (b–f) generated from the boxed region for AZ31B after 4 h in H$_2$O with 1 wt % NaCl (from reference 8).

Technology Transfer Path

Basic understanding of the film formation on Mg alloys and its behavior in different environments will provide insight into how improvements can be made to design and optimize new Mg alloys and conversion coatings to improve corrosion resistance under automotive relevant conditions. The current gap in basic understanding of the film formation mechanics and kinetics and correlation with alloy chemistry and microstructure is a key factor limiting achievement of improved corrosion resistance to permit more widespread use of Mg alloys in automotive applications. Teaming with MENA, a leading Mg alloy producer, on this project will provide a direct path for incorporating insights from this effort into practice.

Conclusions

Isotopic tracer studies in pure water indicated that both Mg film growth mechanisms and hydrogen penetration are significantly influenced by alloying additions. Work in FY 2015 will attempt to extend this approach to the film formation mechanism in NaCl solutions. Although SANS did not prove sensitive to film formation in pure water, SANS did show good promise for characterization of the transition to nanoporous and filamentous Mg hydroxide formation associated with accelerated corrosion of Mg alloys in salt solutions. A key advantage of SANS is the ability to characterize the entire sample volume, which is beneficial for Mg corrosion as the attack tends to be highly heterogeneous and nonuniform, and thus complements more local techniques such as TEM imaging. A further advantage of SANS is the potential to obtain data in situ during Mg corrosion as a function of exposure time, i.e., one could monitor surface area changes as a function of exposure time in situ for Mg alloys in NaCl solutions. The observations of the outer film formation of nanoporous, high surface area Mg hydroxide from Mg alloys in NaCl solutions, as well as penetration of Cl to the inner, more dense MgO-base film regions, begins to provide the basis for an improved mechanistic understanding of the detailed mechanisms by which NaCl breaks down protective film formation accelerates the corrosion of Mg.

Zhili Feng, Principle Investigator
Oak Ridge National Laboratory
Phone: (865) 576-3797
E-mail: fengz@ornl.gov

Contributors
Jian Chen, Oak Ridge National Laboratory
Jerry Brady, Eagle Bend Manufacturing, Inc.

Accomplishments

- Completed the new IR NDE prototype system development by integrating the novel hardware and data analysis algorithms. (FY 2014)
- Completed the prototype evaluation in the laboratory using a large sampling of weld coupons that were made from different advanced high-strength steels, thicknesses, coatings, and stack-up configurations. (FY 2014)
- Further improved the design of the induction coil as the auxiliary heating unit for post-weld NDE inspection ensuring that it is suitable to the assembly production environment. (FY 2014)
- Started the online system evaluation in the assembly production environment at a Tier One auto-body component manufacturer with promising initial testing results for both real-time and post-weld NDE inspections (FY 2014)
- Initiated discussion of technology transfer and licensing with two private companies. (FY 2014)

Future Directions

- Continue to work with industrial partners to complete the full system tests on production lines.
- Demonstrate the performance of the infrared (IR) NDE system to original equipment manufacturers (OEMs).
- Develop a commercialization plan for broad technology transfer.

Technology Assessment

- Target: Develop a system that can meet or exceed the inspection cycle time requirements dictated by the mass production assembly line environment including: (1) collection time less than 2–3 s for online inspection; (2) collection time less than 5–10 s for offline inspection; and (3) data analysis and decision making time less than 1–2 s.
- Target: The prototype spot weld quality inspection system based on IR thermography can detect the stuck weld,

weld nugget size (up to 0.2 mm resolution), and surface indentation (up to 0.1 mm resolution) in both the two layer (2T) and three layer (3T) stack-up configurations.
- Gap: Currently, the effective IR image acquisition and analysis algorithms and hardware system to determine the weld quality within the targeted time period and with the necessary quality and weld attribute special resolution does not exist.

✧   ✧   ✧   ✧   ✧

Introduction

Resistance spot welding is the most widely used technology for assembling auto body structures. Variations in welding conditions, part "fit-up," and other production conditions inevitably occur in the complex, high-volume, body-in-white (BIW) assembly process. These variations can result in out-of-tolerance joints that impair the quality and performance of the vehicles. The increased use of AHSSs and other lightweight metals is expected to pose even more stringent requirements on joint quality. Despite the extensive R&D efforts over the years, nondestructive weld quality inspection still remains a critical issue for the auto industry, largely due to the unique technological and economic constraints of the auto production environment. Any weld quality inspection technique must be fast, low cost, low in false rejection rate, and not interfere with the highly automated welding fabrication process. Today, inspection systems that meet these requirements do not exist.

This project aims at developing a field-deployable, online, weld quality monitoring method based on the IR thermography. A distinct advantage of IR thermography as a NDE tool is its nonintrusive and noncontact nature. This makes IR based NDE methods especially attractive for the highly automated BIW assembly lines

Approach

The project consists of the following major tasks to achieve the project goal.

- Refine and optimize the field-deployable IR measurement techniques that can reliably detect the characteristic thermal signature patterns of various weld quality attributes both in real time and in postmortem online inspection;
- Develop the robust IR image analysis software that, in real-time, can analyze the IR thermal image for the characteristic signature of various weld defects and weld

joint configurations, to provide quantitative measure of the quality;

- Develop a prototype IR weld quality monitoring expert system (hardware and software) that is cost effective and suitable for field demonstration;
- Validate and demonstrate the effectiveness and robustness of the technology for a wide range of spot welds made with different steel grades, coatings, thickness and stack-up configurations with varying quality attributes (nugget size and indentation depth, etc.) commonly encountered in BIW production;
- Conduct field tests in actual auto body assembly production environment to further refine/improve the technology.
- Identify and work with potential industry entities for technology transfer and eventual commercialization.

A unique prerequisite for the IR thermography based NDE technology in automotive applications is that the surface of the materials and welds cannot receive any special treatments. All the development and testing in this project should be on the as-welded or as-received surfaces.

Results and Discussion

In previous years of the project, an initial version of the IR image acquisition system and data analysis algorithm was developed which demonstrated the feasibility for both real-time (online) and post-weld (offline) inspection applications. A wide range of welds made with different steel grades, coatings, thickness and stack-up configurations were produced. Welds with varying attributes (nugget size and indentation depth, etc.) were intentionally made by carefully controlling the welding parameters. Tests showed that the system was able to positively quantify the weld nugget size, shape, and thickness, and identify welding defects including the lack-of-fusion and excessive indentation.

The schematic of a resistance spot weld (RSW) quality inspection system for both real-time and post-weld NDE inspections are illustrated in Figure III-70. The system primarily consists of (1) a computer with specially designed software for system control, data acquisition and IR image analysis, (2) a low-cost IR camera, and (3) input/output instruments for system control and synchronization and (4) an auxiliary heating device (for post-weld inspection).

FY 2014 efforts were focused on field testing and validation of the entire prototype system (software and hardware) in an auto-body assembly production environment. The IR signal analysis algorithms have been further improved to resolve the influence on IR thermal signature from the complex geometry of the real auto body structures. Promising initial testing results have been obtained for both real-time and post-weld NDE inspections.

The field validation trials were performed at COSMA's Eagle Bend Manufacturing Plant in Clinton, Tennessee. Figure III-71 shows one of the auto body subassembly parts.

The geometry of the part was relatively complicated compared to the previously tested flat coupons in the laboratory.
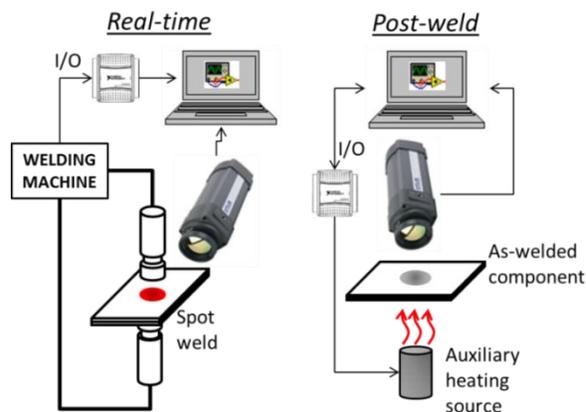
Figure III-70: Schematic of the IR thermography based RSW quality inspection system.

To ease the access to different locations in actual components, the induction heating coil was redesigned. The redesign included reduction of the coil size, improved concentration of the induction heat flux and reduced interference, and improved cooling of the coil to avoid overheating after long-time use at high heating cycle rate in production lines.

The IR image analysis algorithms were also refined to overcome the influence of part geometry on heat flow at the edge or corner of the part. Examples of the real-time weld inspection results obtained by the improved algorithms are plotted in Figure III-72. The calculated thermal signatures were compared to the subsequent destructive measurement. The comparison shows an approximate linear correlation.

Promising results were also obtained for post-weld inspection of spot welds in actual body components. As shown in Figure III-73, the IR measured weld nugget shapes and sizes were very close to the destructive measurements. Defects of 'cold weld' and 'under-sized' weld were positively identified.

Technology Transfer Path

The IR NDE prototype system has been generated strong interests from major auto OEMs and their part suppliers and instrument manufacturers. In particular, ORNL is in discussions with a Tier One supplier (end user) and a specialty measurement equipment manufacturer (potential IR NDE system supplier) for licensing the technology. Further, additional funding from State of Tennessee and ORNL's Technology Transfer Office has been applied for in order to commercialize the technology.

Figure III-71: Production auto body components with multiple spot welds used in field trials.
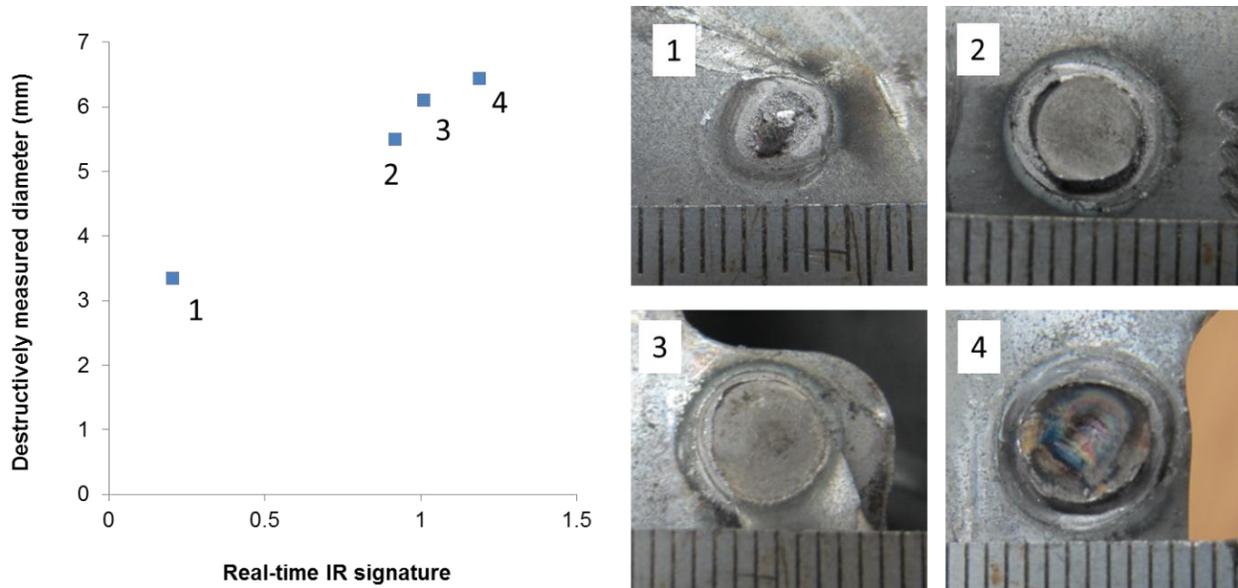
Figure III-72: Real-time IR thermal signature vs. destructively measured weld nugget size from an actual body component.
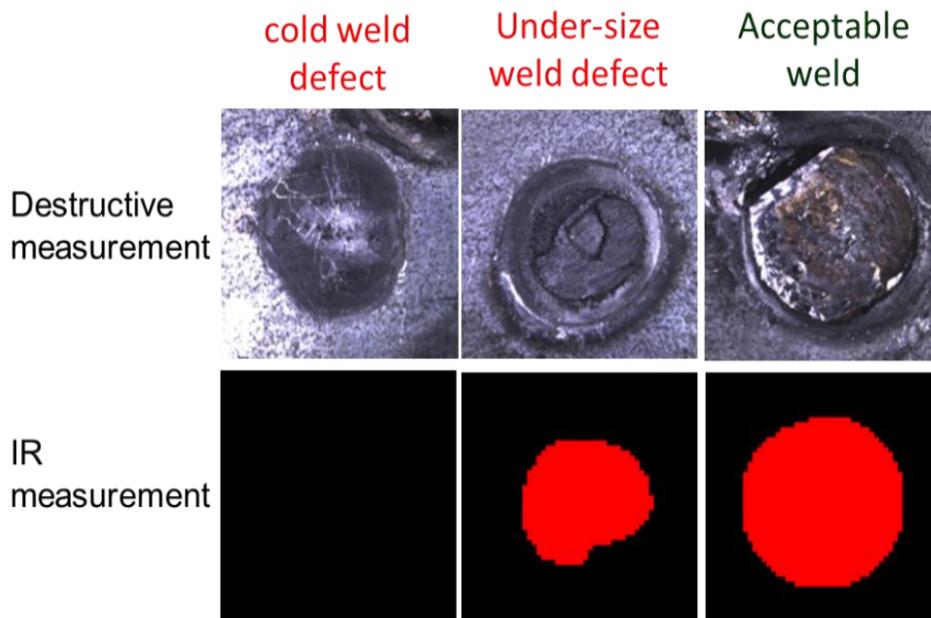
Figure III-73: Post-weld IR thermal signature vs. destructively measured weld nugget.

Conclusion

The accomplishment achieved in FY 2014 was focused on field testing and validation of our prototype IR NDE system. The work addressed technical issues encountered in the automotive body assembly production environment. Both hardware and software were further improved. Very promising results have been produced for both real-time and post-weld IR NDE inspections that were conducted in assembly plants. Potential technology transfer and licensing arrangements are under discussion.

Zhili Feng, Principal Investigator
Oak Ridge National Laboratory
Phone: (865) 576-3797; Fax: (865) 574-4928
E-mail: fengz@ornl.gov

Benda Yan and Sriram Sadagopan, Principal Investigators
ArcelorMittal USA
3300 Dickey Road
East Chicago, IN 46312
Phone: (219) 399-6922
E-mail: benda.yan@arcelormittal.com

Contributors:
ORNL: Xinghua Yu, Don Erdman, Yanli Wang, Wei Zhang, Dongxiao Qiao, Stan David

ArcelorMittal: Wenkao Hou, Steve Kelly

ESAB: Wesley Wang

Colorado School of Mines: Zhifeng Wang, Zhenzhen Yu, Sindu Thomas and Stephen Liu

Accomplishments

- Confirmed reduced weld residual stresses in the low transformation temperature (LTT) welds by means of high-energy synchrotron experiment. (FY 2014)
- Demonstrated the feasibility of alternating weld distortion in thin gage steel sheet metals by means of LTT weld wires. (FY 2014)
- Successfully demonstrated a new weld filler metal design approach and concept that could effectively control the stresses in the high stress concentration region of short stitch weld commonly used in the auto-body structures. Preliminary fatigue testing confirmed a 3–5 × weld fatigue improvement. (FY 2013)
- Successfully developed a mechanical stress management approach and demonstrated that such an approach improves the weld fatigue life between 5 and 10 times at the high cycle fatigue testing range, which is more relevant to the durability of auto-body structures. (FY 2013)
- Completed the initial fatigue testing of baseline welds fabricated with both conventional weld wire and the LTT weld wires to generate the applied stress magnitude verses cycles to failure (S-N) curves. (FY 2012)
- Completed the initial development of weld thermal-metallurgical-mechanical model to gain an understanding on the effect of low-temperature phase transformation on

the formation of compressive weld residual stress at the fatigue cracking initiation region. (FY 2012)
- Developed a new weld fatigue testing specimen configuration that is essential to maintaining the weld residual stress field representative of typical welded automotive body structures. (FY 2011)
- Completed a comprehensive survey of open literature to collect the published chemistry of LTT weld wires. Down-selected and produced three different types of baseline LTT weld wires. (FY 2011)

Future Directions

- Explore technology commercialization strategies to implement the weld fatigue life improvement technology developed in this project.

Technology Assessment

- Target: Develop robust, in-process weld fatigue life improvement technologies that can be used to join AHSS auto-body structural components with cost penalties acceptable to the automotive industry.
- Gap: The weld fatigue strength in the as-welded condition does not increase in proportion to the yield and tensile strength of AHSS. The insensitivity of weld fatigue strength to steel static strength is a major barrier for lightweighting of automotive components through down-gauging for chassis and other load-bearing components.
- Gap: Current weld fatigue improvement techniques are mostly post-weld based. The added steps are cost prohibitive in the high volume mass production automotive environment, and there exists large variability in the fatigue life achieved by various post-weld-based techniques.

✧   ✧   ✧   ✧   ✧

Introduction

Under a cooperative research and development agreement, ORNL and ArcelorMittal USA are working together to develop the technical basis and demonstrate the viability of innovative technologies that can substantially improve the weld fatigue strength and the durability of automotive body structures. Durability is one of the primary metrics in designing and engineering automotive body structures. Fatigue performance of welded joints is critical to the durability of the body structure because the likeliest locations for fatigue failure are often at welds. Recent studies by the Auto Steel Partnership Sheet Metal Fatigue Committee, DOE's Lightweighting Materials Program, and others [9–13] have

clearly revealed that, unlike the base metal fatigue strength, the weld fatigue strength of AHSS is largely insensitive to the base metal composition, microstructure, and strength under typical welding conditions used in automotive BIW. The lack of inherent weld fatigue strength advantage of AHSSs over conventional steels is a major barrier for vehicle weight reduction through down-gauging. Using thinner part cross-sections leads to an increase in applied stresses, thereby reducing durability under the same dynamic road loading conditions. In addition to AHSSs, a recent comparative study revealed that other lightweight alloys such as Al and Mg alloys may not offer improved weld fatigue strengths on a specific weight basis. Therefore, solutions to improve the fatigue strength of welds are critical to BIW lightweighting.

Approach

Instead of using post-welding techniques to improve the weld fatigue strength, this project focuses on developing in-process weld technology as part of the welding operation. The overall goal of the project is to develop effective ways to control and mitigate the key factors limiting the fatigue life of AHSS welds, including weld residual stress, weld profile, and weld microstructure/chemistry. This joint research effort also fully utilizes state-of-the-art integrated computational welding engineering (ICWE), neutron/synchrotron and other advanced residual stress measurement techniques, and fatigue testing and microstructure analysis capabilities at ORNL and ArcelorMittal Global R&D to perform the research and development. Two specific, in-process approaches are being developed in this project. Issues of both technical and economic nature unique to the automotive body structural welding environment were identified and are being addressed.

Results and Discussion

As reported in previous annual reports of the project, the feasibility of the effective weld fatigue life improvement by
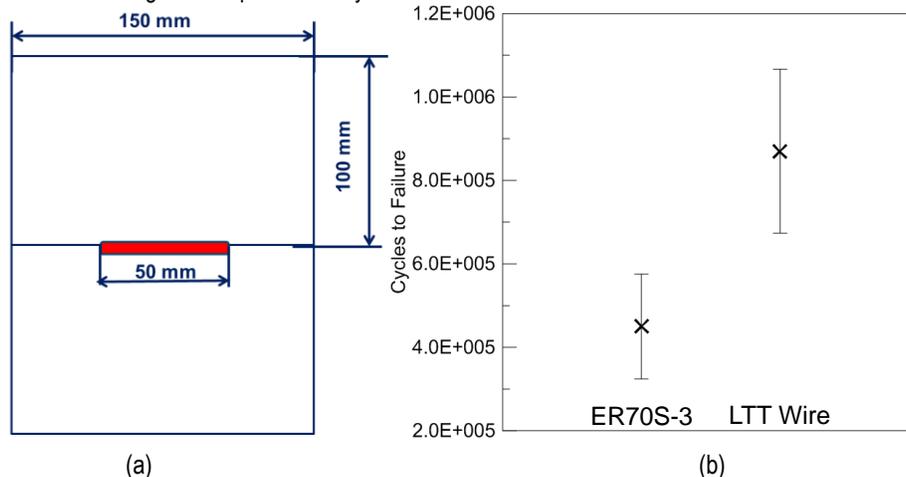
means of the two different in-process weld residual stress mitigation approaches have been demonstrated.

- A new weld metal design could effectively control the stresses in the high stress concentration region of short stitch weld commonly used in the auto-body structures. Fatigue testing confirmed a 3–5 × weld fatigue improvement under high cycle testing conditions.
- A thermomechanical stress management approach improves the weld fatigue life between 5 and 10 × at the high cycle fatigue testing range, which is more relevant to the durability of auto-body structures.

In FY 2014, a new LTT weld wire was evaluated. Once again, the LTT weld showed substantial improvement in weld fatigue life, as shown in Figure III-74. On average a ~2 × increase was demonstrated on 1.8 mm thick DP980 steel sheet at applied nominal stress level of 43 MPa.

More interestingly, the changes in weld residual stresses via LTT wire showed drastic changes in the dimensional changes of the thin gage steel sheet materials. This is illustrated in Figure III-75. In this particular case, two stitch bead-on-plate welds were deposited on a 2 mm thick low carbon steel sheet. Compared to the standard reference ER70S-3 weld wire, the welded steel sheet exhibited complete reversal of the distortion direction. In the case of reference ER70S-3 weld wire, the middle section of the steel sheet was bent downward for about 10 mm. To the contrary, the weld made with the new LTT wire bent the steel sheet upward for about 15 mm. This suggested the complete changes in weld residual stresses in the weld made by the new LTT wire. The changes in weld residual stresses are being investigated by the neutron diffraction technique. It should be noted that such drastic change in distortion mode by the new LTT wire suggests the possibility of control weld distortion by further refinement of LTT weld wire.

(a)

(b)

Figure III-74: Fatigue testing results with a new LTT wire compared with baseline ER70S-3 weld wire: (a) special weld fatigue specimen configuration and (b) fatigue testing results. R=0.1, f=10Hz.
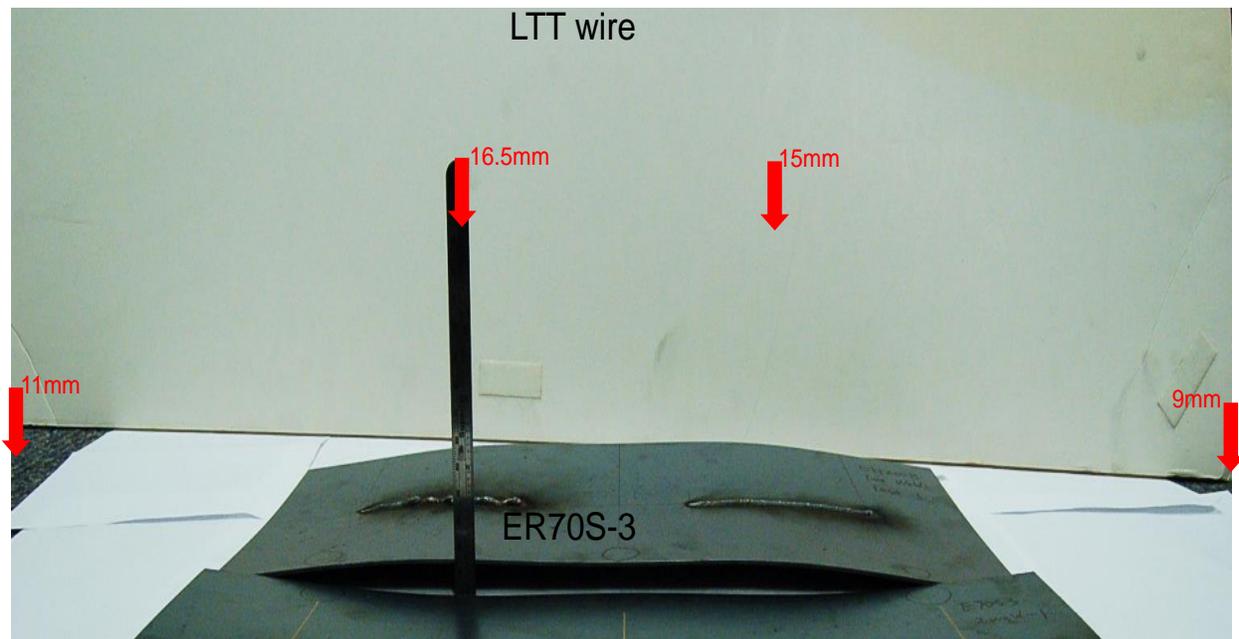
Figure III-75: Reversal of distortion mode with the use of LTT wire.

In FY 2014, we also completed the weld residual stress measurement by means of high-energy synchrotron x-ray diffraction technique that was started in FY 2013. The synchrotron measurement confirmed the substantial reductions of weld residual stresses in the region near the weld (Figure III-76), thereby providing the technical basis for the observed drastic weld fatigue life improvement. Due to experimental difficulties, residual stresses approximately 10 mm away from the weld fusion line were obtained. New experimental setup is being devised to obtain residual stresses closer to the fusion line.

In addition, we are working on direct measurement of the weld stress evolution during welding, based on a unique high-temperature digital image correlation (DIC) measurement technique specifically developed for in situ weld stress/strain measurement at ORNL [14]. We expect that the in situ DIC measurement during welding will provide additional direct evidence on the role of low temperature phase transformation on the suppression of high-tensile weld residual stresses.

(a)

(b)

(c)

(d)
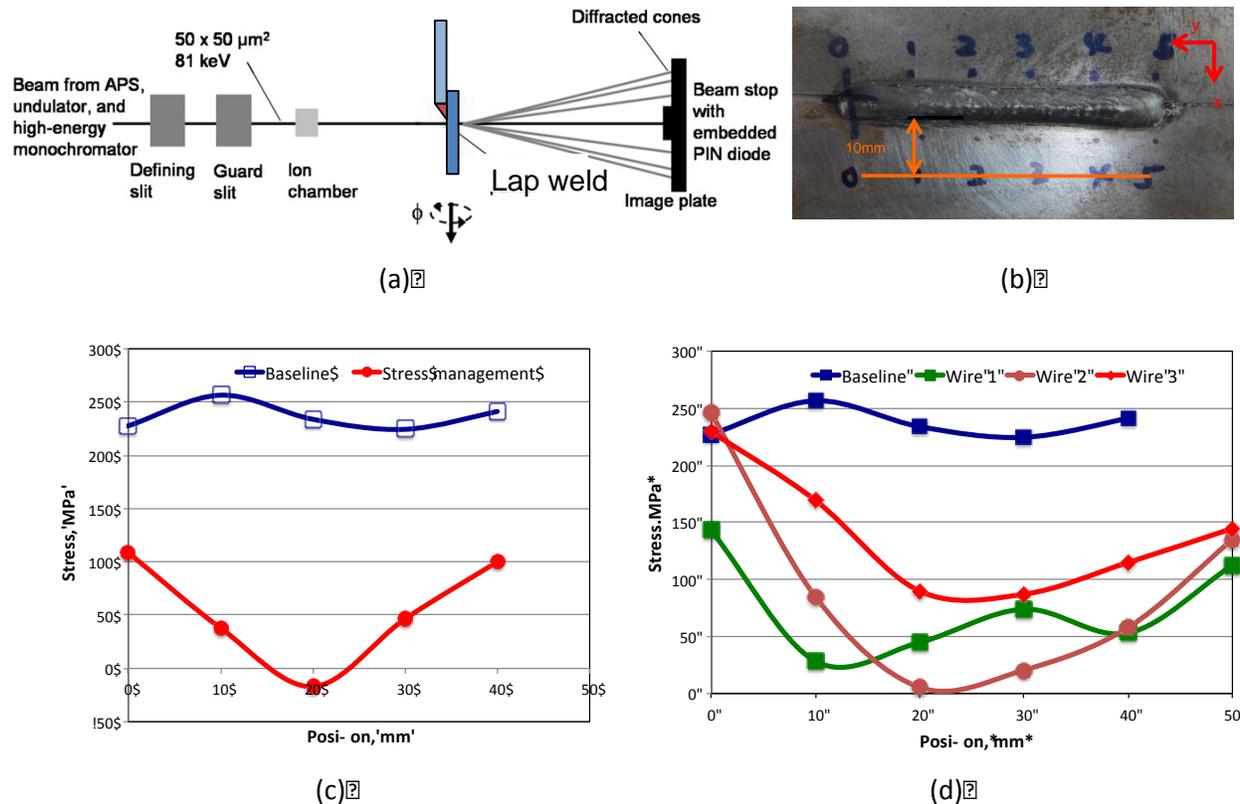
Figure III-76: High-energy synchrotron residual stress measurement. Transverse residual stresses are shown. (a) Synchrotron diffraction experimental setup. (b) Measurement locations relative to the stitch weld. (c) Reduction of weld residual stresses by means of proactive thermomechanical stress management. (d) Reduction of weld residual stresses by means of LTT weld wires with three different LTT wires and the baseline ER70-S weld wire.

Technology Transfer Path

The primary technology transfer path is to work closely with the industry partners of the project – a major steel supplier and a major welding consumables manufacturer – that have the business interests and marketing capability to quickly commercialize the technology developed in this project. In addition, we plan to disseminate the findings and results from the project to automotive OEMs and other interested parties through the extensive communication channels that we have established over the years.

Conclusions

Weld fatigue life has been identified as one of the key technology barriers to widespread use of lightweight materials (AHSS, Al, and Mg alloys) for auto-body structure lightweighting. The technology developed in this project is expected to provide cost-effective and practical solutions to the automotive industry to address this critical issue.

Significant technical progress has been achieved in this project: 3–5 × and 5–10 × weld fatigue life improvement were demonstrated using two different novel approaches to control and mitigate weld residual stresses. The changes in weld residual stresses could also drastically change the welding-induced distortion in thin sheet steels used for auto-body structural components. High-energy synchrotron measurement confirmed the substantial reductions of weld residual stresses in the region near the weld thereby providing the technical basis for the observed drastic weld fatigue life improvement.

III.18 Infrared (IR) Heat Treatment of Cast Bimetallic Joints and Residual Stress Characterization

Thomas R. Watkins, Principal Investigator
Oak Ridge National Laboratory
Phone: (865) 387-6472; Fax: (865) 574-3940
E-mail: watkinstr@ornl.gov

Timothy W. Skszek, Principal Investigator
Cosma Engineering
4121 North Atlantic Boulevard
Auburn Hills, MI 48326
Phone; (248) 786-2584; Fax: (248) 786-2583
E-mail: tim.skszek@vehmaintl.com

Contributors:
ORNL: Adrian Sabau, Donald Erdman III,
Gerald M. Ludtka, Bart Murphy

Promatek Research Centre: Xiaoping Niu

Accomplishments

- Completed a series of heat treatments on flat plates to determine the most promising heat treatment for a modified T6 schedule. Subsequently, heat treated joints. (FY 2006)
- Completed 100% of the neutron residual stress data collection and analysis for a series of conventionally heat-treated joints and one modified T6 heat-treated joint to determine conditions in which beneficial residual stresses are changed. (FY 2014)
- Completed the thermomechanical model to predict the residual stresses in the as-cast condition of a joint. (FY 2014)

Future Directions

- As time allows, the model may be refined further and a publication may follow. The project has now ended.

Technology Assessment

- Target: Complete and document both a modified T6 and a T5 heat treatment schedule for a bimetallic joint. Manufacture demonstration joints and validate that flat casting samples treated according to this schedule meet minimum performance requirements: modified T6: yield strength >250 MPa, ultimate tensile strength >310 MPa, elongation >8%; T5: yield strength >172 MPa, ultimate tensile strength >243 MPa, elongation >7%.
- Target: The developed heat treatment reduced processing time from >280 minutes to less than 70 minutes to produce a modified T6 heat treatment with improved material properties.
- Gap: Traditional heat treatments are either too time consuming or degrade the beneficial residual stresses in bimetallic joints.

✧   ✧   ✧   ✧   ✧

Introduction

The technical objective of this cooperative research and development agreement (CRADA) is to develop and model a heat treatment process based on IR heating of an Al casting and a bimetallic joint to produce a T5 temper in a shorter period of time than is currently achievable and, separately, to produce a modified T6 temper for improved mechanical properties without the loss of joint integrity. IR heat treatments have been demonstrated to provide reduced processing time, reduced energy requirements, and improved material properties of Al components, including strength and elongation, relative to convective thermal heat treatment methods.

This project addresses the DOE Vehicle Technologies Office Lightweighting Materials technology barrier "Joining and Assembly" by facilitating the use of lightweight, high-performance materials that will contribute to the development of vehicles that provide better fuel economy yet are comparable in size, comfort, and safety to current vehicles. The project is focused on a specific application for a high-volume vehicle platform; however, the joining technologies and methods developed will be applicable to multiple joints throughout this and other vehicle architectures.

The bimetallic joints [15] under consideration are part of the automotive front and rear cross-car structure, wherein a capped, steel tube is enveloped by molten Al to form a joint. A novel IR heat treatment approach is being developed to tailor the temperature profile, after casting, to strengthen the Al, better manage the residual stresses, and achieve a superior joint. Fabrication and thermal processing of a bimetallic structure comprising two dissimilar materials presents processing challenges to mitigate, reduce, and optimize many materials issues, such as residual stresses, interfacial reactions, and altered properties.

The A356 alloy is one of the most used Al-Si-Mg casting alloys, especially in the T6 heat-treated condition, because the improvements in mechanical properties make this alloy suitable for load-bearing applications. The first stage of T6 heat treatment is a solution treatment at an elevated temperature (e.g., 540°C), which homogenizes the chemistry and dissolves any preexisting precipitates. At the end of the solution treatment,

castings are typically quenched in water. This serves to retain the solute-rich homogeneous matrix chemistry, formed at high temperature, at room temperature. A subsequent aging treatment capitalizes on this super-saturated solid solution to generate controlled dispersions of very small strengthening precipitates within the matrix of Al grains.

Approach

The project has been organized into three research areas: IR processing experiments and prototype assembly; characterization of castings and joints; and model development and validation. Two distinct sets of samples were examined: flat casting samples and sectioned bimetallic "joint-only" samples. Cosma supplied flat castings and joint-only samples under standard processing conditions (T5 and modified T6) as well as untempered/un-heat-treated flat casting and joint-only samples.

During Phase II of this project, a modified T6 heat treatment method for flat Al-Si-Mg castings (i.e., not bimetallic joints) was developed based on a combined computational and experimental approach. A prototype furnace and quenching scheme were assembled and ordered, respectively. Residual stresses were measured using neutron diffraction and subsequent data analyses were performed. A thermomechanical model for steel deformation during a heating schedule was developed, and a model for the bimetallic joint was developed.

Results and Discussion

A prototype IR oven was assembled, capable of simultaneously heating samples on top and bottom, to minimize thermal gradients (Figure III-77). IR heat treatment experiments associated with ~5 mm thick cast A356 plates were conducted (Table III-9). The experiment included evaluation of a short cycle solutionization, quench, and age hardening process as well as a solutionization, quench, and two-step age hardening process. A heating rate of 1.75°C/s was maintained for all positive thermal gradients. Quench mediums of compressed dry air, compressed moist air, and compressed wet air were evaluated. A 20-minute dwell time at solutionizing temperature was maintained for all thermal events. The yield stress, ultimate tensile strength and elongation results (two samples/condition) indicate that a rapid quench after solutionizing with a double step aging process yielded the best results, close to the targets. Mechanical test results indicate that improved material properties can be realized, as compared to traditional solutionization and age hardening heat treatment cycles of 6 to 10 hours in duration,

in a reduced time period 10% to 16% percent of the time at temperature, providing significant energy reduction as well as improved material properties.

Subsequently, one joint was heat treated with the most promising schedule for a residual stress determination: solutionize at 482°C/900°F for <30 min.; quench with wet air; age in two steps: 134°C/273°F for 20 min., then 195°C/383°F for 20 min.

Table III-9: Summary of heat treatment conditions used with flat plate castings.

Solutionize	Quench*	Age 1	Age 2
482°C, 20 min	Q1	134°C, 20 min	195°C, 20 min
482°C, 20 min	Q2	134°C, 20 min	195°C, 20 min
482°C, 20 min	Q3	134°C, 20 min	195°C, 20 min
482°C, 20 min	Q1	172°C, 30 min	None
482°C, 20 min	Q2	172°C, 30 min	None
482°C, 20 min	Q3	172°C, 30 min	None
525°C, 20 min	Q1	170°C, 120 min	None
525°C, 20 min	Q2	170°C, 120 min	None
525°C, 20 min	Q3	170°C, 120 min	None

*Q1 = compressed air, Q2 = compressed moist air, and Q3 = compressed wet air.

Residual Stress Determination

Residual stresses play an important role in these joints. Previously, a series of conventionally heat-treated joints were examined using neutron diffraction to measure and map the residual stresses in the joint region. In this fiscal year, the residual stress determinations were conducted at the High Flux Isotope Reactor at ORNL using the HB-2B beam line in the joint that was heat treated at 260°C/500°F for 4 hours and then air cooled and the one that received the modified T6 heat treatment described above. The position of the (211) steel reflection and (311) Al reflection were measured in the radial, hoop, and axial directions. The experimental details are similar to those described in the literature (Johnson et al. 2012). Figure III-78 shows the residual stresses in the 500°F and modified T6 samples. Comparison to prior work, indicates that the residual stresses in the 500°F sample are almost unchanged from the as-cast condition. The modified T6 heat treatment shifts the residual stress more compressive by nominally 100 MPa, while the spread of residual stress was nominally unchanged.

A.

B.

C.
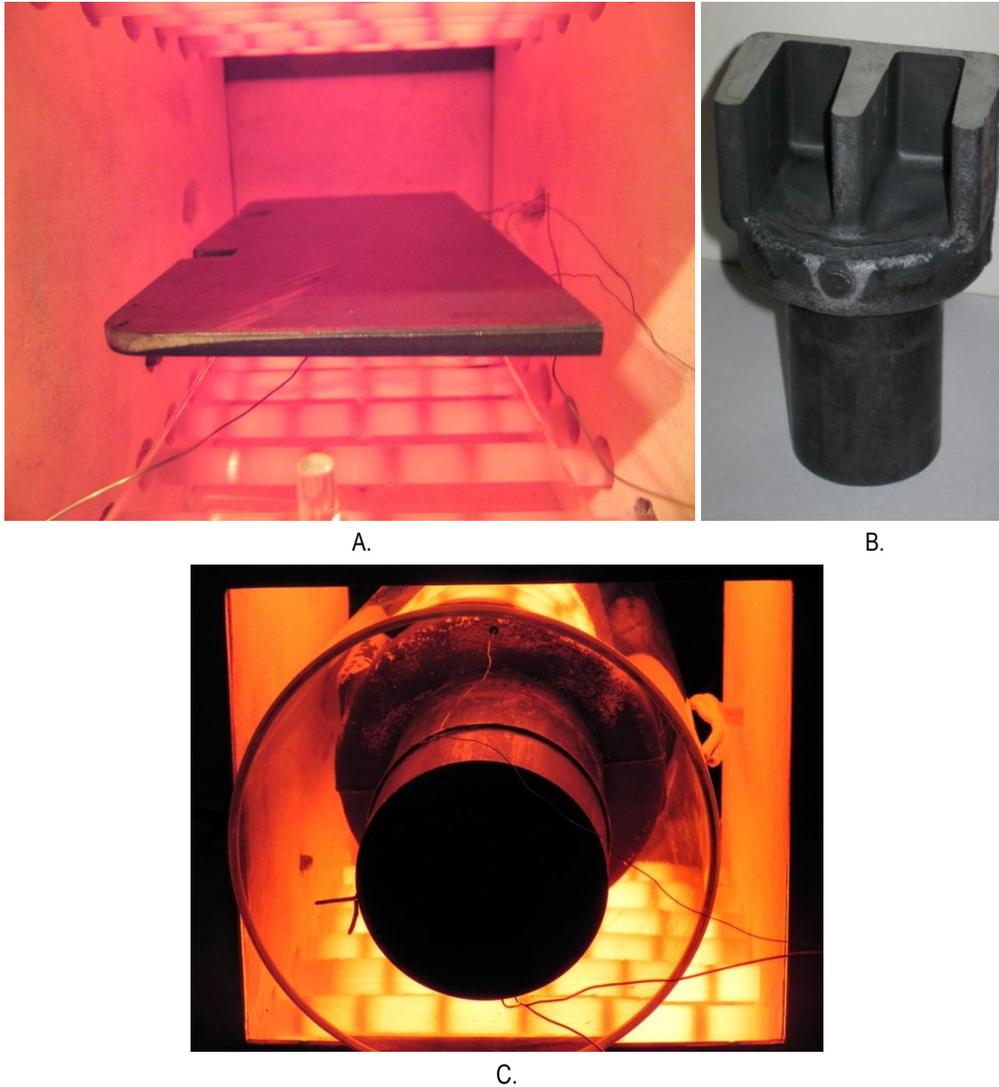
Figure III-77: A. Photograph of the interior (210 × 127 × 203 mm) of the prototype furnace while at temperature. There were 12 halogen bulbs, 6 on top and 6 on the bottom (500 W, 120 V, 56.4 W/ each; 6 kW for entire furnace) spaced 121 mm apart. The A356 plate was 6 × 98 × 180 mm and was supported by a quartz plate resting on four quartz posts. The plate was positioned in the center of the furnace to ensure equal spacing from the IR lamps. B. Photograph of the overcast A356 Al–0.2% C steel tube joint which is ~150 mm tall. C. The Al-steel joint being heat treated. Thermocouple wires can easily be seen in A. and C.
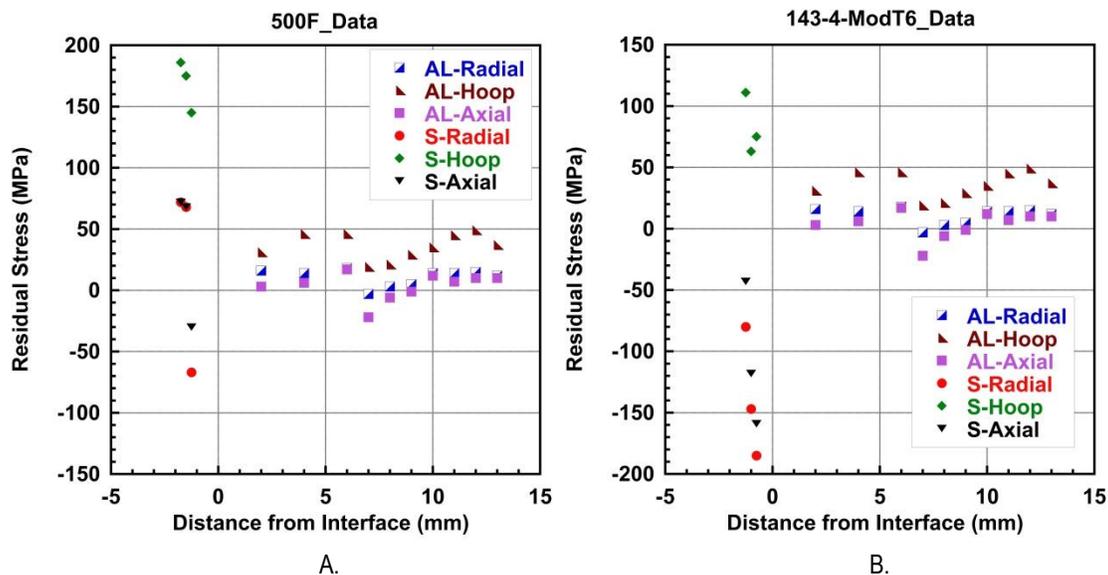
Figure III-78: The residual stresses as a function of distance from the interface for the 500°F (A) and modified T6 samples (B).

Model Development and Validation

A complete thermomechanical simulation was conducted during the metal casting of the Al component around the steel insert using commercial software ProCAST. Some of the main unknowns in the modeling of this process are the heat transfer coefficients at various interfaces. It has to be mentioned that limited experimental data was available for this modeling task. For example, the liquid metal pressure, mold and metal temperature data was limited. The die preheated the steel tube after loading it into the die and during metal casting. The solidification time was between 20 to 40 s. In the absence of experimental data for the heat transfer coefficients, the heat transfer coefficients were obtained by (a) estimating their expected range of variation for similar metal casting processes and (b) conducting a series of preliminary simulations to match, as closely as possible the limited experimental data available. A literature review was conducted to identify typical values used for heat transfer coefficients for the squeeze casting of Al, the closest casting process to those used here. This is turn was used to model the evolution of the solid fraction of solid, solidification times and temperatures during solidification at locations in the joint area.

In order to obtain residual stresses, inelastic properties of both steel and aluminum must be considered. Both aluminum and steel were considered to exhibit a rate-independent isotropic hardening plasticity thermomechanical behavior. Temperature-dependent property data (i.e., Young's moduli and yield stress) were used for both the elastic and plastic properties was predicted and taken from literature. The numerical simulation can be used to obtained data on the distribution of the final deformation and final state of stress of the as-cast sample. From these thermomechanical data, the residual stresses in the radial, hoop and axial directions were obtained at the same locations where neutron scattering

measurements were conducted. This required average the predicted stresses and strains in the model over the area of the gauge area of the neutron residual stress measurement. The results for the residual stresses are shown in Figure III-79 for a joint overcast depth of 5 mm. While the trends are quite similar, the magnitudes are quite different. For example, the results for the hoop stress in the steel are almost seven times those measured. Refinement of this model may continue.

Technology Transfer Path

The primary technology transfer path for this effort is to work closely with the industry partner—Cosma—which has the business interests and marketing capability to quickly commercialize the technology developed in this project. The technology being developed is being put into use on a high-volume vehicle platform as the technology is developed.

Conclusions

ORNL's and Cosma's effort through this CRADA have advanced the overcast technology. The modeling, prototype development, novel heat treatments, and residual stress and mechanical property characterizations have improved the state-of-the-art overcast joining technology and will be applicable to multiple joints throughout this and other vehicle architectures. This work benefits numerous Tier I automotive suppliers and will contribute to achieving DOE's goal of improved fuel efficiency and reduced emissions.
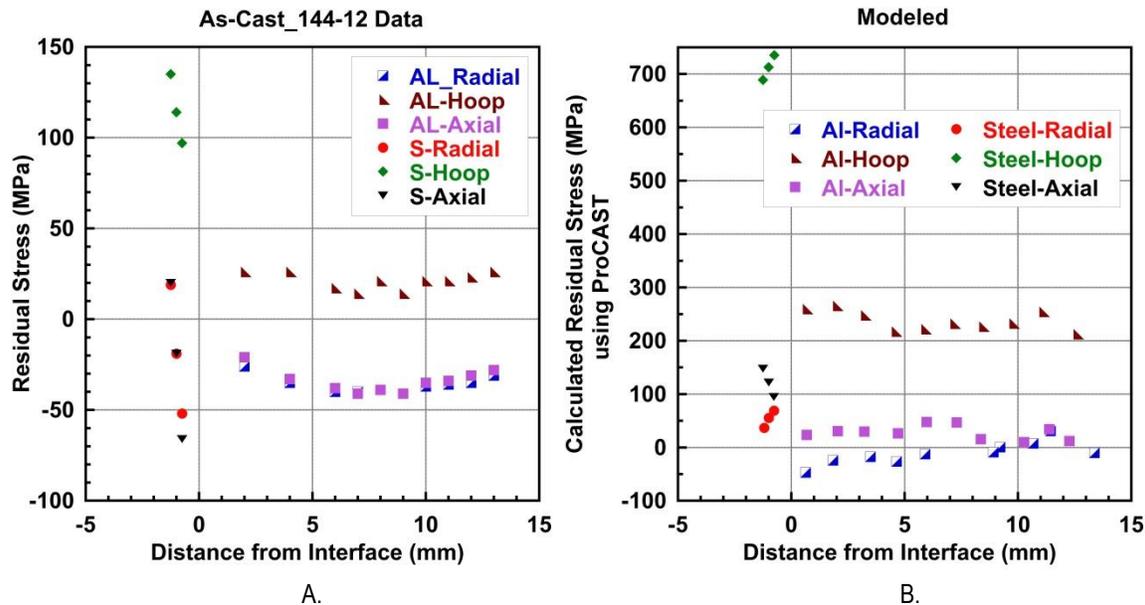
Figure III-79: A, measured, and B, predicted, residual stresses [MPa] for the as-cast condition.

The purpose of this project was to investigate IR heat treatment to increase the yield strength and elongation of the cast Al portion of an Al–steel bimetallic joint to achieve improved material properties, resulting in a superior joint. The modified T6 heat treatment experiments using IR processing are complete. Flat casting samples were heat-treated with an IR heating system. The residual stress characterization of bimetallic joints is complete. A heat transfer model and casting model will provide insight on the evolution of residual stresses in the current and future bimetallic components, indicating how the beneficial residual stresses in Al form and maintain following the heat treatment. A thermomechanical model for the steel was completed. Temperature-dependent property data was used for both the elastic and plastic properties. The computed residual deformation of the steel cap and cylinder is in qualitative agreement with the experimental data. From these thermomechanical data, the residual stresses in the hoop, axial, and radial direction were obtained at the same locations where neutron scattering experiments were conducted.

Conclusions

Research under this task has provided insights into the operating mechanisms of protective films on Mg alloys that provide the scientific community with guidance on the development of protective films and better alloys for reducing the corrosion behavior of future Mg alloys and the automotive parts manufactured from those alloys. Significant progress was made in FY 2013 on the development of a cost-effective, robust, accurate IR thermography-based system to quantitatively inspect spot weld quality in automotive manufacturing plants. Intelligent and automated software was

developed and implemented in the system and tested in automotive assembly plants. Significant technical progress was achieved in reducing the weld fatigue of AHSS joints by 3–10 × using two novel approaches to control and mitigate weld residual stresses. This was improved upon by the development of a new filler wire. IR-based heat treatment schedules were developed for T5 and T6, and these are being implemented in automotive production facilities.

Presentations/Publications/Patents

1. Brady, M. P. Advanced Characterization of Mg Alloy Surface Films, invited presentation at CORROSION 2014, NACE, March 9-13, 2014, San Antonio, Texas, USA.

2. Unocic, K. A.; Elsentriecy, H.H.; Brady, M.P.; Meyer, H.M.; Song, G.L.; Fayek, M.; Meisner, R.A.; Davis, B. Transmission Electron Microscopy Study of Aqueous Film Formation and Evolution on Magnesium Alloys. *Journal of the Electrochemical Society,* 161 (6), C302-C311 (2014).

3. Brady, M.P.; Fayek, M.; Elsentriecy, H.H.; Unocic, K.A.; Anovitz, L.M.; Keiser, J.R.; Song, GuangLing; Davis, B. Tracer Film Growth Study of Hydrogen and Oxygen from the Corrosion of Magnesium in Water. *Journal of the Electrochemical Society,* 161 (9), C395-C404, (2014).

4. Brady, M.P.; Rother, G.; Anovitz, L.M.; Littrell, K.C.; Unocic, K.A.; Elsentriecy, H.H.; Song, G.-L.; Thomson, J.K.; Gallego, N.C.; Davis, B. Film Breakdown and Nano-Porous Mg(OH)2 Formation from Corrosion of Magnesium Alloys in Salt Solutions, submitted for publication.

5. Chen, J.; Feng, Z.; Wang, H.; Zhang, W. Non-destructive Inspections of Welds and Joints Using Infrared Imaging and Post-Weld Heating, ORNL patent application, May 2011.

6. Chen, J.; Feng, Z.; Zhang, W. A Non-destructive and Real-time Inspection System for Monitoring Resistance Spot Welding Using Infrared Thermography, ORNL patent application, August 2012.

7. Chen, J.; Feng, Z.; Zhang, W. Software title "IR Spot Weld Inspect". Copyright Number 50000074, 2014.

8. Chen, J.; Feng, Z.; Warren, Charles D. Nondestructive Inspection of RSW of AHHS by Infrared Technology, International Symposium on Advances in Resistance Welding 2014, Atlanta, Georgia.

9. Chen, J.; Zhang, W.; Yu, Z.; Wang, H.; Feng, Z. Automated Spot Weld Inspection Using Infrared Thermography, Presented at 9th International Conference on Trends in Welding Research, Chicago 2012.

10. Chen, J.; Zhang, W.; Yu, Z.; Feng, Z. Automated Spot Weld Inspection using Infrared Thermography, Proceedings of 9th International Conference on Trends in Welding Research.

11. Chen, J.; Zhang, W.; Feng, Z. Resistance Spot Welding On-line Inspection System Based on Infrared Thermography, Presentation in FABTECH 2012.

12. Chen, J.; Feng, Z.; Zhang, W. An Online Infrared-based Resistance Spot Weld Inspection System, Presentation in SAE 2013 World Congress.

13. Watkins, T.R.; Sabau, A.; Erdman III, D.; Ludtka, G.M.; Murphy, B.; Joshi, P.; Yin, H.; Zhang, W.; Skszek, T.W.; Niu, X. *IR Heat Treatment of Hybrid Steel-Al Joints*; Report No. ORNL/TM-2014/ORNL-10-02839, **2014**, Oak Ridge National Laboratory, Oak Ridge, TN.

14. Johnson, E.M.; Watkins, T.R.; Schmidlin, J.E.; Dutler, S. A. A benchmark study on casting residual stress. *Metall. Mater. Trans. A* **2012,** 43A(5) 1487–1496.

15. Qiao, D.; et al. The Effect of Martensitic Phase Transformation on Weld Residual Stress Distribution in Steel Sheet Lap Joint—A Computational Study, in Proceedings of the 9th International Conference on Trends in Welding Research, Chicago, IL, 2012.

16. Wang, Z.; Yu, Z.; Feng, Z.; Liu, S. Effect of Low Transformation Temperature Welding Consumables on Mechanical Properties of Lap Joints. 2014 AWS Annual Convention, Atlanta, Georgia.

References

1. Song, G.; Atrens, A. Corrosion mechanisms of magnesium alloys. *Advanced Engineering Materials,* **2007**, 9 (3), pp. 177-183.

2. Song, G.L. Recent progress in corrosion and protection of magnesium alloys. *Advanced Engineering Materials*, **2005**, 7 (7), pp. 563-586.

3. Gray J.E.; Luan, B. Protective coatings on magnesium and its alloys--a critical review, *Journal of Alloys and Compounds*, **2002**, 336 (1-2), pp. 88-113.

4. Seyeux, A.; et al. ToF-SIMS depth profile of the surface film on pure magnesium formed by immersion in pure water and the identification of magnesium hydride. *Corrosion Science,* **2009**, 51 (9), pp. 1883-1886.

5. Hara, N.; et al. Formation and breakdown of surface films on magnesium and its alloys in aqueous solutions. *Corrosion Science*, **2007**, 49 (1), pp. 166-175.

6. Nordlien J.H.; et al. A TEM investigation of naturally formed oxide films on pure magnesium. *Corrosion Science,* **1997**, 39 (8), pp. 1397-1414.

7. Brady, M.P.; et al. Tracer film growth study of hydrogen and oxygen from the corrosion of magnesium in water. *Journal of the Electrochemical Society,* **2014**, 161 (9), pp. C395-C404.

8. Brady, M.P.; et al. Film breakdown and nano-porous $Mg(OH)_2$ formation from corrosion of magnesium alloys in salt solutions. **2014,** submitted for publication.

9. Bonnen, J.; Iyengar, R.M. Fatigue of Spot Welds in Low-Carbon, High-Strength Low-Alloy, and Advanced High-Strength Steels and Fatigue of Fusion Welds in Advanced High-Strength Steels. In *2006 International Automotive Body Congress,* pp. 19-30.

10. Yan, B.; Lalam S.H.; Zhu, H. *Performance Evaluation of GMAW Welds for Four Advanced High-Strength Steels.* SAE International Paper No. 2005-01-0904, 2005.

11. Iyengar R.M.; et al, 2008. Fatigue of Spot-Welded Sheet Steel Joints: Physics, Mechanics and Process Variability. 2008 Great Designed in Steel.

12. Feng, Z.; Chiang, J.; Kuo, M.; Jiang, C.; Sang, Y. A New Perspective on Fatigue Performance of Advanced High-Strength Steel GMAW Joints. Sheet Metal Welding Conference XIII, 2008.

13. Feng, Z.; Sang, Y.; Jiang, C.; Chiang, J.; Kuo, M. Fatigue Performance of Advanced High-Strength Steels (AHSS) GMAW Joints. In SEA 2009 World Congress, Detroit, MI, Paper No. 09M-0256.

14. Chen, J.; Yu, X.; Miller, R.G.; Feng, Z. "In-situ Thermal Strain and Temperature Measurement and Modeling During Arc Welding. In *Science and Technology of Welding and Joining*, in press (2014).

15. Buchholz, K. Two-metal cradle from Cosma is production-ready. *Automot. Eng.* [online], **2011,** 15. http://www.sae.org/mags/AEI/9505 (last accessed November 2014).

III.19 Pulsed Joining of Body-In-White Components – Ford Motor Company

John Bonnen, Principle Investigator
Ford Motor Company
MD 3135 RIC
P.O. Box 2053
Dearborn, MI 48121-2053
Phone: (313) 319-1764
E-mail: jbonnen@ford.com

Sergey Golovashchenko, University Partner
Oakland University
2200 N Squirrel Roiad
Rochester, MI 48309
Phone: (248) 370-4051
E-mail: golovash@oakland.edu

Xin Sun, National Laboratory Partner
Pacific Northwest National Laboratory
902 Battelle Boulevard
Richland, WA 99352
Phone: (509) 372-6489
E-mail: xin.sun@pnnl.gov

William Joost, Technology Area Development Manager
U.S. Department of Energy
1000 Independence Avenue, S.W.
Washington, DC 20585
Phone: (202) 287-6020; Fax: (202) 856-2476
E-mail: william.joost@ee.doe.gov

Contractor: Ford Motor Company
Contract No.: DE-EE0006432

Abstract/Executive Summary

The objective of this project was to develop cost efficient high quality pulsed welding (PW) technology for joining 6xxx Al (Al) and high strength steel (HSS) (with tensile strength above 580 megapascals (MPa)) components enabling broad usage of hydroformed parts and leading to substantial weight reduction of cars and trucks to reduce U.S. demand on petroleum, lower carbon emissions and energy expenditures. In general, pulsed welding is a form of impact welding where two dissimilar metal pieces are joined by accelerating one to velocities exceeding 300 meters per second (m/s) at which point the first piece strikes the second and forms a weld. In this work, two methods were used to accelerate the flyer material: electromagnetic (EM) pulse and electrohydraulic (EH) pulse launching. The advantage of pulsed welding techniques is that welds can be formed between two materials that cannot otherwise be welded, such as high strength AlAl and HSS. The technical objectives of the project included: 1) developing cost affordable production feasible tooling design for PW of 6xxx Al to HSS with strengths above 580 MPa; 2) demonstrating that fabricated joints can exceed the required service load strength initially at the coupon level and then at the component level; 3) developing fundamental understanding of the mechanisms of joint formation and conditions leading to formation of high quality PW joint; and 4) creating a numerical model predicting the tooling and electric discharge parameters necessary for the joint formation and that satisfy the targeted strength parameters. The project successfully developed: 1) EM and EH pulsed welds between high strength Al with tensile strengths exceeding 240 MPa and steels exceeding 580 MPa; 2) pulsed welds of extrusions with strengths exceeding project requirements; 3) EM and EH flyer launch models and 4) weld interface formation models. However, the grant holder, Ford Motor Company (FMC), could see no path to commercialization within a reasonable time frame and the work was discontinued at the end of the first budget period.

Accomplishments

- World first development/successful use of Electro-Hydraulic Pulse Welding (EHPW).
- World first welding of high strength Al (Tensile Strength (T.S.) > 200 MPa) to HSS (T.S. > 580MPa) with electromagnetic pulse (EMP) and electrohydraulic pulse (EHP) welding techniques.
- Successfully demonstrated efficacy of single-turn coil design in EM welding of high strength Al to HSS.
- Exceeded weld base metal strength targets by successfully EM pulse welding 6061-T6 Al (326 MPa T.S. vs 240 MPa for T4 condition) to 1045 cold rolled steel (737 MPa T.S. vs. 580 MPa target)
- Successfully demonstrated an EM pulse welded EX-EX (extrusion to extrusion) structure that exceeded the 20 kilonewton (kN) project requirement. The weld did not fail but rather the tube base metal failed at 21 kN.
- Successful EH pulse welds created between dual phase (DP) 600 steel (600 MPa T.S.) and 6022-T4 Al (255 MPa T.S.).
- Successfully modeled electromagnetic pulse welding (EMPW) weld interface morphology based on both shape

and length scales as validated against actual metallographic measurements.

- Successfully modeled and validated the EH launch of the flyer up until the moment of impact, and the flight time and velocity profile.

Future Directions

- FMC None – Project concluded

Technology Assessment

- Target: Demonstrate strength of EX-SH PW with the strength of the weld exceeding 80% of the strength of 6xxx Al sheet.
- Gap: Tooling design for PW of EX-SH has been developed only at the conceptual level. Detailed design and experimental validation of the tool is required.
- Target: Demonstrate PW process satisfying the service requirements at the component level.
- Gap: Design and experimental validation of fixtures and tools feasible for the joint testing for service loads at the component level is required.

❖   ❖   ❖   ❖   ❖

Introduction

Pulsed joining (PJ) technology uses high-velocity impact between similar or dissimilar materials to create a solid-state joint that can be either a metallurgical weld or a mechanical bond. PJ technologies such as explosive welding (EXW) and magnetic pulsed welding (MPW) have been well known for several decades and are well publicized in the literature. They have been commercially exploited in limited industrial applications outside the automotive industry (plate cladding and joining) and limited use on transportation vehicles outside the body in white (BIW) (e.g. drive shaft assemblies). PJ processes are based on high velocity impact between welded materials which removes oxides from the surfaces to be welded and creates high strength bond between the materials. PJ avoids the fusion welding related distortions and microstructural degradation in the molten metal or heat affected zone (HAZ). PW is an autogeneous joining process that introduces no other materials (e.g. filler wire, rivets, interlayer bonding foils, etc.) that add cost both during manufacturing and recycling.

Approach

BIW assembly process requires welding of EX-EX as well as EX-SH metal parts. Space limitations and packaging issues during BIW assembly process require different versions of welding: when the pulsed pressure is applied from the inner part to the outer and vice versa. The project is targeting a solution for each of the required configurations. In order to realize industrial feasibility of PW class of joining, the costs of using a durable MPW coil must be compared to a high efficiency and low cost disposable coil design recently developed at Ford. Therefore, tooling design for MPW and EHPW was developed and demonstrated for EX-EX configuration of the joint during first budget period. Numerical simulation techniques predicting the tooling performance as well as the flyer acceleration process were developed for both processes. Simulation of the bonding process was based upon flyer material velocity distributions predicted at the acceleration stage. Validation of numerical models was to be performed by employing the Laser Doppler Velocimeter technology as well as by metallographic analysis of interface microstructure. Validation of achieved level of strength of both MPW and EHPW was done by mechanical testing of the welded samples.

Results and Discussion

Modeling Effort

Numerical modeling of both MPW and EHPW and validation of the obtained results was a major effort during FY 2014. The coupled model for MPW incorporates the analysis of electromagnetic and high-rate deformation processes that take place during extrusion/flyer acceleration and impact with the target. The LSTC commercial code, LS DYNA, was employed for this effort. Initial simulations of extrusion acceleration with a pulsed electromagnetic field incorporated coupled Maxwell equations, equations of dynamic deformation of a solid, and heat transfer equations.

Prior to constructing the experimental coils, the analysis was performed to define the most suitable material for use in the single turn coil for use in magnetic pulsed welding of tubes. Figure III-80a shows a completed 3-dimensional (3D) model simulating the EM acceleration of a 1 millimeter (mm) extrusion into a mandrel and Figure III-80b shows the von Mises stress distribution within the coil. The results indicated that cold rolled carbon steel is the most appropriate material for constructing the coil.
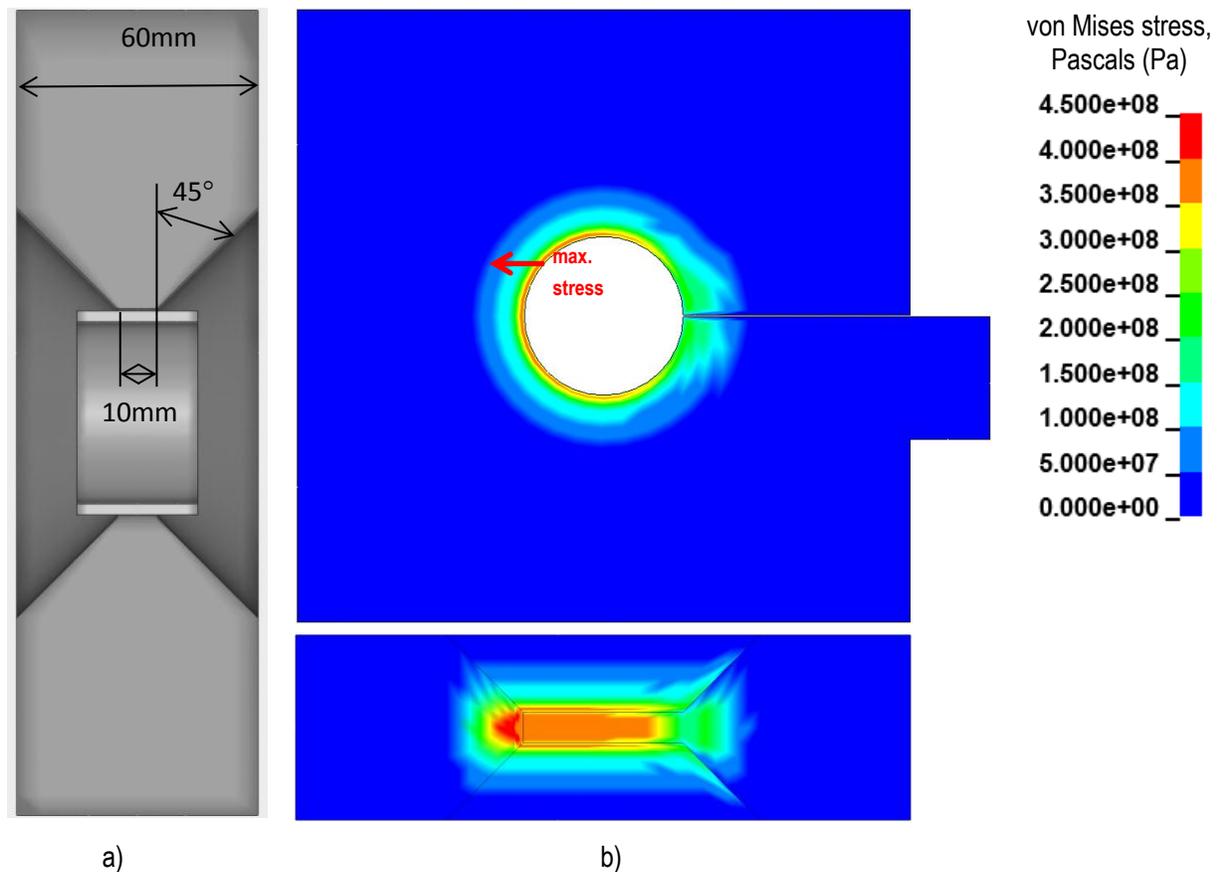
Figure III-80: Single-turn coil used for MPW of tubes: a) geometry, and b) von Mises stress levels during the discharge.

The simulation technique uses the EM module in LS-DYNA. Figure III-81 shows the results for the simulation of the electromagnetic coil accelerating an overaged Al 6061-T7 tube into a 1045 cold rolled 20° mandrel. The coil is in red, the flyer/extrusion is in blue and the mandrel is in green. Note that the impact angle made between the traveling flyer and the mandrel is very shallow and somewhat indeterminate given the mesh density which is already very high for a 3D simulation.

For EHPW, an electrohydraulic nozzle chamber concept was adapted wherein a radial electrode was located in the floor of a cylindrical cavity (height approximately equal to

diameter, $H \approx D$) and at the top of the cavity was placed a funnel (or cone). When a pulse is discharged at the bottom of the water filled cylinder, the water to moves up the cylinder and, once it enters the conical region, it accelerates (because of diminishing cross-sectional area) until it enters the nozzle at the end of the cone. The nozzle was another cylinder of $H \approx D$ = 10 mm intended to collimate the water flow. Thus, high water velocities are achieved which can launch a piece of metal at velocities sufficient for welding.

0.0 μs

4.5 μs

6.5 μs

8.5 μs

10.5 μs

17.5 μs
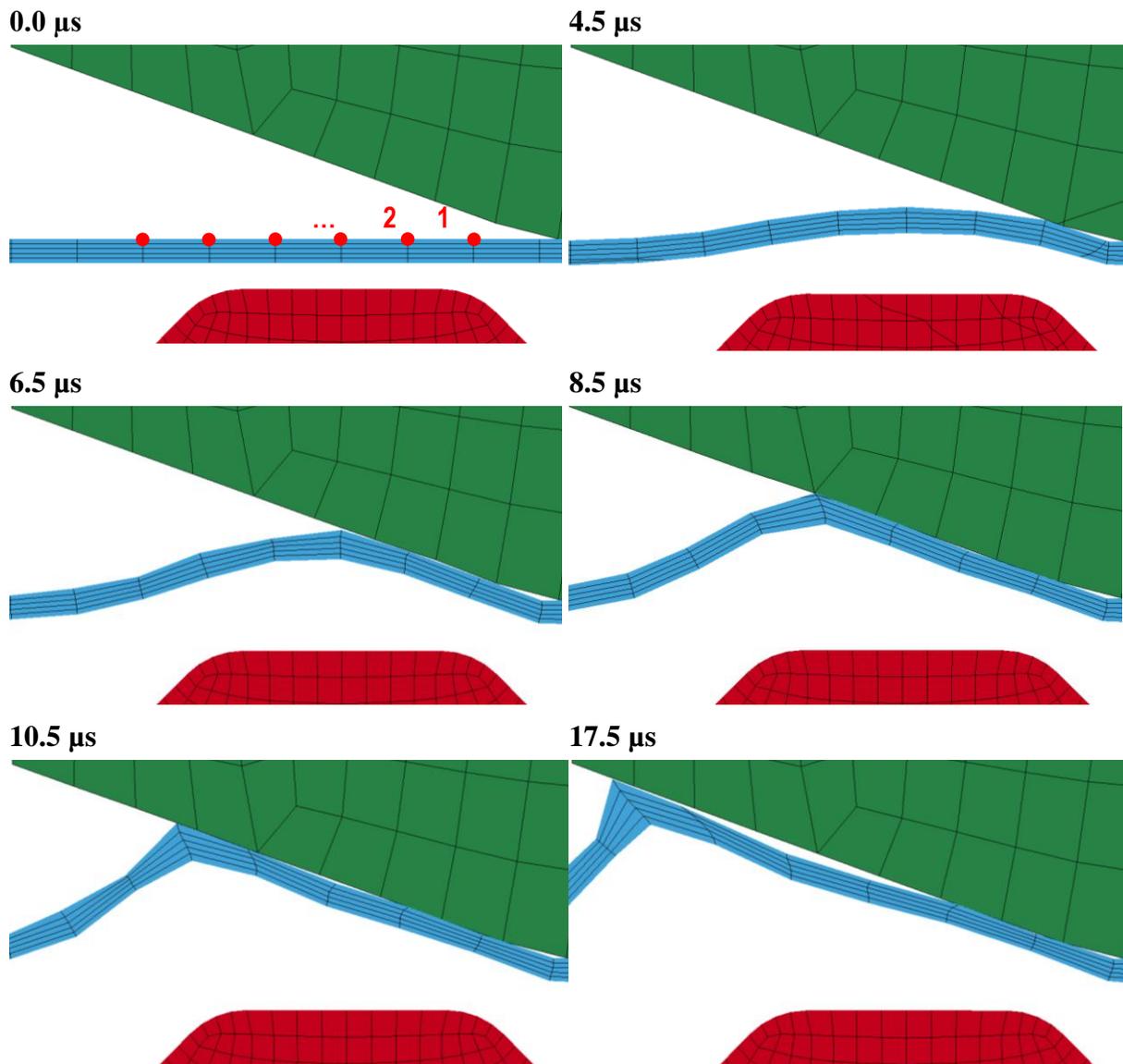
Figure III-81: Simulation for a 16 kilovolt (kV) (41.0 kilojoule (kJ)) discharge accelerating heat treated (350°C) Al 6061 into a 20° 1045 cold rolled (CR) steel mandrel at various time intervals in microseconds (μs). However, simulations indicate that the impact geometry is similar regardless of energy and Al material grade.

Numerical modeling of EHPW involves analysis of all stages of the process starting from the initial discharge channel where energy deposition starts and leads to the initial shock wave propagation, followed by reflection of pressure waves from the chamber walls, and then by the flow of liquid applying pressure to the flyer surface and accelerating it. In order to develop a numerical model of the EHPW process, the following models need to be developed and later on coupled: (1) electrical model of the discharge channel; (2) model of the plasma channel; (3) model of the liquid as a pressure transmitting medium; and (4) a deformable blank in contact with high pressure/high velocity liquid. Each individual model was developed using the capabilities of the LS-DYNA commercial code.

Thus the full model of the electrohydraulic nozzle chamber (or "cannon") was assembled from these component physical models. The energy used in the simulation was 6.8kJ (13kV). The discharge occurs at the bottom of the chamber. A magnified view of the simulation showing the jet of water leaving the nozzle is shown in Figure III-82. This simulation is of the launch of a small Al 6022-T4 flyer towards a DP600 target.

7.2 µs

7.3 µs

7.4 µs

7.5 µs

7.6 µs

7.7 µs

7.8 µs

7.9 µs

8.0 µs
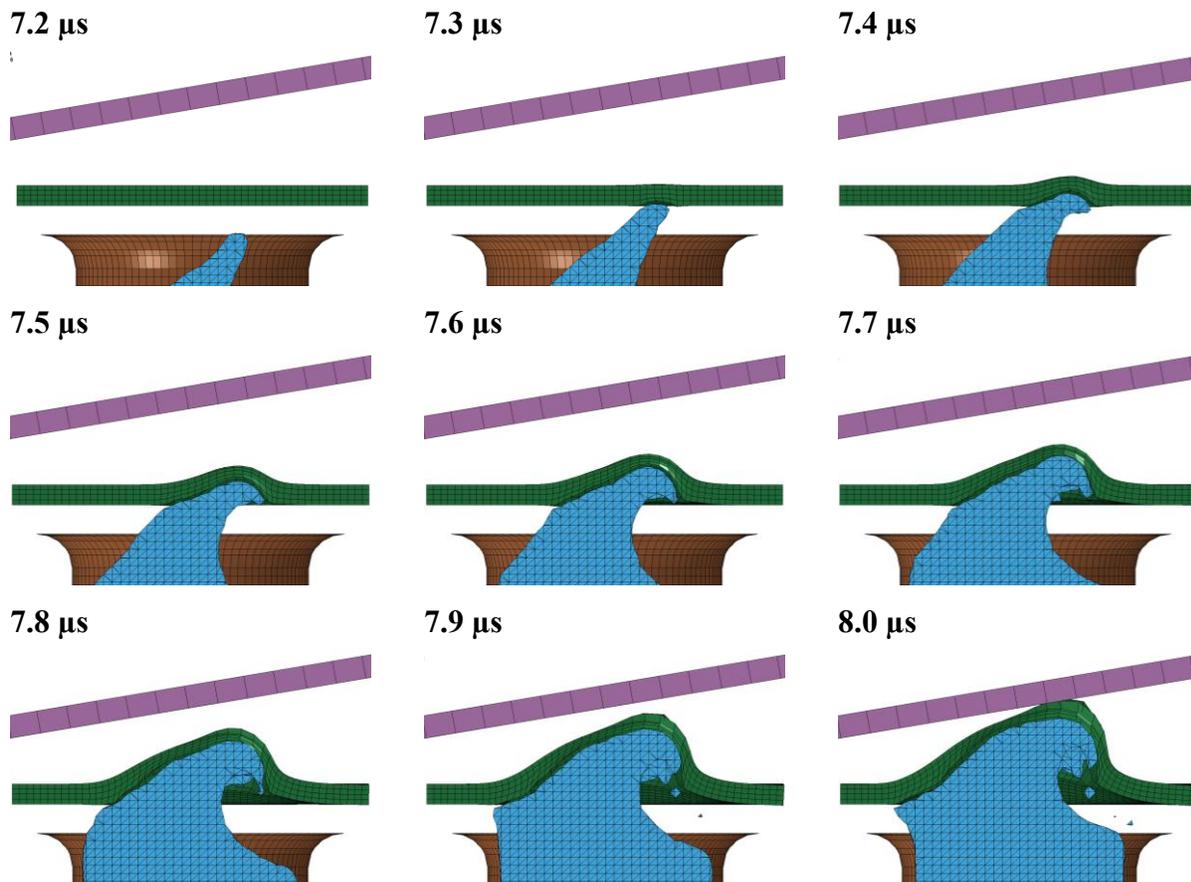
Figure III-82: Simulation of a 6.8kJ (13kV) EH pulse launching an Al 6022-T4 flyer into a DP600 steel target. A 70 µs offset is used on the time values.

Figure III-83 shows the centerline velocities for both the simulation and a Laser Doppler Velocimeter (LDV) experiment sharing the same settings (6.8kJ/13kV). There is a very good correlation between simulation and experiment including the moment of initiation of motion, the moment of impact (79µs), and the final velocity (~570m/s). The simulation was completed before the LDV experiment was run.

Modeling work of the interface in pulsed welding of Al to steel has been focused on developing a predictive thermo-mechanically coupled numerical framework to quantitatively resolve material response under extreme loading conditions. Weld interface modeling development was performed using an Eulerian framework including inelastic deformation induced thermal effects. Figure III-84 shows the effects of the impact velocities where more frequent and significant interfacial waves are observed with increasing velocities due to the energy-driven nature of the pulsed welding process.
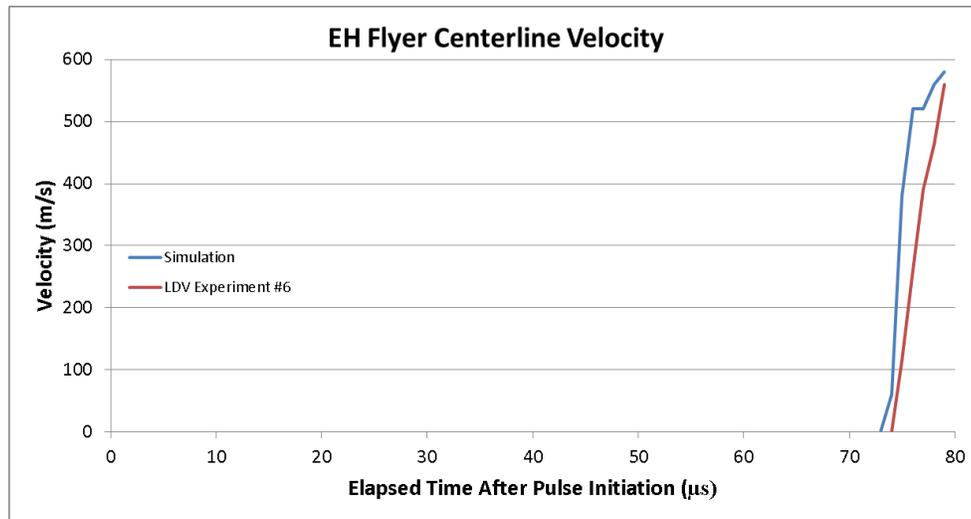
Figure III-83: Comparison of experimental and simulation derived velocities for an Al 6022-T4 flyer plate launched by a 6.8kJ (15kV) EH pulse.
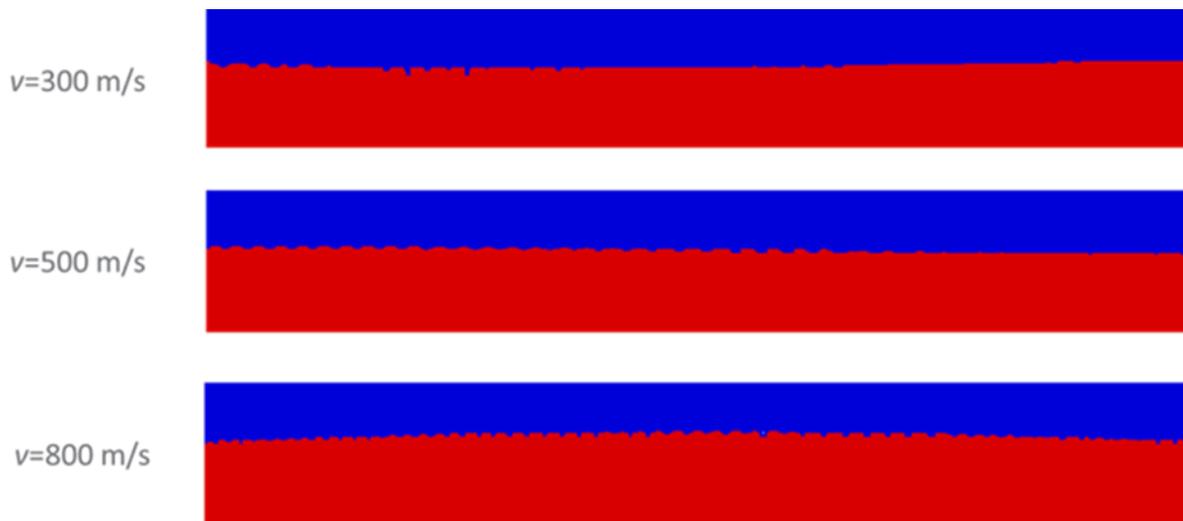
Figure III-84: Effects of impact velocity (v).

Figure III-85 shows a snapshot of the predicted Al-steel interface generated by the simulation. The predicted morphology of the interface varies from location to location with both flat surface and wavy segments observed. If regions with predicted temperatures above the melting temperature of Al are assumed to approximate the size of the intermetallics formed during the pulsed welding process, the average predicted wavelength is found to be around 97.3 micrometers (µm) and the average predicted wave height is about 24.5 µm. Both are in good quantitative agreement with experimental measurements of 84.2 µm and 23.5 µm respectively.
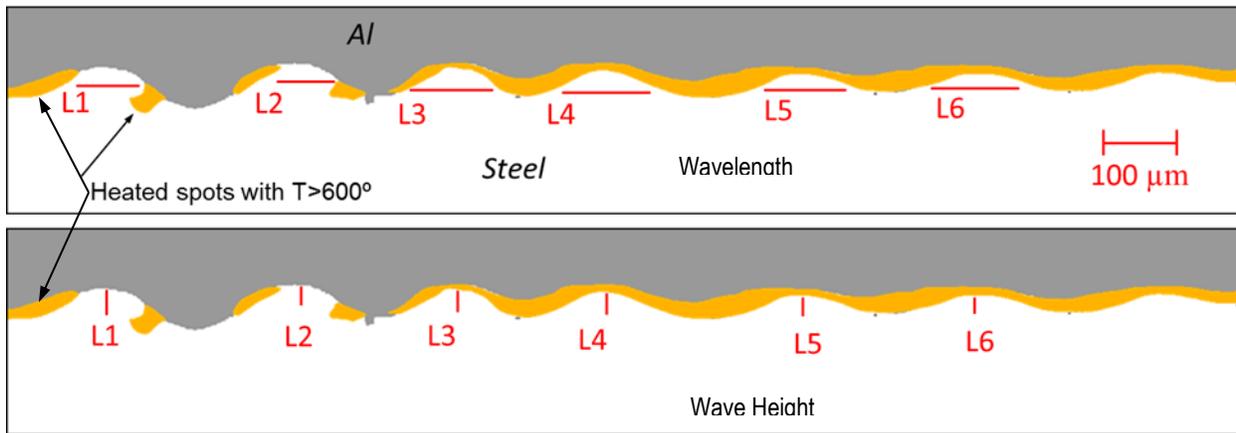
Figure III-85: Prediction of the wavy interface between 6061 Al and 1045 steel. The top of the figure shows wavelength measurements while the bottom shows wave height measurements. Yellow areas indicate localized regions where the temperature has exceeded the melting point of Al (600°C).

Error! Reference source not found.(a) shows a predicted interfacial temperature history profile indicating a rapid increase in local temperatures to levels well in excess of the melting point of Al, and immediately followed by rapid cooling. According to the iron-Al phase diagram (**Error! Reference source not found.**(b)), such extreme conditions can produce a variety of iron-aluminum (Fe-Al intermetallic compounds, and, with coefficient of thermal expansion mismatch, result in considerable in-situ micro-cracking in the vicinity of the weld interface which could further reduce the post-weld strength. In order to explicitly address this effect, a molecular dynamics analysis is currently being developed to investigate intermetallic formation kinetics during the high-velocity impact between Al and steel so that a quantitative relationship between the composition of the intermetallics and

local thermo-mechanical conditions can first be established and later coupled into structural scale PW simulations and predictions.

The work includes numerical simulation to achieve in-depth material science knowledge of the processes taking place at the boundary surfaces of dissimilar alloys during high-speed impact leading to the creation of a metallurgical bond. A finite element-based modeling methodology is being developed to analyze the transient dynamic response of the metal plates during the proposed welding process. This part of the simulation work is focusing on interfacial bond formation mechanisms.
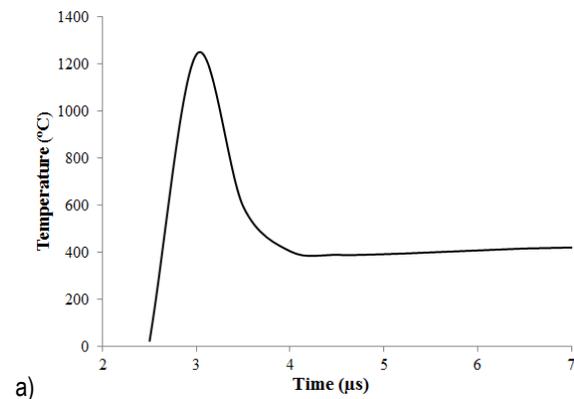
a)

b)

v
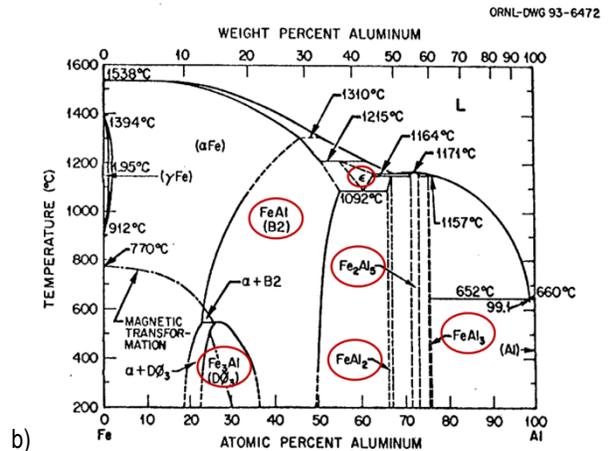
Experimental Effort

The pulsed current generator, or the capacitor bank unit, used in these experiments had a maximum energy capacity of 100 kJ at a maximum charging voltage of 25 kV. Electrical energy was stored in high voltage capacitors charged through a transformer and a set of diodes. Each of them was connected to the discharge circuit through their individual vacuum switch. A set of vacuum switches closes the circuit and delivers high voltage stored in each module of capacitors to the electromagnetic coil tool. The internal inductance of the pulse generator was 20 nanohenries (nH). The electric potential energy, U, of a charged capacitor is given by:

$$U = \frac{1}{2}CV^2$$

where C is the capacitance and V is the charging voltage. The pulse generator was composed of eight modular blocks of capacitors, with 40 microfarads (µF) per block. Therefore, with all eight banks of capacitors connected, the capacitance of the system is 320 µF, and with this value the energy consumption for any given pulse can be calculated as a function of the charging voltage, and vice versa.

The Al tubing that was used as the primary material for our experiments was 6061 Al tube with a 2-inch outer diameter and a wall thickness of 0.035 inch (0.889 mm). The tube was purchased in the T6 temper, which is the high-strength form of the Al 6061 alloy. Some experiments were done using the tube in the T6 temper, while other experiments were done using tubes that had been over-aged at high temperature in order to reduce the yield strength of the material, because prior research on explosive welding techniques have confirmed that materials with lower yield strengths are easier to weld using explosive methods. The specific over-aging profile (which could also be referred to as an annealing profile) used for these experiments was soaking at 350°C for two hours followed by cooling to 250°C over five hours, or at a rate of 20°C per hour. Tensile tests showed that this over-aging profile reduced the yield strength of the Al 6061 tube from 267 MPa to 70 MPa.

The mandrels used during all EM-welding experiments were made of American Iron and Steel Institute (AISI) 1045 steel in a cold drawn condition. Tensile tests done on this material confirmed that it had a tensile strength of 737 MPa, safely above the strength level of 580 MPa set as a target for the pulsed welding project. Mandrels were fabricated to allow testing of three different impact angles: 10°, 15° and 20°. Many preliminary welding experiments were conducted with a wide range of discharge energies, but the range of energy that proved to be successful at producing welds with these materials was 19.6 kJ to 28.9 kJ, at voltages of 14 kV to 17 kV.

Two other types of Al tubing were also used during experimental testing, but these tubes had a larger wall thickness of 2.8 mm along with the same 2-inch outer diameter. One of the thicker walled tubes was Al 6082-T4, and the other was Al 6061-T4, both with a 2-inch outer diameter and a 2.8 mm wall thickness. These tubes were selected for testing because they represent alloy and thickness combinations that are currently being used in the automotive industry for the production of hydroformed parts for body structures. While the EM coil tool was able to significantly crimp these tubes onto the mandrels being used, no welds were formed using the thick-walled tubing and discharge voltages up to 20 kV, so the majority of our testing was done using the tubes with a 2-inch outer diameter and the 0.889 mm wall thickness.

Images showing the weld interface quality of a weld made at 17kV (46.2 kJ) between a Al 6061-T6 extrusion and a 20° 1045CR steel mandrel at two magnifications can be found in Figure III-86.

As simulations indicated, the weld morphology appears to get increasingly finer as the energy is increased for the 20° mandrel.

An intermittent weld structure is seen in Figure III-86 where the clean weld interface between the steel and Al can be seen at the wave peaks that intrude farthest into the Al. On the steel side the troughs tend to be filled with Fe-Al intermetallic. A complete survey of the interface indicates that a roughly 50-50 mix of clean Fe-Al fusion and narrow intermittent intermetallics is observed along the length of the weld. The mixture ratio does vary depending on the position along the weld.

In order to achieve the target of EX-EX welds and determine their overall strength, two mandrels were welded back-to-back and then tensile tested, applying a mixed tensile/shear loading to the weld interface itself. The result of tensile testing was tube wall failure at 21 kN with the result that the weld survived testing.

As with the MPW, successful EHP welds made with the nozzle chamber were examined to determine the geometry of the wavy interface for the purposes of microstructural weld formation model verification. Figure III-87 shows a typical set for two trials of weld interfaces, similar to those found in MPW, obtained using EHPW technology.

Again, the EHP welding nozzle chamber was used to create EX-EX welds, with four spot welds joining two 1045 CR steel extrusions together inside a 1.5mm thick Al 6061-T6 tube. The welds were loaded in shear in the tensile tester and failure was through the weld interface at 15 kN.
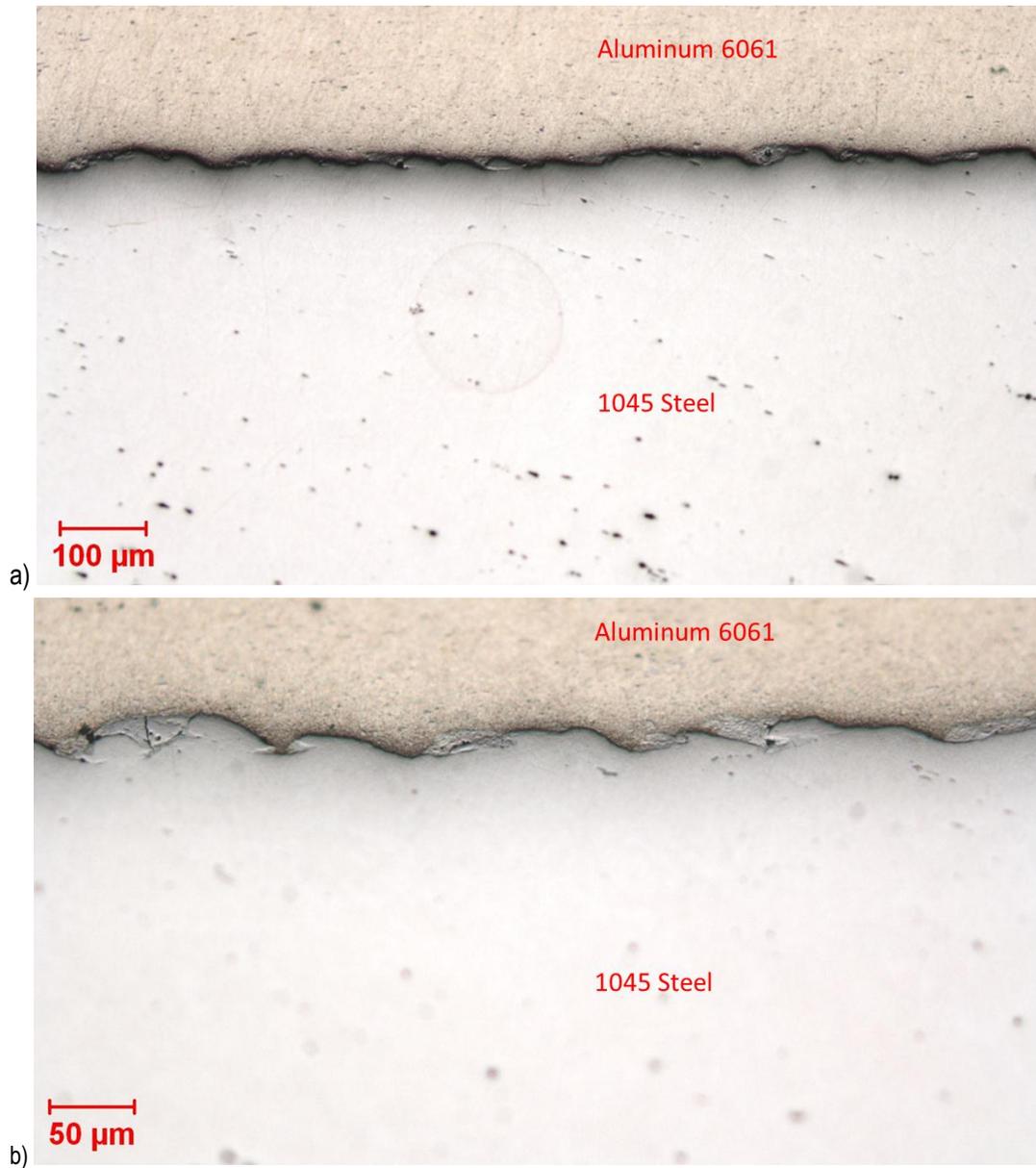
Figure III-86: Micrographs of an 18 kV (51.8 kJ) weld of an Al 6061-T6 extrusion welded to a 20º 1045CR steel mandrel. Images taken at (a) low and (b) medium magnifications.
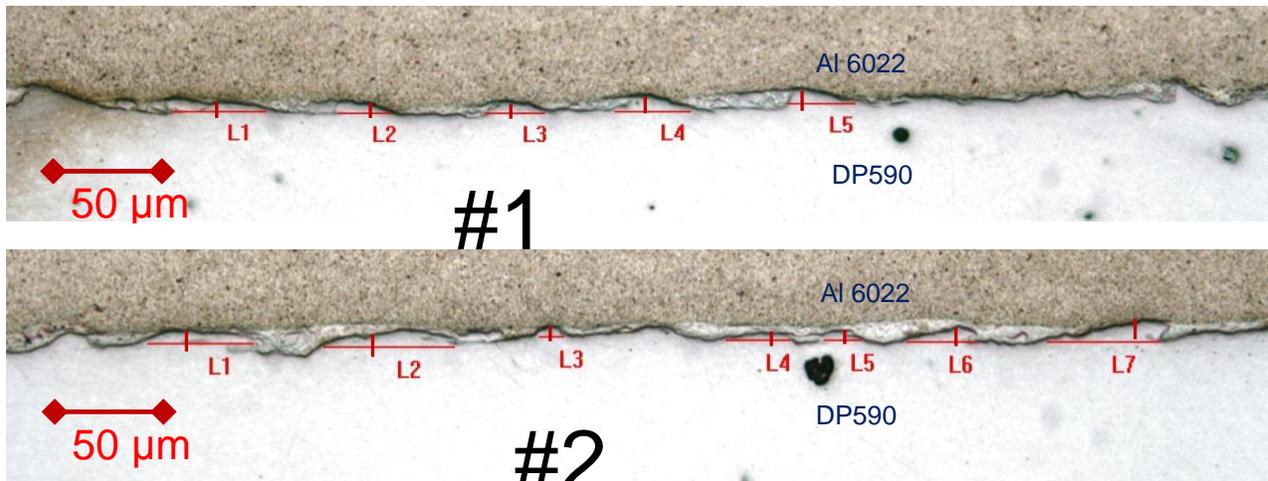
Figure III-87: EHP weld interface showing wavy interface of an EHP weld made at 6.8 kJ (13 kV) between 6022-T4 Al and DP600 steel at a 10o angle. Geometrical measurements of the wavy interface at the weld line were made at the marked locations for correlation with modelling.

Laser Doppler Velocimetry of EHPW

The function of the Velocimeter is to measure the velocities of the flyers in both the EM and EH pulsed welding experiments. The Velocimeter is a 4-channel instrument allowing determination of not only flyer velocity, but flyer orientation and rotational components as the flyer strikes the target. The goal of using this instrument is to remove the vagaries of each tooling setup and produce a complete picture of the process window – a map of where good welds occur in velocity-impact angle space.

The unit is comprised of a 1500 nm Erbium Doped Fiber Amplifier (EDFA) laser, four 1-GHz optical detectors, probes, optical reference junctions and a 1-GHz four-channel oscilloscope. The velocimeter is capable of reliably measuring velocities up to 1 kilometer per second (km/s) and is more than sufficient for our experiments and is able to sense the flyer at distances up to about 6 mm.

Experiments with the LDV were performed on the EH nozzle chamber used to form the welds discussed above. A new anvil was constructed to hold the fiber optics necessary to determine flyer velocities. The results of two separate tests are shown in Figure III-88 for a 6.8 kJ (13 kV) discharge with

the sensor aligned with the Al 6022-T4 flyer centerline. The figure is a conversion of Doppler frequencies in to velocities, and as a consequence the frequency distribution results in a distribution of velocities. The figure shows two peaks – the first peak occurs as the flyer approaches the anvil; then the velocity drops to zero when the flyer hits the anvil. Inertia causes a plug of Al to break free and continue to travel into the laser aperture in the anvil producing the second peak, and then the large noise spike occurs where the plug strikes the fiber optic sensor destroying it.

Technology Transfer Path

Although the technology shows promise for lightweighting and integration into automotive production, the grant holder, FMC, could see no path to commercialization in a reasonable time frame, and the work was discontinued at the end of the first budget period. FMC continues to have an interest in pulsed joining technology and will continue to monitor the progress of university-based research in this field.
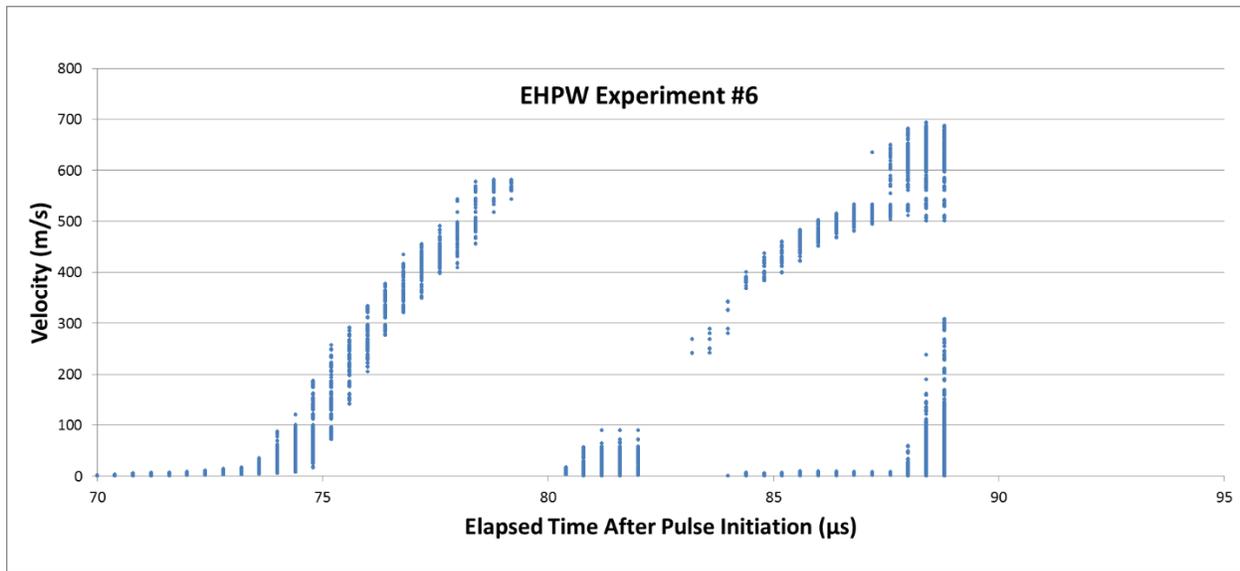
Figure III-88: Flyer plate velocity resulting from a 6.8 kJ (13 kV) EH discharge. The first peak is the flyer as it approaches the anvil, and the second peak is that of the Al plug. The flyer reached a velocity between 550-600 m/s before impact.

Conclusions

1. Successfully created EMPWs of overaged Al 6061 tubes (152 MPa tensile strength) to both 15° and 20° 1045CR steel mandrels (737 MPa T.S.) and Al 6061-T6 tubes to 20° 1045CR steel mandrels.

2. Successfully created EMPWs between two extrusions (EX-EX) welds between overaged Al 6061 tubes and 1045CR steel mandrels that exceeded the 20 kN minimum strength requirement. The tubes failed at 21 kN rather than at the welds.

3. Developed a numerical model of EH flyer launch that successfully predicts the moment of launch, the acceleration profile, and the time of and velocity at the moment of impact as validated by LDV measurements.

4. Developed a numerical model of EM flyer launch that predicts velocities, accelerations and the flyer shape under a range of energies as validated by LDV measurements.

5. Successfully created an EHPW EX-EX extrusion welded structure that achieved 15.1 kN strength level but did fail through the weld.

6. Developed a numerical model of EMW interface formation that, given inputs from the EM flyer launch model, successfully predict wavy interface formation and the length and height scales of the interface as validated by metallographic data.

Presentations/Publications/Patents

1. Golovashchenko, S.F., Bonnen, J.J.F., Dawson, S.A., Mamutov, A., Maison, L.D., de Vries, J., United States

Patent and Trademark Office (USPTO) Application 14/321942, "Solid Cartridge For A Pulse Weld Forming Electrode And Method Of Joining Tubular Members" (8/8/2014).

2. Golovashchenko, S.F., Bonnen, J.J.F., Dawson, S.A., Mamutov, A., Maison, L.D., de Vries, J., USPTO Application 14/454968, "Electrode Cartridge For Pulse Welding" (8/8/2014).

References

1. Massalski, T.B; Okamoto, H.; ASM International (1986), Binary alloy phase diagrams, Materials Park, Ohio: ASM International, ©1990.

2. Okamoto, H.; Beck, Paul A. (1971). "Phase relationships in the iron-rich FeAl alloys." *Metallurgical and Materials Transactions B-Process Metallurgy and Materials Processing Science*, (2:2), pp. 569-574

3. Oki, K.; Hasaka, M.; Eguchi, T. (1973). "Process of Order-Disorder Transformation in Iron-Aluminum Alloys." *Japanese Journal of Applied Physics*, (12:10) p 1522

4. Swann, P.R.; Duff, W.R.; Fisher, R.M. (1969). "The Diagram of State for Iron-Aluminum Solid Solutions." *Trans. Metall. Soc. AIME*, (245:851-853)

III.20 Dealloying, Microstructure and the Corrosion/Protection of Cast Magnesium Alloys – Arizona State University (ASU)

Karl Sieradzki, Principal Investigator
Arizona State University (ASU)
Ira A. Fulton School of Engineering
501 E. Tyler Mall
P.O. Box 876106
Tempe, Arizona 85287
Phone: (480) 965-8990
E-mail: karl.sieradzki@asu.edu

Aaron Yocum, Project Officer
National Energy Technology Laboratory
3610 Collins Ferry Road
P.O. Box 880
Morgantown, WV 26507-0880
Phone: 304-285-4852
E-mail: Aaron.yocum@netl.doe.gov

William Joost, Technology Area Development Manager
U.S. Department of Energy
1000 Independence Avenue, SW
Washington, DC 20585
Phone: (202) 287-6020
E-mail: william.joost@ee.doe.gov'

Contractor: Arizona State University (ASU)
Contract No.: DE-EE0006436

Abstract/Executive Summary

The purpose of this project is to develop an improved understanding of the corrosion behavior in advanced automotive cast magnesium (Mg) alloys through iterative experimental and computational efforts. During the first fiscal year, significant progress has been made on the experimental portion of the project. Commercial alloys including aluminum-zinc (AZ)91D as well as single-phase samples were acquired or fabricated, and synthetic Mg-aluminum (Al) alloys were synthesized using photolithography. The alloys were verified using morphological, structural and compositional characterization methods. AZ91D was subjected to full-immersion/free corrosion in an aqueous chloride environment and characterized using standard methods as well as a newly developed Al assay protocol based on lithium (Li) underpotential deposition (UPD). The synthetic alloys were used to calibrate the Li UPD/Al assay protocol, and the analysis indicated only a small amount of Al enriched on the AZ91D surface. In contrast, preliminary results from potentiostatic corrosion in a nonaqueous ionic liquid (iL) resulted in a complex redistribution and a much more significant degree of Al enrichment on Mg-Al alloys. The accompanying water reduction reaction that occurs during Mg corrosion in aqueous systems

causes a significantly increase in the electrolyte pH that may have led to Al dissolution, which would have prevented the same degree of Al enrichment that was observed for the nonaqueous corrosion. Standard glass electrodes were used to measure the pH in the bulk electrolyte surrounding the Mg-Al alloys during aqueous corrosion. However, in order to determine the effect of the composition and phase distribution, e.g. the spatial length scales of β phase and α/β eutectic, on the change in pH, an oxidized iridium (Ir) microelectrode is under development for use in aqueous corrosion studies.

Accomplishments

- Acquired and characterized commercial alloys AZ31B, aluminum-manganese (AM)60B and AZ91D along with individual samples of the common components found in commercial Mg-Al alloys including solid-solution α phase Mg-Al with various concentrations as well as $Mg_{17}Al_{12}$ β phase and manganese aluminide ($MnAl_3$) compounds. (FY 2014)
- Developed an electrochemical Al assay protocol using Li UPD. (FY 2014)
- Synthetic Mg-Al surfaces representing 5% Al coverage have been fabricated using photolithography. Initial electrochemical characterization results of these samples have been used to calibrate the Li UPD/Al assay protocol. (FY 2014)
- Compiled data on the surface morphology and composition of AZ91D following various durations of full immersion, free corrosion in an aqueous chloride environment. (FY 2014)
- Collected data on the electrolyte pH evolution during full immersion, free corrosion conditions for commercials alloys and common components using a standard glass electrode. (FY 2014)
- Synthesized an oxidized Ir microelectrode that exhibits super-Nernstian behavior that may be used in future experiments to determine how individual components and relative length scales between components effect pH evolution. (FY 2014)
- Observed Al enrichment on Mg-Al alloys under full-immersion, potentiostatic corrosion in a nonaqueous deep eutectic solvent of 1:2 molar ratio of choline chloride:urea based on energy dispersive x-ray spectroscopy (EDS) and Li UPD/Al assay results. (FY 2014)

Future Directions

- Continue to fabricated and validate synthetic Mg-Al alloy behavior with real alloys using electrochemical characterization.
- Expand the study of Mg-Al corrosion in nonaqueous ionic liquids to determine the effect of parameters such as

- duration and electrochemical potential on morphology and aluminum redistribution and enrichment.
- Perform atmospheric corrosion studies on both real and synthetic alloys.
- Perform kinetic Monte Carlo (KMC) simulations incorporating embedded atom method (EAM) potentials to ascertain the anodic dissolution behavior of Mg-Al alloys.
- Develop and test hydrophobic coatings using aprotic hydrophobic ionic liquids.
- Develop and test stainless-like Mg alloys identified using KMC simulations.

Technology Assessment

- Target: Fabricate synthetic Mg-Al alloys based on the relative length scales of real alloys and validate their electrochemical behavior within 10% accuracy.
- Gap: Standard photolithographic techniques have not been designed for the magnesium system including interference from its native oxide.
- Target: Develop an Al assay protocol within 5% accuracy to ascertain the electrochemically active Al on the surface of a corroded Mg-Al alloy due to possible redistribution and enrichment.
- Gap: Conventional compositional techniques such as EDS probe not only the electrochemically-active Al on the surface but also a significant amount of the bulk due to the large interaction volume of the electron beam.
- Gap: Limited experimental results exist on the crystallographic-dependence of the Li UPD shifts for Al.
- Target: Clarify the anodic dissolution behaviors of the Mg-Al phases in nonaqueous iLs containing less than 1 ppm oxygen and 100 ppm water.
- Gap: A limited selection of iLs exist that have a large enough electrochemical potential window to allow for the anodic dissolution/deposition of Mg without the simultaneous breakdown of the solvent.
- Target: Determine the effect of microstructural composition: ranging from 2-8 atomic weight percent (at%) Al in the alpha phase, and length scales, on the order of 1-100 microns (μm), on the local time dependent pH evolution.
- Gap: Standard glass electrodes have inadequate sensitivity over the relevant length scales in Mg-Al alloys.
- Gap: Conventional scanning electrochemical microscopy (SECM) may lack the resolution to ascertain local pH changes over the relevant length scales in most Mg-Al alloys due to the dynamic surface topography during corrosion.
- Target: Develop and validate KMC code that simulates time dependent electrochemical dissolution behaviors including pH dependent chemical dissolution and Al redistribution during corrosion of Mg-Al solid solutions to within 10% accuracy compared to experimental results.
- Gap: Selection of the EAM potential must be chosen from existing potentials in the literature based on convenience of analytical forms and the speed at which they will allow the KMC simulations to run.

- Target: Develop hydrophobic coatings for corrosion protection of Mg-Al alloys.
- Gap: Coatings that provide passive blocking layers often lack self-healing capabilities and suffer from the potential of pin-hole formation.

✧   ✧   ✧   ✧   ✧

Introduction

The objective of this project is to develop an improved understanding of the corrosion behavior in advanced automotive cast Mg alloys. By expanding upon the scientific comprehension in the area of corrosion behavior, this project will help to identify development paths toward novel Mg alloys and coatings. Iterative experimental and computational efforts will be performed to understand the effects of composition and phase distribution, e.g. the spatial length scales of β phase and α/β eutectic, on the corrosion behavior of cast Mg-Al alloys in aqueous environments and in iLs where the absence of water and oxygen will prevent the interference of their corresponding reduction reactions.

Approach

The project will utilize three general approaches for the study of Mg-Al corrosion behavior: 1) artificial or synthetic Mg alloys, 2) iLs, and 3) KMC simulations, which incorporate the effects of and the spatial redistribution of alloying elements during corrosion. During this first fiscal year of the project, major headway has been made with the first two approaches including the synthesis and testing of synthetic alloys using photolithography as well as initial corrosion studies in nonaqueous iL electrolytes. In addition, a complementary protocol has also been developed that is capable of assaying the Al surface composition. This technique relies on the selective underpotential deposition of Li on Al in Mg-Al alloys.

Results and Discussion

During the first fiscal year of the project, the first main task was to acquire and characterize commercial Mg-Al alloys as well as samples of common components found in those alloys. Following the acquisition of AZ31B, AM60 and AZ91D commercial alloys, their microstructure and composition were characterized using SEM, EDS and x-ray diffraction (XRD) and reported in Figure III-89, Figure III-90 and Figure III-91, respectively. The samples were prepared using an oil-based diamond slurry polishing procedure down to a 0.5 μm particle size followed by an acetic picral etching procedure as described in [1] to remove damaged material as well as reveal grain boundaries and secondary phases. The XRD results in Figure III-91a as well as EDS were used to identify the bright contrast secondary phases present in the commercial alloys such as the β $Mg_{17}Al_{12}$ phase in AM60 and AZ91D as well as $MnAl_3$ particulates in AZ31B. They were also used to verify the Al concentration in the solid-solution α phase.
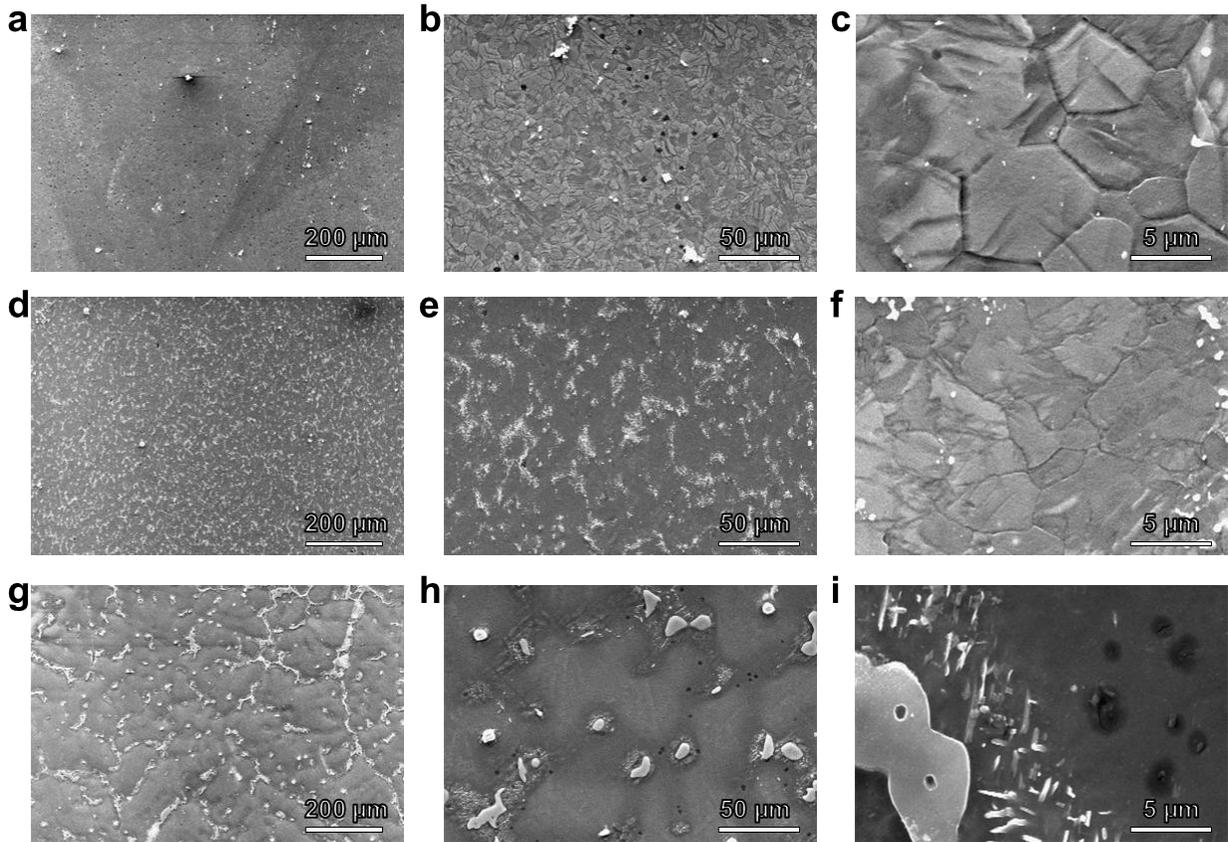
Figure III-89: Microstructural characterization of commercial alloys at various magnifications using SEM for a, b, c) AZ31B, d, e, f) AM60 and g, h, i) AZ91D. The alloys were prepared using oil-based polishing materials down to 0.5 µm and etched using acetic picral solution to expose grain boundaries and phases.
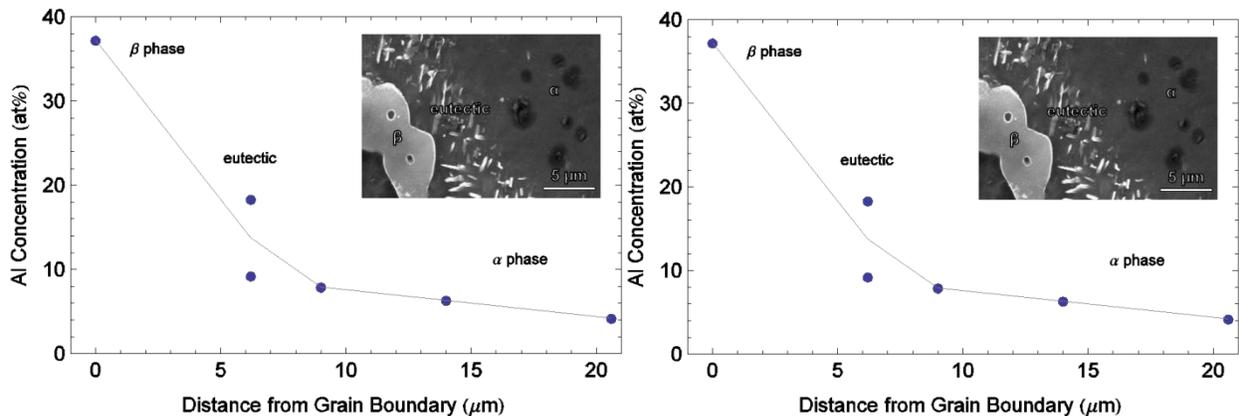
Figure III-90: Distribution of Al concentration in a balance of Mg within a representative AZ91D grain. The $Mg_{17}Al_{12}$ β phase is proximal to the grain boundary, a solid solution α phase 4-8 at% Al is located inside the grain, and between the two phases, a eutectic region exists consisting of both α and β phases. The lowest Al concentration is found at the center of the grain, and it gradually increases outward toward the grain boundaries.
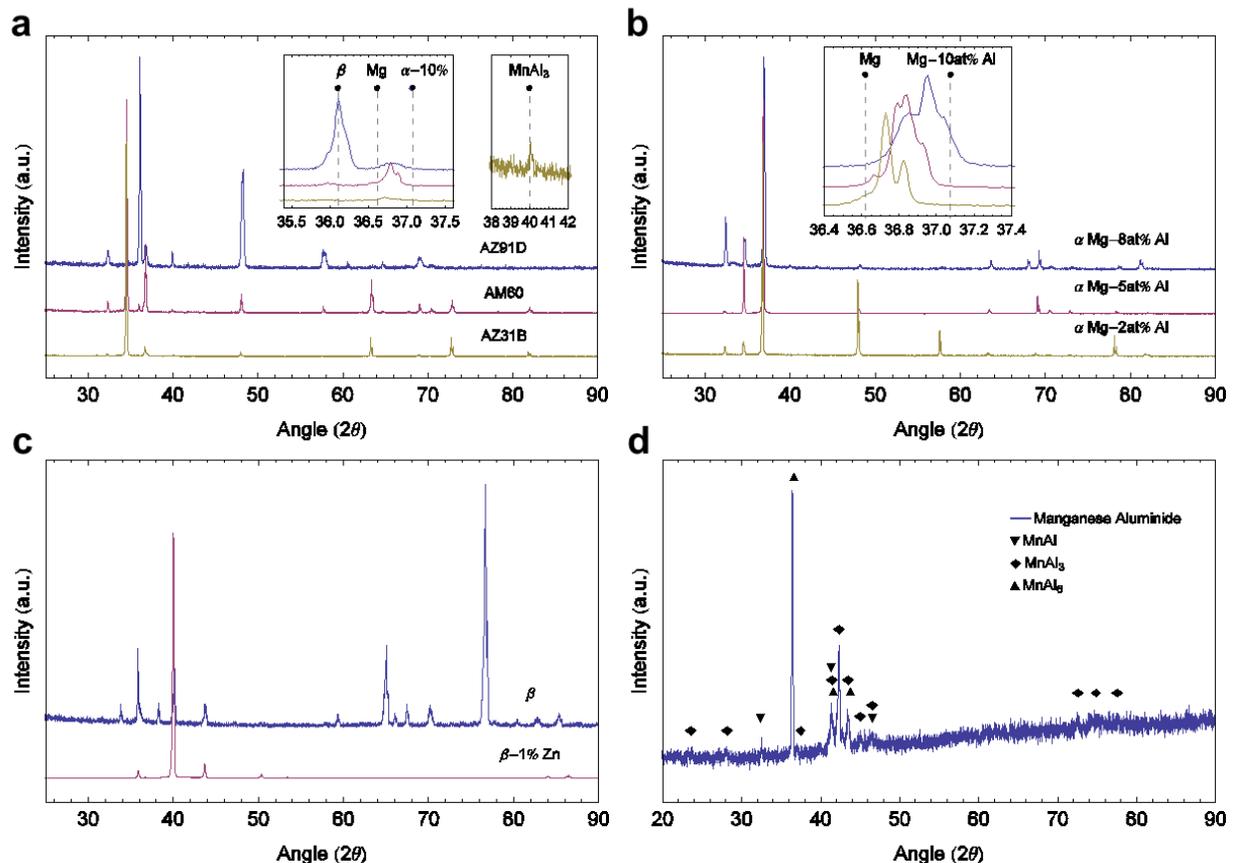
Figure III-91: XRD patterns for a) commercial alloys AZ91D, AM60 and AZ31B, b) solid-solution α phase samples containing approximately 2-8 at% Al, c) Mg$_{17}$Al$_{12}$ β phase with and without 1% Zn and d) MnAl$_3$.

In Figure III-91a, reference patterns for Mg, α Mg-10% Al, β Mg$_{17}$Al$_{12}$ and MnAl$_3$ phases were superimposed over the data and shown in the insets plotted in the two regions most prominent for the listed phases. AZ31B exhibited a peak between Mg and α Mg- 10% Al, which is in good agreement with the 2.7 – 3.2 at% Al probed by EDS. Also, as shown in the second inset graph, a small peak is exhibited associated with MnAl$_3$, as displayed by the bright particulates in Figure III-89b located near the boundaries of 5-10 µm size grains (see Figure III-89c). For AM60, a peak was observed between Mg and α Mg- 10% Al, which is in good agreement with the ~ 4.0 at% Al probed by EDS. Furthermore, in the first inset graph, a small peak is exhibited associated with the β phase, as displayed by the bright particulates in Figure III-89f located near the boundaries of 2-5 µm size grains.

AZ91D exhibited a high intensity peak associated with the β phase as well as a small peak between Mg and α Mg- 10% Al in good agreement with the 4.2-7.9 at% Al measured by EDS across grain sizes ranging from 50-100 µm. This relatively large distribution of Al within the AZ91D grains is plotted in Figure III-90 as measured by EDS. The lowest Al concentration is found at the center of the grain, approximately 4.2 at% Al, and it gradually increases radially outward toward

the grain boundaries to a maximum of approximately 7.9 at% Al. Large secondary β phases reside at the grain boundary, and between the α and β phases, a eutectic region exists containing both phases.

In order to systematically study the effects of the individual phases of the real alloys on their corrosion behavior, samples of the individual components were acquired or fabricated. XRD results in Figure III-91 were used to verify samples of solid solution α phase containing approximately 2, 5 and 8 at% Al (Figure III-91b), β phase with and without 1.0 at% Zn (Figure III-91c) as well as MnAl$_3$ (Figure III-91d). The peaks exhibited in the XRD spectra agree with the desired phases. Furthermore, the peak shift between reference patterns for Mg and α Mg- 10% Al are in good agreement with the desired range of Al composition for the solid solution α Mg-Al alloys.

In conjunction with the acquisition and fabrication of the relevant Mg-Al materials, a procedure was developed to assay the surface composition of Al. This measurement is of potential significance for Mg-Al corrosion studies where preferential dissolution of Mg may cause Al redistribution and enrichment. Correlation between the Al concentration and parameters affecting corrosion such as electrolyte composition and duration of immersion may be used to determine

important factors such as the corrosion rate and mechanism. Standard compositional characterization methods such as EDS may not be sensitive enough to determine small concentration changes in the uppermost surface layers due to the large interaction volume of the electron beam. Therefore, an electrochemical technique was developed based on Li UPD on Al.

Cyclic voltammetry (CV) was performed on Al and Mg separately at increasingly lower potential limits to ascertain the potential regions where the materials may or may not exhibit UPD or alloying with Li. The results of the study are reported in Figure III-92. In Figure III-92a, Li exhibits a broad UPD stripping peak on the curve down to a lower potential limit 500 millivolts (mV) vs. Li/Li+. Li also exhibits a sharp peak most likely associated with stripping from underpotential bulk alloying at lower potential limits approximately 70 mV positive of Li/Li+. At even lower potentials as show in Figure III-92b, the magnitude of the charge density associated with deposition/alloying and stripping/dealloying continues to increase and become more irreversible. The behavior on Mg is different from that of Al. Li UPD does occur but only when the lower potential limit is at or below 70 mV vs. Li/Li+ (see Figure III-92c). As shown in Figure III-92d, bulk alloying of Li and Mg doesn't occur until the potential is driven significantly

below the reversible Li/Li+ potential, between -50 and -100 mV. Therefore, at relatively higher potential limits, such as 500 or 300 mV, the Al surface coverage may be assayed using Li UPD, and in the lower potential regime, down to 50 mV vs. Li/Li+, the electrochemically accessible bulk Al may be assayed using Li underpotential alloying. However, each regime has limitations; the UPD peaks are relatively smaller and broader leading to errors associated with background subtraction, and the bulk peak though larger and sharper may overlap with a small peak associated with UPD on metallic Mg when implemented on Mg-Al alloys.

The assay procedure was further developed for all three potential regimes. To increase the sensitivity of this method, an extended potentiostatic hold or chronoamperometry was employed at the lower potential limit prior to the anodic stripping voltammetry. Figure III-93 reports the anodic stripping curves using this technique for Al and various preparations of Mg. The chronoamperometric step resulted in more pronounced broad peaks on the Al in the UPD region, and the sharp peak associated with dealloying/stripping (see Figure III-93b) is much larger due the increased time allowed for alloying into the bulk of the sample.
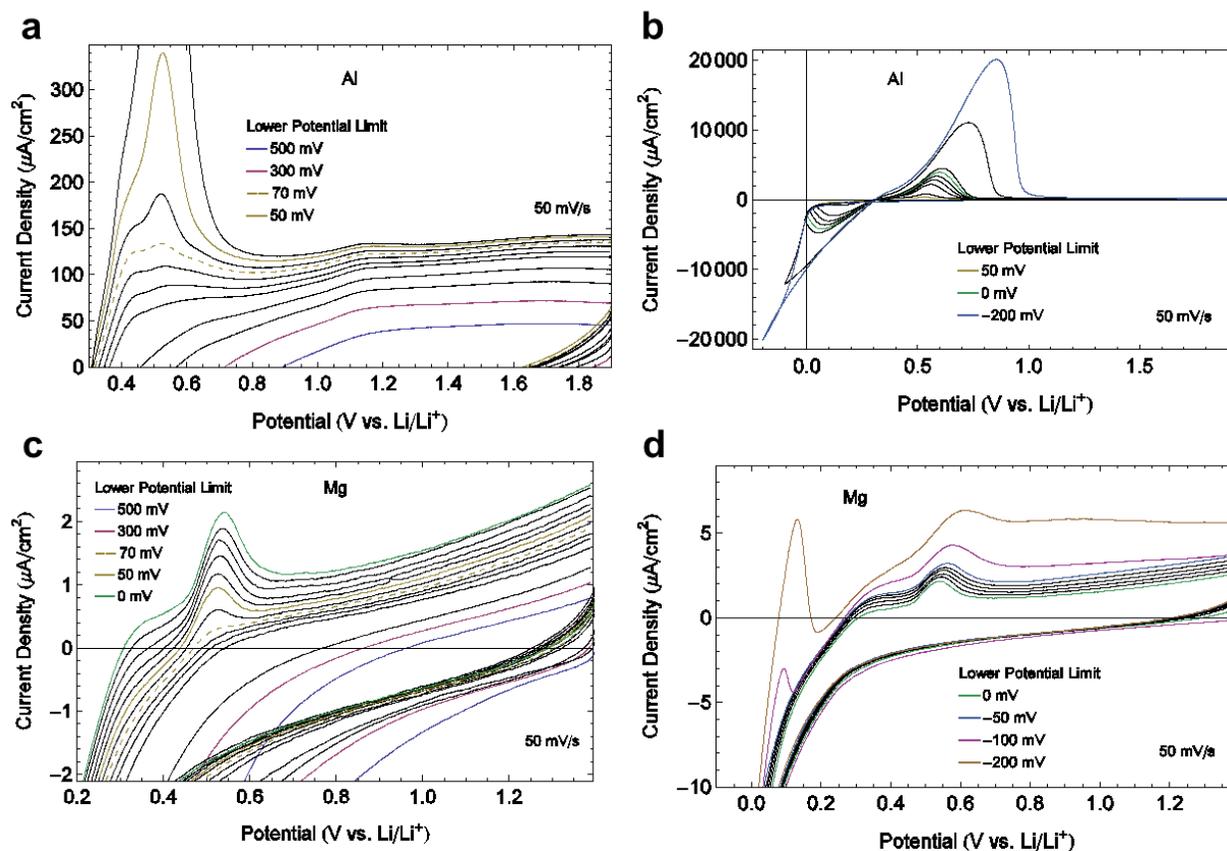
Figure III-92: Cyclic voltammetry performed at 50 millivolts per second (mV/s) in 1.0 molarity lithium perchlorate (M LiClO4) in propylene carbonate at increasingly lower potential limits for a, b) Al sheet, 99.999%, and c, d) Mg, 99.95% sanded down to 1200 grit/p4000 in a UHP argon (Ar) atmosphere to minimize the native oxides. Significant traces are labeled by the CV lower potential limit (V) vs. Li/Li+.
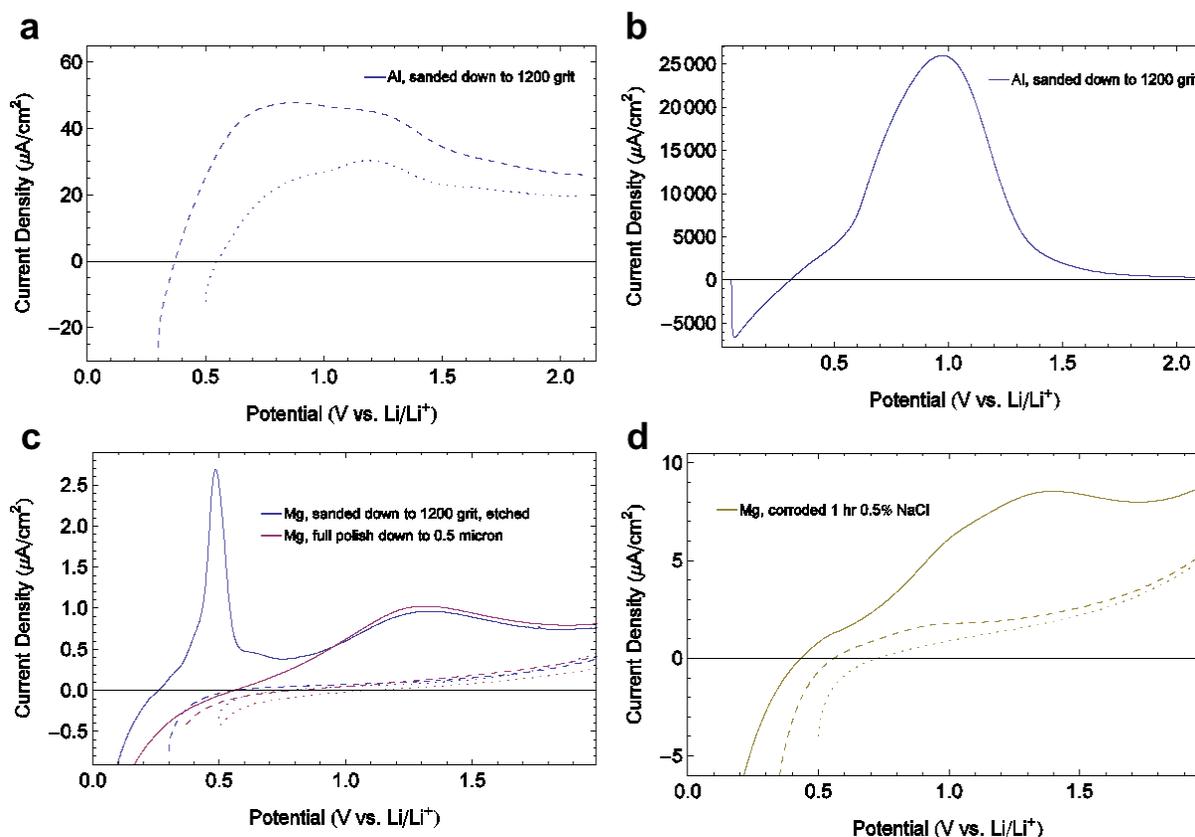
Figure III-93: Anodic stripping curves at 5 mV/s in 1.0 M LiClO$_4$ in propylene carbonate following 600 second chronoamperometry at the lower potential limit: (dotted) 500 mV, (dashed) 300 mV and (solid) 50 mV vs. Li/Li$^+$ for a, b) Al sheet, 99.999%, and Mg, 99.95% for various preparations: c) sanded down to 1200 grit/p4000 vs. fully oil-based polishing down to 0.5 μm and d) corroded under full immersion in 0.5% aqueous NaCl for 1 hr.

The procedure was then repeated for various preparations of Mg. As seen before a sharp peak is observed when stripping from 50 mV vs. Li/Li$^+$ on sanded Mg. However, after full sample polishing using oil-based diamond slurries down to 0.5 μm in air, the sharp peak is missing, and a broad peak is observed at higher potentials. The sharp peak at approximately 500 mV is likely associated with Li UPD on metallic Mg, and the broad peak at approximately 1.3 V vs. Li/Li$^+$ may be due to Li interaction with the native oxide of Mg. In fact, alkali metal atoms, particularly Li, are known to produce a strong bond with magnesium oxide (MgO). [2] In addition, a Mg sample was corroded under full-immersion, free-corrosion conditions in 0.5% aqueous sodium chloride (NaCl) for 1 hour to see how surface species such as MgO and magnesium hydroxide (Mg(OH)$_2$) formed during corrosion effect the Li UPD/Al assay protocol. Unlike the sanded or polished Mg, a small peak was observed on the stripping curve from the lower potential limit of 300 mV in addition to the large broad peak(s) observed from 50 mV vs. Li/Li$^+$. Consequently, an additional limitation in these two potential regimes may exist when utilizing this protocol on corroded Mg-

Al samples where the corrosion products of Mg may contribute to the stripping peaks at high potentials.

Another important accomplishment from this fiscal year has been the design and fabrication of artificial or synthetic alloys. These samples are intended for several purposes including mimicking real alloys for controlled corrosion studies as well as creating standards for calibrating the Li UPD/Al assay results. The samples are synthesized using photolithography, and the SEM and EDS areal mapping results for the first iteration of these alloys are presented in Figure III-94. The pattern was designed based on approximate length scales mimicking the AZ91D microstructure (see Figure III-89h). The pattern is composed of 7.3 μm diameter discs located on the corners and edges of a square 50 μm lattice. In the first fabrication iteration, Al discs were patterned onto a pure Mg substrate. Initially, challenges arose related to the native oxide that forms on the Mg during polishing prior to photolithography. The oxide layer was determined to prevent electrical conductivity to the Al islands which made them electrochemically inaccessible during Li UPD/stripping tests. Therefore, the final procedure was

modified to include a sputtering step following photoresist development but prior to 100 nanometer (nm) thick deposition

of Al.

a

b

Mg   **Al**   **C**   **O**
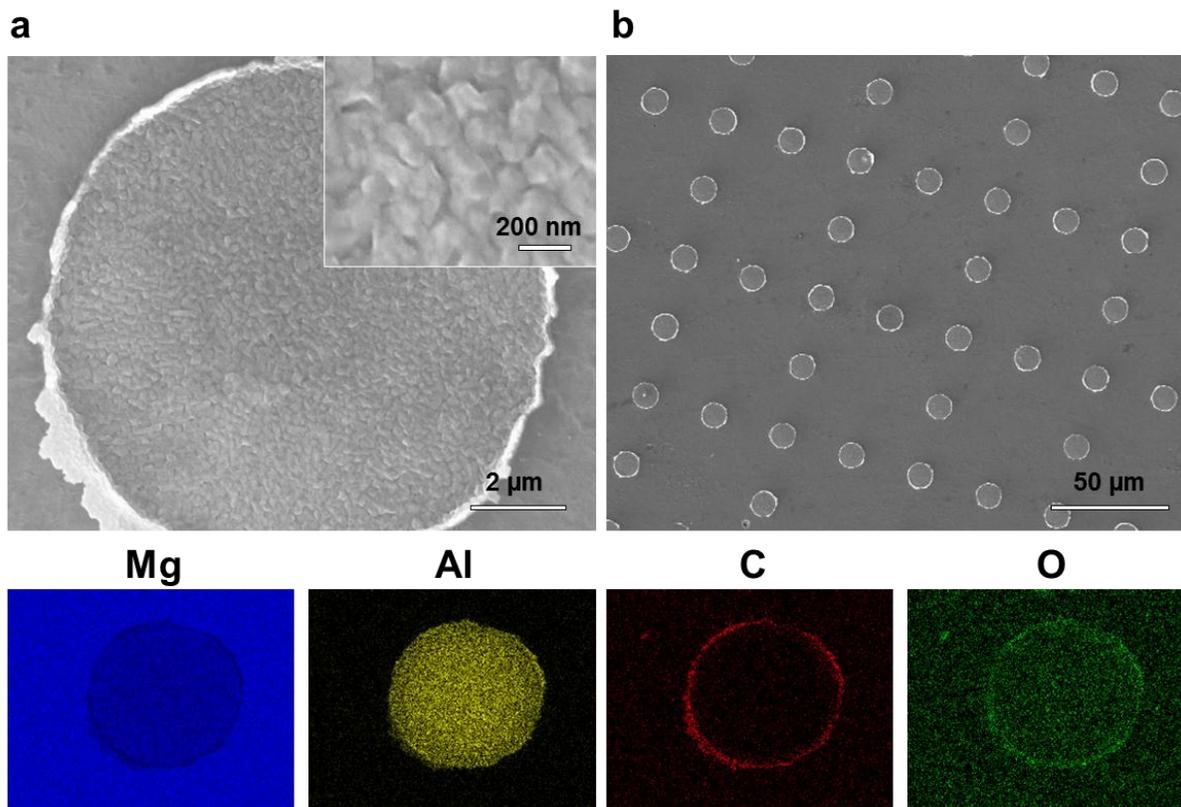
Figure III-94: SEM surface morphology of 5%, 100 nm Al coverage on 99.95% Mg substrates that underwent sputtering during photolithography at a) higher magnification showing the deposit texture and b) lower magnification showing the overall pattern. EDS areal mapping was performed on the island in a) to show the elemental mapping of Mg, Al, carbon (C) and oxygen (O).

A sample similar to that shown in Figure III-94 as well as a full blanket deposition, 100% Al coverage on Mg, were then employed as calibration samples for the Li UPD/Al assay protocol. The results are reported in Figure III-95. Comparison of the peak locations and charge density are reported in Table III-10. The error reported in the charge density is associated with the inherent difficulty in background subtraction of the broad peaks found in the stripping curves from 500 and 300 mV vs. Li/Li+. Apparently, we are exhibiting a contribution from the native magnesium oxide or hydroxide on the uncovered surface of the 5% Al coverage sample (recall Figure III-93c,d). This likely affected the positive peak shift and relative larger charge density of the broad peak exhibited from the 300 mV scan on the 5% Al coverage. It is also evident in the broad peak observed between 1.0 and 1.5 V from the 50 mV lower limit anodic stripping curve. More importantly, the UPD on Mg metal may also contribute to the sharp peak observed at approximately 500 mV on the curve from the 50 mV vs. Li/Li+ lower potential limit.

These calibration curves have further confirmed that the protocol may be used to assay the Al on the surface, but there are current limitations to its application for an Al assay due to

contributions from Mg or MgO/Mg(OH)$_2$ as well as errors introduced by the approximate background subtraction, depending on the stripping lower potential limit. The large broad peaks especially in the stripping curves from lower potential limits 300 and 500 mV vs. Li/Li+ may in fact be a superposition of several peaks associated with crystallographic-dependent Li UPD shifts. Schmickler et al. have calculated large Li UPD shifts ranging from 0.15 V for (111), 0.64 V for (100) and 1.78 V vs. Li/Li+ for (110) face-centered cubic (FCC) crystallographic faces. [3] [4] Schmickler, 2001) Such large peak shifts have been experimentally observed for other FCC metals such as platinum (Pt), [5] but experimental Li UPD shifts have yet to be reported for Al. Future experiments are planned that may help to dissociate the broad peaks by their crystallographic-dependent shifts using single-crystal studies.

All tasks prior to this point have been in preparation for the following aqueous full-immersion, free-corrosion study initiated on AZ91D for various durations. The surface morphology and overall composition was measured using SEM and EDS, respectively, and the Li UPD/Al assay protocol was employed

on the corroded samples to examine the possibility of Al   enrichment.
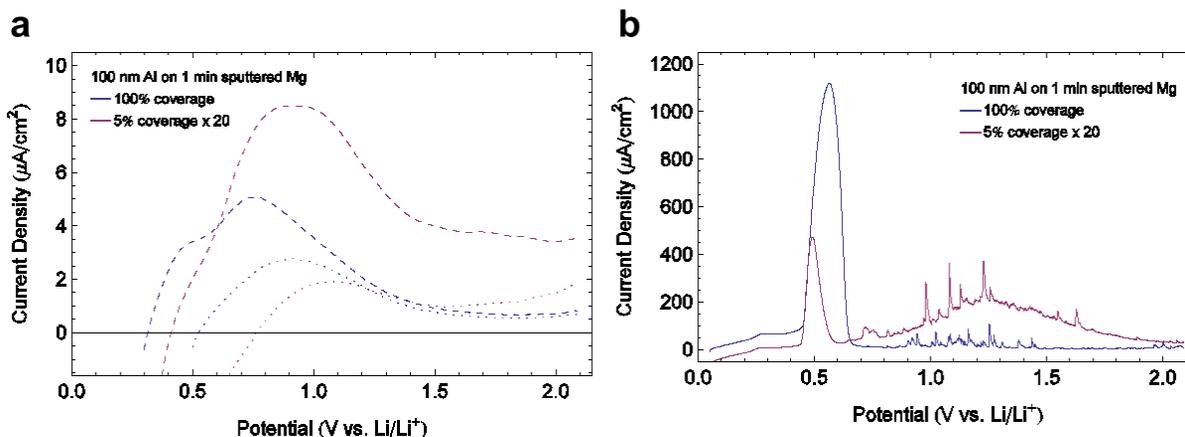
Figure III-95: Anodic stripping curves following 600 second chronoamperometry at the lower potential limit: a) (dotted) 500 mV, (dashed) 300 mV and b) (solid) 50 mV vs. Li/Li+ for a 100% and a 5% coverage of 100 nm Al synthesized using photolithography similar to that in Figure III-94 on Mg. All stripping curves were scanned at 5 mV/s in 1.0 M LiClO4 in propylene carbonate. The current density of the 5% coverage sample was multiplied by a factor of 20 to visually compare to the 100% coverage sample.

Table III-10: Comparison of Li UPD/Al assay Results for Various Coverage of 100 nm Al on Sputtered Mg

Stripping Curve following 600 sec. at lower potential limit (vs. Li$^+$/Li):	Peak Location (mV vs. Li$^+$/Li)		Stripping Charge Density (microcoulomb per square centimeter ($\mu C/cm^2$))		% Stripping Charge (5% stripping charge/100% stripping charge)
	100% coverage	5% coverage	100% coverage	5% coverage	
500 mV	910	1050	320	6.4 - 25	5.0 ± 4.2%
300 mV	489/755	450/910	650	30 - 65	7.3 ± 3.8%
50 mV	287 567	280 493	230 2.7×10^4	8.1 3.0×10^2	3.5% 1.1%

The SEM results for AZ91D that underwent various durations ranging from 5 minutes to 20 hours of full-immersion, free-corrosion in 3.5% NaCl are reported in Figure III-96. After 5 minutes the visually corroded areas that appear highly textured and white in contrast are primarily located in the center of the grains. This is not surprising due to the decreasing Al concentration toward the center of the grains as shown in Figure III-90. As the duration increases, the corroded region spreads outward toward the β phase at the grain boundaries. As the duration increases further, the β phase that appears white in contrast in the un-corroded sample becomes less visible, and the corrosion seems to affect a larger extent of the alloy surface. EDS was performed on the surface, and apart from the increase in oxygen and carbon, the aluminum concentration compared to magnesium decreased slightly from about 10 to 8 atomic percent. This may be due to a decrease in the amount of β phase due to undercutting. Nevertheless, due to the large interaction volume of the electron beam, the data includes a significant contribution from the bulk of the sample. Therefore, this technique may not be sensitive enough to

determine small concentration differences such as Al enrichment in the uppermost surface layers.

In order to determine the electrochemically active Al on the corroded samples, the Li UPD/Al assay protocol was implemented, and the results are recorded in Figure III-97. Representative anodic stripping curves performed on several duplicate samples are recorded in Figure III-97a and Figure III-97b from the lower potential limits: 50 and 500 mV vs. Li/Li+, respectively. A linear background subtraction was performed, and the insets plot the resulting curves. The anodic Li stripping charge density was calculated from the background subtracted curves and converted to an Al surface concentration using the 100% Al coverage sample in Figure III-95 for calibration. This data is compared to the overall EDS data in Figure III-97c. It is important to note here that the protocol was performed on samples of pure β phase, and Li was determined to not undergo UPD on the β phase component of the alloy and thus does not contribute to the charge density calculated in Figure III-97c.
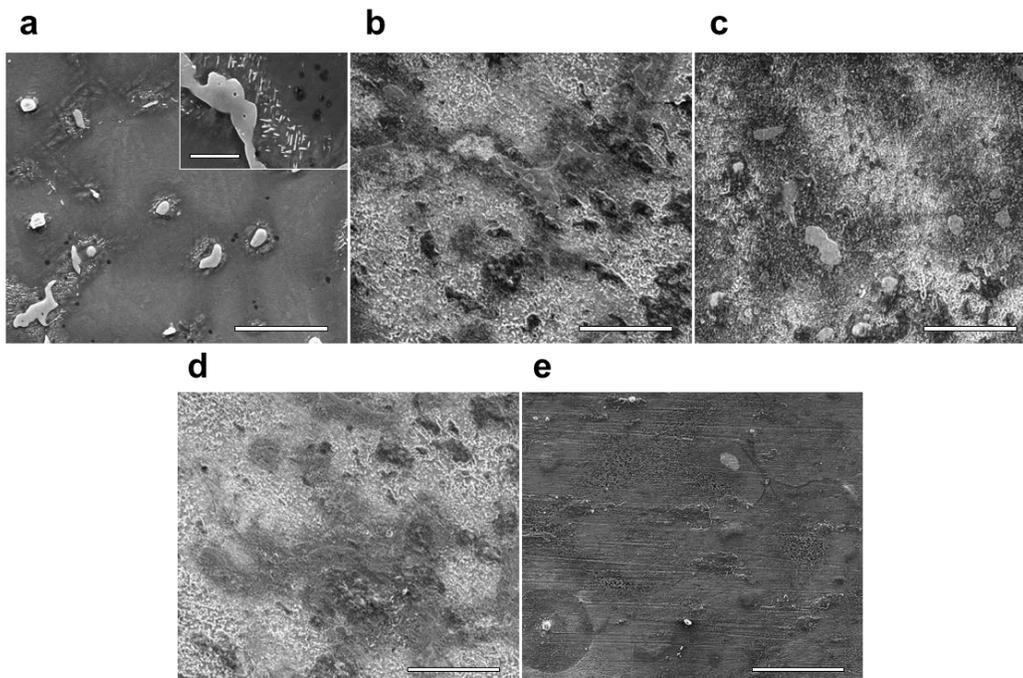
Figure III-96: Surface morphology using SEM of AZ91D: a) un-corroded, and corroded by full-immersion, free-corrosion in 3.5% aqueous NaCl for b) 5 min, c) 20 min, d) 4 hr and e) 20 hr. The inset of a) shows the Mg$_{17}$Al$_{12}$ β phase surrounded by a eutectic region located at the grain boundaries. The scale bars are 50 μm for the main images and 10 μm for the inset.
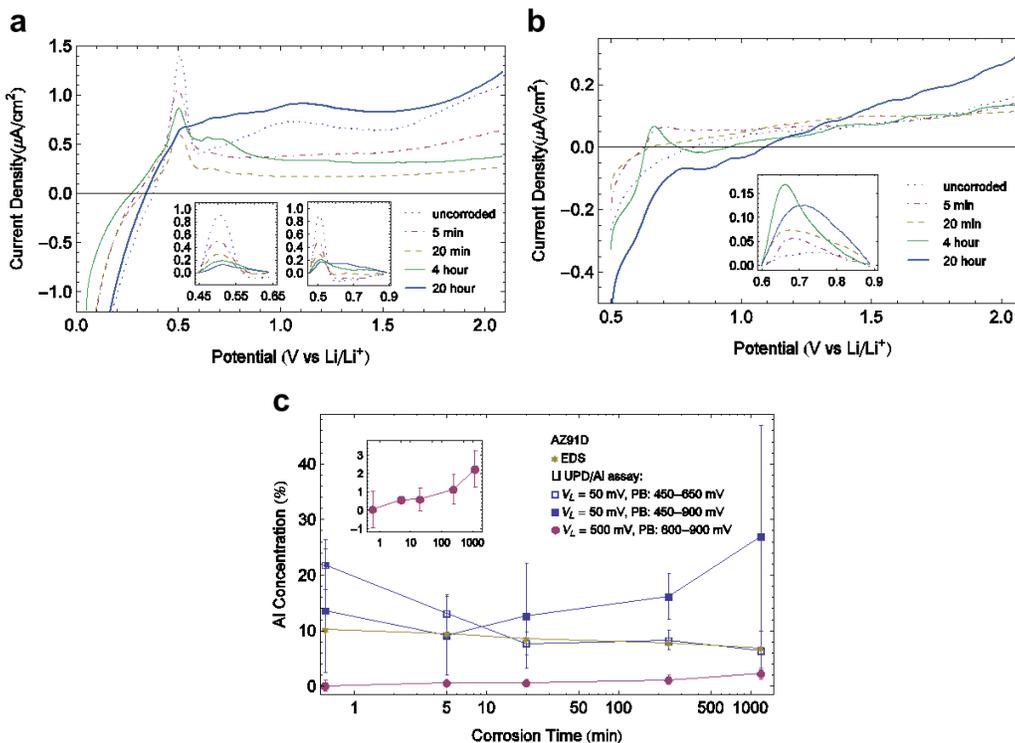
Figure III-97: Li UPD/Al assay results for corroded AZ91D: linear sweep anodic stripping curves following 600 second potentiostatic holds at lower potential limits (V$_L$) a) 50 mV and b) 500 mV vs. Li/Li$^+$ scanned at 5 mV/s in 1.0 M LiClO$_4$ in propylene carbonate; c) the charge density from the peaks in a) and b) converted to an Al concentration using the standard samples in Figure III-93 as calibration compared to an overall concentration measured using EDS. The insets of a) and b) plot the peaks after a linear background subtraction taken between the indicated peak baselines (PB). The inset in c) highlights the slight increasing trend in the 500 mV Li UPD/Al assay data.

According to the stripping curve from 500 mV, the active Al concentration that is capable of Li UPD increases from 0 to 2.2 ± 1.0 at% Al. On the other hand, the calculated Al concentration from the 50 mV lower potential limit shows a different behavior. In the first iteration, a narrow potential window was chosen for the background correction in close proximity to the peak located at ~ 500 mV vs. Li/Li+. However, after close inspection of the data, although the peak appears to be decreasing in height, it also appears to be shifting or broadening to higher potentials as the corrosion duration increases. Considering the large crystallographic-dependent UPD shifts expected for this system, these shifts may also be attributed to Al. Therefore, another background subtraction and charge density calculation was performed on a larger potential window from 450 to 900 mV, which is shown in a second inset in 9a and the calculation also reported in Figure III-97c. Unlike the stripping curve from 500 mV, the charge density calculated from the stripping curve taken from 50 mV may have significant contributions from Mg metal at the ~ 500 mV peak and MgO or Mg(OH)$_2$ at the larger potentials (recall from Figure III-93c,d). For the narrower window, the decreasing charge density may in fact be dominated by the decreasing amount of Mg metal during corrosion, and that from the larger window, may be dominated by the increase in MgO of Mg(OH)$_2$. Therefore, the overall decreasing or increasing trends observed for the narrower or broader peaks, respectively, may be partially or mostly attributable to a change in the abundance of Mg metal and its oxides rather than the change in Al on the surface. Currently, without experimental results for the crystallographic-dependent UPD shifts for Al, these contributions would be difficult to accurately discern.

Another area of development crucial to the understanding of the corrosion of Mg-Al alloys is the measurement of the electrolyte pH evolution during corrosion both on the macroscopic and microscopic scales. During corrosion, Mg undergoes oxidative dissolution simultaneously causing water reduction and an increase in electrolyte pH. To determine the effect of the different alloying elements and intermetallic particles on the pH evolution is of particular interest.

Small pieces of Mg-Al alloys were immersed in 3.5% NaCl under free corrosion conditions, and the bulk electrolyte pH was monitored using a standard glass pH electrode. The results are reported in Figure III-98. The pH of the electrolyte surrounding the corroding Mg increases faster than alloys containing Al, peaks at about 9.8 then gradually decreases. However, the pH of the electrolyte surrounding the Mg-Al alloys increases at a slower rate than Mg alone. There are many competing reactions that are likely affecting the pH evolution including water reduction, Mg oxidation to MgO and also the oxidation of Al to soluble aluminate at high enough pH. This may help to explain the only slight increase in Al content found for the AZ91D samples. Most likely, the aluminum momentarily enriched on the surface due to Mg dissolution and also suffered from dissolution in high pH environments.
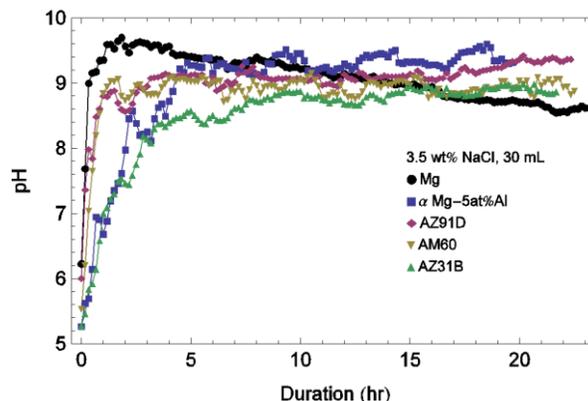
Figure III-98: Evolution of electrolyte pH of commercial alloys and common components under full-immersion, free-corrosion conditions in 3.5% aqueous NaCl using a standard glass electrode.

Although this electrode has been useful for studying the macroscopic change in electrolyte pH on the order of millimeters above the corroding surface, this distance above the surface is too large to determine specific effects from alloy parameters such as compositional distribution and the size and spacing of secondary particles on the order of microns. Therefore, a pH sensor was explored based on a hydrated metal oxide wire whose open circuit potential is linearly related to the solution pH.

The surface of approximately 1.0 mm of exposed Pt-20% Ir and Ir wires were oxidized using repeating multistep chronoamperometry for 10,000 cycles. Figure III-99 reports the open circuit potential (OCP) of the wires against a standard Ag/AgCl reference electrode in various buffer solutions. The oxidized Pt-20% Ir wire exhibited 25 mV/pH sensitivity whereas the oxidized Ir wire presented super-Nernstian behavior with 68 mV/pH. The increased sensitivity makes the oxidized Ir wire the preferred choice for more accurate pH sensing. In addition to buffer solutions, the oxidized Ir wire has further been shown to behave with similar sensitivity and linearity in both sulfate and chloride-containing solutions that have been adjusted with sodium hydroxide. This is an important finding due to the potential for chloride ions to interfere with the oxide surface. Therefore, future studies are envisioned for this electrode to probe the local pH environment of corroding Mg-Al alloys in chloride solutions in either a stationary or atomic force microscope (AFM)-SECM setup.
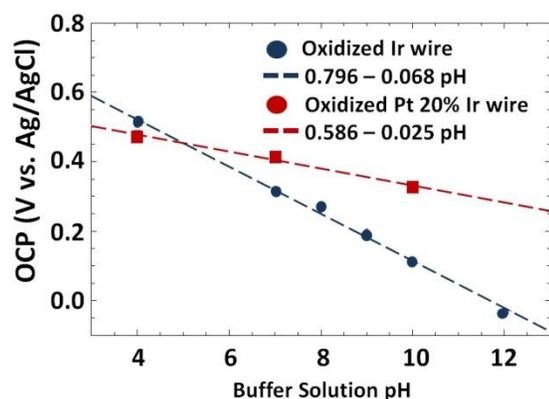
Figure III-99: Calibration curve relating the open circuit potentials of the oxidized microelectrode made from Ir and Pt-20% Ir wires with respect to the solution pH.

The final area of interest that was explored during this fiscal year was the study of the anodic dissolution behaviors of Mg-Al alloys without the simultaneous water or di-oxygen reduction reactions. Toward this end, two ionic liquids have been identified and considered for these studies. The first is a deep eutectic mixture of choline-chloride:urea (CC-urea) in a 1:2 molar ratio and the second is 1-butyl-3-methylimidazolium tetrafluoroborate ($BMImBF_4$). $BMImBF_4$ exhibits a larger electrochemical potential stability window, possibly large enough to study not only Mg dissolution but also deposition. However, preliminary results have shown that even a minimal amount of native oxide present on Mg and Mg-Al alloys significantly hinders electrochemical dissolution. On the other hand, the CC-urea mixture easily breaks down the oxide

allowing subsequent dissolution studies, and preliminary results are reported here for two types of Mg-Al alloys: one containing only solid-solution α phase Mg-5at% Al and one containing β phase in a Mg-8at% Al alloy.

Results of nonaqueous electrochemical corrosion on solid-solution α Mg-5at% Al was performed at -100 mV vs. Al/Al^{3+} in CC-urea at 150°C. SEM and EDS areal mapping images of the resulting surface morphology and composition are shown in Figure III-100. The images indicate Al-enriched nanowires forming ridges around an inset area of mainly Mg. Quantitative EDS measurements indicated that the base, nanowires and ridges contained approximately 8.3, 30 and 65 at% Al, respectively. In addition, Li UPD/Al assay results of the un-corroded and corroded α phase Mg-5at% Al are reported in Figure III-101. The anodic stripping curves confirm the presence of a significant amount of electrochemically active Al. A linear background correction was again implemented on the stripping peaks (see the inset in Figure III-101 for the background-correct peaks), and the peak charge density was compared to the standard 100 nm, 100% Al coverage sample in Figure III-95. In the Li UPD region, chronoamperometry and anodic stripping curves from lower potential limits: 300 and 500 mV vs. Li/Li^+, the corroded sample exhibited the equivalent signal of a 79-84% Al planar surface coverage. In the bulk alloying region, chronoamperometry and anodic stripping curves from lower potential limit of 50 mV vs. Li/Li^+, the corroded sample exhibited the equivalent response of a film 2.0 nm thick.
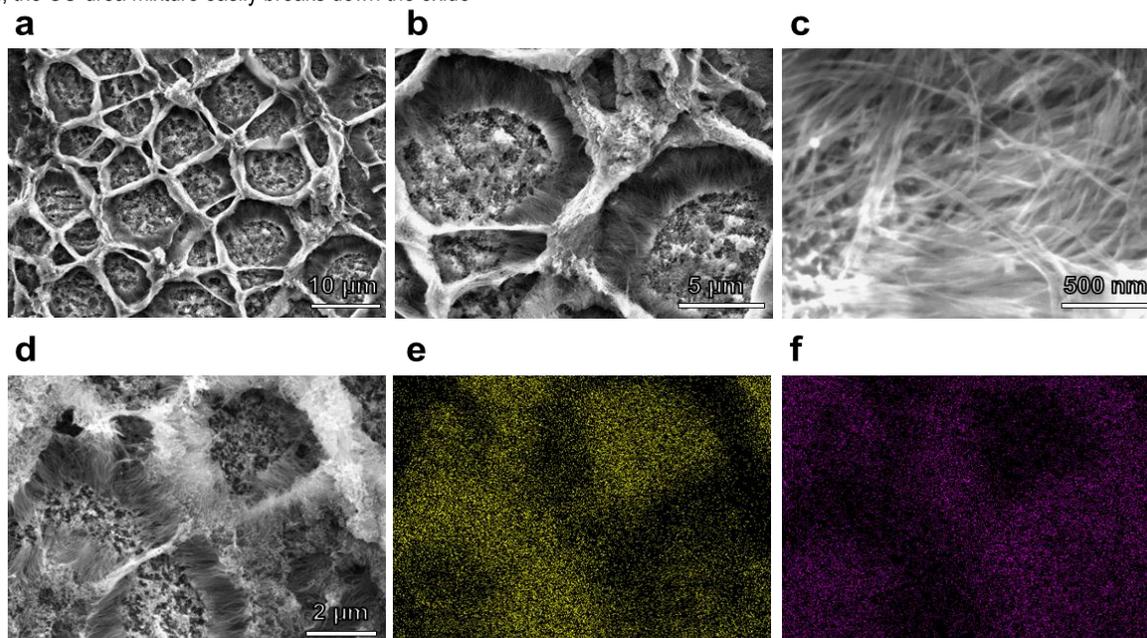
Figure III-100: Surface morphology using SEM of α Mg-5at% Al following potentiostatic corrosion at -100 mV vs. Al/Al^{3+} for 60 min in a deep eutectic 1:2 molar ratio of choline chloride:urea at 150°C shown at increasing magnification (a-c) as well as EDS areal mapping of the base, nanowire and ridge morphology shown in d) for e) Mg and f) Al abundance.
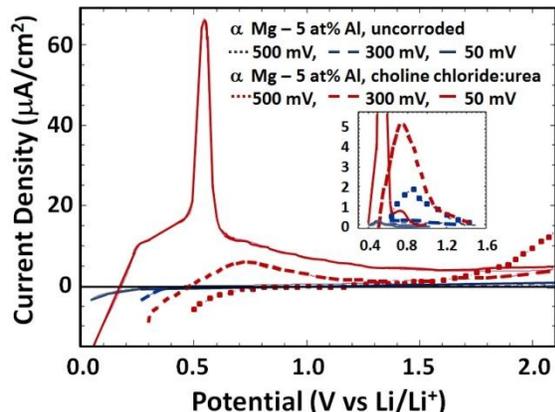
Figure III-101: Anodic stripping curves at 5 mV/s in 1.0 M LiClO$_4$ in propylene carbonate following 600 second chronoamperometry at the lower potential limit: (dotted) 500 mV, (dashed) 300 mV and (solid) 50 mV vs. Li/Li$^+$ for α Mg-5at% Al: (blue) un-corroded and (red) following potentiostatic corrosion at -100 mV vs. Al/Al^{3+} for 60 min in a deep eutectic 1:2 molar ratio of choline chloride:urea at 150°C.

As expected, the absence of water and di-oxygen related reactions allowed for the selective dissolution of Mg and the redistribution and enrichment of Al. However, the mechanism for redistribution which resulted in the complex surface morphology is still under investigation.

A similar study was has also been initiated on a Mg-Al alloy that contains not only the solid-solution α phase but also the β phase to determine the effect of the secondary phase on the corrosion behavior. Figure III-102 shows the SEM surface morphology of an un-annealed Mg-8at% Al alloy before and after electrochemically-controlled corrosion at -100 mV vs. Al/Al^{3+} for 30 min in CC-urea at 150°C. Quantitative EDS measurements indicated an increase in the Al concentration between the un-corroded and corroded surface of the alpha phase from 4.7 to 10.2, of the beta phase from 36.5 to 86.2 and of the overall compositional change from 8.7 to 42.4 at% Al, respectively. In the aqueous corrosion study of AZ91D, as shown in Figure III-96, the corrosion appears to initiate at the center of the alpha grains where the Al concentration is lowest. However, in this nonaqueous study, the opposite appears to be true where the center of the grains appear to be the least corroded. These complex preliminary results have spurred further investigation planned for the next fiscal year of the program into the corrosion behavior of these Mg-Al alloys in nonaqueous systems.
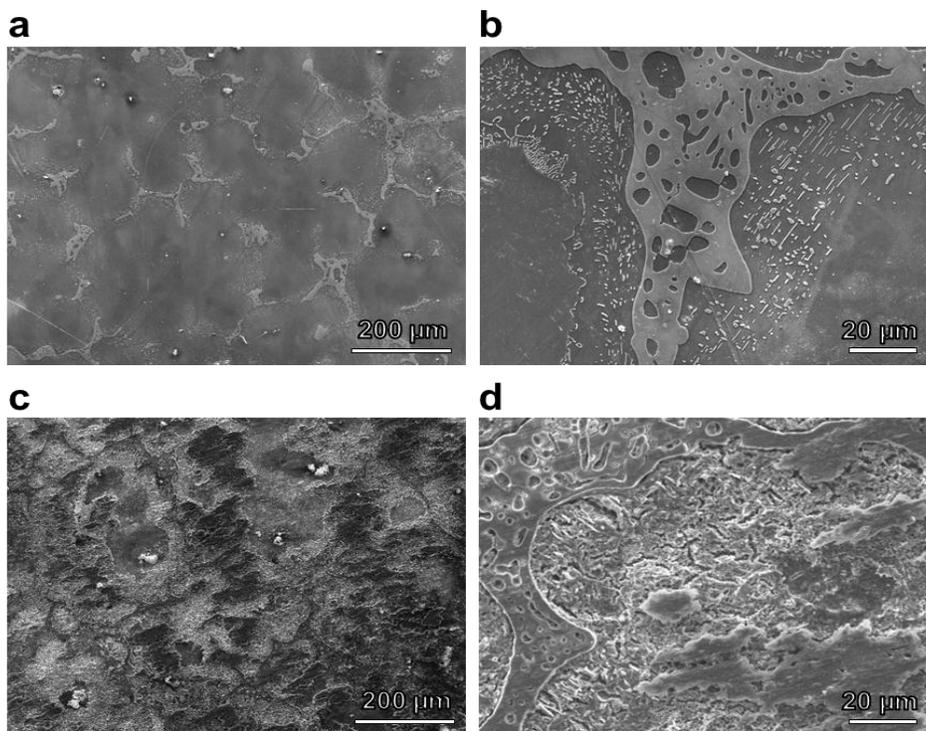
Figure III-102: Surface morphology using SEM of un-annealed Mg-8at% Al alloy: a,b) un-corroded and c,d) corroded at -100 mV vs. Al/Al^{3+} for 30 min in a deep eutectic 1:2 molar ratio of choline chloride:urea at 150°C.

Technology Transfer Path

Technology produced by this program will be disseminated to the automotive engineering community by the development of a web site from which our detailed raw data, reports, source code for KMC simulations and literature publications can be downloaded. The raw data, which is typically unavailable in research publications, will be made available through this site. Future journal publications will contain a citation indicating the location of this site. In addition, the KMC source code and additional relevant information will be recorded in the National Institute of Standards and Technology (NIST) Materials Genome Initiative repository.

Conclusion

During the first fiscal year of the project, significant headway has been made toward the development of a better understanding of the corrosion behavior in advanced automotive cast Mg alloys. In preparation for corrosion studies, commercial alloys including AZ91D as well as single-phase samples were acquired or fabricated and verified using morphological, structural and compositional characterization methods. In addition, synthetic Mg-Al alloys were synthesized using photolithography. These synthetic alloys will not only be useful for corrosion studies, but they have also been used to calibrate an electrochemical Al assay protocol based on underpotential deposition of Li. This protocol was then applied to data from AZ91D that underwent full-immersion, free-corrosion conditions in an aqueous chloride environment. The analysis indicated a slight Al enrichment of 2.2 ± 1.0 at% Al on the alloy surface after 20 hours of corrosion. In contrast, preliminary results from potentiostatic corrosion in a nonaqueous deep-eutectic solvent of choline chloride and urea resulted in a complex redistribution and a much more significant degree of Al enrichment on Mg-Al alloys compared to aqueous corrosion. Results from the Al assay protocol indicated an equivalent signal of 79-84% planar surface coverage, 2.0 nm thick of Al on a corroded surface of α phase Mg-5at% Al. In aqueous systems, Mg corrosion is accompanied by simultaneous water and/or di-oxygen reduction reactions that significantly change the pH of the electrolyte, which may lead to Al dissolution. This may have prevented the same degree of Al enrichment that was observed for the nonaqueous corrosion. Therefore, concurrently with aqueous corrosion studies, an oxidized Ir microelectrode has been developed for future studies to ascertain the local pH evolution on commercial and synthetic Mg-Al alloy surfaces under aqueous corrosion.

Presentations/Publications/Patents

No presentations, publications or patents are available to report for the first fiscal year of the program.

References

1. Voort, G. V. Metallography of Magnesium and Its Alloys. Buehler Tech-Notes 2005, 4, 1-7.

2. Finazzi, E.; Di Valentin, C.; Pacchioni, G.; Chiesa, M.; Giamello, E.; Gao, H.; Lian, J.; Risse, T.; Freund, H. Properties of Alkali Metal Atoms Deposited on a Mgo Surface: A Systematic Experimental and Theoretical Study. *Chem Eur J* **2008**, *14*, 4404-4414.

3. Lehnert, W.; Schmickler, W. A Model for the Adsorption of a Commensurate Layer of Metal Ions on a Single Crystal Substrate. *J Electroanal Chem* **2001**, *310*, 27-37.

4. Schmickler, W. A Model for the Adsoption of Metal Ions on Single Crystal Surface. Chemical Physics 2001, 141, 95-104.

5. Paddon, C. A.; Compton, R. G. Underpotential Deposition of Lithium on Platinum Single Crystal Electrodes in Tetrahydrofuran. *J. Phys. Chem. Lett*. **2007**, *111*, 9016-9018.

III.21 A Systematic Multiscale Modeling and Experimental Approach to Protect Grain Boundaries in Magnesium Alloys from Corrosion – Mississippi State University

Mark F. Horstemeyer, Principal Investigator
Center for Advanced Vehicular Systems
Mississippi State University
200 Research Boulevard,
Mississippi State, MS 39762
Phone: (662) 325-5449
E-mail: mfhorst@cavs.msstate.edu

Santanu Chaudhuri, Principal Investigator
Illinois Applied Research Institute
The University of Illinois, Champion Campus
2100 S Oak St #206
Champaign, IL 61820
Phone: (217) 300-9419
E-mail: santc@illinois.edu

William Joost, Technology Area Development Manager
U.S. Department of Energy
1000 Independence Avenue, SW
Washington, DC 20585
Phone: (202) 287-6020
E-mail: william.joost@ee.doe.gov

Contractor: Mississippi State University (MSU)
Contract No.: DE-FOA-0000793

Abstract/Executive Summary

The goal of the proposed multiscale modeling research is to establish fundamental *structure-property* relationships in cast magnesium (Mg) alloys by investigating critical grain boundary phenomena (intergranular failure) during corrosion coupled with experimental electrochemical studies. This endeavor will lead to an experimentally validated physically based internal state variable (ISV) model developed from lower length scale information to be used in the finite element analysis of structural components.

Accomplishments

- Performed geometry optimization computations within the framework of density functional theory (DFT) on pure and doped Mg(0001) surfaces. Calculated the energy of segregation for the dopant metals (X=Al, Fe, Zn, Ca and Mn) from the bulk of Mg to the topmost layers of Mg(0001), along with the surface energy changes during segregation.

- Identified the preferred adsorption configuration and energetics of molecules relevant to hydrogen evolution, i.e., water (H_2O), hydroxide (OH) and hydrogen (H), on pure and doped Mg(0001) surfaces through DFT.

- Initiated and partially completed the computations on the potential dependent energetics of competitive reaction paths of electrochemical H_2O decomposition, e.g., hydrogen evolution reaction, on pure and doped Mg(0001) surfaces.

- Procured pure Mg (99.95% purity), magnesium-aluminum (Mg-Al) alloys (made from commercial pure Mg (99.95%) and commercial pure Al (99.99%) with 2 percent by weight (2 wt.%), 4 wt.%, and 6 wt.% Al), as well as magnesium-zinc (Mg-Zn) alloys (made from commercial pure Mg (99.95%) and commercial pure Zn (99.99%) with 2 wt.%, 4 wt.%, and 6 wt.% Zn).

- Conducted the corrosion surface characterization to investigate the corrosion properties of the procured Mg alloys by performing preliminary electrochemical studies (quantify the hydrogen oxidation reaction, potential-dynamic polarization curve) and immersion corrosion experiments (quantify general corrosion, localized pitting corrosion, and profilometry analysis).

- Completed the formulation of the kinematics, kinetic, thermodynamics, and mass balance for the corrosion ISV damage model.

Future Directions

- First-principle computations initiated on the adsorption energetics of H_2O, OH and H on Mg-X(0001) surface alloys will be expanded to include the stoichiometric bulk alloy surfaces.

- Vibrational frequencies of the adsorption systems will be computed to obtain the zero point energy and entropic corrections to the electronic energy, which will eventually be used to provide quantitative results on the potential dependence of hydrogen evolution reaction for pure and doped Mg(0001) surfaces.

- The effect of doping on the energy barriers of relevant reactions, e.g., H_2O and H_2 decomposition, will be explored.

- Acquire the remainder of the magnesium alloys, and complete the corrosion surface characterization experiments for all the procured magnesium alloys. For instance, use atomic force microscopy (AFM) to study the nanoscale electrochemical corrosion process, apply scanning electrochemical microscope (SECM) to investigate the hydrogen evolution rate on different kinds of magnesium alloys, and conduct immersion corrosion tests and profilometry analysis to quantify corrosion damage for these materials.

- Integrate the multiscale ISV corrosion damage models, and complete the model calibration and validation with the experimental data.
- Implement model into Finite Element (FE) code, create fitting routine to determine constants for an Abaqus User Material (UMAT) subroutine, and implement into the Abaqus UMAT.
- Update the integrated computational materials engineering (ICME) models and experimental data into the cyberinfrastructure (CI) and NIST dspace repository.

Technology Assessment

- Target: With an overarching goal of creating a mechanistic multiscale modeling framework that captures hydrogen evolution under corrosive environments (a tractable metric associated with Mg corrosion), the specific objectives of this project are as follows: (1) Design and perform first-principles (ab initio) simulations for various element-doping scenarios to inform the next higher length scale dealing with classical molecular dynamics (MD) simulations of diffusion and transport under electrochemical conditions; (2) Develop a multiscale modeling approach using the ISV formalism that links the macroscopic damage evolution to nanoscale hydrogen evolution mechanisms and material properties. Hydrogen evolution kinetics will be explored using first-principles simulations and nanoscale experiments; and (3) Experimentally characterize the electrochemical processes of corrosion through in situ electrochemical atomic force microscopy (EC-AFM).
- Gap: A lack of nanoscale corrosion simulation data with respect to alloying elements that can inform higher length scale models for Mg alloys.
- Gap: No current ISV model for corrosion in Mg alloys that can predict corrosion damage as a function of time and any associated connections to lower length scale simulations.
- Gap: No quantification in the literature for experimental data that delineates pit nucleation, pit growth, and pit coalescence compared to general and intergranular corrosion.

❖   ❖   ❖   ❖   ❖

Introduction

The Mg-Al and/or Mg-Zn alloys have a strong prospect of providing next-generation structural alloys for automotive applications. The objective of this project is to apply multiscale modeling and experimental approaches to provide a fundamental understanding of the corrosion process that leads to intergranular failure and rapid degradation of the mechanical properties of Mg alloys. Corrosion is highly dependent on the alloying elements and microstructure. During the casting process, many of the grain boundaries and their relative orientations may be modified. Some impurity elements prefer segregating to grain boundaries, whereby

they modify the stability of grain boundaries. However, there is no clear knowledge on how doping and grain boundary engineering can be used favorably for altering corrosion rates in promising Mg alloys. In addition, although many rare earth (RE) elements have been shown to improve the corrosion protection, there is a lack of mechanistic understanding on how RE elements can be used effectively to bolster corrosion protection of surface layers and grain boundaries. A significant research effort on fundamental approaches to isolate and mitigate primary mechanisms of corrosion progression is proposed to answer several important questions of fundamental interest: (a) how to identify ideal microstructure and intergranular corrosion mechanisms in Mg-Al/Mg-Zn alloy systems in atomistic detail, (b) how to evaluate the relative role of doping elements (RE and related elements) for corrosion control using localized hydrogen evolution kinetics as a guide to changes in overall corrosion kinetics, and (c) how to implement these findings into a predictive model.

Multiscale modeling techniques provide a powerful approach to accurately model the corrosion effects. Our proposed multiscale physically based modeling methodology is illustrated in Figure III-103. This methodology is adapted from the current modeling philosophy "From Atoms to Autos" at Mississippi State University's (MSU) Center for Advanced Vehicular Systems (CAVS) and will be used as the philosophical foundation to capture the history of effects from lower length scales (i.e., electronics) to the full structural scale material model. Using this philosophy and starting with the end in mind, the ability to use different forms of cast Mg alloys for structural automobile applications would be the end goal. As an example, the Chevrolet Corvette engine cradle was cast from an AE44 (Al-RE ternary) Mg alloy. The success of the engine cradle project, where the principal investigator (PI) was involved in the modeling of the cradle, shows that there is opportunity to create lightweight structural members for automobiles. However, accurately modeling the multiscale effects through downscaling the mechanistic requirements and then upscaling the results will be vital to further improvement.
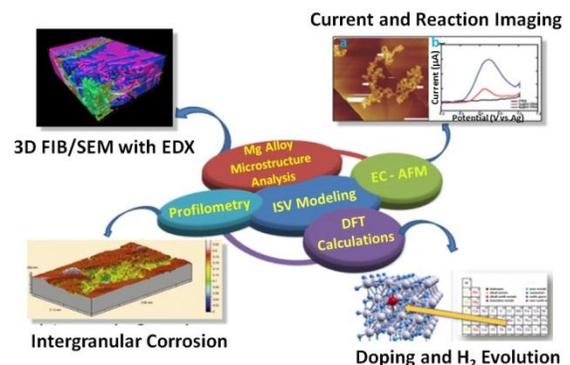
Figure III-103: Multicale modeling strategy that integrates experimentally and computationally obtained information from different material length scales. The structure-property relationships are captured within the macroscale internal state variable (ISV) model for the development of cast Mg alloys.

The importance of defining the downscaling requirements from the environmental conditions and then upscaling from the simulation results from lower length scales creates "bridges" for information flow and the ability for the macroscale model to admit nanoscale information. This project focuses on corrosion mechanisms in a multiscale framework. One of the outcomes of the current project is the scientific understanding of the nanoscale corrosion mechanisms responsible for macroscale material failure. Bridge(s) to the macroscale will be made such that structural finite element analysis may be used to predict material corrosion behavior under different mechanical and thermal environments (the thermal and mechanical environments are already part of the macroscale ISV formulation).

Approach

The goal of the proposed multiscale modeling research is to establish fundamental *structure-property* relationships in cast magnesium (Mg) alloys by investigating critical grain boundary phenomena (intergranular failure) during corrosion coupled with experimental electrochemical studies. In FY 2014, DFT computations were performed to determine the energetics and configurational aspects of hydrogen evolution and the potential dependence of reaction rates, on pure and alloyed Mg(0001) surfaces in a comparative way. Periodic slab computations within the framework of DFT were performed using Vienna ab-initio simulation package - Perdew-Wang 91 (VASP-PW91) on high performance computing clusters. A new consistent formulation coupling kinematics, thermodynamics, chemical mass balance, and kinetics was developed to account for the corrosion damage by using an extended multiplicative decomposition of deformation gradient. The corrosion model, based upon ISV theory, captures the effects of general corrosion, pit nucleation, pit growth, pit coalescence, and intergranular corrosion.

With respect to the multiscale experiments, high purity level magnesium alloys (Mg-2wt.%, 4wt.%, 6wt.% Al, Mg-2wt.%, 4wt.%, 6wt.% Zn) were procured, and these materials were prepared by vacuum induction melting the alloying elements in a hard-fired CoorsTek alumina crucible under an atmosphere of high purity argon. Then, the materials were casted into water-cooled copper chill-molds forming four-inch diameter with thirteen-inch long ingots. The detail chemical composition of the pure Mg and Mg-2 wt.% Al was identified by SpectroMax, and the microstructure of these two alloys was characterized under the optical microscope and scanning electron microscope (SEM). A scanning electro-chemical microscope (SECM) was applied to quantify the hydrogen evolution rate on the specimen surfaces. In addition, corrosion potential of the procured material was investigated by conducting the potential dynamic polarization tests. Corrosion damage caused by general corrosion, integranular corrosion, and localized pitting corrosion was quantified by performing immersion corrosion tests and profilometry analysis.

Results and Discussion

1. First Principle design, simulation, and optimization

DFT computations in this fiscal year briefly aimed to find answers to the following subjects:

- Energetics of surface segregation of impurity atoms from bulk to the surface of Mg(0001)
- Effect of impurity atoms on surface energy and stability of Mg(0001)
- Effect of impurity atoms on energetics of H_2O, H and OH adsorption, and H_2O decomposition.

The energy of segregation of impurity atoms, X, from the bulk of Mg to Mg(0001) surface were found through substitution of an Mg atom from inner and topmost layers, in order, with X, and a following geometry optimization to calculate the change in energy. For X tried here, i.e., X= aluminum (Al), iron (Fe), zinc (Zn), calcium (Ca) or manganese (Mn), the segregation energy was found to be positive except for X=Ca. The assumption is that the driving force that governs the segregation thermodynamics is the electronegativity difference between X and Mg: Ca, the only element with a lower electronegativity than Mg energetically prefers to locate at the surface, whereas the others energetically prefer to reside in the bulk. Computations also revealed that Fe and Mn doping causes magnetization in the alloy.

To understand the effect of impurity segregation on the surface stability of Mg(0001), the surface energy, E_{surf}, before and after doping, i.e., of Mg(0001) and MgX(0001), was calculated according to the formulas

$$E_{surf} = \frac{E_{Mg(0001)} - 54E_{Mg}}{2} \text{ and}$$
$$E_{surf} = \frac{E_{MgX(0001)} - 53E_{Mg} - E_X}{2}$$

The surface energy of pure Mg(0001) was found as 0.56 joules per square meter (J/m^2), approximately 30% lower than the experimental value, as a result of general tendencies of the generalized gradient approximations (GGA) functionals to underestimate the metal surface energies. [1] However, the shortcoming of our functional is not expected to cause a problem in evaluation of the surface energy change with doping, considering that the doping concentration of X in Mg is low. Doping of X= Mn and Fe increases the surface energy of the Mg(0001), whereas X=Al and Zn does not have an effect, and X=Ca decreases it [Table III-11].

Table III-11: Surface energies of MgX(0001).

X	Mg	Fe	Mn	Al	Zn	Ca
E (J/m^2)	0.56	0.69	0.66	0.56	0.56	0.53

For adsorption of the H_2O, OH and H, on pure and doped Mg(0001), all possible adsorption sites, composed of either pure Mg atoms, the single surface X atom, or a combination of Mg and X atoms are tried. Computations revealed that the

presence of surface impurities can cause changes in the adsorption energies and configurations either directly, i.e., when the surface impurity atom binds the adsorbate, or through an indirect interaction in which the impurity changes the electronic and chemical properties of surface Mg atoms and consequently influences the H_2O-Mg bonds, or a combination thereof. The energetically most favored adsorption configurations for H_2O, OH and H are given in Figure III-104, Figure III-105, and Figure III-106.

In the case of H_2O, computations revealed that presence of the impurity decreases the adsorption energy, i.e., increases the strength of H_2O adsorption on the surface. Thus, the presence of H_2O molecules on the surface is a driving force for the diffusion of the impurities from the bulk to the topmost layers.
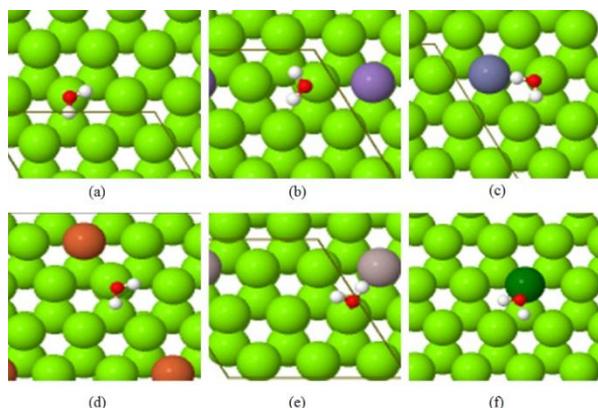
Figure III-104: Most favorable adsorption site of H_2O on Mg-X(0001) with (a) X=Mg, (b) X=Mn, (c) X=Zn, (d) X=Fe, (e) X=Al and, (f) X=Ca.
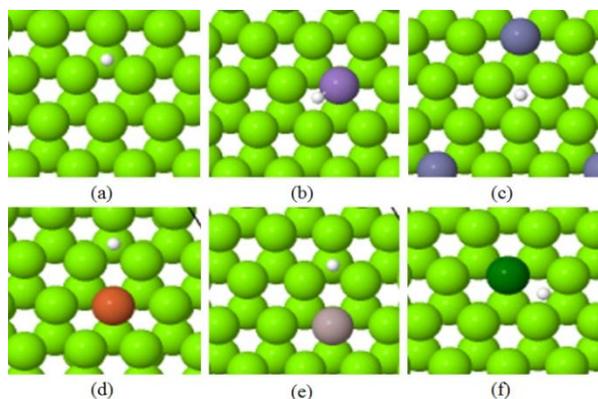
Figure III-105: Most favorable adsorption site of H on Mg-X(0001) with (a) X=Mg, (b) X=Mn, (c) X=Zn, (d) X=Fe, (e) X=Al and, (f) X=Ca.
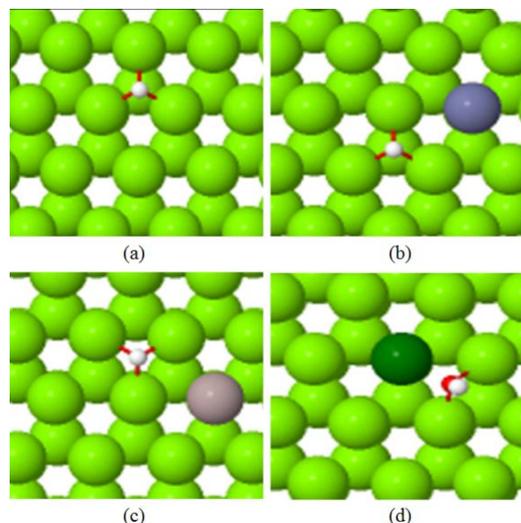
Figure III-106: Most favorable adsorption site of OH on Mg-X(0001) with (a) X=Mg, (b) X=Zn, (c) X=Al and, (d) X=Ca.

In the case of H and OH, computations revealed that presence of the impurity decreases the adsorption energies, i.e., increases the strength of both OH and H adsorption on the surface. Computations overall indicate that impurity atoms on the surface, as well as the neighboring Mg atoms around them are active sites in conversion of H_2O into OH and H.

In an electrochemical environment where water is present, the two reactions can proceed

Reaction (Rxn) 1. $H_2O_{ads} \rightarrow OH_{ads} + H^+(aq) + e^-$

Rxn 2. $H_2O_{ads} + e^- \rightarrow H_{ads} + OH^-(aq)$ or in acidic solutions, $H_3O^+(aq) + e^- \rightarrow H_2O_{ads} + H_{ads}$
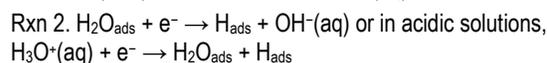
The rate of the two reactions depend on the potential effective on the metal surface. The equilibrium potential, U, (at which the reactions turn into exothermic) with respect to standard hydrogen electrode can be calculated with these two equations where E is enthalpy, ΔZPE is the zero point energy, and ΔTS is the change in entropy. [2]

$U_{Rxn1} = E_{H2O/MgX(0001)} - E_{OH/MgX(0001)} - 1/2E(H_{2,gas}) - \Delta ZPE_{Rxn1} - \Delta TS_{Rxn1}$

$U_{Rxn2} = E_{H/MgX(0001)} - 1/2E(H_{2,gas}) - E_{MgX(0001)} + \Delta ZPE_{Rxn2} + \Delta TS_{Rxn2}$

For potentials below U_{Rxn2}, Rxn 2 becomes exothermic and thus H_{ads} species is produced on the surface, which then react to form $H_{2,gas}$ through $2H_{ads} \rightarrow H_{2,gas}$.

At potentials from U_{Rxn2} to U_{Rxn1}, H_2O is stable, whereas at potentials higher than U_{Rxn1}, the metal surface is covered by OH_{ads} species, through Rxn 1.

Our computations on vibrational frequencies of adsorbate-metal systems to calculate the ΔZPE and ΔTS are in progress. Electronic energy computations that are completed up to now indicate: (i) As compared to the pure Mg(0001) equilibrium potential, the presence of impurities, as modeled by X=Al, Zn and Ca, show negligible influence on U_{Rxn1}, i.e., the potential dependent rate of surface OH_{ads} formation and (ii) U_{Rxn2}, i.e., the potential dependent rate of surface H_{ads} formation. On the

other hand, is affected by impurities. We computed a shift to cathodic potentials by ~0.1 V in the case of X=Al and Zn and by ~0.3 V in the case of X=Ca.

2. ISV corrosion damage modeling

The corrosion model based upon ISV theory is to capture the effects of pit nucleation, pit growth, pit coalescence, and general corrosion in a multiplicative decomposition manner. Using standard continuum mechanics, all of the equations will be written in the current configuration. Any motion or damage within the material can be mapped from the reference, x, to current configuration, $\underline{X}$, by the deformation gradient, $\underline{F}$.

$$\underline{F} = \frac{\partial x}{\partial \underline{X}} \qquad (1)$$

The deformation gradient assumes a sufficient continuity, where the local deformation at $\underline{X}$ is characterized as the gradient of the motion, which is a second order, two-point tensor. The kinematics of motion combine elastic straining, inelastic flow, and formation and growth of damage and is illustrated by the multiplicative decomposition of the deformation gradient. The deformation can be decomposed into the elastic, $\underline{F}_e$, damage, $\underline{F}_\phi$, and plastic, $\underline{F}_p$, deformation gradients given as the following,

$$\underline{F} = \underline{F}_e \underline{F}_\phi \underline{F}_p \ . \qquad (2)$$

The elastic deformation gradient, $\underline{F}_e$, represents lattice displacements from equilibrium. The volumetric inelastic deformation gradient, $\underline{F}_\phi$, represents a continuous distribution of corrosion and mechanical damage throughout the specimen. By this notion, the damage deformation gradient then can be decomposed by the chemical, $\underline{F}_{\phi_c}$, and mechanical, $\underline{F}_{\phi_m}$, deformation gradients as shown in the following equation

$$\underline{F}_\phi = \underline{F}_{\phi_c} \underline{F}_{\phi_m} \qquad (3)$$

The finite strain deformation gradient can then be rewritten as

$$\underline{F} = \underline{F}_e \underline{F}_{\phi_c} \underline{F}_{\phi_m} \underline{F}_p \qquad (4)$$

and is illustrated in Figure III-107.
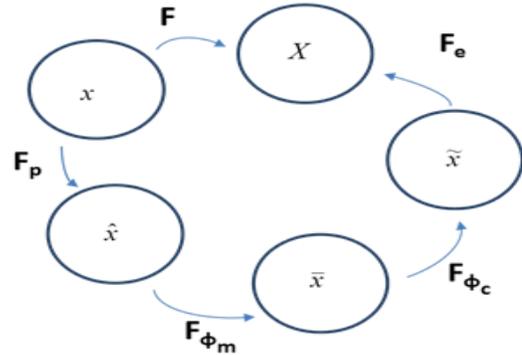
Figure III-107: Multiplicative decomposition of the deformation gradient into the elastic damage (Chemical and mechanical), and plastic parts.

The First Law of Thermodynamics in the local form as given by Malvern [3] will then be consistently written with the additional modification for the chemical corrosion effects with the following equation:

$$\rho \dot{u} = \underline{\sigma} : \underline{d} + \rho r - \nabla \cdot \underline{q} \qquad (5)$$

where u is the internal energy per unit mass, $\underline{\sigma}$ is the Cauchy stress tensor, r is the specific heat generation rate, $\underline{q}$ is the heat flux vector and ρ is the density. The First Law can be defined in the intermediate configuration by pushing forward the symmetric part of the velocity gradient to the tilde configuration.

$$\tilde{\rho}\dot{\tilde{u}} = \underline{\tilde{\sigma}} : \underline{F}_e^T \underline{d}\underline{F}_e + \rho r - \nabla \cdot \underline{q} \qquad (6)$$

For the isothermal deformation we are considering, the First Law can be simplified to the following:

$$\tilde{\rho}\dot{\tilde{u}} = \underline{\tilde{\sigma}} : \underline{F}_e^T \underline{d}\underline{F}_e \qquad (7)$$

The chemical reactions occurred during the degradation process can be simplified as the evolution of alloy composition with time due to dissolution-diffusion-segregation processes. In the electrolyte domain Ω_e, the dynamic mass change of each species, i, was caused by the ion migration and the homogeneous reactions. [4] The mass balance equation can be mathematically exppressed as:

$$\frac{\partial C_i}{\partial t} = \nabla \cdot (D_i \nabla (C_i)) + \nabla (v_{solution} C_i) + \frac{z_1}{RT} F D_i \nabla (C \nabla \varphi) + P_i \qquad (8)$$

where C_i is the concentration (mole/m³) of species i,

$$C_i = \frac{n_i}{V}$$, n_i is the total number of species i in the system,

V is the volume of electrolyte solution; $v_{solution}$ is the average velocity of the solution; D_i is the effective dissolution coefficient (m²/s) of species i, P_i is a term that accounts for the dissolution/precipitation phenomena (reaction rate in moles per cubic meter – second (mol/m³s)); Z is the charge indicates the ion migration, F is the Faraday constant (96,485.34 Coulomb per mole (C/mol)), R is the gas constant (8.314 J/(mol K)), T is the temperature (K), and φ is the electrochemical potential (V). Where $\nabla \cdot (D_i \nabla (C_i))$ and

$\nabla(v_{solution} C_i)$ characterize the diffusion and convective phenomena occurred in the system, respectively. In our case, the convective transport will be neglected, as the corrosive solution is not refreshed by a moving liquid; ion migration can be regarded as a kind of diffusion phenomena.

For the kinetics of this corrosion model, the total damage has been previously discussed in our group's work. The proposed model is as follows:

$$\phi_c = \phi_{gc} + \phi_{pc} + \phi_{ic} \qquad (9)$$

where ϕ_c is the total damage from corrosion arising from any type of corrosion mechanism, ϕ_{gc} is the damage from general corrosion (loss of thickness), ϕ_{pc} is the damage from pitting corrosion, and ϕ_{ic} is the damage from intergranular corrosion. General corrosion is signified by volume loss of the material. Pitting corrosion is used as localized corrosion for the sake of our theoretical model's paradigm and implementation. Lastly, the definition of intergranular corrosion in our context is localized corrosion that occurs at the grain boundaries caused by precipitates and segregation leading to the formation of microgalvanic cells. The pitting and intergranular mechanisms have been examined using a scanning electron microscope in Figure III-108 for an "as cast" AE44 alloy.

For pitting corrosion damage, different rate equations are given for each mechanism of nucleation, growth, coalescence. The volume fraction of pits can also be defined as the multiplicative decomposition in the form of,

$$\phi_{pc} = \eta_p v_p c \qquad (10)$$

Pit nucleation, η_p, is defined as the number density that changes as a function of time that is driven by the local galvanic electrochemical potential between base matrix material and second phase material. Pit growth, v_p, is

defined as either pit depth increases or pit surface area growth or both. Pit coalescence, c, is the interaction of the pits as they grow together and is often characterized by transgranular corrosion. This natural coalescence process is illustrated in Figure III-109.
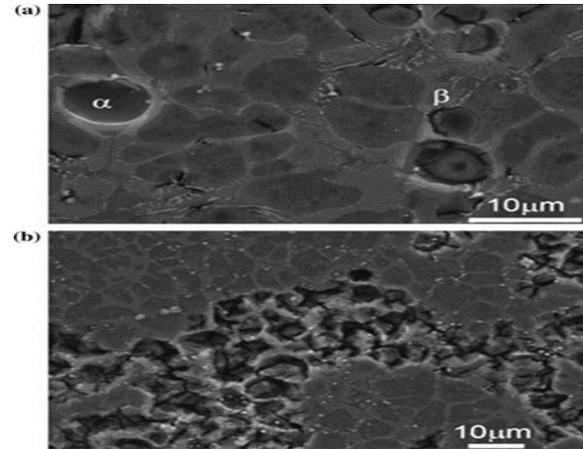
Figure III-108: Scanning electron micrographs of polished AE44 coupons at different times during the immersion test. Corrosion of the polished AE44 surface at two different times. Notice two types of corrosion present: (a) pitting and (b) intergranular corrosion [5].
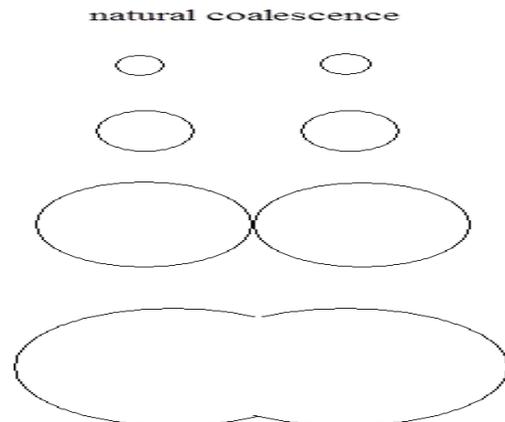
Figure III-109: Impingement coalescence illustrated by Horstemeyer [6].

3. Corrosion characterization

The chemical composition of the tested pure Mg and Mg-2%Al magnesium alloy is listed in Table III-12. Specimens prepared for the microstructure observation were initially cut from three different orthogonal directions, and cold mounted with epoxy resin. Then, surfaces of the metallographic samples were ground on progressively finer emery paper ranging from 1200 grit to 4000 grit, polished by 3, 1, and 0.05 micrometers (µm) diamond suspension solutions, and then etched with solution consisting of 5 milliliter (ml) acetic acid, 3 grams (g) picric acid, 10 ml H_2O, and 100 ml ethanol to observe the microstructure morphology. Figure III-110a and Figure III-110b show the microstructure features for the

Table III-12: Nominal composition of the material tested (weight percentage).

Element	Al	Zn	Mn	Si	Fe	Ca	Th	Cu	Pb	Mg
Pure Mg	0.026	0.0046	0.013	0.012	0.048	0.011	0.110	0.0036	0.039	99.6
Mg-2%Al	1.82	0.0025	0.016	0.012	0.027	0.0041	0.025	0.0088	0.014	98

casting Mg-2%Al alloy and pure Mg, respectively. The grain size for Mg-2% Al alloy (Figure III-110a) in the three different orientations is almost the same, around 500 μm. Some second phase particles were distributed along the grain boundaries and grain interiors, and with the overall averaged particle size of 34.2 square micrometers ($μm^2$), had a nearest neighbor distance of 59.4 μm. In addition, dendritic arms can be clearly observed in the grains. Figure III-110b shows the microstructure character of pure Mg, with a grain size range from 1 millimeter (mm) to 3 mm, and the grain size and formation are quite different for different directions.
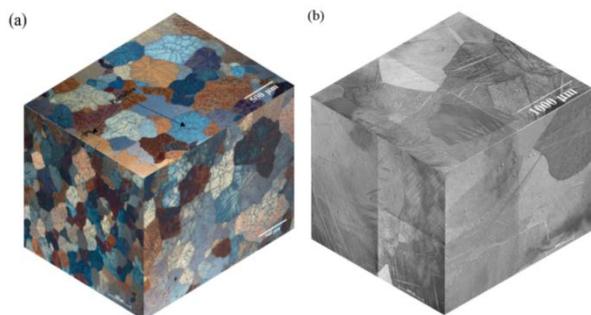
Figure III-110: Optical microstructure of Mg-2%Al alloy (a) and pure Mg (b) with three orthogonal directions. For Mg-2% Al alloy, the scale bar for every direction is the same and is 500 μm. For pure Mg, the scale bar for every direction is the same and is 1000 μm.

The electrochemical behavior of Mg-2%Al alloy and pure Mg was evaluated by potential dynamic tests. The specimens were cut into one centimeter (cm) by one cm square size, and mechanically polished using 2000-4000 grit silicon carbide (SiC) papers. Specimens were tested in 3.5% sodium chloride (NaCl) aqueous solution with a standard 3-electrode glass cell. The polarization scan started from the open potential, and scanned towards the cathodic and anodic directions separately, with scan rate of 0.3 millivolts per second (mV/s). A platinum gauze was selected as counter electrode and a saturated calomel electrode (SCE) was used as reference electrode. Figure III-111 presents the potentiodynamic polarization curves for freshly prepared specimens immersed in the solution. The open circuit potential (OCP) for Mg-2% Al alloy was more positive than the one for pure Mg. In addition, checking the specimens after the anodic polarization tests, the surfaces turned black and corroded. Specimen surfaces were rougher for pure Mg and many large localized corrosion pits were observed on surfaces, while not found on Mg-2%Al alloy surfaces. The better electrochemical behavior of the Mg-2% Al alloy can be caused by the better protective corrosion film

generated on the specimen, or the relatively higher grain boundary density which restricted the expanding of localized corrosion pits. [7]
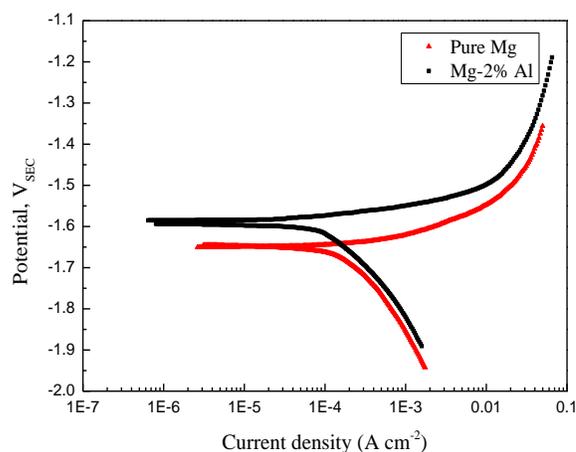
Figure III-111: Polarization curves for pure Mg and Mg-2% Al alloy in 3.5% NaCl solution.

Technology Transfer Path

The simulation/experimental results (intellectual capital, such as information, data, models, and tools) will be enabled to automakers, the materials science community, and researchers in the field of Mg alloys.

Conclusion

DFT computations proved a strong influence of the second metal, e.g., Al, Ca, Mn, Fe, Zn, on the adsorption energetics of reactants, intermediates and products of hydrogen evolution on Mg. The findings point out changes in the potential dependent reaction rates due to the dopant presence on the surface. A physically based ISV model was developed to capture the fundamental mechanisms of corrosion through kinematics, thermodynamics, and kinetics. The model will fit into the cradle-to-grave ICME-based design system that contains an ageing process. The model included the effects of hydrogen evolution rates and corrosion damage mechanics in Mg corrosion events (general, pitting, and intergranular). Preliminary microstructure characterization, electro-chemical tests, and immersion tests were performed for two materials (pure Mg and Mg-2% Al alloy). The results

show the Mg-2%Al alloy had better electro-chemical and corrosion resistant properties.

Presentations/Publications/Patents

1. W. Song, H.J. Martin, M.Lugo, C. A. Walton, M.F. Horstemeyer, P.T. Wang, "Corrosion Fatigue Behavior of an Extruded AM30 Magnesium Alloy in Sodium Chloride Solution Environment". Presented at The Minerals, Metals, and Materials Society Annual Meeting and Exchange, San Diego, California on Feb. 15- Feb. 21, 2014.

References

1. Da Silva, J. L.; Stampfl, C.; Scheffler, M. Converged properties of clean metal surfaces by all-electron first-principles calculations. *Surface science* **2006,** *600,* pp 703-715.

2. Rossmeisl, J.; Nørskov, J. K.; Taylor, C. D.; Janik, M. J.; Neurock, M. Calculated phase diagrams for the electrochemical oxidation and reduction of water over Pt (111). *The Journal of Physical Chemistry B* **2006,** *110*, pp 21833-21839.

3. Malvern, L.E. Introduction to the Mechanics of a Continuous Medium. Englewood Cliffs, NJ: Prentice-Hall, Inc. (1969).

4. Xiao, J.; Chaudhuri, S., Predictive modeling of localized corrosion: An application to aluminum alloys. *Electrochimica Acta* **2011,** *56*, pp 5630-5641.

5. Alvarez, R. B.; Martin, H. J.; Horstemeyer, M. F.; Chandler, M. Q.; Williams, N.; Wang, P. T.; Ruiz, A. Corrosion relationships as a function of time and surface roughness on a structural AE44 magnesium alloy. *Corrosion Science* **2010,** *52*, pp 1635-1648.

6. Horstemeyer, M. F.; Bammann, D. J., Historical review of internal state variable theory for inelasticity. *International Journal of Plasticity* **2010,** *26*, pp 1310-1334.

7. Ralston, K. D.; Birbilis, N.; Davies, C. H. J., Revealing the relationship between grain size and corrosion rate of metals. *Scripta Materialia* **2010,** *63*, pp 1201-1204.

III.22 Corrosivity and Passivity of Metastable Mg Alloys—Oak Ridge National Laboratory

Guang-Ling Song, Principle Investigator
Oak Ridge National Laboratory
1 Bethel Valley Road
Oak Ridge, TN 37831
Phone: (865) 574-4451; Fax: (865) 574-6098
E-mail: songg@ornl.gov

Aaron Yocum, Contract Manager
National Energy Technology Laboratory
3610 Collins Ferry Road
Morgantown, WV 26507-0880
Phone: (304) 285-4852; Fax: (304) 285-4403
E-mail: aaron.yocum@netl.doe.gov

Will Joost, Technology Area Development Manager
U.S. Department of Energy
1000 Independence Avenue, SW
Washington, DC 20585
Phone: (202) 287-6020; Fax: (202) 856-2476
E-mail: William.Joost@ee.doe.gov

Contractor: Oak Ridge National Laboratory (ORNL)
Contract No.: 0793-1594

Abstract/Executive Summary

The purpose of this project to investigate the possibility of forming a passive film on a Mg (magnesium) alloys through adding some strong passivating elements in Mg solid solution. In the first year, the film nature of pure Mg was investigated and magnetron-sputtered Mg-Ti (magnesium-titanium) alloys were produced. Their polarization behavior and film compositions were measured. These form a critical basis for studying other more complicated MgX (X represents other elements) alloys in subsequent years.

Accomplishments

- Investigated and characterized the anodic surface film formed on pure Mg ingot, which is important and essential knowledge for understanding the corrosion resistance of metastable Mg alloys (FY 2014).
- Prepared a series of magnetron-sputtered Mg-Ti alloys for subsequent studies (FY 2014).
- Completed electrochemical tests, XPS (X-ray photo spectroscopy) measurements, and SEM/TEM (scanning electron microscope/transmission electron microscope) samples of Mg-Ti alloys (FY 2014).

Future Directions

- Repeat all the corrosion, electrochemical, XPS, SEM/TEM experiments on a few alloys selected among the following systems based on ongoing project findings: Mg-Cr (magnesium-chromium), Mg-Fe (magnesium-iron), Mg-Ni (magnesium-nickel), Mg-Mn (magnesium-manganese), Mg-Sn (magnesium-tin), and Mg-Al (magnesium-aluminum) alloys.

Technology Assessment

- Target: Gain an understanding of the effect of strong passivating alloying elements, such as Ti and Cr in Mg solid solution on Mg passivity and corrosivity.
- Target: Gain an insight into the detrimental effect of impurity Fe on Mg corrosion resistance.
- Gap: There is very limited knowledge of producing and characterizing magnetron-sputtered Mg-Ti alloys. No work has been done on other magnetron-sputtered MgX alloys. If Mg can become passive by alloying with these strong passivating elements, then insight into the development of corrosion-resistant Mg alloys or coating can be gained from this knowledge.

✧   ✧   ✧   ✧   ✧

Introduction

Significant efforts have been undertaken to understand the corrosion behavior [1] and improve the corrosion performance [2] of Mg alloys. The corrosivity of numerous Mg alloys has been investigated for through casting, forming, and heat-treatment approaches. However, almost none of the previously studied alloying systems are adequately corrosion resistant for automotive applications[3,4]. As a result, industry has found that it is difficult to develop a corrosion-resistant, light-weight Mg alloy [5].

Surface alloying offers a promising potential to dramatically enhance corrosion resistance without significantly altering a material's bulk properties and density. To have a corrosion-resistant surface layer, it is important to know what alloying elements can significantly improve Mg corrosion resistance.

It is well known that passivated metals have very low corrosion rates. An example is stainless steel, which is produced by the addition of passivating elements. It may be possible to obtain a corrosion-resistant Mg alloy through

alloying with passivating elements such as Cr, Ti, Al, or Ni. In a Mg alloy, the critical constituent is its matrix phase, which is always a corrosion resistance weak region that is preferentially attacked by corrosion. If the matrix phase became passive after alloying with a strong passivating element, a significant step toward improvement in corrosion resistance of the Mg alloy would be expected. Some existing research has indicated that amorphous Mg alloys containing Ni, Y (yttrium), or Nd (neodymium) show a distinct passive region when anodically polarized in a chloride containing solution [6]. Passivation can significantly nobly shift the corrosion potential and dramatically inhibit the anodic dissolution. A passivated Mg alloy would not have a high galvanic corrosion rate. Therefore, even if it were in contact with cathodic metals, its galvanic corrosion damage would not be significant. The mitigation of galvanic corrosion based on the natural passivation behavior of Mg alloys is most reliable because a naturally formed passive film could self-heal if damaged.

Corrosivity or passivity is closely associated with the formation and dissolution of surface films on Mg alloys. However, the influence of the alloying elements on the film composition and stability has not been systematically examined, and the possible effect of the substrate metallurgical defects on the film imperfection and protectiveness has not been carefully addressed. There is a lack of fundamental understanding of surface films on Mg alloys. This gap will be closed in this study.

Approach

The following steps are being undertaken in this project.

1. MgX alloys are being produced, where the alloying element X = Ti, Cr, Mn, Fe, Al, Ni and Sn. The supersaturated single-phase MgX binary alloys are produced by means of magnetron sputtering.

2. Corrosion testing in solution [0.1 wt % NaCl (sodium chloride) + saturated $Mg(OH)_2$ (magnesium hydroxide), pH~11] and electrochemical techniques (including polarization curve and AC impedance measurements) are employed to characterize the corrosivity and passivity of the sputtered single-phase MgX alloys to demonstrate the effect of the supersaturated alloying element X and the metastable microstructure on the alloy's corrosivity and passivity [7].

3. SEM/TEM and XPS analyses are carried out to detect the compositions and microstructures of the surface films on the sputtered single-phase MgX alloys to illustrate the influence of the alloying elements on the film composition and microstructure.

In the first fiscal year, the basic methodology has been established by using ingot pure Mg and MgTi alloys.

Results and Discussion

Figure III-112 shows the polarization curves of ingot Mg and magnetron-sputtered MgTi alloys in a saturated $Mg(OH)_2$ + 0.1 wt % NaCl solution. From Figure III-112 it can be seen that the magnetron sputtering negatively shifts the polarization curve of ingot pure Mg. The shifted curve has a more negative open circuit potential (OCP) and higher anodic current densities than the ingot pure Mg, suggesting that the sputtered Mg is more active than the latter. The addition of Ti into Mg positively shifts the curve and reduces anodic current densities. Particularly, the anodic current density reduction in the region (pointed to by the arrows in the figure) next to the OCP is evident for $Mg^{51.6}Ti^{48.4}$. There is a step decrease in the anodic current densities for $Mg^{21.9}Ti^{78.1}$. These mean that the $Mg^{51.6}Ti^{48.4}$ alloy has a passivation tendency, and $Mg^{21.9}Ti^{78.1}$ should have been passivated at its OCP.
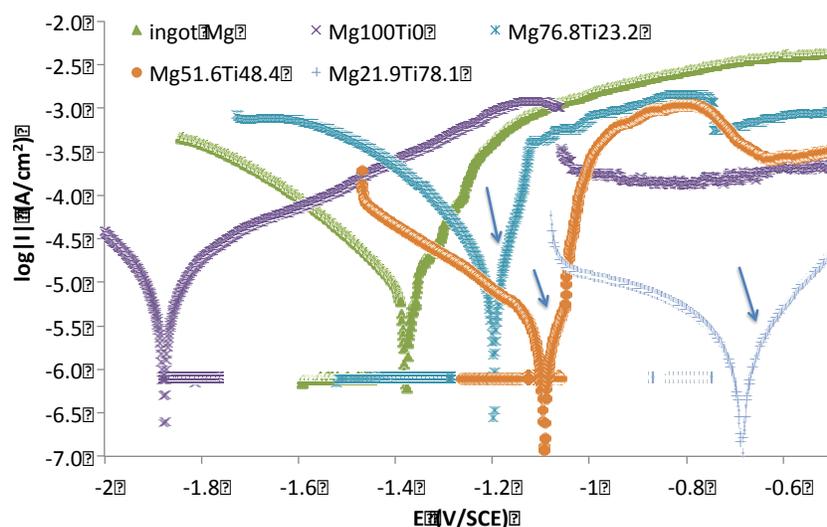
Figure III-112: Polarization curves for ingot pure Mg and magnetron-sputtered MgTi alloys in saturated $Mg(OH)_2$ + 0.1 wt % NaCl solution.

AC electrochemical impedance spectroscopies (EISs) of ingot pure Mg and magnetron-sputtered MgTi alloys in saturated $Mg(OH)_2$ + 0.1 wt % NaCl solution are shown in Figure III-113. It is found that ingot pure Mg, $Mg^{100}Ti^0$, $Mg^{76.8}Ti^{23.2}$, and $Mg^{51.6}Ti^{48.4}$ have a similar EIS behavior, while $Mg^{21.9}Ti^{78.1}$ has a "tail" extending to infinity. This means that the last alloy in the list, a high-Ti content alloy, is much more corrosion resistant than the first four specimens, which have low-Ti content. The dramatic increase in corrosion resistance for $Mg^{21.9}Ti^{78.1}$ further supports its step decrease in anodic polarization current density on the polarization curve.

The above electrochemical results, including the polarization curve and the EIS measurements, suggest that a stable, passive film may be formed when the Ti content is higher than 50%.

XPS was employed to analyze the film composition. The air-formed films on the MgTi alloys are shown in Figure III-114. On all the magnetron-sputtered MgTi specimens, a dramatic oxygen decrease can be detected at 25~50 nm depth, suggesting that the oxide films on these MgTi alloys are relatively thin, only about 25~50 nm thick. Even though the oxygen levels on these specimens after 50 nm etching are still much higher than 0%, and Mg levels are still lower than the Mg concentrations of corresponding substrate alloys, this does not mean that the air-formed films on the magnetron-sputtered MgTi alloys are thicker than 50 nm, because the substrate alloys can be further oxidized during ion etching. Moreover, it should be noted that no Ti enrichment was detected in these films. This implies that no preferential oxidation of Ti from the substrate alloys has occurred under the atmospheric condition.
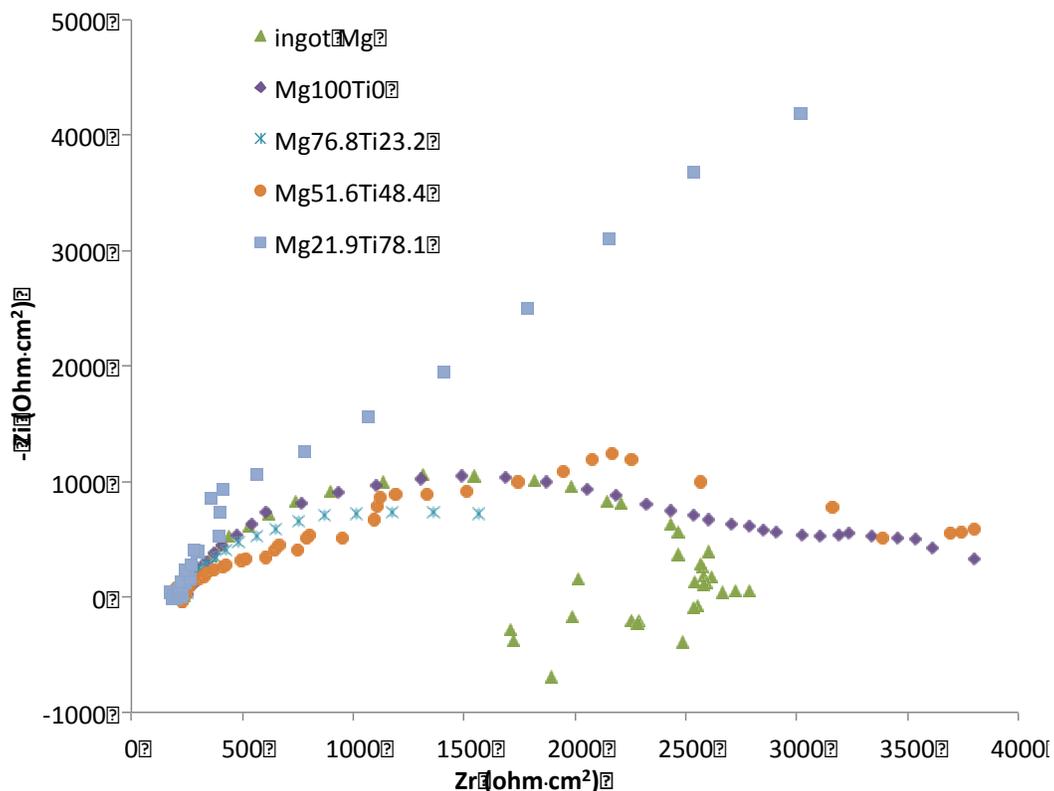
Figure III-113: Electrochemical impedance spectroscopies for the ingot pure Mg and magnetron-sputtered MgTi alloys in saturated $Mg(OH)_2$ + 0.1 wt % NaCl solution.
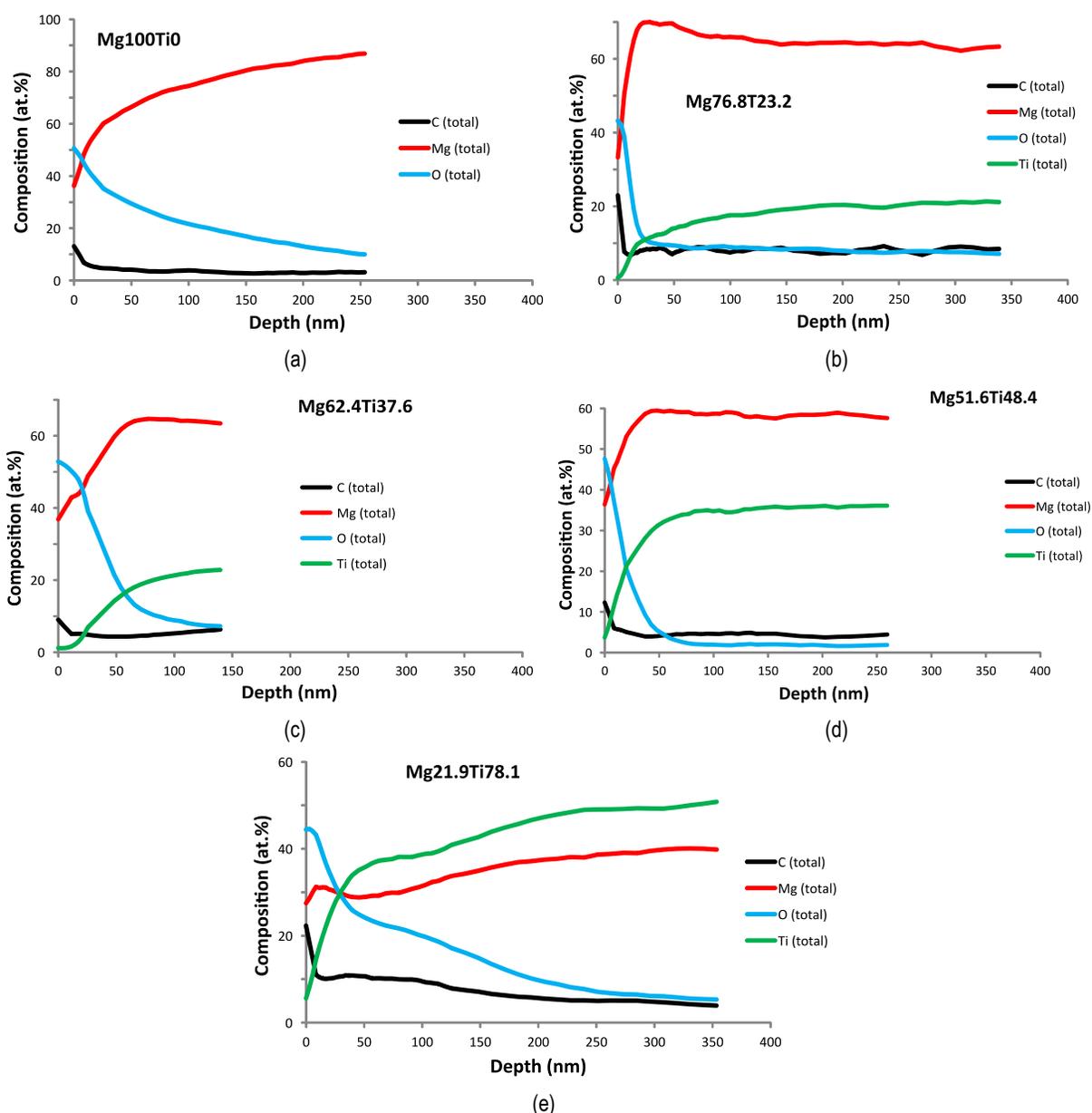
Figure III-114: XPS profiles for MgTi alloy surfaces in air.

The films on the magnetron-sputtered MgTi alloys after 24 h immersion in saturated $Mg(OH)_2$ + 0.1 wt % NaCl solution are shown in Figure III-115. After immersion, the corrosion product film on magnetron-sputtered $Mg^{100}Ti^0$ is about 300 nm thick. The ratio of Mg:O (magnesium:oxygen) is close to 1:1, suggesting that the composition of the film is mainly MgO (magnesium oxide, Figure III-115a). These results are consistent with the thick MgO film on high purity ingot Mg [8]. Some Ti enrichment is observed in the film for $Mg^{76.8}Ti^{23.2}$ (Figure III-115b). This could be caused by rapid selective dissolution of Mg from the substrate alloy. On this alloy, the film is very thick, and the O level is relatively high (>30 at. %) throughout the etching depth. The film becomes slightly thinner on $Mg^{62.4}Ti^{37.6}$ (Figure III-115c), as the O level decreases to 20 at. % at 350 nm. However, there is no distinct interface between the film and substrate metal on this alloy. This could be a result of a non-uniform surface film formed on the alloy surface; corrosion penetration is very deep in some areas, whereas in other locations, the surface is not corroded. A step reduction in film thickness occurs on $Mg^{51.6}Ti^{48.4}$ (Figure III-115d). The film on $Mg^{21.9}Ti^{78.1}$ has similar thickness as that on $Mg^{51.6}Ti^{48.4}$ (Figure III-115e). The step reduction in film thickness suggests a sudden increase in film protectiveness, which is in consistence with the observation of dramatically decreased anodic current densities next to the OCP potential for $Mg^{51.6}Ti^{48.4}$ (Figure III-112).

(a)

(b)

(c)

(d)

(e)
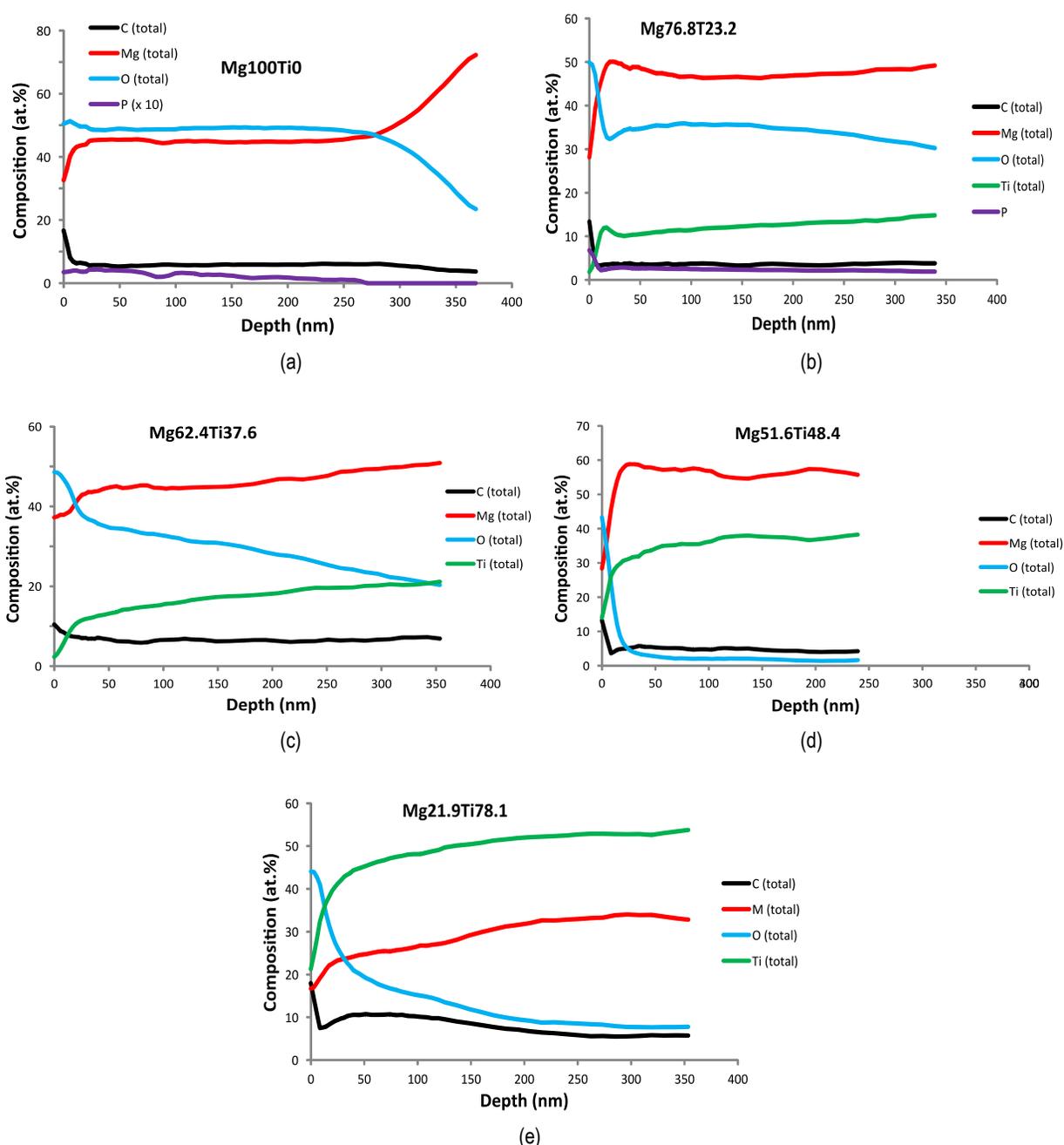
Figure III-115: XPS profiles for MgTi alloy surfaces after 24 h immersion in saturated Mg(OH)₂ + 0.1wt.% NaCl solution.

The surface SEM images of the non-immersed surface areas of the sputtered MgTi alloys are shown in Figure III-116. Mg^{100}Ti^{0} is not uniform in surface morphology (Figure III-116a). There are many corroded spots in the non-immersed regions. This kind of corrosion damage is less severe on Mg$^{76.8}$Ti$^{23.2}$ (Figure III-116b). The corrosion spots are completely inhibited when the sample contains 37.7 at. % Ti (Figure III-116c), but many cracks can be seen on the surface area of Mg$^{62.4}$Ti$^{37.6}$. It is unknown if the sample cracking can be attributed to the Ti addition. The surface quality is improved evidently when Ti content is 48.4 at. %. Nevertheless, the pinholes as shown on the surface of Mg$^{51.6}$Ti$^{48.4}$ (Figure III-116d) may be weak points for corrosion under immersion conditions. The best surface quality is obtained on Mg$^{21.9}$Ti$^{78.1}$ (Figure III-116e).

(a) Mg^{100}Ti^{0}

(b) Mg$^{76.8}$Ti$^{23.2}$

(c) Mg$^{62.4}$Ti$^{37.6}$

(d) Mg$^{51.6}$Ti$^{48.4}$

(e) Mg$^{21.9}$Ti$^{78.1}$
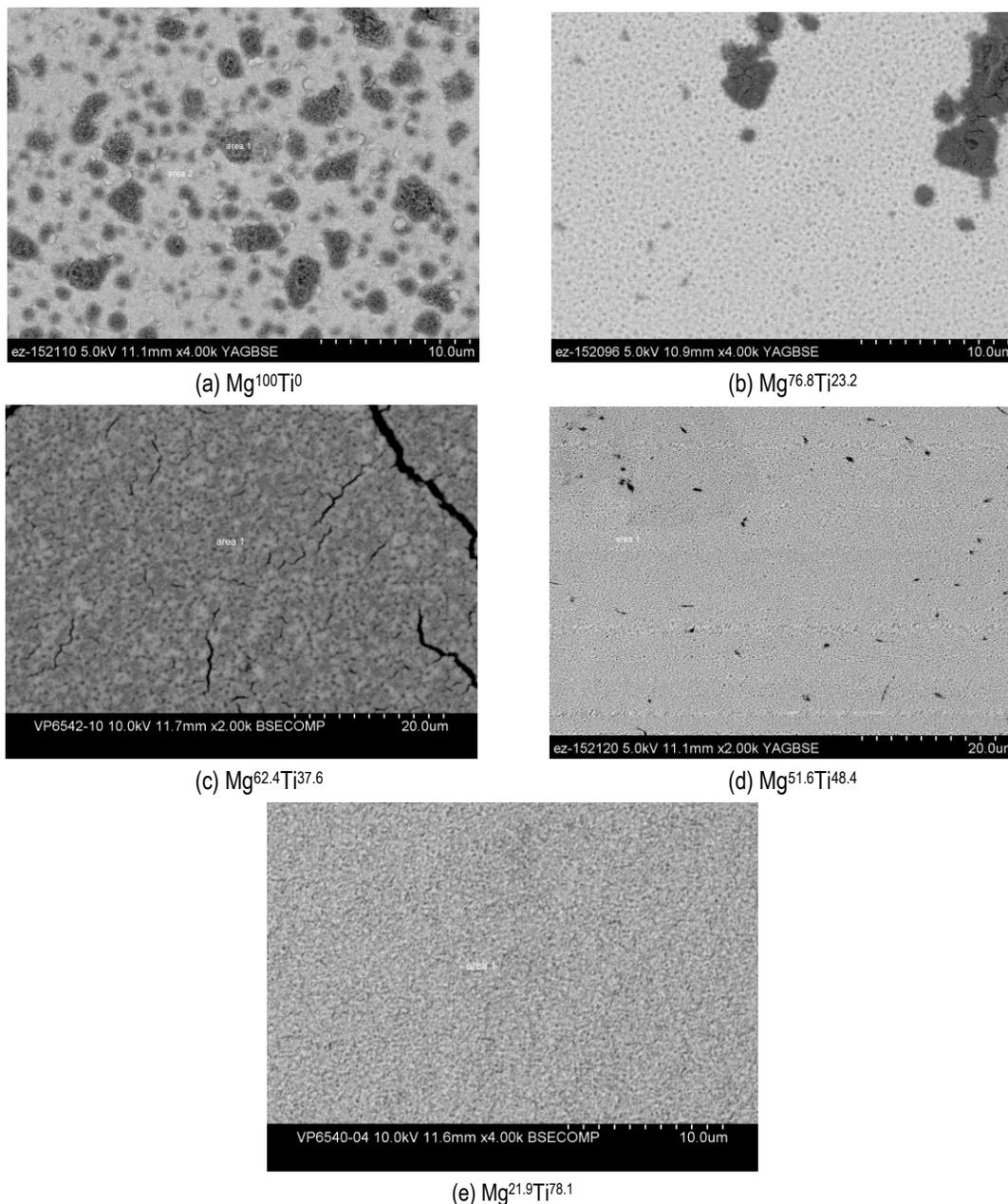
Figure III-116: Topographic SEM images of non-immersed surface regions of MgTi surfaces in air.

After 24 h immersion in a saturated Mg(OH)$_2$ + 0.1 wt % NaCl solution, the surface corrosion morphologies of these sputtered MgTi alloys are shown in Figure III-117. The whole surface of Mg^{100}Ti^{0} has been corroded, covered by a thick uniform corrosion product film with some large cracks (Figure III-117a). The cracking damage is to some degree inhibited and the cracks become smaller within the corroded areas when 23.3%Ti is added into Mg (Figure III-117b). On this alloy surface, the corrosion becomes non-uniform, and some areas are not corroded. When the Ti concentration is increased to 37.6% and 48.4% (Figure III-117c and Figure III-117d), the alloy surfaces are only partially corroded in the solution. On Mg$^{62.4}$Ti$^{37.6}$ (Figure III-117c), cracks can still be seen in some corroded areas. They could be the cause, rather than the result, of the corrosion of Mg$^{62.4}$Ti$^{37.6}$. Cracks disappear on the Mg$^{51.6}$Ti$^{48.4}$ (Figure III-117d). On this alloy, the corrosion damage may result from the pinholes that were originally in the alloy (Figure III-116d), and the uncorroded area on the alloy could be covered by a protective surface film. In other words, a passive film may be formed on this alloy, but the passive film is not stable or integrated enough to provide protection. After the alloy content of Ti is raised as high as 78.1%, the corrosion is completely inhibited (Figure III-117e).

At such a high Ti content, a stable and integrated protective

passive film is formed on the alloy surface.
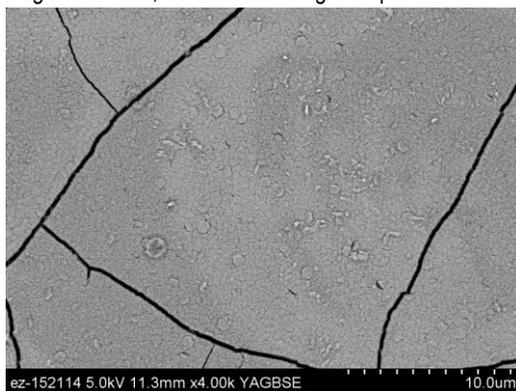
(a) Mg^{100}Ti^0
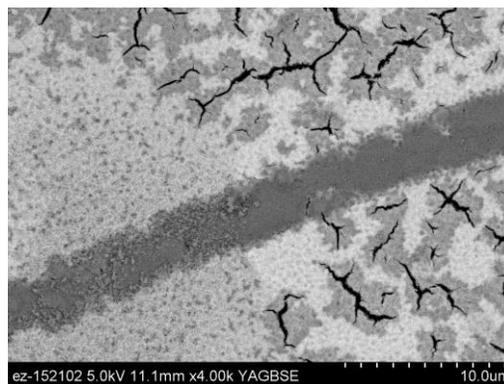
(b) Mg$^{76.8}$Ti$^{23.2}$
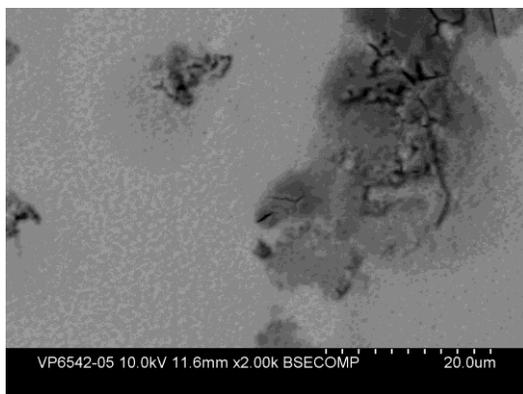
(c) Mg$^{62.4}$Ti$^{37.6}$
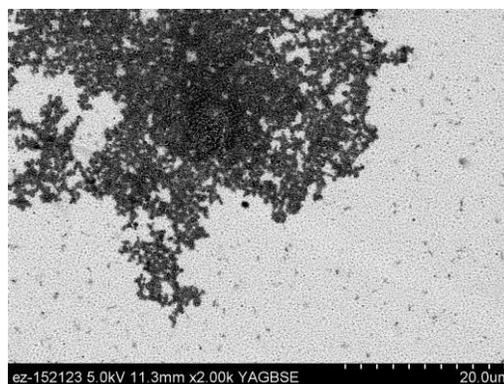
(d) Mg$^{51.6}$Ti$^{48.4}$
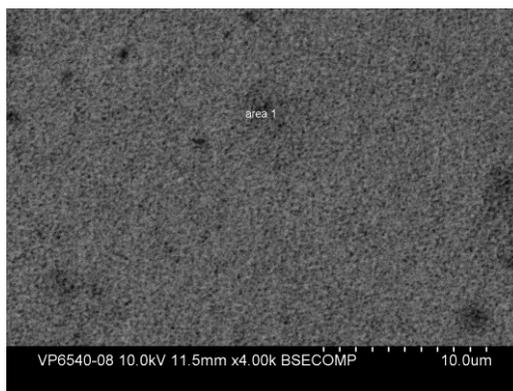
(e) Mg$^{21.9}$Ti$^{78.1}$

Figure III-117: Topographic SEM images of MgTi surfaces after 24 h immersion in saturated Mg(OH)$_2$ + 0.1 wt % NaCl solution.

BF-STEM (bright field scanning transmission electron microscope) images of the cross sections for the magnetron-sputtered MgTi alloys before and after 24 h immersion in saturated Mg(OH)$_2$ + 0.1 wt % NaCl solution are shown in Figure III-118. The sputtered Mg on glass appears to have a columnar structure (Figure III-118a and Figure III-118b). Before immersion, its surface film is very thin (Figure III-118a), which confirms the XPS estimation (Figure III-114a). After immersion, a ~0.3 µm thick continuous film is formed on its

surface (Figure III-118b). The TEM-estimated film thickness corresponds very well to the XPS-indicated film thickness (Figure III-115a). Alloying with a small amount of Ti does not change the columnar microstructure of the substrate (Figure III-118c). Before immersion, the air-formed surface film is still very thin (Figure III-118c), and the surface corrosion damage becomes non-uniform (Figure III-118d). Corrosion penetrates deeply in some areas. This

(a) Sputtered Mg^{100}Ti^0 before immersion

(b) Sputtered Mg^{100}Ti^0 after immersion

(c) Sputtered Mg$^{76.8}$Ti$^{23.2}$ before immersion

(d) Sputtered Mg$^{76.8}$Ti$^{23.2}$ after immersion

(e) Sputtered Mg$^{51.6}$Ti$^{48.4}$ before immersion

(f) Sputtered Mg$^{51.6}$Ti$^{48.4}$ after immersion
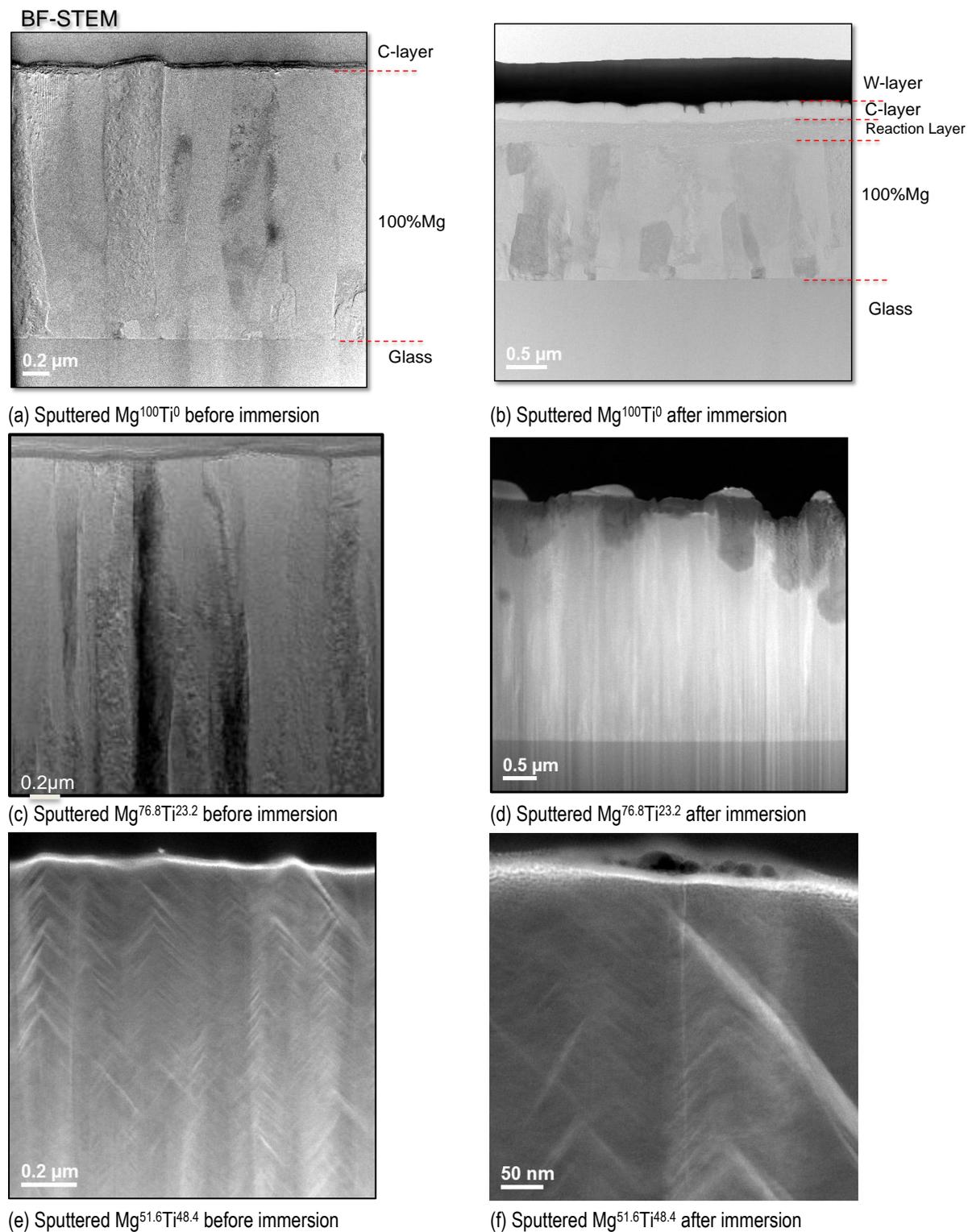
Figure III-118: BF-STEM cross-section images for magnetron-sputtered Mg and Mg-Ti alloys before and after 24 h immersion in saturated Mg(OH)$_2$ + 0.1 wt % NaCl solution.

also supports the XPS expectation that the film is not uniform and that there is no distinct film/metal interface. A further increase in Ti concentration results in a different microstructure of the substrate. Figure III-118e and Figure III-118f show that the substrate alloy has a zig-zag microstructure. Again, the surface films on the alloy before and after immersion are not clear under TEM inspection (Figure III-118e and Figure III-118f). Further high-resolution TEM investigation needs to be carried out for the thin surface film. Nevertheless, the TEM observations of the non-immersed and immersed $Mg^{51.6}Ti^{48.4}$ alloy (Figure III-118e and Figure III-118f) are consistent with the XPS results (Figure III-114e and Figure III-115e). These results suggest that the film formed in the solution is very protective and that no corrosion damage occurs in the measured area. These TEM and XPS results also provide a reasonable explanation for earlier polarization curve/EIS behaviors.

Technology Transfer Path

The above results and analyses provide primary insight into the film stability and the influence of substrate on the film, which may lead to better alloys and coatings being developed to improve the corrosion resistance of Mg alloys. Particularly, the knowledge about Al, Mn, and Fe alloying developed in this project can be used in the development of GM alloy AT72. The knowledge of Ti and Cr alloying may be employed to modify and improve this GM alloying system. The implementers of the knowledge developed in this project are the magnesium alloy producers and their customers, the automotive original equipment manufacturers. This project has significant involvement from both industries.

Conclusions

Based on these preliminary results, the following conclusions were obtained:

1. Magnetron-sputtered Mg normally is purer than ingot Mg. Thus, impurity cannot be responsible for the higher activity of sputtered $Mg^{100}Ti^{0}$. The only explanation is that the magnetron-sputtering process results in a metastable microstructure, which activates Mg. Therefore, the magnetron-sputtered Mg has a more negative OCP and higher anodic current densities than ingot Mg.

2. A small amount of Ti added to Mg solid solution may inhibit to some extend the oxidation of Mg in air, but it cannot effectively inhibit the anodic dissolution of Mg. In this case, selective dissolution of Mg occurs. Due to its nonequilibrium microstructure and chemical composition, the Mg alloy with such a small amount of alloying Ti may have an even faster corrosion rate than ingot Mg. It is unclear why cracks are formed in the alloy with the small amount of alloying Ti.

3. A very thin but protective passive film may be formed on a MgTi alloy when the Ti content in solid Mg solution is high enough (e.g., >50%). The passive film may become even more stable, continuous, and protective when the Ti content is >78 at. %. The passive film is so thin that it cannot be easily detected by conventional TEM methods. High-resolution TEM will be required on perfectly prepared specimens to characterize the passive film.

4. Based on the MgTi results, it is important to investigate the passivity of MgCr alloys. Chromium may have a stronger passivating capacity with Mg than Ti, which may make Mg passive at a concentration lower than 50 at. % Cr. Magnetron-sputtered MgCr alloys have been ordered. The electrochemical, XPS, and SEM/TEM tests have been planned, and experimental results will be obtained in the near future.

Presentations/Publications/Patents

1. Song, G.-L.; Unocic, K. A. The Anodic Surface Film and Hydrogen Evolution on Mg (submitted to Corrosion Science)

2. Song, G.-L. Corrosion and Protection of Mg Alloys, invited seminar, University of Brno, Czech Republic, April 12, 2014.

References

1. *Corrosion of Magnesium Alloys*; Song, G.-L., Ed.; Woodhead Publishing, Cambridge, UK, 2011.

2. *Corrosion Prevention of Magnesium Alloys*; Song, G.-L., Ed.; Woodhead Publishing, Cambridge, UK, 2013.

3. Song, G.; Atrens, A. Corrosion Mechanisms of Magnesium Alloys. *Advanced Engineering Materials*, **1999**, 1(1), 11–33.

4. Gu, X.; Zheng, Y.; Cheng, Y.; Zhong, S.; Xi, T. In Vitro Corrosion and Biocompatibility of Binary Magnesium Alloys. *Biomaterials*, **2009**, 30, 484–498.

5. Song, G-L. Corrosion Behavior and Mitigation Strategy of Magnesium Alloys. In *Surface Engineering of Light Alloys—Al, Mg and Ti*; Dong, H., Ed.; CRC Press, Woodhead Publishing, 2010.

6. Yao, H.; Li, Y.; Wee, A. Corrosion Behavior of Melt-spun $Mg_{65}Ni_{20}Nd_{15}$ and $Mg_{65}Cu_{25}Y_{10}$ Metallic Glasses. *Electrochimica Acta*, **2003**, 48, 2641–2650.

7. Song, G.-L.; Xu, Z. Effect of Microstructure Evolution on Corrosion of Different Crystal Surfaces of AZ31 Mg Alloy in a Chloride Containing Solution. *Corrosion Science*, **2012**, 54, 97–105.

8. Unocic, K. A.; Elsentriecy, H. H.; Brady, M. P.; Meyer, H. M.; Song, G. L.; Fayek, M.; Meisner, R. A.; Davis, B. *J. Electrochem. Soc.*, **2014**, 161(6), C302–C311.

III.23 High-Throughput Study of Diffusion and Phase Transformation Kinetics of Magnesium-Based Systems for Automotive Cast Magnesium Alloys – The Ohio State University (OSU)

Alan A. Luo, Principle Investigator
Ohio State University
137 Fontana Labs
116 W. 19th Avenue
Columbus, OH 43210
Phone: (614) 292-5629
E-mail: luo.445@osu.edu

Ji-Cheng Zhao, Principle Investigator
Ohio State University
286 Watts Hall
116 W. 19th Avenue
Columbus, OH 43210
Phone: (614) 292-9462
E-mail: zhao.199@osu.edu

Adrienne Riggi, Project Officer
National Energy Technology Laboratory
3610 Collins Ferry Road
P.O. Box 880
Morgantown, WV 26507-0880
Phone: 304-285-5223
E-mail: Adrienne.riggi@netl.doe.gov

William Joost, Technology Area Development Manager
U.S. Department of Energy
1000 Independence Avenue, S.W.
Washington, DC 20585
Phone: (202) 287-6020; Fax: (202) 856-2476
E-mail: william.joost@ee.doe.gov

Contractor: The Ohio State University
Contract No.: DE-EE0006450

Abstract/Executive Summary

The objective of this study is to establish a scientific foundation on kinetic modeling of diffusion, phase precipitation, and casting/solidification in order to accelerate the design and optimization of cast magnesium (Mg) alloys for weight reduction of U.S. automotive fleet. The team will: 1) study the diffusion kinetics of six Mg-containing binary systems using high-throughput diffusion multiples to establish reliable diffusivity and mobility databases for the magnesium-aluminum-zinc-tin-calcium-strontium-manganese (Mg-Al-Zn-Sn-Ca-Sr-Mn) system; 2) study the precipitation kinetics (nucleation, growth and coarsening) using both innovative dual-anneal diffusion multiples (DADMs) and cast model alloys to provide large amounts of kinetic data (including interfacial energy) and microstructure atlases to enable implementation of the Kampmann-Wagner numerical (KWN) model to simulate phase transformation kinetics of non-spherical/non-cuboidal precipitates in Mg alloys; 3) implement a micromodel to take into account back diffusion in the solid phase in order to predict microstructure and microsegregation in multicomponent Mg alloys during dendritic solidification especially under high pressure die-casting (HPDC) conditions; and, 4) widely disseminate the data, knowledge and information using the Materials Genome Initiative (MGI) infrastructure as well as publications and digital data sharing to enable researchers to identify new pathways/routes to better cast Mg alloys.

Accomplishments

- Made 11 solid-liquid diffusion multiple samples for high temperature investigation and 10 solid diffusion multiple samples for low temperature investigation. Sixteen of them have been analyzed using Scanning Electron Microscopy (SEM). Two Mg-Zn and Mg-Mn diffusion multiple samples have been examined using Electron Probe Micro-Analysis (EPMA) to obtain the diffusion profiles. The forward simulation method was used to generate the interdiffusion coefficients from the diffusion profiles. (FY 2014)
- Collected diffusion data on hexagonal close-packed (hcp) Mg phase of Mg alloy system from literature and established a preliminary atomic mobility database for Mg alloys. (FY 2014)
- Developed a precipitation model for Mg-Al-Zn, Mg-Sn and Mg-Al-Sn alloys to simulate the precipitation kinetics during aging treatment. Prepared Mg-Al-Sn alloy samples of various compositions and carried out heat treatment for experimental validation of the precipitation model. (FY 2014)

Future Directions

- Further characterize the diffusion multiple samples using SEM and EPMA and make more diffusion multiple samples to generate more mobility data. Revise the forward simulation code and improve the preliminary atomic mobility database using our experimental data.
- Carry out aging experiments on the Mg-Al-Sn samples and investigate the microstructure evolution of precipitation using transmission electron microscopy

(TEM). Verify and calibrate the simulation on Mg-Al-Sn alloys.

- Develop a code to simulate the solidification of Mg alloys including back diffusion.

Technology Assessment

- Target: Establish the diffusivity database of Mg-Al-Zn-Mn-Sn-Ca-Sr system by diffusion experiments
- Gap: Difficult to make diffusion samples due to the high reactivity of Ca and Sr and oxidation tendency of Mg and Mn. Special measures such as vacuum induction melting are promising.
- Target: Quantitatively simulate the microstructure evolution of precipitation in Mg-Al-Sn alloys (as an example).
- Gap: No quantitative microstructure evolution data on the precipitation of Mg-Al-Sn alloys during aging process in literature. Experimental work is needed to generate these data to verify and calibrate the model.
- Target: Develop a code to simulate the solidification of Mg alloys including back diffusion.
- Gap: Current commercial codes such as Pandat™ do not include back diffusion in kinetic simulation.

✧   ✧   ✧   ✧   ✧

Introduction

Lightweighting is an effective way to increase energy efficiency and reduce green-house gas emissions. Magnesium, the lightest structural metal, will thus see increased use in a wide range of structural and functional applications for energy generation, energy storage, propulsion, and transportation. The lack of diffusivity data for Mg alloys is hindering the computational design of high performance Mg alloys using an Integrated Computational Materials Engineering (ICME) approach. Simulation of precipitation hardening in Mg alloys is needed to assist the development of high-strength Mg alloys. Moreover, the Scheil solidification model does not take the back diffusion into account and may not be able to accurately predict the microstructure under casting conditions. A code which takes the back diffusion into account should be developed. In this research period, the major work is on diffusion and precipitation. Several diffusion multiples have been made and

characterized. The forward simulation has been used to extract the interdiffusion coefficient from the diffusion profiles measured by EPMA. Using the CALculation of PHAse Diagrams (CALPHAD) approach, a preliminary atomic mobility database of Mg alloys has been established based on literature data and estimation from empirical equations. The microstructure evolution of precipitation of Mg-Al-Zn, Mg-Sn and Mg-Al-Sn alloys during aging process have been simulated by coupling Mg thermodynamic database and the preliminary atomic mobility database. Several Mg-Al-Sn alloys for verifying the simulation have been prepared and solution-treated before aging and characterization using TEM).

Approach

Two types of diffusion multiples are designed to measure the diffusion profiles. One is the liquid-solid diffusion multiple aimed at high temperature investigation, as shown in Figure III-119a. The pure iron (Fe) is used to isolate the steel screw from Mg in order to prevent carbon contamination. The multiples are encapsulated in quartz tubes filled with argon (Ar) before placing them in furnaces for heat treatment. The other multiple shown in Figure III-120 is the solid diffusion multiple for measurements at low temperatures. Figure III-120a and Figure III-121 are the original design and preparation procedure, respectively. After the raw materials are assembled, the multiple is sealed by welding, hot-isostatically-pressed (HIP) and encapsulated in a quartz tube before heat treatment. In the updated design shown in Figure III-120b, an Al cartridge was used instead of Mg, due to the better weldability of pure Al than pure Mg. After heat treatment, the samples are polished and examined using optical microscopy, SEM and EPMA. The forward simulation method [1] is used to extract the interdiffusion coefficients from the diffusion profiles.

A preliminary atomic mobility database of Mg-Al-Zn-Mn-Sn-Ca-Sr system has been established based on assessment of diffusion data in literature using the CALPHAD approach. [2] The self-diffusion, impurity diffusion and interdiffusion coefficients are used as input to generate the atomic mobility for each element. Empirical methods for estimating the self-diffusion and impurity diffusion coefficients are used to fill the gaps in diffusion data. In the next research period, this database will be improved using our own diffusion data obtained from the diffusion multiples.
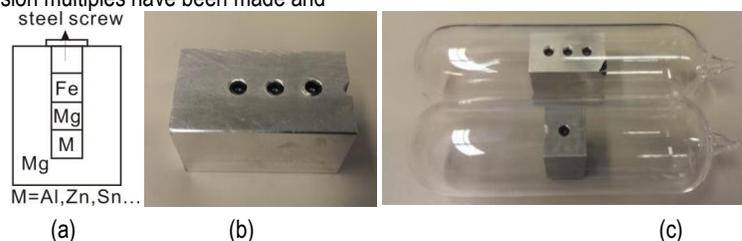
Figure III-119: Design and preparation of liquid-solid diffusion multiple: (a) design; (b) assembly; and (c) encapsulated in quartz tubes.

- Mg$_2$Sn: 3X5X6;
- Mg 1: 4X6X10;
- Mg 2: 5X7X10;
- Mg 3: 2X5X6;
- Mg cap: 2X5X7.
- Diffusion system:
  **Mg-Sn; Mg-Al;
  Mg-Mn; Mg-Ca
  Al-Mn**

(a)   (b)
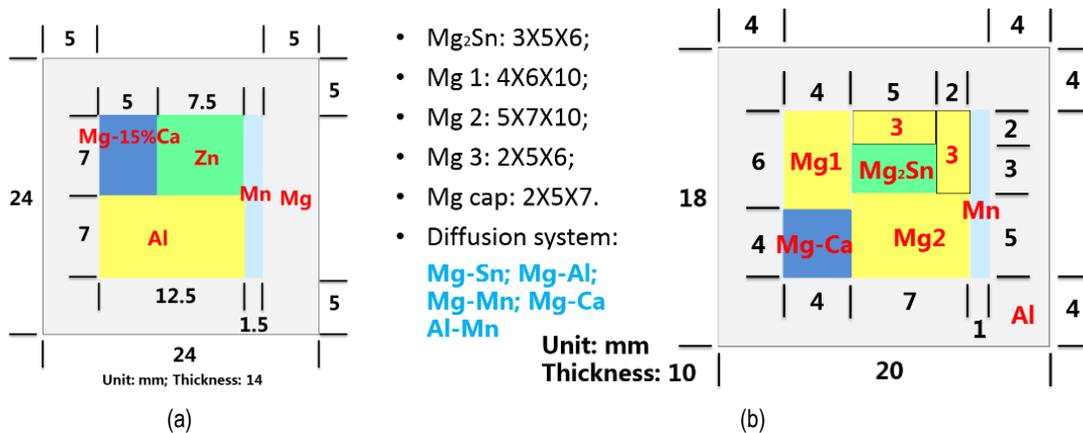
Figure III-120: Design of solid diffusion multiple: (a) the original design using a Mg cartridge; and (b) the updated design using an Al cartridge.

(a)   (b)   (c)   (d)
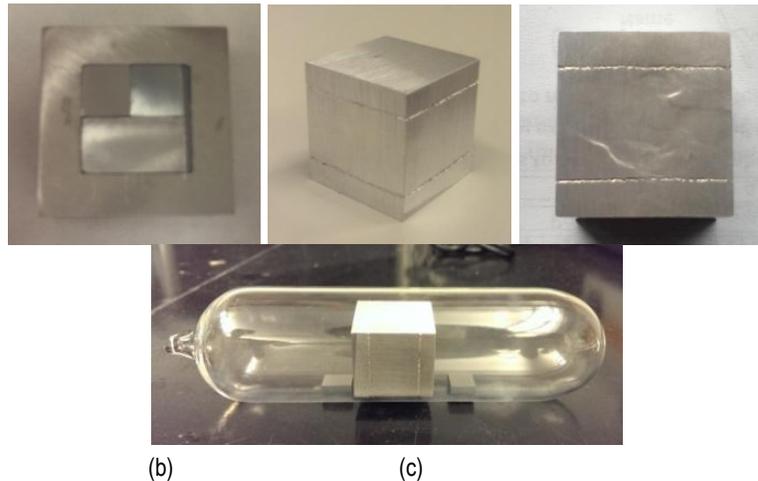
Figure III-121: The preparation procedure of solid diffusion multiples: (a) assembly; (b) welded; (c) hot- isostatically-pressed; and (d) encapsulated in a quartz tube.

The classical precipitation model KWN [3] implemented in the PanPrecipitation module of Pandat™ software is used to simulate the precipitation of Mg alloys during aging process. This model features the capability of modeling nucleation, growth and coarsening simultaneously. The PanMagnesium thermodynamic database and the preliminary atomic mobility database are used to generate the driving force, phase equilibria and diffusivity for quantitative simulation. During this research period, the alloys simulated are Mg-Al-Zn, Mg-Sn and Mg-Al-Sn alloys. The simulation on Mg-9Al-1Zn (by weight percent (wt.%)) alloy is a modification of previous simulation[4] by using new experimental data in the literature. The shape of magnesium stannide (Mg$_2$Sn) and Mg$_{17}$Al$_{12}$ precipitates are not spherical according to experimental observations. By assuming shape-preserved growth of the precipitates, the shape of the precipitates could be treated as sphere for simplification. [4] In order to verify and refine the simulation on Mg-Al-Sn alloys, experiments need to be carried out to obtain the microstructure evolution data during aging

process. Mg-Al-Sn alloys with different compositions have been prepared and solution-treated to dissolve Mg$_{17}$Al$_{12}$ and Mg$_2$Sn. After aging, the samples will be characterized using TEM to investigate the precipitation kinetics.

Results and Discussion

Diffusion multiples for high temperature measurement

Table III-13 lists the diffusion multiples made during this research period. The elements Al, Mn, Sn and Zn are used in the two types of diffusion multiples. Ca is considered in the solid diffusion multiple and Sr has not been considered so far. Ca and Sr are very reactive. Special measures are needed and the experiments on these two elements will be carried out in the next research period. Figure III-122 and Figue III-124 present the analysis of Mg-Mn diffusion multiple heated at 600

degrees Centigrade (°C) for 48 hours. The temperature of reaction Liquid + (Mn) → (Mg) is 650.6°C, so no liquid will form. No intermetallics layer is observed and the concentration profile measured by EPMA in Figure III-125 suggests that the solubilities of Mg in (Mn) and Mn in (Mg) are very low, which is consistent to the Mg-Mn phase diagram. By using the forward

simulation method, the interdiffusion coefficients are extracted, as shown in Figure III-125. To our knowledge, this is the first time that the interdiffusion coefficients of the hcp(Mg) phase of Mg-Mn system are reported.

Table III-13: List of the diffusion samples made during this research period.

	System	No.	Heat Treatment	SEM	EPMA
liquid-solid diffusion multiples for high temperature measurement	Mg-Al	3	450°C(2), 550°C, 8hours	√	
	Mg-Mn	1	600°C, 48hours	√	600°C 48hours
	Mg-Sn	4	450°C(2), 500°C, 550°C, 8hours	√	
	Mg-Zn	3	450°C(2), 500°C, 8hours	√	450°C 8hours
solid diffusion multiples for low temperature measurement	See Figure III-120a	4	315°C,790 hours 275°C, 1760 hours	√	
	See Figure III-120b	6			
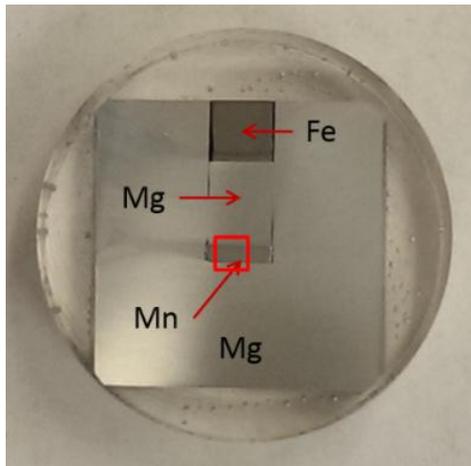
Figure III-122: The polished section of Mg-Mn diffusion multiple heated at 600°C for 48 hours.
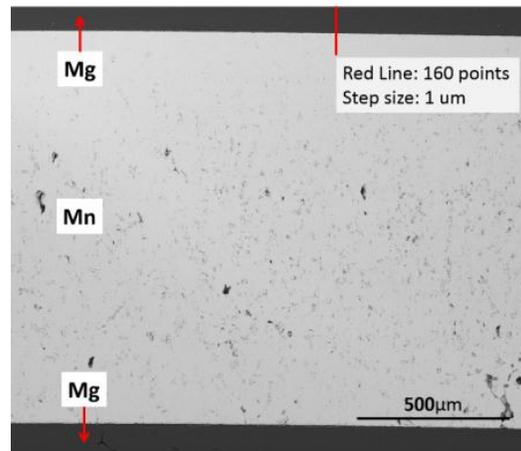
Figure III-123: Back-scattered Electron (BSE) image of the region labeled by red square in Figure III-122. The red line is for EPMA scanning.
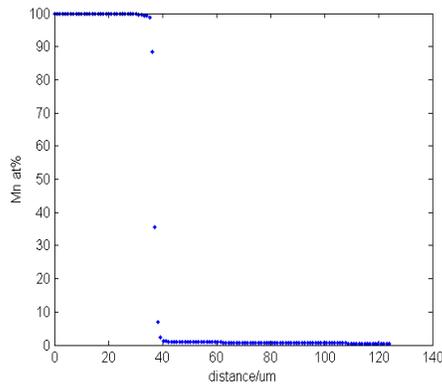
Figure III-124: Concentration profile measured by EPMA.
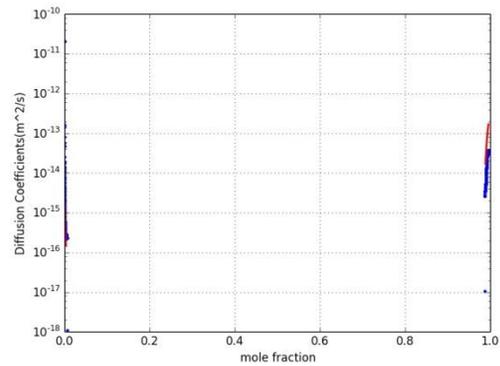
Figure III-125: Comparison of the interdiffusion coefficients obtained from the forward simulation [1] (red lines) with those obtained by the Sauer-Freise method [5] (blue lines).

Figure III-126 to Figure III-130 present the analysis of Mg-Zn diffusion multiple heated at 450°C for 8 hours. The heat treatment temperature is higher than the melting point of Zn, so Zn melts during the heat treatment and diffuses into the Mg area around it. A big hole is observed after quenching, marked as "black epoxy" in Figure III-126. Figure III-127 and Figure III-128 indicate MgZn$_2$ phase forms during the heat treatment, which is in agreement with the Mg-Zn phase diagram. In order to analyze the Mg-Zn concentration profile by the forward simulation method, constant concentration is assumed for the liquid region. Figure III-130 shows the interdiffusion coefficients extracted using the forward simulation method and Sauer-Freise method, respectively. In order to obtain a more reliable result, modification of the original code on forward simulation will be carried out in the next research period.

The Mg-Al diffusion at 450°C for 8 hours shown in Figure III-131a is similar to the Mg-Zn sample discussed

above. A hole formed and the boundary is not very "straight". According to the Mg-Al phase diagram, there should be intermetallics of Mg$_{17}$Al$_{12}$ and Al$_3$Mg$_2$; however, they are not observed in Figure III-131b. The reason may be that the heat treatment time is not long enough. The diffusion images between Mg and Sn at 550°C for eight hours are presented in Figure III-132, where the formation of Mg$_2$Sn phase is evident. Compared with Mg-Al or Zn diffusion multiples, the diffusion region in Mg-Sn sample is smaller, which may be due to slower diffusion of Sn. In the next research period, these diffusion multiples will be further examined by SEM and EPMA. According to the results from Mg-Zn system above, this kind of design for high temperature measurement is feasible. Several multiples will be made and heat treated at different times and temperatures to generate more diffusion profiles. The forward simulation code will also be improved to extract more accurate diffusivity data.
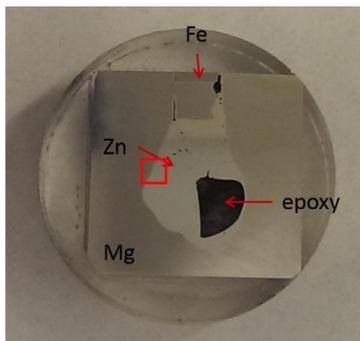
Figure III-126: The polished section of Mg-Zn diffusion multiple heated at 450°C for 8 hours.
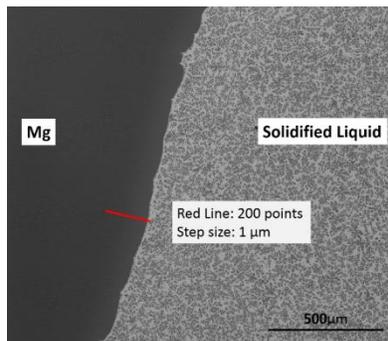
Figure III-127: BSE image of the region labeled by red square in Figure III-126. The red line is for EPMA scanning.
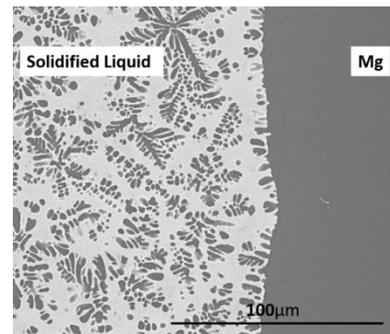
Figure III-128: Magnified BSE image around the interface.
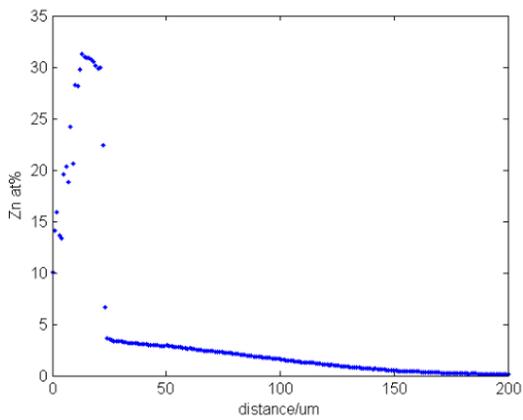
Figure III-129: Concentration profile measured using EPMA.
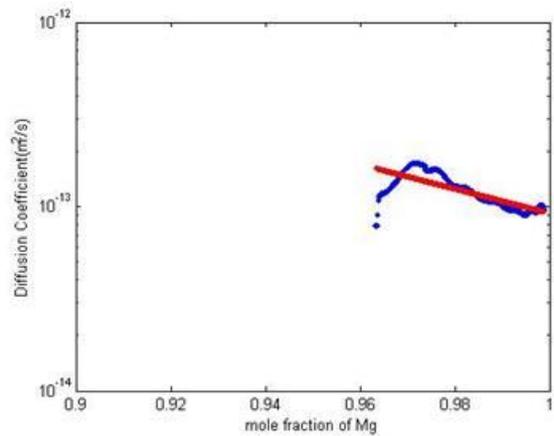
Figure III-130: Comparison of the interdiffusion coefficients obtained from the forward simulation [1] (red lines) with those obtained by the Sauer-Freise method [5] (blue lines).

(a)   (b)
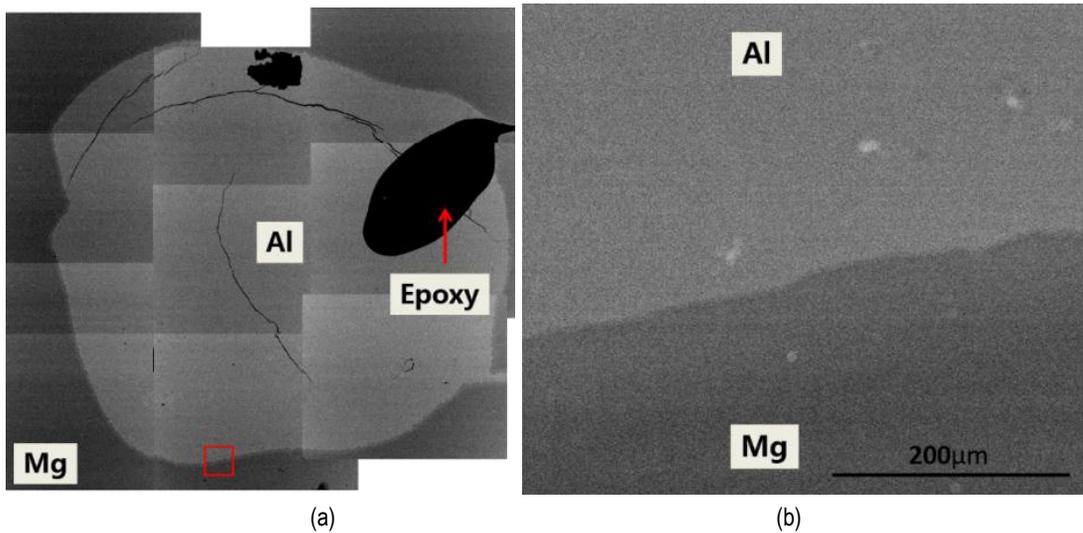
Figure III-131: BSE image of the Mg-Al diffusion multiple heat treated at 450°C for 8 hours: (a) the whole region; and (b) local region labeled by red square in Figure III-131a. The image of Figure III-131a is a combination of several images since the SEM could not take a picture of the whole region at one time.

(a)   (b)   (c)
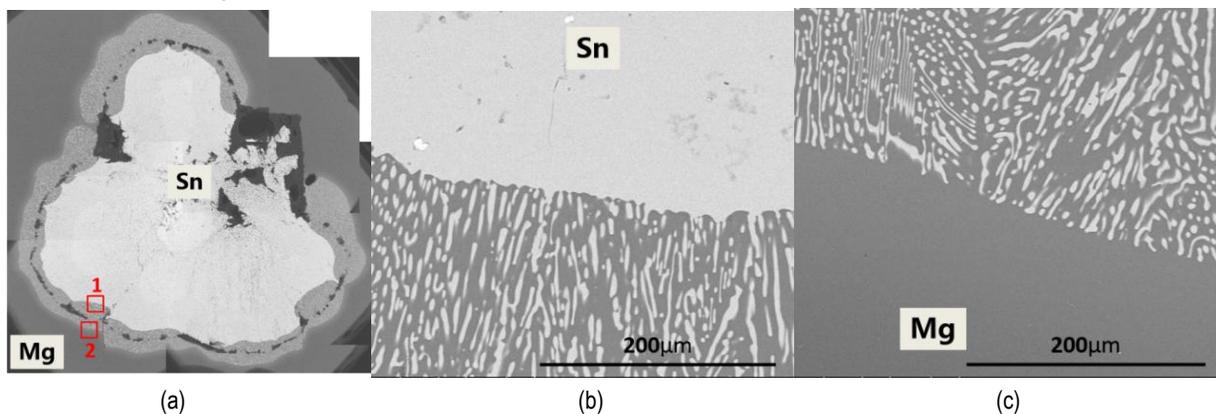
Figure III-132: BSE image of the Mg-Sn diffusion multiple heat treated at 550°C for 8 hours. (a) the whole region; (b) local region labeled by red square 1; and (c) local region labeled by red square 2.

Diffusion multiples for low temperature measurement

Figure III-133 shows the sections of the diffusion multiples heated at 315°C for 790 hours and 275°C for 1760 hours, respectively. They contain Mg-Zn, Mg-Al, Mg-Mn, Mg-Ca, Al-Zn, Mn-Zn and Al-Mn diffusion systems. A gap is observed along Mg/MgCa boundary in Figure III-133a, which may be caused by the differences of thermal expansion coefficients or else the pressure of HIP was not high enough to make the MgCa piece contact closely with Mg. In the next research period, higher pressure will be used. Figure III-134 shows the BSE images of the diffusion of three systems. There are intermetallics layers formed during the diffusion between Mn and Zn. Substantial information will be obtained from the diffusion multiple with further measurement. The diffusion multiple heated at 275°C for 1760 hours shows very similar results under optical microscope and will be examined by SEM and EPMA. Other 6 diffusion multiples listed in Table III-13 using Al as the cartridge instead of Mg will be heat treated at 370°C and 420°C for three different times after welding and pressing.

(a) (b)
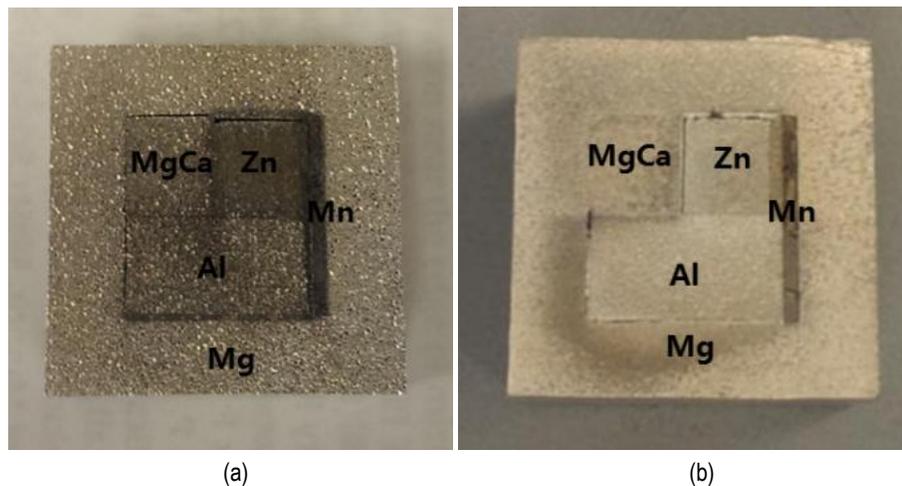
Figure III-133: Mg diffusion multiples for low temperature measurement. (a) 315°C for 790 hours; and (b) 275°C for 1760 hours.
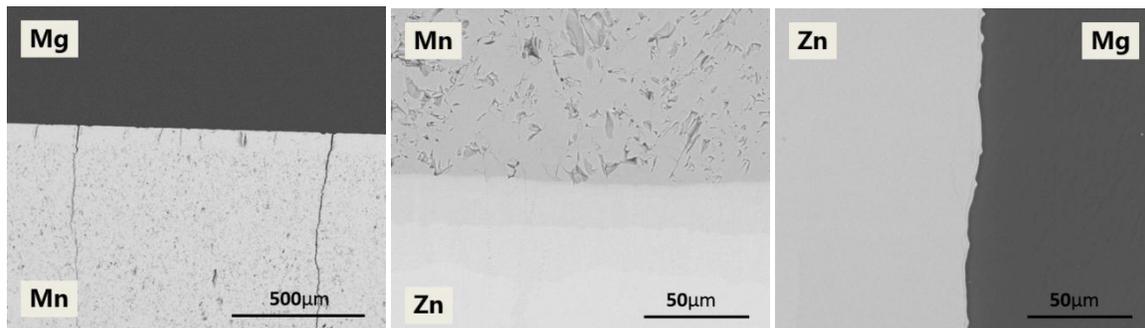
Figure III-134: BSE images of three diffusion systems in the diffusion multiple heated at 315°C for 790 hours.

Establishment of a preliminary atomic mobility database

The literature on the diffusion of hcp(Mg) phase of Mg-Al-Zn-Mn-Sn-Ca-Sr system was searched and collected. Using the CALPHAD approach and the literature data as input, a preliminary atomic database for Mg alloys is established. Most of the literature data are on the diffusion of Mg-Al binary system below 420°C. Impurity diffusion coefficients of Zn and Sn in (Mg) are reported. For Mn, Ca and Sr, there are no experimental data so far. Since Al, Mn, Ca, Sn and Sr do not have stable hcp structure, the related atomic parameters are estimated using empirical methods. Due to the scarcity of literature data, the preliminary database is preliminary and will be improved by our diffusion experiments in the next research period. Figure III-135 shows the calculated interdiffusion coefficients in the Mg-rich region of Mg-Al system along with the experimental data. Indications are that more diffusion experiments are needed to clarify the discrepancy on Mg-Al systems.

Precipitation simulation and preparation of precipitation experiment

By coupling to the thermodynamic database PanMagnesium and the preliminary atomic mobility database described above, the precipitation of Mg_2Sn at 200°C in two supersaturated Mg-Sn alloys is simulated. Figure III-136 shows the calculated number densities for the two Mg-Sn alloys are in agreement with the experimental data. Figure III-137 shows the predicted radius for Mg-1.9 atomic percent (at.%) Sn alloy at 240 hours is 128 nanometers (nm), which is consistent with the experimental value of 112 nm. However, for the Mg-1.3 at.% Sn alloy, the simulated radius at 1000 hours is 160 nm, which is lower than the experimental value of 197 nm, but still within the

experimental error range. Figure III-138 indicates during precipitation of Mg_2Sn, the precipitation contribution to yield strength increases while the solution contribution decreases. The predicted hardness evolution is consistent with the experimental data in Figure III-139. Based on a previous work [4], the simulation of precipitation of $Mg_{17}Al_{12}$ in Mg-9Al-1Zn alloy at 200°C is modified using the new experimental data from Zeng [10]. The simulated number density, average radius and volume fraction of $Mg_{17}Al_{12}$ with the experimental data are shown in Figure III-140. By combining the parameters for Mg_2Sn and $Mg_{17}Al_{12}$, the simulation of concurrent precipitation of $Mg_{17}Al_{12}$ and Mg_2Sn in Mg-7Al-2Sn (wt.%) alloys is achieved. Figure III-141 is the predicted microstructure evolution of Mg_2Sn and $Mg_{17}Al_{12}$.
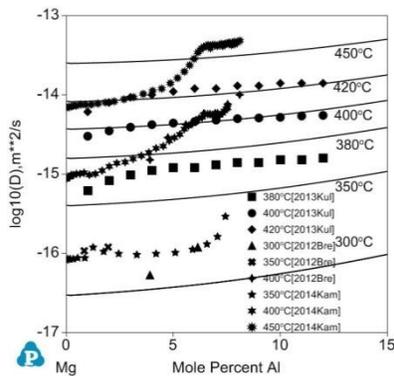
Figure III-135: Calculated interdiffusion coefficients in the Mg rich region of Mg-Al system along with the experimental data [6-8].
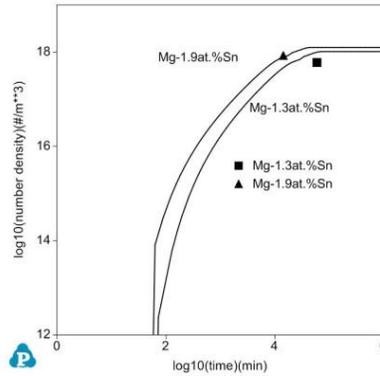
Figure III-136: Predicted number density of Mg_2Sn precipitate in Mg-1.3 at.% Sn and Mg-1.9 at.% alloys along with the experimental data [9]
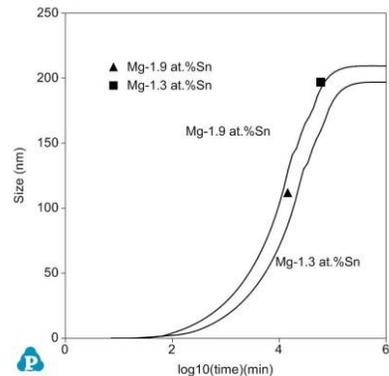
Figure III-137: Predicted radius of Mg_2Sn precipitate in Mg-1.3 at.% Sn and Mg-1.9 at.% alloys along with the experimental data [9].
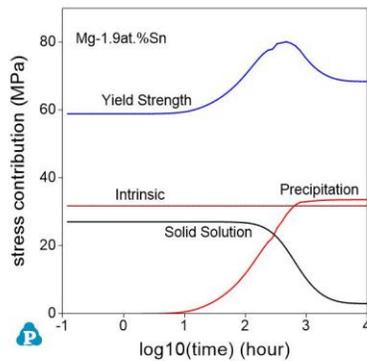
Figure III-138: Predicted yield strength including each contribution for Mg-1.9 at.% Sn. The prediction on Mg 1.9 at.% Sn is similar and not shown here to save space.

(a)   (b)
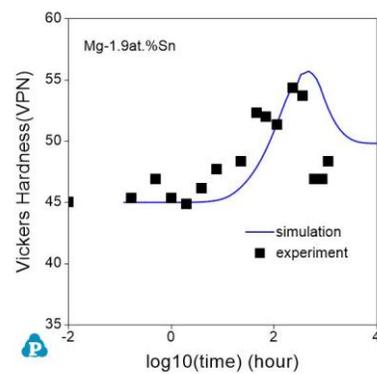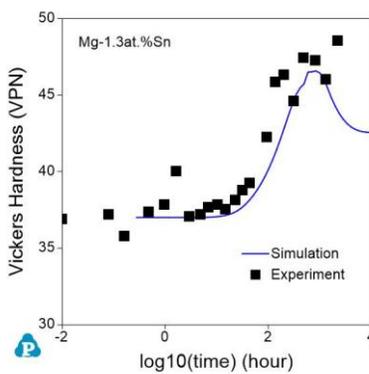
Figure III-139: Predicted hardness evolution with the experimental data [9]: (a) Mg-1.3 at.%Sn; and (b) Mg-1.9at.%Sn.

(a)   (b)   (c)
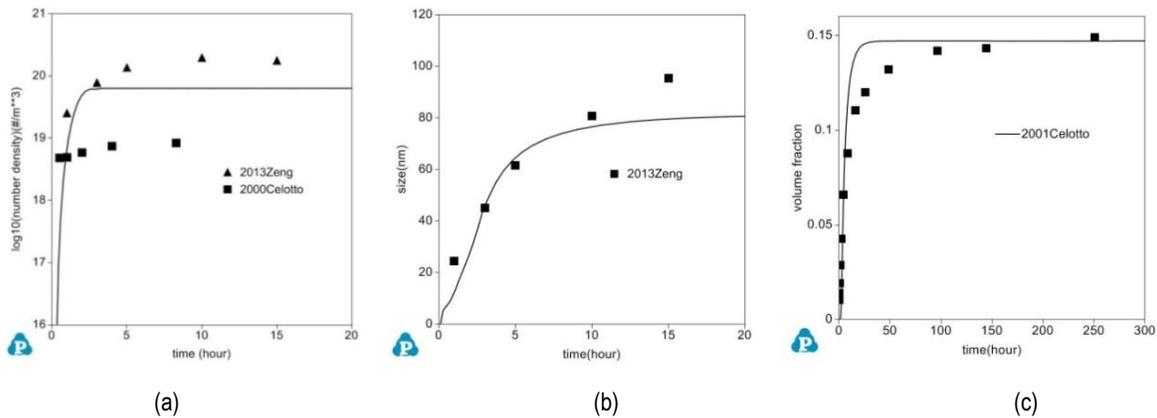
Figure III-140: Predicted (a) number density; (b) size; and (c) volume fraction of Mg17Al12 precipitate in Mg-9Al-1Zn alloy at 200°C with the experimental data [10-12].

(a)   (b)   (c)
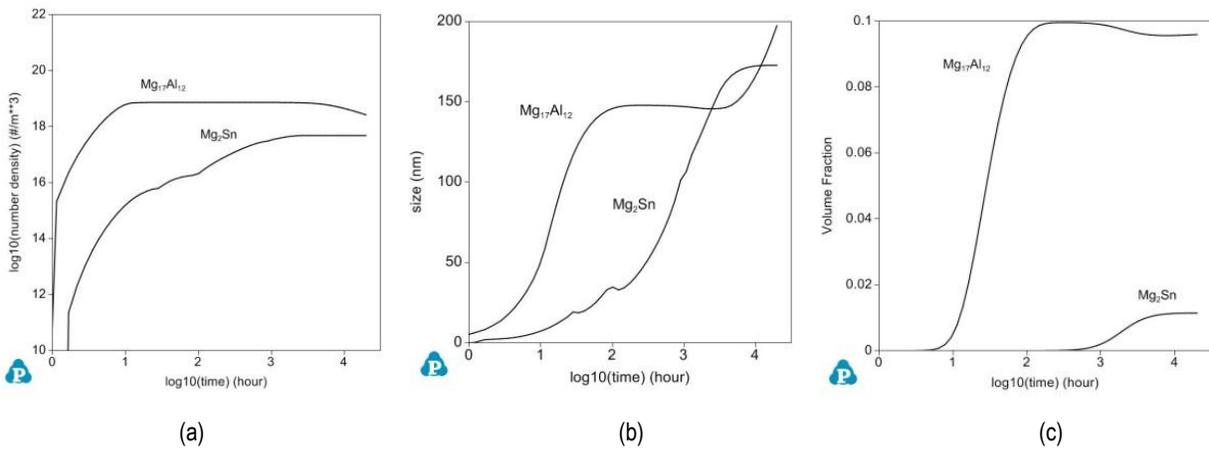
Figure III-141: Predicted (a) number density; (b) size; and (c) volume fraction of Mg$_{17}$Al$_{12}$ and Mg$_2$Sn precipitates in Mg-7Al-2Sn alloy at 200°C.

(a)   (b)
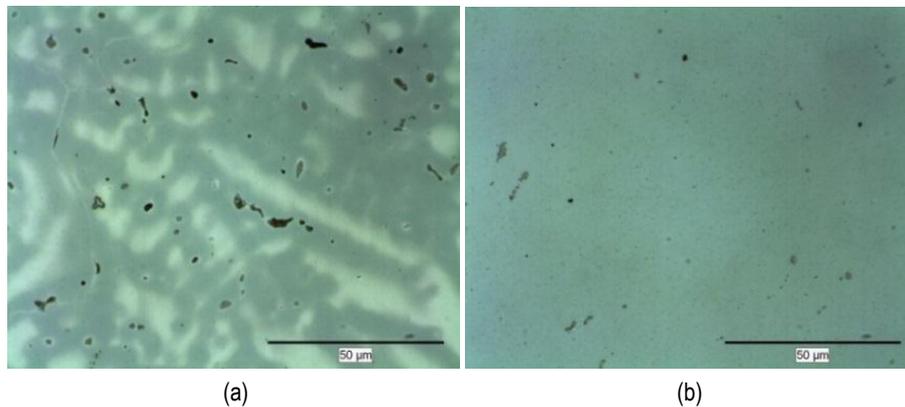
Figure III-142: Optical micrograph of Mg-2Al-8Sn alloy: (a) as cast; and (b) after solution treatment at 510°C for 70 hours. (Note the round Mg$_2$Sn particles).

In order to verify and improve the simulation, experiments are needed to measure the microstructure evolution during the aging process. Mg-Al-Sn alloys with different compositions were prepared. Based on thermodynamic calculations and literature, Mg-2Al-8Sn, Mg-3Al-6Sn and Mg-7Al-2Sn alloys are solution treated at 510°C, 490°C and 420°C for 70 hours to

dissolve Mg_2Sn and/or $Mg_{17}Al_{12}$ phases. Compared with $Mg_{17}Al_{12}$, the Mg_2Sn phase is very difficult to be dissolved. Even after 70 hours heat treatment at 510°C, a few Mg_2Sn particles with round shape could still be observed in (Mg) matrix, as shown in Figure III-142. The reason may be that the diffusion of Sn is slower than that of Al, and Mg_2Sn is more thermally stable than $Mg_{17}Al_{12}$. Solution treatment with longer time and higher temperatures will be carried out to achieve more dissolution of Mg_2Sn phase.

Technology Transfer Path

The experimental diffusion data obtained from this project will improve the Mg alloy diffusivity database, which is presently insufficient for Mg alloy and process development. These data and the precipitation model can provide quantitative and reliable information in the design of high performance Mg alloys and processing techniques using the ICME approach.

These databases and models will be made available to the automotive industry and the general public. Furthermore, OSU will work closely with the automotive industry to apply these databases and models to optimize several new Mg alloys such as Mg-Al-Ca, Mg-Al-Sr and Mg-Al-Sn alloys for lightweight applications.

Conclusions

1. Several solid-liquid diffusion multiples and solid diffusion multiples were made and examined. The interdiffusion coefficients of Mg-Mn and Mg-Zn at 600°C and 450°C were extracted from the diffusion profiles using a forward simulation method. The results from the Mg-Zn solid-liquid diffusion multiple demonstrated the practicability of the diffusion multiple design. The forward simulation code will be further refined. More diffusion multiples and characterization work will be carried out in the next research period to generate more data and improve the preliminary Mg atomic mobility database.

2. A preliminary atomic mobility database for Mg alloys was established based on literature data and estimation from empirical equations. This database will be improved using the diffusion experiments in the next research period.

3. The precipitation simulations on Mg-Al-Zn, Mg-Sn and Mg-Al-Sn alloys were carried out. The predicted microstructure evolution for Mg-Al-Zn and Mg-Sn alloys were in agreement with the experimental data. The predicted microstructure of Mg-7Al-2Sn alloys showed concurrent precipitation of $Mg_{17}Al_{12}$ and Mg_2Sn phases. Several Mg-Al-Sn alloys were prepared and solution treated to dissolve $Mg_{17}Al_{12}$ and Mg_2Sn before aging process and TEM characterization.

Presentations/Publications/Patents

Zhang, C.; Cao, W.; Chen, S.L.; Zhu, J; Zhang, F.; Luo, A.A.; Schmid-Fetzer, R.(2014) "Precipitation Simulation of AZ91 Alloy", *JOM*, **2014**, *66*, (3), pp. 389-396.

References

1. Zhang, Q.; Zhao, J.C. Extracting interdiffusion coefficients from binary diffusion couples using traditional methods and a forward-simulation method. *Intermetallics*. **2013**, *34*, pp 132-141.

2. Saunders, N.; Miodownik, A.P. CALPHAD *(Calculation of Phase Diagrams): A Comprehensive Guide*, Elsevier, 1998

3. Kampmann, R.; Wagner, R. Kinetics of precipitation in metastable binary alloys-theory and application to Cu-1.9 at % Ti and Ni-14 at % Al. In *Decomposition of Alloys: the early stages, Proceedings of the 2nd Acta-ScriptaMetallurgica Conference*; Haasen P., Gerold V., Wagner R., Eds.; Pergamon Press, 1983, pp 91-103.

4. Zhang, C.; Cao, W.; Chen, S.L.; Zhu, J.; Zhang, F.; Luo, A.A.; Schmid-Fetzer, R. Precipitation Simulation of AZ91 Alloy. *JOM* **2014**,*66(3)*, pp 389-396.

5. Sauer F.; Freise V.Z. *Elektrochem*.**1962**,*66*, pp 353.

6. Kammerer, C.; Kulkarni, N.; Warmack, R.; Perry, K.; Belova, I.; Murch G.; Sohn Y. Impurity diffusion coefficients of Al and Zn in Mg determined from solid-to-solid diffusion couples. In *Magnesium Technology 2014*; Alderman M., Manuel, M.V., Hort N., Neelameggham N.R., Eds.;TMS,2014, pp 505-509

7. Brennan, S.; Bermudez, K.; Kulkarni, N. S.; Sohn, Y. Interdiffusion in the Mg-Al System and Intrinsic Diffusion in β-Mg_2Al_3. *Metall. Mater. Trans. A*.**2012**,*43(11)*, pp 4043-4052.

8. Kulkarni, K.N.; Luo, A.A. Interdiffusion and Phase Growth Kinetics in Magnesium-Aluminum Binary System. *J. Phase Equilib. Diff.***2013**, *34(2)*, pp 104-115.

9. Mendis, C. L.; Bettles, C. J.; Gibson, M. A.; Gorsse, S.; Hutchinson, C. R. Refinement of precipitate distributions in an age-hardenable Mg–Sn alloy through microalloying. *Phil. Mag. Let.***2006**, *86(7)*, pp 443-456.

10. Zeng R. Precipitation hardening in AZ91 magnesium alloy, PhD thesis, 2013, University of Birmingham, UK.

11. Celotto, S. TEM study of continuous precipitation in Mg–9 wt% Al–1 wt% Zn alloy. *Acta Mater.***2000**, *48(8)*, pp 1775-1787.

12. Celotto, S.; Bastow, T. J. Study of precipitation in aged binary Mg–Al and ternary Mg–Al–Zn alloys using 27Al NMR spectroscopy. *Acta Mater* **2001**, *49(1)*, pp 41-51.

III.24 In situ Investigation of Microstructural Evolution During Solidification and Heat-Treatment in a Die-Cast Magnesium Alloy – Pacific Northwest National Laboratory

Aashish Rohatgi, Principal Investigator
Pacific Northwest National Laboratory
Phone: (509) 372-6047
E-mail: aashish.rohatgi@pnnl.gov

Nigel D. Browning, Principal Investigator
Pacific Northwest National Laboratory
Phone: (509) 375-7569
E-mail: nigel.browning@pnnl.gov

William Joost, Technology Area Development Manager
U. S. Department of Energy
1000 Independence Avenue. S.S.
Washington, DC 20585
Phone: (202) 287-6020; Fax: (202) 856-2476
E-mail: william.joost@ee.doe.gov

Contractor: Pacific Northwest National Laboratory
Contract No.: DE-AC05-00OR22725 & DE-AC06-76RL01830

Abstract/Executive Summary

The goal of this project is to understand the microstructural evolution in AZ91 (9 weight percent (wt.%) aluminum (Al) and 1 wt.% zinc (Zn)) magnesium (Mg) alloy under non-equilibrium solidification conditions of die casting and during subsequent heat-treatment. The two primary objectives of this work are: 1) understand the solidification kinetics of AZ91 melt at high cooling rates and 2) understand the kinetics of phase evolution of β-Mg$_{17}$Al$_{12}$ and α-Mg during heat-treatment. The purpose of the first objective is to understand the nucleation and growth kinetics of the dendrites, Mg$_{17}$Al$_{12}$ and eutectic under non-equilibrium high-rate cooling (~100–1000 degrees Centigrade per second (°C/s)), as experienced by the molten AZ91 Mg alloy during high-pressure die casting (HPDC). The purpose of the second objective is to understand the kinetics of phase evolution when the casting, comprising a non-equilibrium microstructure, is heat-treated between 150-300°C.

To investigate solidification under high cooling rates, in situ experiments using ultrafast techniques in a dynamic transmission electron microscope (DTEM) will be employed. Thin film Mg-Al alloy samples were prepared by sputtering for in situ solidification experiments. The as-sputtered films showed an average grain size of 15-20 nanometers (nm) and

a composition close to the Al content in commercial bulk AZ91. Ex situ laser melting was conducted to guide future in situ solidification experiments, and laser energy of 0.2-0.35 millijoules (mJ) was found suitable to locally melt the sputtered Mg-Al film. Heat-transfer in the ex situ melted Mg alloy film was modeled to estimate the cooling rate during solidification. Initial results suggest a cooling rate greater than 1000°C/s. Aging heat-treatment experiments were conducted on sputtered films and on lamellae that were milled out of bulk HPDC AZ91 using the focused ion beam (FIB) technique. The latter specimens showed formation of magnesium-gallium (Mg-Ga) intermetallic precipitates due to contamination by Ga ions that are inevitable in the FIB technique. Thus, the influence of Mg-Ga precipitates needs to be considered when analyzing the evolution of Mg-Al microstructure in FIB-milled specimens. Finally, adjustments were made to the modified embedded atom method (MEAM) parameters of an existing potential of the Mg-Al system. The resulting data shows a significant improvement in the calculated values of Mg$_{17}$Al$_{12}$, especially for heat of formation and bulk modulus.

Accomplishments

- Determined suitable substrate and manufacturing conditions for sputter coating Mg-Al binary and Mg-Al-Zn ternary thin film samples. Calibrated the composition and thickness of the sputtered films and evaluated their microstructure. (FY 2014)
- Determined the laser energy required to locally melt sputtered Mg-Al films. (FY 2014)
- Developed FIB procedures to "lift out" thin film specimens from bulk HPDC AZ91D Mg alloy and analyzed the evolution of Mg$_{17}$Al$_{12}$ upon heat-treatment at three temperatures. (FY 2014)
- Improved the existing MEAM potential for Mg-Al system and calculated physical properties for Mg, Al, Mg-Al solid-solution and Mg$_{17}$Al$_{12}$. (FY 2014)

Future Directions

- Analyze microstructural evolution and speed of the solidification front via in-situ melting/solidification experiments in DTEM.
- Quantify the incubation time and growth kinetics of Mg$_{17}$Al$_{12}$ in Mg-Al binary thin films at 150, 200, and 300°C.
- Evaluate the effect of Zn on the incubation time and growth kinetics of Mg$_{17}$Al$_{12}$ in Mg-Al-Zn ternary thin films at 150, 200, and 300°C.
- Modify PNNL's recently developed object kinetic-Monte Carlo (kMC) code Kinetic Simulation of Microstructure

Evolution (KSOME) into an atomistic kMC code to study nucleation and growth of $Mg_{17}Al_{12}$.

- Develop a database of local environment-dependent activation energies for vacancy jumps, using nudged-elastic band method, as an input to the KSOME code.
- Use solidification software to simulate as-cast AZ91D microstructure at cooling rates between 1-1000°C/s and compare against experimentally observed microstructures.

Technology Assessment

- Target: Quantify the nucleation and growth kinetics during solidification in molten AZ91 Mg alloy under high-rate cooling (~100-1000°C/s).
- Gap: Traditional analytical techniques cannot image the microstructural evolution in situ during solidification of molten metals at high cooling rates. Thus, existing research is restricted to post-solidification analysis, or to in situ analysis at cooling rates much lower than 100°C/s.
- Target: Develop solidification models that can predict the non-equilibrium microstructures developed in AZ91 Mg alloy during die casting.
- Gap: Microstructural evolution data during solidification of Mg alloys at high cooling rates is not available to validate existing models. Hence, solidification models cannot accurately predict the non-equilibrium as-cast microstructure that is formed during die casting of Mg alloys.

✧   ✧   ✧   ✧   ✧

Introduction

Mg has the potential to provide 60%-75% mass savings relative to steel or cast iron [1] and HPDC can be used to economically produce large, thin-wall Mg castings to replace steel subsystems. Mg castings can take advantage of its mass-saving potential for automotive applications because castings do not have to overcome the limited room-temperature formability of Mg, an aspect that has hindered the widespread use of Mg sheets in automotive applications.

High cooling rates during HPDC lead to formation of a non-equilibrium microstructure comprising $Mg_{17}Al_{12}$ precipitates and inhomogeneous α-Mg-Al solid-solution. However, the kinetics of the solidification process during HPDC is not well understood because the associated high cooling rates (~100-1000°C/s) make it virtually impossible for traditional analytical techniques to image the microstructural evolution in situ during solidification of molten metals. Thus, existing research on in situ solidification analysis is restricted to cooling rates up to ~40°C/s using differential scanning calorimetry. Alternately, post-solidification analysis can be used for rapidly cooled samples but without detailed understanding of the solidification history. Further, current solidification models are limited mainly to mold filling and thermal and stress analyses but without the ability to predict

the post-solidification microstructure extensively. This limitation is due to the inadequacy of the current modeling techniques to model non-equilibrium phase transformation, diffusion, etc. processes. In this work, we propose to perform in situ melting and solidification experiments inside a DTEM to address the above knowledge gap. This information will feed into the commercially available solidification modeling software, ProCAST (process casting evaluation software from ESI North America), to help enable its use for predicting HPDC microstructures in Mg alloys.

Once cast, high-pressure die castings are generally not heat treated to avoid blister formation caused by the presence of porosity. Although alloy development and process improvement efforts are ongoing to reduce/eliminate the porosity and enable heat-treatment to improve the mechanical performance of die castings, post-solidification heat-treatment investigations have been limited to sand/gravity-castings where the casting is solutionized and then aged. The solutionizing step helps homogenize the microstructure, but the influence of the starting non-equilibrium as-die-cast microstructure on its subsequent evolution during heat-treatment is lost. This project will characterize the early stages of heat-treatment for the nucleation and growth of the $Mg_{17}Al_{12}$ phase. As diffusion is bound to occur on shorter lengths scales during early stages of heating, in situ heat-treatment in a transmission electron microscope (TEM) is the ideal technique to observe those early changes.

From atomistic modeling perspective, a quantitative prediction of segregation and precipitation kinetics requires a precise description of the point defect diffusion mechanisms. In AZ91, vacancy binding with Al atoms within the Mg matrix plays an important role, and therefore solute diffusion kinetics mediated by vacancy diffusion is a key factor controlling the kinetics of $Mg_{17}Al_{12}$ precipitates. The simulation of clustering and precipitation combines the attention to microscopic aspects like diffusion, nucleation, and aggregation of solute atoms in the bulk that are of interest for practical applications. Thus, understanding gained from atomistic simulations would be helpful in designing compositions and thermal treatments aimed at controlling the size, spatial distribution, and morphology of precipitates at the nanoscale.

Approach

The project is divided into four major tasks related to determination of in situ kinetics during solidification and during heat-treatment, solidification modeling, and atomistic modeling. Progress in each of these tasks in FY 2014 is described below.

In Situ Solidification Kinetics

Conventional TEM is usually limited by the low refresh rate of the charge-coupled device (CCD) detector that is insufficient to image high-rate solidification kinetics. Therefore, this project aims to use a novel DTEM approach to capture the solidification evolution in real time under high-cooling rates.

DTEM uses a laser beam that can locally heat and melt the TEM specimen, while a second laser beam, delayed by a known duration, is used to generate discrete electron bursts for ultrafast imaging of microstructure evolution during melting and solidification. Thus, for an AZ91 sample, the volume fraction of solid and liquid phases and nucleation and growth of $Mg_{17}Al_{12}$ precipitates can be determined as a function of time. DTEM experiments require an electron transparent film of uniform thickness and composition for a repeatable response in each melting run. Sputter coating is the preferred method to make DTEM film specimens because they can be batch fabricated in a repeatable manner; they have greater lateral dimensions than films fabricated by FIB "lift out" technique; and they are uniform in thickness compared to the wedge-shaped geometry obtained by traditional electro-polishing methods.

The project used in-house fabricated membrane chips as a substrate for magnetron sputtering of binary and ternary alloy films with homogeneous thickness and composition. To avoid oxidation in the time between fabrication and analysis, the films were stored in an argon-purged vacuum desiccator.

The grain-size distribution in the film was measured in TEM bright-field and dark-field images using Gatan Digital Micrograph, while the composition of the film was analyzed with energy dispersive spectroscopy (EDX) in the TEM. Ex situ experiments were used to determine the laser energies required for melting Mg-Al films during the planned in situ experiments in the DTEM (see Figure III-143(a)). A neodymium-doped yttrium aluminum garnet (Nd:YAG) laser system with a wavelength of 532 nm was used to generate single pulses of 10 nanoseconds (ns) length with a beam diameter of ~100 micrometers (μm) (the beam profile was not Gaussian, so the accurate pulse shape could not be determined). A series of shots, ranging in energy from 0.1-5 mJ, were directed at a *nanocrystalline* Mg-9 wt.% Al film (~80 nm thick) deposited on a standard silicon (Si) wafer (see Figure III-143(b) and Figure III-143(c)). Low-energy laser shot experiments, at laser energies which produced melting in the above described Si-supported film, were also conducted on a film supported by a membrane chip. These membrane supported films were examined in the TEM.
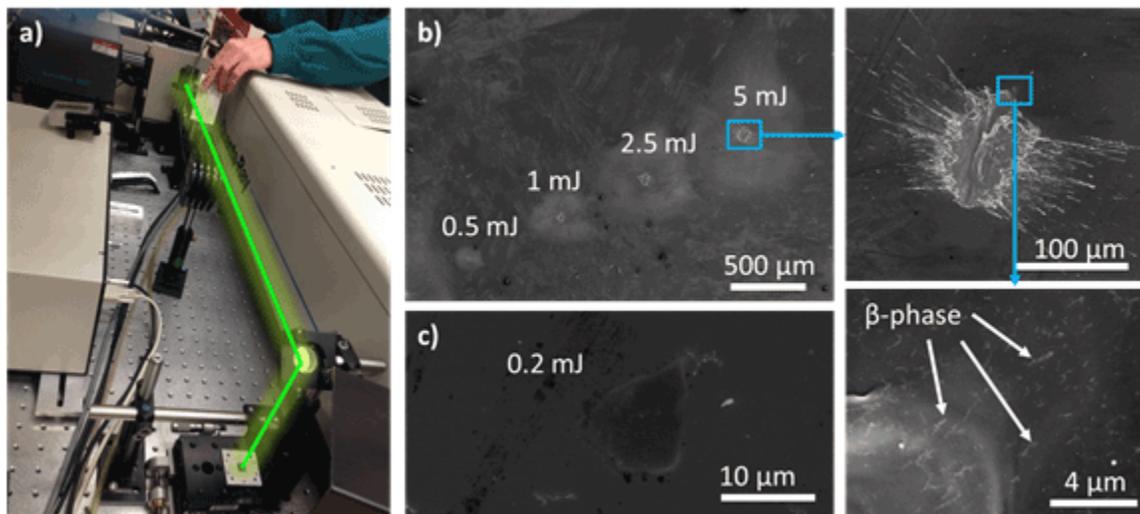
Figure III-143: a) Photograph of the laser set up used for ex situ laser-melting (the laser-beam path is indicated schematically by the green-colored line). b) A scanning electron microscope (SEM) micrograph (secondary electron image) showing the laser damage to the Si-supported Mg-alloy film as a function of the pulse energy. The first cut-out shows a magnified splatter, and the second cut-out shows bright contrast features, believed to correspond to the β-phase (Mg17Al12), adjacent to the ablated regions. c) At 0.2 mJ pulse energy, the Mg-alloy film was melted rather than ablated.

III.x In situ Investigation of Microstructural Evolution During Solidification and Heat-Treatment in a Die-Cast Magnesium Alloy – Pacific Northwest National Laboratory

Rohatgi and Browning–PNNL

In Situ Heat-Treatment

One limitation of the traditional TEM specimen preparation (i.e., using mechanical and electropolishing techniques) for in situ investigation is that one does not have control over which microstructural features within the specimen are amenable for TEM investigation. Hence, the FIB approach was selected to prepare site-specific TEM samples for in situ heat-treatment studies. However, the FIB approach poses two experimental challenges:

1) Platinum, which is commonly used for "welding" the specimen lamella to the specimen manipulator during FIB milling, may catalyze the oxidation of Mg/Al (with the residual oxygen in the microscope)—especially at elevated temperatures during in situ heat treatment.

2) FIB uses a Ga ion beam to mill the specimen; hence, Ga implantation cannot be entirely avoided even though a low-voltage cleaning step can reduce the extent of the damage layer. At temperatures relevant to the present work with Mg, the Ga-Mg phase diagram suggests the formation of Ga-Mg intermetallics at very low Ga concentrations (<1 wt.%).

Issue 1) above was solved by removing and replacing the initially necessary platinum welds with carbon in a subsequent manufacturing step. Issue 2) cannot be avoided using the FIB technique; therefore, the project employed best efforts to keep Ga ion implantation at a minimum. A Gatan heating holder in a probe-corrected FEI Titan 200 kilovolt (kV) field emission gun (FEG) scanning transmission electron microscope (STEM) was used to conduct in situ heat treatment in the as-cast FIB lift-out specimens and the magnetron sputtered thin films.

Solidification Modeling

Our industrial collaborator, ESI North America, developed a computer-aided design model of Mg-9 wt.% Al film on top of the membrane chip. The thermal model was run with a melt pool of diameter 10 micrometers (μm) and at an initial temperature of 610°C (i.e., initial temperature near the liquidus for AZ91). Cooling was simulated in the model as due to conduction only.

Atomistic Modeling

A molecular dynamics simulation approach, using empirical interatomic potentials, was chosen to calculate defect formation and migration energies, solute-vacancy binding energies, and to study their effect on nucleation and growth kinetics of $Mg_{17}Al_{12}$. Two recently developed second-nearest neighbor MEAM type potentials, for the Mg-Al system [2] and for Al, Si, Mg, Cu and Fe system [3], were analyzed using the molecular dynamics simulation package, Large-scale Atomic/Molecular Massively Parallel Simulator (LAMMPS) [4]. Calculations were performed for bulk (lattice constants, elastic constant) and point defect properties (vacancy, interstitial formation energies, substitutional impurity energies, activation energy of vacancy diffusion). All calculations were performed at zero degrees Kelvin (0 ˚K), allowing full relaxation of atoms. Adjustments were made to the MEAM parameters of the existing potential [2] to achieve good correlation between the molecular dynamics calculated values and the experimentally measured and density functional theory (DFT) calculated values.

Results and Discussion

In Situ Solidification Kinetics

Figure III-144a and Figure III-144b show the bright-field and the dark-field image of Mg-9 wt. % Al sputtered film, and Figure III-144c shows the resulting grains-size histogram. The measured grain-size ranged from 9 – 33 nm, with an average grain-size of 15 – 20 nm. The crystalline nature (as opposed to amorphous) of the film is a desirable structure, as diffraction—and therefore phase identification during future low-signal DTEM experiments—will be possible (see diffraction ring pattern in the inset in Figure III-144b). Table III-14 shows the composition of the sputtered film, and the data shows that the Al content of the as-sputtered Mg-Al binary film is very close to the nominal Al content in AZ91 (i.e., 9 wt.% Al). Hence, under identical cooling conditions and to a first approximation, the solidification behavior of this film (upon melting in the DTEM) is expected to be comparable to the solidification behavior of a bulk alloy of similar composition.
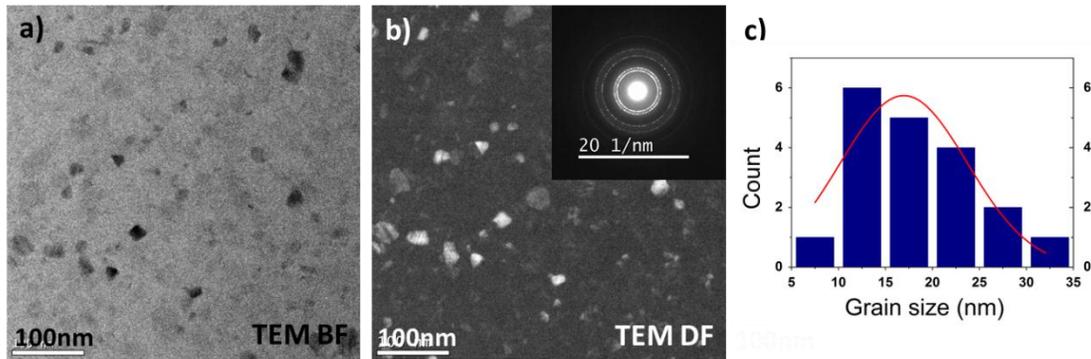
Figure III-144: a) TEM bright-field image of the Mg-9wt.% Al film. b) TEM dark-field image of the film, inset selected area diffraction pattern. c) Histogram showing the grain-size distribution in the film (blue bars) and a Gaussian fit to the histogram (red line) showing that the average grain size is between 15 and 20 nm.

Table III-14: Composition of the film as measured from the respective K-lines with EDX in the TEM. The X-ray signal from the silicon nitride (Si_3N_4) membrane was neglected in the quantification.

Element	Weight %	Atomic %	Uncertainty %
Mg(K)	90.7	91.6	1.14
Al(K)	9.3	8.4	0.38

In the ex situ laser-melting experiments, laser shots with 0.5 – 5 mJ pulse energy caused the AZ91 sputtered films to ablate and left splatter marks that were visible in an optical microscope. Figure III-143b shows a scanning electron microscope image of those splatter marks. In the edge regions of the laser-damaged area, the film was melted, and it appears that small regions of $Mg_{17}Al_{12}$ phase (bright contrast) developed. The experiment was repeated at lower pulse energies of 0.1, 0.2 and 0.35 mJ respectively. At these energies, although the Mg alloy film appeared undamaged when viewed in the optical microscope, closer examination of the exposed areas in the SEM revealed that in the cases of 0.35 and 0.2 mJ pulse energy, the sample melted and subsequently solidified in a ~10 µm wide area. When 0.1 mJ pulse energy was used, no signs of melting/solidification were detected.

While high laser pulser energies (0.5 – 5mJ) caused ablation (Figure III-143a and Figure III-143b), moderate pulse energies (0.2 – 0.35 mJ) were suitable to locally melt the Mg-9 wt.% Al without damaging/ablating rest of the film. Lower energies—comparable to the energies used by Kulovits et al. [5] for melting Al—were insufficient to induce melting in the Mg alloy film in air. However, the energy required for melting (0.2

mJ) is higher only by a factor of four than it was in the case of Al. Although the melting point of Al (~660°C) is greater than the liquidus temperature of AZ91 (~610°C), the relatively greater energy required for melting the AZ91 film in the current work could be due to the differences in thermal conductivity, specific heat, and latent heat of the films, as well as due to differences in the laser beam profile and the testing environment (open air in this work versus ultra-high vacuum inside the TEM [5]).

An attempt was made to melt the film on a support membrane with different (low) laser energies. One attempt with a 0.35 mJ beam was successful (Figure III-145). The observed melt pool is comparable in size and microstructure to the melt pool reported by Kulovits et al. [5] (Figure III-145b) on Al film. Although the laser melting experiment was conducted in air, oxide formation was not observed in the solidified area which was encouraging to note. EDX did not reveal any local variations in the chemical composition of the solidified area. From these results, an assumption can be made that laser melting of Mg-9wt.% Al films in the DTEM can be achieved at pulse energies of 0.2 – 0.35 mJ with the Nd:YAG 532 nm laser system.
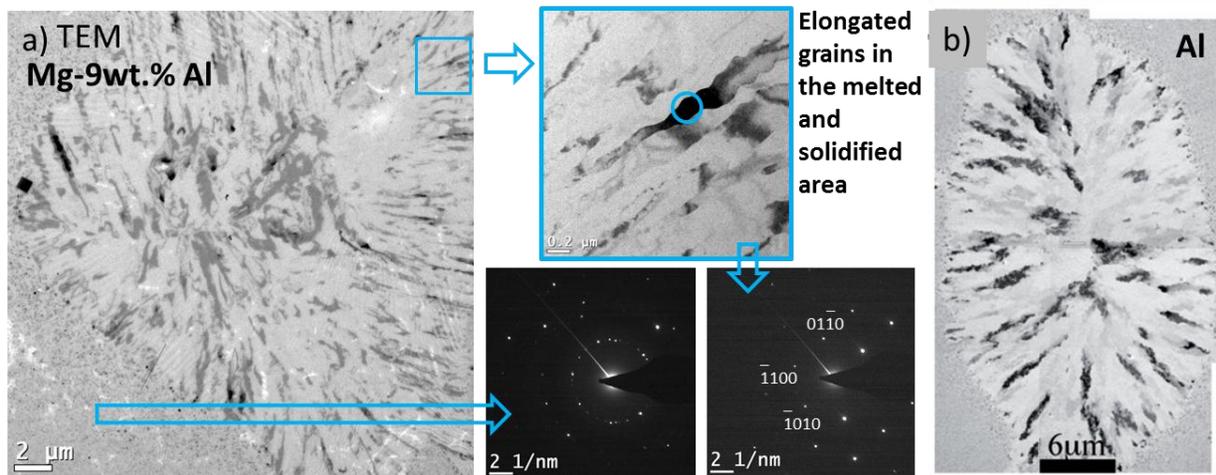
Figure III-145: a) TEM image of the laser-shot region in Mg-9wt.% Al film showing the elongated grains in the melted and solidified area and the diffraction patterns of the as-deposited structure and (0001) pattern of one of the grains in the as-cast microstructure. The circle in the cut-out shows the region imaged by the selected area aperture. b) Laser-melt/solidified pool in an Al film taken from Kulovits et al [5].

In Situ Heat-treatment

Figure III-146 and Figure III-147 show the microstructural evolution in FIB-milled specimens made from a bulk HPDC AZ91D. Figure III-146 shows that while no changes to the $Mg_{17}Al_{12}$ β-phase were observed at 80°C, small (~20 nm) Ga-Mg intermetallic precipitates formed within the Mg-Al α-phase (Figure III-146a). These precipitates grew during additional heating at 150°C. We observed a particularly high density of Ga-Mg intermetallic precipitates at the α/β phase boundary. When the temperature was increased to 200°C, larger particles started to appear; in some cases, they appeared very thick and spherical, suggesting that a Ga-rich liquid phase had formed. At this stage, the β-phase appeared to grow. At present, no conclusion can be made as to what the influence of the Ga is on the evolution of β-phase at this temperature. Figure III-147 shows the microstructural evolution in the second FIB-milled specimen during the early stages of heat-treatment at 400°C. Unlike the first specimen heated to a maximum temperature of 200°C, no Ga-rich precipitates were observed here. An assumption was made that at 400°C, Ga-Mg phase is molten and is located out of the field of view. The

β-phase started to grow immediately and appeared to develop a polygonal morphology.

Figure III-148 shows the microstructural evolution during in situ heating of a Mg-9 wt.% Al sputtered film. EDX measurements showed that the as-sputtered film was homogeneous in composition across different grains. After an initial heating to 200°C, a number of β-phase particles had nucleated and grown across the film. One of these β-phase particles was observed during additional heating to 400°C and, as shown in Figure III-148, the area-fraction of this particle almost doubled within 45 minutes at test temperature.

Solidification Modeling

Preliminary modeling results showed that the cooling rate within the melt pool may exceed 1000°C/s. It is presently not feasible to have thermocouples (or any other temperature measurement technique) integrated within the in situ melting setup. Therefore, alternatives are being evaluated, such as modifications in specimen geometry, to improve the control over the cooling rate during solidification.
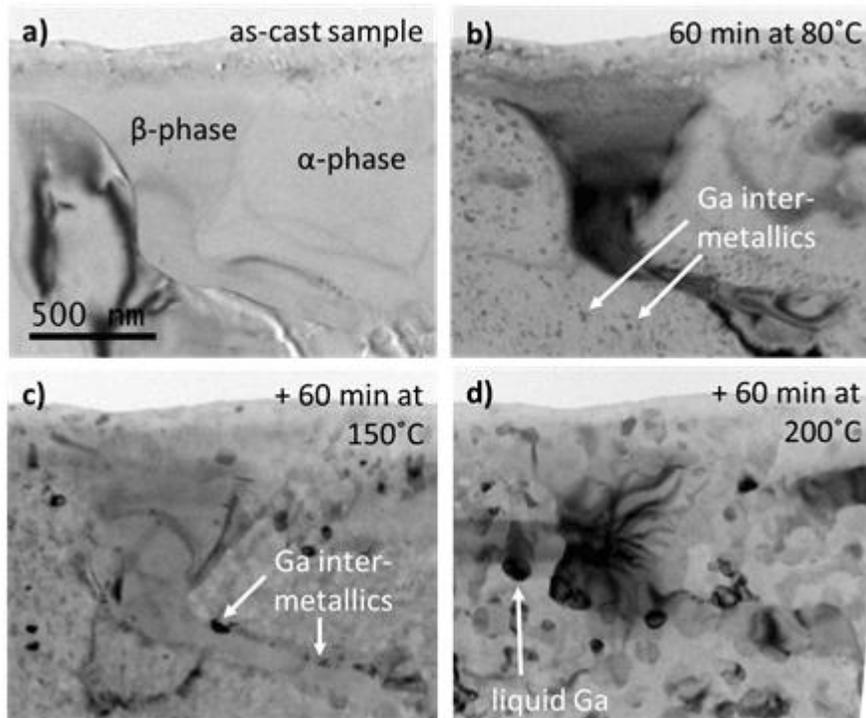
Figure III-146: TEM images of HPDC AZ91 alloy. a) As-cast sample showing the α- and β-phase before heat treatment, b) after 60 minutes at 80°C, c) after an additional 60 minutes at 150°C, and d) after a further 60 minutes at 200°C. All figures are at the same magnification as indicated by the scale bar shown in (a).
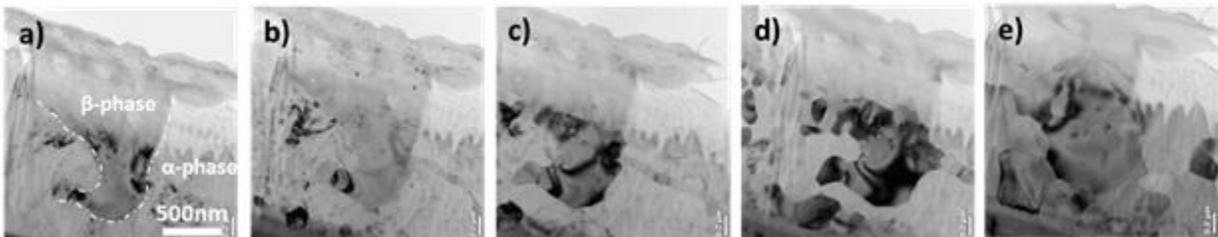
Figure III-147: TEM images of HPDC AZ91 alloy heat treated at 400°C. These images were captured in quick succession from a) to e) in less than 5 minutes, while the sample was heated to a maximum temperature of 400°C. The β phase is outlined in white in a). Scale bar for all images is as shown in (a).
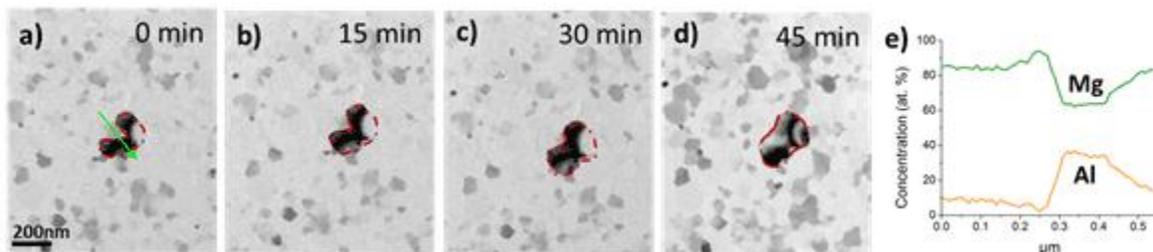
Figure III-148: TEM images of a β-phase particle (outlined in red) in Mg-9 wt.% Al film heat-treated at 400°C after a) 0 minutes, b) 15 minutes, c) 30 minutes, and d) 45 minutes. e) Electron energy loss spectroscopy (EELS) line profile across the original particle along the green arrow in a).

Atomistic Simulations of Mg-Al

Table III-15 compares the experimental values (from the literature) of $Mg_{17}Al_{12}$ properties with those calculated using various potentials and DFT. The data in Table III-15 shows a significant improvement in the calculated values, especially for heat of formation and bulk modulus, after PNNL's adjustments to existing MEAM potential [2]. Table III-16 shows the elastic constants for pure Al, Mg and $Mg_{17}Al_{12}$ (A_{12} structure) and shows a good correlation between the values obtained by MEAM potential of the present work and the experimental (for Al and Mg) or DFT (for $Mg_{17}Al_{12}$) values. Table III-17 shows

comparison of formation energy of single vacancy and self-interstitial and substitutional impurities of Al in bulk Mg and Mg in bulk Al. The MEAM potential reproduced experimental (exp.) values of Mg and Al vacancy formation energies. Self-interstitial formation energies were calculated for Mg and Al at octahedral (octa.) and tetrahedral (tetra.) sites. Overall, the agreement between MEAM, experimental, and DFT values for the vacancy and self-interstitial formation energies, and substitutional impurity energies is quite good and within few electron volts (eV).

Table III-15: Comparison of experimentally measured properties of Mg17Al12 with those calculated using different approaches.

Property	[2]	PNNL MEAM	[3]	DFT [3, 6]	Experimental [3]
Heat of Formation (meV)	-44.2	-33.90	49.40	-17.0 – -48.0	-32.65 – -34.10
Cohesive Energy (eV)	-2.254	-2.33	-2.22	-2.03 – -2.47	Not Available
Lattice Constant (Å)	10.41	10.56	10.73	10.54 – 10.55	10.54 –10.56
Atomic Volume (Å³)	19.45	20.31	21.28	18.65 –20.25	20.13 – 20.30
Bulk Modulus (GPa)	70.32	50.25	48.29	49.53 – 50.1	49.6

Table III-16: Comparison of experimentally measured elastic constants of Al, Mg and Mg17Al12 with those calculated using MEAM potential (using PNNL's adjustments).

Material	Al		Mg		$Mg_{17}Al_{12}$	
(GPa)	MEAM	Experimental [7]	MEAM	Experimental [7]	MEAM	DFT [8]
C_{11}	114.33	107.3	62.81	59.7	83.364	86.8
C_{22}	114.33	107.3	62.81	59.7	83.364	86.8
C_{33}	114.33	107.3	69.61	61.7	83.364	86.8
C_{12}	61.91	60.9	25.97	26.2	32.142	29.0
C_{13}	61.91	60.9	21.18	21.7	32.142	29.0
C_{23}	61.91	60.9	21.18	21.7	32.142	29.0
C_{44}	31.56	28.3	17.14	16.4	14.005	20.0
C_{55}	31.56	28.3	17.14	16.4	14.005	20.0
C_{66}	31.56	28.3	18.42		14.005	20.0

Table III-17: Comparison of DFT measured defect formation energies in Al and Mg with those calculated using MEAM potential (using PNNL's adjustments).

Material	Vacancy (eV)		Intersitial (eV)				Substitutional Atom (eV)			
			MEAM		DFT [3]		MEAM		DFT [3]	
	MEAM	DFT (Exp.) [3]	Octa.	Tetra.	Octa.	Tetra.	Mg	Al	Mg	Al
Al	0.68	0.55 (0.67)	2.65	3.11	2.8	3.3	0.04	-	0.05	-
Mg	0.89	0.7 (0.5-0.89)	2.54	2.57	2.2	2.2	-	0.013		0.06

III.x In situ Investigation of Microstructural Evolution During Solidification and Heat-Treatment in a Die-Cast Magnesium Alloy – Pacific Northwest National Laboratory

Rohatgi and Browning–PNNL

Technology Transfer Path

ESI will use the results and knowledge developed in this work to identify modifications that may be necessary in their solidification modeling code, ProCAST, for predicting microstructures in die-cast Mg alloys. Such validated and commercially available microstructural codes will allow automotive original equipment manufacturers to reduce time for casting trials and speed up implementation of Mg alloy castings in production vehicles.

Conclusion

Sputtering techniques were developed to reproducibly fabricate thin (~80 nm) and electron transparent Mg-Al films on a support membrane. The TEM micrographs show that the average grain-size in the films is 15-20 nm, while EDX shows that the films contain 9±0.38 wt.% Al and 91±1.14 wt.% Mg—i.e., very close to the Al content in AZ91. Multiple specimens of such alloy films can be produced per sputtering run and these films are ideal for planned in situ melting-solidification experiments in the dynamic TEM.

FIB milling and in situ heating procedures were developed to perform aging heat-treatment on thin films of AZ91 FIB-milled from bulk HPDC AZ91 alloy. Future experiments on AZ91 films will be used to quantify the kinetics of $Mg_{17}Al_{12}$ evolution at elevated temperatures. Such experimental data will be correlated to the predictions of atomistic modeling work.

The existing MEAM potentials were adjusted for the Mg-Al system and a significant improvement was obtained in the calculated values of $Mg_{17}Al_{12}$, especially the heat of formation and bulk modulus. Hence, in future work, these adjusted MEAM potentials will be used to calculate point defect properties, binding energies of vacancy and solute atoms to different cluster sizes, substitutional energies, and diffusion mechanisms at various concentrations of both Al and vacancies in Mg. This information will be used as input to a simulation tool, Kinetic Simulation of Microstructure Evolution, which is an object kMC code developed at PNNL. PNNL is modifying this code in the current project to study nucleation and growth of $Mg_{17}Al_{12}$.

Presentations/Publications/Patents

Kruska K, Rohatgi A, Vemuri R, Evans JE, Kovarik L, Abellan P, Parent LR, Mehdi LB, Browning ND, Dynamical TEM Investigation of Solidification Kinetics in an AZ91 Mg Alloy, PNNL Post-Doc Research Symposium 2014, July 30, 2014 (Poster).

References

1. Powers, W.F. "Automotive Materials in the 21st Century." *Advanced Materials and Processes* (157), 2000; pp. 38-41.

2. POSTEC CMSE LAB. https://cmse.postech.ac.kr/lammps/3707. Accessed June 10, 2014.

3. Jelinek, B.; Groh, S.; Horstemeyer, M. F.; Houze, J.; Kim, S. G.; Wagner, G. J.; Moitra, A.; Baskes, M. "Modified Embedded Atom Method Potential for Al, Si, Mg, Cu, and Fe Alloys." *Phys Rev B* (85), 2012; pp. 245102.

4. Plimpton, S. "Fast Parallel Algorithms for Short-Range Molecular Dynamics." *J Comp Phys.* (117), 1995; pp. 1-19.

5. Kulovits, A.; Wiezorek, J.M.K.; LaGrange, T.; Reed, T.W.; Campbell, G.H. "Revealing the Transient States of Rapid Solidification of Aluminum Thin Films using Ultrafast In-situ Transmission Electron Microscopy." *Philosophical Magazine Letters* (91), 2011 ; pp. 287-286.

6. Kim, Y.-M.; Kim, N. J.; Lee, B.-J. "Atomistic Modeling of Pure Mg and Mg–Al Systems." *CALPHAD: Computer Coupling of Phase Diagrams and Thermochemistry* (33), 2009; pp. 650–657.

7. Simmons, G.; Wang, H. *Single Crystal Elastic Constants and Calculated Aggregate Properties. A Handbook.* MIT Press Cambridge, Mass., 1971.

8. Wang, N.; Yu, W -J.; Tang, B. -Y.; Peng, L –M.; Ding W –J. "Structural and Mechanical Properties of $Mg_{17}Al_{12}$ and $Mg_{24}Y_5$ from First-principles Calculations." *J. Phys. D. Appl. Phys.* (41), 2008; pp. 195408.

III.25 Transformation Kinetics and Alloy Microsegregation in High Pressure Die Cast Magnesium Alloys – The University of Michigan

John E. Allison, Principle Investigator
The University of Michigan
500 South State Street
Ann Arbor, MI 48109
Phone: (734) 971-3989
E-mail: johnea@umich.edu

Aaron Yocum, Project Officer
National Energy Technology Laboratory
3610 Collins Ferry Road
P.O. Box 880
Morgantown, WV 26507-0880
Phone: 304-285-4852
E-mail: Aaron.yocum@netl.doe.gov

William Joost, Technology Area Development Manager
U.S. Department of Energy
1000 Independence Avenue, S.W.
Washington, DC 20585
Phone: (202) 287-6020; Fax: (202) 856-2476
E-mail: william.joost@ee.doe.gov

Contractor: University of Michigan
Contract No.: DE-EE0006434

Abstract/Executive Summary

High pressure die casting (HPDC) is the predominant manufacturing method for magnesium (Mg) alloy automotive components, however, the phase transformation kinetics that occur in this process are, at best, poorly understood. The cooling rates during solidification in HPDC are far from equilibrium and have not been the subject of significant quantitative research. Improved understanding of microstructural kinetics and alloy segregation are required to refine industrial processes and to develop new alloy systems. Improvements in this understanding will be accomplished by combining systematic and quantitative experiments and state-of-art modeling and simulation.

The primary objectives of this project are:

- To conduct a systematic, quantitative study of phase transformation kinetics and microsegregation in high pressure die cast Mg alloys under conditions that occur in automotive component production.
- To conduct a systematic, quantitative study of phase transformation kinetics and changes in microsegregation during solution treatment and aging of super vacuum die cast Mg alloys.

- To develop physics-based phase transformation kinetics micro-models that quantitatively capture microstructural evolution and microsegregation during high pressure die casting and heat treatment of Mg alloys.
- To transfer this knowledge to industry and the wider research community through these micro-models and through the experimental data that will be stored in the National Institute of Standards and Technology-Department of Energy- Office of Energy Efficiency and Renewable Energy (NIST-DOE-EERE) Advanced Automotive Cast Mg Alloys Repository and in a new repository, The Materials Commons.

To accomplish the above goals a systematic and comprehensive experimental study is being combined with computational modeling and simulation.

The University of Michigan (UM) is conducting all experimental characterization of microstructures and microsegregation in the HPDC/Super Vacuum Die Casting (SVDC) materials. The microstructure and chemical compositions of as-cast HPDC Mg alloys are being quantitatively and systematically characterized using a combination of methods including electron probe micro-analysis (EPMA) and optical, scanning electron microscopy (SEM) and transmission electron microscope (TEM). This comprehensive characterization has been initiated in the ternary alloys, AM60 and AZ91. These initial results have shown that while Scheil solidification kinetics appear to describe the Al segregation profile at mid-thickness in 2.5 mm and 5.0 mm plates, Scheil models do not describe the microsegregation that occurs during rapid solidification at the edge of the plate. Continued characterization will provide new insights in understanding phase transformation kinetics during high cooling rate solidification, micro-segregation of different alloying elements, and the impact of casting parameters like cooling rate and casting thickness on as-cast microstructure and microstructure evolution during subsequent heat treatment processes. Ford Motor Company and Professor Shoumei Xiong of Tsinghua University, Beijing China are providing support to this project in supplying HPDC/SVDC Mg plates and complex-shaped castings.

Based on quantitative experimental results, a solidification micro-model will be developed in close collaboration with Dr. Mei Li at Ford Motor Company to predict the evolution of the primary microstructure features of as-cast HPDC Mg alloys. Micro-models will also be developed to predict the dissolution of eutectic phases and redistribution of alloying elements during solution treatment and the precipitation of strengthening phases during aging. These micro-models will be validated using quantitative results obtained on complex-shaped HPDC/SVDC casting of AM50 and AZ91.

III.x Transformation Kinetics and Alloy Microsegregation in High Pressure
Die Cast Magnesium Alloys – The University of Michigan

Allison–University of Michigan

The experimental data and models will made available to the technical community via the NIST DOE-EERE Advanced Automotive Cast Mg Alloys Repository and the UM-DOE Materials Commons, a new knowledge repository under development within the UM Center for Predictive Integrated Structural Materials Science (PRISMS) funded by DOE Basic Energy Sciences (BES).

This project is planned to span four years and will be conducted in one phase consisting of six tasks.

Accomplishments

- Produced plates of ternary Mg alloys AM60B, AM70, and AZ91 using a high pressure SVDC technique. (FY 2014)
- Completed initial precision MagmaSoft HPDC simulation of the SVDC casting conditions and geometry.
- Established reliable and consistent EPMA and metallographic procedures on the above ternary alloys. (FY 2014)
- Developed a Monte Carlo simulation of microsegregation behavior as measured by EPMA in HPDC Mg alloys. (FY 2014)
- Characterized microsegregation behavior in HPDC AM60B (of two plate thicknesses), AM70, and AZ91, as well as in Mg-9 aluminum (Al) produced under different casting conditions. (FY 2014)
- Completed quantitative characterization of beta-phase area fraction in HPDC AM60B. (FY 2014)
- Completed EBSD characterization of HPDC AM60B (of two plate thicknesses) and AZ91 as-cast microstructure. (FY 2014)

Future Directions

- Complete SVDC of Mg-Al binaries, and magnesium-aluminum-manganese (Mg-Al-Mn), magnesium-aluminum-zinc (Mg-Al-Zn), magnesium-aluminum-calcium (Mg-Al-Ca), and magnesium-aluminum-strontium (Mg-Al-Sr) ternaries
- Complete phase transformation and microsegregation characterization of binaries and Mn and Zn ternaries
- Complete phase transformation and microsegregation characterization of Ca and Sr ternaries and in complex casting of AM50 and AZ91
- Complete study of precipitation kinetics and of eutectic phase transformation and microsegregation during heat treatment in selected binary and ternary alloys
- Complete micro-model for Mg-Al binaries and Mg-Al-Mn, Mg-Al-Zn, Mg-Al-Ca, and Mg-Al-Sr ternaries for HPDC and heat treatment conditions
- Incorporate experimental data for Mg-Al binaries and Mg-Al-Mn, Mg-Al-Zn, Mg-Al-Ca, and Mg-Al-Sr ternaries into Materials Commons and release to public
- Incorporate micro-model into NIST DOE-EERE Repository and Materials Commons and release to public

Technology Assessment

- Target: Improved predictive capabilities for HPDC Mg alloy microstructures and precipitation kinetics.
- Gap: There is a lack of quantitative info on phase transformations and microsegregation in HPDC Mg alloys.

✧   ✧   ✧   ✧   ✧

Introduction

HPDC is used to manufacture over 90% of the commercial Mg products. [1] This process is fast, economical and produces complex thin-wall Mg components that cannot be fabricated by other means. The cooling rate involved in HPDC and SVDC is extremely high and ranges from 10 to 1000 degrees Centigrade per second (°C/s) [2] [3] as depicted in Figure III-149. The solidification processes experienced in this region are far from equilibrium conditions. Under such extreme conditions, the solidification kinetics, phase transformations and the redistribution of alloying elements cannot be predicted using equilibrium thermodynamics or the typical modifications to predict alloy partitioning, such as those represented by a Scheil model. [4] As shown in Figure III-149, even a straight-forward microstructural characteristic such as secondary dendrite arm spacing has not been characterized in detail in this cooling rate regime. There is essentially no systematic, quantitative information on eutectic phase formation or microsegregation in this region. This represents a major and distinct gap in our scientific understanding of this important manufacturing process.

The redistribution of alloying elements during non-equilibrium solidification leads to micro-scale segregation across the dendrite/cell and this micro-scale segregation is strongly dependent on the cooling rate. Although microsegregation has been the subject of a limited number of investigations in Mg alloys [5-7], there is no known microsegregation study for Mg alloys under HPDC conditions in the open literature. Previous studies of microsegregation in Mg alloys have been obtained in directionally solidified castings or in samples cast under moderate cooling rate conditions.
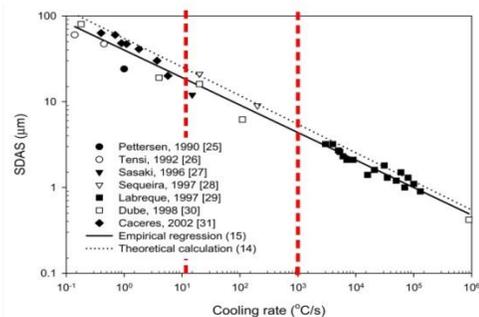
Figure III-149: Effect of cooling rate on secondary dendrite arm spacing (SDAS) in micrometers (μm) of AZ91 Mg alloy. [3] Cooling rate bounds have been added for HPDC/SVDC casting practices.

III.x Transformation Kinetics and Alloy Microsegregation in High Pressure
Die Cast Magnesium Alloys – The University of Michigan

Allison–University of Michigan

Research on heat treatment of die cast Mg alloys has been limited due to the blistering that occurs when entrapped air expands during solution treatment. A new processing technology, SVDC for Al and Mg alloy components [8] [9] significantly reduces or eliminates air entrapment thus enabling heat treatment of die casting alloys and components. This advanced processing route offers new approaches for alloy development and improved Mg component properties. To date, studies of the dissolution of eutectic phases and precipitate evolution during heat treatment of die cast alloys has been very limited [10-12] and there has been no systematic investigation of alloying and processing effects.

Precipitation hardening has the potential to be a major strengthening mechanism in heat treatable SVDC Mg alloys, however SVDC Mg alloys have not yet been the subject of extensive studies. Gradients in alloy microsegregation and eutectic phase transformation that will be exhibited during SVDC will likely have a key influence on the development of new alloy systems. In addition, quantitative characterization of precipitation microstructure under different heat treatment condition is crucial to optimize the effects of precipitation strengthening and building physics-based strengthening models.

Approach

1. Manufacture of high pressure die cast plates and complex-shaped castings & simulation

The alloy compositions to be used in this study are shown in Table III-18. The alloy matrix was selected to include a wide range of compositions that will provide for optimization of current commercial alloys AM50/AM60 and AZ91 as well as pave the way for development of advanced, high-temperature Mg-Al-Ca and Mg-Al-Sr alloys. Through arrangements with the Ford Motor Company, the majority of castings are being provided by Tsinghua University. These castings will be processed using SVDC casting procedures.

Die casting process controls linked with precision MagmaSoft HPDC simulation will be used to provide an estimate of the cooling rate as a function of location in casting and casting geometry. The simulations use a fine finite difference mesh (at least 5 -10 elements through the cross section) and high-fidelity HPDC interfacial heat transfer coefficients for HPDC developed by Li and Allison and co-workers [13-15] to estimate cooling rate as a function of location.

Table III-18: Planned alloy compositions (Bal stands for balance).

Alloy Compositions (wt%)					
Mg	Al	Zn	Mn	Ca	Sr
Bal	3				
Bal	5				
Bal	9				
Bal	12				
Bal	9	0.5			
Bal	9	1			
Bal	9	2			
Bal	5		0.5		
Bal	5		1		
Bal	5		2		
Bal	5			3	
Bal	5				3

2. Quantitative characterization of phase transformation kinetics and microsegregation in high pressure die castings

Solidification phase transformation kinetics will be quantified using comprehensive microstructural characterization, including optical metallography and SEM coupled with advanced image analysis. The primary characteristics that will be quantified are eutectic volume fraction and size and alpha grain/cell size as a function of alloy, location, sample thickness and process condition. Microsegregation profiles of alloying elements (Al, Mn, Zn, Ca, Sr) versus solidification fraction will be quantitatively characterized using the EPMA scan method. [5-7] These microsegregation results will be compared with Calphad-based Scheil solidification estimates of alloy partitioning. Phase transformation kinetics and microsegregation profiles will also be quantified in a complex casting of both AM50 and AZ91 to confirm the experimental findings and to validate the phase transformation kinetics micro-models described below.

3. Quantitative characterization of phase transformation kinetics and microsegregation during heat treatment of super vacuum die castings.

This task will quantitatively characterize phase transformation kinetics and changes in microsegregation profiles during heat treatment of super vacuum die cast plates. Eutectic phase dissolution and changes in microsegregation will be characterized as a function of solution treatment time and temperature. Phase transformation kinetics will be

III.x Transformation Kinetics and Alloy Microsegregation in High Pressure
Die Cast Magnesium Alloys – The University of Michigan

Allison–University of Michigan

quantified using quantitative microstructural characterization, including x-ray diffraction, optical metallography and SEM. The primary characteristics that will be quantified are changes in eutectic volume fraction and size as a function of alloy, location, sample thickness and process condition. Solution treatment induced changes in microsegregation profiles of alloying elements (Al, Mn, Zn, Ca, Sr) will be quantitatively characterized using the electron microprobe area scan method. Precipitate evolution will be characterized in selected alloys using quantitative TEM techniques. [11] Precipitate evolution will be captured in the form of isothermal transformation curves. Beta phase dissolution kinetics and changes in microsegregation profiles will also be quantified in complex castings of AM50 and AZ91 to validate the phase transformation kinetics micro-models.

4. Develop physically-based phase transformation kinetics micro-models that quantitatively capture microstructural evolution and microsegregation during high pressure die casting and heat treatment.

The quantitative and systematic results described above will be used to develop state-of-art phase transformation kinetics micro-models for high pressure die cast alloys. A comprehensive *solidification kinetics micro-model* will be developed which considers solute trapping, dendrite arm coarsening, and dendrite tip undercooling and couples these calculations directly with multicomponent phase diagram computations. Given solidification conditions and alloy compositions, this micro-model will be capable of predicting secondary dendrite arm spacing, types and fractions of various non-equilibrium phases, liquid concentrations and solute concentration profiles in the primary Mg phase under

the extreme high heat extraction conditions that exist in HPDC and SVDC. A *dissolution kinetics micro-model* will be developed to account for eutectic phase dissolution and compositional homogenization. In addition, an analytical *precipitation kinetics micro-model* for predicting precipitate kinetics will also be developed.

5. Transfer the project knowledge to industry and research community through micro-models and experimental data housed in the UM DOE PRISMS Materials Commons.

The information produced in this study will be uploaded to the NIST-DOE EERE Advanced Automotive Cast Mg Alloys Repository and the UM-DOE Materials Commons, a knowledge repository that is under development within the UM-DOE PRISMS Center. Data schemas that are being developed are being done in coordination and consultation with NIST.

Results and Discussion

1. HPDC of AM60, AM70 and AZ91and HPDC simulations

AM60B and AZ91 Mg alloy plates of three different thicknesses (2.5 mm, 3.75 mm and 5 mm) were produced using a high pressure SVDC technique at Tsinghua University. In addition, SVDC plates of AM70 were supplied by Ford Motor Company. Figure III-150 schematically illustrates the die and casting geometry used for the (a) AM60B and AZ91 and (b) AM70.
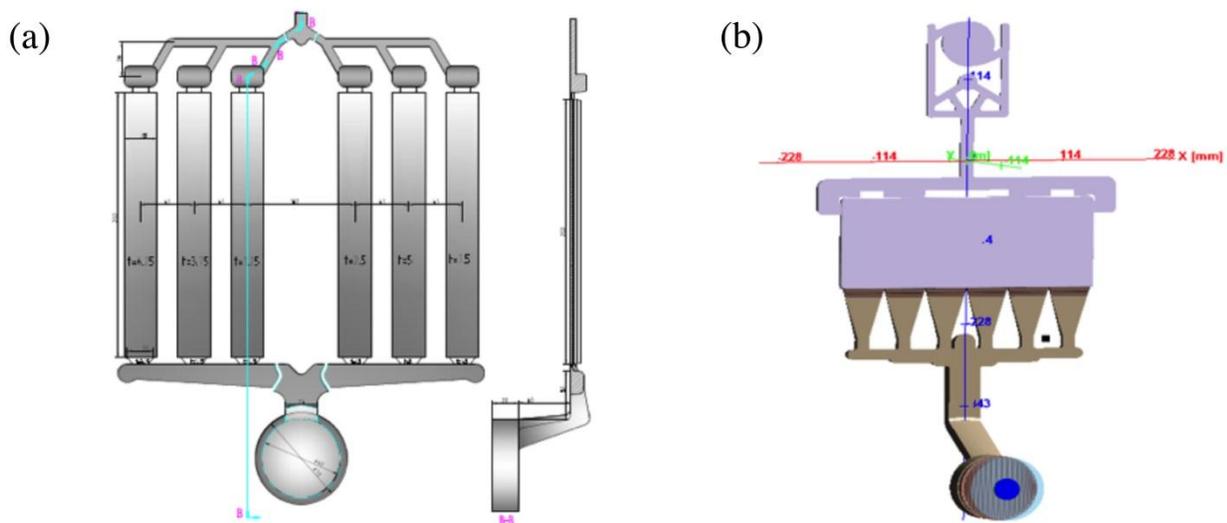
Figure III-150: Schematic illustration of die geometry for producing HPDC (a) AM60B and AZ91 at Tsinghua University and (b) AM70 at Ford Motor Co.

III.x Transformation Kinetics and Alloy Microsegregation in High Pressure
Die Cast Magnesium Alloys – The University of Michigan

Allison–University of Michigan

To develop a physics-based "micro-model" to predict the volume fraction of eutectic phases during non-equilibrium HPDC solidification conditions, an accurate and quantitative understanding of the relationship between cooling rate and microsegregation across the thickness of the castings is crucial. To reveal the local cooling conditions, precision MagmaSoft HPDC simulation with refined meshes and high-fidelity HPDC interfacial heat transfer coefficients have been used. Figure III-151(a) shows the refined meshes with 10 and 35 layers cross the 2.5 mm thickness of a casting plate, and Figure III-151(b) illustrates that the local cooling rates can be revealed using these fine meshes. Analysis of these results is ongoing; however, initial results indicate a cooling rate that varies from approximately 150°C/s in the center of the casting to 300°C/s at the edge. This is consistent with the expectation depicted in Figure III-149.
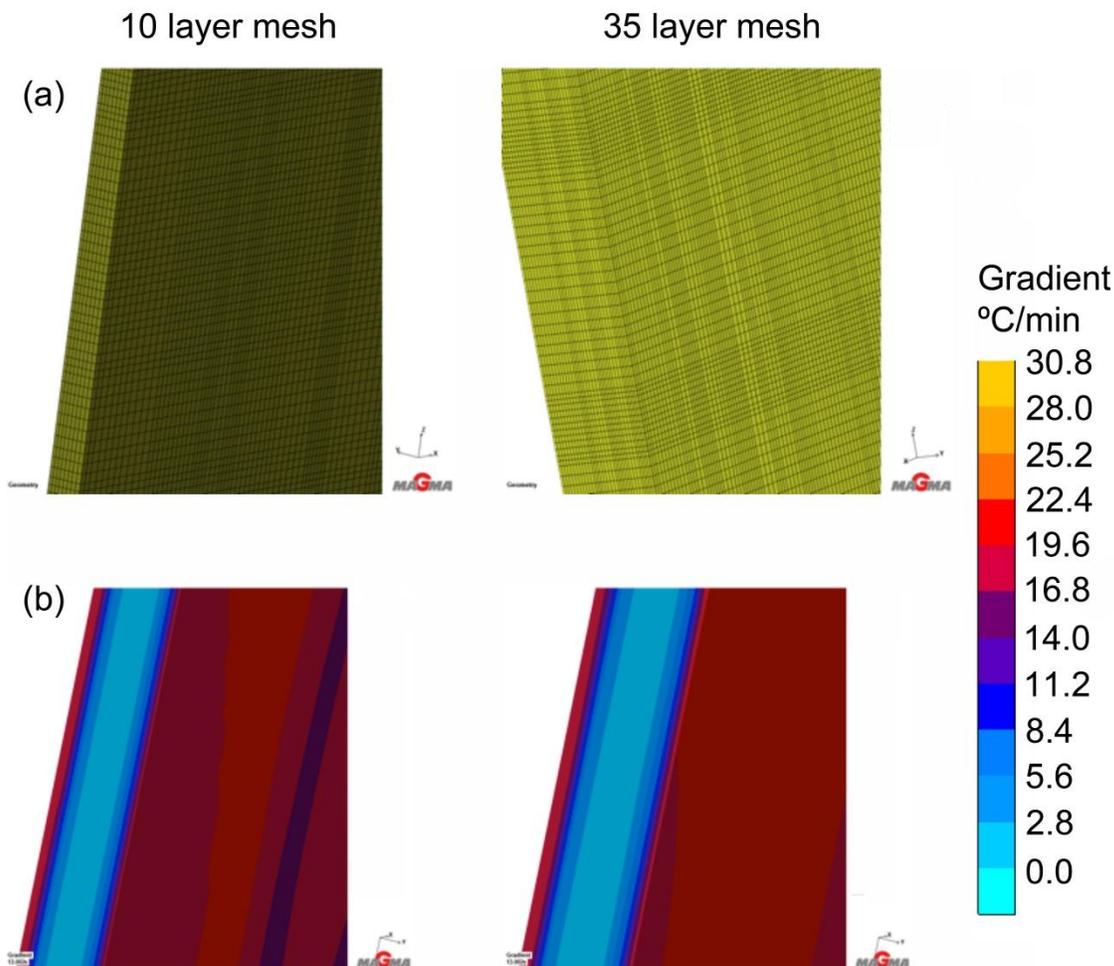
Figure III-151: MagmaSoft simulation of a plate casting with 2.5 mm thickness. (a) Refined meshes of 10 and 35 layers across the thickness; (b) Predicted local cooling rates using the refined meshes.

2. Microstructure Characterization of HPDC Alloys

The area fraction of $Mg_{17}Al_{12}$ (beta) phase was quantified using SEM in combination with the image analysis software ImageJ. Figure III-152 shows secondary SEM images of the general microstructure features in AM60B at the center and edge locations of the cast plates, with major phases identified on the images. Current work includes developing an automated image processing routine in Mathematica based on partitioning the phases using contrast. This code will address the need to have reproducible quantification, regardless of analyst or moderate variations in the image brightness and contrast settings.
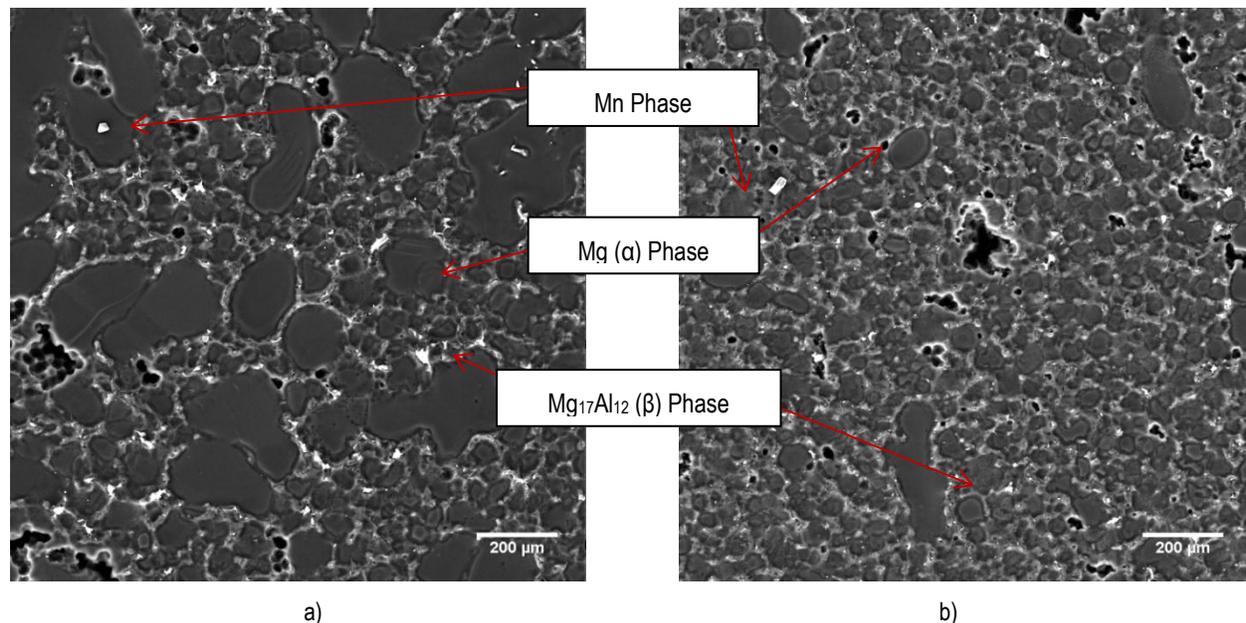
Figure III-152: Secondary electron micrographs of 2.5 mm HPDC AM60B castings at a) center and b) edge of plate.
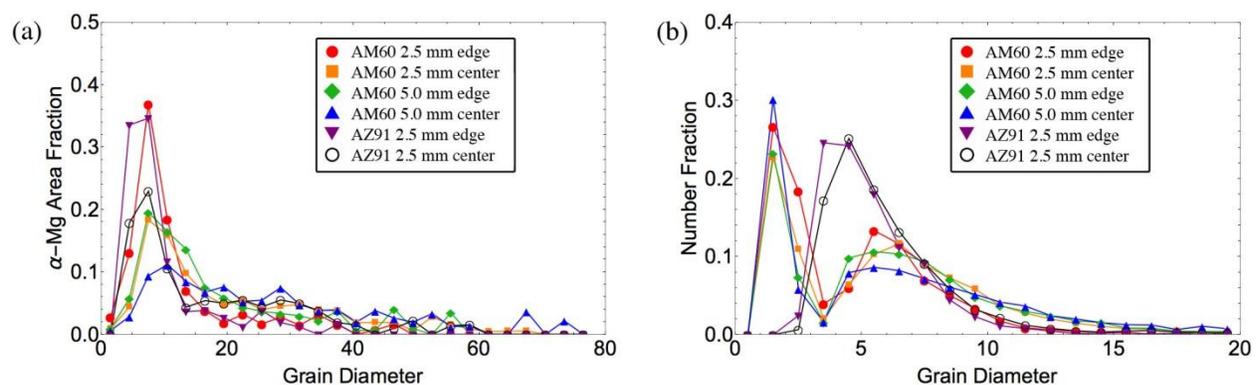
Figure III-153: Grain size distribution in the HPDC AM60 and AZ91 plates, represented as (a) the fraction of indexed area filled by grains of a given diameter and (b) the number fraction of grains with a diameter less than 20 μm.

The grain size distribution of edge and center locations for 2.5 mm HPDC AM60B, 5.0 mm HPDC AM60B, and 2.5 mm HPDC AZ91 was determined through electron backscatter diffraction (EBSD). The data for each condition was collected over a square area of at least 300 μm on edge with a step size between 0.5 and 0.8 μm. Histograms of the grain size distributions are shown in Figure III-153. In the 2.5 mm thick castings, a high fraction (0.8 or 80%) of the area at the edge of the sample is filled with fine grains less than 10 μm in diameter. In the center of the AZ91 plate, the area fraction of fine grains is only slightly lower than at the edge (0.7). However, in the thinner AM60B plates, the area fraction of small grains drops to 0.5 in the center. In the 5.0 mm thick AM60B casting, the area fraction of fine grains is 0.5 and 0.4 at the edge and center, respectively. The area fraction of fine grains is lower in the thicker casting. Only a few percent of the grains in the AZ91 casting are less than 3 μm.

3. Microsegregation Behavior in HPDC AM60 and AZ91

Considerable effort in this reporting period has been invested in the establishment and refinement of the procedures used study microsegregation behavior in the HPDC Mg alloys. For this purpose, we have developed high quality EPMA data acquisition and analysis procedures.

3.1 Established Experimental Procedure

Specimens for EPMA are mounted in epoxy and polished to 1 μm. Water is avoided during the polishing stages to prevent oxidization. Pure (>99.9%) metal elemental standards (Mg, Al, Mn, Zn) are prepared using the same process. The samples and standards are polished no earlier than the day before EPMA analysis to limit oxidation. After polishing, the materials are coated with a 150-200 angstrom carbon layer.

III.x Transformation Kinetics and Alloy Microsegregation in High Pressure
Die Cast Magnesium Alloys – The University of Michigan

Allison–University of Michigan

The carbon layer thickness is gauged using a brass block that is coated at the same time and turns from gold to red-orange at the correct carbon thickness. Coating the pure metal standards at the same time as the specimen of interest avoids errors with calibration due to coating dependent variations in X-ray yield. EPMA data is collected using a Cameca SX-100 equipped with wavelength-dispersive spectrometers (WDS). The acceleration voltage, beam current, and beam emissions for current data collection are 15 kilovolts (kV), 10 nanoamps (nA), and 60 microamps (μA), respectively.

EPMA data is collected in a 20 x 20 point grid with a 10 μm step size. Only points with a total concentration between 98 and 101 wt% are used for analysis. In most data grids, more than 70% of the points meet this criterion. Different methods for sorting solute profile data have been evaluated and we have selected the weighted-interval ranking sort (WIRS) method [16] as the method which provides the most consistent quantitative analysis.

3.2 Monte Carlo Simulation of Microsegregation behavior in HPDC Mg Alloys

A Monte Carlo simulation model was developed to quantitatively evaluate the effect of microstructure parameters (like cell size) and experimental parameters used in the EPMA test on the measured microsegregation behavior in HPDC Mg alloys. The EPMA variables included electron accelerating voltage and dataset size. The method developed currently is a one-dimension analysis. The main assumptions used to develop the simulation are a circularly shaped 2D cell (Figure III-154(a)) and, for the purpose of testing the model, that the distribution of alloying elements follows Scheil

segregation from the center of the cell to the edge of cell (Figure III-154(b)). The size of electron beam interaction volume is calculated using a Monte Carlo simulation of electron interactions. Each dataset is randomly sampled along the cell and eutectic region until the desired number of data points is reached. The model is being used to explore how variations in microstructure and EPMA operating conditions influence the measured microsegregation profile.

3.3 Microsegregation Behavior in HPDC AM60 & AZ91

Figure III-155 shows the comparison between EPMA results of 2.5 mm (a) AM60 and (b) AZ91 and the Scheil solidification models. For both alloys, the microsegregation behavior at the center location is very close to the Scheil simulation results up to a high solid fraction (around 0.8), while the experimental results for the edge location have a large deviation from microsegregation predicted for Scheil conditions. These preliminary results suggest that the Scheil model may be useful for predicting microsegregation behavior of Al at center location for HPDC AM60B plate, which could be a very significant finding. A new micro-model must be developed in order to predict the segregation profiles at the edge of the plate where solidification is more rapid.

Two plate thicknesses of HPDC AM60 have been studied. Figure III-156 shows the comparison of the experimental microsegregation profiles measured in the 2.5 mm and 5 mm plate. The microsegregation behavior is comparable between the two plate thicknesses. More data scans are needed to confirm this trend across different locations along the length of the plate and in additional alloys.
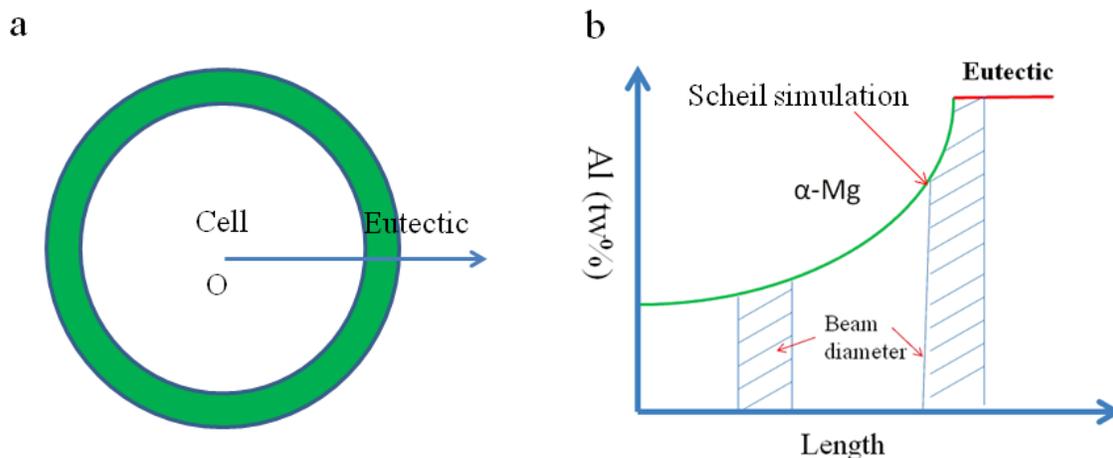
Figure III-154: Illustration of Monte Carlo simulation of the EPMA characterization of microsegregation: a) model of HPDC as-cast microstructure, b) illustration of the one-dimensional distribution of Al across a Mg cell from the center of the cell to the eutectic region.

III.x Transformation Kinetics and Alloy Microsegregation in High Pressure
Die Cast Magnesium Alloys – The University of Michigan

Allison–University of Michigan
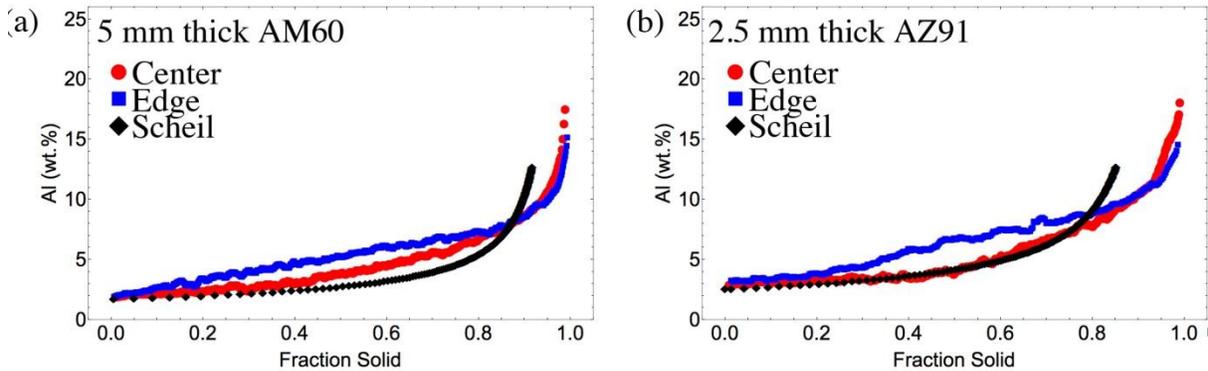
Figure III-155: Comparison of microsegregation behavior determined using EPMA with Scheil simulation in HPDC plates of a) 5.0 mm thick AM60B and b) 2.5 mm thick AZ91. A 10 point moving average was used when plotting the experimental data.
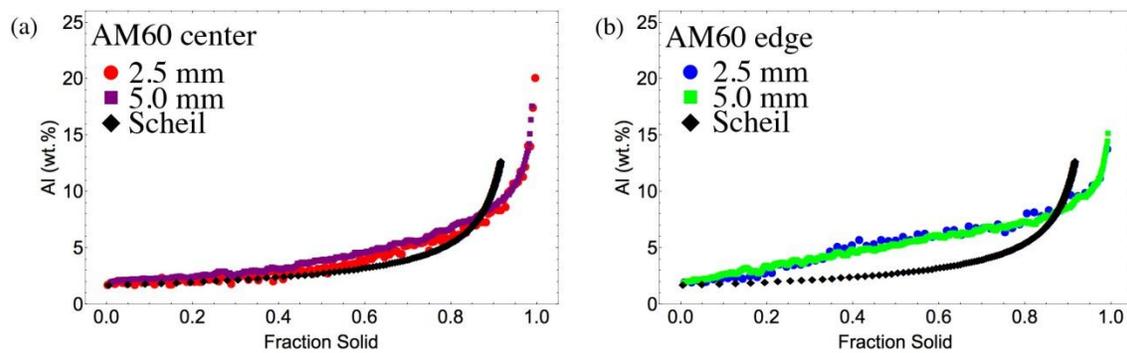
Figure III-156: Thickness effect on microsegregation behavior in AM60 at (a) center-line and (b) edge of plate.

Technology Transfer Path

In addition to publications and presentations at national and international conferences, project knowledge including experimental data and micro-models will be transferred to industry and the research community through the NIST DOE-EERE Mg Kinetics Repository and the UM DOE PRISMS Materials Commons. The database structure and content used for The Materials Commons is being constructed in coordination with national Materials Genome Initiative repository efforts lead by NIST. Discussions with key repository experts at NIST and elsewhere have already commenced. This will ensure that the information developed in this program will be broadly accessible to the technical community.

Conclusion

During FY 2014, the focus has been on developing and refining the techniques that will be used for quantitative characterization of the microsegregation behavior of HPDC Mg alloys and eventually in SVDC alloys following heat treatment. Current commercial ternary alloys, AM60 and AZ91 were used to develop and validate the methods. The sample preparation and data analysis procedures have been well established both for determining grain size using EBSD and

for the construction of microsegregation profiles using EPMA. When considering the breadth of the proposed experimental alloy matrix, it was essential to arrive at consistent methods that will yield high quality data. Future data acquisition and analysis will be straightforward and effective.

Microstructural analysis has shown that due to rapid solidification at the edges of the casting, there is a higher volume of Al-rich phases at the edge of the castings that at the center. This is consistent with a higher average Al concentration in EPMA scans of the edge regions compared with measurements from the center of castings. This indicates that macrosegregation of Al occurs during HPDC. EBSD scans have revealed that the alpha-Mg microstructure in HPDC AM60 and AZ91 consists of both fine (~5 μm) grains and larger (20 to 80 μm) externally solidified crystals. Nearly 10,000 grains have been characterized in one of the material conditions. These large scans facilitate meaningful comparisons as a function of plate thickness, alloy, and through-thickness location. In addition, when made available to the technical community through the NIST Repository and the Materials Commons, these comparisons will provide excellent statistics for the construction of structure-property models.

Measurements of microsegregation at edge and mid-thickness locations in the cross-section of HPDC AM60B and AZ91 plates reveal location dependent Al microsegregation

III.x Transformation Kinetics and Alloy Microsegregation in High Pressure
Die Cast Magnesium Alloys – The University of Michigan

Allison–University of Michigan

behavior. At the center locations, the microsegregation results are consistent with Scheil solidification modeling predictions. There is a large deviation from Scheil predictions in the microsegregation behavior at the edge of the plates. In contrast, plate thickness did not have a significant effect on microsegregation behavior of Al as measured at edge and mid-thickness in 2.5mm and 5.0 mm thick AM60B plates.

Presentations/Publications/Patents

Allison, J.E. (November 2013). "Phase Transformation Kinetics and Alloy Microsegregation in High Pressure Die Cast Magnesium Alloys", Program Kick-Off, Washington.

References

1. Slade, S. Magnesium : Bridging Diverse Metal Markets. In *Magnesium Technology*; Agnew, S. R.; Neelameggham, N. R.; Nyberg, E. A.; Sillekens, W. H., Eds.; Wiley, 2010; pp. 91–95.

2. Gjestland, H.; Westengen, H. Advancements in High Pressure Die Casting of Magnesium. *Adv. Eng. Mater.* **2007**, *9*, 769–776.

3. Kim, J. S.; Isac, M.; Guthrie, R. I. L. Metal-Mold Heat Transfer And Solidification Of Magnesium Alloys In Belt Casting Processes. In *Magnesium Technology*; Luo, A. A., Ed.; Metallurgical Society of AIME, 2004; pp. 247–255.

4. Porter, D. A.; Easterling, K. E. *Phase Transformations in Metals and Alloys*; 2nd ed.; Nelson Thornes Ltd.: Cheltenham, UK, 1992; pp. 185–262.

5. Mirković, D.; Schmid-Fetzer, R. Directional Solidification of Mg-Al Alloys and Microsegregation Study of Mg Alloys AZ31 and AM50: Part I. Methodology. *Metall. Mater. Trans. A* **2009**, *40*, 958–973.

6. TerBush, J. R.; Saddock, N. D.; Jones, J. W.; Pollock, T. M. Partitioning of Solute to the Primary α-Mg Phase in Creep-Resistant Mg-Al-Ca–Based Cast Alloys. *Metall. Mater. Trans. A* **2010**, *41*, 2435–2442.

7. Zheng, X.; Luo, A. A.; Zhang, C.; Dong, J.; Waldo, R. A. Directional Solidification and Microsegregation in a Magnesium-Aluminum-Calcium Alloy. *Metall. Mater. Trans. A* **2012**, *43*, 3239–3248.

8. Sadayappan, K.; Kasprzak, W.; Brown, Z.; Quimet, L.; Luo, A. A. Characterization of Magnesium Automotive Components Produced by Super-Vacuum Die Casting Process. *Mater. Sci. Forum* **2009**, *618-619*, 381–386.

9. Luo, A. A. Advanced Casting Technologies For Lightweight Automotive Applications. *China Foundry* **2010**, *7*, 463–469.

10. Li, M.; Zhang, R.; Allison, J.E. Modeling Casting and Heat Treatment Effects on Microstructure in Super Vacuum Die Casting (SVDC) AZ91 Magnesium Alloy. In *Magnesium Technology*; Agnew, S. R.; Neelameggham, N. R.; Nyberg, E. A.; Sillekens, W. H., Eds.; Wiley, 2010; pp. 623–627.

11. Miao, J.; Li, M.; Allison, J. E. Microstructure Evolution During Heat Treatment In A Super Vacuum Die Casting AZ91 Alloy. In *Proceedings of Magnesium 2012*; pp. 493–498.

12. Wang, J.; Li, M.; Ghaffari, B.; Chen, L.-Q.; Miao, J.; Allison, J. A Microstructural Evolution Model For Mg 17 Al 12 Precipitates In AZ91.in *Proceedings of Magnesium 2012*, WJ. Poole, Editor, Vancouver, BC, Canada, **2012**, 163–170.

13. Guo, Z.-P.; Xiong, S.-M.; Liu, B.-C.; Li, M.; Allison, J.E. Effect of Process Parameters, Casting Thickness, and Alloys on the Interfacial Heat-Transfer Coefficient in the High-Pressure Die-Casting Process. *Metall. Mater. Trans. A* **2008**, *39*, 2896–2905.

14. Guo, Z.-P.; Xiong, S.-M.; Liu, B.-C.; Li, M.; Allison, J.E. Determination Of The Heat Transfer Coefficient At Metal–Die Interface Of High Pressure Die Casting Process Of AM50 Alloy. *Int. J. Heat Mass Transf.* **2008**, *51*, 6032–6038.

15. Li, S.; Xiong, S.; Liu, B.; Li, M.; Allison, J. E. Numerical Simulation Of Flow-Induced Air Entrapment Defects In The High Pressure Die Casting Process. In *Magnesium Technology*; Agnew, S. R.; Neelameggham, N. R.; Nyberg, E. A.; Sillekens, W. H., Eds.; Wiley, 2010; pp. 613–616.

16. Mirković, D.; Schmid-Fetzer, R. Directional Solidification of Mg-Al Alloys and Microsegregation Study of Mg Alloys AZ31 and AM50: Part II. Comparison between AZ31 and AM50. *Metall. Mater. Trans. A* **2009**, *40*, 974–981.

IV CARBON FIBER AND POLYMER COMPOSITES

IV.1 Development and Commercialization of a Novel Low-Cost Carbon Fiber–Zoltek Companies, Inc.

Bill Regan, Principal Investigator
Vice President of Engineering and Technology
3101 McKelvey Road
St. Louis, Missouri 63044
Phone: (314) 291-5110
E-mail: bill.regan@zoltek.com

Carol Schutte, Technology Area Development Manager
U.S. Department of Energy
1000 Independence Avenue, SW
Washington, DC 20585
Phone: (202) 586-1022
E-mail: carol.schutte@ee.doe.gov

Aaron Yocum, Contract Manager
National Energy Technology Laboratory
3610 Collins Ferry Road
Morgantown, WV 26507-0880
Phone: (304) 285-4852; Fax (304) 285-4403
E-mail: aaron.yocum@netl.doe.gov

Contractor: Zoltek Companies, Inc.
Contract No.: DE-EE0005394

Abstract/Executive Summary

The objectives of this project are to develop and commercially validate a low cost carbon fiber meeting the target cost of $5.00/lb. and target properties of strength > 250,000 pounds per square inch (psi), modulus of elasticity > 25,000,000 psi, and strain-to-failure > 1%. This project is a joint development effort of Zoltek Companies, Inc. and Weyerhaeuser Company. The bases of this development are innovative, patent pending technology for wet-spinning of lignin/polyacrylonitrile (PAN) blended polymer precursor fibers combined with modifications to existing commercial precursor and carbon fiber manufacturing processes. This approach, which combines the fiscally conservative use of existing carbon fiber infrastructure with the innovative development of a new low cost, renewably based lignin precursor material, provides the greatest chance of near term commercial adoption and a line of sight to low cost carbon fiber suitable for light-weighting automotive structures as well as other energy efficient applications.

The objectives of Phase 1 were to optimize the precursor technology and carbon conversion parameters to achieve a precursor fiber with maximum lignin content that converts to a carbon fiber exceeding the defined property requirements. The final objective of Phase 1 was to validate the scale up of this technology to full scale commercial production using existing spinning and carbon fiber manufacturing facilities. Phase 1 of the project was successfully completed during FY 2013, and composite performance objectives were validated with 25% lignin/PAN carbon fiber early in the current fiscal year.

From the technical issues encountered and knowledge gained during from the Phase 1 commercial scale trial, the technical plan formulated for Phase 2 sought to (1) develop and optimize pilot and commercial precursor polymer and spinning parameters to eliminate production problems identified in Phase 1 and to maximize lignin content to > 35% to achieve lowest possible precursor cost; (2) develop and optimize oxidation and carbonization parameters for lowest cost, highest performance carbon fiber; and (3) identify and implement improved manufacturing concepts and equipment that will further drive down costs toward project objective of $5.00/pound. The final objective of Phase 2, scheduled to take place during FY 2014, was to validate the scale up of the improved precursor and carbon fiber manufacturing technologies to full scale commercial production using manufacturing facilities that have been modified for operational efficiency and energy reduction.

Accomplishments

- Over 140 pilot scale polymer runs and 500 pilot scale spinning trials have been completed to evaluate various blends of lignin and PAN polymers, various solution parameters, and various spinning conditions to define best polymer and spinning conditions to achieve precursor fibers that can convert to carbon fibers meeting project objectives. (FY 2012 – 2014)

- Over 200 pilot oxidation trials were completed to establish processing parameters required to fully stabilize the pilot precursor fibers so that they can survive the carbonization process. A small number (< 25) of these pilot oxidized fibers have been successfully carbonized into carbon fiber exceeding project objectives. These results helped define the polymer, precursor spinning, and oxidation parameters used for the Phase 1 full scale commercial validation executed in FY 2013.

- These pilot scale precursor fibers, oxidized fibers, and carbon fibers were fully characterized for physical, chemical and mechanical properties and have also been

examined using scanning electron microscopy (SEM) to assess fiber morphologies. (FY 2012 – 2014)

- A large database of thermal properties was generated to determine the chemical reaction behavior of lignin/PAN precursor fibers to understand the oxidation/stabilization process required to produce carbon fiber. This data includes differential scanning calorimetry (DSC), thermal gravimetric analysis (TGA), and dynamic mechanical analysis (DMA). (FY 2012 – 2014)

- In preparation for the Phase 1 commercial scale validation of the lignin/PAN precursor and carbon fiber technologies, 10,000 pounds of high purity lignin polymer were produced, commercial scale polymer mixing equipment was developed and readied for production operation, and a commercial scale spinning line was prepared for the commercial trial conducted in FY 2013. (FY 2012)

- The Phase 1 commercial scale precursor spinning trial was completed in March 2013, producing a total of 13 metric tons of lignin/PAN precursor with lignin contents of 25% and 35%. Precursor fiber spools with acceptable quality and sufficient spool lengths, approximately nine metric tons, were shipped to the Zoltek Hungary plant for carbon conversion. (FY 2013)

- The Phase 1 commercial scale lignin/PAN carbon fiber production was completed in June 2013. Various problems were encountered during this first commercial scale trial resulting in a lower than expected volume of carbon fiber produced. 1000 kilograms of the 25% lignin/PAN carbon fiber were successfully spooled. (FY 2013)

- The commercial scale carbon fibers produced were tested and properties exceeded project targets. Subsequently, the fibers were used to produce prepreg tapes, pultruded bars, unidirectional stitched fabrics, and carbon sheet molding compounds (SMC). The prepreg tapes were molded into panels and tested with results indicative of expected properties. The pultruded bars were also tested with similar results. Tests on composites made from fabrics and SMC were completed in early FY 2014, completing all Phase 1 efforts. (FY 2014)

- Pilot scale technical efforts in the current year evaluated a broad range of PAN polymer molecular weights, comonomer ratios, and spinning conditions to produce the best precursor morphologies obtained to date for polymer blends ranging from 25% to 45% lignin. The principal objective to eliminate the presence of macrovoids, believed to be partially responsible for the low process yield in carbonization, was achieved. Fibrillation, however, was still observed in the higher lignin content precursor blends. (FY 2014)

- Two 10,000-pound quantities of high purity lignin were produced by Weyerhaeuser, dried, and delivered to the Zoltek Mexico facility in preparation for the Phase 2 commercial spinning run. (FY 2014)

- Following computational fluid dynamics (CFD) studies conducted in FY 2013 to upgrade performance of the oxidation process, a single oxidation oven was modified on the commercial line designated for lignin carbon fiber production in Mexico. Validation of the upgrade was completed in June, 2014, confirming improved air flow uniformity within the oven and lower energy consumption per unit of output. The longer effective heated length of the re-configured oven offers the potential for higher process speed and further cost reduction. The remaining two oxidation ovens in the same line are being modified in likewise fashion with completion expected in the first quarter of FY 2015. (FY 2014)

Future Directions

The overriding objective and enabling event to successfully complete the project is the development of an acceptable solution to the lignin leaching problem. The technical approach will focus efforts in the evaluation of an alternate set of wet spinning conditions which suppress lignin leaching while maintaining acceptable precursor spinnability and morphology. The use of filtration techniques could also be advantageous provided the degree of leaching can be reduced to a very low level. Contingent on finding an acceptable solution to the lignin leaching problem:

- Pilot scale development of precursor polymer and spinning will continue to optimize materials and process parameters for commercial product with a lignin content of $\geq$ 35% at the lowest possible precursor cost. In addition, development and optimization of oxidation and carbonization parameters will be continued to achieve lowest cost, highest performance carbon fiber possible.

- Commercial spinning line modifications (yet to be defined) will be made to support the Phase 2 objectives.

- Multiple industrial scale reactor runs will be performed to develop and validate scale up of high molecular weight PAN required. This will lead to multiple commercial scale spinning trials to fully validate polymer and precursor spinning prior to final product production validation in 3rd quarter of calendar 2015.

- Final validation of commercial scale process and product will be accomplished during fourth calendar quarter of 2015 followed by the development of a final cost model as well as a commercial product implementation plan.

- Final task of the project will be to complete characterization of commercial carbon fiber produced from lignin/PAN precursor fiber, including putting the fiber into various intermediate product forms for composite testing. Some of these products will be distributed to various automotive original equipment manufacturers (OEMs) and Tier 1 suppliers for their evaluations and part demonstrations.

Technology Assessment

- Target: Achieve a $ 5.00/pound carbon fiber with tensile strength > 250,000 psi and tensile modulus > 25,000,000 psi using renewable (non-petroleum based) raw materials.

- Technology target: Produce lignin/PAN blend precursors at ≥ 35% lignin content with no macrovoids and under process conditions that support low cost commercial production.
- Gap: Lignin/PAN blend precursors with low macrovoid content have been produced at pilot scale with lignin contents as high as 40-45%, but the wet spinning conditions necessary to achieve this result lead to excessive leaching of lignin from the spin dope. This level of leaching (10-20%) cannot be managed in a commercial process without incurring an unacceptable cost penalty.
- Technology target: Demonstrate that high molecular weight PAN polymer produced in the pilot scale reactor can be reproduced in the commercial scale reactor.
- Gap: Production of acceptable lignin/PAN polymer blends has required the use of PAN polymer with a higher molecular weight than standard polymer. Reproducing pilot scale PAN polymer at commercial scale was problematic in Phase 1.
- Technology target: Increase the process yield of lignin/PAN blend precursor in the carbonization step.
- Gap: In the Phase 1 commercial demonstration and in subsequent pilot studies, the process yield of oxidized precursors passed through the carbonization furnaces has been unacceptably low.

✧   ✧   ✧   ✧   ✧

Introduction

The objectives of this project are to develop and commercially validate a low cost carbon fiber meeting the target cost of $5.00/lb. and target properties of strength > 250,000 psi, modulus of elasticity > 25,000,000 psi, and strain-to-failure > 1%. This project is a joint development effort of Zoltek Companies, Inc. and Weyerhaeuser Company. The bases of this development are innovative, patent pending technology for wet-spinning of lignin/PAN blended polymer precursor fibers combined with modifications to existing commercial precursor and carbon fiber manufacturing processes. This approach, which combines the fiscally conservative use of existing carbon fiber infrastructure with the innovative development of a new low-cost, renewably based lignin precursor material, is believed to provide the greatest chance of near term commercial adoption and a line of sight to low-cost carbon fiber suitable for light-weighting automotive structures as well as other energy efficient applications.

Initial feasibility of technology was demonstrated during Phase 0 in FY 2011, prior to award of this project. The objectives of Phase 1 were to optimize the precursor technology and carbon conversion parameters to achieve a precursor fiber with maximum lignin content that converts to a carbon fiber exceeding the defined property requirements. The final objective of Phase 1 was to validate the scale up of this technology to full scale commercial production using existing spinning and carbon fiber manufacturing facilities. Phase 1 of

the project was successfully completed with 25% lignin/PAN carbon fiber during fiscal year FY 2013.

From the technical issues encountered and knowledge gained during from the Phase 1 commercial scale trial, the technical plan formulated for Phase 2 sought to (1) develop and optimize pilot and commercial precursor polymer and spinning parameters to eliminate production problems identified in Phase 1 and to maximize lignin content to ≥ 35% to achieve lowest possible precursor cost; (2) develop and optimize oxidation and carbonization parameters for lowest cost, highest performance carbon fiber; and (3) identify and implement improved manufacturing concepts and equipment that will further drive down costs toward project objective of $5.00/pound. The final objective of Phase 2, scheduled to take place during FY 2014, was to validate the scale up of the improved precursor and carbon fiber manufacturing technologies to full scale commercial production using manufacturing facilities that have been modified for operational efficiency and energy reduction. Phase 2 was initiated in FY 2013 in parallel with completion of Phase 1 and, under a revised schedule, will continue through FY 2015. The project has encountered a technical hurdle (excessive lignin leaching from the polymer dope during precursor spinning) that, as of the end of FY 2014, lacks an acceptable solution.

Approach

The approach used for this project consists of a logical sequence of series and parallel tasks focused on achieving the project objectives. These tasks develop and validate the required technologies through a classical building block approach from lab scale through pilot scale to full scale commercial demonstration. Descriptions of tasks performed during Phase 1 of project and, in some cases, continuing into Phase 2 are outlined below:

Task 1 – Cost Model Development: An initial spreadsheet cost model was developed early in Phase 1 based on Zoltek standard costs to produce PAN precursor and resulting carbon fiber and using estimated material substitution cost savings replacing various percentages of PAN with lignin polymer. This cost model will be refined based on process improvements achieved during Phase 2.

Task 2 – Polymerization and Solution Studies: Solution studies have been done throughout the project to assess solubility, stability, and spinnability of lignin/PAN spinning solution dopes. Phase 1 identified that PAN polymers with higher molecular weights would be required to achieve needed spinning viscosities for the blended polymer solutions. Significant technology development in this area was continued in Phase 2 with considerable success achieved in preventing macrovoid formation in trial precursors. Little success was achieved, however, in the effort to eliminate the leaching of lignin from polymer dopes during coagulation.

Task 3 – Lab and Pilot Scale Spinning: Develop and validate spinning parameters at lab scale leading to spinning of larger tow precursor fibers at pilot scale for batch and

continuous oxidation studies. Approximately 500 pilot scale precursor spinning trials have been performed to date in the project. This work will continue through Phase 2 to define optimum parameters for commercial product validation.

Task 4 – Pilot Scale Oxidation and Carbonization Development: Perform pilot oxidation and carbonization studies leading to selection of candidate product and process conditions for full scale development and validation. Approximately 200 pilot oxidation trials have been performed throughout Phase 1 and early stages of Phase 2. This effort will continue in Phase 2 to define optimum parameters for commercial product validation.

Task 5 – Analytical Studies: Perform thermal analysis, chemical analysis, microscopy, mechanical and physical property testing at all stages of development. Hundreds of analytical tests have been performed throughout the program and this will continue through evaluations of final product validation. In addition, hundreds of SEM images have been generated on precursor fibers, oxidized fibers, and carbon fibers. Microscopy is a primary tool for assessing morphologies and quality of the development products.

Task 6 – Large Scale Lignin Production: In Phase 1, 10,000 pounds of high purity lignin polymer was produced at Weyerhaeuser pilot facility to be used for full commercial scale validation of lignin/PAN precursor fiber and resulting carbon fiber. In Phase 2, approximately 20,000 pounds of lignin polymer was produced to allow for more large scale studies prior to final commercial validation and to allow for a larger quantity of carbon fiber production during the validation trial.

Task 7 – Commercial Scale Equipment: In Phase 1, large scale lignin/PAN mixing equipment was developed to provide the blended polymer dope for commercial scale trial. Zoltek commercial spinning line 1 also underwent slight modifications prior to producing the lignin blend precursor used for Phase 1 commercial carbon conversion. Spinning line 1 is also earmarked for commercial scale production of precursor for the final commercial carbon fiber demonstration. Based on the level of success achieved in addressing the lignin leaching problem, further modifications to spinning line 1 may be required.

Equipment modifications made to the oxidation ovens on the Zoltek line selected for final carbon fiber demonstration were implemented in calendar year 2014 to reduce energy consumption and increase production efficiencies toward the objective of achieving the lowest possible production costs.

Task 8 – Commercial Scale Validation: Each Phase of the project is completed with a commercial scale validation of process and product technologies. Phase 1 commercial scale validation was completed in FY 2013, successfully producing 25% lignin/PAN carbon fiber with properties exceeding target requirements. The Phase 1 commercial validation also identified process and product issues that needed further development and resolution as discussed earlier in this report. As a result, the Phase 2 commercial ready process and product validation has been delayed until the fourth quarter of calendar 2015.

Results and Discussion

Phase 2 Summary Results and Discussion

Although the Phase 2 work plan was actually initiated in late FY 2013 in parallel with Phase 1, the principal Phase 2 work was conducted in FY 2014. The objectives as defined at the beginning of the fiscal year were as follows:

Phase 2 Objectives

- Develop and optimize precursor polymer and spinning parameters for commercial product
  - eliminate problems identified in Phase 1
  - maximize lignin content; $\geq$ 35%
  - achieve lowest possible cost
- Develop and optimize oxidation and carbonization parameters for lowest cost, highest performance carbon fiber
- Identify and implement improved manufacturing concepts and equipment that will further drive down costs toward project objective of $5.00/pound
- Validate full commercial scale, production ready processes and products
- Define and initiate commercialization implementation plan

Technology Development

The course for technology development in Phase 2 was set by the results of the first commercial spinning trial conducted in Phase 1, which produced 25% and 35% lignin/PAN precursors. The major operational problem encountered during the spinning trial was excessive leaching of lignin from the spin dope in the coagulation and pre-stretching baths (see Figure IV-1). The problem was recognized at that time as a potential impediment to low cost commercial production of lignin/PAN precursor blends. While a technical solution to the problem (alternative solvent, adjustment to spinning conditions, etc.) was anticipated, a parallel effort was launched to cope with the problem by modifying the spinning process to filter lignin from the spinning solution and re-use the lignin filtrate in a closed loop process. Irrespective of the details of the various engineering options under consideration, cost implications associated with any approach selected would likely be unfavorable.

Figure IV-1: Heater coil in pre-stretching bath saturated with non-soluble residue during commercial spinning trial

A second technology objective was to improve filament morphology by eliminating the formation of macrovoids during coagulation and to do so with polymer blends containing ≥ 35% lignin to reduce the cost of the starting raw material. After many polymer and pilot spinning runs during which the PAN polymer molecular weight, comonomer ratio and spinning conditions were varied over a broad range, filament morphologies were obtained which met the stated objective for precursor blends as high as 45%. The SEM micrographs of coagulated filaments produced from higher molecular weight, batch-prepared (BP) PAN polymers and lignin in 35, 40 and 45% blends are presented in Figure IV-2, Figure IV-3 and Figure IV-4. In parallel, analytical techniques were developed at Weyerhaeuser to characterize the molecular weight of the various polymers formulated.
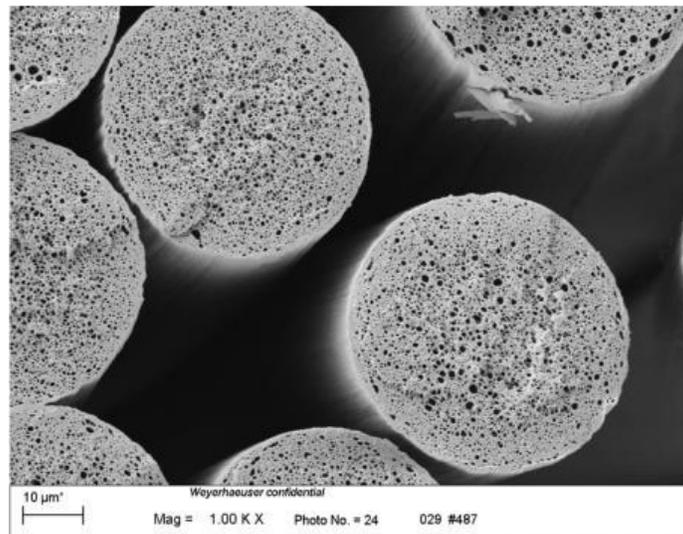
35% lignin/PAN precursor fiber from BP with standard co-monomer ratio – coagulated bath

Figure IV-2: Precursor fiber sample #487.
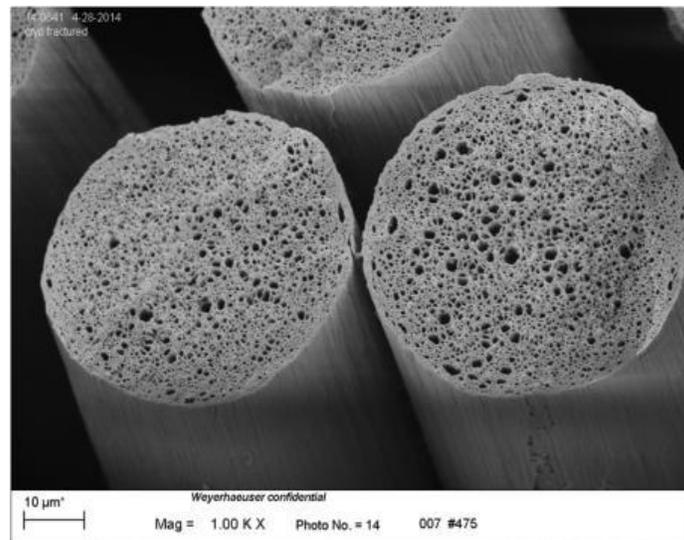
40% lignin/PAN precursor fiber from BP with standard co-monomer ratio – coagulated bath

Figure IV-3: Precursor fiber sample #475.
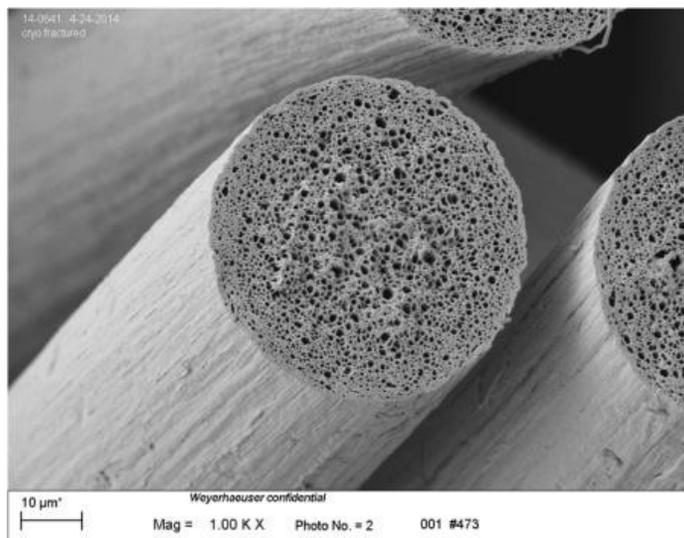
45% lignin/PAN precursor fiber from BP with standard co-monomer ratio – coagulated bath

Figure IV-4: Precursor fiber sample #473.

The improvement in morphology of the precursors is clear from the micrographs (no macrovoids). However, use of these batch polymers can also increase the dynamic viscosity of the polymer dope solution causing difficulties in the spinning process, placing an upper limit on the PAN molecular weight.

One other feature to emphasize is the increase in fibrillation that occurs with increasing lignin content, evident in the following SEM shots (Figure IV-5 and Figure IV-6). Fibrillation can lead to bridging between filaments (filament sticking), which can develop during oxidation and negatively impact tensile property development during carbonization.

Follow-on studies were conducted with lignin/PAN blends using batch polymers formulated with a higher comonomer

ratio which demonstrated that fibrillation can be reduced using this approach, although additional work is required to confirm a performance enhancement in oxidation and carbonization.

Another set of experiments was also carried out wherein precursors were spun from standard PAN polymer (no lignin) and sized with different recipes and concentrations of spin finish to quantify the impact of the finish on the thermal reaction profiles of the fibers during oxidation. The family of DSC curves shown in Figure IV-7 for various precursor fibers (PF) demonstrates that a finish applied to the surface of the fibers, even at low levels, can influence the thermal behavior of the fibers during oxidation. Certain of the size components are specifically formulated to lubricate the filaments to

suppress filament breakage and sticking. The use of additional lubricant was implemented to good advantage during the Phase 1 commercial carbon conversion trial to promote carbonization.

Operational Efficiencies Concepts Development and Modifications to Commercial Equipment

Increasing process throughput represents the greatest potential for reducing unit conversion costs. Toward this objective, computational fluid dynamics (CFD) analyses of oxidation oven air flow were performed in FY 2013 to assess the potential for increasing throughput through oxidation. This effort identified needed oven equipment modifications which were installed and validated in FY 2014 in a single oxidation oven on the commercial carbon line at Zoltek Mexico earmarked for conversion of lignin blend precursor.

Validation of the modifications was carried out under real-world production conditions using Zoltek standard PAN precursor (with a historical database). The two-week trial yielded the expected improvements – greater recirculation air

flow volume with improved vertical and horizontal flow uniformity within the heated chamber. The net result was the creation of an oven with a longer usable heated length, a more uniform environment for oxidation of the tows with reduced potential for a destructive exotherm, and at approximately 5% lower energy input. The remaining two ovens in the line were subsequently modified in a likewise fashion with validation of the entire line scheduled to take place in the first quarter of FY 2015.

After analyzing various engineering options to modify spinning line 1 to deal with the leaching problem via continuous filtration of the spinning solution and capture of the lignin for re-use, it was decided that none of the options present a viable commercial solution at the current level of leaching (10-20% loss of lignin from the spin dope). A novel filtration technique which uses an oscillating membrane to execute filtrate separation may offer some advantage provided the level of leaching can be reduced by an order of magnitude.
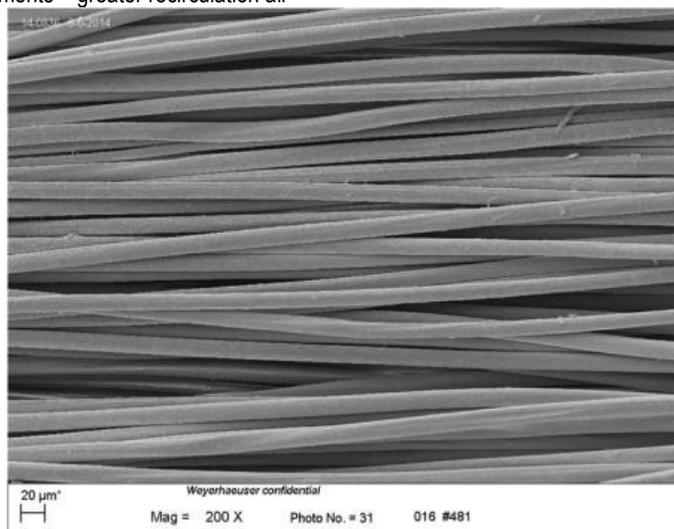
25% lignin/PAN precursor fiber from BP with standard co-monomer ratio – longitudinal view

Figure IV-5: Precursor fiber sample #481.
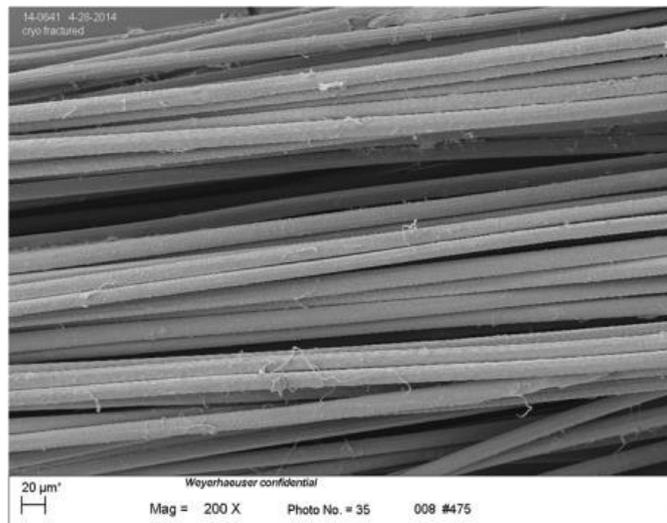
40% lignin/PAN precursor fiber from BP with standard co-monomer ratio – longitudinal view

Figure IV-6: Precursor fiber sample #475.
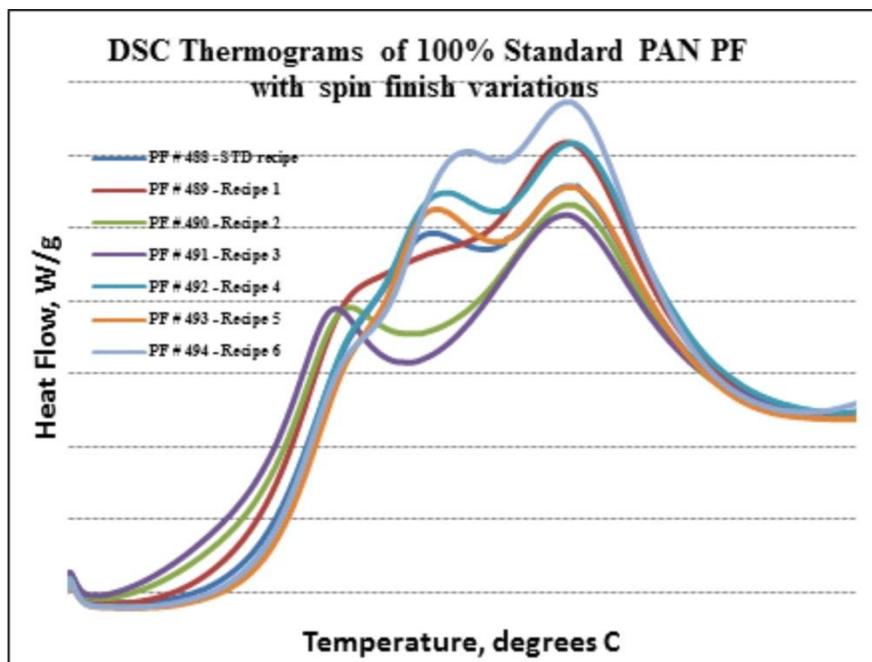
Figure IV-7: DSC Thermograms.

Lignin Production

The lignin pilot plant (LPP) has operated most of the year to produce high purity lignin for the commercial polymer and spinning runs originally planned for FY 2014. Two 10,000-pound quantities of lignin were produced, toll-dried at an external location, and shipped to Zoltek Mexico for storage. The shipments were received in Mexico in April and September 2014. The LPP has now been mothballed since no further lignin is expected to be needed to fulfill the project objectives.

Technology Transfer Path

The carbon fibers produced during the Phase 1 commercial trial were tested with properties exceeding project targets. Subsequently, the fibers were used to produce prepreg tapes, pultruded bars, unidirectional stitched fabrics, and carbon SMC. The prepreg tapes were molded into panels

and tested, indicating expected properties. The pultruded bars and composites made from fabrics and SMC were also tested with similar results.

A similar validation will be done at the end of Phase 2 of the project to demonstrate the performance of the fully commercialized lignin/PAN precursor and carbon fiber technology. The culmination of Phase 2 would validate the fully commercially robust process and product for lignin/PAN based carbon fiber. After successful validation of the Phase 2 commercial product, efforts can then be devoted to implementation of a commercialization plan to be developed in the last quarters of the project.

Conclusions

The technical activities conducted during Phase 1 of the project successfully demonstrated the feasibility of producing lignin/PAN blend precursors and converting those precursors to carbon fiber on a commercial scale. The carbon fibers produced possessed mechanical properties which exceeded project objectives and further gave acceptable property translation in a range of downstream intermediate and composite processes. However, several operational problems and material deficiencies were encountered in the course of Phase 1, which defined the plan for the follow-on work addressed during Phase 2 in FY 2014.

Foremost among the operational problems was the inability to retain all of the lignin in the precursor during the spinning operation, resulting in excessive lignin leaching into the coagulation and first stretching baths. The cost implications of implementing an engineering fix to handle this amount of leaching on a continuous basis are considered to be unacceptable in light of the cost objectives of the project. Efforts were re-directed to address this problem as discussed in previous sections of this report.

A second objective was to increase the lignin fraction of the precursor blend from 25% to ≥35% without generating macrovoids during the spinning operation. Technical efforts were successful in achieving this objective although the set of spinning conditions required to do so are not complementary to lowering the leaching level.

Although several of the improved precursors were successfully converted to carbon fiber using pilot and commercial facilities, the yield obtained in the carbonization step of the process is still below target and will remain an area of focus.

Presentations/Publications/Patents

Presentations

1. Husman, G. (April 2012) "Development and Commercialization of a Novel Low-Cost Carbon Fiber." Presented at the SAE 2012 World Congress & Exhibition, April 24, 2012.

2. Husman, G. (May 2012) "Development and Commercialization of a Novel Low-Cost Carbon Fiber." Presented at the DOE Vehicle Technologies Office Annual Merit Review, May 16, 2012.

3. Husman, G. (June 2012) "Development and Commercialization of a Novel Low-Cost Carbon Fiber." Presented at the International Lignin Biochemicals Conference in Toronto, Canada, June 21, 2012.

4. Husman, G. (September 2012) "Development and Commercialization of a Novel Low-Cost Carbon Fiber." Presented at the Society of Plastics Engineering / Advanced Composites Conference and Exhibition, SPE /ACCE, September 13, 2012.

5. Husman, G. (November 2012) "Development and Commercialization of a Novel Low-Cost Carbon Fiber." Presented at the JEC Americas Composites Show and Conference, November 8, 2012.

6. Husman, G. (May 2013) "Development and Commercialization of a Novel Low-Cost Carbon Fiber." Presented at the DOE Vehicle Technologies Office Annual Merit Review, May 15, 2013.

7. Husman, G. (September 2013) "Development and Commercialization of a Novel Low-Cost Carbon Fiber." Presented at the Plastic Modification for Automotive and Durable Goods Conference, Chicago, IL, September 4, 2013.

Patents:

U. S. Patent 8,771,832 B2, Lignin/polyacrylonitrile-containing dopes, fibers, and methods of making same, Bissett, Paul J. and Carole W. Herriott (This patent covers base technology developed at Weyerhaeuser prior to contract.)

IV.2 Advanced Oxidative Stabilization of Carbon Fiber Precursors— Oak Ridge National Laboratory

Felix L. Paulauskas, Principle Investigator
Oak Ridge National Laboratory
1 Bethel Valley Road
Oak Ridge, TN 37831
Phone: (865) 576-3785; Fax: (865) 574-8257
E-mail: paulauskasfl@ornl.gov

Truman Bonds, Jeremey Jackson, and Corey Bounds, Principal Investigators
RMX Technologies (RMX)
835 Innovation Drive, Suite 200
Knoxville, TN 37932
Phone: (865) 777-2741; Fax: 865-671-0650
E-mail: tbonds@rmxtechnologies.net

C. David Warren, Field Technical Monitor
Oak Ridge National Laboratory
1 Bethel Valley Road
Oak Ridge, TN 37831
Phone: (865) 574-9693; Fax: (865) 574-6098
E-mail: warrencd@ornl.gov

Carol Schutte, Technology Area Development Manager
U.S. Department of Energy
1000 Independence Avenue, SW
Washington, DC 20585
Phone: (202) 586-1022
E-mail: carol.schutte@ee.doe.gov

Ed Owens, Technology Area Development Manager
U.S. Department of Energy
1000 Independence Avenue, SW
Washington, DC 20585-0340
Phone: (202) 586-4830; Fax: (202) 856-2476
E-mail: Edwin.Owens@ee.doe.gov

Contractor: Oak Ridge National Laboratory
Contract No.: DE-AC05-00OR22725

Abstract/Executive Summary

The cost of producing carbon fiber (CF) is the single largest obstacle to its incorporation in future automotive systems. According to a cost study, 51% of the cost of producing CF is attributable to the cost of the precursor; 43% of the cost of CF is attributable to the conversion of the precursor into CF and activating the surface for resin compatibility; and the remaining 6% of the cost is for spooling and handling [1]. Significant effort is being expended on developing lower cost, higher rate production technologies. Conversion work includes development of a higher speed, lower cost oxidative stabilization process and development of a microwave-assisted plasma process carbonization method that is funded through a separate DOE program.

This task is aimed at developing an atmospheric plasma processing technique to rapidly and inexpensively oxidize polyacrylonitrile (PAN) precursor fibers. Conventional oxidation is a slow thermal process that typically consumes more than 80% of the processing time in a conventional CF conversion line. A rapid oxidation process could dramatically increase the conversion line throughput and appreciably lower the fiber cost.

The strategy for transitioning this technology to industry is to involve industry as early in the development process as is practical; this strategy will also reduce investment risk. The advanced oxidation task will be mature enough in the next 18 months to start involving oxidation oven manufacturers.

Accomplishments

- Completed a process-to-properties correlation on the bench-scale small reactor using a variety of techniques including chemical characterization using Fourier transform infrared spectroscopy to correlate chemical properties to physical and mechanical properties. The purpose was to understand the relationship between process parameters and final properties. (FY 2014)
- Completed construction and made operational the 1 ton/year plasma oxidation oven (the large reactor). (FY 2014)
- Conducted initial trials of the large reactor and resolved most engineering issues to optimize operation. (FY 2014)
- Processed two tows of commodity-grade, 24,000-filament precursor fiber in the large reactor in 30 min, reducing the oxidation time from the 80–120 min conventional process. Produced two spools of 100 ft each that were submitted to Oak Ridge National Laboratory (ORNL) for subsequent carbonization and mechanical testing. All properties exceeded DOE thresholds of 250 kilopounds per square inch (ksi) tensile strength, 25 million pounds per square inch (Msi) tensile modulus, and 1% strain to failure. (FY 2014)
- RMX Technologies established an industrial partnership with a major CF manufacturer to further commercialize the plasma oxidation technology. A letter of commitment was provided to DOE. (FY 2014)

Future Directions

- Further optimize performance of the large reactor to maximize mechanical properties of the fiber and minimize the required oxidation time.
- Expand capacity of the winding equipment to 4-6 tows to maximize throughput and economics.
- Demonstrate robustness of the plasma oxidation technology with long duration runs.
- Examine the stability and consistency of the process and equipment by examining and reducing variability in oxidized PAN fiber (OPF) density to less than 0.2 grams per cubic centimeter (g/cc) and mechanical properties along both the length of the fiber and the width of the large reactor.

Technology Assessment

- Target: Develop higher throughput (approximately 3 times faster) oxidation of CF, thus lowering the manufacturing costs of CF and increasing the material throughput and production rate.
- Gap: Conventional oxidation methods require 80-120 min, thus limiting CF production rates. Faster oxidation could reduce the cost per pound for downstream processes such as the carbonization, surface treatment, and sizing for manufacturing CF because mass throughput rates would be increased.
- Gap: Conventional oxidation methods contribute $1.78/pound (lb) [2] to the cost of CF and, more importantly, are the rate limiting and mass throughput limiting steps due to the long residence times required. Increasing the mass throughput would decrease the cost per pound attributable to oxidative stabilization for CF.
- Gap: The advanced oxidative stabilization process has been successfully demonstrated in the laboratory but has not yet been demonstrated while integrated with other parts of the CF conversion process or at speeds and reliability levels required for industrial adoption of the technology.

✧　　✧　　✧　　✧　　✧

Introduction

The purpose of this project is to develop a plasma processing technique to rapidly and inexpensively oxidize PAN precursor fibers. Conventional oxidation is a slow thermal process that typically consumes more than 80% of the processing time in a conventional CF conversion line. A rapid oxidation process could dramatically increase the conversion line throughput and appreciably lower the fiber cost. Atmospheric pressure plasma is a new technology that is relatively inexpensive to implement in industrial processes [3]. The oxidation residence time must be greatly reduced to effect fast conversion and match the speed of the advanced carbonization technology. This project is developing an

atmospheric plasma oxidation technology that could be used in line with conventional conversion equipment or integrated with other advanced fiber conversion processes to produce lower cost CF with properties suitable for use by the automotive industry. Critical technical criteria include (1) DOE programmatic goals (≥25 Msi tensile modulus, ≥250 ksi tensile strength, and ≥1.0% ultimate elongation in the finished fiber); (2) uniform properties over the length of the fiber tow; (3) repeatable and controllable processing; and (4) significant unit cost reduction compared with conventional processing. This effort is aimed at further developing those technologies to be able to continuously process 12-50 K tows of fiber and achieve properties meeting or exceeding program minimum property requirements with tow-to-tow and along-the-tow property variation within ±15%. The goals also include significantly reducing the time required for oxidative stabilization (conventionally 80-120 min) by a factor of 3 times which would permit greater fiber production rates and improved economics.

Approach

For this project, the researchers are investigating PAN precursor fiber oxidation using nonthermal plasma at atmospheric pressure. As illustrated in Figure IV-8, conventional oxidative stabilization produces a "core-shell" geometry with a distinct interphase between the (slowly growing) fully oxidized shell and the (shrinking) stabilized inner core. Plasma processing enhances oxygen diffusion and chemistry in the PAN oxidation process, accelerating the oxidized layer growth rate and oxidizing the fiber more uniformly, with a considerably less pronounced interface between the two regions. Previous work has shown that this approach can reduce the required residence time for complete oxidation.

The overall project approach is to develop and validate the plasma processing process up to the 1 ton/year scale. The successful operation of the large reactor now permits continuous operation at a pilot scale for demonstration. Once that is completed, a preproduction scale prototype unit will be designed. Construction of the preproduction scale prototype unit, in collaboration with an industrial partner, will be funded separately from this effort.

Results and Discussion

This fiscal year, the research effort focused on bringing the large reactor online. Once this was completed, two tows of commodity-grade, 24,000-filament precursor fiber were successfully processed, meeting a key go/no-go DOE milestone. During this process, significant engineering issues were resolved that enabled good performance from the large reactor.

Early in FY 2014, data analysis of experiments performed with the small reactor in FY 2013 was completed. These results are summarized in a quarterly progress report that was submitted to DOE. Several relationships were discovered that influenced the final implementation of the large reactor.
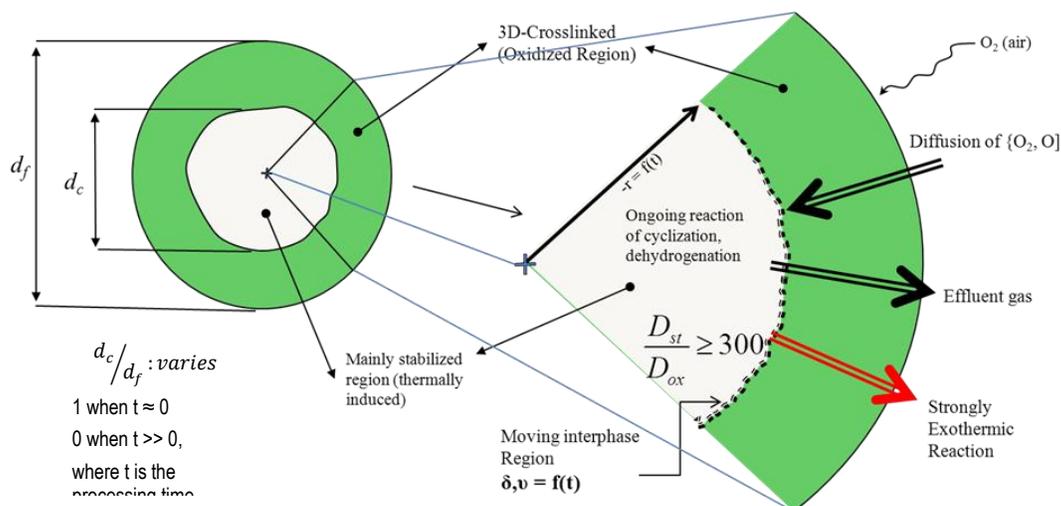
Figure IV-8: Single filament cross section during conventional oxidative stabilization process [4-6].

Figure IV-9: Processing two commodity-grade, 24,000-filament tows of precursor fiber in the large reactor.

The construction of the large reactor was completed in the spring of 2014. The stretcher system was fully expanded to operate using four independent zones. Winding equipment was installed that allows 1-3 tows to be processed simultaneously. Operations commenced in April 2014, and trial processing runs with a single tow revealed several equipment reliability issues that needed to be resolved. Nearly 4 months were required to work out these issues and to optimize the processing parameters to achieve the desired density metric for OPF. Once these issues were resolved, two spools of 100 ft each of OPF were processed (Figure IV-9) and sent to ORNL for carbonization. Even without any optimization of the stretch parameters, the carbonized fiber passed the mechanical property target of the DOE program.

RMX has learned from multiple industry sources that typical conventional oxidation unit energy consumption is in the range of 17 to 26 kilowatt hours per kilogram (kWh/kg) OPF when produced in the range of 1500 to 2500 tons/year.

This takes into account the full economy of scale savings realized at this level of operation. In comparison, the large reactor, at the 1 ton/year level, has exhibited a unit energy consumption of 44.8 kWh/kg of OPF while processing only two tows. Once the large reactor is processing six tows (its capacity), the unit energy consumption is estimated to be 14.9 kWh/kg of OPF. More work will be conducted to evaluate the energy requirements for larger scale reactors and confirm these numbers.

Because of equipment optimization an "enriched" air process gas is no longer necessary. In all the experiments discussed above, only plain, dried air was used-no additional process gas chemistries. This is an important milestone for maximizing the economic benefits of this technology.

The final deliverable for this project is the design of a larger plasma oxidation system scaled to be compatible with the CFTF. The follow-on of this project will be the construction of an advanced technology pilot line that will then be installed

at CFTF, and be used to validate the system performance and scalability as well as to produce the required quantities of advanced technology CFs to support the Vehicle Technologies Office's advanced development activities. The follow-on activity for scale-up will be a separate project from the current effort.

Technology Transfer Path

RMX Technologies has an exclusive option to license ORNL's rights to the intellectual property (IP) covering plasma oxidation. (RMX already has rights to this IP through co-invention.) RMX will therefore lead the commercialization effort and has already executed a plan to win industry commitments to support scaling this technology to industrial levels. A large CF manufacturer has become a partner to scale-up efforts. Several CF conversion equipment manufacturers are interested and conducting discussions with RMX.

Conclusion

The technology has now been proven at the 1 ton/year level. Further optimization will be made to maximize the performance of the large reactor and to examine various aspects of the advantages of this technology. At the conclusion of the current phase of this project (projected to be the end of FY 2015), researchers will be positioned to procure, install, test, and operate a pilot-scale (25 tons/year) plasma oxidation module in an advanced technology pilot line. The final deliverable for this project is the design of a larger plasma oxidation system scaled to be compatible with the CFTF.

Presentations/Publications/Patents

1. Bonds, T. A. (presenter); Paulauskas, F. L. October 2014) "Plasma Oxidation Commercialization Status Update." Presented at the Carbon Fiber Consortium meeting, Knoxville, TN.

2. Paulauskas, F.L., Advanced carbonization internal invention disclosure: 3164. Spinoff of oxidation technology.

3. Paulauskas, F. L. (February 2014) "Plasma Oxidation Commercialization Status Update." Presented at the Material Technical Team Meeting, Detroit, Michigan.

4. Paulauskas, F. L. (presenter); Bonds, T. A. (June 2014) "Advanced Oxidation & Stabilization of PAN-Based Carbon Precursor Fibers". Presented at the 2014 U.S. Department of Energy Hydrogen and Fuel Cells Program

and Vehicle Technologies Office Annual Merit Review and Peer Evaluation Meeting. Washington, DC.

5. Paulauskas, F. L. (presenter); Bonds, T. A. (March 2014) Internal presentation for programmatic evaluation for DOE presentation at ORNL. Oak Ridge National Laboratory, Oak Ridge, TN.

6. Paulauskas, F. L. (presenter); Bonds, T. A. (March 2014) "Plasma Oxidation Commercialization Status Update." Presented at the Carbon Fiber Consortium meeting, Knoxville, TN.

7. Paulauskas, F. L. et al., "Apparatus and Method for Carbon Fiber Surface Treatment." U.S. Patent 8,227,051 B1, (July 24, 2012).

8. Paulauskas, F. L. et al., "Rapid Oxidation of Polymeric Fibers for Producing Flame Retardant Fibers." 13/163,134 filed June 2011. U.S. Patent Office action 8/20/2014: 13/163134. Advanced oxidation high density. Docket 28107.

9. Paulauskas, F.L.; Ozcan, S., "Thermochemical surface treatment. Spin off of oxidation technology." US. Patent Office action: 13/163711, Docket 26789.

References

1. Friedfeld, B. (January 2007) "Cost Assessment of Lignin- and PAN-Based Precursor for Low-Cost Carbon Fiber." Presented at the Automotive Composites Consortium, Detroit, Michigan.

2. Wheatley, A.; Warren, D.; Das, S. (2014) "Low-Cost Carbon Fibre: Applications, Performance and Cost Models, Chapter 17, *Advanced Composite Materials for Automotive Applications.* John Wiley & Sons, Ltd.

3. Roth, J. R. (2001) "Atmospheric Pressure Plasma Sources," Chapter 15, *Industrial Plasma Engineering, Vol. 2: Applications to Nonthermal Plasma Processing.* Institute of Physics. Publishing: Philadelphia, 2001.

4. Paulauskas, F. L. (June 2010) "Advanced Oxidation and Stabilization of PAN-Based Carbon Precursor Fibers." Presented at the *DOE Annual Merit Review*, Washington, DC.

5. Paulauskas, F. L. (May 2004) "Temperature-Dependent Dielectric Measurements of Polyacrylonitrile Fibers." Presented at *SAMPE 2004,* Long Beach, CA.

6. White, S. M.; Spruiell, J. E.; Paulauskas, F. L. (May 2004) "Fundamental Studies of Stabilization of Polyacrylonitrile Precursor, Part 1: Effects of Thermal and Environmental Treatments." Presented at *SAMPE 2004,* Long Beach, CA.

IV.3　Carbon Fiber Technology Facility—Oak Ridge National Laboratory

Ronald Ott, Principle Investigator
Oak Ridge National Laboratory
Post Office Box 2008
Oak Ridge, TN 37830-6186
Phone: (865) 574-5172
E-mail: ottr@ornl.gov

Carol Schutte, Technology Area Development Manager
U.S. Department of Energy
1000 Independence Avenue, SW
Washington, DC 20585
Phone: (202) 586-1022
E-mail: carol.schutte@ee.doe.gov

Ed Owens, Technology Area Development Manager
U.S. Department of Energy
1000 Independence Avenue, SW
Washington, DC 20585-0340
Phone: (202) 586-4830; Fax: (202) 856-2476
E-mail: Edwin.Owens@ee.doe.gov

Contractor: Oak Ridge National Laboratory
Contract No.: DE-AC05-00OR22725

Abstract/Executive Summary

In March 2009, the US Department of Energy's (DOE's) Office of Energy Efficiency and Renewable Energy (EERE) issued a competitive call for proposals to construct and operate a highly flexible, highly instrumented, low-cost carbon fiber technology demonstration facility for demonstrating and evaluating new low-cost manufacturing technologies at a pilot scale. Oak Ridge National Laboratory (ORNL) responded to the call and was awarded the project. Construction of the Carbon Fiber Technology Facility (CFTF) began in March 2011, and the facility was commissioned for operations in March 2013.

The CFTF offers a unique, highly flexible, highly instrumented carbon fiber line for demonstrating advanced technology scale-up and for producing market-development volumes of prototypical carbon fibers. The CFTF has unique capabilities, with the flexibility to process a range of feed stocks and product forms that is unmatched anywhere in the world. The CFTF bridges the "valley of death" between laboratory research and commercial scale deployment of low-cost carbon fiber technologies, thus filling a critical need for promoting industrial competitiveness for the manufacture of carbon fiber in this nation.

The objective of this project is to accomplish the safe and reliable operation of the CFTF and to further DOE's objectives for large-scale commercialization of low-cost carbon fibers (LCCFs). The Vehicle Technologies Office (VTO) and the Advanced Manufacturing Office (AMO) provided operating funds for the project, which supports EERE's efforts towards transitioning technologies to industry, specifically with respect to cost-effective carbon fiber for composite materials in high-volume energy applications.

Activities funded under this project include the development and implementation of management systems to ensure safe, compliant, and reliable facility operations; the production of sufficient quantities of carbon fibers from lower-cost precursor materials to place LCCF in the hands of industry partners for the development of prototypical composite applications; and the establishment of a skilled workforce and a training system that can be leveraged to assist industry in the development of a skilled carbon fiber and composites workforce.

Accomplishments

- Operations during this period primarily focused on converting carbon fibers in a variety of formats in anticipation of supporting projects approved by AMO and VTP. Approximately 1275 kg were produced during the period from a variety of traditional polyacrylonitrile (PAN) precursor and textile acrylic fiber (T-PAN) precursor materials in small tow (12 K), medium tow (24 K and 48 K) and large tow (610 K) formats. (FY 2014)
- Progress was made in the development of the conversion protocol for the textile acrylic fibers supplied by the Kaltex Group, a large textile fiber producer located in northern Mexico. Tests of these production runs showed that tensile strength and tensile modulus values were improving, reaching up to 511 Ksi and 33.6 Msi, respectively. These results indicated that this material might be a good candidate for full-scale production of lower-cost carbon fibers. (FY 2014)
- During the second year of operation, the CFTF exhibited a perfect record of safety and environmental compliance. (FY 2014)

Future Directions

- ORNL will support a project sponsored by AMO and lead by Graftech International Holdings, Inc., based in Parma, Ohio. The project, "Low-Cost, Bio-Based Carbon Fiber for High Temperature Processing," will focus on developing a viable alternative to petroleum-based carbon fibers using biomass. The goal is to use this fiber in thermal insulation such as that used for high-temperature furnaces used to manufacture solar panel components.

- ORNL will continue the safe and reliable operation of the carbon fiber conversion line and the melt spinner, with a focus in FY 2015 on providing lower-cost carbon fibers produced from multiple textile acrylic fibers to industry partners for development of prototypical composite applications. The primary objective for this activity is to create industry "pull" for carbon fibers from this textile material and, ultimately, large-scale investment by industry in building production lines for mass producing lower-cost carbon fiber to supply automotive and other markets. Discussions with industry partners about scaling the textile PAN conversion process will continue with the intent of signing a cooperative research and development agreement (CRADA) in FY 2015.
- There are plans to scale up other alternative precursor materials, including lignin-based carbon fibers, cellulosic paper carbon materials, and polyolefin-based carbon fibers.

Technology Assessment

- Target: Scale up alternative, low-cost precursors and precursor-specific processing technologies for the manufacture of LCCFs. Alternative materials include multiple sources of textile acrylic fiber (FY 2015) and lignin for functional applications (FY 2015).
- Target: Scale up alternative, lower-cost processing methods for converting precursors into carbon fiber. Alternative processing methods include advanced oxidation and microwave-assisted plasma carbonization, as well as other processes that are under development.
- Target: Increase the production rate of textile acrylic precursors to match the capacity of the CFTF.
- Gap: Development of process science for stabilization and carbonization of these materials requires significant effort, including the collection of process data and correlation of large amounts of data sets to outcomes (e.g., material properties) to determine optimum processing conditions. For lignin-based carbon fibers, the melt spin-ability and stabilization times remain technical challenges.
- Gap: New processes can be developed as individual units at the laboratory. Interfacing of these new processes can be demonstrated for short-term operation at the pilot scale with 1-6 tows being simultaneously processed for 1-2 hours. Without the CFTF facilities and expertise, it would not be possible to scale the technologies to the level of continuous operation for days or weeks, which is a necessary step for the new technologies to be commercialized by private industry.
- Gap: Due to the large tow format (over 600,000 filaments) and the need to significantly stretch the material during the conversion process, achieving maximum throughput is challenging. Techniques are being developed in order to achieve a 2-fold increase in the throughput of the large tow format textile precursors.

✧   ✧   ✧   ✧   ✧

Introduction

The objective of this project is to accomplish the safe and reliable operation of the CFTF for the purpose of furthering DOE's objectives for large-scale commercialization of LCCFs. The tasks covered under this project are co-funded by the VTP and the AMO; they support the EERE's efforts towards transitioning technologies to industry, specifically with respect to cost-effective carbon fiber for composite materials in high-volume energy applications. Key strategies to be implemented by the project are to (1) develop and implement the process science for the conversion of alternative precursor materials into LCCF, (2) produce and disseminate quantities of LCCF to industrial partners for evaluation in composite components, and (3) develop a skilled workforce for the carbon fiber and composites industries.

Approach

The CFTF is open for tours in order for industry and others to see the technology and the process science being developed to produce LCCF from alternative precursor materials with industry appropriate mechanical properties. There is currently no commercial manufacturer of this particular LCCF, so the CFTF plans to produce enough of it for industry to evaluate. This is intended to produce industry demand for the technology, showcasing the quality of the LCCF in a multitude of end user platforms. The CFTF staff continues to hold discussions with industrial partners that are interested in scaling the processes being developed at the CFTF. The financial investment for industry to scale the technology is significant, and one not quickly decided upon. One of the missions of the CFTF is to transition this technology to industry for scaling, but numerous technical challenges remain that must be overcome to further reduce the risk for industry to implement the technology. These technical challenges are being addressed at the CFTF in collaboration with industry in order to reduce implementation risks. Some of these challenges are handling the large tow, increasing throughput, splicing and splitting the large tow, and developing appropriate sizing for the LCCF for specific composite applications. The CFTF continues to be a training ground for technical staff in the production of carbon fiber. Multiple tools have been developed to establish a training program for future carbon fiber production facilities.

Results and Discussion

CFTF staff took an aggressive approach in scaling up the conversion of a textile acrylic fiber to carbon fiber. The team established availability of textile acrylic fiber from the Kaltex Group, a large textile fiber producer located in northern Mexico, 200 miles south of Brownsville, Texas. Other sources of textile fiber are currently being evaluated because multiple sources of precursor materials will be needed for industry to truly scale and commercialize LCCFs. Significant progress

has been made toward developing the appropriate process science to achieve better than required properties for automotive production. The DOE automotive targets are tensile strength exceeding 250 Ksi and a modulus exceeding 25 Msi. To date, carbon fiber produced from the Kaltex precursor material has achieved over 450 Ksi tensile strength and 33 Msi tensile modulus. Figure IV-10 shows the development of these mechanical properties for the textile-based carbon fiber. All samples were tested using American Society for Testing and Materials (ASTM) D 4018 [1].
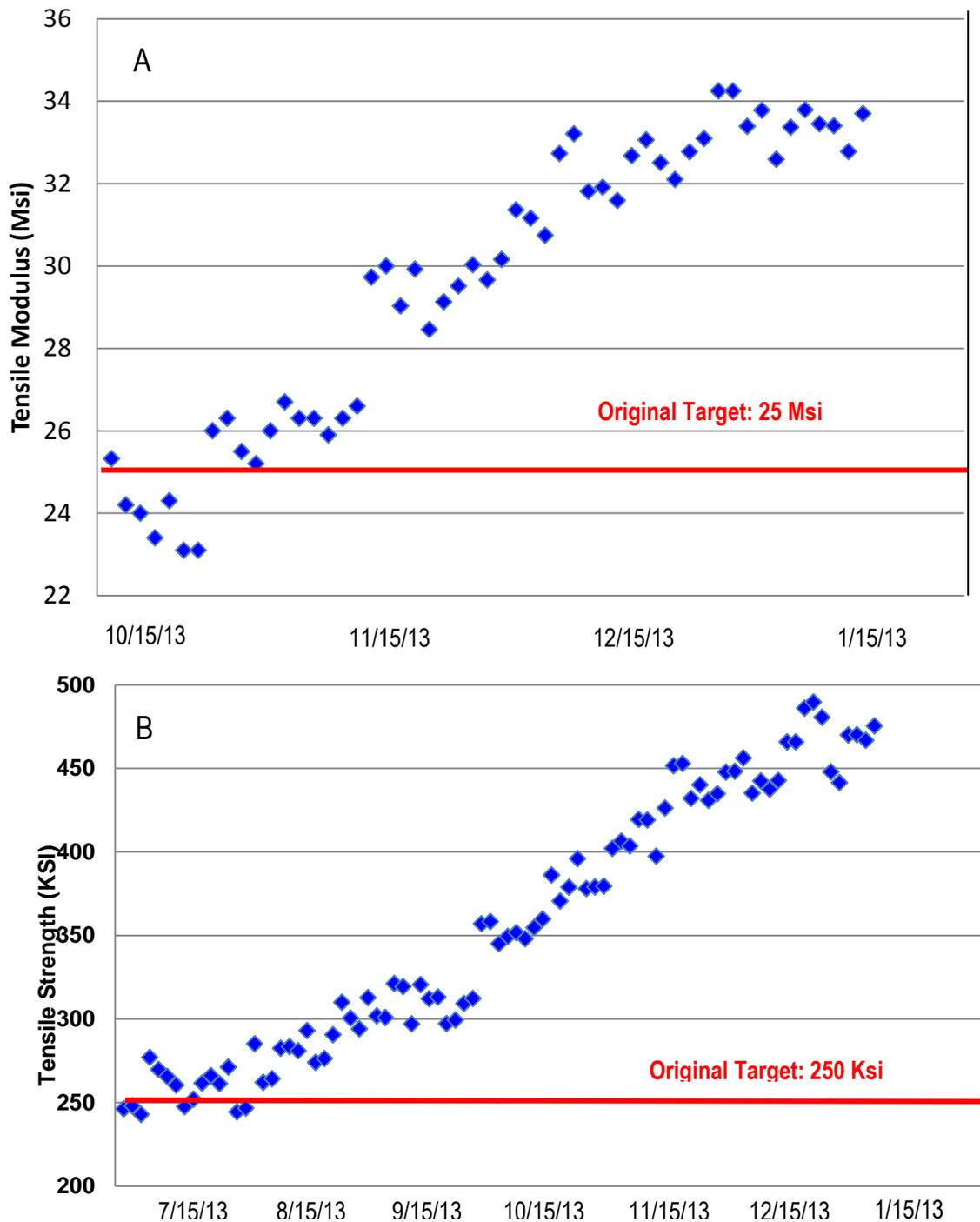
Figure IV-10: Progression over time of tensile modulus and tensile strength of carbon fiber produced from the Kaltex precursor during the project; (A) modulus progression and (B) strength progression.

Chopped carbon fiber made from the Kaltex precursor was sent to Plastics Analytics Laboratory for comparison to a commercially available carbon fiber product using standard test methods [2–5]. These results for mixtures of 30% carbon fiber and polycarbonate, Ultem, polypropylene and nylon are shown in Table IV-1–Table IV-4. They show that for this type of composite material (bulk molding compound) the textile PAN-based carbon fiber (K20-c) performed very similarly. This type of compound would be used in injection molding applications, which will probably be one of the targeted automotive composite processes because the necessary infrastructure is available. Additional testing in continuous form, including non-crimped fabrics, is also under way. The continuous processes have more composite manufacturing handling challenges because of the ultra-large tow format.

Table IV-1: Polycarbonate with 30% carbon fiber.

	Commercial carbon fiber	K20-c (ORNL carbon fiber)
Impact	2.74 [ft lb/in.]	2.72 [ft lb/in.]
Tensile strength	19,084 [psi]	21,993 [psi]
Elongation at break	2.26 [%]	2.36 [%]
Tension modulus	2,043,534 [psi]	2,589,919 [psi]
Flex strength	32,181 [psi]	31,400 [psi]
Flex modulus	1,744,876 [psi]	1,480,280 [psi]
Surface resistivity	2.5110e2 [ohms cm]	3.3110e2 [ohms cm]

Table IV-2: Ultem with 30% carbon fiber.

	Commercial carbon fiber	K20-c (ORNL carbon fiber)
Impact	2.50 [ft lb/in.]	1.69 [ft lb/in.]
Tensile strength	24,879 [psi]	23,693 [psi]
Elongation at break	1.46 [%]	1.06 [%]
Tension modulus	2,013,005 [psi]	2,412,854 [psi]
Flex strength	35,914 [psi]	34,338 [psi]
Flex modulus	1,909,275 [psi]	2,256,877 [psi]
Surface resistivity	1.310e3 [ohms cm]	2.6510e2 [ohms cm]

Table IV-3: Propylene with 30% carbon fiber.

	Commercial carbon fiber	K20-c (ORNLcarbon fiber)
Impact	1.10 [ft lb/in.]	0.95 [ft lb/in.]
Tensile strength	5,941 [psi]	6,092 [psi]
Elongation at break	3.56 [%]	2.80 [%]
Tension modulus	2,370,609 [psi]	2,262,048 [psi]
Flex strength	10,920 [psi]	11,618 [psi]
Flex modulus	1,221,171 [psi]	1,261,083 [psi]
Surface resistivity	43.1 [ohms cm]	106.1 [ohms cm]

Table IV-4: Nylon with 30% carbon fiber.

	Commercial carbon fiber	K20-c (ORNL carbon fiber)
Impact	2.89 [ft lb/in.]	2.41 [ft lb/in.]
Tensile strength	27,071 [psi]	25,667 [psi]
Elongation at break	2.39 [%]	2.59 [%]
Tension modulus	2,900,566 [psi]	2,517,068 [psi]
Flex strength	43,524 [psi]	38,707 [psi]
Flex modulus	1,912,504 [psi]	1,634,937 [psi]
Surface resistivity	84.1 [ohms cm]	102.1 [ohms cm]

Since the target performance metrics have been achieved and are reproducible, research has turned to the handling aspects of the large tow fiber. Figure IV-11 pictorially compares typical industrial-grade 24 K tows of carbon fiber and the ultra-large tow of carbon fiber produced from the Kaltex tow. While this could be an advantage in some intermediate and composite processes in the long term, such as the production of non-crimped fabrics and prepregs, the composites industry is currently built around lower tow carbon fiber (i.e, ~24 K tows versus up to 600,000 filament tows for the textile fibers). In order to be able to use the existing compositing infrastructure, large tow fiber must be split into smaller, more manageable tows for the composites industry. This is only one of several handling concerns that must be addressed and solved to truly commercialize this LCCF.

CFTF staff is evaluating additional sources of textile PAN materials. High volumes of textile PAN are available at much lower prices than traditional PAN carbon fiber precursor materials. This business model and volume could be used by new entrants into the carbon fiber industry for high-volume industrial, transportation, wind, and automotive applications. This approach would eliminate the commercialization barrier of secondary capitalization (up to $200M), depreciation and operational expense for PAN solution spinning operations that new entrants will face if they are required to produce their own precursor materials.

The CFTF provides an optimal research and development platform to further establish best practices for the carbon fiber production process. The CFTF is a conventional conversion facility with many advanced capabilities that allow a unique understanding of the influence that different processing parameters have on the properties of carbon fiber. With this in mind, evaluating and establishing cost-effective in-situ

monitoring and characterization tools should be a major focus for the CFTF. The possibility exists to increase the energy efficiency of a conventional processing line, establish these best practices, and distribute them across the industry. This would have a significant impact on the cost of the conversion process since approximately half the cost of carbon fiber is associated with the conversion process; the other half is associated with the price of the precursor material. ORNL, in collaboration with industry, has unique capabilities to develop in-situ monitoring and characterization tools such as visible polarized spectroscopy using changes in fiber reflection characteristics to determine the degree of cross-linking present in the fiber during the oxidation process. Another characterization tool, infrared thermography, could be used to measure fiber temperature as well as the emissivity change that could be correlated to different states of fiber conversion such as carbonization.

Conclusion

In a relatively short amount of time, the CFTF has demonstrated that a lower-cost carbon fiber can be produced from a textile-grade acrylic fiber, an accomplishment that has resulted in many inquiries from industry partners about the use of LCCF and, ultimately, scaling up the technology. Through technical collaborations, lower-cost carbon fibers and other products (such as oxidized PAN fibers) can be placed in the hands of industry for the development of prototypical composite applications to prove the value of these fibers. The CFTF staff continues to collaborate with industry to understand their specific needs in order to minimize the risk in scaling this technology for commercialization.

Figure IV-11: Typical spools of (a) 24 K industrial-grade carbon fiber and (b) 610 K rolls of textile-based carbon fiber.

Presentations/Publications/Patents

1. McGetrick, L. B. Presentation to the Aviation and Missile Research, Development, and Engineering Center (ARMDEC), Oak Ridge, TN, July 9, 2014.

2. McGetrick, L. B.; Jackson, C. D. Presentation to Friends of Oak Ridge National Laboratory (FORNL), Oak Ridge, TN, June 10, 2014.

3. McGetrick, L. B. DOE Vehicle Technologies Office Annual Merit Review. Washington, D.C., June 17, 2014.

4. McGetrick, L. B. Presentation to the USDRIVE Materials Technical Team. Oak Ridge, TN, February 12, 2014.

5. McGetrick, L. B. Presentation to Electric Power Research Institute (EPRI) Advanced Manufacturing Workshop. Knoxville, TN, November 13, 2013.

References

1. ASTM Standard D 4018-11, Standard Test Methods for Properties of Continuous Filament Carbon and Graphite Fiber Tows, ASTM International, West Conshohocken, PA, 2011, DOI: 10.1520/D4018-11; www.astm.org.

2. ASTM Standard D 256-10, Standard Test Methods for Determining the Izod Pendulum Impact Resistance of Plastics, ASTM International, West Conshohocken, PA, 2010.

3. ASTM Standard D 638-10, Standard Test Method for Tensile Properties of Plastics, ASTM International, West Conshohocken, PA, 2010; DOI: 10.1520/D0638-10; www.astm.org.

4. ASTM Standard D 790-10, Standard Test Methods for Flexural Properties of Unreinforced and Reinforced Plastics and Electrical Insulating Materials, ASTM International, West Conshohocken, PA, 2010, DOI: 10.1520/D0790-10; www.astm.org.

5. ASTM Standard D 792-13, Standard Test Methods for Density and Specific Gravity (Relative Density) of Plastics by Displacement, ASTM International, West Conshohocken, PA, 2013, www.astm.org; DOI:10.1520/D0792

IV.4 Predictive Engineering Tools for Injection-Molded Long-Carbon-Fiber Thermoplastic Composites– Pacific Northwest National Laboratory

Ba Nghiep Nguyen, Principal Investigator
Pacific Northwest National Laboratory
902 Battelle Boulevard
P.O. 999 – MSIN J4-55
Richland, WA 99352
Phone: (509) 375-3634
E-mail: ba.nguyen@pnnl.gov

Leonard S. Fifield, Project Manager
Pacific Northwest National Laboratory
902 Battelle Boulevard
P.O. 999 – MSIN K4-18
Richland, WA 99352
Phone: (509) 375-6424; e-mail: leo.fifield@pnnl.gov

Aaron Yocum, Project Manager
National Energy Technology Laboratory
3610 Collins Ferry Road
P.O. Box 880
Morgantown, WV 26507-0880
Phone: 304-285-4852
E-mail: Aaron.yocum@netl.doe.gov

Carol Schutte, Technology Area Development Manager
U.S. Department of Energy
1000 Independence Avenue, SW
Washington, DC 20585
Phone: (202) 586-1022
E-mail: carol.schutte@ee.doe.gov

Contractor: Pacific Northwest National Laboratory (PNNL)
Contract No.: DE-AC05-00OR22725 & DE-AC06-76RLO1830

Abstract/Executive Summary

This project aims to integrate, optimize, and validate the fiber orientation and length distribution models previously developed and implemented in the Autodesk® Simulation Moldflow® Insight (ASMI) software package for injection-molded long-carbon-fiber (LCF) thermoplastic composites. The project is organized into two phases: Phase 1 demonstrates the ability of the advanced ASMI package to predict fiber orientation and length distributions in LCF/polypropylene (PP) and LCF/polyamide 6,6 (PA66) plaques within 15% of experimental results. Phase 2 will validate the advanced ASMI package by predicting fiber orientation and length distributions to within 15% of experimental results for a complex three-dimensional (3D) Toyota automotive part injection-molded from LCF/PP and LCF/PA66 materials. PNNL will estimate weight savings and cost impacts for the vehicle system using ASMI and structural analyses of the complex part.

This report describes Phase 1 activities performed by the team comprising PNNL; PlastiComp, Inc. (PlastiComp); Purdue University (Purdue); Autodesk, Inc. (Autodesk); Toyota Research Institute North America (Toyota); Magna Exteriors and Interiors Corp. (Magna); and University of Illinois. The work includes (a) compounding 30 and 50- weight percent (wt%) LCF/PP, and 30 and 50-wt% LCF/PA66 pellets, (b) characterizing rheological and physical properties of selected materials for process modeling, (c) improving and implementing advanced process models in ASMI for fiber orientation and length prediction, (d) molding 7 inches (in) x 7 in x 0.125 in center-gated and edge-gated plaques, (e) molding similar plaques using the PlastiComp Pushtrusion® in-line direct-injection long-fiber manufacturing technology molding process (D-LFT), (f) developing methods for fiber orientation and length measurement, (g) conducting fiber measurements for PlastiComp plaques, (h) validating the ASMI fiber orientation predictions for the plaques within 15% of measured data, and (i) performing pre-analyses of the 3D complex parts with and without ribs to guide tool design and modifications for part molding.

Accomplishments

- PlastiComp, Inc. compounded 30-wt% and 50-wt% LCF/PP (55 pounds (lbs) each) and 30-wt% and 50-wt% (55 lbs each) LCF/PA66 and shipped these compounds to Autodesk for rheological, thermal, and mechanical characterization. (FY 2014)
- Autodesk completed the material characterization for the rheological, thermal, and mechanical properties for the selected materials, and distributed the material data files to all the project partners. (FY 2014)
- Autodesk delivered a research version of ASMI to PNNL for process modeling. (FY 2014)
- PlastiComp injection-molded 160 center-gated and edge-gated 30-wt% and 50-wt% LCF/PP and 30-wt% and 50-wt% LCF/PA66 (7 in x 7 in x 0.125 in) plaques under fast- and slow-fill conditions. (FY 2014)

- PlastiComp molded 160 center- and edge-gated 20-to-30-wt% LCF/PP and 20-to-30-wt% LCF/PA66 (7inin x 7 in x 0.125 in) plaques by the Pushtrusion®D-LFT process. (FY 2014)
- PlastiComp conducted pre-analysis of the 3D complex part using similar materials and recommended a wall thickness, molding pressure, and gating conditions. This valuable contribution aided PNNL in analyzing the target materials of the project with data received from Autodesk. (FY 2014)
- PNNL cut 0.9 in x 0.9 in samples out of PlastiComp plaques at the selected locations (named A, B, and C) and shipped these samples to Purdue for fiber orientation and length measurement. (FY 2014)
- Purdue validated the fiber orientation measurement method using fiber orientation data obtained using the Leeds technique [1] and manually measured data by University of Illinois. (FY 2014)
- Purdue developed a software tool for fiber length measurement. (FY 2014)
- Purdue conducted fiber orientation measurements for three PlastiComp plaques: fast-fill 30-wt% LCF/PP edge-gated plaques, slow-fill 50-wt% LCF/PP edge-gated plaques, and slow-fill 50-wt% LCF/PP center-gated plaques. Purdue delivered the data at the selected locations to PNNL. (FY 2014)
- PNNL conducted ASMI mid-plane analyses and compared the predicted fiber orientations with Purdue measured data at plaque locations A, B, and C. The team used the tensile elastic and flexural moduli computed for the flow and cross-flow directions with predicted and measured fiber orientations to evaluate the prediction at given locations. (FY 2014)
- Toyota, Magna and PlastiComp discussed tool modification for molding the 3D complex parts with PNNL. Toyota sent the computer-aided design (CAD) files of the complex parts with and without ribs to PNNL to build ASMI models of these parts for mold-filling pre-analysis. (FY 2014)
- PNNL performed ASMI analyses for the Toyota complex parts with and without ribs, having different wall thicknesses, and using the PlastiComp 50-wt% LCF/PP, 50-wt% LCF/PA66, 30-wt% LCF/PP, and 30-wt% LCF/PA66 materials to provide guidance for tool design and modifications for part molding. (FY 2014)
- Magna injection-molded plaques from the 50-wt% LCF/PP and 50-wt% LCF/PA66 materials received from PlastiComp in order to extract machine purge materials from Magna's 200-ton injection-molding machine, which is targeted to mold the complex part. Magna shipped the purge materials to Purdue for fiber length analysis. (FY 2014)
- University of Illinois advised Autodesk on fiber length and orientation simulations. (FY 2014)
- Autodesk implemented a new fiber length distribution (FLD) model based on an unbreakable length assumption with Reduced Order Modeling (ROM) by the Proper Orthogonal Decomposition (POD) approach in the mid-plane, dual-domain, and 3D ASMI solvers. (FY 2014)

- Autodesk improved the ASMI 3D solver for fiber orientation prediction using the anisotropic rotary diffusion (ARD) reduced-strain closure (RSC) model [2]. (FY 2014)

Future Directions

- The team will use fiber orientation and fiber length distribution data from locations A, B, and C in composite plaques to validate ASMI predictions and complete a go/no-go list.
- Agreement within 15% of the mechanical performance values in terms of the principal elastic tensile and flexural moduli calculated from the experimentally determined and computed fiber orientation and length data for the 2D plaques on the go/no-go list will enable transition to Phase 2 to focus on the 3D complex automotive part.
- Magna will build tooling for the complex 3D part at the beginning of Phase 2.
- Magna will mold the 3D complex parts with and without ribs from PlastiComp 30-wt% LCF/PP and 30-wt% LCF/PA66 compounds using the conventional injection-molding process.
- PlastiComp will mold the 3D complex parts with ribs targeting 30-wt% LCF/PP and 30-wt% LCF/PA66 materials using the D-LFT process and benchmark with conventional LFT outcomes.
- The molded complex parts will be shipped to PNNL for sampling at selected locations for fiber orientation and length measurements.
- PNNL will perform ASMI analyses of the complex parts and compare predicted fiber orientation and length results with the measured data using the same method used for plaques to evaluate the 15% accuracy criterion.
- At the end of Phase 2, PNNL and Toyota will investigate weight savings and cost impact vis-à-vis program requirements defined in Table 2 of DE-FOA-0000648 (Area of Interest 1) with the assistance of Autodesk.[3]

Technology Assessment

- Target: Demonstrate fiber length distribution with 10% variation between the machine purge materials (from PlastiComp, Magna, and Autodesk molding equipment) that is sufficient to achieve 'long fibers' (average fiber length exceeding 2 mm) in 3D molded parts.
- Gap: Isolating carbon fibers from the resin matrix through heating in air oxidizes the fibers, promotes fiber breakage, and leads to underestimation of fiber length.
- Target: Achieve D-LFT molding with high fiber loadings to achieve enhanced mechanical properties.
- Gap: Current PlastiComp D-LFT technology is limited to fiber content of 30-wt% for carbon fiber reinforced PP and PA66 molded parts. Upgrading of PlastiComp D-LFT capabilities to higher fiber content is beyond the scope of the current program.

- Target: Validate the ASMI fiber orientation and length predictions for PlastiComp plaques at selected locations within 15% of the measured data.
- Gap: Fiber orientation and length data have not been available for all materials of interest.

✧   ✧   ✧   ✧   ✧

Introduction

The two phases of this project aim to advance the predictive engineering (PE) tool to accurately predict fiber orientation and length distribution in injection-molded LCF thermoplastic composites to enable optimum design of automotive structures that meet weight reduction and cost impact requirements as defined in DE-FOA-0000648 (Area of Interest 1, Table 2). [3]

Phase 1 Objective and Scope: Phase 1 integrates, optimizes, and validates the fiber-orientation and length-distribution models previously developed and implemented in the ASMI package for injection-molded LCF/PP and LCF/PA66 plaques. Phase 1 demonstrates the ASMI package as a PE tool that accurately predicts fiber orientation and length distributions within 15% of experimental results.

Phase 2 Objective and Scope: Phase 2 will focus on validating the ASMI package to predict flow-induced fiber orientation and length distribution in a complex, injection-molded, 3D Toyota automotive part (Figure IV-12). The project will compare predicted fiber orientation and length for key locations on the complex LCF/PP and LCF/PA66 parts with experimental results. Agreement within 15% will validate the PE tool. At the end of Phase 2, the team will evaluate the ASMI tool for weight and cost impact for the relevant vehicle system.

Approach

This project integrates, optimizes, and validates injection-molded, LCF thermoplastic composite PE tools. Figure IV-12 illustrates the technical approach that progresses from compounding LCF/PP and LCF/PA66 materials, to process model improvement and implementation, to molding and modeling LCF/PP and LCF/PA66 plaques. The lessons learned from the plaque study will help to mold, model, and optimize the 3D complex part when the project enters Phase 2.

Results and Discussion

Material compounding and plaque molding (PlastiComp)*: After holding the project kick-off meeting at PlastiComp Global Headquarters in Winona, MN, PlastiComp compounded 30-wt% and 50-wt% LCF/PP (55 lbs each) and 30-wt% and 50-wt% (55 lbs each) LCF/PA66 materials and shipped these compounds to Autodesk labs for rheological, thermal, and mechanical characterization. Purdue received representative samples of these 12-mm-long pellets for fiber-length analyses [4].

Compounding LCF/PP & LCF/PA66

Process model improvement/ Implementation of molding and modeling LCF/PP & LCF/PA66 plaques

Molding/modeling/ optimize the 3D complex part

Candidate part can be used at many locations in the automobile as shown in the picture above
1) Rocker to B pillar reinforcement
2) A pillar reinforcement
3) B pillar reinforcement
4) Roof rain reinforcement
5) Cross member
6) Front rail reinforcement
7) Interior pillar

Proposed component shown in the vehicle

Figure IV-12: Schematic picture illustrating the technical approach to integrate and validate the tools for designing injection-molded LCF thermoplastic automotive structures.

PlastiComp fabricated the fan-edge-gated plaque mold and used an existing center-gated plaque mold, both illustrated in Figure IV-13, for the molding trials. PlastiComp molded 30-wt% and 50-wt% LCF/PP and LCF/PA66 center-gated and edge-gated plaques using the conventional injection-molding process under controlled slow- and fast-fill conditions. The molded plaques were delivered to PNNL. The injection speeds and processing conditions used in the various molding trials were also sent to PNNL for preparing ASMI models and analyses of PlastiComp plaques [5].

During the third quarter of fiscal year (FY) 2014, the team used the edge-gated and center-gated plaque molds (Figure IV-13) for molding trials using PlastiComp exclusive Pushtrusion® D-LFT processing, illustrated in Figure IV-14. In contrast to LFT molding with pre-compounded pellets, Pushtrusion® directly feeds the molten resin and cuts fibers into the mixing zone of the injection barrel. In the molten resin stream, Pushtrusion® cuts fiber lengths to desired length by a rotary cutter (not shown in Figure IV-14) at the exit of the capillary tube. The speed of the cutter, the number of cutting

edges, and lineal speed of the fiber/resin stream are selected to determine chopped fiber lengths. D-LFT fiber lengths of 12-mm were selected, consistent with the pre-compounded pellets. Since fiber-chopping in Pushtrusion® occurs in the molten phase, there is tight control on fiber-length distribution, whereas fibers in pre-compounded pellets used in the conventional injection-molding process are subject to severe length attrition during pellet melting in the injection barrel. Pushtrusion® routinely compounds 20-wt% to 50-wt% glass-fiber compounds. However, the process is currently limited to 30-wt% carbon-fiber compounds [6]. Equipment upgrade for higher fiber content was deemed a stretch goal and was eliminated from the project scope due to the late start of program and schedule risk to subsequent analytical tasks. Therefore, 20 to 30-wt% fiber loadings were selected for PlastiComp molding of center-gated and edge-gated LCF/PP plaques and LCF/PA66 (7 in x 7 in x 0.125 in) plaques by the D-LFT process.

(a)   (b)   Fan gate
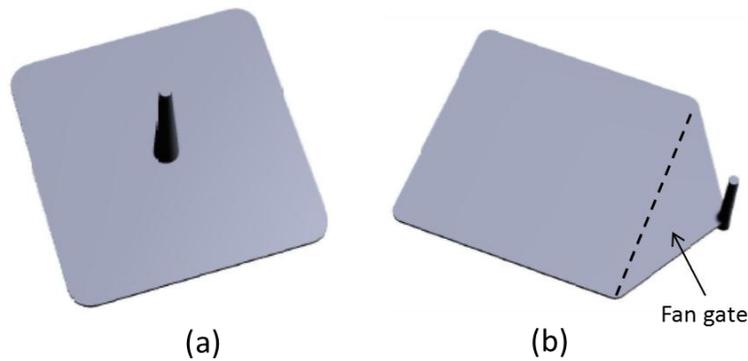
Figure IV-13: (a) Center-gated and (b) edge-gated 7 in x 7 in x 0.125 in PlastiComp plaque designs.

Pushtrusion ® Operating Principle
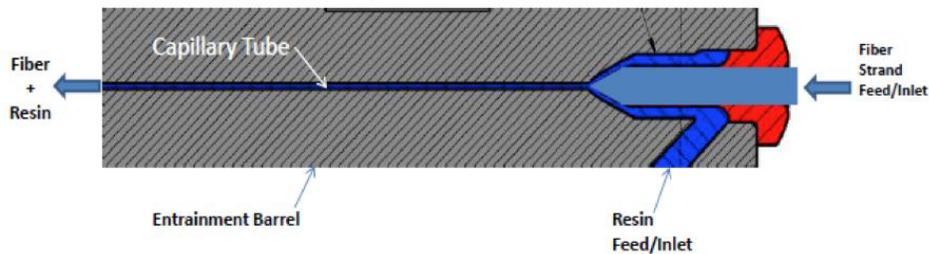
- Fiber strands (tow-ends) are placed in resin-flow in a capillary tube
- The resin drags the fiber strands along with it
- The cross-sectional area of the capillary tube determines the volumetric ratio of the fiber to resin

Figure IV-14: Principle of the Pushtrusion® D-LFT used by PlastiComp.

Characterization of compound materials (Autodesk):
Autodesk completed material characterization of four LCF thermoplastic compounds including 30-wt% LCF/PP, 30-wt% LCF/PA66, 50-wt% LCF/PP, and 50-wt% LCF/PA66. The characterization provided viscosity, thermal properties, mechanical properties, and pressure-volume-temperature (PVT)/density data for the selected materials. All project participants received the material data files [7, 8, 9, 10]. Illustration of data from the characterization is presented in Figure IV-15(a) and Figure IV-15(b), including specific heat (C_p) versus temperature (in °C) data done in cooling for the 30-wt% LCF/PA66 and 50-wt% LCF/PA66. From this data the transition (solidification) temperature was observed to be 231°C for both PA66 grades, while the ejection temperature was observed to be 219°C for the 30-wt% LCF/PA66 and 221°C for the 50-wt% LCF/PA66. The glass transition temperature (T_g) and melting temperature (T_m) for PA66 are approximately 70°C and 262°C, respectively (values supplied by PlastiComp).

Isolating samples from PlastiComp plaques (PNNL):
Upon receiving molded plaques from PlastiComp, PNNL cut the 0.9 in x 0.9 in samples from these plaques at three locations named "A", "B", and "C" (Figure IV-16) for shipping to Purdue for fiber orientation and length measurement. All three locations in a given plaque are located on the same centerline. Location A is near the gate while location C is near the plaque end. Location B is equally distant from locations A and C. Figure IV-16 (a) and 5(b) show these locations defined on the edge-gated and center-gated plaques.

Fiber orientation and length measurement (Purdue):
To facilitate fiber length and orientation measurement, Purdue set up an optical microscope, Olympus BX51, as shown in Figure IV-17. A software-controlled motorized stage attached to the microscope allows for automated image stitching at high magnification. Additionally, high dynamic range and extended-focus imaging capabilities capture in-focus, high-contrast images at varying heights. This system provides the function of the need for the Leeds system and provides measurement fidelity.
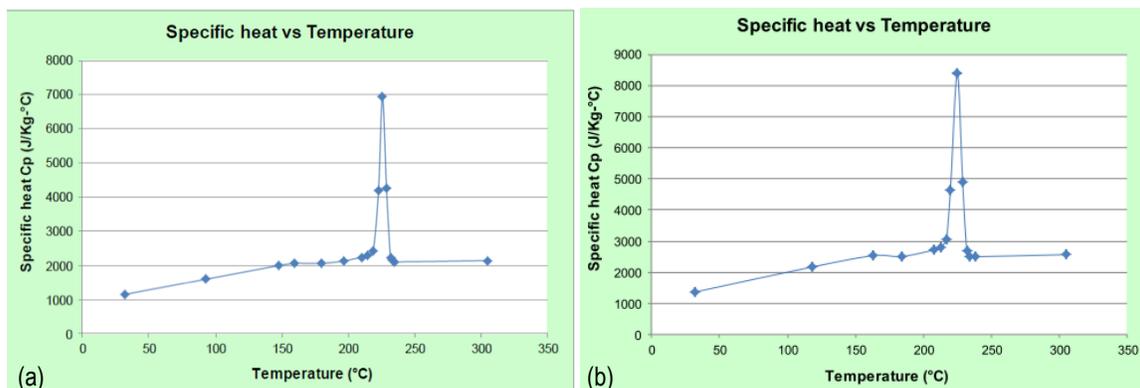
Figure IV-15: Specific heat vs. temperature curves recorded during cooling for (a) 30-wt% LCF/PA66 and (b) 50-wt% LCF/PA66 materials.
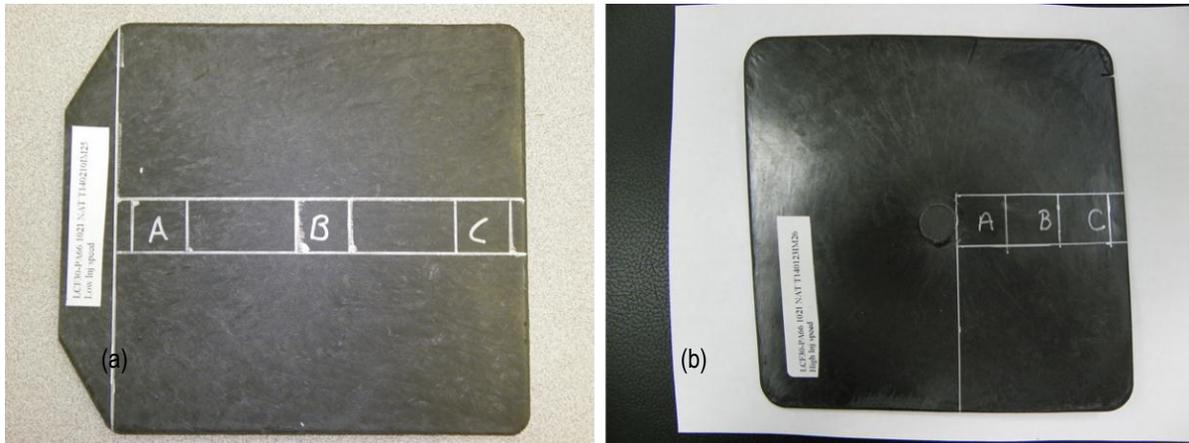
Figure IV-16: Locations A, B, and C defined on the (a) edge-gated and (b) center-gated plaques were isolated for shipping to Purdue for fiber orientation and length measurement.

Figure IV-17: Optical microscope system with motorized stage for use in fiber measurements.

Purdue developed a fiber orientation measurement method and validated this method using the previous fiber orientation data obtained from the Leeds machine and manually measured data by the University of Illinois. The work includes:

- Developing a new polishing routine, utilizing the automated polishing machine, to reduce fiber damage during surface preparation.

- Using a marker-based watershed segmentation routine, in conjunction with a hysteresis thresholding technique, for fiber segmentation.

- Verifying the orientation measurement method using images and results obtained by Phelps [2] using the Leeds method. The orientation results obtained by Purdue's method were compared with the data obtained using the Leeds machine and those obtained using manual segmentation by Phelps [2]. Purdue's fiber orientation results agree within 10% of a reference analysis on data acquired by the Leeds system, thereby verifying the Purdue method.

The comparison of the fiber orientation tensor components A_{11}, A_{22}, A_{33} and A_{31} are shown in Figure IV-18. The 1- and 2-directions denote the flow (A_{11}) and cross flow (A_{22}) directions, respectively. There was good agreement between the three methods and validation of Purdue's fiber orientation measurement method was confirmed [6].
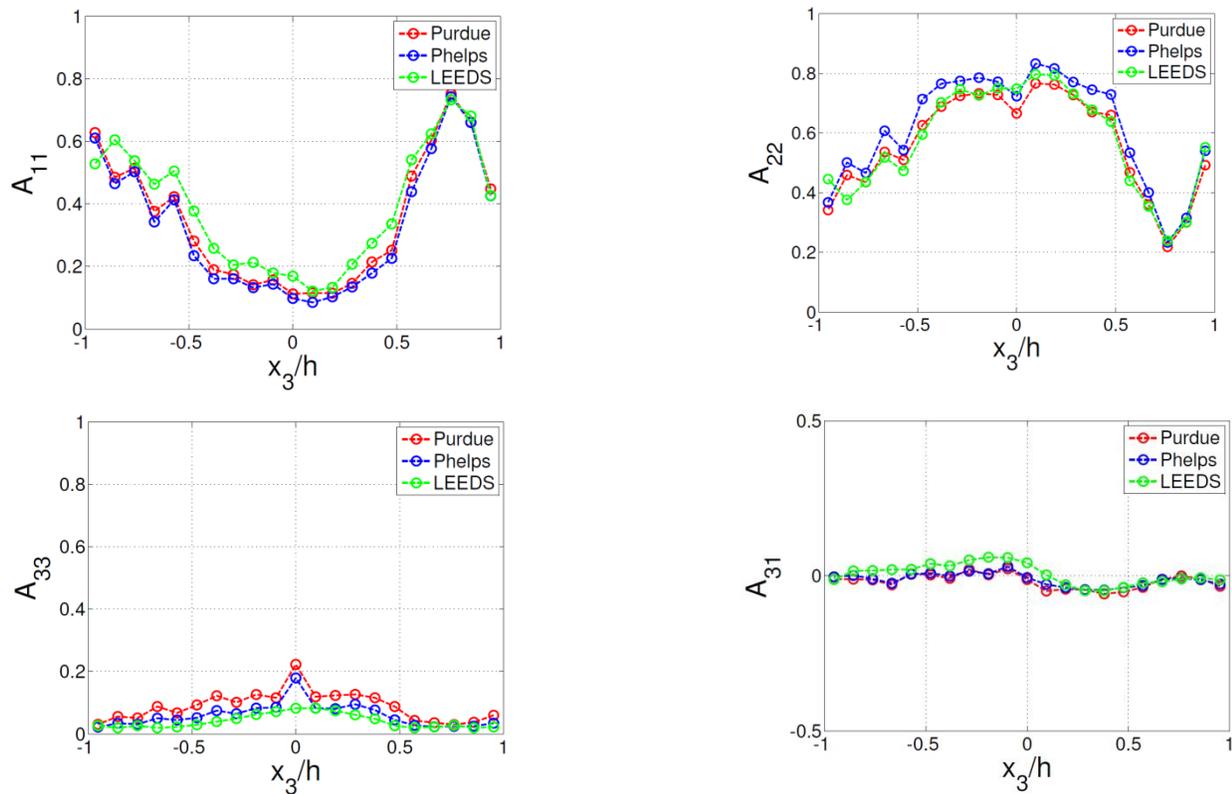
Figure IV-18: Comparison of fiber orientation tensor components obtained using Purdue's method, Phelps' manual segmentation, and Leeds machine (x_3 denotes thickness direction and h the plaque thickness).

Fiber length distribution measurements require identifying and measuring the length of individual fibers present in the down-selected batch of carbon fibers. The current accepted method involves manual selection and identification of individual fibers. To automate this process, the team wrote fiber length measurement software using Matlab®. Using high resolution microscope images as input, the software identifies and labels individual fibers, measures their length, and outputs the fiber length distribution present in the input image. The software is capable of improving contrast by performing image histogram analysis and correctly distinguishing fibers crossing over each other, as shown in Figure IV-19. The use of this software will improve productivity and greatly increase the fiber length measurement workflow.

Fiber orientation measurement for PlastiComp plaques (Purdue): Purdue used their developed automated software method to measure fiber orientations for samples taken at locations A, B, and C on a fast-fill 30-wt% LCF/PP edge-gated plaque, slow-fill 50-wt% LCF/PP edge-gated plaque, and slow-fill 50-wt% LCF/PP center-gated plaque. The comparison between measured and predicted fiber orientation is discussed below.

ASMI analysis of PlastiComp plaques (PNNL): PNNL received three sets of fiber orientation data from Purdue for the samples at locations A, B, and C (Figure IV-16) of the PlastiComp plaques. In discussion with Autodesk, PNNL used these data to validate ASMI fiber orientation prediction. From the measured data, the team selected a target fiber orientation tensor, and from this target, they identified acceptable b_i parameters for the ARD-RSC model [2] [11]. The b_i parameters were identified following the procedure proposed by Phelps and Tucker [11]. The steady-state solution in a simple shear flow was fit to the selected target orientation. This requires physically valid fiber-interaction tensor **C** in all flows and stable transient-orientation solutions in simple shear, planar, uniaxial, and biaxial elongation flows. The team selected the target steady-state fiber orientation of the model based on the measured orientation in the shell layers. Figure IV-20(a) and Figure IV-20(b) show the ASMI finite element models for the edge-gated and center-gated plaques used in the analyses. The ASMI simulations used the actual process parameters that PlastiComp used when molding the plaques. The b_i and RSC parameters identified for the 30-wt% LCF/PP fast-fill molding are:

$$b_1 = -0.002074, b_2 = 0.1512, b_3 = 0, b_4 = 0.01209, b_5 = 0, RSC = 0.008,$$

and those for the slow-fill 50-wt% LCF/PP are:

$b_1 = 0.001654, b_2 = 0.0054, b_3 = 0.025, b_4 = -0.0008676, b_5 = -0.005,$ *RSC*=0.02
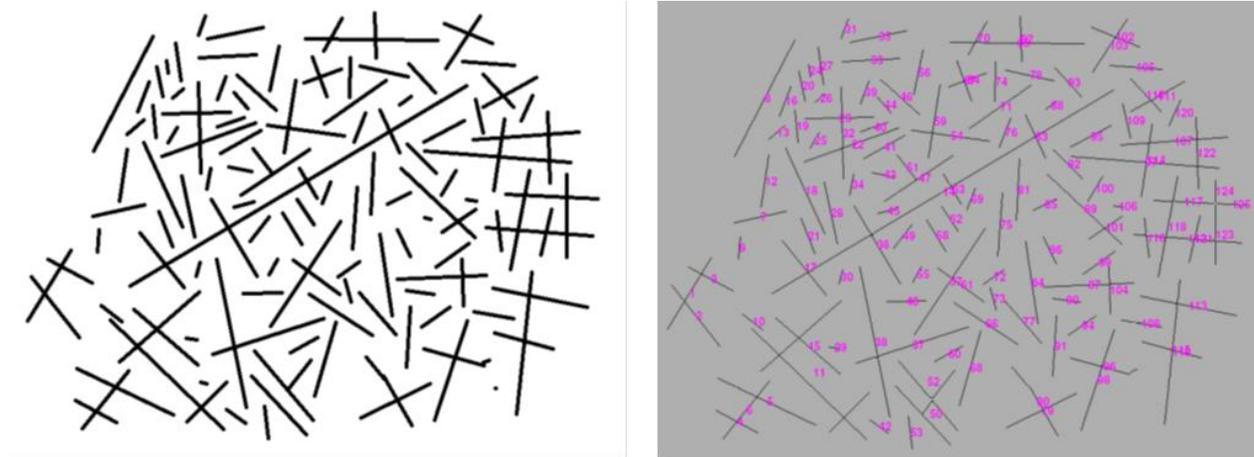
Figure IV-19: Automated identification and labeling of a sample image with multiple fiber crossings.
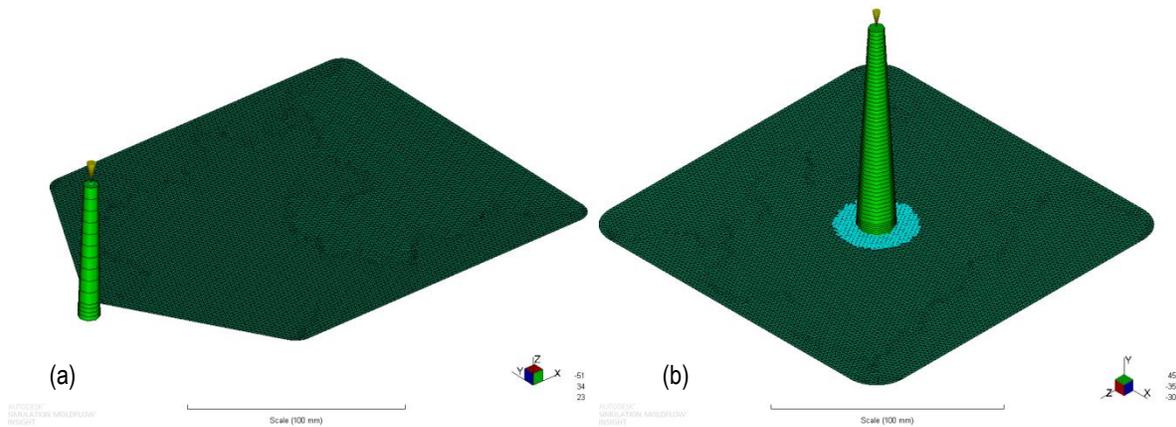
Figure IV-20: ASMI models for the PlastiComp (a) edge-gated plaque and (b) center-gated plaque.

As fiber orientation strongly varies through the sample thickness, it is not possible and meaningful to have point-by-point comparisons between the predicted and measured fiber orientations for all the components of the second-order fiber orientation tensor. Instead, a quantitative method [12] for comparing measured and predicted fiber orientation using the calculated mechanical properties provides a meaningful and relevant basis for assessing accuracy in fiber orientation prediction. To evaluate whether ASMI fiber orientation prediction at a given location agrees with measured data within 15%, the team used tensile elastic moduli and flexural moduli computed for the flow and cross-flow directions with

predicted and measured fiber orientations. Typical values of elastic properties of the carbon fiber and resin matrix were used in the calculations assuming a uniform fiber aspect ratio of 200.

Figure IV-21 to Figure IV-23 show the predicted and measured through-thickness evolutions of the orientation components A_{11} (flow-direction) and A_{22} (cross-flow direction) at locations A, B, and C on the fast-fill 30-wt% LCF/PP edge-gated plaque. Good global trend and value agreement was found for all three locations. Table IV-5 to Table IV-8 shows reasonable agreement in tensile and flexural modulus

predictions using predicted and measured fiber orientation for this plaque. The team performed ASMI analyses for the slow-fill 50-wt% LCF/PP edge-gated and center-gated plaques for which the orientation data are available. All the results were reported and discussed in Nguyen et al. [12]. For all the analyzed cases ASMI captured the experimental tendency reasonably well and globally found good agreement in the

trends and values for all three locations except for the flexural modulus, D_{11} at location B that did not meet the 15% agreement. This was due to the significantly lower values of the predicted orientation tensor component, A_{11} than the corresponding measured values at the skin and shell layers for this location (Figure IV-22).
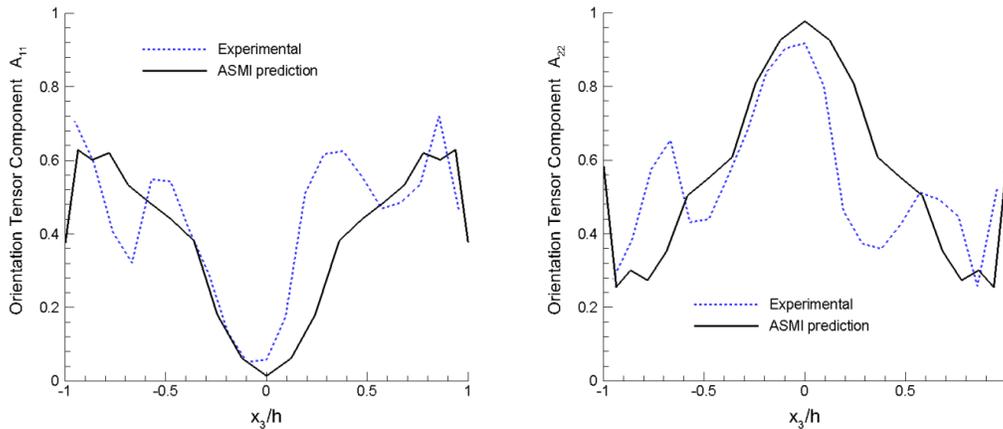
Figure IV-21: Predicted and measured fiber orientation tensor components in the flow- and cross-flow directions: (left) A_{11}, (right) A_{22}, for the edge-gated fast-fill 30-wt% LCF/PP plaque at location A.
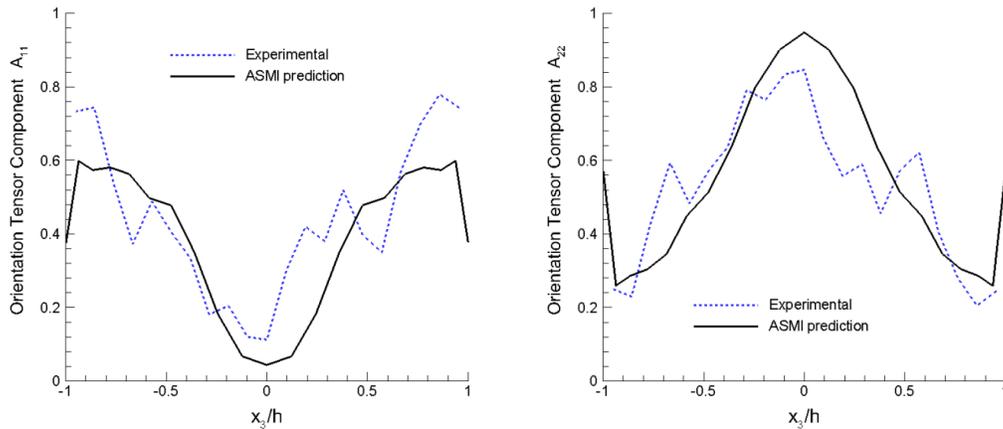
Figure IV-22: Predicted and measured fiber orientation tensor components in the flow- and cross-flow directions: (left) A_{11}, (right) A_{22}, for the edge-gated fast-fill 30-wt% LCF/PP plaque at location B.
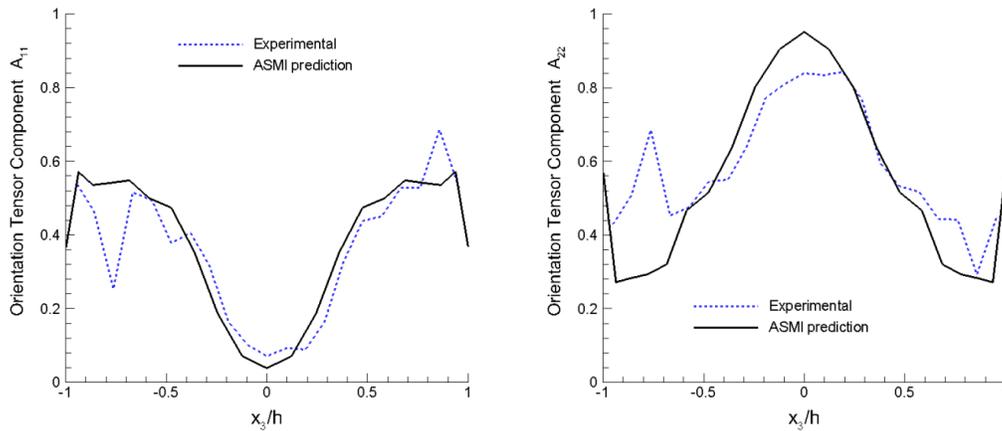
Figure IV-23: Predicted and measured fiber orientation tensor components in the flow- and cross-flow directions: (left) A$_{11}$, (right) A$_{22}$, for the edge-gated fast-fill 30-wt% LCF/PP plaque at location C.

Table IV-5: Computed E_{11} based on predicted and measured fiber orientations at locations A, B, and C in the edge-gated fast-fill 30-wt% LCF/PP plaque.

Tensile Modulus	E_{11} (predicted orientation) MPa	E_{11} (measured orientation) MPa	Agreement within
Loc. A	14382	15791	8.9%
Loc. B	14001	16127	13.2%
Loc. C	13360	12573	6.3%

Table IV-6: Computed E_{22} based on predicted and measured fiber orientations at locations A, B, and C in the edge-gated fast-fill 30-wt% LCF/PP plaque.

Tensile Modulus	E_{22} (predicted orientation) MPa	E_{22} (measured orientation) MPa	Agreement within
Loc. A	20300	19819	2.4%
Loc. B	19638	19305	1.7%
Loc. C	19669	21665	9.2%

Table IV-7: Computed D_{11} based on predicted and measured fiber orientations at locations A, B, and C in the edge-gated fast-fill 30-wt% LCF/PP plaque.

Flexural Modulus	D_{11} (predicted orientation) MPa.mm3	D_{11} (measured orientation) MPa.mm3	Agreement within
Loc. A	25794	28483	9.4%
Loc. B	25479	33002	22.8%
Loc. C	24644	25202	2.2%

Table IV-8: Computed D_{22} based on predicted and measured fiber orientations at locations A, B, and C in the edge-gated fast-fill 30-wt% LCF/PP plaque.

Flexural Modulus	D_{22} (predicted orientation) MPa.mm3	D_{22} (measured orientation) MPa.mm3	Agreement within
Loc. A	36788	35557	3.5%
Loc. B	35823	31575	13.5%
Loc. C	35818	37038	3.3%

Complex part mold-filling pre-analysis (PNNL): In the mold-filling pre-analysis for the Toyota complex part, the team used four PlastiComp materials to provide guidance for mold design and modifications: 30-wt% LCF/ PP, 30-wt% LCF/PA66, 50-wt% LCF/PP, and 50-wt% LCF/PA66. Autodesk characterized these materials and provided rheological and physical data to PNNL for process simulations using ASMI. A reasonable weighted average fiber length of 4-mm in the charge at the injection-molding machine nozzle was suggested by PlastiComp and used in the analysis since FLD data for the purge materials was not available at the time of this report.

The first round of mold-filling pre-analyses conducted for the complex part considered 50-wt% LCF/PP and 50-wt% LCF/PA66 materials, targeting 50-wt% carbon fiber loading for the complex part. The results highlighted the difficulty of mold filling with 50-wt% LCF/PA66 for both 2.0 mm and 3.0 mm part thicknesses. The predicted pressures at the end of fill exceeded maximum levels desired for preserving fiber length in the part and the team has consequently prioritized 30-wt% over 50-wt% fiber loadings.

ASMI predicted successful mold filling of the complex part using both 30-wt% LCF/PP and 30-wt% LCF/PA66, for the 2.0 mm, 2.8 mm and 3.0 mm wall thicknesses considered, and for complex parts both with ribs and without ribs. Predicted values for weighted average fiber length significantly exceeded the 1-2 mm range for the locations analyzed on parts filled with 30-wt% LCF/PP and 30-wt% LCF/PA66 based on the 4 mm fiber length inlet condition. Nguyen et al. [13] completed and submitted a formal report on this work to DOE. The distribution of predicted pressure at the end of fill for the 2.8 mm wall, 30-wt% LCF/PA66 complex part with ribs in Figure IV-24 reveals acceptable maximum pressure levels.

The larger wall thickness values of 2.8 mm and 3.0 mm for the part are considered so that the tool can be used for fiber-loading values higher than 30-wt%.
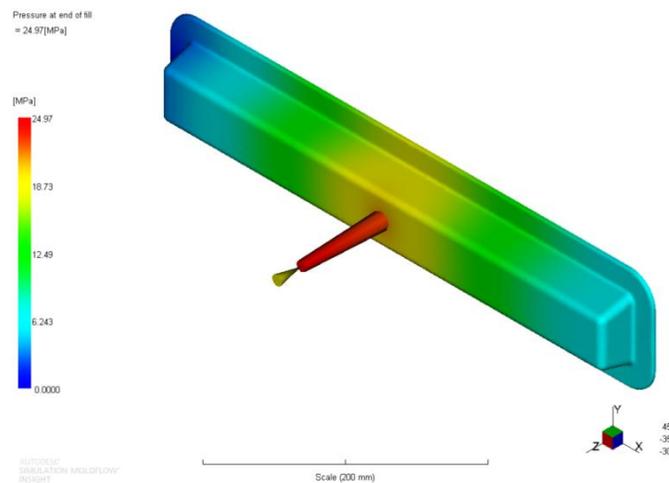
Implementation of a fiber length distribution (FLD) model (Autodesk): Autodesk implemented a new FLD model based on an unbreakable length assumption with ROM by the POD approach in the mid-plane, dual-domain, and 3D solvers. Recent work focused on removing the need for a preliminary snapshot analysis to determine the POD modes. The snapshot analysis previously used required long computation time and large computation memory while running the full-flow and FLD models to pre-determine the POD modes for use in the ROM scheme. Using a dynamic look-up table that covers a wide spectrum of shear-rate and viscosity variations in the analysis removed the need for snapshot analysis. In 3D analysis testing, the POD approach predicted FLD results that reasonably match those of the full model as illustrated in Figure IV-25 and Figure IV-26. The initial fiber length condition of 4.0 mm was adopted at the injection location as a reasonable anticipated value in the absence of available data from FLD measurements in the sprue to inform what the initial fiber length should be. Given this initial fiber length, the distribution of fiber lengths predicted for the full model (Figure IV-25) shows that most of the fibers are expected to have lengths below 1.0 mm in all three locations indicated, while two of those locations are predicted to have some fibers retained at the initial fiber length (4.0 mm). These characteristics of the fiber length prediction are well matched in the FLD calculation using ROM with 5 POD modes (Figure IV-26). Nguyen et al. [12] compared and reported the computational memory required when using ROM with five POD modes and the full FLD model for a dual-domain analysis of the complex part with 150 length segments in the FLD distribution. The memory required for the FLD calculation was reduced by 61% when ROM with five POD modes is used. A subsequent memory usage analysis of the 3D FLD calculation indicated an 85% memory reduction.

Figure IV-24: Distribution of pressure at the end of fill predicted for the 2.8 mm, 30-wt% LCF/PA66 complex part with ribs, including an acceptable level of the maximum pressure at the end of fill.
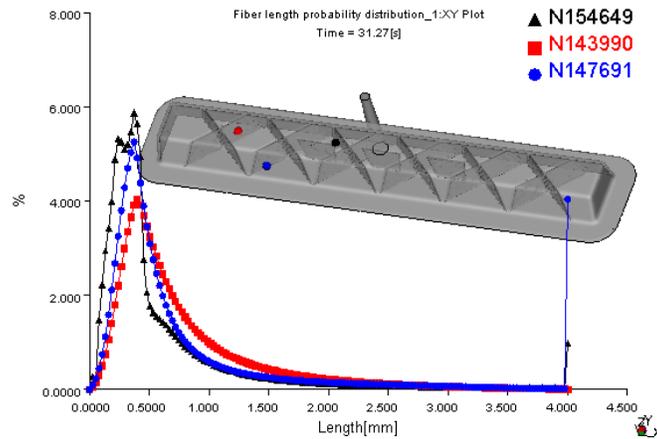
Figure IV-25: Example of 3D prediction of FLD for the complex part using the full fiber breakage model based on unbreakable length: 150 segments, drag coefficient, D_g = 3.0, shear rate constant, C_b = 0.02, and probability profile control factor, S = 0.25.
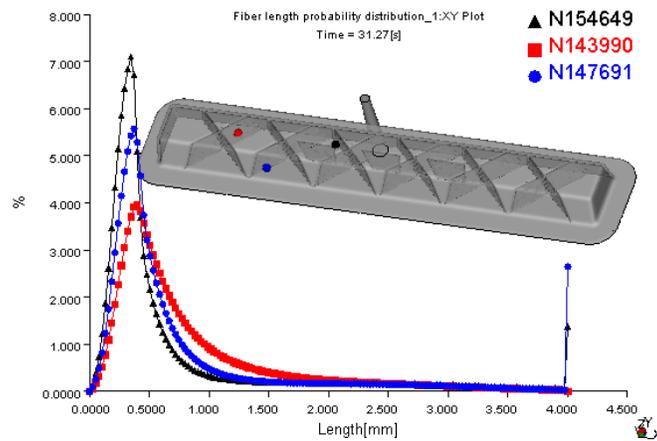
Figure IV-26: Example of 3D prediction of FLD for the complex part using five POD modes of the fiber breakage model based on unbreakable length: 150 segments, D_g = 3.0, C_b = 0.02, S = 0.25.
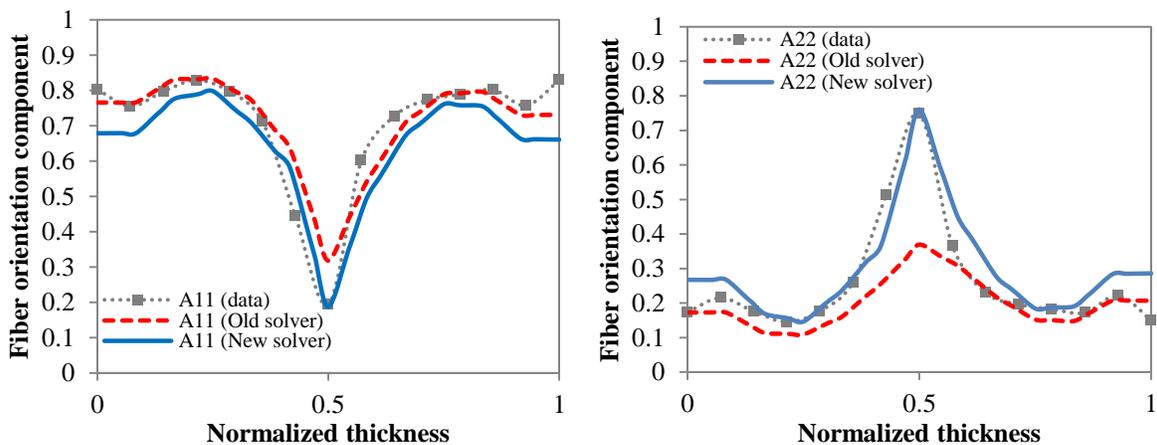
Figure IV-27: Comparison of fiber orientation data (from Wang 2007) with ASMI 3D predictions.

Fiber orientation prediction improvement in the ASMI 3D Solver (Autodesk): Autodesk improved the fiber orientation prediction by the RSC model in 3D analysis and used the RSC with the ARD model to predict fiber orientation for LCF composites. Previous comparisons indicated that ASMI reasonably predicts the orientation component in the flow direction but tends to over-predict orientation in the thickness direction and hence under-predict the orientation component in the cross-flow direction. Also, the orientation near the mid-thickness plane is nearly always predicted to be fully random, regardless of the flow geometry, processing conditions, and materials. The team carefully studied the RSC model, and the implementation improved, especially near the gate region where the elongation flow is dominant as the melt polymer enters the cavity. Autodesk tested the new ASMI 3D RSC solver for a number of injection-molded short-fiber composites, and the fiber orientation prediction shows good agreement with most experimental data. Figure IV-27 shows the probability of fibers to be orientated in flow direction (A_{11}) and cross-flow direction (A_{22}) and compares measured orientation data (from Wang [14]) with the previous and the new predictions. The improved RSC 3D fiber solver provides results in much better agreement of the orientation components, particularly in the cross-flow direction (A_{22} in the core region).

Technology Transfer Path

The participation of industrial partners (i.e., Autodesk, PlastiComp, Toyota, and Magna) in this project supports a path for the PE tool and research results to be transferred to U.S. automotive and plastics industries, where ASMI is widely used. The advanced PE capability developed here will be available to these industries in the future to help achieve affordable, light-weight vehicles systems.

Conclusion

During FY 2014, the team completed important key steps that will enable the project to transition to Phase 2 to demonstrate predictive engineering of long carbon fibers in a complex 3D part. We successfully compounded, characterized, and molded prioritized fiber reinforced thermoplastic materials. We developed fiber orientation and length measurement methods to acquire data for model validation. We also built and executed ASMI mid-plane models to predict fiber orientation in PlastiComp plaques. The good agreement between the ASMI orientation predictions and the measured orientation data supports the validity and usefulness of the ARD-RSC model and ASMI for LCF thermoplastic composites. Accurate prediction of fiber orientation is crucial for the subsequent prediction of the fiber length distribution and mechanical properties used in structural analyses. At the end FY 2014, we completed the implementation of a ROM for fiber length in ASMI, and the improved 3D ASMI solver was demonstrated to provide more accurate fiber orientation predictions.

Presentations/Publications/Patents

None

References

1. Hine PJ, RA Duckett, N Davidson, AR Clarke (1993). "Modelling of the Elastic Properties of Fibre Reinforced Composites: I. Orientation measurement," Composites Science and Technology, 47:65-73.

2. Phelps, J.H. (2009). Processing-Microstructural Models for Short- and Long-Fiber Thermoplastic Composites. Ph.D. Thesis. Urbana, IL: University of Illinois at Urbana-Champaign.

3. U. S. Department of Energy, National Energy Technology Laboratory, Funding Opportunity Number: DE-FOA-0000648. "Predictive Modeling for Automotive Lightweighting Applications and Advanced Alloy Development for Automotive and Heavy-Duty Engines". Announcement Type: 003. CFDA Number: 81.086 Conservation Research and Development, Issue Date: 05/04/2012

4. Nguyen, B.N., Sanborn, S.E., Simmons, K.L., Mathur, R.N., Sangid, M.D., Jin, X., Franco, C., Gandhi, U.N., Mori, S., Tucker III, C.L. (2014 a) Predictive Engineering Tools for Injection-Molded Long-Carbon-Fiber Thermoplastic Composites – FY 2014 First Quarterly Report. PNNL-23139. Richland, WA, Pacific Northwest National Laboratory.

5. Nguyen, B.N., Sanborn, S.E., Simmons, K.L., Mathur, R.N., Sangid, M.D., Jin, X., Franco, C., Gandhi, U.N., Mori, S., Tucker III, C.L. (2014 b). Predictive Engineering Tools for Injection-Molded Long-Carbon-Fiber Thermoplastic Composites – FY 2014 Second Quarterly Report. PNNL-23325. Richland, WA, Pacific Northwest National Laboratory.

6. Nguyen, B.N., Sanborn, S.E., Mathur, R.N., Sharma, B.N. Sangid, M.D., Jin, X., Franco, C., Gandhi, U.N., Mori, S., Tucker III, C.L. (2014 c). Predictive Engineering Tools for Injection-Molded Long-Carbon-Fiber Thermoplastic Composites – FY 2014 Third Quarterly Report. PNNL-23499. Richland, WA, Pacific Northwest National Laboratory

7. Autodesk, Inc. (2014a), "Material Testing Report MAT5404"

8. Autodesk, Inc. (2014 b). "Material Testing Report: MAT5405"

9. Autodesk, Inc. (2014 c). "Material Testing Report: MAT5406"

10. Autodesk, Inc. (2014 d). Material Testing Report: MAT5407"

11. Phelps, J.H.; Tucker III, C.L. (2009). "An Anisotropic Rotary Diffusion Model for Fiber Orientation in Short- and

Long-Fiber Thermoplastics," Journal of the Non-Newtonian Fluid Mechanics (156:3); pp.165-176.

12. Nguyen, B.N., Fifield, L.S., Wang, J., Jin, X., Franco, C., Sharma B.N., Kijewski, S.A., Sangid, M.D., Mathur, R.N., Mori, S., Gandhi, U.N., Tucker III, C.L. (2014 d). Predictive Engineering Tools for Injection-Molded Long-Carbon-Fiber Thermoplastic Composites – FY 2014 Fourth Quarterly Report, Submitted. Richland, WA, Pacific Northwest National Laboratory.

13. Nguyen, B.N., Fifield, L.S., Gandhi, U.N., Mori, S., Mathur, R.N., Franco, C. (2014 e). Mold Filling Pre-Analysis of the 3D Complex Part – Milestone Report. PNNL-23772. Richland, WA, Pacific Northwest National Laboratory.

14. Wang, J. (2007). Improved Fiber Orientation Predictions For Injection-molded Composites. Ph.D. Thesis, University of Illinois at Urbana-Champaign, Urbana, IL.

Vlastimil Kunc, Principle Investigator
Oak Ridge National Laboratory
1 Bethel Valley Road
Oak Ridge, TN 37831
Phone: (865) 919-4595; Fax: (865) 574-4357
E-mail: kuncv@ornl.gov

C. David Warren, Principal Investigator
Oak Ridge National Laboratory
1 Bethel Valley Road
Oak Ridge, TN 37831
Phone: (865) 574-9693; Fax: (865) 574-6098
E-mail: warrencd@ornl.gov

Aaron Yocum, Contract Manager
National Energy Technology Laboratory
3610 Collins Ferry Road
Morgantown, WV 26507-0880s
Phone: (304) 285-4852; Fax (304) 285-4403
Email: aaron.yocum@netl.doe.gov

Carol Schutte, Technology Area Development Manager
U.S. Department of Energy
1000 Independence Avenue, SW
Washington, DC 20585
Phone: (202) 586-1022
E-mail: carol.schutte@ee.doe.gov

Ed Owens, Technology Area Development Manager
U.S. Department of Energy
1000 Independence Avenue, SW
Washington, DC 20585-0340
Phone: (202) 586-4830; Fax: (202) 856-2476
E-mail: Edwin.Owens@ee.doe.gov

Contractor: Oak Ridge National Laboratory (ORNL)
Contract No.: DE-AC05-00OR22725

Abstract/Executive Summary

The objective of this project is to validate three-dimensional (3D) models for long carbon fiber (CF) reinforced, thermoplastic, injection-molded composites. Advanced characterization techniques are being used to generate data on CF orientation and CF length distribution within a component for a database of experimental results. Computational models, validated using a part with features representative of an automotive component, and the database of results will be made available to the general public via the worldwide web. Additionally, this predictive technology will be used to create a demonstration part, which will lead to production implementation of a separate part by Ford Motor Company.

ORNL is mainly responsible for generating and distributing experimental data, generated using proven measurement techniques, and coordinating the project. Ford Motor Company is responsible for system specification and weight-reduction analysis. BASF and PlastiComp are preparing and supplying materials for the project and will assist with part molding. ASPN/Minco and BASF are responsible for molding the final part. The University of Illinois will assist by supporting model integration with Virginia Polytechnic Institute (VPI). Moldex3D North America is responsible for implementation and commercialization of validated models.

Accomplishments

- Established acceptable temperatures for fiber length sample pyrolysis in atmosphere and in nitrogen. (FY 2014)
- Qualified molding machines intended for plaque molding and complex part molding by performing fiber length distribution measurements from purges. (FY 2014)
- Produced material for molding trials: polypropylene (PP) with 20% and 40% CF, polyamide (PA) with 20% and 40% CF. (FY 2014)
- Established target molding parameters and molded plaque samples with all materials under target. (FY 2014)
- Performed rheology measurements with cone and capillary rheometers and established model input rheology data for PP materials. (FY 2014)
- Performed preliminary flow analysis in complex part. (FY 2014)

Future Directions

- Use modified screw in a large injection molding machine to produce complex parts.
- Perform flow simulation of complex parts.
- Perform fiber length and fiber orientation measurements in complex part.
- Report comparison of flow simulations and experimental measurements.

Technology Assessment

- Target: Validate CF length to 15% of model prediction on flat plaques using the reduced-order fiber breakage model.
- Target: Validate CF length to 15% of model prediction for the complex part using the reduced-order fiber breakage model.
- Target: Validate CF orientation to 15% of model prediction for complex part using the fiber orientation model.
- Gap: A reduced-order fiber breakage model is not available in a commercial code. A reduced-order model has not been validated for injection-molded CF-reinforced thermoplastics.
- Gap: Fiber orientation and length models have not been validated in commercial codes for long fiber injection-molded CF-reinforced thermoplastics.
- Gap: An experimental dataset for validation of fiber orientation and fiber length models, specifically for CF, is not available for parts with complex geometries.

✧   ✧   ✧   ✧   ✧

Introduction

The objectives of the project are to implement and validate computational tools for predicting fiber orientation and fiber length distribution in injection-molded, long-CF, thermoplastic composites for automotive applications. Validation on a complex part with realistic features will be conducted, and the experimental results will be made available to the public. The intent is to validate prediction tools on an actual 3D automotive part made from a long–CF thermoplastic material for weight savings at an acceptable cost.

Analysis of the preliminary design indicates the potential for a weight reduction greater than 50% from both part consolidation and material substitution. Ford Motor Company, with the support of this project team, has committed to bringing the technology toward production implementation with an integrated, long–CF, injection-molded thermoplastic system. In FY 2014, the team focused on satisfying U.S. Department of Energy (DOE) requirements for part and molder qualification and generating data necessary for successful project execution upon DOE approval.

Approach

Extensive documentation and evidence were provided to DOE to document features of the selected part and prior experience of molders. Trials were performed in which the target material was purged through two different injection molding machines targeted for molding of plaques and large complex parts. The purges were evaluated for fiber length distribution to establish the suitability of the equipment for production of long-fiber-length samples.

Measurements revealed that both machines produced long-length CFs, in excess of values measured in previous projects, and DOE approved proceeding with the next project steps. Upon inspection of the fiber length data, the industrial partners judged that further improvements could be made to the large injection molding machine intended for production of a complex part. A new injection screw was designed and is being procured at the expense of BASF to support this effort. This modification has delayed the project; however, the expected improvement in fiber length distribution should make this project more valuable for the industry and provide better data to promote the application of long fiber thermoplastic use in automotive applications.

Technical work focused on refining measurement techniques for fiber length measurement and for rheology measurement. Preliminary flow analysis was performed for a seat back part. This analysis was used to make initial selections of measurement locations that would not coincide with weld lines in the sample. The runner system and other features of the mold will be modified based on best industry practices and this preliminary simulation to increase the probability of retaining long fiber lengths in the final part. The technical work is detailed below.

Results and Discussion

In anticipation of approval of the molding trial, the team prepared to perform the fiber length measurements necessary for qualification of the molding machines. The researchers had developed reliable techniques for fiber length measurements in the past [1]; however, the vast majority of that work was done with glass fiber–reinforced polymers. Working with CFs during this project requires attention to details that may not have been critical for work with glass fibers. The technique for fiber length measurement relies on multiple steps of pyrolysis during which the matrix material is burned, with a mass of fibers remaining for further processing and analysis. It is critical that the length of fibers does not change during the pyrolysis step. This was not a significant concern with glass fibers; however, CFs can be damaged easily by excessive temperature in an oxidative atmosphere. To verify our previously established pyrolysis temperatures for PP and PA materials, a series of thermogravimetric analysis (TGA) experiments [2] was performed. In these experiments, a small sample of material was continuously weighed as the temperature was slowly increased. The changes in weight identify critical temperatures at which components of the material volatilize. Figure IV-28 shows a TGA of commercial CFs. The heating profile was a continuous increase in temperature of 5°C per minute in ambient air and in nitrogen. The plot indicates significant loss of fiber mass above 600°C in ambient air and negligible loss of mass in nitrogen. A small loss of weight up to 500°C can be assigned to volatilization of fiber sizing and experimental error.

Figure IV-30 and Figure IV-31 show TGA with temperature holds at 450°C and 600°C, respectively. The results confirm that the mass loss at 450°C can be considered

negligible over an extended period of time, while 600°C temperature results in complete loss of carbon fiber mass. This validates the previous procedure in which PP and PA

materials with CFs were pyrolyzed between 400°C and 450°C.
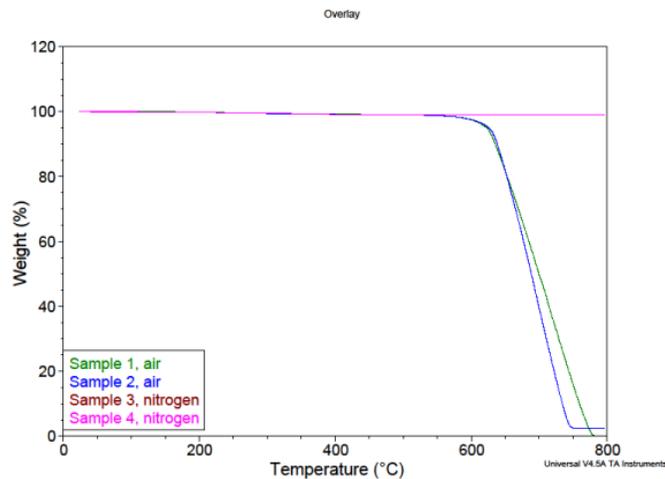
Figure IV-28: TGA of CFs with 5°C/min temperature increase in ambient air and in nitrogen.
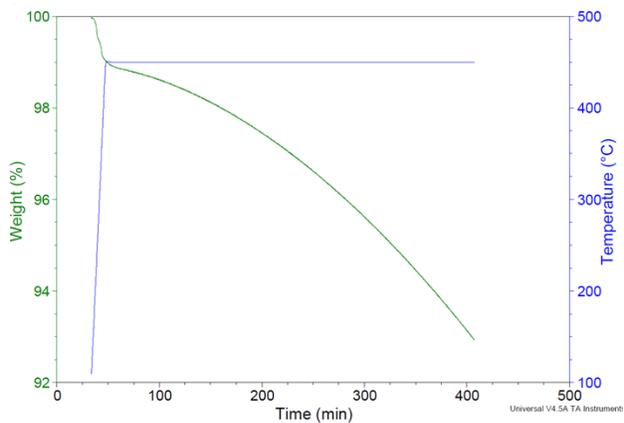
Figure IV-29: TGA analysis of CFs with a temperature increase held at 450°C in ambient air.
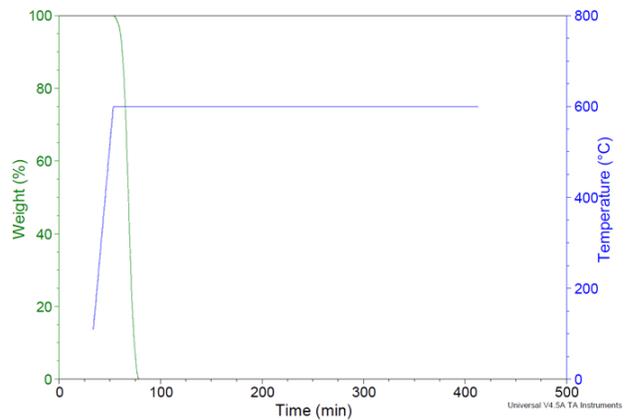
Figure IV-30: TGA analysis of CFs with a temperature increase held at 600°C in ambient air.

After approval to proceed with initial molding trials was received, purges of PA material with 40% CF were performed at PlastiComp and ASPN/Minco using best molding practices. ASPN/Minco also molded under slow and fast fill rate conditions.

To satisfy the requirement of molder qualification, the team performed fiber length measurements for purge samples from injection molding machines at PlastiComp and ASPN that will be used for plaque and part molding. The measured weight average fiber lengths were 7.33 mm and 4.44 mm, respectively, for the PlastiComp and ASPN purges. The input fiber length was 10 mm. The measurements show significant retention of long fibers, resulting in long fiber injection-molded material, and confirm that subsequent validation efforts will generate fiber orientation and fiber length distribution data

significantly different from previously investigated short fiber materials with average fiber lengths of 2 mm or less.

The material selected for this trial was PA-40% CF, which is the material with the highest fiber loading and highest molding temperature considered in this project. High fiber loading and high resin temperatures result in increased fiber breakage due to fiber-fiber interaction and increased shear gradients. Results presented therefore represent the worst case scenario, with all other materials considered in the project producing equivalent or greater fiber length retention.

The purge trials were performed using the same batch of material at PlastiComp in collaboration with senior research staff from ASPN/Minco and BASF. The purges were performed with best molding practices and the industry typical setup for each machine. In addition, ASPN performed at high

IV.5. Predictive Engineering Tools for Injection-Molded Long Carbon
Fiber Thermoplastic Composites—Oak Ridge National Laboratory

Kunc and Warren–ORNL

screw rotations per minute (RPMs) test to study the degradation of material as a function of screw speed.

Figure IV-31 shows PlastiComp and ASPN purges as supplied to ORNL for fiber length measurements. Both purges presented significant challenges for fiber length measurement because the content of long fibers was so high that the standard method for sample selection and filament separation had to be modified. Figure IV-32 shows a nonuniformity of purge and the presence of voids, which will influence fiber length measurement results depending on the particular location in the sample selected for measurement. Multiple sample isolations and partial measurements were performed to confirm that reported data were representative of the samples. All qualitative observations and partial measurement

steps confirmed the significant presence of long fibers, an excellent fiber length retention.

Figure IV-33 and Figure IV-34 show isolated fiber samples for ASPN and PlastiComp samples. Both samples contained primarily long fibers. ASPN fibers appear aligned in a layered fashion, while PlastiComp filaments appear to be more entangled. Fiber length distributions for these samples are shown in Figure IV-35 and Figure IV-36, with averages and maximums summarized in Table IV-9. Figure IV-37 shows the fiber length distribution for the sample produced at ASPN with high screw RPMs. Clearly, high screw RPMs degrade fiber length significantly and demonstrates the ability to modify material microstructure by varying processing conditions.

Figure IV-31: Purges as supplied to ORNL for measurement.

Figure IV-32: Nonuniform profile and voids within ASPN purges.

Figure IV-33: Selected ASPN fibers showing long-aligned fibers.
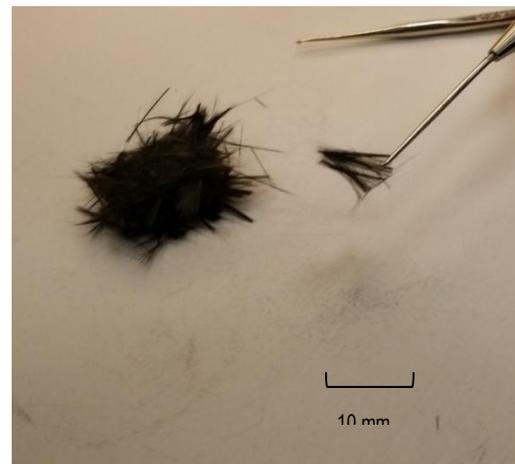
Figure IV-34: Selected PlastiComp sample showing long-entangled fibers.

IV.5. Predictive Engineering Tools for Injection-Molded Long Carbon
Fiber Thermoplastic Composites—Oak Ridge National Laboratory

Kunc and Warren–ORNL
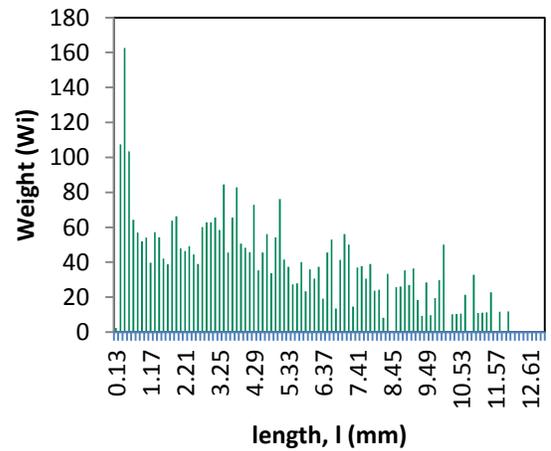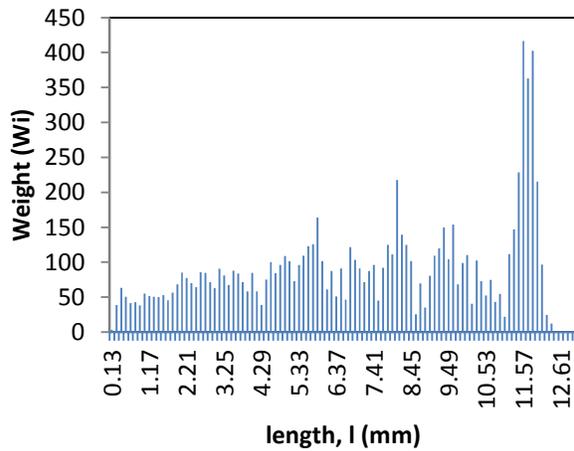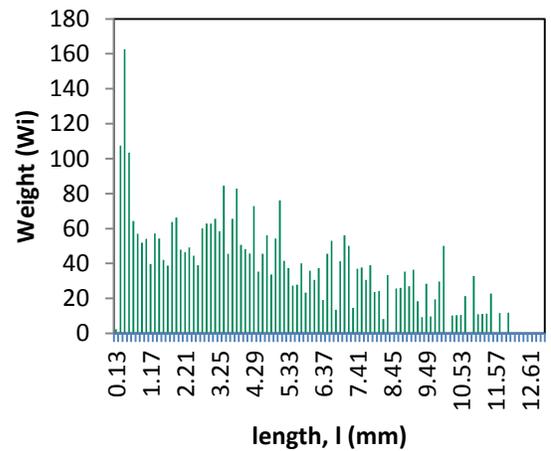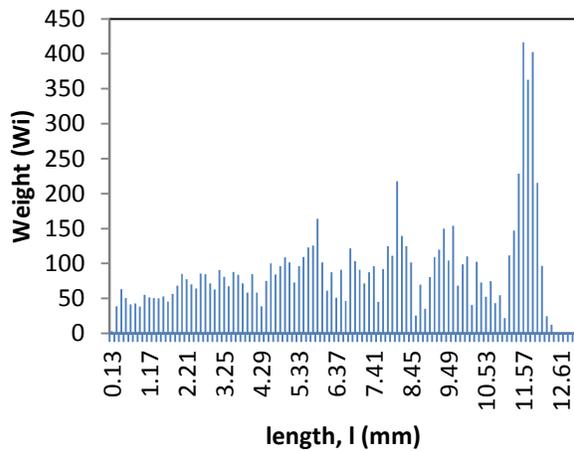
Figure IV-35: PlastiComp fiber length distribution.

Figure IV-36: ASPN fiber length distribution.

Table IV-9: Fiber length averages for measured samples.

Specimen description	Number of fibers measured	Fiber length Average (mm)	Fiber width Maximum (mm)
PlastiComp	2,185	4.06	7.33
ASPN	2,134	1.69	4.44
ASPN-high RPMs	*2,898*	*0.46*	*1.76*

IV.5. Predictive Engineering Tools for Injection-Molded Long Carbon
Fiber Thermoplastic Composites—Oak Ridge National Laboratory

Kunc and Warren–ORNL
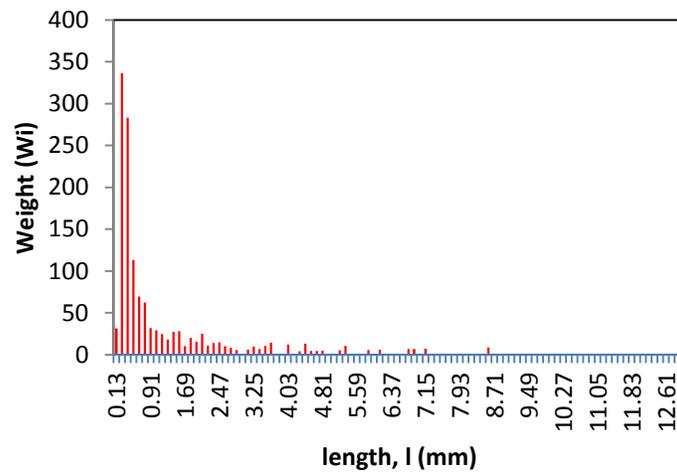
Figure IV-37: ASPN fiber length distribution for sample produced with high screw RPMs.

Progress has been made on the rheological characterization [3] of the PA 66 and PP materials. Processing these materials through a single screw extruder disperses the fibers and causes significant fiber attrition. Transient shear measurements were attempted using the 20 wt % PP suspension in a cone and plate rheometer (Figure IV-38) with a donut shaped sample and a sliding plate rheometer (Figure IV-39). In both cases, the flow was not uniform and the sample geometry changed, which made stress measurements unreliable.

Results for steady shear viscosity were obtained in a capillary rheometer at 220°C for the PP materials. Two

capillary dies were used: one with a 2 mm diameter and a 30 mm length, one with a 1 mm diameter and 20 mm length. The 20 and 40 wt % materials exhibit a power-law dependency in viscosity (η) with respect to shear rate (γ or ω), shown in Figure IV-40. The viscosity of the pure PP matrix was measured using a combination of cone and plate and capillary rheometers. The pure matrix viscosity can be fit using the Carreau-Yasuda generalized Newtonian fluid model. A zero shear viscosity was observed in the pure matrix that was not evident in the fiber suspensions.

Figure IV-38: Cone and plate rheometer with a sample.

Figure IV-39: Sliding plate rheometer with a sample.

IV.5. Predictive Engineering Tools for Injection-Molded Long Carbon
Fiber Thermoplastic Composites—Oak Ridge National Laboratory

Kunc and Warren–ORNL
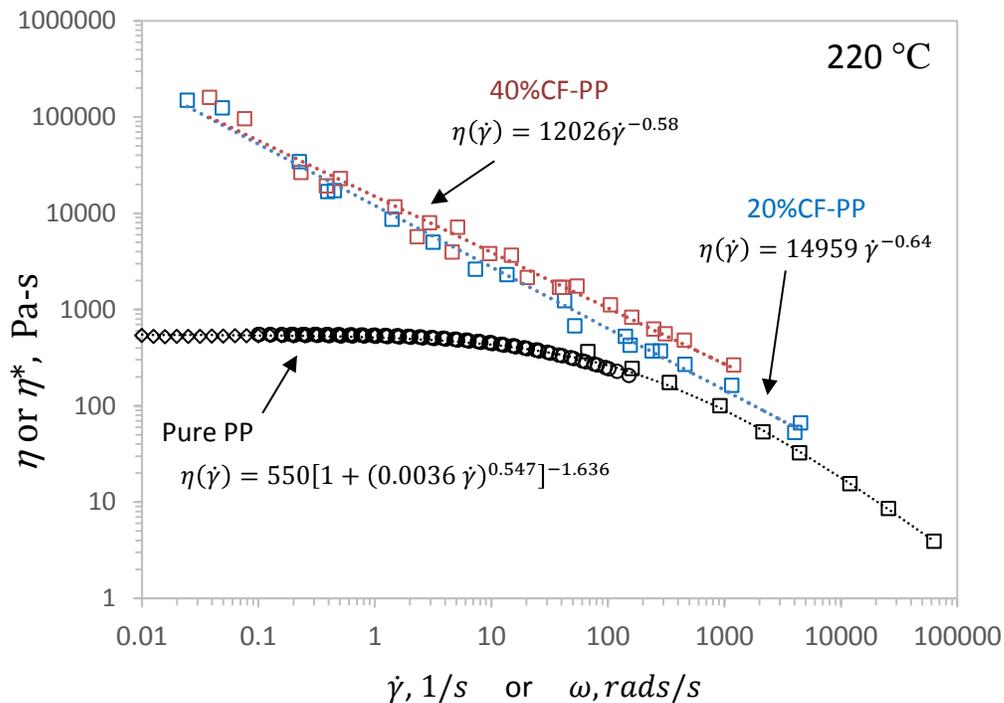
Figure IV-40: Viscosity versus shear rate data for the pure matrix (black) and 20 wt % (blue) and 40 wt % (orange) CF suspensions in PP. Data were obtained by cone and plate steady shear (◊), cone and plate small amplitude oscillatory (○), and capillary (□) measurements.

Viscosity results for the PA 66 matrix produced poor agreement between test methods and temperatures. Continuing work will focus on obtaining these data. Testing the CF-PA suspensions in the capillary rheometer has also produced poor results. Possible bridging of fibers at the capillary entrance is causing unstable flow through the capillary. To remedy this issue, a larger capillary die, 4 mm in diameter, is currently being constructed.

Moldex3D North America is responsible for providing accurate predictions of fiber orientation and fiber length using Moldex3D software. The predictive capabilities of Moldex3D's iARD-RPR model are being validated using experimental data generated at VPI with plaques molded in a separate effort. An end-gated plaque with 40 wt% long carbon fiber-nylon 66 is being used for this study. Local fiber orientation and length distributions at key regions in the part are being measured. Moldex3D's fiber orientation and fiber length predictions are briefly presented below.

Measurements were taken at 10 locations on the plaque (Figure IV-41). In Moldex3D analysis, three locations—(0,0), near the gate; (50,90), at 50% length and 90% width; and (90,10), at 90% length and 10% width—were chosen for a comparison of the experimental and predictive fiber orientation tensor components distribution through the normalized thickness. Those results are shown in Figure IV-42–Figure IV-44 for orientation component vs. normalized thickness (z/h). Moldex3D predictions are in good agreement with experimental data. Critical features are clearly exhibited, including (1) core extreme point, (2) core width, (3) shell height, (4) skin layer, (5) A11–A22 core cross sections, and (6) constrained small A33. Measured fiber lengths were compared to fiber lengths predicted by the model. An overall accuracy assessment of these results, based on the average A11 value, shows that there is about a 10% deviation between experiment and prediction. The models will be further scrutinized against data from plaques with optimized fiber lengths.

IV.5. Predictive Engineering Tools for Injection-Molded Long Carbon
Fiber Thermoplastic Composites—Oak Ridge National Laboratory

Kunc and Warren–ORNL
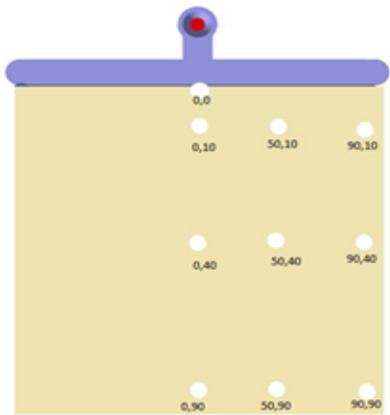
Figure IV-41: Measured points of fiber orientation taken at 10 locations on end-gated plaque.
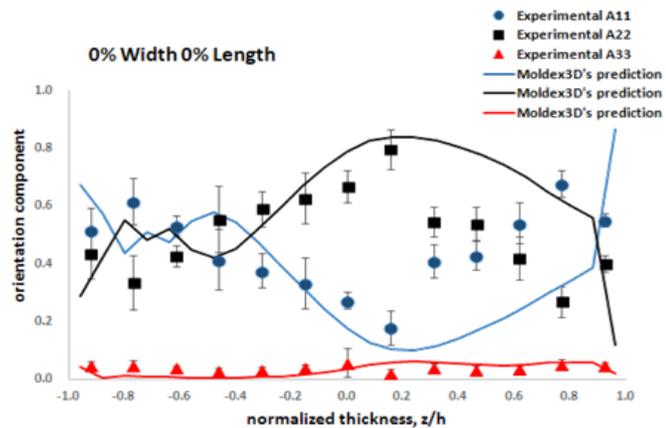
Figure IV-42: Experimental and predictive fiber orientation tensor components distribution through the normalized thickness at location (0, 0), near the gate.
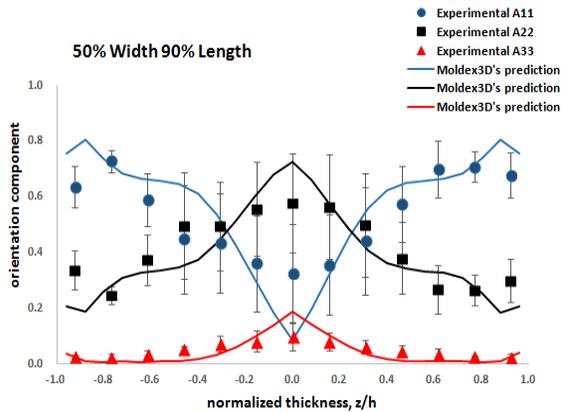
Figure IV-43: Experimental and predictive fiber orientation tensor components distribution through the normalized thickness at location (50, 90).
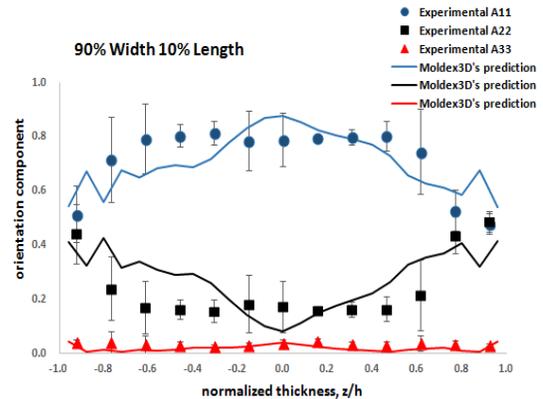
Figure IV-44: Experimental and predictive fiber orientation tensor components distribution through the normalized thickness at location (90, 10).

Preliminary flow analysis was performed by Moldex3D on the complex part to understand the locations of weld lines and to support modification of the mold before performing molding trials. Figure IV-45 shows the model of the validation part with the existing runner system. Some features of the runner system and potentially the part will be modified to increase the likelihood of retaining long fibers in the part. Figure IV-46 illustrates flow time with major weld lines. The locations of weld lines must be well understood to avoid sampling from regions containing weld lines. Figure IV-47 and Figure IV-48 show locations of all predicted weld lines on the front and back sides of the part.

More conclusive simulations will be performed when the modification to the runner system has been completed and all rheological data are available. Fiber length and fiber orientation measured from plaques using previously developed methods [4–6] will be used to establish model parameters for fiber orientation and fiber breakage models.

These measurements are ongoing and will be reported in future reports.

Technology Transfer Path

The primary technology transfer path for this effort is to work closely with the industry partners—Minco, BASF, Moldex, and Ford—which have the business interests and marketing capability to commercialize the technology developed in this project. Moldex will integrate the computational models into its computational software, and Ford will use those models and the molding technology developed in future vehicle designs. Because the computational models and the database of results will be made available to the general public via the World Wide Web, commercial molders will have access to data generated by this project to assist them in determining molding parameters.

IV.5. Predictive Engineering Tools for Injection-Molded Long Carbon
Fiber Thermoplastic Composites—Oak Ridge National Laboratory

Kunc and Warren–ORNL
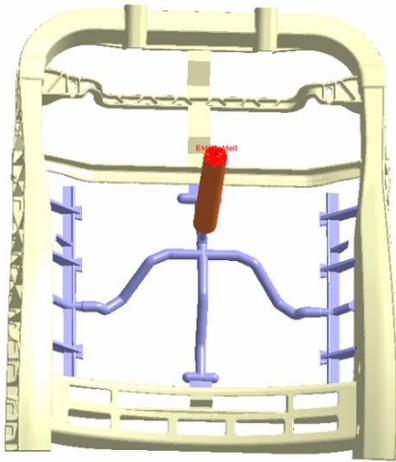
Figure IV-45: Model of complex part including the existing runner system.

Figure IV-46: Visualization of flow time with major weld lines. Yellow indicates shorter flow times and red longer flow times which will correspond to the suspected location of weld lines.
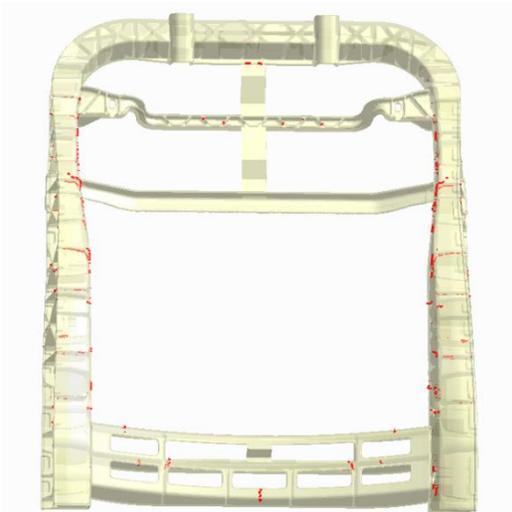
Figure IV-47: Visualization of weld lines in the front section of the complex part.
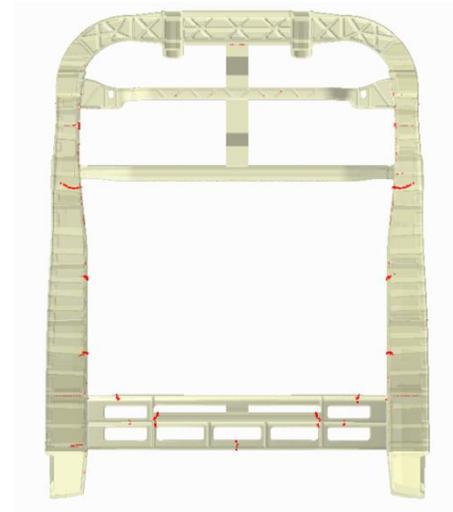
Figure IV-48: Visualization of weld lines in the back section of the complex part.

Conclusion

In FY 2014, the team satisfied DOE requirements for part selection and molder qualification, clearing two go-no go milestones in the project. Fiber length measurement results from purge trials have shown the ability of the molders to retain long fiber length in injection-molded CF-filled thermoplastics. The team produced materials for all molding trials and molded plaques used for establishing model parameters. Initial simulations of the complex part have revealed a significant number of potential weld lines that will have to be avoided during sampling. Technical details of fiber length measurements and rheology measurements are discussed in this report.

Presentations/Publications/Patents

None this year.

References

1. Kunc, V.; Frame, B.J.; Nguyen, B.N.; Tucker III, C.L.; Velez-Garcia, G. "Fiber Length Distribution Measurement for Long Glass and Carbon Fiber Reinforced Injection

IV.5. Predictive Engineering Tools for Injection-Molded Long Carbon
Fiber Thermoplastic Composites—Oak Ridge National Laboratory

Kunc and Warren–ORNL

Molded Thermoplastics." *Proceedings of the 7th Annual SPE Automotive Composites Conference and Exposition,* Troy, Michigan, 2007.

2. Coats, A.W.; Redfern, J.P. "Thermogravimetric Analysis: A Review." *Analyst* , *(88)*, 1963, pp. *906–924.*

3. Macosko, Christopher W. Rheology: Principles, Measurements, and Applications; Wiley-VCH, 1994.

4. Eberhardt, C.; Clarke, A. "Fibre-orientation measurements in short-glass-fibre composites. Part I: automated, high-angular-resolution measurement by

confocal microscopy." *Compos. Sci. Technol.***,** (61:10), 2001, pp. 1389–1400.

5. Velez-Garcia, G.M.; et al. "Unambiguous orientation in short fiber composites over small sampling area in a center-gated disk." *Composites, Part A***,** (43:1), 2012, pp. 104–113.

6. Velez-Garcia, G.M.; et al. "Sample preparation and image acquisition using optical-reflective microscopy in the measurement of fiber orientation in thermoplastic composites." *J. Microsc.* (248:1), pp. 23–33.

IV.6 Validation of Carbon-Fiber Composite Crash Models Via Automotive Crash Testing– USAMP, LLC

Omar Faruque, Principal Investigator
Passive Safety Department
Ford Motor Company Research and Innovation Center
Post Office Box 2053
Dearborn, MI 48121
Phone: (313) 322-1044
E-mail: ofaruque@ford.com

Libby Berger, Principal Investigator
Chemical Sciences & Material Systems Lab
General Motors R&D Center
MC 480-106-710
30500 Mound Road
Warren, MI 48090
Phone: (248) 930-5018
E-mail: libby.berger@gm.com

Aaron Yocum, Project Manager
National Energy Technology Laboratory
Post Office Box 880
3610 Collins Ferry Road
Morgantown WV 26507-0880
Phone: (304) 285-4852
E-mail: aaron.yocum@netl.doe.gov

Carol Schutte, Technology Area Development Manager
U.S. Department of Energy
1000 Independence Avenue, SW
Washington, DC 20585
Phone: (202) 586-1022
E-mail: carol.schutte@ee.doe.gov

Contractor: United States Automotive Materials Partnership, LLC
Contract No.: DE-EE0005661

Abstract/Executive Summary

The objective of this project is to validate physics-based crash models for simulating primary load carrying automotive structures made of production-feasible carbon fiber composites for crash energy management. This will include the two Automotive Composites Consortium/USAMP-developed meso-scale models from the University of Michigan (UM) [1-3] and Northwestern University (NWU) [4] [5], as well as existing composite crash material models in four major commercial crash codes (LS-DYNA [6-10], RADIOSS [11-13], PAM-CRASH [14] [15], ABAQUS [8] [16-18]). The models will be used to predict quasi-static and dynamic crash behavior of a vehicle front end sub-system made of carbon-fiber composites. The project goal is to validate the models for simulating crash of a lightweight carbon-fiber composite front bumper and crush can (FBCC) system. In order to do this, we are determining the crash behavior of a reference steel FBCC; designing, building, and crash testing a composite FBCC predicted to have equivalent crash behavior; and comparing the predictions with the physical crash tests. The crash performance of the composite FBCC should be equivalent to the steel FBCC under various crash-loading modes. The successful validation of these crash models will allow the use of lightweight carbon-fiber composites in automotive structures for significant mass savings.

During Year 2, the project team completed the baseline crash testing for both high-speed and low-speed load cases for the steel FBCCs, as well as the baseline predictions of crash outcomes by four leading commercial finite element analysis codes. The crash energy and peak loads from the steel FBCC tests were used to set targets for driving the design of the composite FBCCs. After analysis of several crush can and bumper beam concepts, the project team has narrowed down the options and settled on a C-channel bumper design with internal ribs, and a two-piece hat section (square or circular) for the crush cans. These components will likely be compression molded from thermoset epoxy fabric with unidirectional reinforcements, with chopped carbon fiber sheet molding compound (SMC) and joined by adhesive bonding with mechanical peel stoppers. These decisions have been supported by molding of plaques and simple shapes, and the testing of material properties required by the commercial codes, with more specialized material testing requirements for the academic codes. Procurement of several material systems of thermoplastic (TP) laminate materials was also completed in Year 2, and material property measurements and manufacturability evaluations are planned in Year 3.

Accomplishments

- Completed development of a thermoset (TS) materials design database of minimum material property data required to support composite FBCC design and crash model validation at element, coupon and component - level.
- Conducted a second round of TS compression molding trials, and molded closed-end TS hat-shape parts for evaluation. The hat samples served to evaluate four-point bending properties and will be used as an intermediate step in validation of university-led material models via axial crush testing, as well as for screening using two non-destructive evaluation (NDE) methods.
- Completed all physical baseline steel bumper/crush can assembly crash testing, including high speed – full frontal,

40% frontal offset, 30 degree angular and midpoint frontal pole; low speed – midpoint and quarter frontal. Data analysis is complete for all six crash load cases, and test protocols are documented. The steel crash data analysis was used to set the performance targets for the composite FBCC.

- Completed predictive modeling of all steel baseline steel bumper/crush can assemblies for all four commercial codes (PAM-CRASH, LS-DYNA, ABAQUS and RADIOSS).
- NDEs using ultrasonic pulse/echo and soft x-rays were demonstrated on both flat plaques and hat section forms via inter-ply inserts. Structural health monitoring (SHM) using microelectromechanical systems (MEMS) accelerometers and fiber Bragg grating strain sensors was also initiated.

Future Directions

- Complete correlation analyses between commercial crash code predictions and crash test data for all six load cases for the baseline steel FBCC crash testing and analyze results for validity and reproducibility. Compare with predictive modeling results using the selected commercial codes.
- Obtain detailed material property test data as inputs for the various modeling strategies and computational codes and select composite material and process system.
- Using the findings from baseline steel crash tests and computer-aided engineering (CAE) with down-selected composite FBCC concepts, complete the design of a composite FBCC such that it is predicted to perform at least as well as the steel FBCC in the six crash modes.
- Procure tooling and fabricate thermoset carbon fiber composite FBCCs for crash testing and correlation with targets determined from the crash of the steel FBCCs; develop joining strategy and validate with joining trials; identify opportunities for thermoplastic composite materials and lower-cost carbon fiber reinforcements.
- Procure fiber Bragg grating dynamic strain analyzer and compare its impact detection capabilities to low cost MEMS accelerometers for SHM.

Technology Assessment

- Target: Assess the validity of material models for crash performance of carbon-fiber composites. Design, fabricate and crash-test a composite FBCC to provide equivalent crash performance to a steel FBCC, while demonstrating a 33% weight savings over the baseline steel structure.
- Gap: Unvalidated meso-scale material models developed by the UM and NWU through Automotive Composites Consortium (ACC)/USAMP support for crash-critical carbon fiber composite structures.
- Gap: Unknown failure modes and composite material properties for micro- and meso-scale material models.
- Gap: Unproven NDE methods for detection of crash damage or durability issues.
- Gap: Error band for steel FBCC not established, defaulting to "industry best practice" of $\pm$10%.

✧　　✧　　✧　　✧　　✧

Introduction

Several new material models for predicting the behavior of carbon-fiber composites were developed by academic collaborators over the last decade under the oversight of the ACC and USAMP, sponsored by the DOE. These included micro-scale and meso-scale models of braided carbon fabric composite materials, as well as random fiber composites. [19-22] Of these, two models in particular – UM's RUC-based meso-scale material model [1-3] and NWU's micro-plane representative unit cell (RUC) mode; [4] [5] – are promising enough to be used for crash simulation of composite structures. In addition, several engineering design houses and commercial crash software developers have also implemented many advanced constitutive models to characterize highly nonlinear crash response of composite structures in the four major finite element-based commercial crash codes – i.e., LS-DYNA, RADIOSS, ABAQUS and PAM-CRASH. To enable ongoing lightweighting initiatives incorporating advanced materials such as carbon-fiber composites, these models require validation and are the subject of the USAMP - Validation of Material Models (VMM) Project.

Approach

Our approach to validating these models consists of selecting a production steel FBCC, utilizing commercial crash codes to predict the FBCC's crash performance, crashing it and comparing the crash predictions to the crash results to determine the appropriate targets. These targets will be utilized to design the carbon-fiber composite FBCC. A carbon-fiber composite FBCC will then be fabricated, crash behavior predicted (using commercial codes and the UM and NWU material models), experimentally crash tested, and the predictions will be compared to the crash results.

The USAMP Project is organized into seven main tasks to be executed over the 48-month period with results and discussion at the end of Year 2 given below – the status of active tasks is indicated:

Task 1: Project Administration/Management - ongoing

Task 2: Experimental/Analytical Characterization of Crash Performance of a Baseline Steel FBCC – completed

Task 3: Design and Crash Performance Predictions of a Composite FBCC – in progress

Task 4: Manufacture/Assembly of the Composite FBCC – recently begun

Task 5: Crash Test Composite FBCC – begins in Year 4.

Task 6: NDE of Composite Structure – in progress

Task 7: Compare Experimental Results with Analytical Predictions – begins in Year 4.

Results and Discussion

Task 1: Project Administration/Management

Members from the USAMP companies organized a vertically integrated research and management team. The team includes leading academic researchers proficient in modeling, automotive design/engineering service suppliers, composite manufacturers, and crash test vendors. The National Center for Manufacturing Sciences, an experienced research and technology management organization, coordinates the technical and management tasks for this project.

Task 2: Experimental/Analytical Characterization of Crash Performance of a Baseline Steel FBCC

Crash testing for the remaining load cases (low-speed frontal and quarter impacts) was conducted and analyzed by Wayne State University (WSU). In parallel, Engineered Solutions, Inc. (ESI) completed simulations of all load cases using the agreed upon commercial codes (PAM-CRASH, LS-DYNA, ABAQUS and RADIOSS). Similar to the high-speed testing completed last year, accelerometers were used for calculating velocity and to describe the overall system level deceleration profile, high-speed video was used to determine system displacement and deformations and impact wall load cells were used to measure impact force to compare to the mass-acceleration calculation obtained from accelerometers. Once again, test-to-test variability was minimized with a high coefficient of variation (CoV) in impact speeds obtained/measured as evident in Table IV-10.

Table IV-10: Impact velocities for low-speed frontal quarter impact test mode.

Bumper #	Velocity (mph)
54	9.17
55	9.17
56	9.62
57	9.73
58	9.73
59	9.4
Average	**9.47**
Stand Dev.	**0.26**
CoV	**2.76**

For the remaining low-speed testing, a similar test setup was employed to that of the high speed testing completed last year. Figure IV-49(a) Overhead view and Figure IV-49(b) Side view illustrates schematics of the impact load cases.

Figure IV-50 demonstrates a real world depiction of the test setup. It is important to note that the impactor on the sled was built specific to Federal Motor Vehicle Safety Standards (FMVSS) part 571, specific for low-speed damageability and differed from that used in the high-speed load case scenarios completed last year. However, the overall sled-on-sled test methodology was maintained.

Post processing for all test modes, including the recently completed low-speed testing is complete. Similar to high-speed testing, redundant measures were put in place in order to guarantee time history integrity as well as minimize number of tests per mode. Once again, excellent repeatability was witnessed from test to test. Figure IV-51 and Figure IV-52 illustrate this looking at force-time histories and force-displacement histories respectively.

Once again, excellent agreement was found in the redundant measures and can clearly be seen in Figure IV-53 comparing the calculated force of the impact using the mass of the system and deceleration profile compared to that of the directly measured load cells.

WSU has completed the preliminary final report and submitted to the project task leaders that are currently editing the document, which should be complete by December of quarter four 2014. An investigation into the correlation of steel commercial code predictions and results of physical testing is ongoing using the objective rating metrics for dynamic systems standard. Preliminary assessment shows good correlation of the full frontal and frontal offset impact tests to the commercial code predictions. In Figure IV-54(a), Figure IV-54(b), Figure IV-54(c) and Figure IV-54(d), such an example of the comparison to four commercial CAE code predictions with respect to physical testing demonstrates the overall score and the time history of a given input, here impact force from the full frontal high-speed load case. Using this methodology, the scores are normalized to one hundred.
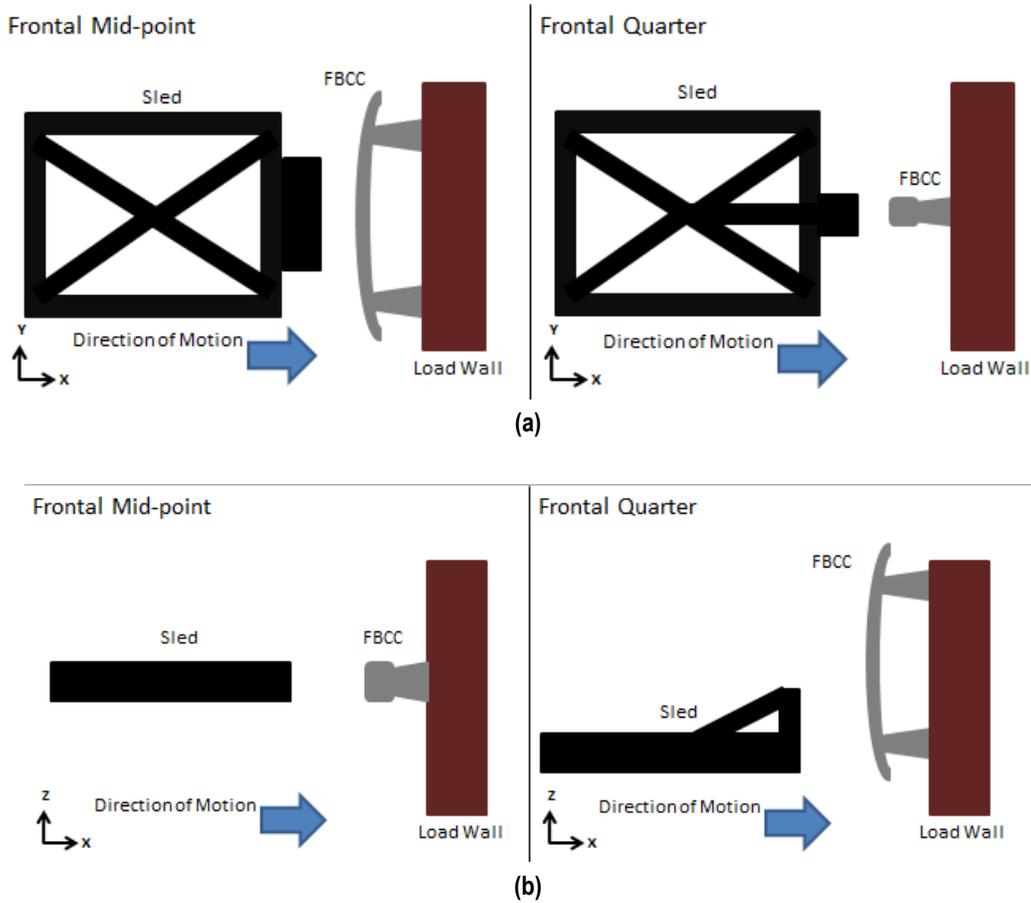
Figure IV-49: (a) Overhead schematic of low-speed tests; (b) Side schematic of low speed tests.
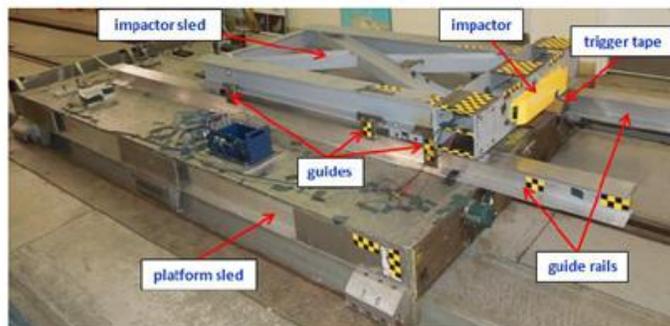
Figure IV-50: Set-up of sled-on-sled system used for low-speed test modes.
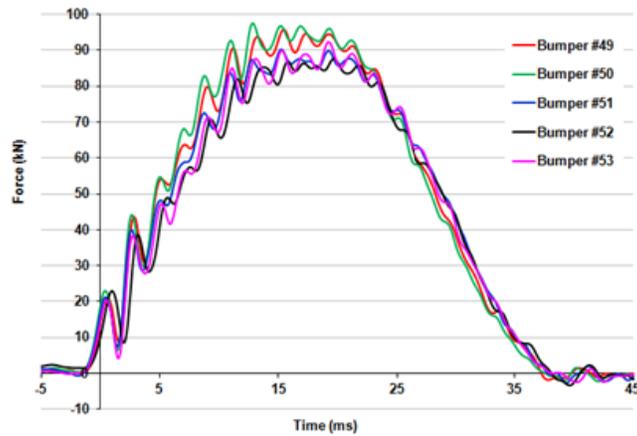
Figure IV-51: Impact force vs. time of frontal mid-point impact tests.
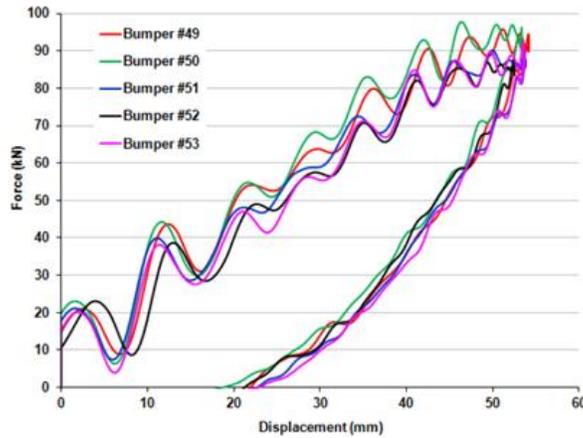
Figure IV-52: Impact force vs. displacement of frontal mid-point impact tests.
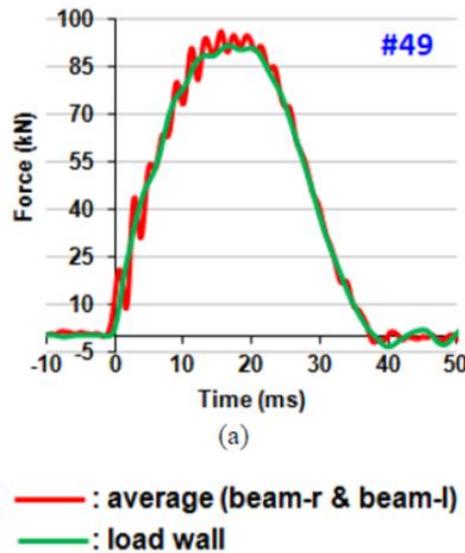
Figure IV-53: Impact force vs. time comparing discrete measurements from load cells with calculated force.
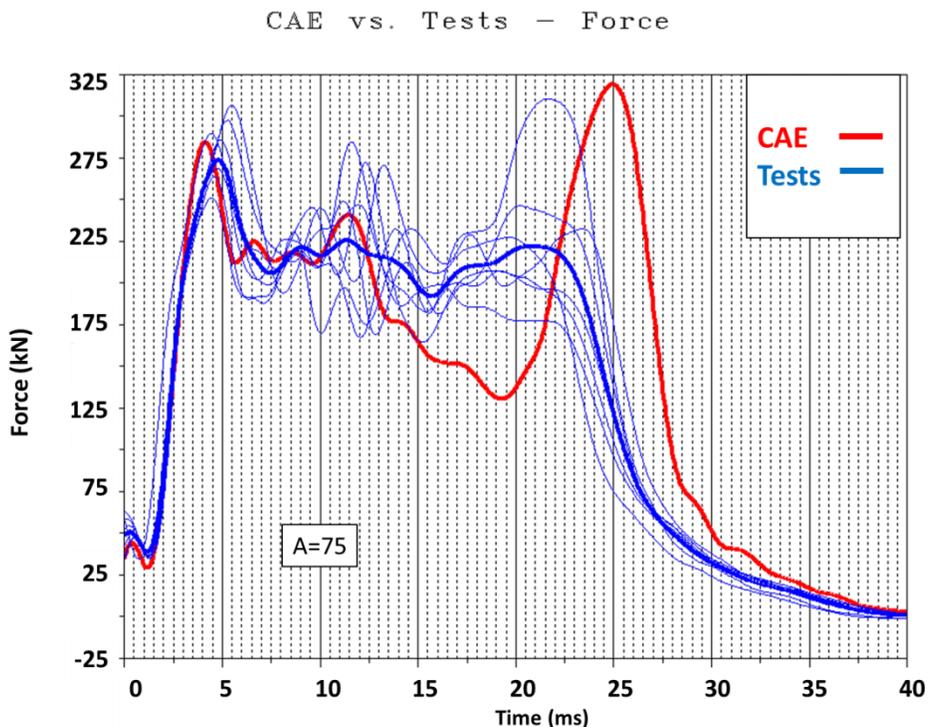
(a) Force-time history comparison of commercial code A to physical tests. Dark blue curve represents average of all physical tests.
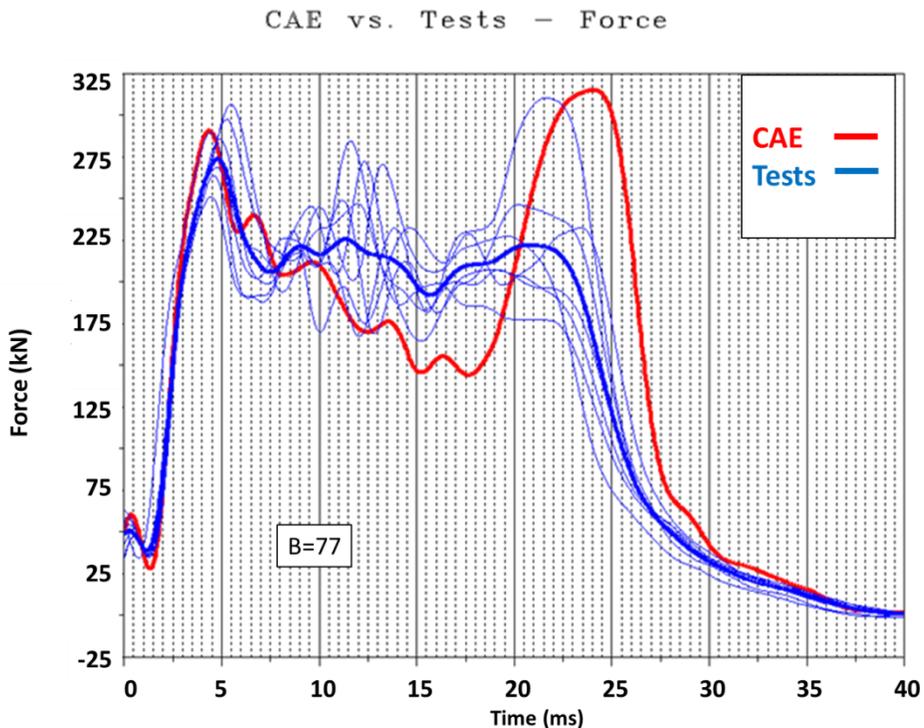
(b) Force-time history comparison of commercial code B to physical tests. Dark blue curve represents average of all physical tests.
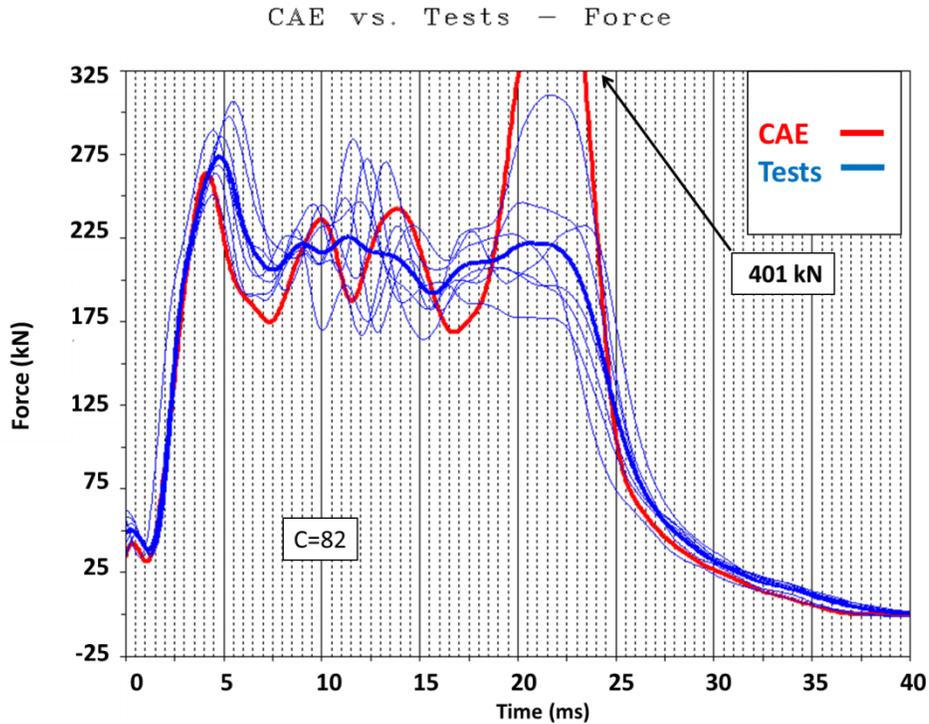
(c) Force-time history comparison of commercial code C to physical tests. Dark blue curve represents average of all physical tests.
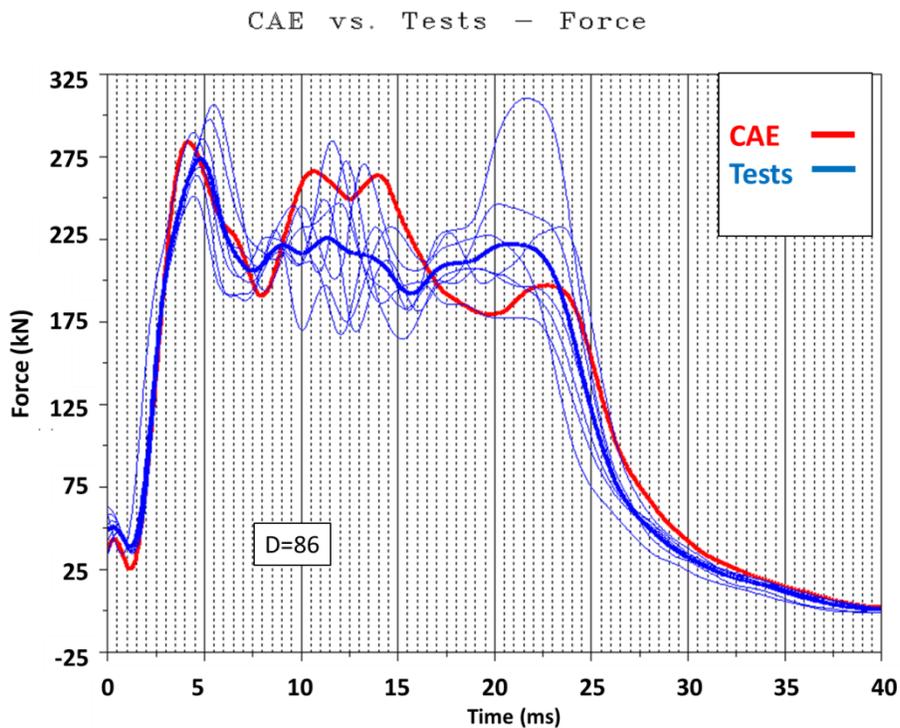
(d) Force-time history comparison of commercial code D to physical tests. Dark blue curve represents average of all physical tests.

Figure IV-54a-d: Comparison of physical crash modes (dark blue is average of all tests, light blue represents each test, red is CAE prediction) to CAE predictions for impact force.

Task 3 Design and Crash Performance Predictions of a Composite FBCC

Task 3.1 Material and Process Selection:

Extensive USAMP collaborations with NWU, UM, and ESI - the selected design/CAE source - have resulted in a consolidated list of critical material properties which will provide all of the required data for the crash modeling with commercial codes and the university codes. This includes tensile, compression, shear, and flexural testing, as well as cyclic tension, interlaminar fracture toughness [G_{1c} (Double Cantilever Beam) and G_{2c} a(End Notch Flex)] at three thicknesses, notched tension at three sizes, and micrography analysis of the geometry of the woven samples. [23-29] In order to obtain material properties for the modeling, 250 mm x 450 mm plaques were compression molded in a variety of configurations. These include:

- Unidirectional carbon/epoxy prepreg
  - $(0)_8$
  - $(0/90)_{2s}$
  - $(0/45/-45/90)_s$ (quasi-isotropic (QI))
- Woven carbon/epoxy prepreg, 2x2 twill
  - $(0/90)_{2s}$
  - $(0/45/-45/90)_s$ (QI)

The material property database development for these plaques has been completed at Delsen Labs, Glendale, CA, and includes:

- tensile
- compression
- rail shear
- bending (flex)
- cyclic tensile
- thermal analysis glass transition temperature (T_g)
- fiber content testing

All of these tests are quite standard except for the cyclic tension. Figure IV-55 shows an example of the cyclic tension testing, which measures the shear damage to the sample by repeated loading to partial strain. The shear damage, d_{12}^i, is the loss in shear modulus at the tested strain as a ratio with the beginning shear modulus:

$$d_{12}^i = 1 - G_{12}^i / G_{12}^0 \qquad (1)$$

where G_{12} is the shear modulus. The partial strain values were taken as 10%, 17.5%, 25%, 37.5%, 50%, 70%, and 90% of the ultimate strain. The sample is stressed to 10% of the ultimate strain, then returned to zero load, then stressed to 17.5%, returned to zero, stressed to 25%, returned to zero, and so forth. This test is required by PAM-CRASH for the unidirectional plaques molded as $(0)_8$ and $(0/90)_{2s}$, and tested in tension at 45°, and for woven plaques at $(0/90)_{2s}$ tested in tension at 0° and 45°, and in compression at 90°. Table IV-11 shows the shear damage after the cycle, up to 90° loading, and Figure IV-56 shows the shear damage as a function of the loading to the specified strains.

The second plaque molding trial of compression molding epoxy prepreg plaques used a larger plaque tool of 610 mm x 610 mm. A variety of configurations, including unidirectional, woven, and mixed unidirectional and woven plaques were molded. The unidirectional and woven $(0)_8$ and $(0/90)_{2s}$ plaques provide samples for properties as further necessary for the calibration of the material cards in the various codes used for the design of the FBCC. The QI plaques allow for the verification of the material cards. The mixed materials will serve as models for a possible bumper beam layup configuration.

Plaques from this molding trial will also be used to provide material properties for fracture toughness and size effects, as required by the models from NWU and UM. The fracture toughness testing, G_{1c} and G_{2c}, requires molded-in crack initiators, for which we used strips of polytetrafluoroethylene (PTFE) tape as interlaminar initiators in some of the plaques. The size effect testing investigates the effect of sample size on the fracture properties, and ideally uses factors of 3 and 9 for the length and thickness of the G_{1C} and G_{2C}, and length and width for the notched tensile testing, compared to the standard sample size. [30-33] Because of the limitations of our plaque size, we compromised these factors to 3 and 5 for the G_{1C} and 2.5 and 4 for the G_{2C}, with the lengths being the non-insert molded portion of the sample. These tests will be done at NWU, and are expected to be completed in early Q1 of FY 2015.

Table IV-11: Shear damage after seven cycles of loading at progressive strain rates, up to 90% of the expected ultimate strain.

Material	Loading Mode		Shear damage
Uni $[0]_8$	Tension @ 45°	mean	**0.010**
Uni $[0/90]_{2s}$	Tension @ 45°	mean	**0.189**
Woven $[0/90]_{2s}$	Tension @ 0°	mean	**-0.010**
Woven $[0/90]_{2s}$	Compression @ 45°	mean	**-0.002**
Woven $[0/90]_{2s}$	Tension @ 45°	mean	**0.133**

WF – C25 – 11 – 45T – C – R3 Cyclic Tension

Cycle	Color	Elastic Modulus (msi)	Poisson's Ratio	Shear Modulus (msi)	Shear Damage
1	Red	1.934	0.677	0.577	0.000
2	Green	1.924	0.682	0.572	0.009
3	Blue	1.875	0.693	0.554	0.040
4	Cyan	1.779	0.692	0.526	0.088
5	Magenta	1.723	0.705	0.505	0.124
6	Yellow	1.675	0.709	0.490	0.150
7	Black	1.628	0.703	0.478	0.171
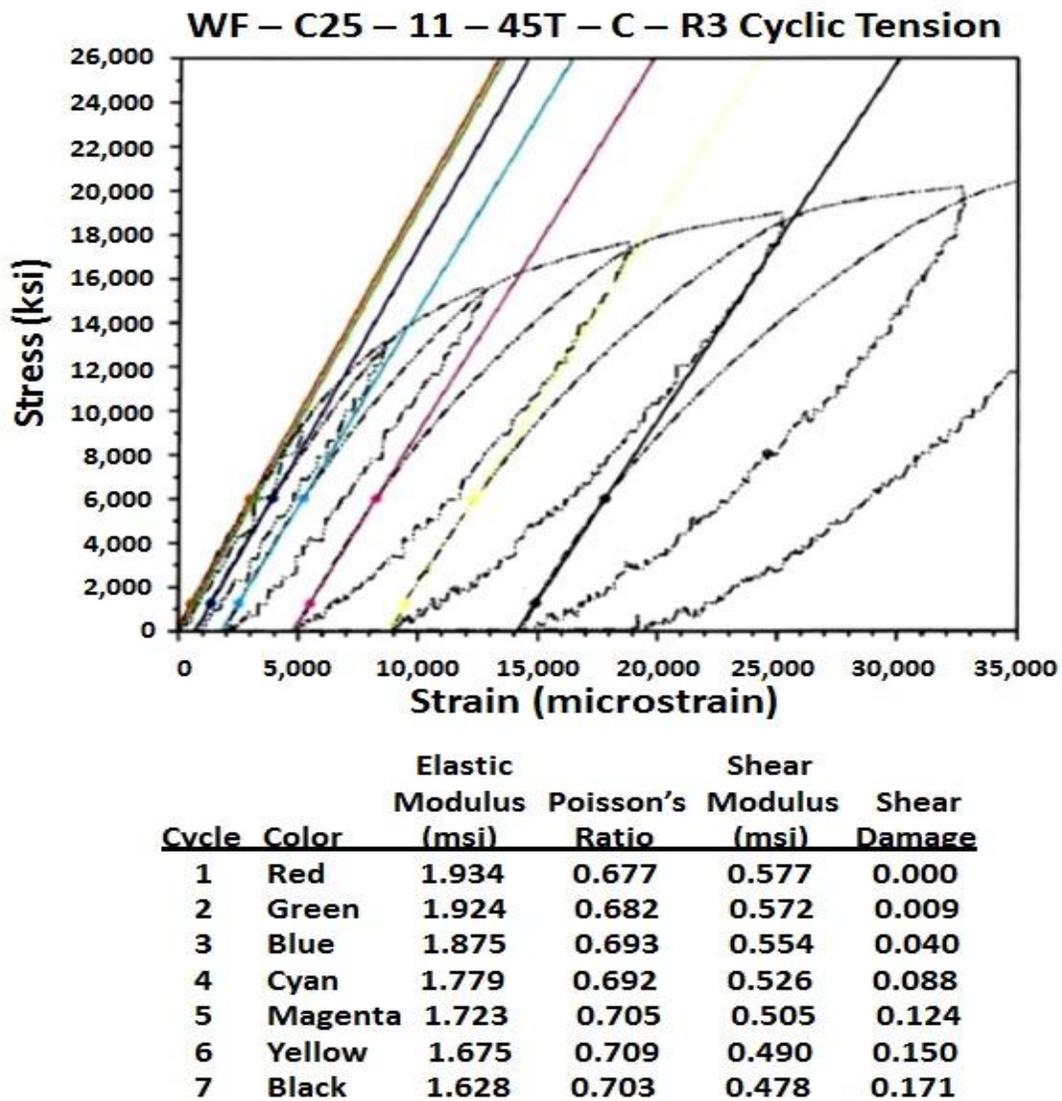
Figure IV-55: Cyclic tensile testing of carbon/epoxy twill weave (0/90)$_{2s}$ plaques, tested at 45 degrees to partial strain in a cyclic manner. This test measures the shear damage induced in the sample by the cyclic loading.
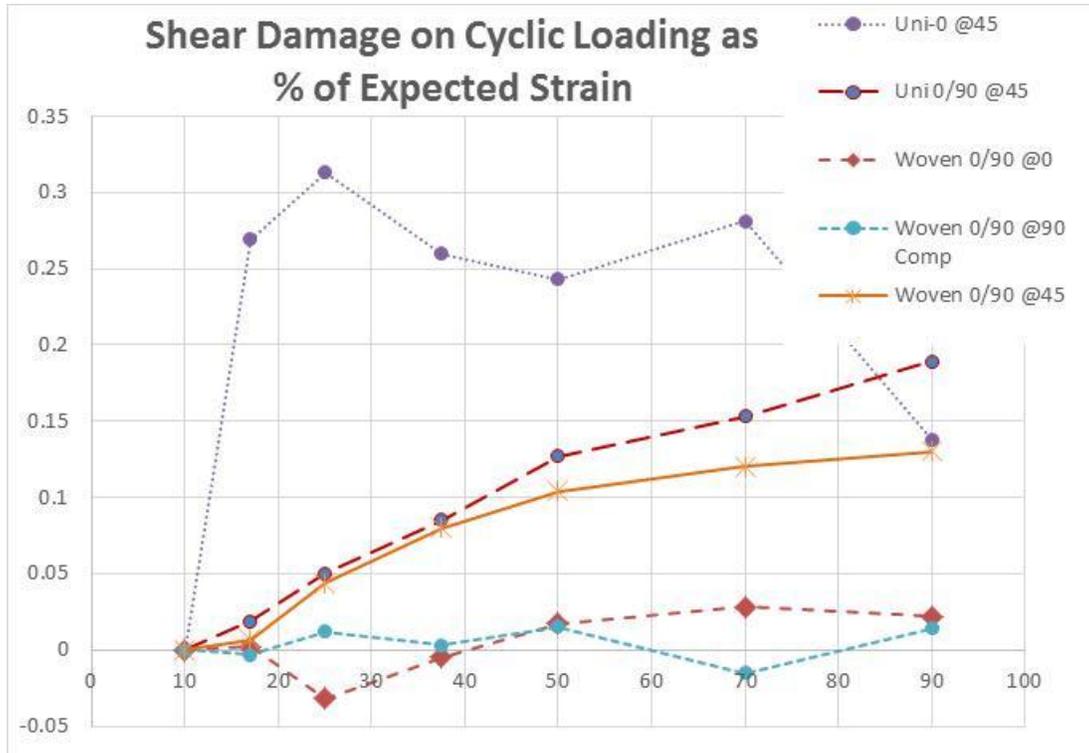
Figure IV-56: This chart shows the degradation of the shear properties of the unidirectional $(0)_8$ and $(0/90)_{2S}$ and the woven $(0/90)_{2S}$ after cyclic loading at seven increasing strain loads. The unidirectional and woven materials tested at 45° degraded at an increasing pace, while the unidirectional $(0)_8$ immediately lost considerable structure, and the woven tested in tension and compression show good resistance to the loading.

Representative Small Part:

Our next molding trial utilized a closed-end hat section to understand the behavior of these materials in a complex shape. We are also utilizing these samples to provide further opportunities for initial validation of the crash models of UM and NWU, by bonding the hats to flat sections of the same layup cut from the plaques in the molding trial described above, cutting off the closed ends, and testing them in axial crush. This will also give us a chance to test our joining strategy of bonding flanges and using rivets or bolts at set spacing as peel stoppers.

The hat section molding trial was run near the end of FY 2014 Q3. The fiber orientations are shown in Table IV-12, with 10 specimens being molded of each layup.

In addition to the planned axial crush testing, we tested the hat sections in 4-point flex as another opportunity for the evaluation of the models and commercial codes. Figure IV-57 shows the configuration for this testing, and a comparison of the three layups, for an average of 4 parts per layup.

Table IV-12: Description of the Closed End Hat Section Molding Layups.

Designation	Layup	Thickness (mm)
Woven 0/90	0/90/0/90/0/90/0/90/0/90/0	2.4
Woven QI	0/90/45/-45/0/90/0/-45/45/90/0	2.4
Uni/Woven QI Mix	0/0/0/90/45/90/-45/90/0/0/0	2.4
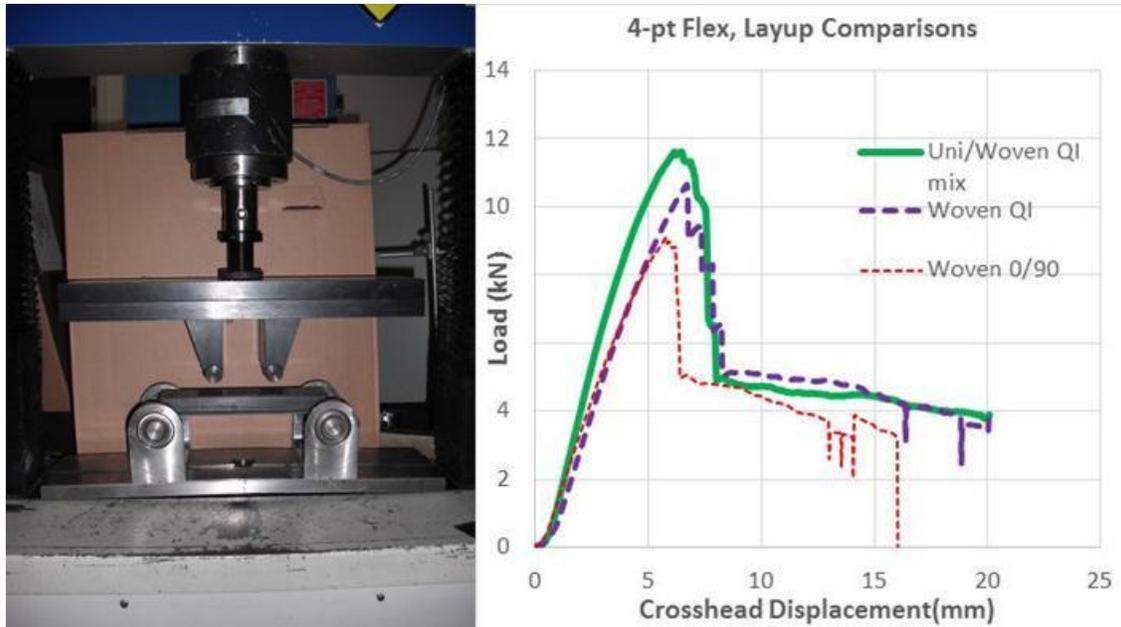
Figure IV-57: Configuration of the 4-pt flex test and comparison of the three layups. Curves are an average of 4 parts per layup. The sawtooth effect at the end of the displacement is an artifact of the averaging.

Joining Methodologies:

In order to fabricate the tubes for the axial crush testing, we are working with Dow Automotive to select the most appropriate adhesive. Dow has recommended three two-component adhesives:

- An epoxy adhesive, with lap shear about 1 gigapascal (GPa) and elongation about 13%
- A polyurethane (PU) adhesive, with lap shear less than 11 megapascals (MPa) and elongation about 115%
- A second PU adhesive, with lap shear less than 5 MPa and elongation about 150%.

In general, the epoxy adhesives had a much higher lap shear strength, but a lower elongation and thus were more brittle, while the PU adhesives had higher elongation, but lower lap shear. Dow suggested that they would test these three adhesives with our materials in lap shear, quasi-static cleavage peel, and impact peel. When these results are available in the first quarter of Fiscal Year 2015, we will model axial crush for our geometry to determine whether lap shear or elongation is the more important for the joint, and select our adhesive accordingly.

Processes for Molding the FBCC:

The composite FBCC will be a combination of bumper beam and two crush cans. The function of these two is different, with the dominant function of the beam being to pass

the load of the crash onto the crush cans, and the dominant function of the crush can being to absorb the crash energy. Thus, the geometry and fiber layup of the two components is quite different. Until recently, different molding methods for the beam and the crush cans were investigated, with the beams probably being molded via compression molding, and the crush cans via pultrusion. However, based on input from the modeling sources, this plan changed to make both beam and crush cans by compression molding.

The design for the bumper beam is a C-channel with ribs in the channel as shown in Figure IV-58, and will be molded with a carbon/epoxy prepreg layup for the C-channel and carbon SMC charges laid on top of the prepreg before molding for the ribs. This is a technique utilized with glass composites in the Automotive Composites Consortium Structural Composites Underbody project for a predominately glass fabric structure with ribs in certain areas.

For the crush cans, however, the square ribbed constant cross-section geometry will not be used as earlier planned via pultrusion, but a two-piece, joined cone will be used. An example of this flanged crush can geometry is also shown in Figure IV-58. The two cone sections will be joined with the same bonding and bolting scheme used for the hat sections bonded to the flat plaques for axial crush described above.
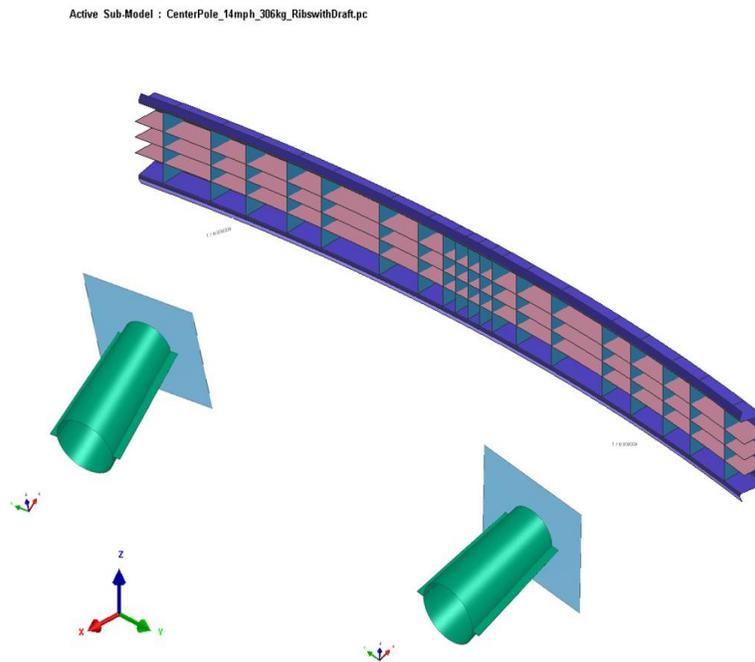
Figure IV-58: Tentative designs for the crush cans made from two compression-molded conical hat sections joined at the flanges, and the bumper beam, a C-channel with ribs on the included side, also compression molded.

Task 3.2 Design/CAE Analysis of Composite FBCC:

The primary focus of Year 2 activity for the Design/CAE Team was to optimize design concepts for the composite FBCC, implementing the material test and fracture characteristics obtained from experimental testing in Task 3.1, and develop a bumper beam concept to meet the full system performance requirements.

The final predictions for the steel FBCC in each of the identified commercial codes were submitted for correlation assessment, following agreement and finalization of the physical test set-up. The CAE Design team then established energy absorption and crush mode targets for the composite FBCC from the experimental and CAE simulations of the steel FBCC for each investigated load case. The full correlation report will be completed for the first quarter of 2015.

Composite Material Model Characterization and Calibration:

Both of the microplane models implemented in ABAQUS were calibrated against uniaxial tests (tension/compression) and V-notched shear tests on twill woven composite coupons performed by Delsen Testing Laboratories (Delsen). Analysis

conducted by NWU of the received test data from Delsen showed that (1) the stiffness is not sensitive to the present load rate; (2) the load rate is far lower than that in the dynamic crushing experiment; and (3) the compressive strength is different than the corresponding tensile strength. A model which is able to consider the difference of the tensile and compressive strength is under development by the UM.

The PAM-CRASH composite material model (Mat 131) was calibrated with physical test data obtained from coupon tests to fulfill the required material parameters. Figure IV-59 shows the results for the PAM-CRASH Mat 131 model for Tension, Compression and Cyclic Shear.

The Microplane model was calibrated for two approaches: The Microplane Model with Preferential Orientations, and the Spectral Stiffness Microplane Model. Figure IV-60 and Figure IV-61 show the comparison of the calibrated models against the test data for a $[0,90]_{2s}$ laminate, and for a quasi-isotropic laminate for the Microplane model with Preferential Orientations. Figure IV-62 shows the calibration results for the spectral stiffness microplane model for the same $[0,90]_{2s}$ laminate, and for a quasi-isotropic laminate.
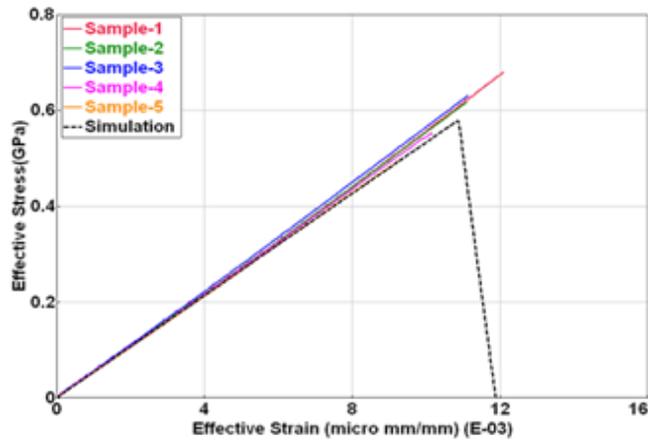
a)
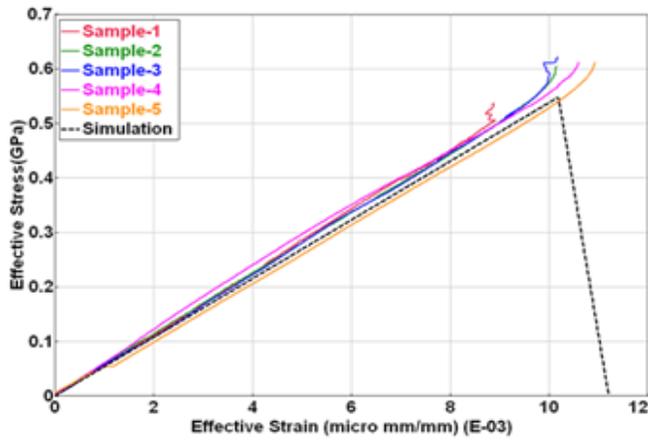
b)
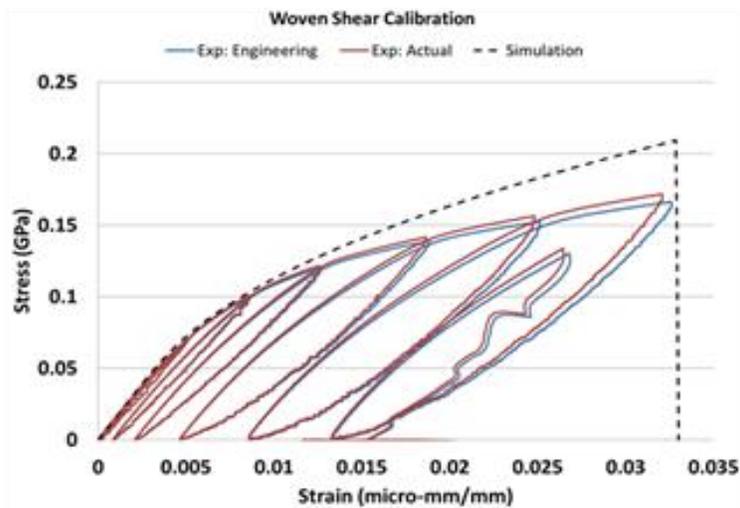
c)

Figure IV-59: Material Model Calibration Results for PAM-CRASH Material 131 (a) Tension, (b) Compression, (c) Cyclic Shear.
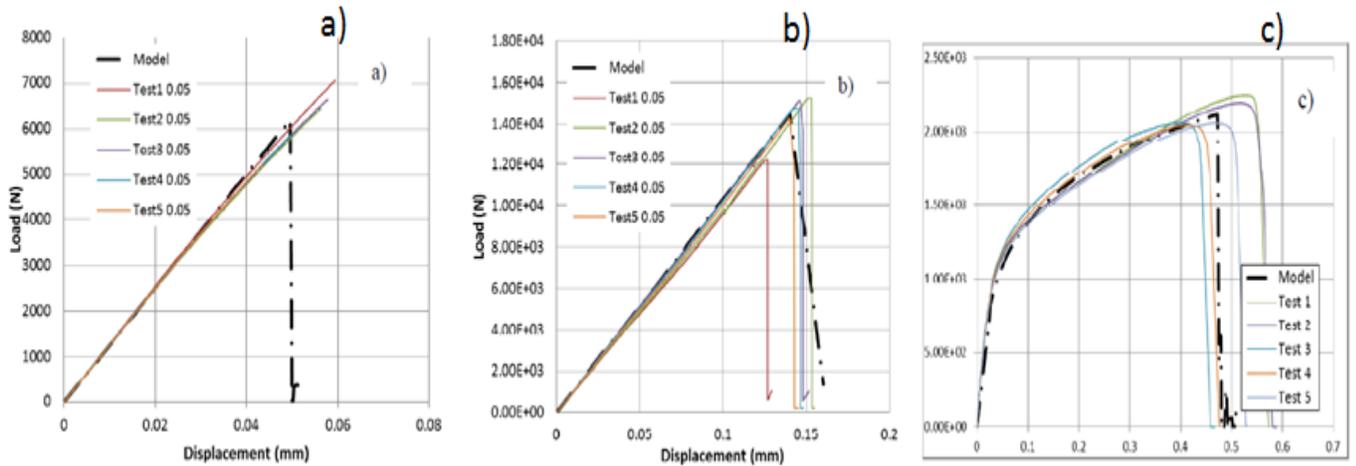
Figure IV-60: Material Model Calibration Results of the Microplane Model with Preferential orientations for (a) Tension, (b) Compression, (c) In-plane Shear ([0,90]$_{2s}$ laminate).
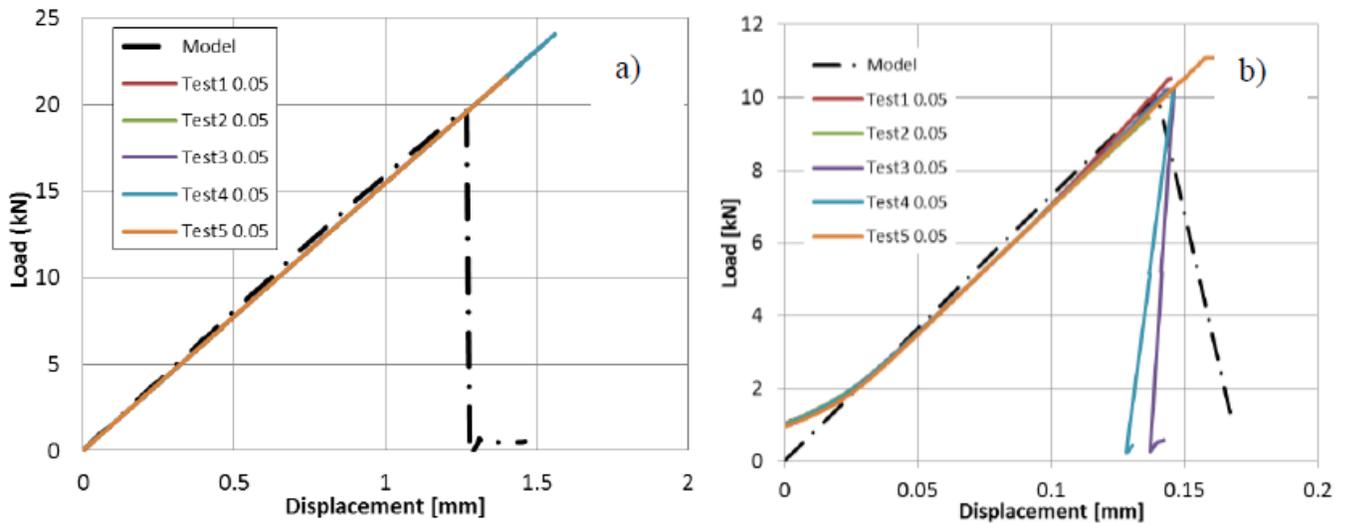
Figure IV-61: Material Model Calibration Results of the Microplane Model with Preferential orientations for (a) Tension, (b) Compression (Quasi-Isotropic configuration).
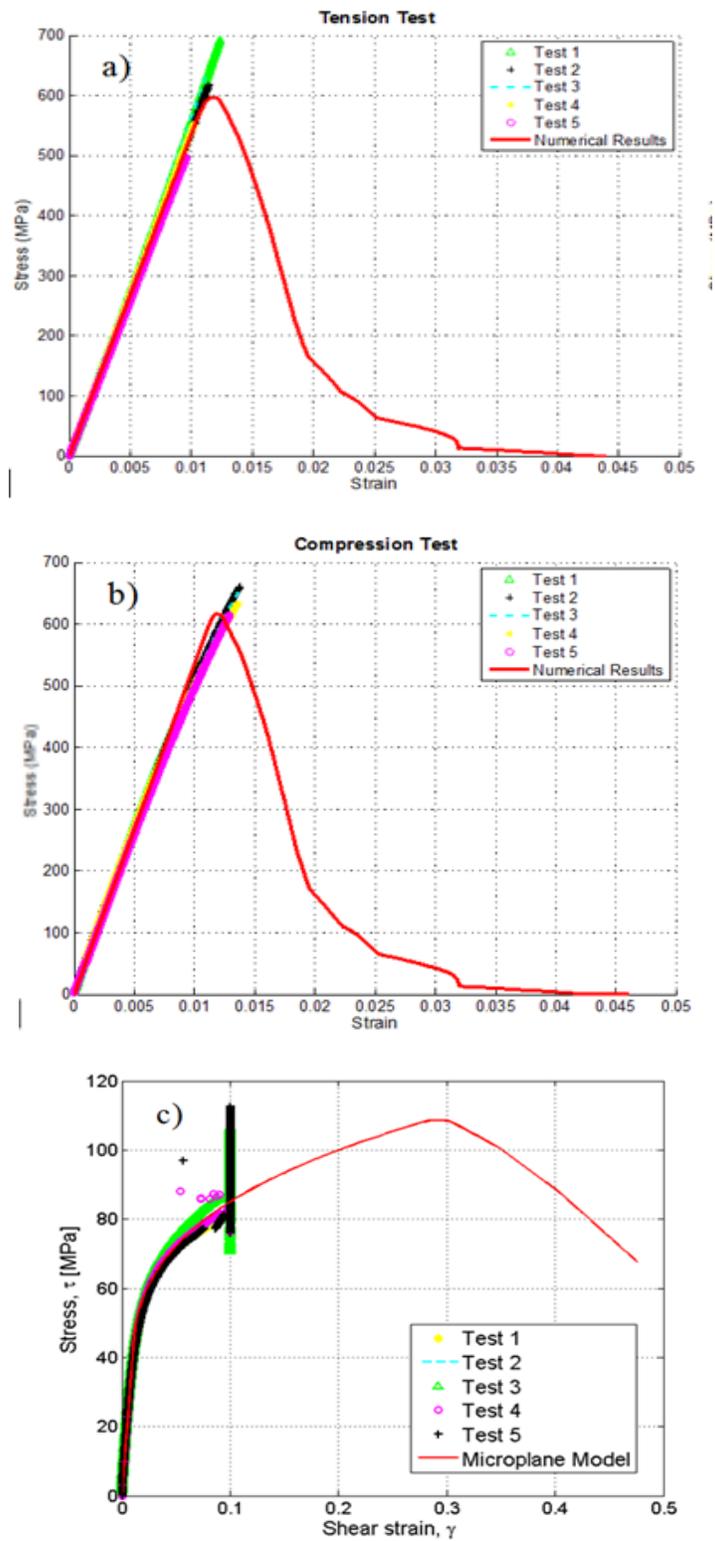
Figure IV-62: Material Model Calibration Results of the Spectral Stiffness Microplane Model for (a) Tension, (b) Compression, (c) Shear.

The results show that the model can realistically predict the orthotropic elastic constants and the strength limits for twill woven composites. In particular, the highly non-linear behavior of the material in shear is fully captured.

UM also tested two types of tensile specimens, dog bone specimen and Single Edge Notched Tensile (SENT) specimens are tested in UM to obtain the tensile strength and fracture energy. The geometries are shown in Figure IV-63. Two different sizes of SENT specimens are tested to get tensile fracture energy which is required in the material model. Detailed dimensions are also shown in these figures. The fracture location of the dog bone specimen is shown in Figure IV-63(b). From the linear elastic finite element analysis, fracture occurs at the stress concentration location introduced by change of the cross-section. The average nominal tensile strength from the dog bone test is 702 MPa. The true tensile strength is expected to be larger than the nominal strength.

The simple tensile tests are used to obtain the material properties. The nominal tensile strength from the dog bone tensile test is less than the real tensile strength. In the present study, the tensile strength will be calculated from the simulation.

The nonlinear shear and crack band model are combined in the material model proposed by Xu and Waas. For the simple tensile tests, the inputs for the crack band model are

tensile strength and fracture energy. These two parameters are determined by trial and error. That is the tensile strength and fracture energy are determined until the corresponding predicted load-response match the experimental data well. After several iterations, the tensile strength and the tensile fracture energy are estimated to be 820 MPa and 80 newtons per millimeter (N/mm). The predicted load response and the experimental data match well as shown in Figure IV-64. Notably, the experimental displacement is obtained from the digital image correlation (DIC) analysis. In order to make the comparison, the location where the displacement is measured in the finite element model and DIC were the same. In the present study, the Young's modulus for the dog bone specimens are $E_x=62.0\pm3.0$ GPa, and Poissons ratio, ν_{xy}, =0.05, which are obtained from the DIC analysis. The shear response from Delsen test results are used. These material properties are used in the crack band model, the predicted response is given in Figure IV-64. A very good agreement is observed form the model calibration.

At the time of writing, the Mode I and Mode II inter and intra-laminar fracture testing is being finalized and implemented into the microplane and RUC model for better characterization of the fracture mechanics within the crush can laminate.

Dimensions used in the tests		
mm	Small specimen	Large specimen
D	25	50
L₁	75	150
D × L	25 × 151	50 × 226
a	5	10
b	1	1.3
w_a	2.25	0.26
w_b	2.25	0.26

(a)   (b)
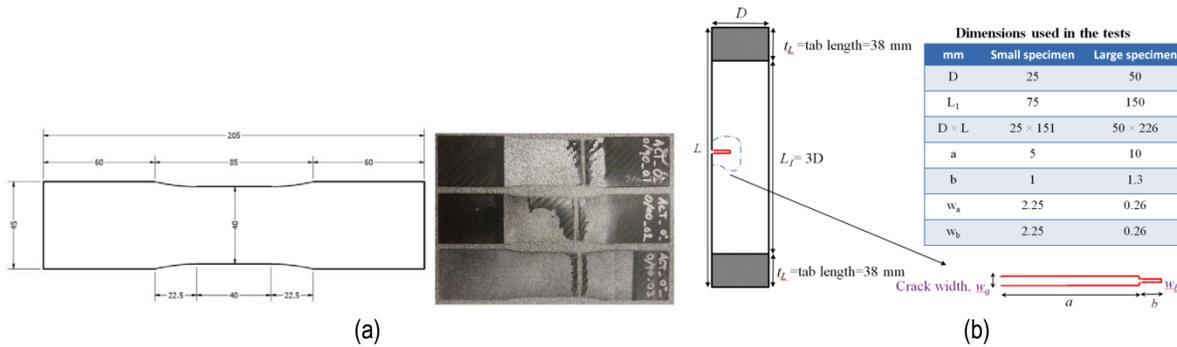
Figure IV-63: (a) 1 Dog bone tensile test specimen, geometry and failure mode, (b) Single Edge Notch Tensile (SENT) specimen, geometry and dimensions.
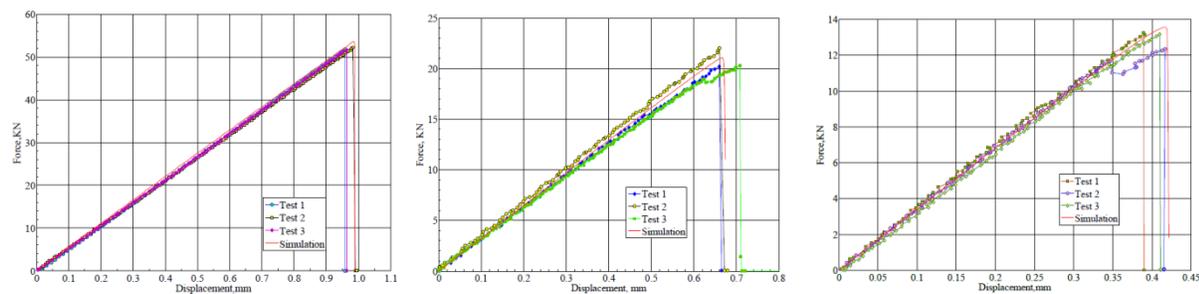
Figure IV-64: Calibration results for the (a) Dogbone, (b) Large SENT and (c) Small SENT specimens.

The correct prediction of the energy dissipated by intra- and inter-laminar crack initialization and propagation requires the experimental characterization of the fracture energy involved in the fracturing process. For quasi-brittle materials (such as the woven composites under investigation) the only way to correctly measure the fracture energy is size effect testing. After the work done in the previous quarter on the design of suitable tests, the NWU team has begun conducting the size effect testing and test data analysis. All the activity involved with the experiments, including the specimen preparation, has been done in the mechanical testing lab at the Department of Civil and Environmental Engineering of NWU. Intra-laminar size effect tests on SENT specimens of three radially scaled sizes have been carried out on a 20 kip MTS Systems Corporation (MTS) servo-loop hydraulic machine. Figure IV-65 shows test set-up, maximum principal strain contour, and the force-displacement plots for all the tested sizes. The results are currently being used to calibrate the NWU models and to provide a precise estimation of the intra-laminar fracture energy of the material.

The inter-laminar tests are currently being run. The mode I inter-laminar size effect tests are completed and the NWU team is starting the tests on End Notch Flexure specimens to investigate the mode II inter-laminar size effect.

Composite Crush-Can Development - Flat Frontal Loadcase:

To understand the crush mode and required lay-ups and wall thickness of the crush can, much of the virtual development focused on component analysis of the crush can itself, with the crush performance compared to a target energy absorption (17-19 kJ) and average force (approx. 110 kN). Studies conducted in year indicated that a progressive, axial crush mode provided higher energy absorption than the

circumferential peel mode and could be better suited to the high loads required of this crush can application. It also mitigated the need for a heavy initiator "plug" which would save weight, investment and piece cost.

Due to the material testing being carried out on compression molded samples, the previously investigated pultrusion concept had to be disregarded, as the resulting fiber volume and laminate material properties from the pultrusion manufacturing process would be significantly different from those obtained in compression molding, used to make plaques based on which all Delsen coupon tests were conducted.

Two geometries were refined for comparison and concept selection for tooling kick-off; a 2-piece, square hat section and a 2-piece conical section, both glued and riveted at the flanges. The concepts are shown in Figure IV-66. The tapered, conical geometry investigate in Year 1 of the project had shown stable, axial crush, and the new analyses in each of the investigated codes still supported this finding, even with the updated material parameters and test set-ups.

While concepts with the shear plate exhibited higher average forces, there were some large assumptions regarding the joining at the flanges. The team decided that it would reduce the chance of error or unpredicted and un-desired failure modes if the flanged joint were limited to two pieces of material, instead of three. Since the conical and hat section crush cans showed adequate energy absorption without the shear plate, the preliminary analysis gives a promising indication that the performance targets can be met with this design, as shown in Figure IV-67.

a)   b)   c)
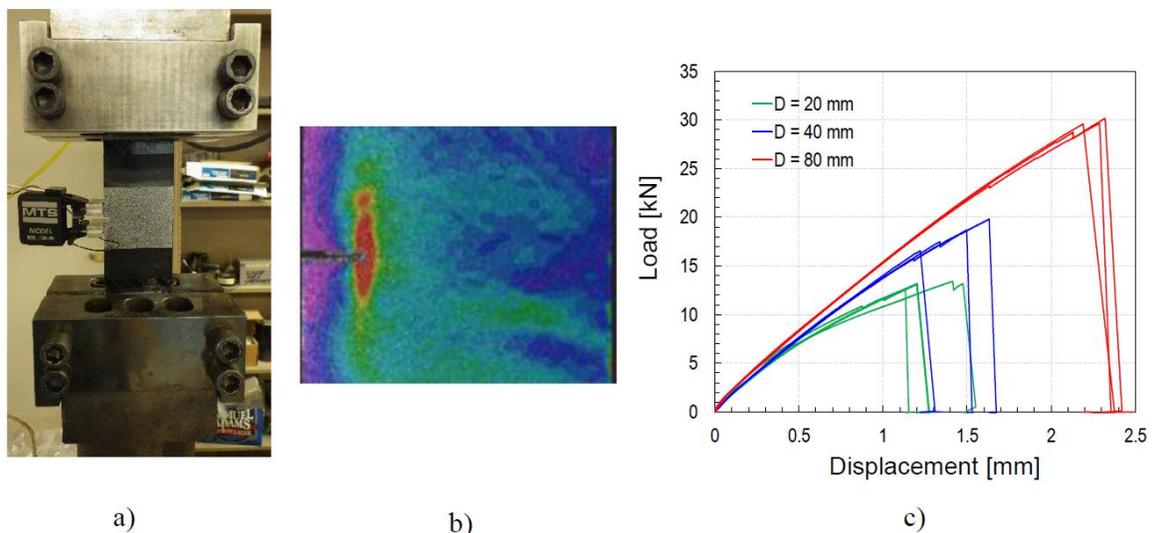
Figure IV-65: (a) Medium size SENT specimen under tensile loading in Crack Mouth Opening Displacement (CMOD) control, (b) Contour plot of the maximum principal strain measured by DIC used for model calibration, (c) Force-displacement curves for all the investigated sizes.
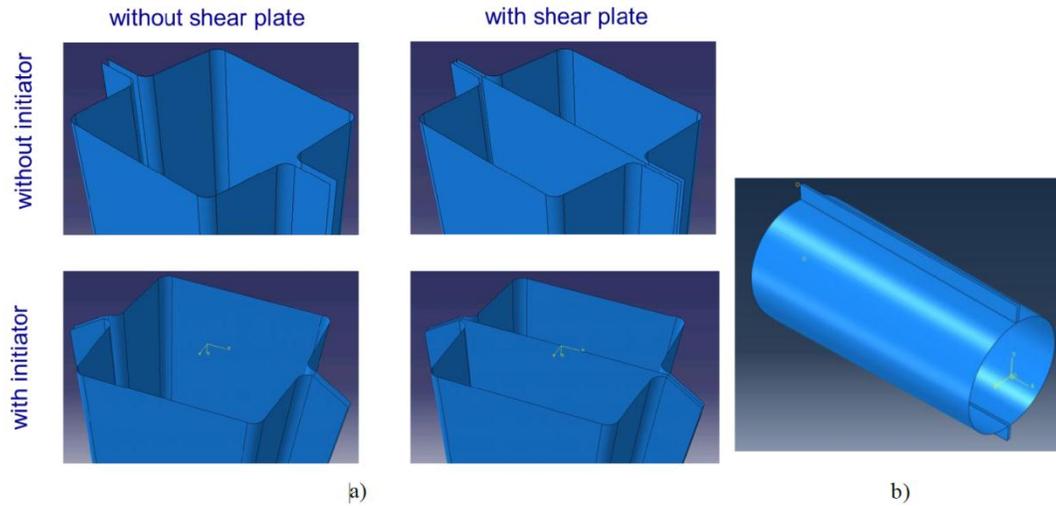
Figure IV-66: Compression molded 2-3 piece crush can concepts: (a) Hat section geometries, (b) Conical section geometries.
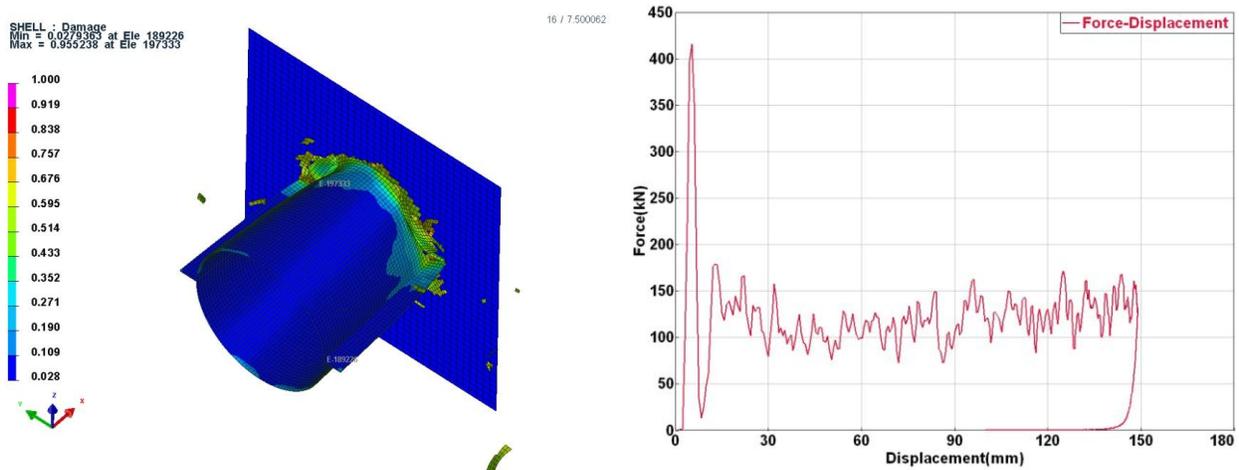
Figure IV-67: Preliminary analysis results for 2-piece conical crush can concept.

Due to the improved crush stability and potential to more easily integrate the crush cans into the SMC ribs of the bumper beam, the tapered, conical crush can section has been selected for tool kick-off, with optimization of the lay-up and manufacturing process to be carried out through the remainder of 2014 in alignment with Milestone 5 completion.

Composite Bumper Beam Development

After evaluation of the manufacturing requirements and design feasibility against the functional objectives of a bumper beam (which was supported by preliminary CAE assessment of the concepts), the team decided to pursue Concept 3 (shown in Figure IV-68) for the bumper beam. This concept employs a compression molded, continuous fiber C-Section beam, with chopped, random carbon fiber SMC ribs. These ribs allow for final tuning and optimization of the crush, as well as strength and elastic characteristics of the bumper beam for the different impact modes.

For design development, the beam was subjected to a low velocity impact loadcase in the elastic regime, for which no damage is allowed and an elastic+failure simulation provides some guidance on the stiffness of the bumper, its failure mechanisms and suitability to higher velocity loadcases. Two different ply types (unidirectional (UD) and Woven) were utilized for this study. For this simple elastic analysis of the bumper beam system, steel crush cans were used in the model.

UD, Woven and combination of UD/Woven materials were used along with various laminate stacking sequences to understand the behavior (shown in Figure IV-69). The design with upturned flange and 3-degree open draw angle was selected as the best design to meet the functional objectives of the bumper beam.
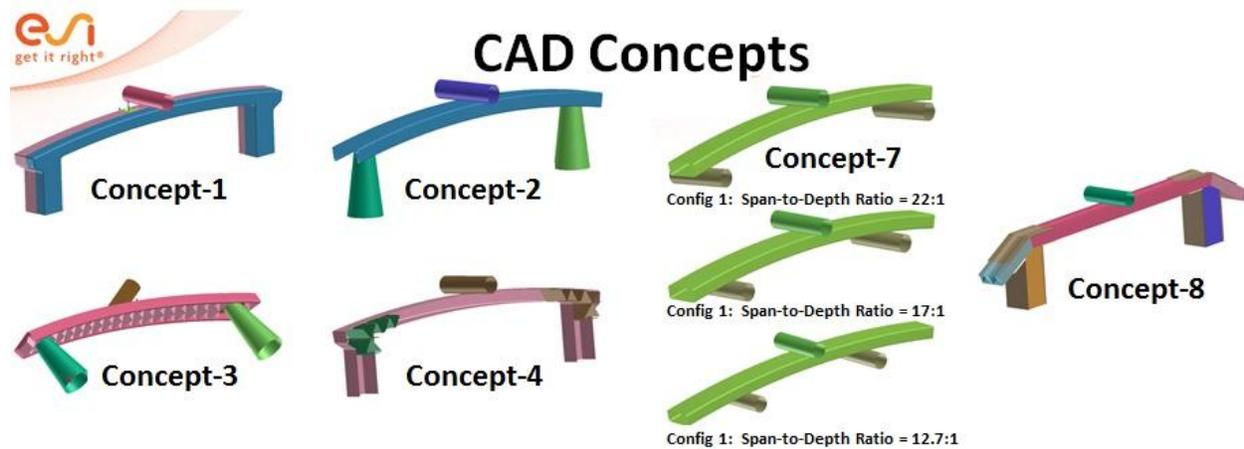
Figure IV-68: Composite Bumper Beam Concepts
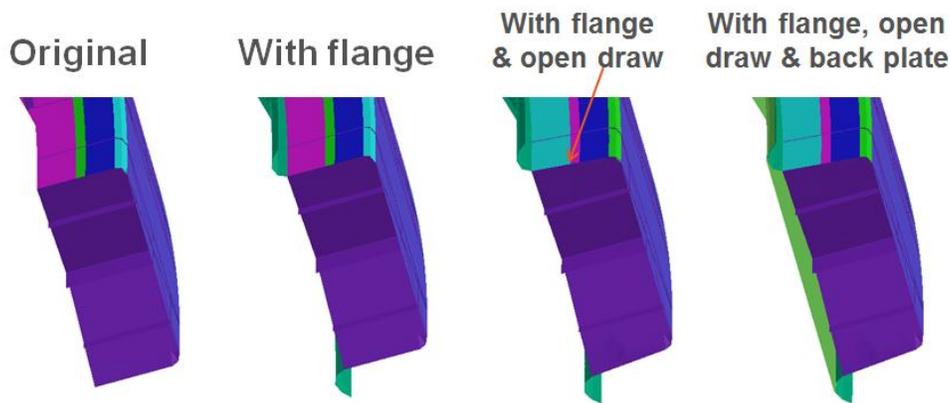
Figure IV-69: Composite Bumper Beam Concepts.

The Center Pole loadcase was studied using updated bumper design from linear elastic analysis. Damage, plasticity and failure data was used to understand damage mechanisms and evaluate the performance of the composite bumper during standard center pole impacts.

Task 6: Non-destructive Evaluation ((NDE) of Composite Structure

The NDE capabilities of both ultrasonic pulse/echo and low-energy radiography have now been demonstrated on all the materials generated by the project to date. These include both thermosets and thermoplastic matrices re-enforced with uni-directional, woven, and random chopped carbon fibers. Small, thin phantoms were built into these materials at each inter-ply to demonstrate the NDE performance. Each of the phantoms can be imaged with sub-millimeter resolution at each inter-ply for both 8- and 11-ply composites (see 70). Moreover, using ultrasonic pulse/echo, the tows within each ply can be resolved. In unidirectional and woven materials, the tow directions can be measured to an accuracy of a few degrees. This required developing a two-dimensional fast Fourier transform correlation analysis. The ultrasonic capabilities have been demonstrated

with both a conventional raster-scanner and with a manual, surface following ultrasonic phased-array.

The nondestructive detection of internal damage was also demonstrated on two very different sets of damaged parts. The first set used American Society for Testing and Materials (ASTM) standard impacts at a range of impact energies spanning from no damage to complete penetration. The three dimensional shape of the damage cone and extent of lateral delamination was imaged. The effect of these impacts on compressive strength was also being measured. Even with 15-mm diameter penetration, there is a negligible effect on the compressive strength of a 4-inch wide plaque. The second set of damaged parts was comprised of hat-sections that had been broken in 4-poing flex. Typically these ruptured at one of the middle, top-of-hat points leaving a little or no visible cracking below the three other flex points. Again, non-visible delaminations could be imaged in three dimensions as shown in Figure IV-1.

Current plans call for straight, flat sections to be inspected with ultrasonic pulse/echo using raster scanning in an immersion tank as described above. Curved sections would

be inspected with the surface-following ultrasonic phased-array that has also been demonstrated.

A general strategy for structural health monitoring in the automotive environment has been developed. While traditional NDE methods, such as tap tests and ultrasound, can be used in the manufacturing environment, they require too much training and capital expense for most repair shops. This drives the need for on-board sensors to detect in-service impacts that may have damaged the composites. While there is a deep literature for SHM of composites, most of these methods are probably too expensive for the automotive market. Our current, primary strategy is to evaluate very low-cost microelectromechanical systems (MEMS) accelerometers, such as those found in cellphones, to determine optimal detector locations and the range of impact energies that can be detected. These will be mounted as self-powered, remotely accessible devices. A comparison study is being planned which would use an optical-fiber Bragg grating (FBG) strain sensor. Multiple locations (gratings with different spacing) will be accessed on a single fiber using wavelength-division multiplexing.
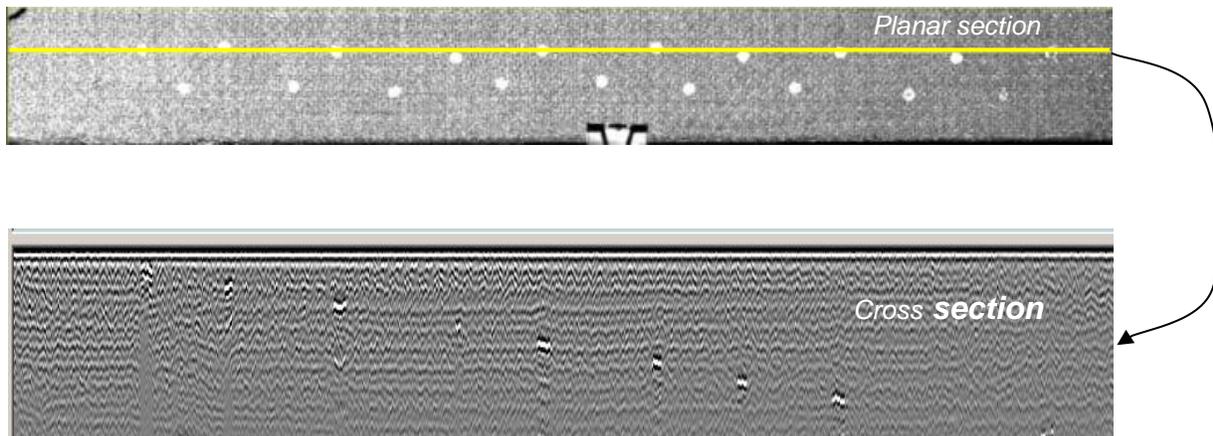
Figure IV-70: Ultrasonic images of an 11-ply woven carbon fiber composite with polyethylene (PE) and PTFE inserts. The upper image is the peak reflection within the material. The lower image is a cross-section showing the inter-ply locations of some of the PE inserts as well as some of the inter-ply and tow structure. Taken at 0.5-mm resolution using a pulsed 15-MHz transducer. Sample is 610-mm W x 75 H x 2.5 thick.
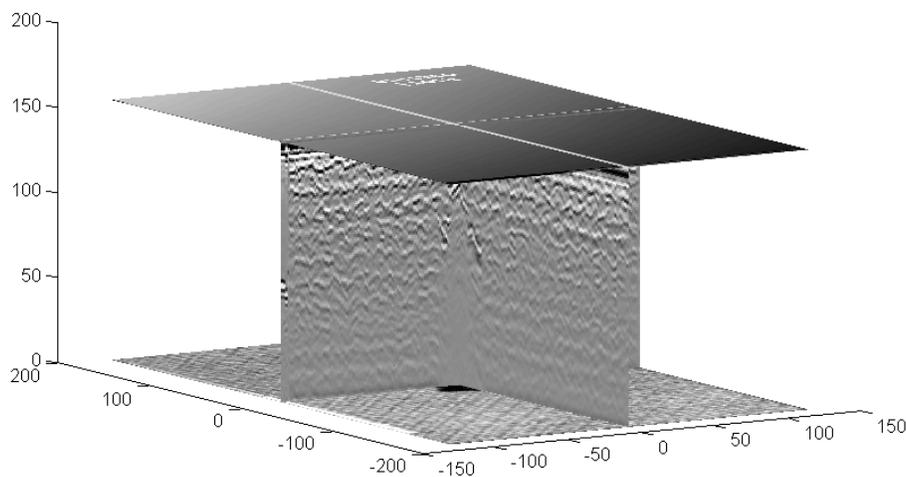
Figure IV-71: Ultrasonic images of an 11-ply woven carbon fiber composite subjected to impact with a standard hemispherical impactor. The top slice is the top indentation, while the other slices are the local reflectivity in three orthogonal planes and indicate the conical damage zone. Damage propagates from the bottom surface towards the front. There is no visible damage on the impacted top surface. The vertical height is exaggerated: the sample is 2.5 mm thick.

Technology Transfer Path

The FBCC was selected because it represents the primary energy absorbing structural members in frontal crashes and is a challenging structural application of composites for crash energy management. Two USAMP-facilitated material models and four major commercial crash codes (LS-DYNA, RADIOSS, PAM-CRASH and ABAQUS) are being evaluated for the crush cans and bumper beam application in predictive modeling followed by validation with fabricated structures via crash and physical testing and analyses. At all levels, a broad group of technology stakeholders are involved so as to help accelerate the evaluation of the models and for early identification of key knowledge gaps. Advances made in crash modeling will be quickly implemented by the respective crash code vendors into the major commercial crash codes for crash analyses of carbon composite structures.

Successful demonstration of such challenging structures opens new lightweighting application opportunities for composites in passenger vehicles and light trucks, with the near-term potential to drive U.S. industrial capacity and economies of scale in carbon fiber production. The project outcomes are expected to advance the readiness levels of composite material modeling, and crash-modeling technologies so as to prove their feasibility for broader application of primary automotive composite structures. Periodically, the research will be reported by the Original Equipment Manufacturer, vendor and academic experts in subject-matter reports, as well as disseminated through publications in the open literature and/or subject-matter conferences.

Conclusion

During the Year 2 following kick-off, considerable progress has been made to complete the majority of baseline steel FBCC crash testing with detailed analysis of crash responses completed. Definitions of equivalency were developed that can be incorporated in crash models to help drive the design of innovative composite structures that leverage the strength and lightweighting potential of carbon fiber product forms. Several composite FBCC design concepts for crush cans and bumper beam were evaluated, and FEA-based analysis was performed to yield a short-list of viable composite FBCC components for detailed design, joining and assembly analyses in Year 3. Tooling discussions were initiated with a vendor, and several adhesive joining candidate materials evaluated. Development of methodologies suitable for NDE evaluation of complex composite structures has also progressed.

Presentations/Publications/Patents

Several papers or conference presentations were published by the USAMP team members:

1. Berger, L.; Faruque, O.; Mehta, M. (2014) " Validation of Crash Models for Carbon Fiber Composites: A Project Overview," *17th U.S. National Congress on Theoretical and Applied Mechanics*; June 15-20, 2014, Michigan State University, East Lansing, Michigan.

2. A. Seyed Yaghoubi, A.; Newaz, G.; Begeman, P.; Board, D.; Chen, Y.; Faruque, O. (2014) "Rigid Full Frontal Response of Generic Steel FBCC Samples." *Society of Automotive Engineers 2014 World Congress,* April 8-10, 2014, Detroit, Michigan.

3. Seyed Yaghoubi, A.; Newaz, G.; Begeman, P.; Board, D.; Chen, Y.; Faruque, O. (2014) "Generic Steel FBCC Samples Subjected to Rigid Offset Frontal Impact." *Society of Automotive Engineers 2014 World Congress*, April 8-10, 2014, Detroit, Michigan.

4. Seyed Yaghoubi, A.; Newaz, G.; Begeman, P.; Board, D.; Chen, Y.; Faruque, O. (2014) "Load History Assessment of Generic Steel FBCC Samples Subjected to Rigid Center Pole Impact." *2014 Society of Experimental Mechanics' Conference & Exposition on Experimental and Applied Mechanics*, June 2-5, 2014, Greenville, South Carolina.

5. Seyed Yaghoubi, A.; Newaz, G.; Begeman, P.; Board, D.; Chen, Y.; Faruque, O. (2014) "Rigid Angular Impact Response of Generic Steel FBCC Samples: Correlation of Multiple Velocity-Measurement Techniques." *2014 Society of Experimental Mechanics' Conference & Exposition on Experimental and Applied Mechanics*, June 2-5, 2014, Greenville, South Carolina.

6. Xu, W. and Waas, A.M. (2014) "Crush Analysis and Energy Absorption of Woven Textile Composite Tubes." *17th U.S. National Congress on Theoretical and Applied Mechanic*s, June 15-20, 2014, Michigan State University, East Lansing, Michigan.

7. Kirane, K.; Salviato, M.; and Bazant, Z.P. (2014) "A Multi-Scale Microplane Model for Fracturing Damage of Woven Composites." *17th U.S. National Congress on Theoretical and Applied Mechanics*, June 15-20, 2014, Michigan State University, East Lansing, Michigan.

REFERENCES

1. Song S.; Waas, A.M.; Shahwan, K.W.; et al. "Braided textile composites under compressive loads: Modeling the response, strength and degradation." *Composites Science and Technology*, (67:15-16), 2007; pp. 3059-3070.

2. Quek, S.C.; Waas, A.M.; Shahwan, K.W.; Agaram, V. "Analysis of 2D Flat Triaxial Braided Composites.", *Int.J. Mechanical Sciences*, (45:6-7),2003; pp. 1077-1096.

3. Song, S.; Waas, A.M.; Shahwan, K.W.; Faruquec, O.;
    Xiao, X. "Compression response, strength and post-peak
    response of an axial fiber reinforced tow." *International
    Journal of Mechanical Sciences*, (51), 2009; pp. 491–
    499.

4. Caner, F.C.; Bazant, Z.P.; Hoover, C.G;, Waas, A.M.;
    Shawan, K.W.,"Microplane Model for Fracturing Damage
    of Triaxially Braided Fiber-Polymer Composites." *Journal
    of Engineering Materials and Technology*, (133:021024-
    1-12), April 2011.

5. Cusatis, G.; Beghini, A.; Bazant, Z.P. "Spectral Stiffness
    Microplane Model for Quasibrittle Composite Laminates
    – Part 1: Theory." *Journal of Applied Mechanics*,
    (**75**:021009-1-6), 2008.

6. Chang, F.K.; Chang, K.Y. "A progressive damage model
    for laminated composites containing stress
    concentrations.", *Journal of Composite Materials*, (21:
    834-855), 1987.

7. Feraboli, P.; Wade, B.; Deleo, F.; Rassian, M.; Higgins,
    M.; and Byar, A.; 'LS-DYNA MAT54 modeling of the axial
    crushing of a composite tape sinusoidal specimen.',
    Composites (Part A), (42), 2011; pp. 1809-1125.

8. Matzenmiller, A.; Lubliner, J.;Taylor, R.L. "A Constitutive
    Model for Anisotropic Damage in Fiber-Composites."
    Mechanics of Materials, (20), 1995; pp. 125–152.

9. Xiao, X. " (2008) "Simulation of Composite Tubes Axial
    Impact with a Damage Mechanics Based Composite
    Material Model."10th International LS-DYNA Users
    Conference, June 8-10, 2008; Dearborn, Michigan, pp.
    43-54.

10. Goldberg, R.K.;Carney, K.S. (2006)"Modeling the
    Nonlinear, Strain Rate Dependent deformation of Shuttle
    Leading Edge Materials with Hydrostatic Stress Effects
    Included". 8th International LS-DYNA Users Conference,
    June 4 – 6, 2006, Dearborn, Michigan, (3), pp. 45-56.

11. Gatti, M.; Vescovi, L.; Sperati, M.; Pagano, P.; Ferrero, L.
    (2007) "Characterization of Composite Materials,
    Unidirectional and Fabric Samples." *Autosim Technology
    Workshops & Csc*, Paris, France, July 5-6, 2007.

12. Tsai, S. W.; Wu, E. M. "A general theory of strength for
    anisotropic material.", *J. Compos. Mater.,*; (5:1), 1971,
    pp. 58–80.

13. Daniel, I.M.; Ishai, O. (2006). Engineering Mechanics of
    Composite Materials. (2nd Edition. New York, NY: Oxford
    University Pres; pp. 122-147.

14. Ladevèze, P.; Le Dantec, E. "Damage Modelling of the
    elementary ply for laminated composites", *Composites
    Science and Technology*, (43:3), 1992, pp. 257-267.

15. Johnson, A.K.; Pickett, A.K.;Rozycki, P. "Computational
    methods for predicting impact damage in composite
    structures", *Composites Science and Technology*,
    (61:15), 2001, pp. 2183-2192.

16. Hashin, Z. "Failure Criteria for Unidirectional Fiber
    Composites," *Journal of Applied Mechanics*, (47), 1980,
    pp. 329–334.

17. Abaqus Analysis Users Manual, v6.11. Dassault
    Systemès Simulia Corp.

18. Heimbs, S. "Bird Strike Simulations on Composite
    Aircraft Structures." 2011 Simulia Customer Conference,
    May 19, 2011, Providence, Rhode Island.

19. Yi Pan; Lucian Iorga; Assimina A. Pelegri. "Numerical
    generation of a random chopped fiber composite RVE
    and its elastic properties." *Composites Science and
    Technology,* (**68**), 2008; pp. 2792–2798.

20. Flesher, N.D.; Chang, F-K. (2003) "Effect of Cross-
    Section Configuration on Energy Absorption of Triaxially
    Braided Composite Tubes." 18th Annual Technical
    Conference American Society for Composites. Oct. 19-
    22, 2003, University of Florida, Gainesville, Florida.

21. Yuan, Z.; Fish, J. "Hierarchical Model Reduction at
    Multiple Scales," *International Journal for Numerical
    Methods in Engineering*." 2008.

22. ASTM D3039, Standard Test Method for Tensile
    Properties of Polymer Matrix Composite Materials.

23. ASTM D6856, Standard Guide for Testing Fabric-
    Reinforced "Textile" Composite Materials

24. ASTM D5379, Standard Test Method for Shear
    Properties of Composite Materials by the V-Notched
    Beam Method

25. ASTM D7078, Standard Test Method for Shear
    Properties of Composite Materials by V-Notched Rail
    Shear Method

26. ASTM D3410, Standard Test Method for Compressive
    Properties of Polymer Matrix Composite Materials with
    Unsupported Gage Section by Shear Loading

27. ASTM D5528, Standard Test Method for Mode I
    Interlaminar Fracture Toughness of Unidirectional Fiber-
    Reinforced Polymer Matrix Composites

28. ASTM E132, Standard Test Method for Poisson's Ratio
    at Room Temperature

29. Hsiao, H.M.; Daniel, I.M. "Strain rate behavior of
    composite materials*." Composites Part B 29*, 1998, pp.
    521–533.

30. Bažant, Z. P.; Daniel, I. M.; Li, Z. "Size effect and fracture
    characteristics of composite laminates," *ASME J. Eng.
    Mater. Tech.*, (118), 1996, pp. 317-324.

31. Bažant, Z.P.; "Scaling theory for quasibrittle structural
    failure." *Proc., National Academy of Sciences*, (101:37),
    2004, pp. 13400-13407 (inaugural article).

32. Bažant, Z. P.; Kim, J. -J. H.; Daniel, I. M.; Becq-
    Giraudon, E.; and Zi, G. "Size Effect on Compression
    Strength of Fiber Composites Failing by Kink Band
    Propagation," *Int. J. Fract.*, (**95**), 1999, pp. 103–14.

33. Bazant, Z.P.; Zhou, Y.; Novak, D.; and Daniel, I.M. "Size
    effect on flexural strength of fiber-composite laminate." *J.
    of Engrg. Materials and Technology ASME*, (126), 2004,
    pp.29-37.

V Crosscutting

V.1 Demonstration Project for Multi-Material Lightweight Prototype Vehicle as Part of the Clean Energy Dialogue with Canada –Vehma International of America, Inc. and Ford Motor Company

Tim Skszek, Principle Investigator
Vehma International of America, Inc. and Ford Motor Company)
750 Tower Drive
Troy, MI 48098
Phone: (248) 631-5375
E-mail: tim.skszek@magna.com

Aaron Yocum, Project Officer
National Energy Technology Laboratory
3610 Collins Ferry Road
P.O. Box 880
Morgantown, WV 26507-0880
Phone: 304-285-4852
E-mail: Aaron.yocum@netl.doe.gov

Carol Schutte, Technology Area Development Manager
U.S. Department of Energy
1000 Independence Avenue, SW
Washington, DC 20585
Phone: (xxx) xxx-xxxx
E-mail: carol.schutte@ee.doe.gov

Contractor: Vehma International of America, Inc.
Contract No.: DE-EE0005574

Abstract/Executive Summary

The intent of the Multi-Material Lightweight Vehicle (MMLV) is to assess the feasibility of achieving a significant level of vehicle mass reduction, enabling engine downsizing resulting in a tangible fuel reduction and environmental benefit. The MMLV project includes the development of two lightweight vehicle designs, referred to as Mach-I and Mach-II MMLV variants, based on a 2013 Ford production C/D segment production vehicle (Fusion). Weight comparison, life cycle assessment (LCA) and limited full vehicle testing are included in the project scope. The Mach-I vehicle variant is comprised of materials and processes that are commercially available or previously demonstrated. The 363 kilogram (kg) mass reduction associated with the Mach-I design, enabled use of a one-liter, three-cylinder powertrain while maintaining the performance and utility of the baseline vehicle. In FY 2014, seven MMLV Mach-I "concept vehicles" were manufactured for the purpose of testing and evaluation. Full vehicle test

results and the LCA benefit assessment are in-process and will be reported in FY 2015.

Lightweight Materials and Technologies – MMLV Mach-I Vehicle

Body in White (BIW)	Aluminum (Al) vacuum die casting, Al 6xxx stamping and extrusion, high-strength low alloy (HSLA) stamping, Al 5xxx stamping, press hardened steel (PHS) safety cage
Closures	Al 6xxx outer panel, Al 5xxx inner panel, PHS intrusion beam, Al cast hinge
Bumpers	Al 6xxx extrusion and crush can
Glazing	Hybrid chemically toughened/soda lime laminate front and side, polycarbonate (PC) rear
Engine	Al cast block, forged Al connecting rod, carbon fiber (CF) front cover, oil pan and cam carrier
Transmission	Al clutch hub, pump support and bolts, magnesium (Mg) valve body
Chassis	Al cast front and rear subframe, hollow steel F/R stabilizer bars fiber reinforced composite, titanium and hollow steel rear springs Al cast rotors with thermal spray coating
Interior	CF composite seat back and cushion structure CF composite instrument panel (IP)/cross car beam
Tires	155/70R19 tires
Wheels	CF composite
Electrical	12 volts direct current (VDC) lithium (Li) battery

The Mach-II vehicle design is comprised of advanced materials and manufacturing processes which offer potential for future vehicle lightweighting application and not commercially available or previously demonstrated in a high volume application. The Mach-II design is intended to identify future product application areas and highlight technology gaps which need be addressed to enable commercial use of the lightweight material or manufacturing technology. The MMLV Mach-II design continues to be a work in-process to realize the 50% mass reduction target. The mass associated with the CF and Mg-intensive Mach-II design is currently 911kg (40%) lighter than the baseline vehicle.

Accomplishments

Quantifiable accomplishments during the course of the project during FY 2014 include:

Mach-I Design, Vehicle Build and Test

- Joint testing to facilitate computer aided engineering (CAE) predictive modeling
- Component-level CAE predictive modeling
- Full-Vehicle CAE Predictive Modeling: noise, vibration and harshness (NVH), durability and safety
- Tool Fabrication: BIW and chassis castings, stampings, extrusion, instrument panel, seats, tires, wheels, springs
- Manufacture Lightweight Components: castings, stampings, extrusion, instrument panel, seats, wheels, springs, rotors
- Module Subassembly: BIW, closures, bumpers, engine, transmission, subframes, tires/wheels, seats
- Corrosion: Anodize Al castings, Electrocoat (E-coat) subassemblies and BIW assembly
- Vehicle Integration: Teardown and integration of lightweight subassemblies with baseline vehicles
- Component-level Testing: doors, subframes, springs, seats, rotors
- Vehicle-level Testing: Commenced corrosion, NVH, durability and safety tests

Mach –II Vehicle Design

- BIW - CAE predictive modeling, topology optimisation, modal analysis, local point stiffness, cast Al body structure and CF passenger compartment
- Full Vehicle CAE predictive modeling of NVH, durability and safety
- Closures and Chassis – CAE predictive modeling, Mg sheet and castings
- Engine – Naturally aspired 1.0 liter inline three-cylinder (I3) lightweight concept
- Interiors – Structural trim panels, reduced function seats

Future Directions

Mach-I Design, Vehicle Build and Test

- Vehicle-level Testing: Complete and document full vehicle corrosion, NVH, durability and safety tests
- Life Cycle Analysis (LCA) – Complete analysis and document expected fuel reduction and environmental benefit

Mach –II Vehicle Design

- MMLV Mach-II: Document material changes plus the reduction in vehicle content and features necessary to realize 50% mass reduction objective

Technology Assessment

Al/Al Joining

- **Target:** Achieve 100% Al/Al spot weld joint efficiency of wrought and cast Al substrates ranging between 1.0 and 2.0 millimeters (mm) thick for two-layer (2T) and three-layer (3T) joint configurations in a manufacturing environment.
- **Gap:** Conventional welding techniques (e.g. spot, laser) result in inconsistent joint integrity due to presence of Al oxide ($Al_2O_{3)}$ oxide layer and material expulsion issues.
- **Gap:** Advanced joining techniques (e.g. friction stir welding (FSW) and self-pierce riveting (SPR) for Al have not been demonstrated within 1.5 second cycle time increment. SPR materials present cost and corrosion issues.

Body Panels: Mg and Al Formability

- **Target:** Achieve equivalent formability between Steel, Al and Mg sheet using existing stamping infrastructure to enable ability to form radii <2T in Class A applications of Mg and Al 5xxx and Al 6xxx sheet 1.0 and 2.0 millimeter (mm) gauge.
- **Gap:** Mg and Al alloys lack room temperature formability to achieve forming radii less than 2T. The result is the application of steel substrates in highly styled Class A sheet applications, compromise in styling features or additional progressive room temperature forming operations relative to steel sheet processing.

Body Panels: Mg Paint Finishing and Corrosion

- **Target:** Achieve equivalent reflectance (R-value), Distinctness of Image (DOI) and corrosion resistance characteristics for Class A Mg sheet, as compared to traditional Steel and Al body panels.
- **Gap:** Paint finishing methods have not been developed and demonstrated for Mg Class A automotive sheet applications. Process specifications need be developed which characterized sheet, forming and finishing operations to achieve the application requirements.

Vacuum Die Cast Material Properties

- **Target:** Utilize publicly-available material property characteristics for Al vacuum die cast body structure components in CAE predictive analysis.
- **Gap:** Material cards do not exist in the public domain that characterize the material properties of vacuum die cast body structure Aural-2™T7 and Aural-5™T5 alloys for both quasi-static, high strain rate, low cycle fatigue applications.

FRC Material Properties

- **Target:** Utilize publicly-available material property characteristics for fiber reinforced composite structural component applications in CAE predictive analysis.

- **Gap:** Material cards do not exist in the public domain which characterize the material properties of fiber reinforced composite materials for specific fiber characteristics resin and processing systems.

Joining of Press Hardened Steel (PHS) to Mg, Al and Fiber Reinforced Composite (FRC) Body Structure

- **Target:** Joining of PHS safety cage to lightweight body structure materials.
- **Gap:** The relative strength, hardness and galvanic potential of press hardened steel presents joining issues relative to the attachment to the lightweight body structure.

<div align="center">✧   ✧   ✧   ✧   ✧</div>

Introduction

Lightweighting associated with passenger vehicles has typically been limited to primary mass reduction including material substitution or bolt-on subassemblies such as doors, hoods and deck lids. The fuel reduction benefit associated with secondary mass reduction and engine downsizing has been estimated, using a multiplier factor of the total primary mass reduction.

Approach

The Mach I vehicle design approach included target setting associated with each of the vehicle subsystems to realize a total vehicle mass reduction of 25%, relative to the 2014 Ford Fusion baseline vehicle. Realization of the 25% mass reduction target enabled application of an existing engine/powertrain set used in a current B segment vehicle, By matching the target weight of Mach I vehicle with that of the existing B-segment production vehicle, similar acceleration performance and fuel usage is expected. Utilization of a current model baseline vehicle (2013 Fusion) provided the benefit of integrating the MMLV lightweighted vehicle subsystems with the production baseline vehicle to facilitate full vehicle testing, as well as utilization of carryover component parts and subsystems which were not lightweighted. In order to realize the benefits associated with the use of the 2013 Ford Fusion as the baseline vehicle, subsystem "hardpoints" associated with the baseline vehicle were maintained.

Results and Discussion

Mach-I Concept Vehicles

Figure V-1 gives an illustration of the MMLV prototype concept vehicle showing a paint scheme that depicts the areas where lightweight materials were applied. During fiscal year FY 2014, project activities included fabrication and integration of MMLV Mach I lightweight subassemblies and lightweight component parts with 2013 Fusion baseline vehicles to manufacture seven test vehicles. Corrosion, durability, NVH tests commenced in the fourth quarter (Q4) of 2014. Test results associated with the Mach I vehicles will be reported in FY 2015.

Figure V-1: The MMLV Prototype Concept Vehicle.

BIW

Fabrication of the Mach-I BIW design and integration with 2013 Fusion baseline vehicles were completed in FY 2014. The mass associated with the Mach-I BIW is 250 kg, a 77 kg weight savings (or 23.5%) relative to the 2013 Fusion BIW.

The MMLV BIW is a multi-material design comprised of Al castings, extrusions and stampings (64% Al) and steel front rails, floor cross members and safety cage (36% steel). The eight high pressure vacuum die cast body structure components and the PHS safety cage are common to both the Mach I and Mach II design variants. Figure V-2 and Figure V-3 provide a breakdown of component materials and a picture of the actual prototype construction.

Due to the low volume requirement, some of the materials and thickness specified in the Mach I design release were not commercially available. As such, comparable material grades and material thickness substitutions ranging between 5% and 10% of the specified material thickness were used.

The Mach-I design specified SPR as the primary joining method. In a limited number of cases, where SPR guns of the specified size were not available in the prototype shop, structural Huck® rivets were substituted. Joints which imposed a single-sided access, flow screw and RIVTAC® technology were specified. All joints incorporated structural adhesive to mitigate galvanic corrosion between dissimilar materials and to distribute stress. E-coated modules utilized heat activated Dow Betamate™ 73305. Dow Betamate™ 73326 air- cured adhesive was used for non-E-coated BIW modules and in the final framer.
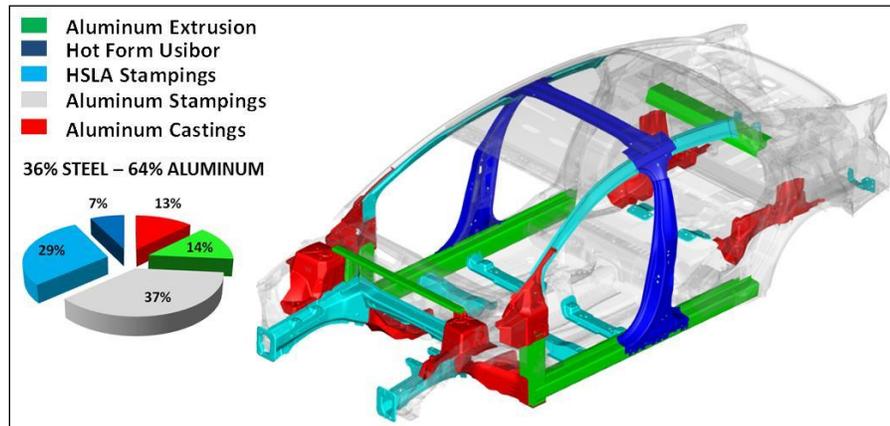
Figure V-2: Mach I BIW Architecture.

Figure V-3: Mach I BIW Prototype Build.

The MMLV Mach I design and prototype vehicle build project included the development of an alternative final assembly sequence and corrosion strategy, enabling use of materials not compatible with e-coat chemistry and processing temperatures. The Corrosion A test vehicle includes processing of the BIW in a traditional manner, which includes assembly of the complete BIW structure, followed by E-coat on the entire BIW to mitigate corrosion. The Corrosion B vehicle was processed using a modified assembly sequence, Bill-of-Process (BOP) and alternate corrosion protection strategy. The Corrosion B vehicle included E-coat of only the Class A painted surfaces and steel components prior to assembly of the BIW. The alternative BIW assembly sequence enables use of materials in the BIW construction which are not compatible with e-coat chemistry and elevated temperature processing. Figure V-4 illustrates the assembly sequence associated with the alternative (non-traditional) assembly and corrosion mitigation. The modular assembly process also enables integration of preassembled and corrosion protected BIW modules manufactured by the tier 1 supplier, as well as potential cost savings and capital cost avoidance associated with E-coat infrastructure. The cost avoidance associated with

the body shop may be of specific interest in niche markets which mandate local vehicle manufacture.

CAE analysis was completed on the MMLV BIW design for global and local stiffness, durability, and selected crash events. Torsion and bending global stiffness results were compared to the 2013 Fusion baseline vehicle and MMLV targets. Due to timing and budgetary constraints, three vehicle-level safety simulations were conducted; Federal Motor Vehicle Safety Standards (FMVSS) 216 Revision A roof crush resistance, Insurance Institute for Highway Safety (IIHS) Offset Deformable Barrier (ODB) frontal impact protection, and FMVSS 214 Revision D side impact protection.

FMVSS 216A roof crush target of 3.625 times the unloaded vehicle weight (UVW) of 1195 kg is 42.45 kilonewton (kN). This loading causes the roof to have a maximum displacement of 127 mm. This test is performed in full vehicle trim as a two-part test loading both sides of the vehicle. The displacement is stopped early if the target is met. Figure V-5 shows the CAE simulation results with the target load being meet on both sides for the MMLV BIW.
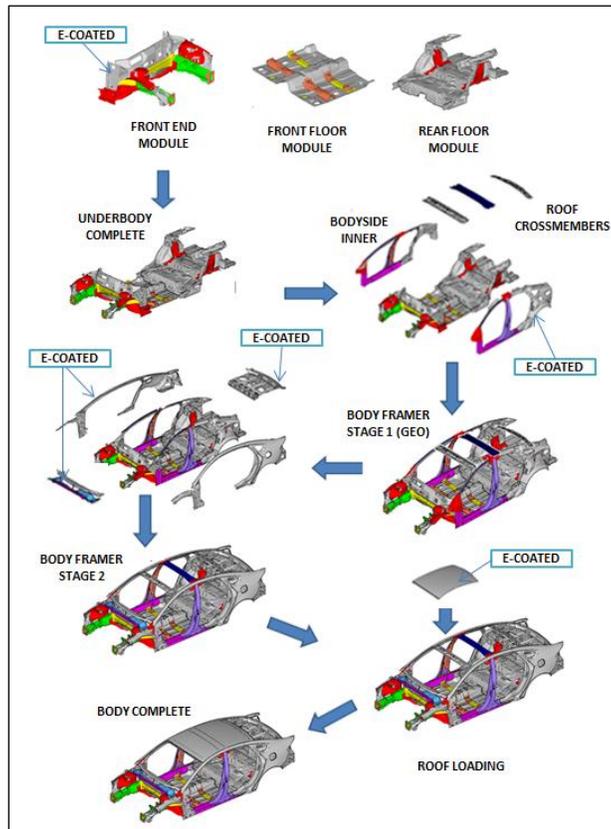
Figure V-4: Alternative Assembly and Corrosion Mitigation.
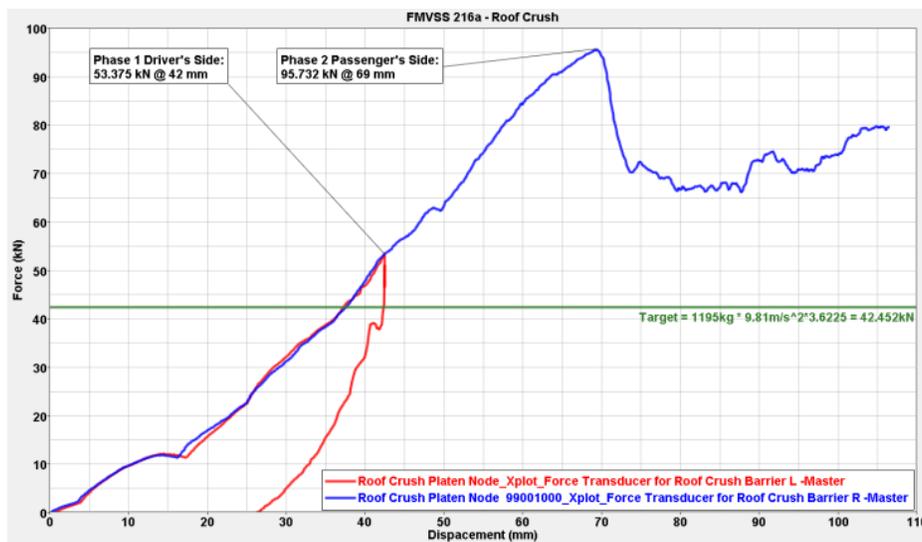
Figure V-5: MMLV FMVSS 216A Roof Crush Results.

IHSS ODB is a 40% frontal offset impact test at 64.4 kilometers per hour (km/h) (40 miles per hour (mph)). The CAE design target was to achieve a GOOD rating for structure, minimizing the magnitude of intrusion into the driver's compartment area. Figure V-6 shows the CAE simulation result with the target intrusion being met for the MMLV BIW. The positive simulation prediction (GOOD) is attributed to the Al body casting at the kick-down rail location in the BIW, providing added stiffness to the structure, minimizing intrusion into the occupant compartment resulting in the GOOD predicted rating for this test.
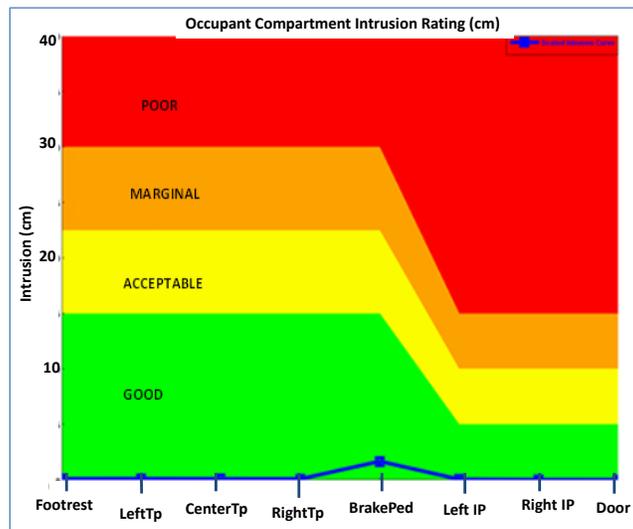
Figure V-6: MMLV IHSS ODB Frontal Impact Results.
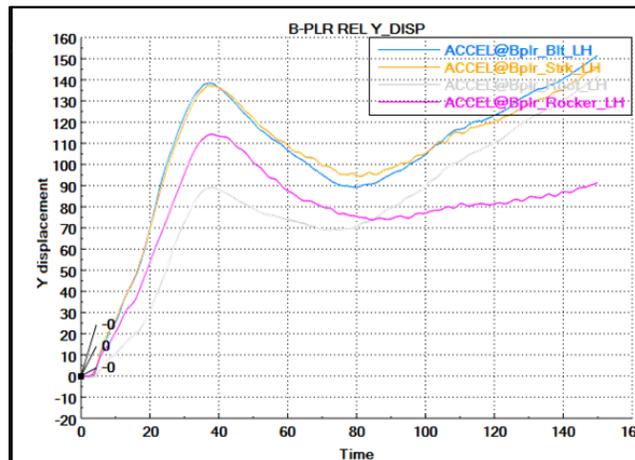
Figure V-7: MMLV FMVSS 214D Side Impact Results (units: x-axis msec, y-axis millimeters).

FMVSS 214D side impact target is a combination of dummy velocity and intrusion into the vehicle compartment. Since the CAE analysis is performed without safety dummies, a door beltline intrusion velocity is tracked and compared to the baseline vehicle of 7 meters per second (m/s) from 20 to 40 milliseconds (ms). Due to the weight reduction on the vehicle and conservation of momentum, this belt line velocity target could not be achieved. The intrusion results were compared to the baseline vehicle and were within acceptable levels as shown in Figure V-7.

Closures

Fabrication of the Mach-I closures-in-white was completed in FY 2014. The mass associated with the Mach-I closures-in-white is 69kg, 29 kg weight savings (29.7%) relative to the 2013 Fusion closures-in-white. Interestingly, the 2013 Fusion

has an Al hood so the design includes no weight saving for the hood in the closures calculation.

The MMLV door styling and sealing package and frame behind glass architecture is carry-over from the 2013 Fusion baseline vehicle. This door architecture consists of a full stamped 5xxx-series inner, 6xxx-series half-door outer and press hardened steel impact beam. The distribution of door materials for the MMLV Mach I door design are given in Figure V-8. The sealing package includes a seal mounted on the sidewalls of the door as well as a secondary flange mounted seal that runs around the bodyside door opening, and several tertiary seals such as a lip seal that seals the bottom of the door to the sill and a seal at the gap between the doors. The critical requirement for seals is a consistent, smooth surface for mounting and touchdown facilitated by a one-piece door inner panel. Figure V-9 is a picture of the prototype doors for the MMLV Mach I design.
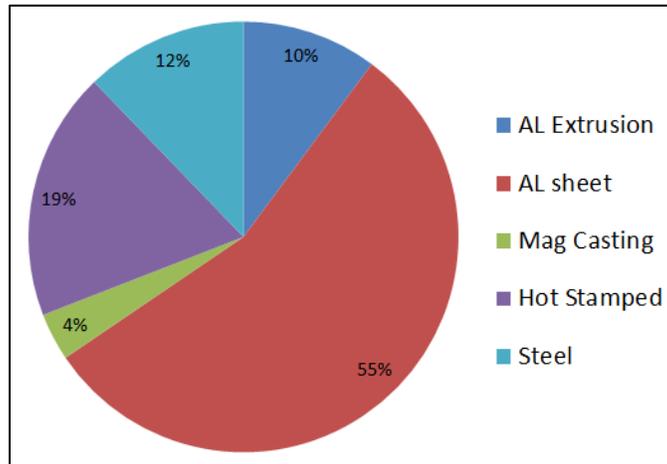
Figure V-8: MMLV Mach I Door Materials 65% Al, 21% Steel and 4% Mg.
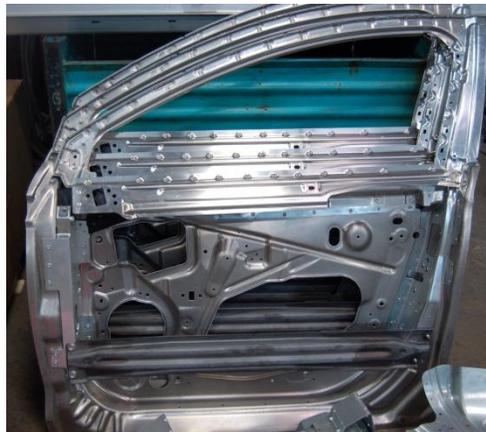
Figure V-9: MMLV Prototype Doors.

Bumpers

Fabrication of the Mach-I front bumper was completed in FY 2014. The total mass associated with the Mach-I front and rear bumpers is 25kg, 11 kg weight savings (30.9%) relative to the 2013 Fusion bumpers. MMLV Mach I bumpers are comprised of 6063-T6 and 6082-T6 MIG welded Al extrusion assemblies. A prototype front bumper is shown in Figure V-10.

Chassis – Subframes

Fabrication of the Mach-I front subframe was completed in FY 2014. The mass associated with the Mach-I front and rear subframes is 30kg, 27 kg weight savings (37.6%) relative to the 2013 Fusion bumpers. MMLV Mach I cradles are comprised of A356-T6 low pressure castings and 6063-T6 MIG welded Al extrusion assemblies. The front cradle for the Mach I design is shown in Figure V-11.

Figure V-10: MMLV Prototype Front Bumper.

Figure V-11: MMLV Front Cradle.

Cylinder Block (-41%)   Oil Pan (-41%)   Cam Carrier (-15%)   Front Cover (-26%)   Connecting Rod (-38%)

Figure V-12: Engine Weight Savings Investigations.

Powertrain and Driveline Development

The Mach-I powertrain design was completed in FY 2014. The Mach-I design powertrain weighs in at 266 kg, an 84 kg weight savings (24%) from the 2002 Taurus powertrain. Figure V-12 shows engine components and their respective percentages of weight saved.

Engine

The engine design includes an Al cylinder block with powder metal bulkhead inserts which features fractured split main bearing caps, carbon fiber oil pan, carbon fiber cam carrier, carbon fiber front cover and an Al connecting rod, see Figure V-12.

Fatigue bench rig testing on the bulkhead sections failed to get the required 10 million cycles at the determined engine maximum bearing loads. The bulkhead insert material was changed and inserts redesigned. CAE analysis, Figure V-13, was performed on the bulkhead insert and indicated much higher acceptable fatigue safety factors. Fatigue bench rig testing on the new inserts verifies the CAE results with loads of 1.5 x the maximum main bearing loads at 10 million cycles. Five new cylinder blocks castings have been poured with the new bulkhead inserts and a slight cylinder block casting change. These revised cylinder blocks have been delivered and the finished cylinder blocks are ready for engine builds.

Carbon fiber front cover and oil pan designs are the prime directive. The computer aided design (CAD) and CAE analysis are complete for both the front cover and oil pan. The finished parts have been delivered and are ready for engine builds.

The cam carrier design has been completed and the first billet lightweight carbon fiber phenolic material cam carrier was delivered. The billet material has demonstrated good machinability and dimensional stability. Al camshaft bearing inserts and bronze alloy tappet bore inserts are being bonded into the carrier. The use of the insert is to provide an adequate surface for the required oil film of the rotating camshaft and direct acting mechanical bucket movement. The results for the fastener testing has demonstrated that this material provides similar fastener retention characteristics and load capability to cast Al.

The CAD design, CAE analysis and tooling associated with the forged Al connecting rods are complete. Al forged connecting rods were made in Q4 of FY 2014 and have been verified to have acceptable material properties. Final machined connecting rods with polymer coated pin and crankshaft surfaces are scheduled to be delivered by Oct. 15, 2014.

The Mach-I prototype engine is scheduled to be built by Oct. 31, 2014 and engine testing is scheduled to be completed by end of 2014 CY.

The lightweight engine technologies are not planned to be integrated with the drivable Mach-I prototype vehicles. The lightweight engine parts will be tested on engine dynamometer and bench labs.

For Mach-II design, the engine will be a naturally aspirated, direct injection, three cylinder, and 1.0 liter gasoline engine. The research team has included a carbon fiber engine block with Al cylinder liners as a further weight reduction for the Mach-II engine.
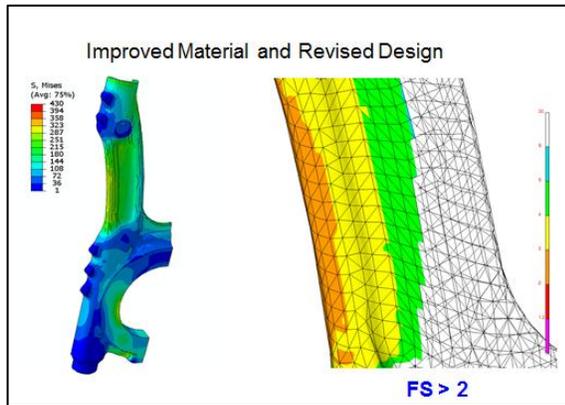
Figure V-13: Bulkhead Insert Fatigue Analysis.

Transmission

The transmission team envisioned a lighter six-speed automatic transmission with Al pump support, Mg valve body, Al clutch hub and Al bolts as illustrated in Figure V-14 with their respective weight savings.

Mg Valve Body

- Clamp load, body distortion analysis complete
- Valve body build and functional testing complete – met acceptance criteria
- Completed Tests:
    – Al bolt installation torque development and clamp load distribution test
    – Static thermo cycle test - met acceptance criteria
- Test in progress: Valve Body Cycling Test

- Planned actions: functional test in transmission

Al Pump Support

- Distortion and stress analysis complete
- Al pump assembly build and functional test complete - met acceptance criteria
- Stator shaft ultimate torque and fatigue tests complete - exceeded acceptance criteria
- Planned actions: pump performance and pump seizure test

Al Clutch Hub / Gear Assembly

- Stress, deformation analysis complete.
- Hub/Gear prototype complete.
- Completed tests:
    – Weld joint ultimate torque and torsional fatigue – exceeded acceptance criteria
    – High speed spin – radial deflection comparable to production steel part
    – Clutch hub brinelling test – met acceptance criteria
    – Clutch hub wear test – met acceptance criteria

A transmission assembly will be built and function-tested with lightweight components. In addition to the components reported above the team also completed CAE assessments. Powertrain bending analysis for Mg transmission case and formability analysis for Al valve body cover were completed to investigate further weight reduction opportunities. The team did not proceed to prototype phase due to limited resource and funding.
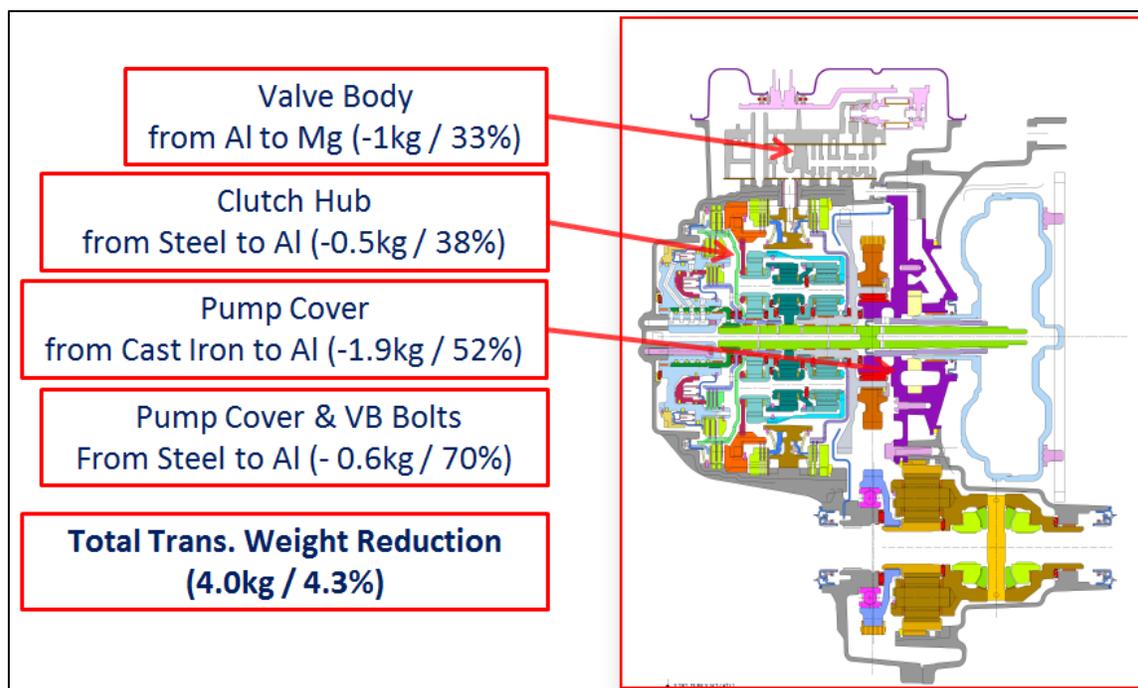
Figure V-14: Transmission Weight Savings Investigations.

For the Mach-II design, the transmission will be a six speed manual transmission with additional weight reduction actions. The clutch and transmission housings will be designed in Mg and the differential will be designed in AlAl. These actions will produce a transmission at approximately 27 kg.

Interior Systems Development

The Mach I design for the interiors includes CF composite seat structures shown in Figure V-15 and Figure V-16, and a CF composite instrument panel cross-car beam shown in Figure V-17.

The seat design passes the four critical load cases for design: front impact, rear impact, cargo retention, and headrest loading. Weight savings is 6% for the seat back structure and 26% for the cushion structure for a total weight savings of 17% per seat. Prototype design yields 1.6 kg weight savings per vehicle.

Figure V-15: CF Composite Seat Back and Cushion Structures (Production Steel Seat Structure Illustrated for Comparison).
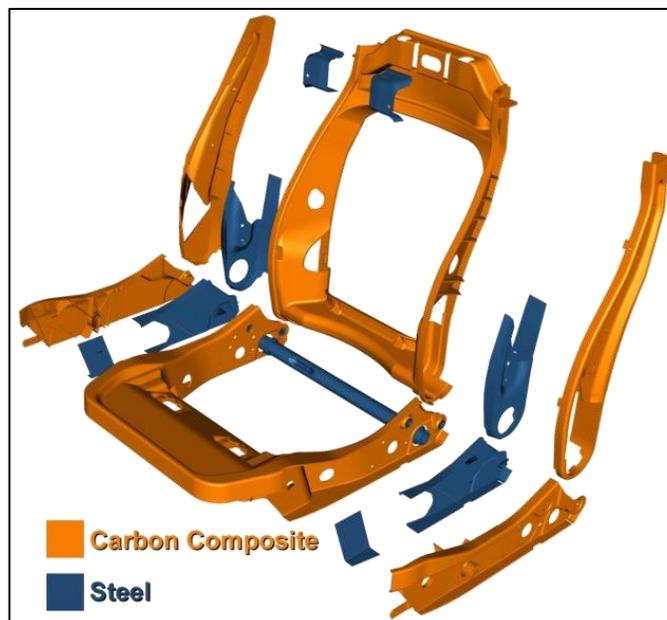
Figure V-16: CF Composite Seat Parts and Material Break Up.
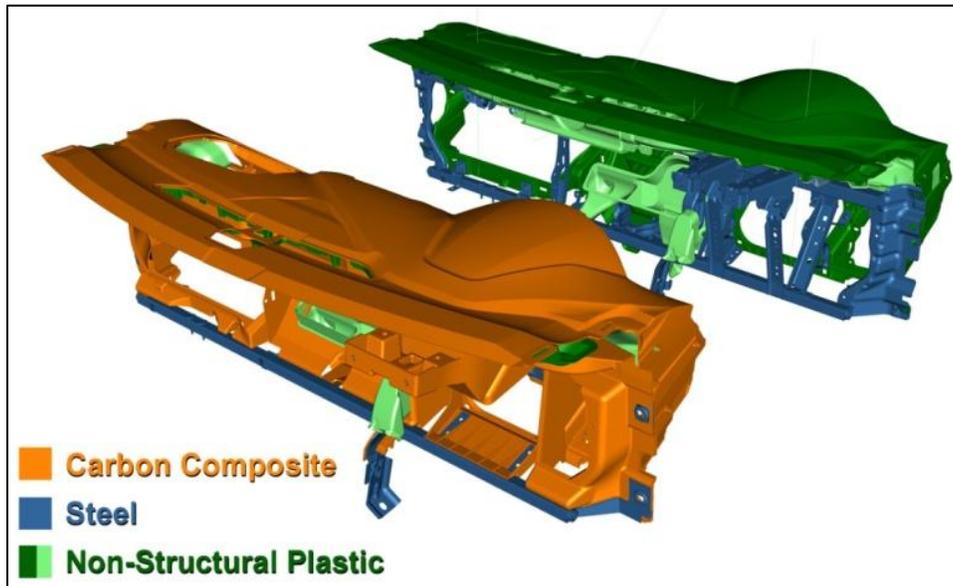
Figure V-17: CF Instrument Panel Cross Car Beam (CCB) (Production Steel/Plastic IP/CCB Illustrated for Comparison).

Design iteration has resulted in a CF reinforced nylon instrument panel/cross car beam (CCB) that meets design targets for performance with a vertical steering column frequency of 37.2 Hz against a design target of 37 Hz. The design has also been verified to meet the passenger airbag and knee bolster deployment loads in front impact. After successful design optimization, a total weight savings of 5.2 kg is realized. This is a 30% weight reduction. The design also reduces part count from 71 parts to 21 parts as illustrated in Figure V-18 below.
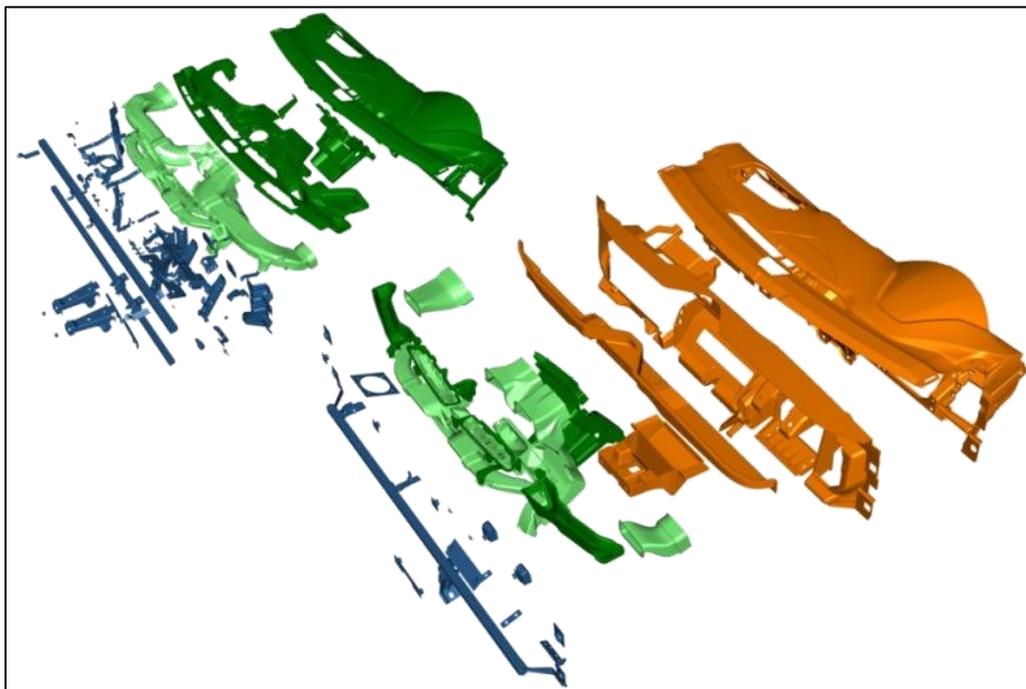
Figure V-18: CF IP/CCB Part Count Comparison.

Interiors Prototype Build

MMLV prototypes parts are produced for the vehicle builds and testing using low-cost prototyping methods. Single sided composite tooling was built. Typical tools, along with some of the first parts produced, are shown in Figure V-19 below. Parts were produce with hand-laid CF fabrics and epoxy resigns with a vacuum-bagging process.

Prototype parts that are weight equivalent to the production intent process were produced. A total of six fully trimmed, fully functional sets of driver and passenger seats were produced for the vehicle builds along with additional subassemblies for testing and spare parts. A complete seat assembly less the foam and trim is shown in Figure V-20.

Figure V-19: CF Upper Duct and Plenum Bracket Parts and Tools.

Figure V-20: CF Composite Prototype Seat.

Figure V-21 below is the first complete prototype IP/CCB built to support the vehicle builds. A total of six complete instrument panel assemblies were produced for the Mach-I vehicle builds along with additional subassemblies for testing and spare parts.

Prototype seats and instrument panel completed the in-vehicle durability testing with no known issues. Finally, evaluation will be made following teardown of the durability vehicle. Additional validation testing of the seats and instrument panels will be completed by the end of the 2014 calendar year.

LightWeight Tires Development

Ford has continued the development and evaluation of a lightweight tire using a unique 155/70R19 tall and narrow design, in collaboration with Michelin. The project is segmented into two primary phases: Phase I- Selection of Preferred Tire Submission and Phase II- Evaluation of

Lightweight Tire. As part of Phase II, Michelin completed a custom build of 56 tires for use on the tire evaluation process and MMLV durability vehicles. The selected tire construction (8.0 kg) successfully passed both Department of Transportation (DOT) and high speed testing.

Tires were submitted for laboratory evaluation of key performance criteria. The Mach-I prototype tires were evaluated for footprint metrics, dimensional measurements and assessment of rolling resistance and traction performance. An illustration, Figure V-22, shows the contact footprint map for the tire. The patch has a length of 142 mm and width of 104 mm.

The Flat-Trac® CT (Cornering and Traction) System was used to measure the lateral force the tire generates including peak grip versus load. The Society of Automotive Engineers (SAE) method J2452 was used to determine the rolling resistance coefficient. The laboratory testing results are shown in Table V-1 below.

Figure V-21: Complete Carbon Composite MMLV IP/CCB.
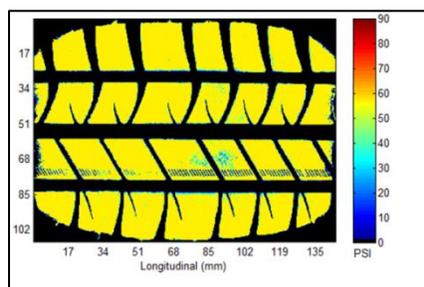
Figure V-22: Contact Patch of MMLV Tire.

Table V-1: Results From Lightweight Tire Tests.

Test	Purpose	Value	Units
Flat-Trac® CT System Test for Lateral Forces Peak Mu (Fy/Fz)	Traction	0.970	Newton/Newton (N/N)
SAE J2452 Rolling Resistance Coefficient	Rolling Resistance	7.25	lbs. per 1000 lbs.

Results of the laboratory evaluation indicate that the Mach-I prototype tire, with 20% weight savings, has similar laboratory performance for traction and rolling resistance compared to the P225/50R17 control tire. The prototype tires are currently being evaluated as part of the durability vehicle studies.

Lightweight Wheel Development

The component testing for the lightweight CF wheels is now complete with few issues identified for further development. The plan included most of the usual wheel verification tests but did not include all the repeats of the tests due to the limited availability of CF prototype wheels. Many tests included only two or three samples.

The component tests include:

- Durability testing   OK
- Dynamic cornering fatigue   OK
- Radial fatigue testing   OK
- Outer rim impact   OK
- Inner rim impact   OK
- Wheel strike impact   OK (critical load test)
  (vehicle test)
- Bolt retention and torque   OK
- Attachment key life testing OK
- Thermal shock   issue with outer coating hazing
- Weathering resistance   issue with outer coating hazing

The CF wheels successfully passed the critical durability test of 100 strikes at a square edged pothole. Little damage was observed on the test wheel. There was some unexpected degradation in the thermal shock and accelerated long term weathering tests where the outer clear coat layer showed hazing, an appearance issue.

For Mach-II design the wheels and tires will need to be reduced in diameter since the team sees no further lightweighting potential from material changes. Any diameter reduction while keeping tire and wheel width at five inches will reduce ride and handling and customer comfort.

Lightweight Brake Rotor Development

The MMLV design incorporates lightweight brake rotors composed of a cast AlAl A356 rotor that is thermally-sprayed with a stainless steel alloy. This combination creates a lightweight, wear-resistant rotor having the proper frictional values to ensure current stopping distances are maintained. The engineered iron-manganese-chromium-aluminum (Fe-Mn-Cr-Al) austenitic steel alloy has undergone several modifications that have improved its stability while maintaining the coefficient of thermal expansion (CTE), corrosion resistance, friction, and wear-resistance. A total of six rotors have undergone a series of tests on a brake dynamometer to determine their response to operating conditions. Figure V-23 shows the comparison for a rotor before and after testing. These tests have shown that the thermal spray coating has friction equivalent to that of a cast iron rotor and that it is capable of meeting the specific dynamometer-based durability tests. Three sets of brake rotors are currently on test vehicles to evaluate their durability and corrosion resistance in the field.

(a) Coated Rotor Prior to Test   (b) Coated Rotor After Test
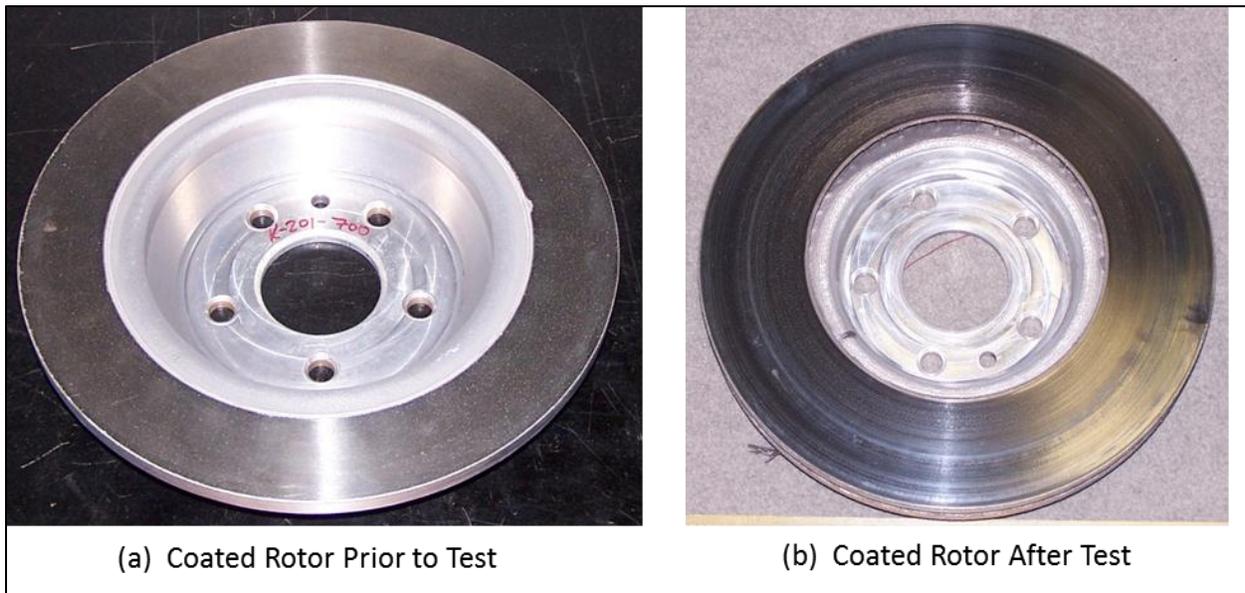
Figure V-23: Mach-I Prototype Brake Rotors.

Front and Rear Coil Springs

Component tests of MMLV lightweight coil springs and proving ground full vehicle durability test were complete. The spring performance was evaluated against design targets. Results are summarized as following:

All three springs, the composite front spring, the hollow steel rear spring, and the titanium rear spring, met the component design requirements:

1. Load/rate targets
2. Dry fatigue life cycles
3. Key life (corrosion fatigue) cycles

Additional test procedures were proposed and developed for the composite spring including relaxation test, fatigue test under high temperature, hydrofluoric acid resistance test, and underwater with alternate temperature fatigue test. The composite spring passed all the additional tests with no degradation on fatigue life comparing with dry fatigue test. Figure V-24 demonstrates the underwater with alternate temperature test procedure.

The composite front coil spring and the hollow steel coil spring were installed in the MMLV durability prototype vehicle. Both springs survived the proving ground durability test for structure and powertrain. There were no damages observed on the springs. There were no spring related vehicle performance issues during the test. The vehicle ride height changes that were associated with spring height losses were well below the 20 mm standard. The residual life of the springs will be test by the end of December 2014.

Front and Rear Stabilizer Bars

Component tests of MMLV hollow steel stabilizer bars and proving ground full vehicle durability test were complete. The stabilizer bar performance was evaluated against design targets. Results are summarized as follows:

Both the front and rear stabilizer bars met the design targets on bar rates. The front bar passed required 70,000 cycles in fatigue test and 1000 newtons (N) in slip force test. The rear bar passed 1000 N in slip force test but failed to meet the required 70,000 cycles in fatigue test. This was an expected result due to the bar size available for the prototype had less capacity then the desired designed bar. The fatigue test setup is shown in Figure V-25.

The hollow steel front and rear stabilizer bars were installed in the MMLV durability prototype vehicle. The front bar survived the proving ground durability test for structure and powertrain. There were no damages observed on the front stabilizer bar. The rear bar survived the structure run of the durability test but failed during the powertrain run. More investigation will be conducted on the post-test front stabilizer bar. The residual life of the bar will be tested by the end of 2014.

Lightweight Glazing

The lightweight glazing used on the MMLV included a polycarbonate (PC) backlite and hybrid chemically strengthened laminated glass for the windshield and side doors. The actual weight saved for the glazing on the MMLV totaled 13.8 kg (34.5%) vs. the production Fusion glass.

Installation of the lightweight glazing was successfully completed on all seven MMLV vehicles with no issues. In addition, component level Taber Industries abrasion testing was completed on both lightweight glazing materials used on the MMLV and each material met the federal American National Standards Institute (ANSI)/SAE Z26.1 abrasion requirements of < 2% change in haze for this application.

Structural durability testing at Ford's Michigan Proving Grounds was completed on the MMLV test vehicle. There were no issues identified during the durability testing on the backlite or front windshield however, both the front and rear left hand side door glazing experienced cracks in the chemically strengthened layer of the laminate at approximately 95% completion of the structural durability test. Both panels were replaced and the vehicle was returned to complete testing. Analysis to determine root cause of the cracking is ongoing.

Vehicle level door slam and window cycling testing as well as testing to evaluate glass lateral bending stiffness, NVH performance, crash, and resistance to obstacle induced damage is planned to be completed in late 2014.

Closures

Cast AlAl Door Hinges:

Seven sets of cast Al front and rear door hinges (left hand side only) have been produced and installed in the MMLV vehicles. No issues were identified.

Lightweight Sound Package for Interior

The Mach-I design includes the industry leading ultra-lightweight sound package technologies to improve acoustical performance of the lightweight vehicle design without increasing the total sound package weight from the baseline vehicle.

These ultra-light acoustical technologies are

- RUS™ lightweight underbody technology
- Ultra Light™ ECO+ floor insulator
- RIMIC™ perforated acoustical heat shield
- Theta fiber Cell™ structural-acoustical material for engine compartment applications.

Benchmarking and acoustical testing of production Fusion parts were conducted to identify weight saving and performance improvement opportunities. Full vehicle Statistical Energy Analysis (SEA) simulations were conducted to evaluate and optimize the performance of ultra-light sound package designs.

a) Springs at the Beginning of the Test
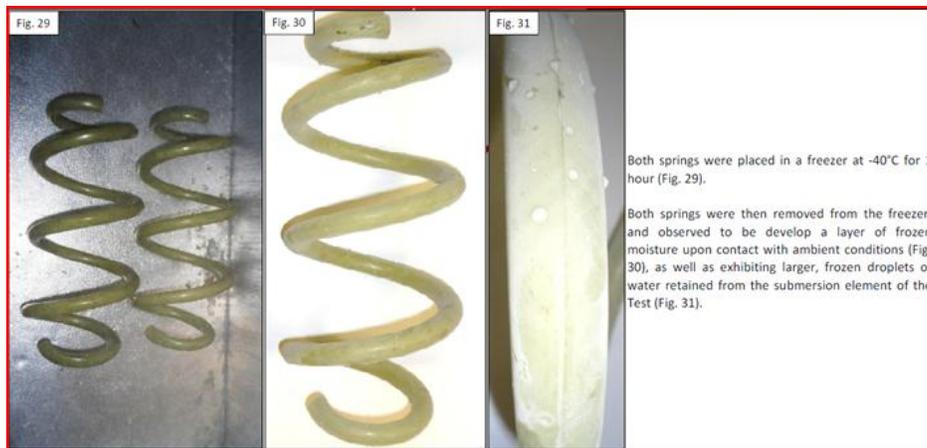
b) Springs During Freeze/Thaw Cycles
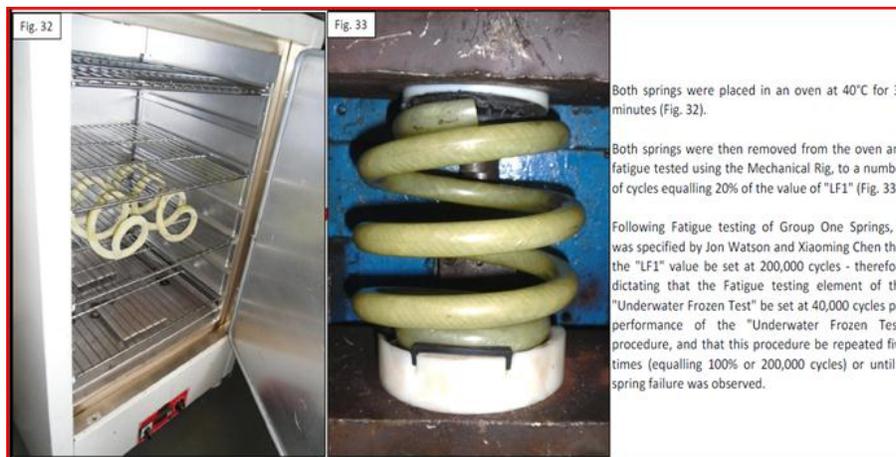
c) Springs Undergoing Heating Cycle and Fatigue Testing

Figure V-24: Composite Spring Test Pictures.
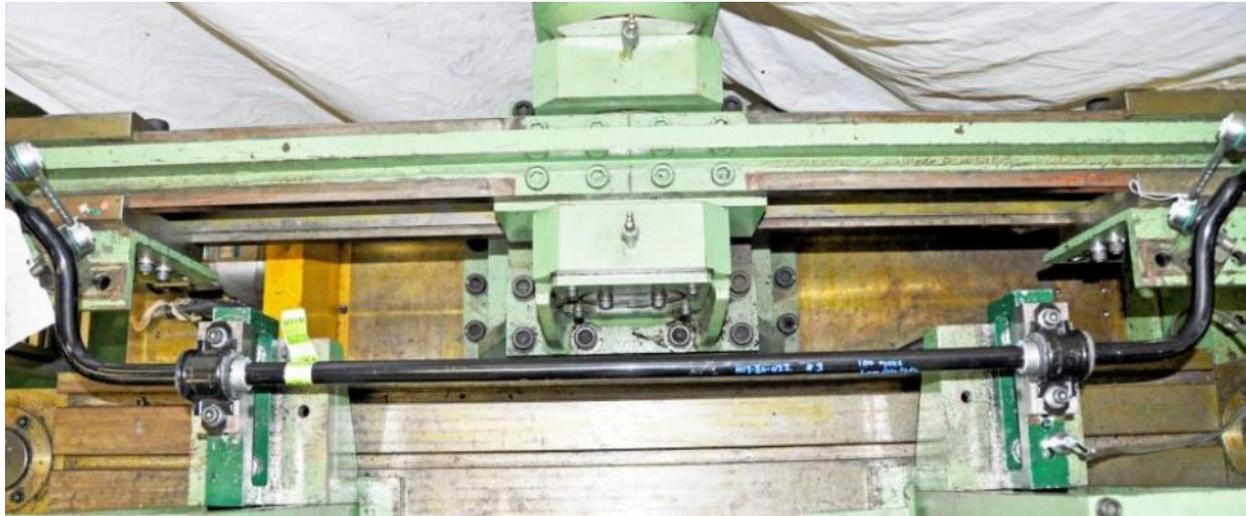
Figure V-25: Rear Stabilizer Bar Fatigue Test Setup.

Full Vehicle Engine Noise Reduction tests indicate that the Engine Encapsulation and Engine Cover Prototype in a donor Fusion improve the NVH performance by 2.7 dB and SEA simulation predicts 2.6 dB improvements. Figure V-26 and Figure V-27 show the prototype parts.

Figure V-26: Theta-Fiber™ Cell Engine Encapsulation and Engine Cover Prototype.
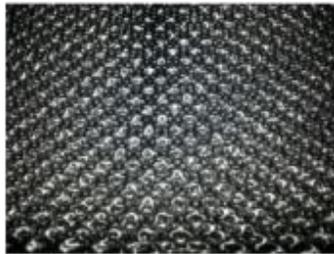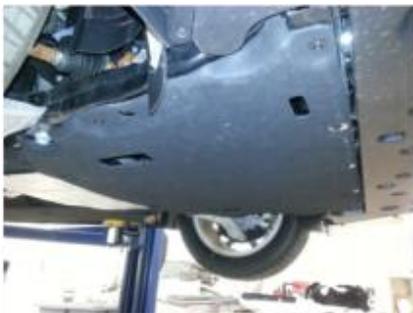
Figure V-27: Ultra-light Sound Package Prototypes on a Fusion Vehicle.

These prototype parts together improved the vehicle Engine Noise Reduction (ENR) by 3.9 decibels (dB), and Tire Patch Noise Reduction (TPNR) by 1.3 dB without increasing the sound package weight in the current Fusion vehicle.

These results indicate that it is possible to significantly improve the acoustical performance of lightweight vehicle design with the use of new ultra-lightweight sound package materials without adding additional weight.

These ultra-light sound package components will be installed on the MMLV Mach-I NVH vehicle to improve the vehicle's acoustical performance as much as 3 dB. Full vehicle NVH tests will be completed by the end of 2014.

Lightweight 12Volt (V) Li Ion Starter Battery

The Energy Storage Research Department has continued investigating the feasibility of using a Li ion battery as the vehicle's starter battery due to the potential for weight reduction when compared to a traditional lead acid battery. Over the past year, the team has identified and acquired relevant test hardware, selected a test facility, and finalized the test setup.

Ongoing independent supplier developments have resulted in changes to cell chemistry and optimization. The outcome of this supplier development activity has delayed the start of planned testing and led to a focus on a reduced subset of supplier chemistries than initially anticipated. Moving forward, the reduced testing subset will proceed to in-depth characterization of actual capability.

A number of test facilities have been evaluated and testing requirements jointly discussed. A test facility has been selected, and a detailed test plan has been finalized. Characterization is expected to begin during the fourth quarter of 2014, with testing completed by the end of the first quarter of 2015.

While Li ion technology is expected to provide sufficient useable energy and power to perform the function of a starter battery, sufficient challenges remain at low temperature and at low state of charge energy windows. Among the actual hardware that has been acquired and is now in-house, available 12V Li ion modules are included, and the team plans to test these to better understand the challenges of current Li ion starter battery technology at low temperatures. These modules are expected to be able to support cold crank at temperatures above 0°C, but power capability at subzero temperatures needs to be characterized.

Component Validation Testing

The detailed plans for all the component testing have been completed and test scheduling has begun within the Ford testing labs. Many of the testing results have been reported in the component descriptions above.

The component testing for the engine and transmission will begin in late summer when the prototype components are available. These components are not included in the MMLV Mach-I vehicle builds.

MMLV Testing Timing 2014 (September '14 update)

		Mar '14	Apr	May	Jun	Jul	Aug	Sep	Oct	Nov	Dec '14	Jan '15	Feb '15
Parts	Component Testing	OOOO	OOOO	X================	====OO=	==============	======X	==============	=================	==========	======X		
Buck #1	NVH + Durability		O O	X==========	============	==============	==============	=============	=======X				
Veh #2	Durability			OO	prep & media show	X====	==============	==============	=======X				
Veh #3	Corrosion - A MMLV			OO				X=======	==============	====X			
Veh #4	Corrosion - B Traditional			O------	-------------	O------OO		X=======	==============	====X			
Veh #5	Safety - A				OO	prep	X=============	============	=======X				
Veh #6	Safety - B						OO	prep	X=**XX**=========	========X			
Veh #7	NVH							OO Engine	X==============	=============	====X		
notes:	OO Delivery X====X Testing **XX** NCAP Frontal Test, Oct 22											

Figure V-28: Full Vehicle Test Timeline.

Vehicle-Level Testing

The vehicle level testing for the MMLV Mach-I prototypes, six full vehicles, one buck (body + closures + glazing + bumpers + front subframe), are underway. The key tests to confirm the lightweight designs will be conducted following Ford testing standards. The timing of the testing is approximate given the uncertainties in Ford testing facility availability; however, the current schedule has the last vibration testing being completed in February 2015 as shown in the timeline of Figure V-28. A key test, the New Car Assessment Program (NCAP) full frontal crash test at 35 mph into a rigid barrier is scheduled for Wednesday, October 22, 2014 at the Ford Safety Crash Barrier facility in Dearborn, Michigan.

The first full vehicle tests of vibration on the body (Buck #1) have been completed. Vibration and stiffness testing was performed on a prototype Body-In-Prime (BIW + Fixed Glass).

Body Structure Laser Scan Testing for Damping Placement

This testing determined areas of the floor to receive damping treatment. The process involved using vibration measurement as a surrogate for structure-borne noise. The assumption was that reducing vibration reduces noise in the vehicle passenger compartment.

Soft boundary conditions were used in the laboratory to simulate a free-free condition (floating body). Force inputs were at two locations: the first at the front subframe left rear mount and the other attached to the rear subframe right front attachment point. A shaker at each input location was directed at oblique angles in order not to bias the results.

The procedure was to scan the bare structure from 50-500 hertz (Hz). After the first scan, constrained layer damping material was hand applied at the locations of highest vibration. The second scan was to verify the reduction in panel vibration. The damping material used was Nitto Denko 1432F Foil Constrained Layer Damper due to its availability and ease of

application at room temperature with no heat cure requirements. The total weight of the added damping material was approximately 4.8 kg. Results are shown below, Figure V-29– Figure V-31, for the rear floor panel area and are typical for the remainder of the floor.
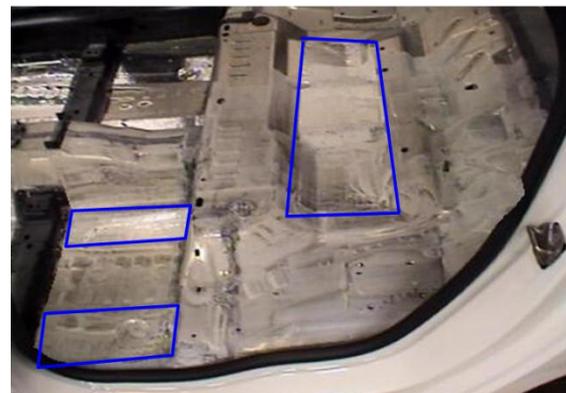
⇦ Forward

Figure V-29: Picture Showing Rear Floor View Through Rear Door Opening. Blue Outlines Indicate Locations Where Damping Treatment Was Added.
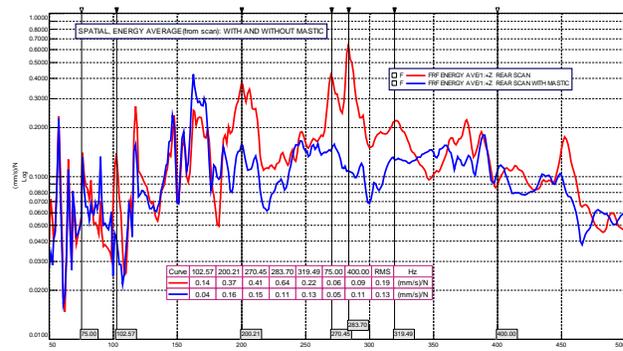
Figure V-30: Rear Floor Laser Scan Results Plot Of Spatial Energy Average Over All Scan Points. The Red Curve is Bare Floor Panel Before Damping Treatment and the Blue Curve is After Application of Damping Treatment.

Without Damping   With Damping
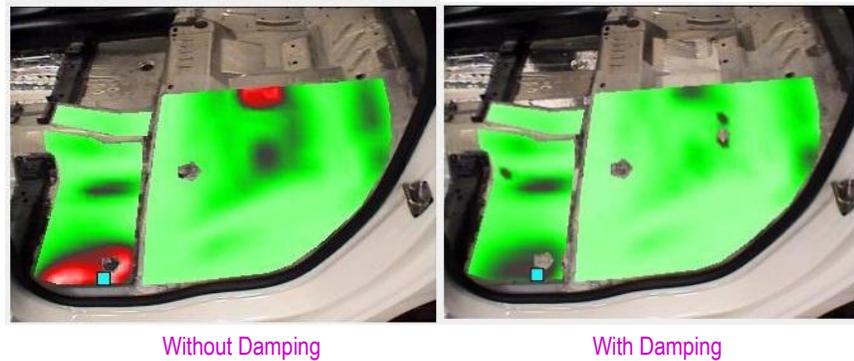
Figure V-31: Rear Floor Laser Scan Results Showing RMS Average Over Each Scan Point. The Red Colors Are Areas of Higher Vibration.

Body Structure Modal Frequency Testing

Global mode shapes and frequencies were measured on the MMLV lightweight body structure. Soft boundary conditions were used in the lab to simulate a free-free condition (floating body). Table V-2 below contains the five modal frequencies and mode shape descriptions determined from the test.

Table V-2: Table of modal frequency results.

Mode Description	Test (Hz)	CAE (Hz)
Global Torsion	44.17	44.78
Rear-End Bending	46.09	40.89
Vertical Bending	48.53	48.07
Rear Match-Boxing	49.25	48.73
Lateral Bending	54.40	54.71

Body Structure Global Stiffness Testing

Global body stiffness was measured on the MMLV lightweight body structure. Table V-3 below contains the values measured in test.

Table V-3: Table of global stiffness results.

	Test	CAE	Target
Global Bending (N/mm)	12,695	12,148	11,458
Global Torsion (kNm/radian)	1,079	1,207	1,100

Full Vehicle Durability Testing

The Durability vehicle began rough road durability testing at the Ford Michigan Proving Grounds in Romeo, MI in mid-July. The vehicle completed the accelerated testing sequence representing 150,000 miles of severe customer use in late September. The testing report will be completed within a

month. The vehicle performed well during the test with only the following seven issues.

1. Rear stabilizer bar bracket bolt cracked at 85%. (this production part had been repeatedly removed and re-attached during the build)
2. Rear hollow steel stabilizer bar cracked at ~90%. (this was expected since the chosen bar size was under capacity)
3. Front Al thermally sprayed brake rotor had coating degrade at ~90%.
4. Left front door chemically toughened laminated glass cracked at ~95%.
5. Left rear door chemically toughened laminated glass cracked at ~95%.
6. Left front lower ball joint softened ~95%. (this production part saw higher loads due to the thin wheels)
7. Left rear door chemically toughened laminated glass cracked at 100%.

Full Vehicle Corrosion Testing

The two companion MMLV vehicles began corrosion testing at the Ford Michigan Proving Grounds in Romeo, MI in early September 2014. The testing is expected to be complete in early December 2014. The two vehicles have different surface treatment strategies, the MMLV system with selected sub-assemblies e-coated prior to full body assembly and the Traditional system with the complete BIW treated in a typical rinse, dip and bake e-coat process.

Full Vehicle Safety Testing

MMLV Mach-I CAE Virtual Analysis

Ford Safety provided vehicle safety performance targets in frontal, side, rear and roof crush modes to guide MMLV vehicle development. Ford Safety also shared crash safety CAE common best practice with Vehma to convey CAE modeling, quality assurance and performance assessment. The Mach-I intermediate designs were constantly reviewed and recommendations to improve design had been suggested.

Vehma had delivered a Mach-I final design to meet all safety target except side impact door intrusion velocity requirements (IIHS side and Lateral Impact New Car Assessment Program (LINCAP)). Ford also suggested side impact structure target and restraint solution for lightweight vehicle. The Vehma crash models were transferred to Ford Safety in the format of LS-DYNA. Crash simulations were conducted using the updated Ford model and the results were compared to those reported by Vehma in their reports. The results generally compared well with base vehicle. Higher NCAP pulse was observed due to the addition of material strain rate effect, but the design can be tailored to obtain a more favorable crash pulse. The models were subsequently updated per vehicle build bill of materials (BOM) and vehicle test weight to more closely represent the prototype Mach-I for testing. Primarily the material properties, sheet-metal gauges, weld patterns and local geometries were modified in accordance with the prototype build. Simulations were conducted to generate predictions for low speed damageability (LSD), IIHS offset impact, and frontal NCAP test modes. The robustness study is conducted considering the variation of material properties, especially element deletion criteria for material fracture characterization. Numerical results show some changes in local deformation. However, on a global scale, the responses are found to be relatively stable.

Crash Vehicle Build and Testing

Ford Safety developed the crash plan based on vehicle re-hit strategy to minimize the cost of vehicle prototype build and adequate instrumentation to optimize data collection. Based on common vehicle crash plan, two prototypes were built to assess critical crash modes include LSD, 40% offset IIHS impact and frontal NCAP tests. The LSD test was successfully completed on August 25, 2014. The test showed mild damages in the form of plastic deformation in exchangeable parts in the impact zone, Figure V-32. The observed damages compared well with the CAE predictions and model is updated through further correlation effort. The observed damage levels were also comparable to the baseline donor vehicle. The crash tests were conducted on the bumper-crush can sub-assembly to obtain sub-system force-deflection response. These results were used

for further CAE model calibration. The vehicle preparation for the IIHS front 40% offset impact test has been completed. The vehicle is scheduled to be tested at the Ford's test barrier facility on early October, 2014. Vehicle preparation for the NCAP test is currently in-progress. The vehicle is scheduled to be tested on October 22nd, 2014.

Mach-I Design Technologies

The Mach-I Design includes existing commercially available materials and production processes that are reasonable for high volume manufacturing (see Table V-4). Not all of the designs were realized in the Mach-I prototype vehicles due to cost and value considerations. For example, the Mach-I prototypes include lightweight left-hand side doors. Producing lightweight right-hand side doors costs twice as much but adds no additional learning or test data.

MMLV Mach-II Design

The Mach-II design is not yet finalized due to the focus on the component and vehicle testing. The Mach-II design is now 150 kg above the design weight target of 751 kg. The Mach-II will be designed without architectural constraints and will obtain a mass reduction of 50%, as compared to the 2002 Taurus baseline vehicle. A comparison of the baseline vehicle subsystem weights and the MMLV (Mach-I and Mach-II) subsystems weight targets is given in Table V-5. Mach-II design will incorporate materials and manufacturing process that "show potential" but are not yet proven commercially viable for high volume production. Examples include Mg wrought body components for both class A surfaces and inner panels and CF materials in structural and sheet components. The use of these materials poses a large challenge in joining and corrosion. The Mach-II design concept will identify the joint and material combinations that will need further research to mitigate corrosion and joint challenges.
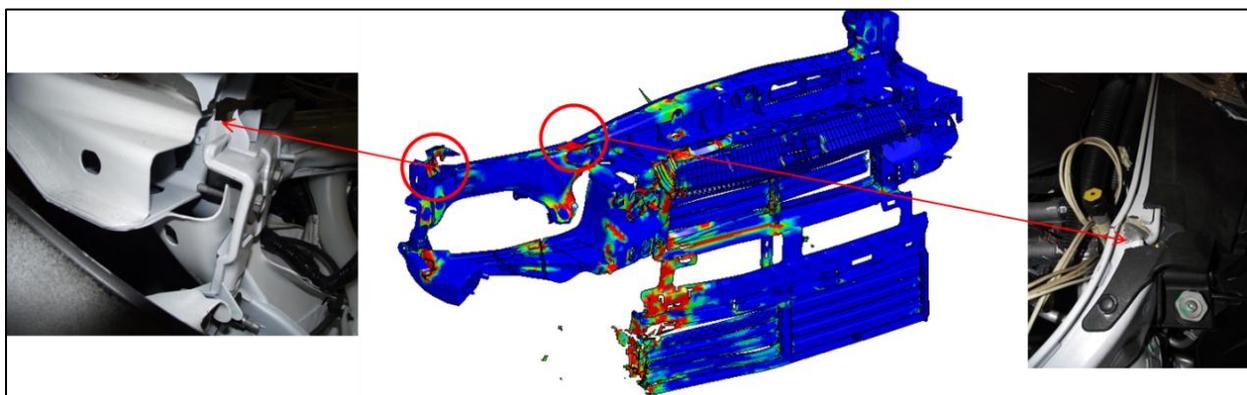
Figure V-32: CAE-vs.-Test Comparison in LSD – Example of Grill Opening Reinforcement Module Damage.

Table V-4: Mach-I DESIGN Technologies.

System	Component	Technologies
Body	BIW	HLSA steel sheet
		Boron steel sheet
		5xxx aluminum sheet
		6xxx aluminum sheet
		6xxx aluminum extrusions
		Aluminum high pressure castings
	Bumpers	6xxx aluminum sheet
		Chemically foamed plastic fascia
	Closures	Boron steel intrusion beam
		5xxx aluminum sheet
		6xxx aluminum sheet
		6xxx aluminum extrusions
		Magnesium high pressure castings
	Glazings	Chemically strengthened hybrid laminated glass windshield
		Chemically strengthened hybrid laminated glass door drop glass
		Polycarbonate rear window (backlite)
	Door Hinges	Cast aluminum door hinges
	Dynamic Seals	Tape-on secondary weather strip
Interiors	Seats	Carbon fiber composite seat structures
	Instrument Panel	Carbon fiber composite cross car beam with integrated HVAC ducts
	HVAC Ducts	Chemically foamed plastic ducts
	Trim	Chemically foamed plastic trim
	Sound Package	Equal weight, improved performance
Chassis	Front Subframe	Aluminum castings plus extrusions
	Rear Subframe	Aluminum castings plus extrusions
	Front Rotors	Thermally sprayed aluminum castings
	Rear Rotors	Thermally sprayed aluminum castings
	Front Springs	Glass + epoxy composite coil springs
	Rear Springs	Hollow steel coil spring
	Front Stabilizer Bar	Hollow steel stabilizer bar
	Rear Stabilizer Bar	Hollow steel stabilizer bar
	Wheels	Carbon fiber composite 19 x 5
	Tires	Low rolling 155/70R19
Powertrain	Engine	Aluminum block with thermally sprayed bo
		Powdered metal forged bulkhead inserts
		Aluminum connecting rods
		Carbon fiber / polyamide oil pan
		Carbon fiber / polyamide front cover
		Carbon fiber / aluminum carrier
	Transmission	Aluminum pump cover
		Aluminum / steel FSW clutch hub
		Magnesium case
		Magnesium valve body
	Driveline	Carbon fiber composite half shafts
Electrical	Battery	Li-ion starter battery
	Distribution Wiring	Aluminum wiring
	Lighting	LED lighting

Table V-5: MMLV Weight Update.

MMLV — PMT Description	2002 Taurus	2013 Fusion	MMLV Mach I DESIGN FINAL	MMLV Mach I Prototype Planned	MMLV Mach II Design Targets (PRELIM)	MMLV Mach II Design Status (4 Mar '14)
Body Exterior and Closures (kg)	574	594	456	489	237	355
Body-in-White	n.a.	326	250	251		183
Closures-in-White	n.a.	98	69	88		56
Bumpers	n.a.	37	25	31		24
Glazings - Fixed and Movable	n.a.	37	25	25		21
Remainder - trim, mechanisms, paint, seals, etc.	n.a.	96	87	94		70
Body Interior and Climate Control (kg)	180	206	161	191	137	116
Seating	n.a.	70	42	61		34
Instrument Panel	n.a.	22	14	15		11
Climate Control	n.a.	27	25	27		11
Remainder - trim, restraints, console, etc	n.a.	88	80	88		60
Chassis (kg)	352	350	252	269	144	212
Frt & Rr Suspension	n.a.	96	81	85		66
Subframes	n.a.	57	30	44		19
Wheels & Tires	n.a.	103	64	58		57
Brakes	n.a.	61	49	50		43
Remainder - steering, jack, etc.	n.a.	33	29	32		27
Powertrain (kg)	350	340	267	299	190	181
Engine (dressed)	n.a.	101	71	101		64
Transmission and Driveline	n.a.	106	92	54		38
Remainder - fuel, cooling, mounts, etc.	n.a.	133	104	143		79
Electrical (kg)	67	69	59	66	53	47
Wiring	n.a.	28	25	28		23
Battery	n.a.	14	8	10		8
Remainder - alternator, starter, speakers, etc.	n.a.	27	26	27		17
Total Vehicle (kg)	1523	1559	1195	1313	761	911

	Mach I DESIGN FINAL	Mach I Prototype Planned	Mach II Targets
Weight save w.r.t. 2013 Fusion	23.3%	15.7%	51.2%
Weight save w.r.t. 2002 Taurus	21.5%	13.8%	50.0%

Further progress on the Mach-II design will be the focus of the next quarter.

Technology Transfer Path

The design and preliminary test results associated with the Mach I lightweight subsystems have been presented to the Product Development teams associated with future vehicle platforms and are being evaluated for cost/benefit considerations for future vehicle platforms.

Conclusion

FY 2014 included the manufacture of MMLV Mach I subsystems and component parts, integration with baseline vehicles and commencement of full vehicle testing. Additionally, much of the design for Mach-II lightweight systems has been completed and the remaining efforts will complete the 50% weight reduction, perhaps through reduction in vehicle content and features.

Presentations/Publications/Patents

MMLV Mach-I Media Announcements

Following the delivery of the first drivable Mach-I durability prototype vehicle, upper management at both Vehma/Magna and Ford used the vehicle to make press announcements on the MMLV project and research efforts on lightweight strategies. The announcements were well received and repeated across many media outlets. Here is a partial list of press releases to MMLV:

1. **Ford Demonstrates Lightweight Fusion Concept**
   http://www.automobilemag.com/features/news/1406-ford-demonstrates-lightweight-fusion-concept/#14053651510851and188,shopper
   by Jake Holmes | United States **Automobile Magazine** | Jun-4-2014

Ford revealed a new lightweight concept version of the Fusion sedan that is nearly 25 percent lighter than the standard car. As a result, the lightweight Fusion weighs as much as the Ford Fiesta hatchback. According to Ford, a 2014 Fiesta weighs 2537-2628 pounds, while a non-hybrid 2014 Ford Fusion tips the scales at 3323-3681 pounds, putting the weight loss somewhere in between 800-900 lbs.

2. Ford Launches Lightweight Concept –
http://www.pistonheads.com/news/default.asp?storyId=30115 *PistonHeads.com*

3. Ford Unveils Ultra-Light Fusion Sedan Concept –
http://www.thedetroitbureau.com/2014/06/ford-unveils-ultra-light-fusion-sedan-concept/ *The Detroit Bureau*

4. Ford's Fusion Lightweight Concept Sheds a Quarter of the Sedan's Bulk –
http://wallstcheatsheet.com/automobiles/fords-fusion-lightweight-concept-sheds-a-quarter-of-the-sedans-bulk.html/?a=viewall – *Wall St. Cheat Sheet*

5. Ford builds on advanced materials use in all-new F-150 with Lightweight Concept Car » Automotive World
http://www.automotiveworld.com/news-releases/ford-builds-advanced-materials-use-new-f-150-lightweight-concept-car/ *Automotive World*

6. Ford unveils Fusion Lightweight Concept, partners with Samsung on lightweight battery research
http://mms.tveyes.com/ExpandGuest.asp?ln=995903 – *WJBK-TV (Fox) Channel 2 (Detroit)*

7. Ford unveils Lightweight Fusion Concept
http://mms.tveyes.com/ExpandGuest.asp?ln=995768 – *WXYZ-TV (ABC) Channel 7 (Detroit)*

8. Ford shows off experimental Fusion 23% lighter than normal
http://www.tweaktown.com/news/38222/ford-shows-off-experimental-fusion-23-lighter-than-normal/index.html – *Blog: TweakTown*

9. **Ford Unveils Special, Lighter-Weight Fusion**
Prototype Is 23% Lighter, Sets Road Map for Next-Generation Weight-Reduction Efforts
by Mike Ramsey | United States
The Wall Street Journal | Jun-4-2014–
http://online.wsj.com/articles/ford-unveils-special-lighter-weight-fusion-1401831431?mod=WSJ_qtoverview_wsjlatest
Associated Press – Ford unveils lightweight concept car
By Dee-Ann Durbin June 3, 2014
http://www.miamiherald.com/2014/06/03/4155763/ford-unveils-lightweight-concept.html

10. **CNET – Ford concept car shows benefits of weight loss**
Electrification and efficient drivetrains play a part in increased fuel economy, but making cars lighter delivers the coup de grace.
By Wayne Cunningham June 3, 2014

http://www.cnet.com/news/ford-concept-car-shows-benefits-of-weight-loss/

11. **USA Today – Ford shows off lightweight car concept**
By Chris Woodyard June 3, 2014
http://www.usatoday.com/story/money/business/2014/06/03/ford-fusion-lightweight/9928467/

12. **The Wall Street Journal**
Ford Unveils Special, Lighter-Weight Fusion
Prototype Is 23% Lighter, Sets Road Map for Next-Generation Weight-Reduction Efforts
By Mike Ramsey June 3, 2014
http://online.wsj.com/articles/ford-unveils-special-lighter-weight-fusion-1401831431

13. **San Francisco Chronicle – Ford, partners unveil projects to improve cars' efficiency**
By David R. Baker June 3, 2014
http://www.sfchronicle.com/business/article/Ford-partners-unveil-projects-to-improve-cars-5526228.php

14. **Jalopnik – Ford Just Unveiled A Fusion That Weighs As Little As A Fiesta**
By Michael Ballaban June 3, 2014
http://jalopnik.com/ford-just-unveiled-a-fusion-that-weighs-as-much-as-a-fi-1585576176

15. **LA Times –Ford Fusion loses 25% of its weight in lightweight concept version**
By Charles Fleming June 3, 2014
http://www.latimes.com/business/autos/la-fi-hy-ford-lightweight-concept-car-20140529-story.html

16. **Ubergizmo – Ford and Samsung Car Dual-Battery Presented in San Francisco**
By Eliane Fiolet une 3, 2014
http://www.ubergizmo.com/2014/06/ford-and-samsung-car-dual-battery-presented-in-san-francisco/

17. **DailyTech – Ford Lightweight Concept Removes 800 lbs. from Fusion Midsize Sedan**
By Brandon Hill June 3, 2014
http://www.dailytech.com/Ford+Lightweight+Concept+Removes+800+lbs+from+Fusion+Midsize+Sedan/article35006.htm#sthash.V9OcoNRE.dpuf

18. **Detroit Free Press**
Ford future technology unveiled in Lightweight Concept
By Alissa Priddle June 3, 2014
http://www.freep.com/article/20140603/BUSINESS0102/306030181/Ford-Fusion-lightweight-concept-F-150-AlAl-auto

19. **Detroit News – Ford reduces Fusion concept's weight 23%**
By Karl Henkel June 3, 2014
http://www.detroitnews.com/article/20140603/AUTO0102/306030097/1361/Ford-reduces-Fusion-concept-s-weight-23-

20. **Motor Trend – Ford Lightweight Concept First Look**
By Frank Markus June 3, 2014
http://www.motortrend.com/future/concept_vehicles/1406
_ford_lightweight_concept_first_look/

21. **WardsAuto – Ford Concept Car Takes Lightweighting to Extreme**
By Byron Pope June 3, 2014
http://wardsauto.com/vehicles-technology/ford-concept-car-takes-lightweighting-extreme

22. **CarAdvice – Ford Lightweight Concept Car**
By Derek Fung June 3, 2014
http://www.caradvice.com.au/289218/ford-lightweight-concept-car-a-fusionmondeo-that-weighs-as-little-as-a-fiesta/

23. **TheFastLaneCar.com – Ford LightWeight Concept turns a Fusion into a Fiesta [Preview]**
By Andre Smirnov June 3, 2014
http://www.tflcar.com/2014/06/ford-lightweight-concept-turns-a-fusion-into-a-fiesta-preview/

24. **MotorAuthority – Ford Fusion Lightweight Concept Car Goes All-Out with High-Tech Weight Savings:Video**
By Nelson Ireson June 3, 2014
http://www.motorauthority.com/news/1092484_ford-fusion-lightweight-concept-car-goes-all-out-with-high-tech-weight-savings-video

25. **Motoring.com – Ford's Feather-Weight Fusion** June 3, 2014
http://www.motoring.com.au/news/medium-passenger/fords-feather-weight-fusion-43905

Websites(s) or Other Internet Site(S)

No dissemination of results of research activities on URL for any internet site(s) took place during the reporting period.

Technologies / Techniques

No technologies/techniques have resulted from the research activities took place during the reporting period.

Inventions, Patent Applications, and/or Licenses

No inventions, patent applications and/or licenses have resulted from the research.

Other Products

No other significant products were developed under this project.

V.2 Chrysler Upset Protrusion Joining Techniques for Joining Dissimilar Metals – Fiat Chrysler Automobiles (FCA) US LLC

Stephen Logan, Principle Investigator
FCA US LLC
800 Chrysler Drive
Auburn Hills, MI 48326
CIMS #482-00-13
Phone: (248) 512-9485
E-mail: stephen.logan@fcagroup.com

Chuck Alsup, Project Officer
National Energy Technology Laboratory
3610 Collins Ferry Road
P.O. Box 880
Morgantown, WV 26507-0880
Phone: 304-285-5432
E-mail: Charles.alsup@netl.doe.gov

William Joost, Technology Area Development Manager
U.S. Department of Energy
1000 Independence Avenue, S.W.
Washington, DC 20585
Phone: (202) 287-6020; Fax: (202) 856-2476
E-mail: william.joost@ee.doe.gov

Contractor: FCA US LLC
Contract No.: DE-EE0006442

Abstract/Executive Summary

The overall project goal is to develop and demonstrate a robust, cost effective, and versatile joining technique, known as Upset Protrusion Joining (UPJ), for joining challenging dissimilar metal combinations, especially those where one of the metals is a die cast magnesium (Mg) component. This project will develop process variants to enable joining of Mg die castings to aluminum (Al) and steel sheet components of various thicknesses, strengths and coating configurations. A variant of the process will be evaluated for joining mixed metals that do not necessarily include Mg or Al die cast components.

Joints are evaluated through conventional microstructure and joining induced defect characterization, as well as through tensile lap shear and cross-tension testing, and fatigue and drop tower impact energy tests. The galvanic corrosion performance of the joints is evaluated through Chrysler's prescribed accelerated corrosion testing procedure, American Society for Testing Materials (ASTM) G85-A2, which has shown to be aggressive for galvanic corrosion on dissimilar metal joints. At the end of the corrosion test, selected

configurations will be re-evaluated for fatigue and impact performance.

Accomplishments

- Obtained large plates and sheets of Mg, Al and steel material, and cut them into several hundred 40 millimeter (mm) by 110 mm shear tension (ST) and 40 mm by 120 mm cross tension (CT) joining test coupons to support Self-Pierce Riveting (SPR) and UPJ joint development work. (FY 2014)
- Obtained 200 aluminum-magnesium (AM) 60B and 200 aluminum-zinc (AZ) 91D Mg die castings (each including two bosses for a total of 400 AM60B and 400 AZ91D bosses) and machined them to appropriately sized (11 mm diameter by 14 mm height) cylindrical test samples to support thermo-mechanical characterization being conducted at McMaster University and CANMET-MTL. (FY 2014)
- Completed two repetitions of each measurement of thermo-mechanical compression behavior for die cast AM60B and AZ91D Mg alloys at eight temperatures and two strain rates using cylindrical shaped compression test specimens cut from die-castings to support computer simulations of UPJ forming behavior. (FY 2014)
- Evaluated 17 different SPR designs to down-select those that could join the 2.0 mm thick Mg AM60B to 2.2 mm thick Al6013 T4 materials while minimizing cracking of the Mg material and eliminating cracking of the Al material. (FY 2014)
- Produced over 200 SPR Mg (AM60B) to Al 6013 joint samples to be evaluated as a benchmark comparison for UPJ joints. (FY 2014)
- Conducted 105 initial (pre-corrosion) benchmark SPR mechanical/structural tests, including microstructure evaluations, joining induced defect characterization, and quasi-static, impact, and fatigue tests, of four unique coating combinations each of shear and cross tension joint configurations. (FY 2014)
- Commenced and completed 12 weeks of accelerated corrosion exposure test and evaluation of 122 benchmark SPR joints in four unique coating combinations of shear and cross tension joint configurations. (FY 2014)
- Conducted extensive process modeling and simulation development work and additional experimental work conducted during this reporting period. This simulation work primarily used surrogate thermo-mechanical data established before the start of this program, as well as additional test samples that have been produced at Applied Engineering & Technology Integration, Inc. (AET) during this period. (FY 2014)
- Obtained 500 die cast AM60B magnesium test coupons (each including two bosses for a total of 1000 bosses)

with7 mm diameter round bosses and 700 coupons (each including two bosses for a total of 1400 bosses) with 8 mm diameter round bosses to support round boss UPJ joining process development and modeling correlation work as well as to support assembly of joining test coupons for later tasks. (FY 2014)

- Optimized round boss UPJ joint electrode shapes and process parameters using a combination of extensive simulation and actual physical experiments. This included machining and evaluating over 10 unique round boss UPJ electrodes in order to develop optimum robust head shapes for 7.0 and 8.0 mm diameter protrusions. (FY 2014)

- Machined and polished final optimized round boss electrode geometries to support process optimization and production of joined assemblies. (FY 2014)

- In addition to optimizing the electrode shape, conducted numerous simulations and physical experiments comparing the effects on joint development performance of varying force and current rates throughout the process. Several process variations were found to be acceptable. This information is utilized in the final process optimization being used to produce joints for evaluation in the next fiscal year. (FY 2014)

- Pretreated appropriate Mg die castings for round boss UPJ joining. (FY 2014)

- Optimized boss geometry for oval boss configurations using computer aided engineering (CAE) simulation tools. (FY 2014)

Future Directions

- Conduct post-corrosion evaluation of benchmark SPR joints.

- Finish producing round boss UPJ joints and conducting mechanical/structural evaluation of these joints as well as conduct accelerated corrosion evaluation and post-corrosion evaluation of these joints.

- Finish optimizing oval boss UPJ joining processes, produce oval boss UPJ joints, and conduct structural/mechanical evaluation of these joints. These joints will not be exposed to accelerated corrosion aging as there is no reason to expect them to perform differently from the round boss UPJ samples.

- Develop and optimize round boss UCR (Upset Cast Riveting) process for joining dissimilar metals that do not include a casting, produce joint evaluation samples, conduct structural/mechanical evaluation of these joints, conduct accelerated corrosion evaluation, and conduct post corrosion evaluation of these joints.

Technology Assessment

- Target (Project): Develop a robust low cost method to join Mg die-castings to dissimilar metal components such as Al and steel sheet.

- Gap: No method currently available for joining Mg die castings to dissimilar metals.
  - Fusion welding cannot be used to join Mg to dissimilar metals because of the formation of brittle intermetallic structures.
  - Although solid state welding should theoretically offer some advantages in joining Mg to dissimilar metals without forming brittle intermetallic formations, actual attempts to do so have shown this to be a substantial challenge requiring perfect joining conditions in order to be successful.
  - Mechanical joining with steel fasteners creates a strong potential for galvanic corrosion between the steel fastener and the Mg die casting. Attempts to rectify this are only partly successful because 1) any coatings on the steel fastener typically get damaged during the insertion of the fastener, and 2) attempts to use Al fasteners are typically cost prohibitive.

- Target (Task 1): Develop optimized joint geometry and process parameters for producing robust Mg to dissimilar metal UPJ joints at industry acceptable cycle times without damaging coatings (if applicable) on the cathodic material.

- Gap: Robust boss and electrode design and process parameters have not been developed to ensure UPJ can be used reliably in volume production applications

- Gap: Insufficient thermo-mechanical compression material data exists for common die cast Mg alloys.

- Gap: Most common die cast Mg alloys do not have ideal forming characteristics and may be susceptible to cracking during the forging process, even with substantial heat application

- Target (Task 2): Produce joined assemblies for testing and evaluation

- Gap: No joined assemblies currently available for testing and evaluation

- Target (Task 3): Conduct initial (pre-corrosion) mechanical/structural testing and evaluation

- Gap: No data currently exists to compare performance of UPJ process to existing joining processes for strength and durability

- Target (Task 4): Conduct accelerated corrosion testing and evaluation on benchmark SPR joints as well as on UPJ variants

- Gap: No data currently exists to compare corrosion performance of UPJ process to existing joining processes.

✧   ✧   ✧   ✧   ✧

Introduction

The UPJ process, shown conceptually in Figure V-33, is somewhat similar to heat staking of plastic components. The simplest form of the process uses a cast-in protrusion on a die cast component, which is aligned with a clearance hole in the mating component prior to application of force and heat which are used to essentially upset forge the protrusion into a larger diameter boss that fills the clearance hole and forms a mushroom-shaped head to solidly lock the two components together.

The process was conceived primarily for the purpose of joining Mg die-castings to each other and to dissimilar metals because die casting is the most common and cost effective process for producing light weight Mg components. This is one of the most common processes for producing aluminum components as well, yet there has been relatively little work aimed at joining components produced from this process (other than bolting).

While alternative dissimilar metal joining processes have been investigated with varying levels of success, galvanic corrosion has consistently been demonstrated to be a key challenge. Particularly:

1) Metallic bonding such as fusion or solid state welding processes, which require a clean (no coatings, or a specific coating designed to improve intermetallic bonding rather than corrosion performance) surface on both metals and does not allow for any isolation between the two metals.

2) Separate fastener (rivet, bolt, etc.). Typically, the separate fastener is made of steel for high strength and low cost. However, steel fasteners will promote galvanic corrosion in aluminum and will aggressively promote galvanic corrosion in magnesium. This galvanic activity is even worse if one of the two light metals is joined to a steel component. Additionally, any coatings on the steel fasteners intended for corrosion protection tend to get damaged during the installation process and the fasteners also tend to damage any coatings on the components being joined, thus rendering any preliminary coatings to be useless since the isolation has been broken, or even magnifying the galvanic attack on the anode if a small defect is created in the coating of the anode. Figure V-34 shows an example of this magnified galvanic attack when a coated steel screw is driven into a coated magnesium component and then exposed to a corrosive environment.

By contrast, the UPJ process relies on a robust mechanical joint rather than intermetallic bonding, so the more cathodic material can be coated prior to joining to protect against galvanic attack on the more anodic material. Additionally, since the UPJ protrusion is going through a hole that can be pre-drilled or pre-punched prior to coating, the UPJ process is much less likely to damage the coating when the joint is being made. Furthermore, since there is no additional cathodic material (such as a steel fastener) used to create the joint, there is no joining induced galvanic activity beyond that between the two parent materials.
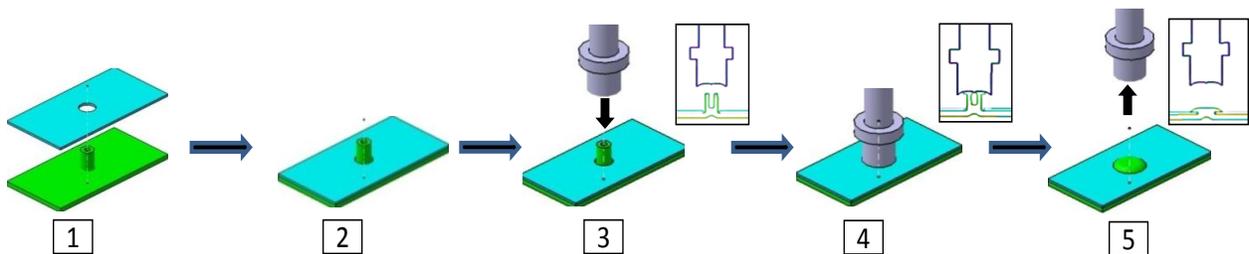
Figure V-33: Initial conceptual schematic of UPJ process – assembling parts, applying heat and force, assembly complete.

Figure V-34: Galvanic corrosion effects of steel screws in a magnesium component exposed to 240 hours of ASTM B117 salt spray testing.

Approach

The project technical approach is summarized as follows:

1. Establish **benchmark** performance of magnesium to aluminum joints produced through SPR, a currently available commercial process, **for comparison purposes _only_**.

2. Obtain additional knowledge and understanding of thermo-mechanical behavior of magnesium alloys through Gleeble® testing being conducted in Canada at no cost to the U.S. Department of Energy (DOE).

3. Take advantage of knowledge that Chrysler has already gained on the UPJ process, as well as additional CAE forming simulations based on the knowledge gained through the Gleeble® testing, to develop optimized cast protrusion and welding electrode shapes to reduce electrical current requirements and provide more robust, repeatable forming performance for each of the joint configurations being considered.

4. For each configuration (AM60B to Al6022, Al6013, and high-strength steel (HSS) in bare, pretreated, and coated conditions, and round and oval shaped joints), produce tensile shear and cross tension test coupons, and send select assemblies back for additional coating layer prior to actual start of mechanical/structural and corrosion evaluations.

5. Subject a substantial number of samples (five of each configuration) to initial mechanical/structural tests as described above.

6. Subject a substantial number of samples to Chrysler's accelerated corrosion tests, reviewing visually every two weeks and removing three samples of each configuration at four week intervals for quasi-static testing.

7. Finally, at the end of the 12-week accelerated corrosion exposure, subject select configurations to fatigue and impact testing for comparison to pre-corrosion performance.

Joint performance is validated through:

- Characterization of material microstructure in the joint region
- Characterization of joining-induced defects in the joint region
- Quasi-static tensile shear tests
- Quasi-static cross-tension tests
- Drop tower impact tests of select tensile shear and cross-tension samples Cyclic fatigue testing of select tensile shear and cross-tension samples
- Exposure to 12 weeks of Chrysler's accelerated corrosion test (ASTM G85-A2) with quasi-static lap shear failure and cross tension failure being evaluated after each 4-week increment, and fatigue testing and impact testing to be re-evaluated on select samples at the end of corrosion exposure
- Characterization of failure mechanisms for each of the mechanical tests described above.

Results and Discussion

As the project approach requires establishing benchmark performance data from a current state of the art joining process that is amenable to joining dissimilar light metals, the SPR process was chosen as being the most likely option for joining dissimilar Mg to Al materials to provide benchmark data. This report will begin by describing the results of the evaluation of the SPR process.

The team developed a test/evaluation matrix to help guide the evaluation of different coating configurations. This test matrix, shown in Table V-6, prescribes the evaluation of four different coating configurations in both ST and CT testing configurations. Table V-6 is color coded to show the current status of evaluation of these joints. The squares highlighted in **green** indicate that pre-corrosion mechanical/structural testing is complete. The squares highlighted in **yellow** indicate that corrosion testing has been completed on those configurations but the post –corrosion mechanical/structural evaluation has not yet been completed. The boxes highlighted in **red** indicate that those parts were removed from the corrosion test chamber prior to completing the prescribed 12 weeks of testing due to a high number of parts within those configurations experiencing premature failures (i.e., the assemblies were coming apart inside the corrosion chamber without having any load applied to them), and meaningful post-corrosion testing may not be possible. This is certainly true of the post-corrosion fatigue testing, which may not be possible due to an insufficient number of intact assemblies available to produce a fatigue curve.

In order to optimize the SPR joining process to produce high quality dissimilar metal (Mg AM60B to Al6013 T4) joints of 2.0 mm Mg to 2.2 mm Al, 17 different rivet configurations were evaluated before down-selecting four that looked the most promising (best rivet engagement, fewest cracks, etc.). Figure V-35 (a) shows cross sections of four different rivet designs evaluated during the optimization of this process while Figure V-35 (b) shows test results for peak quasi-static loads in newtons (N) related to the appropriate rivet sections in Figure V-35(a). Note that it was not possible to join AM60B to Al6013 T4 without some cracking in the Mg coupons. The slight cracking observed in this configuration has been observed in previous research and development (R&D) projects but has been shown to have no significant effect on the mechanical performance of these joints. Note also that all joints are made by driving the rivet through the Mg plate and into the Al plate. This is because the higher ductility of the Al plate allows for ductile formation of the rivet in the Al plate without damage to the plate, whereas the formation of the rivet would have caused substantial cracking in the less ductile Mg plate.

Table V-6: Benchmark SPR Test and Evaluation Matrix.

Material	Test Type Configuration	Surface Condition	Material	Thickness (mm)	Surface Condition	Coated Assembly?	Microstructure Characterization and Defect Evaluation	Quasi-Static ST	Quasi-Static CT	Fatigue ST	Fatigue CT	Impact ST	Impact CT	4 wks Quasi-Static ST	4 wks Quasi-Static CT	8 wks Quasi-Static ST	8 wks Quasi-Static CT	12 wks Quasi-Static ST	12 wks Quasi-Static CT	12 wks Fatigue ST	12 wks Fatigue CT	12 wks Impact ST	12 wks Impact CT
Mg AM60B	Shear Tension	Bare	Al 6013 T4	2.2	Bare	No	5	5						3		3		3					
		Pre-Treat	Al 6013 T4	2.2	Pre-treat	Yes		5		20		5		3		3		3		20		5	
					Coated	No		5						3		3		3					
					Coated	Yes		5						3		3		3					
	Cross Tension	Bare	Al 6013 T4	2.2	Bare	No			5						3		3		3				
		Pre-Treat	Al 6013 T4	2.2	Pre-treat	Yes	5		5		20		5		3		3		3		20		5
					Coated	No			5						3		3		3				
					Coated	Yes	5		5						3		3		3				

Figure V-35: Examples of rivet configurations and joint strengths evaluated for selecting optimum configuration to produce benchmark SPR samples.

Over 200 shear and cross tension assemblies were then produced for the purpose of evaluating the mechanical/structural performance of these joints before exposing a substantial number of un-tested joints to an accelerated corrosion procedure.

Figure V-36 shows photos of actual tested samples. Figure V-36(a) shows the result of a shear tension test, while Figure V-36(b) shows the result of a cross tension test. Similar to the results shown in these photos, all SPR joint samples failed in the Mg parent material at the head of the rivet.

Figure V-37 shows results of quasi-static shear tension and cross tension testing. The different coating configurations were not expected to show any substantial difference in performance in these pre-corrosion mechanical/structural tests. The primary purpose of this set of tests is to provide the baseline for the post-corrosion tests to be conducted in the next fiscal year.

Figure V-38 shows results of quasi-static vs. impact performance results for pre-treated Mg to pretreated Al in (a) ST and (b) CT. In both ST and CT testing, impact performance is significantly better than quasi-static performance. While this is typical for many similar metal joining processes, this behavior was important to validate for the dissimilar metal SPR joints being investigated in this report because these joints will establish the benchmark performance for the UPJ process under development.
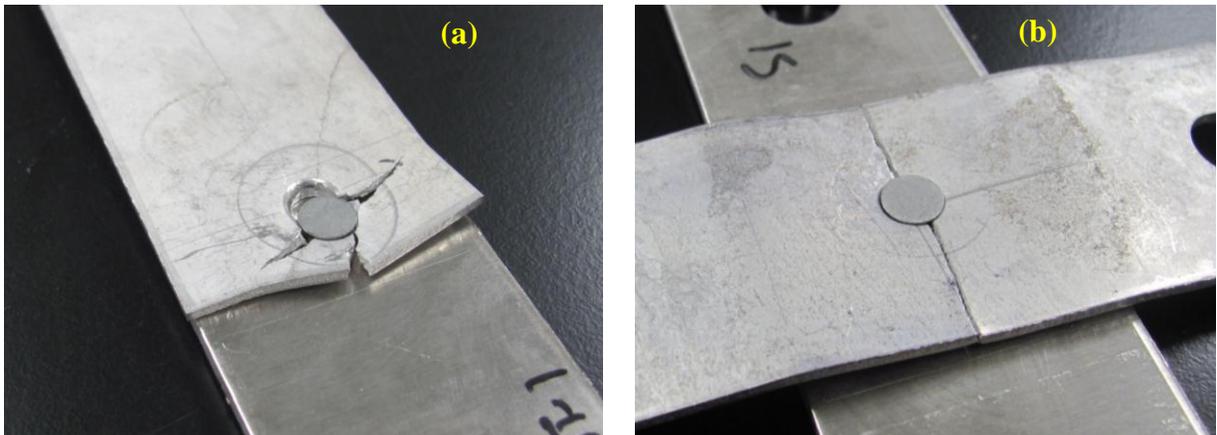
Figure V-36: Preliminary test samples of SPR Mg AM60B to Al6013 T-4 joints.
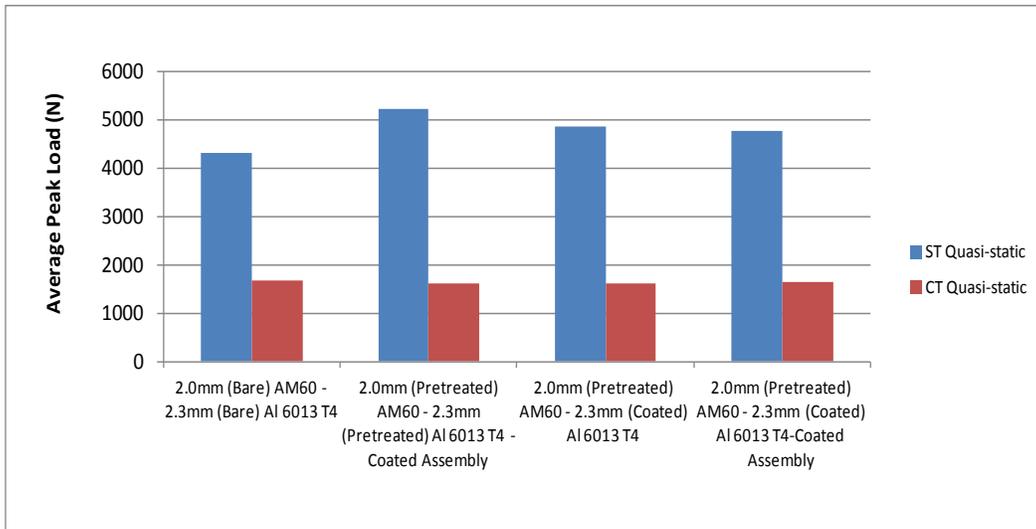
Figure V-37: Quasi-static shear tension and cross tension test results for selected coating configurations of Mg AM60B to Al6013 T-4 SPR joints.
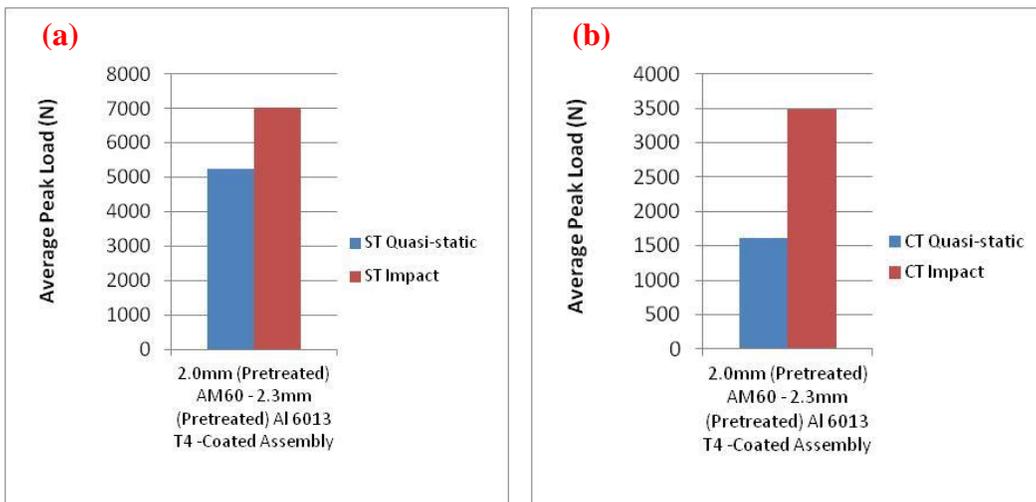
Figure V-38: Comparisons of quasi-static vs impact performance for shear tension (a) and cross tension (b) for pretreated Mg AM60B to Al6013 T-4 SPR joints.

Figure V-39 shows fatigue results for the same configuration as Figure V-38 in (a) ST and (b) CT. As shown in Figure V-36, all pre-corrosion joint failures (including fatigue) occurred in the parent material.

While the mechanical/structural evaluation of the SPR joints was typical of results published elsewhere, based on previous experience, we did not expect this type of joint to perform well in accelerated corrosion exposure. In fact, potential for galvanic corrosion in this type of joint was one of the primary reasons for development of the UPJ process.

Figure V-40 shows results of SPR rivets that cracked after only 6 weeks (1000 hours) of exposure to Chrysler's ASTM G85-A2 accelerated corrosion procedure. This is a cyclic salt spray test with the addition of acetic acid. Figure V-40(a) and (b) are sections from a shear tension sample. Figure V-40 (c) is from a cross tension sample. These samples were not subjected to any mechanical load. The samples came apart simply as a result of pressure from growth of corrosion products between the aluminum and magnesium plates during the accelerated corrosion exposure. This failure mode was surprising since most previous experience with steel fasteners

in Mg (see Figure V-34) had exhibited severe erosion of the Mg panel surrounding the rivet as a result of galvanic corrosion. However, in this evaluation, the cracked rivet failure mode was very typical, being displayed by a large number of samples and resulting in many samples being removed from the test prior to the prescribed exposure time.

Further scanning electron microscopy (SEM) evaluation (Figure V-41) showed that fracture in the steel rivet was a result of hydrogen-induced cracking (hydrogen embrittlement) as a result of high residual stresses on the inner surface of the rivet from the self-pierce riveting process, and a high level of hydrogen generated during the corrosion process and accumulating in the rivet, which is cathodic to Mg and Al. Figure V-41(a) and Figure V-41(b) show mixed fracture modes: inter-granular + trans-granular (quasi-cleavage) with some secondary cracking along the grain boundaries, while Figure V-41(c) shows inter-granular dominant fracture mode in region A from Figure V-41(b) indicating the hydrogen content was relatively high. The rivet was made from high strength steel, which is more susceptible to hydrogen-induced cracking.
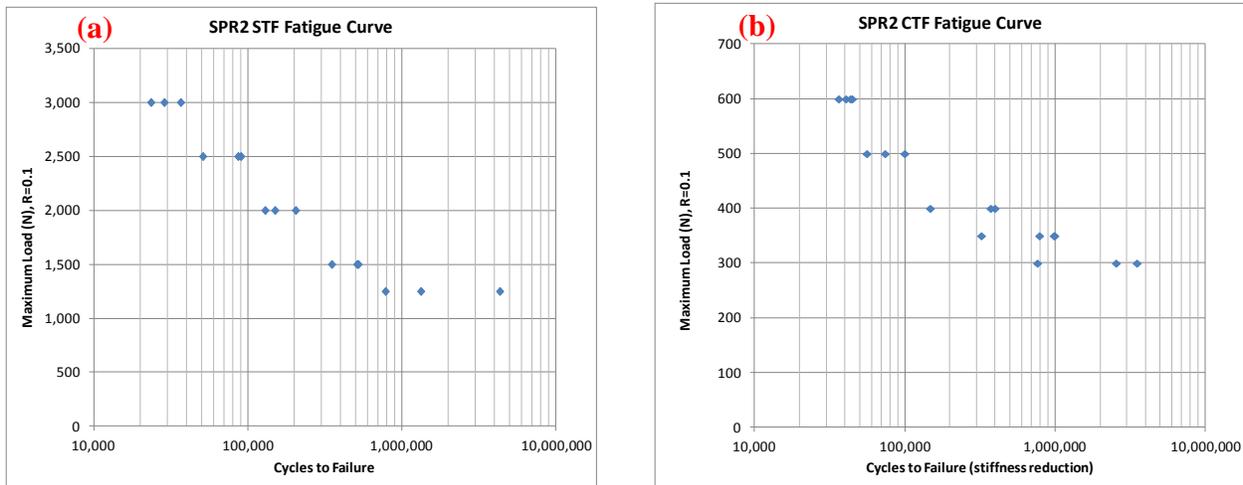
Figure V-39: Fatigue curves for pretreated Mg AM60B to Al6013 SPR joints for shear tension joints (a) and cross tension joints (b).
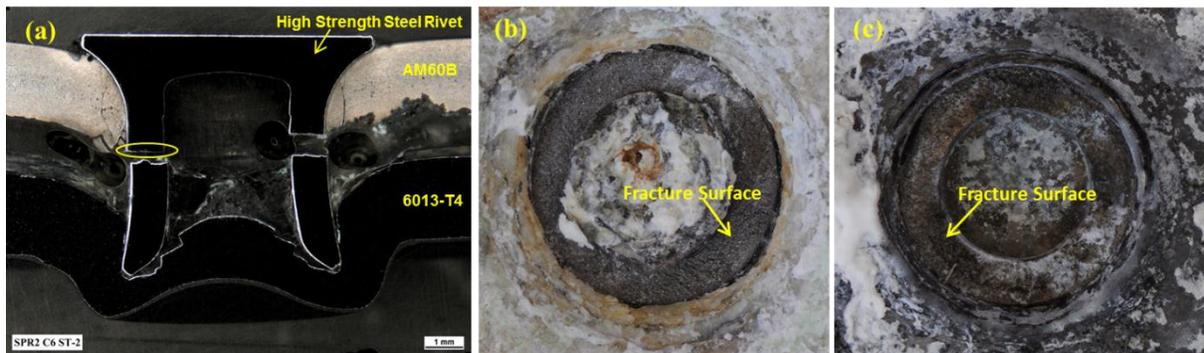
Figure V-40: SPR joint failure after 6 weeks of ASTM G85-A2 accelerated corrosion exposure.
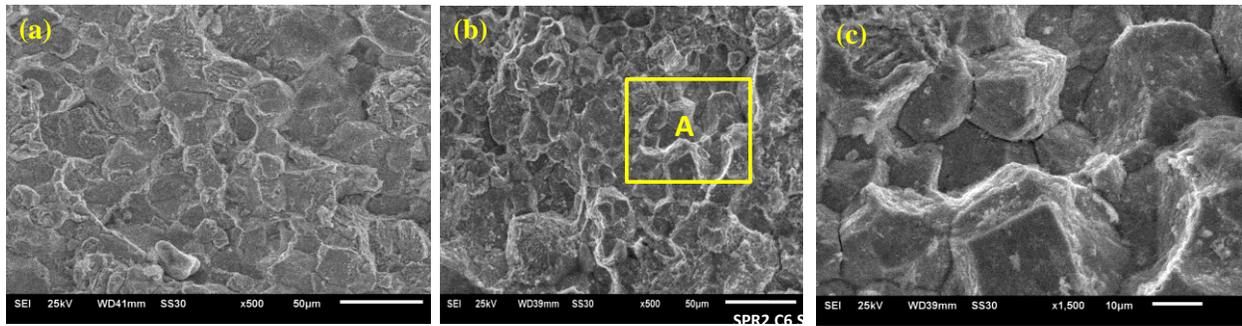
Figure V-41: SEM analysis of SPR joints failed after 6 weeks of ASTM G85-A2 accelerated corrosion exposure showing typical fracture morphology near inner surface of rivet.

Process optimization and development of the UPJ process began with characterization of the thermo-mechanical behavior of common die cast Mg alloys to be used in numerical forming simulation activities.

McMaster University and CANMET-MTL (both located in Hamilton, Ontario, Canada) conducted thermo-mechanical compression testing of die cast AM60B and AZ91D bosses that were machined from ST and CT plates provided by Meridian. Unfortunately, the bosses from the CT plates exhibited excessive porosity, so only the bosses machined from ST plates were used in producing the stress-strain curves for use in the simulation software. Figure V-42(a) shows results for temperatures below 200°C for slow strain rates of 0.1 per second (s^{-1}) and Figure V-42(b) results for fast strain rates of 1 s^{-1} both with stress in megapascals (MPa). Figure V-43(a) shows results for temperatures above 200°C for slow strain rates of 0.1 s^{-1} and 12 (b) shows results for fast strain rates of 1 s^{-1}.

During this fiscal year, the team investigated literally dozens of boss and electrode design configurations, as well as load/current rate process parameter configurations while attempting to optimize the design and process to provide robust joints requiring minimal energy usage and cycle time,

and resulting in minimal damage as a result of heat to coatings on mating components. Figure V-44 below shows one example of the type of design and process simulations conducted to develop an optimum electrode shape for the round boss configuration. In this particular example, when comparing the electrode in (a) to the electrode in (b), at the same point in time and using the same process parameters, the electrode shown in (b) results in lower theta stress, which may reduce the risk of cracking during the forming process.

While Figure V-44 shows potential for improved joint robustness as a result of electrode shape, actual physical process evaluation showed numerical prediction of damage during the forming process to be more difficult than originally anticipated. Extensive physical experimentation was required in addition to numerical simulations in order to optimize the process. Table V-7 shows just one example of numerous experimental evaluations conducted to compare effects of forging force and current rate on joint quality. In this table, the numbers and corresponding colors (1 - green, 2 - orange, and 3 - red) indicate relative subjective ratings for full head formation (larger diameter is better), absence of cracks, and absence of flash, on a scale of 1 (best) to 3 (worst).
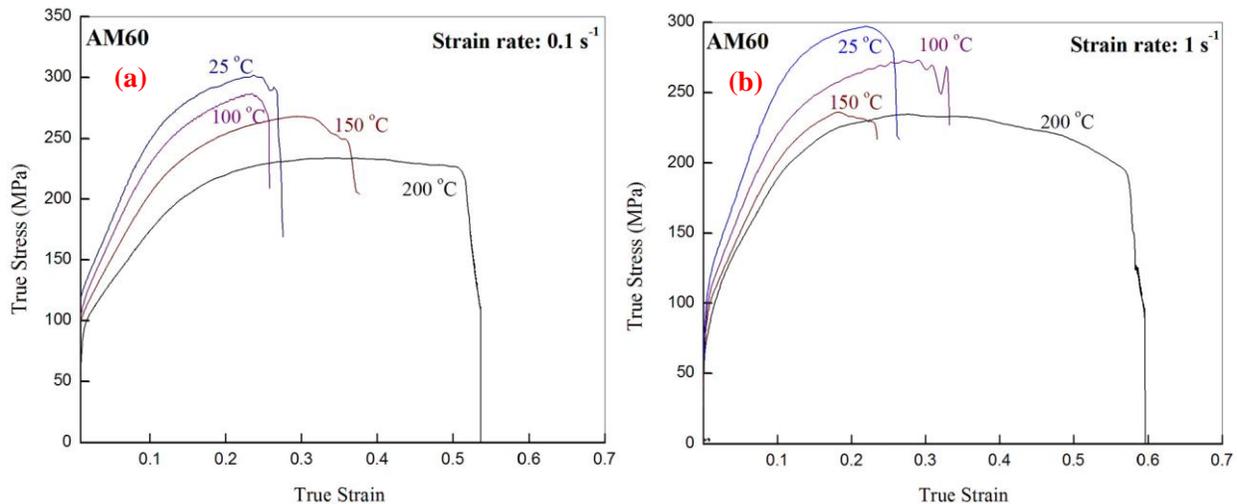
Figure V-42: Gleeble® test results for Mg AM60B alloy at low (<=200°C) temperatures.
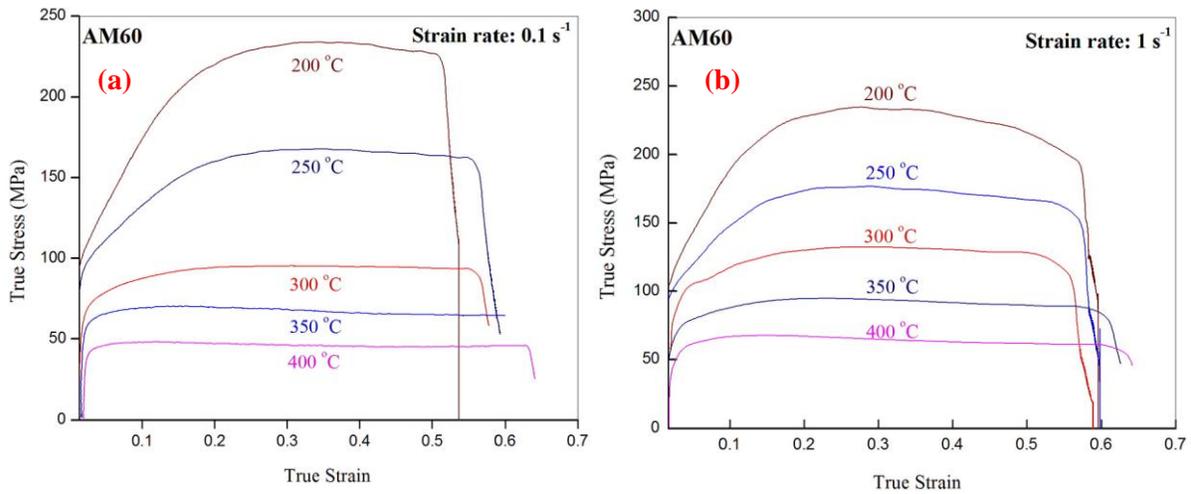
Figure V-43: Gleeble® test results for Mg AM60B alloy at high (>200°C) temperatures.
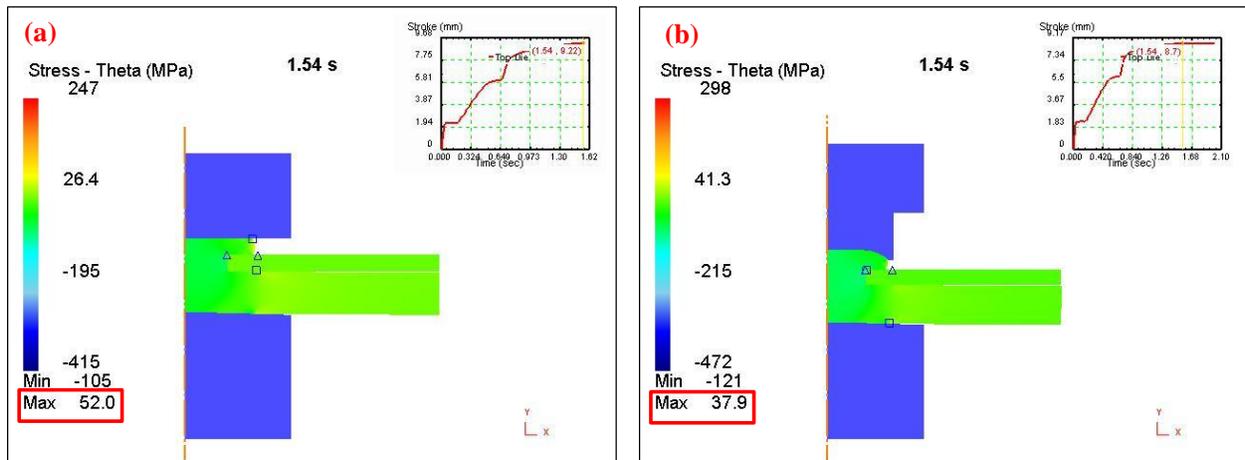
Figure V-44: Example simulation comparison of theta (hoop) stress created by two different electrode shapes.

Table V-7: Example of one of many evaluations of forging force and current rate application effect on joint quality.

Sample	Initial Electrode Force (kN)	Forge Electrode Force (kN)	Forge Timing (ms)	Current 1 (kA)	Time 1 (ms)	Ramp to Current 2 (ms)	Current 2 (kA)	Time 2 (ms)	Current 3 (kA)	Time 3 (ms)	Hold Time (ms)	Head Diameter (mm)	Full Formation	Absence of Cracks	Absence of Flash
D333	8.5	0	0	4	-	3000	8	-	-	-	250	12.0	2	1	1
D357	8.5	15	2500	4	-	3000	8	-	-	-	250	13.0	1	1	1
D354	8.5	22	2500	4	-	3000	8	-	-	-	250	13.2	1	2	1
D356	8.5	28	2500	4	-	3000	8	-	-	-	250	14.0	1	2	1
D355	8.5	35	2500	4	-	3000	8	-	-	-	250	14.3	1	3	1
D339	8.5	0	0	4	1000	3000	6	1000	8	1000	250	12.7	2	1	1
D349	8.5	15	2500	4	1000	3000	6	1000	8	1000	250	13.0	1	2	3
D348	8.5	18	2500	4	1000	3000	6	1000	8	1000	250	13.3	1	2	1
D347	8.5	22	2500	4	1000	3000	6	1000	8	1000	250	13.5	1	3	1
D340	8.5	0	0	5	1000	0	7	1000	9	1000	250	13.0	2	1	2
D334	8.5	0	0	4	-	3000	9	-	-	-	250	12.9	2	1	3
D335	8.5	0	0	5	-	3000	8	-	-	-	250	12.5	2	3	2
D336	8.5	0	0	5	-	3000	9	-	-	-	250	12.9	2	2	2

Technology Transfer Path

Chrysler, a U.S. automotive manufacturer, is leading this project. Since two of the key obstacles preventing more widespread use of light metals in high volume automotive applications are lack of robust joining techniques (especially for dissimilar metal joining) and susceptibility to galvanic corrosion (also, especially for dissimilar metal joining), successful completion of this project will provide a key enabler to high volume application of lightweight materials, allowing Chrysler to accelerate the development of new lightweight vehicle designs that utilize multiple lightweight materials in order to aggressively reduce mass on future vehicle programs.

Conclusion

During this fiscal year, extensive thermo-mechanical material characterization, modeling/simulation and physical experimentation has been used to optimize process parameters for round boss UPJ joints, which are currently being produced to support mechanical/structural evaluation and accelerated corrosion evaluation in the next fiscal year.

Additionally, a full test matrix of over 200 SPR joints have been produced and evaluated for mechanical/structural performance and subjected to Chrysler's accelerated corrosion exposure to serve as a benchmark for UPJ design and process development. Most benchmark SPR joints were unable to pass the full test exposure prescribed by Chrysler Corrosion Engineering without losing integrity before the full test was completed.

Presentations/Publications/Patents

None

References

None

V.3 Brazing Dissimilar Metals with a Novel Composite Foil – Johns Hopkins University

Timothy P. Weihs, Principle Investigator
Johns Hopkins University (JHU)
3400 North Charles Street
Baltimore MD, 21218
Phone: (410) 516-4071
E-mail: weihs@jhu.edu

Judith Dyer, Project Officer
National Energy Technology Laboratory
3610 Collins Ferry Road
P.O. Box 880
Morgantown, WV 26507-0880
Phone: 304-285-1347
E-mail: **Aaron.yocum@netl.doe.gov**

William Joost, Technology Area Development Manager
U.S. Department of Energy
1000 Independence Avenue, S.W.
Washington, DC 20585
Phone: (202) 287-6020; Fax: (202) 856-2476
E-mail: william.joost@ee.doe.gov

Contractor: Johns Hopkins University
Contract No.: DE-EE0006441

Abstract/Executive Summary

The aim of this project is to develop, characterize, and assess novel reactive foils that are based on reduction-oxidation (redox) chemical reactions for use in dissimilar alloy bonding applications. Upon ignition, these foils self-propagate through the bond area and produce heat and molten metal. This represents a significant advantage over traditional joining techniques such as welding, soldering, and furnace brazing, as the heat and braze are delivered locally and heating of the bulk components is not required. In the interest of cost and scalability, the Redox Foils are fabricated from powder compacts that are swaged and rolled into thin foils. The reactive properties can be tailored by altering the extent of mechanical processing and varying the starting chemistry. Bond strength and durability are expected to depend on a number of factors, including but not limited to joining materials, foil chemistry and microstructure, applied pressure, surface preparation, and bond thickness.

In the past fiscal year, Redox Foils were studied for three systems, aluminum:nickel(II) oxide (Al:NiO), aluminum:copper (II) oxide (Al:CuO), and aluminum:copper (I) oxide (Al:Cu$_2$O), and tests were performed to determine baseline bond

strength for several joining materials. Also, the mass ejection was quantified for each system as a function of metallic dilution. During their reactions, Al:NiO foils show negligible mass ejection after dilution with small amounts of nickel, while Al:CuO foils yield substantial mass ejection for all levels of copper dilution. Reaction velocities show similar trends with dilution; highly-diluted Al:NiO and Al:CuO foils differ in velocity by an order of magnitude. In an effort to increase reactivity, composite thermite particles were fabricated via high-energy ball milling.

Accomplishments

- Fabricated 23 batches of Redox Foil representing 11 unique chemistries by mechanical consolidation and processing of elemental powders. (FY 2014)
- Determined baseline strengths for bonding aluminum (Al) 6061, magnesium (Mg) AZ31 (aluminum 3% and zinc 1%), aluminum coated boron steel (ACBS), and hot stamped boron steel (HSBS) with Al:CuO-based, Al:Cu$_2$O-based and Al:NiO-based Redox Foils using initial Redox Foil fabrication techniques. (FY 2014)
- Quantified the mass ejected from the Redox Foils as a function of dilution. (FY 2014)
- Obtained high energy ball mill to mechanically fabricate composite thermite particles, thus increasing the reactivity of starting powders before mechanical consolidation and fabrication of Redox Foils. (FY 2014)

Future Directions

- Improve Redox Foil mechanical fabrication techniques to increase quantity of braze available for joining while maintaining the self-propagating nature of the reactive foil.
- Fabricate sputter deposited Redox Foils to understand how changes in microstructure affect velocity and heats of reaction.
- Alter the dilution chemistry to tailor the braze product of the reaction for specific bonding substrates.
- Determine optimal bonding parameters for given Redox Foil/base metal couples, including optimization of surface preparation, bonding pressure, and foil thickness.
- Create statistically signification datasets for shear strengths of bonds and determine the modes of failure in the joint.
- Analyze the braze and base metal interface for any changes in mechanical properties of base metal due to heating from the reaction of the Redox Foil.

Technology Assessment

- Target: Bonds with a lap shear strength of 20 MPa.

- Gap: Current bonds fabricated with Redox Foil are on the order of five to eight megapascals (MPa), the shear strength can be increased by decreasing the porosity of the bond area.
- Target: Create a Redox Foil where the product contains less than 30% alumina by volume.
- Gap: Current Redox Foils produce upwards of 40% alumina by volume.

◇   ◇   ◇   ◇   ◇

Introduction

Joining of dissimilar engineering materials can be challenging due to differences in chemistry and melting temperatures. Joining can also be complicated by mismatches in thermal contraction on cooling, which can introduce unacceptably high stresses to the bond interface or prevent joining altogether. Brazing and soldering methods can limit thermal mismatch with low melting temperature materials such as Al, Mg, and related alloys. The last two decades have seen the development and commercialization of reactive, self-propagating multilayer foils as local heat sources for joining materials [1-2]. When used in conjunction with solder or braze, these foils can join dissimilar materials without heating either component significantly, as only the area near the interface is heated [3-4]. The standard NanoBond® practice of pre-wetting components with solder, however, adds cost, slows dissemination of the technology, and limits bond strength. Ideally, no pre-wetting would be required and stronger braze bonds would be enabled.

The aim of this project is to develop, characterize, and assess novel reactive foils that are based on redox chemical reactions. Many redox reactions are noted for their exothermic heats of reaction and molten metallic products, making them intriguing candidates for solder-free bonding applications. These are typically known as thermite reactions. Figure V-45 gives a schematic of a possible bonding configuration using a Redox Foil. In addition, the reactive properties of thermite foils may be tailored in a controllable manner by altering the chemistry of the reactants and refining the foil microstructure. The relationships between foil properties and bond characteristics for several thermite systems and dissimilar alloys, including Al 6061, Mg AZ31, ACBS, and HSBS need to be understood. Of particular interest are the shear strengths of the bond, mass ejection (gas and particle) during the reaction, wettability of braze materials, and extent of joint corrosion.

Approach

A technique was developed to produce self-propagating Redox Foils via mechanical processing of metal and oxide powders with initial diameters on the order of tens of microns. These powders are mixed and packed into steel tubes, where they are further compacted into foils through swaging and rolling. Figure V-46 illustrates the process for one redox

chemistry. Foils are typically rolled to thicknesses between 0.4 millimeter (mm) and 0.6 mm, although the final thickness is adjustable. Following rolling, the steel jackets are removed and the bare samples (Figure V-46) are used for testing or bonding. Cross-sections of the powder compacts in Figure V-46 show the refinement of microstructure resulting from the swaging and rolling steps.

The stoichiometry of the reactants is determined from the complete chemical reaction (e.g. $2\ Al + 3\ CuO \rightarrow Al_2O_3 + 3\ Cu$); however, the ratio of the metallic product to the oxide product may be altered by diluting the reactants with excess metal (e.g. $2\ Al + 3\ CuO + X\ Cu \rightarrow Al_2O_3 + [3+X]\ Cu$ where X Cu is the excess copper). Ideally, the metal diluent acts as an inert, heat-sinking material, decreasing the temperature of the reaction. The phase of the diluent at the maximum reaction temperature depends on a number of factors, including heat of reaction, specific heat and amount of diluent, melting/vaporization temperature, and efficiency and modes of heat transfer. As expected, dilution has multiple effects on the reactive properties of the foils, including reducing reaction velocity and mass ejection. These effects will be discussed later.

Work at JHU in FY 2014 has focused on three redox systems, Al:NiO, Al:CuO, and Al:Cu$_2$O. Samples from each system were fabricated at several levels of dilution and ignited in bonds to establish baseline bond strengths. Reaction velocities were measured to assess the effect of dilution on reactivity. Furthermore, experiments were performed to quantify the degree of mass ejection for each redox system, an effect generally not seen in systems that self-propagate via intermetallic formation reactions. Mechanical fabrication of composite thermite particles via high-energy ball milling was begun in an effort to reduce reactant spacing before swaging and rolling.

Results and Discussion

The focus of FY 2014 was fabricating various chemistries of Redox Foils and analyzing the properties of the reactions, as well as performing some baseline bonding experiments. Before fabricating Redox Foils, however, loose compacts of the starting powders were analyzed to determine the effect of dilution on the reactivity of powders, as illustrated in Figure V-47. As the Al:NiO powders are diluted with excess Ni, the amount of heat released (J/g), which is the time integral of the differential scanning calorimeter (DSC) trace, decreases. In addition to combining pure elemental and oxide powders, compacts were fabricated using core-shell powders, whereby elemental nickel was oxidized in air for a given amount of time. These core-shelled particles contained an inner core of elemental nickel, surrounded by a layer of nickel oxide. DSC traces of core-shell particles, red in Figure V-47, have earlier onset temperatures, indicating a more reactive structure due to the intimate contact of the aluminum fuel and oxide. Increasing the reactivity of the reaction is important since it allows for more dilution, and therefore more braze material, to be added to the reactive structure without the risk of quenching during bonding.
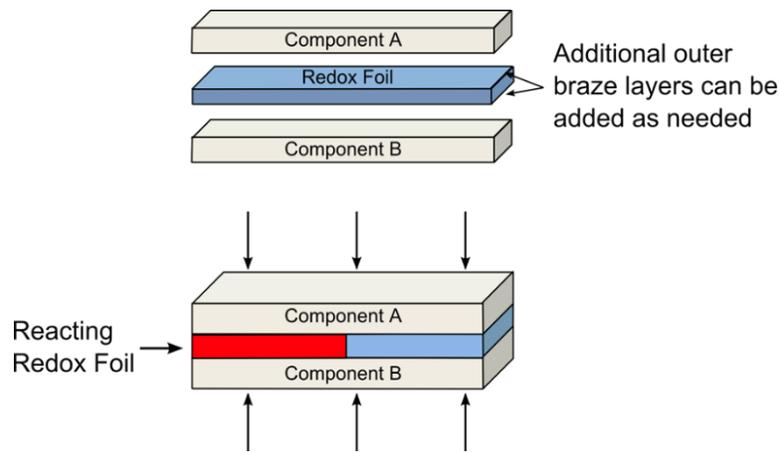
Figure V-45: A schematic representation of bonding with a Redox Foil. After ignition, the foil self-propagates through the bond interface.
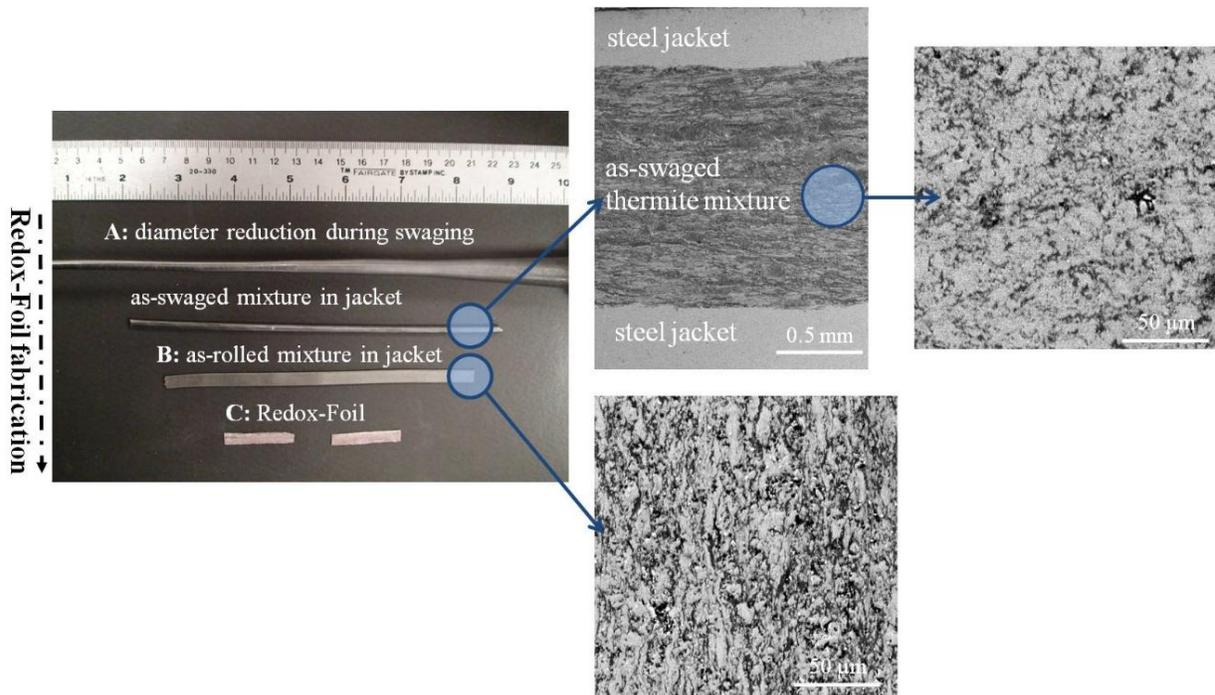
Figure V-46: Sequence of swaging and rolling steps. Typical microstructures of cross-sections taken from as-swaged and as-rolled Al:CuO samples are shown.
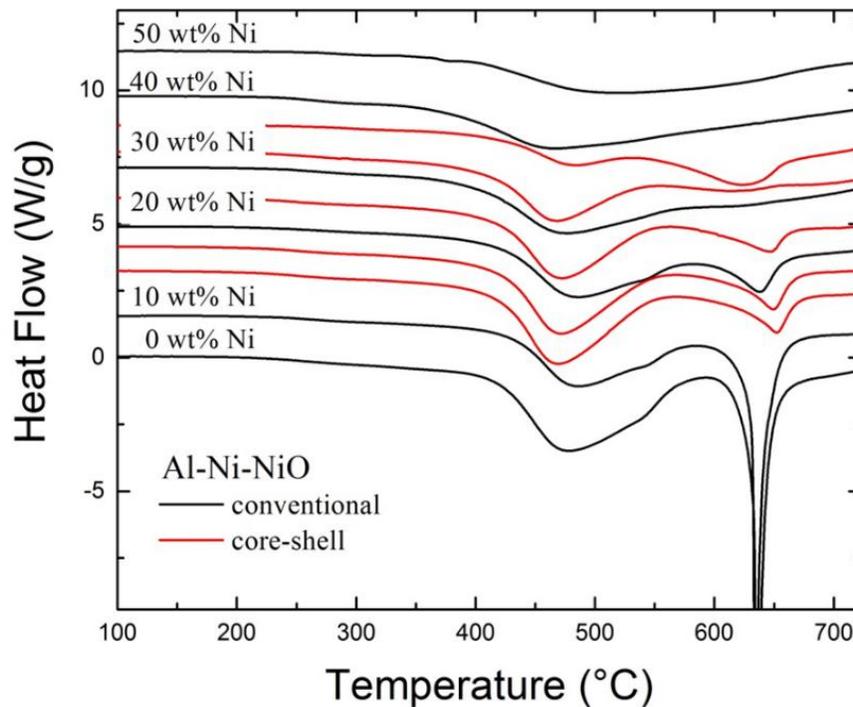
Figure V-47: DSC traces of loose compacts of Al, NiO, and Ni powders for various Ni dilutions. Exothermic reactions are identified by a negative heat flow. However, most curves are offset vertically for clarity.

As seen in the DSC traces from Figure V-47, if the system is diluted with too much inert material, then the total heat released decreases substantially. The dilution also decreases the rate of heat production. During bonding, if the Redox Foil does not produce heat faster than it is dissipated into the rest of the foil or the surroundings (the bonding substrates and atmosphere), then the reaction will quench. In this case the reaction no longer self-propagates across the Redox Foil and much of the foil remains unreacted. To understand the limitations of the current Redox Foils, bonds were performed on Al 6061 and Mg AZ31 to determine the amount of dilution that could be added while the reaction still self-propagates in a bonding configuration. Figure V-48(a) displays a table of the results from the quenching experiment and an image of a reacted foil that quenched as it entered the bond interface is at Figure V-48(b). The CuO system can be diluted the most while still self-propagating in the bond.

Another key reason to increase dilution is to decrease the amount of gas generated by the reaction. Thermites can generate a significant amount of gas [5] as a result of the reaction. Gas generation can also lead to particulate ejection from pressure build up during the reaction. Gas production and particulate ejection are detrimental to the strength of the bond because together they lead to the formation of pores and a non-continuous braze interface. Figure V-49 displays the normalized mass ejection fraction as a function of dilution for the three oxide chemistries examined so far. Normalized mass ejection is defined as the mass of the ejected material collected divided by the mass of the original Redox Foil for the experiment. For all three systems, as dilution increases, the average particulate ejection decreases. For the Al:NiO:Ni system, the particle ejection becomes negligible once dilution increases above 10% by mass, whereas for both CuO systems there is still considerable mass ejection even as dilution is increased. Copper (I) oxide ejects less mass than copper (II) oxide, but because copper (I) oxide is more copper-rich, it is a less energetic formulation and thus is harder to self-propagate with added dilution.

Quenching Summary			
System	Dilution	Al 6061	Mg AZ31
NiO	0	Bond	Bond
NiO	10	Bond	Bond
NiO	20	Quenched	Quenched
CuO	0	Bond	Bond
CuO	10	Bond	Bond
CuO	20	Bond	Bond
CuO	30	Bond	Bond
CuO	40	Bond	Bond
CuO	50	Quenched	Quenched
CuO	60	No Propagation	No Propagation
Cu2O	0	Bond	Bond
Cu2O	10	Quenched	Bond
Cu2O	20		Quenched

Bond	(green)
Quenched	(red)
No Propagation	(dark red)

a)   b)
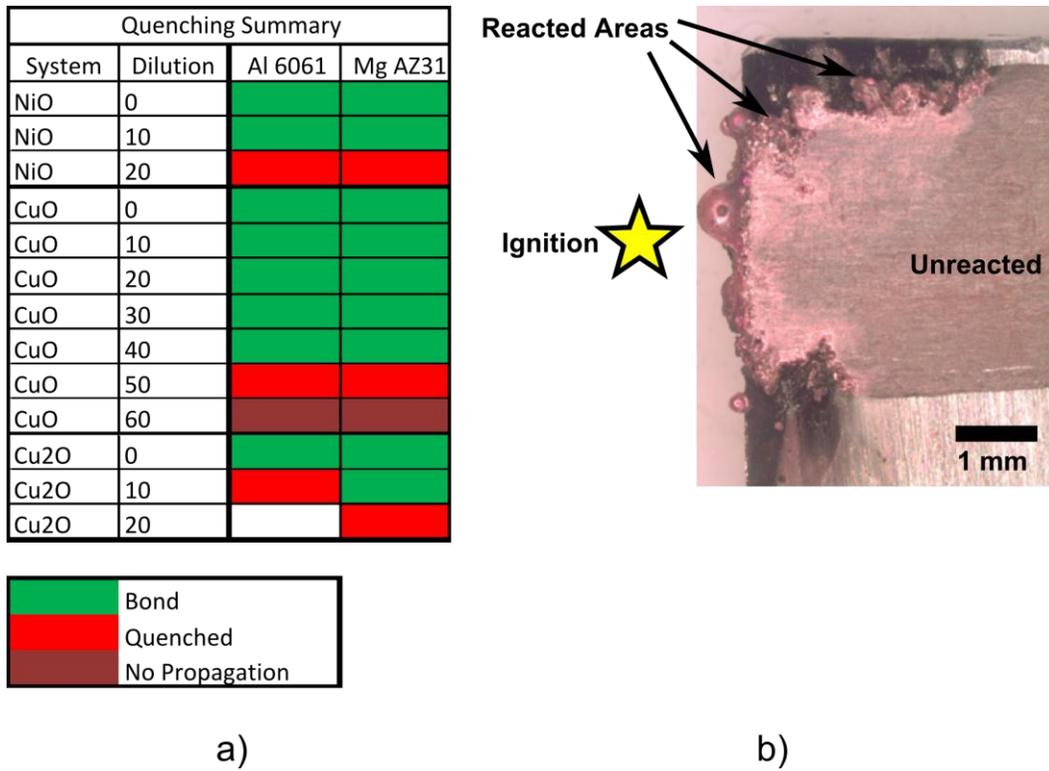
Figure V-48: a) A summary of chemistries that either propagated and produced a bond or quenched during joining for aluminum 6061 and magnesium AZ31 substrates. b) A quenched Al:Cu₂O:10%Cu Redox Foil on an aluminum 6061 substrate. The foil was ignited outside of the bond interface at the location of the yellow star, but quenched once it reached the metal.
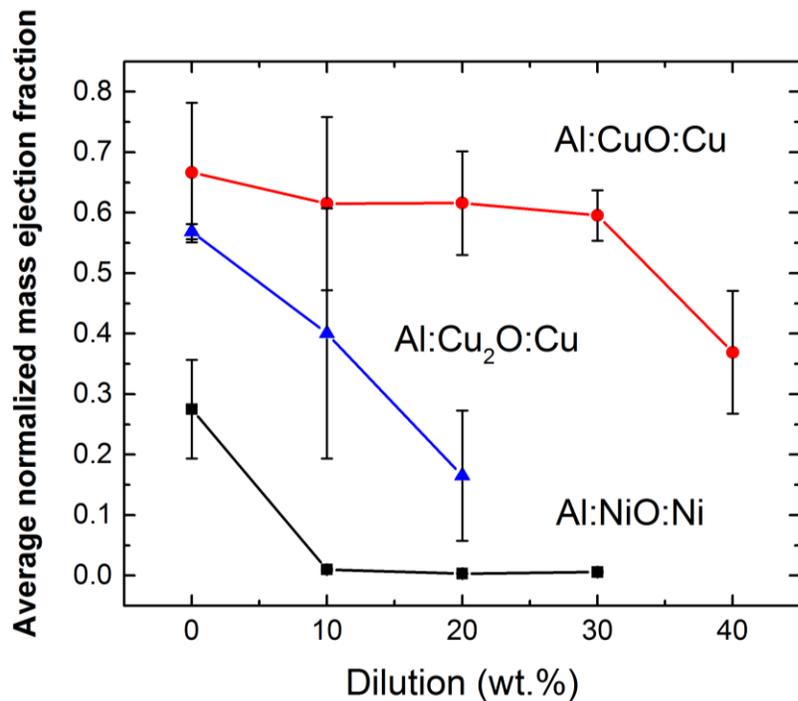
Figure V-49: The average normalized mass ejection as a function of dilution for different weight percents of Al:NiO, Al:CuO, and Al:Cu₂O foils, where the diluent is the metal from the starting oxide.
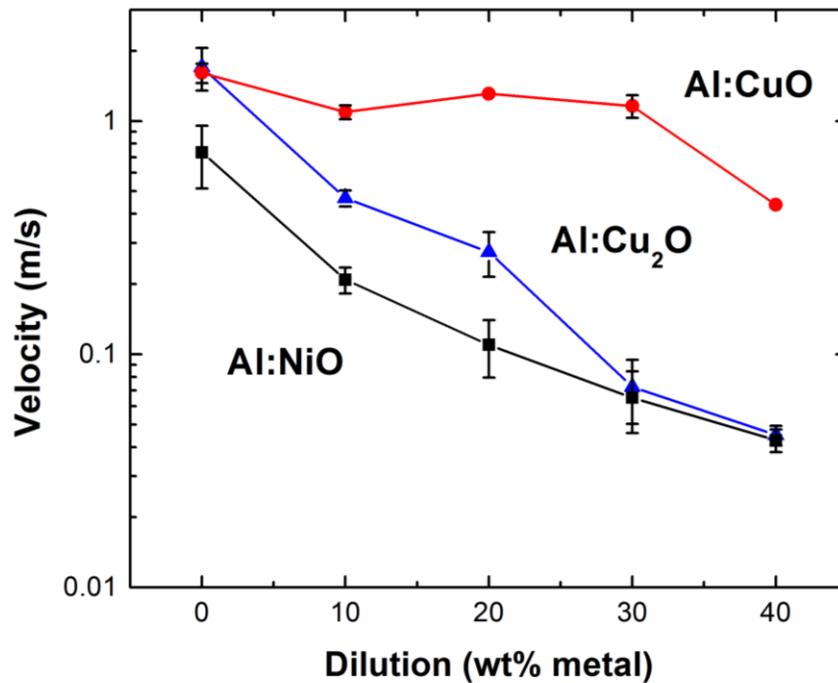
Figure V-50: Average propagation velocities of Al:NiO, Al:CuO, and Al:Cu2O foils as a function of dilution.

To assess the reactivity of as-rolled Redox Foils, velocity measurements were performed on samples from the Al:NiO, Al:CuO, and Al:Cu$_2$O systems. The results are plotted in Figure V-50. Trends are similar to those seen for mass ejection. Al:CuO foils appear relatively insensitive to dilution, with average velocity values between 1-2 meters per second (m/s) until 40% Cu, while velocity in Al:NiO foils drops off considerably after only 10% Ni dilution. Differences in velocity between the Al:NiO and Al:CuO systems increase by nearly an order of magnitude as the respective diluents are added. In theory, increasing the dilution will also increase the average reactant spacing between the metal fuel and oxide powders. Studies on reactive multilayer foils [6-7] confirm that velocity is inversely proportional to reactant spacing and increases with maximum temperature of the reaction. However, the use of powders with micron scale dimensions, coupled with extensive mechanical processing, yield reactant spacings that are not nearly as uniform as those observed in sputter deposited foils. Studies on Redox Foils deposited via magnetron sputtering will be needed to establish the effects of microstructure on reactivity.

In addition to analyzing the properties of the Redox Foils in FY 2014, preliminary bonds were made using Redox Foils. The Al:CuO foils created porous braze interfaces due to the mass ejection caused by the gas generated by the thermite reaction. Even the heavily diluted case of Al:CuO:40%Cu resulted in substantial particulate ejection from the bond interface. Despite these limitations, the Al:CuO:40%Cu foil was still able to bond all substrates, including Al 6061, Mg AZ31, HSBS, and ACBS. The Al:NiO foils did not produce any noticeable particulate ejection, but the strength of the resulting bonds was less than that of the Al:CuO system as depicted in Figure V-51(a). There are two reasons that the NiO-based foils did not perform as well as the CuO-based foils. First, the Al:NiO systems produced more alumina, by volume than the Al:CuO system due to their lower reactivity and smaller degrees of dilution that still allow propagation within a bond. Second, the molten nickel from the thermite reaction does not wet the bonding substrates as well as the molten copper as shown in Figure V-51(b) where a high speed camera captures the molten nickel balling up on the surface of the aluminum substrate.
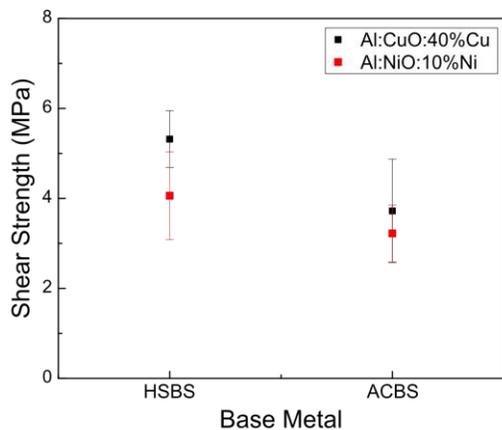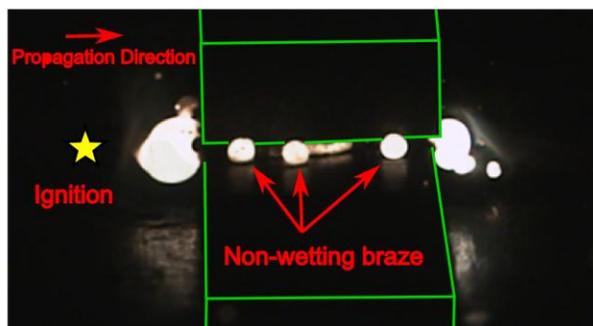
a)   b)

Figure V-51: a) Shear strengths for bonding HSBS and ACBS with Al:CuO:40%Cu and Al:NiO:10%Ni. b) A frame from high speed video showing molten braze from Al:NiO:10%Ni not wetting the aluminum bonding substrates; bonding substrates have been outlined in green for clarity.

Technology Transfer Path

We are currently in the process of patenting the technology. In the future, we plan to license the technology to a materials manufacturer, who will then sell to the automobile industry.

Conclusion

The initial fabrication of Redox Foils during FY 2014 shows that it is possible to make heavily diluted reactive foils whose reaction products can be utilized to braze metals together. Initial testing has found that added dilution does decrease the amount of gas generated by the reaction. However, more dilution can be achieved by further refining the average reactant spacing within the Redox Foils. Methods for refining reactant spacing and thereby allowing for more diluent include ball milling powders to make composite particles that will enhance the reactivity of the systems. With enhanced reactivity, more diluent can be added to the foil to increase the quantity of braze available for joining. The diluent chemistry can also be altered to specifically tailored to enhance wetting of the components by the resulting braze product, which will be explored in detail in subsequent years of the project.

Presentations/Publications/Patents

1. Slusarski, K.A.; Woll, K.; Kinsey, A.H.; Gibbins, J.D.; Ku, A.Y.; Weihs, T.P. (2014) "Quantifying Reaction Velocity and Mass Ejection in Thermite Composite Foils." Presented at the Energetic Materials Gordon Research Seminar and Conference, Newry, ME, 2014.

2. Kinsey, A.H.; Gibbins, J.D.; Slusarski, K.A.; Ku, A.Y.; Woll, K.; Weihs, T.P. (2014) "Optimizing Mechanically Processed Thermite Foils for Bonding Dissimilar Metals." Presented at the Energetic Materials Gordon Research Seminar and Conference, Newry, ME, 2014.

References

1. Ma, E.; Thompson, C. V.; Clevenger, L. a.; Tu, K. N. *Appl. Phys. Lett.* **1990**, *57*, 1262.

2. Duckham, A.; Newson, J. E.; Brown, M. V.; Rude, T. R.; Knio, O.; Heian, E. M.; Subramanian, J. S. Method For Fabricating Large Dimension Bonds Using Reactive Multilayer Joining, 2008.

3. Wang, J.; Besnoin, E.; Duckham, a.; Spey, S. J.; Reiss, M. E.; Knio, O. M.; Powers, M.; Whitener, M.; Weihs, T. P. *Appl. Phys. Lett.* **2003**, *83*, 3987.

4. Swiston, a. J.; Hufnagel, T. C.; Weihs, T. P. *Scr. Mater.* **2003**, *48*, 1575–1580.

5. Fischer, S. H.; Grubelich, M. C. *Int. Pyrotech. Semin.* **1998**.

6. Knepper, R.; Snyder, M. R.; Fritz, G.; Fisher, K.; Knio, O. M.; Weihs, T. P. *J. Appl. Phys.* **2009**, *105*, 083504.

7. Adams, D. P. *Thin Solid Films* **2014**.

V.4 Active, Tailorable Adhesives for Dissimilar Material Bonding, Repair and Reassembly – Michigan State University

Mahmoodul Haq, Principal Investigator
Michigan State University
428 S. Shaw Lane, Room 3569
Engineering Building,
East Lansing, MI 48824.
Phone: (517) 402-3409
E-mail: haqmahmo@egr.msu.edu

Lawrence T Drzal, Principal Investigator
Michigan State University
428 S. Shaw Lane, Room 2100
Engineering Building,
East Lansing, MI 48824.
Phone: (517) 353-5466
E-mail: drzal@egr.msu.edu

Adrienne Riggi, Project Officer
National Energy Technology Laboratory
3610 Collins Ferry Road
P.O. Box 880
Morgantown, WV 26507-0880
Phone: 304-285-5223
Adrienne.riggi@netl.doe.gov

William Joost, Technology Area Development Manager
U.S. Department of Energy
1000 Independence Avenue, S.W.
Washington, DC 20585
Phone: (202) 287-6020; Fax: (202) 856-2476
E-mail: william.joost@ee.doe.gov

Abstract/Executive Summary

The objective of this project is to demonstrate the feasibility of 'active adhesive' technology for structural joining of dissimilar materials, with the ability to dis-assemble/re-assemble and repair while in-service. Thermoplastic adhesives modified by the incorporation of electrically conductive graphene nanoplatelets at a concentration above the percolation point provide a unique synergy of mechanical, thermal and electrical properties. While the choice of the thermoplastic is governed by the desired application the addition of the graphene nanoplatelets allows energy to be deposited primarily in the adhesive. The percolated network of graphene particles in the adhesive at less than 2% can quickly couple to ultra-high frequency (UHF) microwave (MW) radiation via non-contact methods and increase the adhesive temperature to above the required processing temperatures. The adhesive melts and flows over the adherends and upon cooling forms a structural adhesive bond. Furthermore, the process can be used to disassemble the adhesive joint if repair or reworking is required. The dissimilar material joints in this study include fiber reinforced polymer composites (FRP) made of glass and carbon fibers being joined with metals such as advanced high strength steel (AHSS) and aluminum (Al). The global objectives of the proposed work will be achieved through: a) processing, material development and optimization of the active adhesive, b) lab-scale evaluation and detailed material characterization and, c) design, testing and applications. An integrated experimental and numerical approach that adopts novel non-destructive evaluation techniques at every length scale is used in this project. This allows for development of experimentally validated design tools and databases, along with a possibility of a wide range of industrial and large-scale structural joining. The work-to-date has shown great promise in the use of the active adhesives for multi-material joining. Critical experiments and parametric studies are in progress to fully exploit the benefits offered by these active adhesives. [1]

Accomplishments

- Completed the processing of graphene nanoplatelets (GnP) in thermoplastics. (FY 2014)
- Determined optimal content of GnP to achieve synergy of multi-functional coupling and mechanical properties (e.g. stiffness-toughness balance) (FY 2014)
- Evaluated active adhesives for assembly and repair, bonding/dis-bonding of resulting lap joints. (FY 2014)
- Characterized mechanical and thermo-mechanical properties of the adhesives and the adherends. (FY 2014)
- Manufactured high-temperature resistant glass-fiber composite substrates.(FY 2014)
- Completed morphology analysis for fracture surfaces of both pristine and GnP modified adhesives based single lap joints. (FY 2014)
- Developed nano-homogenization simulations to obtain effective properties of novel adhesives. (FY 2014)

Future Directions

a) Functionalization of GnP (improving chemical compatibility with host polymer) to improve the performance of resulting bonded multi-material joints.
b) Develop low-cost, out-of-autoclave, liquid molding techniques to obtain fiber-reinforced composite adherends.

c) Experimental characterization of multi-material joints : a) in-plane (lap-joints), b) out-of-plane (T-joints) and c) torsional joints (rotors, will be tested in collaboration with EATON®)

d) Evaluate the re-assembly/repair of joints using of nondestructive evaluation (NDE) tools such as embedded sensor and infrared (IR) thermography

e) Development of design tools (experimentally validated simulations (EVS)): nano-, meso-, and macro- (large scale) level structural simulations.

Technology Assessment

- Target: Develop active adhesive technology for structural joining of similar and dissimilar materials, with the ability of reversible bonding (dis-assemble/re-assemble), in-service repair, enhanced mechanical properties, and acceptable industrial practices.

- Gap: Joints are mostly considered the 'weak-links' of a structure due the complex phenomena and interactions of several elements of either similar or dissimilar materials. Strategic incorporation of nanographene in adhesives allows for improvements in stiffness, toughness and delamination resistance.

- Gap: Unlike bolted joints, adhesive/bonded joints do not allow disassembly and repair. Industry still lacks the full exploitation and utilization of bonded joints as they are usually considered a one-time 'permanent joint' with moderate strengths and inability to dis-assemble or repair.

✧   ✧   ✧   ✧   ✧

Introduction

Joining of materials and components is inevitable as it allows versatility in assembly and repair along with reduction in time and cost of manufacturing. However, joints are mostly considered the 'weak-links' of the structure due the complex phenomena and interactions of several elements of either similar or dissimilar materials. These complexities combined with the need for lightweight structures and increased safety requires better understanding and development of robust dissimilar material joints. The proposed technique uses 'active adhesives' and inherits all the advantages of bonded joints, such as lightweight, elimination of holes and associated stress-concentrations, and overcomes the shortcomings of disassembly and repair. Additionally, manufacturing flaws and

in-service damage such as impact-induced delamination can be repaired through strategic-targeted heating of the adhesive without affecting the adherends.

The objective of the project is to demonstrate the feasibility of the proposed active adhesive technology for structural joining of dissimilar materials, with the ability to dis-assemble/re-assemble and in-service repair. The outcomes of this work will accelerate the development of efficient active adhesive technology to join multi-materials lightweight structures in different sectors, such as automotive, aerospace, and marine applications.

Approach

Thermoplastic adhesives modified by the incorporation of electrically conductive GnP at a concentration above the percolation point provide a unique synergy of mechanical, thermal and electrical properties. While the choice of the thermoplastic is governed by the desired application the addition of the graphene nanoplatelets allows energy to be deposited primarily in the adhesive. The percolated network of graphene particles in the adhesive at less than 2% can quickly couple to UHF MW radiation via non-contact methods and increase the adhesive temperature to above the required processing temperatures. The adhesive melts and flows over the adherends and upon cooling forms a structural adhesive bond. Furthermore, the process can be used to disassemble the adhesive joint if repair or reworking is required. A schematic of the proposed technology is provided in Figure V-52. To the best of the investigators knowledge, such active adhesives with repeatable healing/repair and facile disassembly are unique and have not been used in structural joining, and offer a possibility in a wide range of applications.

The approach used in this work follows the "materials by design" philosophy by incorporating an integrated experimental and computational approach to strategically explore the design possibilities and limits of the proposed active adhesive technology. This approach eliminates the costly 'trial-and-error' approach and allows a rational development of resulting materials and joints. The EVS developed through this approach will allow exploring material designs beyond the experimental matrix studied. Furthermore, EVS can be used as design tools and can allow prediction of residual strength and design of novel joints. A schematic of the approach is provided in Figure V-53.
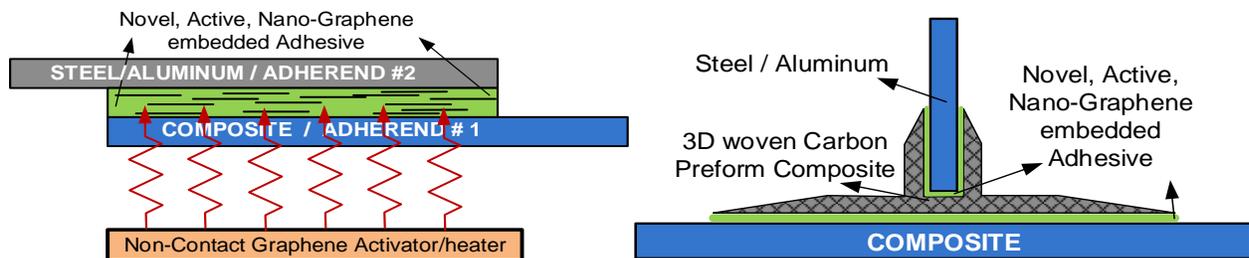
Figure V-52: LEFT: Schematic of the concept shown for in-plane joints, RIGHT: out-of-plane joints.
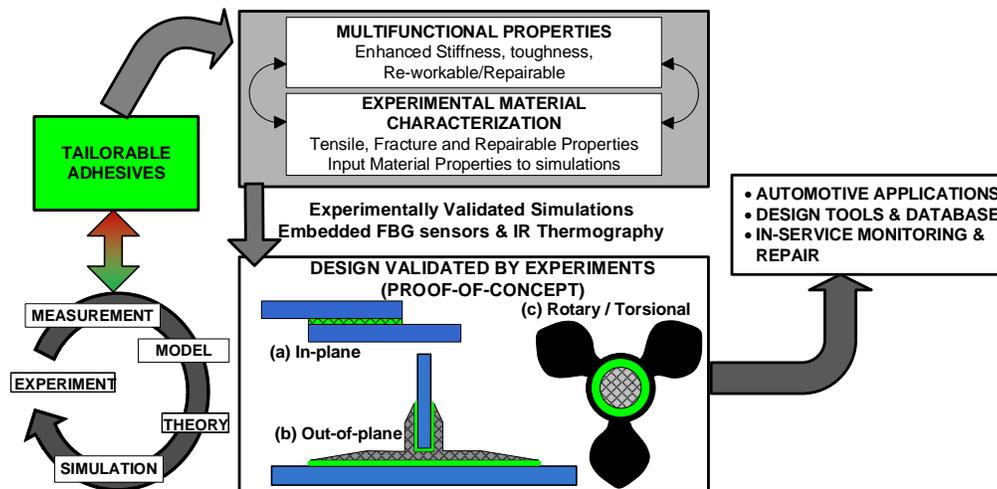
Figure V-53: Schematic of Overall Approach.

Most structural joints development studies focus solely on in-plane behavior. This work evaluates the feasibility of proposed technique in: a) in-plane (lap-joints), (b) out-of-plane (three dimensional (3D) woven Pi- shaped or T- shaped joints), and c) torsional/rotatory (super-charger) joints. Measurement techniques such as embedded fiber-Bragg grating (FBG) optic sensors and infrared thermography will be used to accurately measure the in-service performance and observe the repair efficiency of resulting dissimilar material joints. Such a thorough study is directed to cover all possible automotive and ground vehicle applications.

The above mentioned approach of developing 'active adhesives' will be achieved through the following sub-objectives/tasks:

A. Processing, Material Development and Optimization of the Active Adhesives:

- Task #1: Evaluation of processing parameters, determination of optimal graphene content for synergy of multi-functional, microwave coupling and mechanical properties (e.g., stiffness-toughness balance),

B. Lab-Scale Evaluation and Detailed Material Characterization:

- Task #2: Lab-scale evaluation includes strategically selected experiments for characterization of both adhesives and adherends. Also includes low-cost manufacturing of fiber-reinforced composite adherends.
- Task #3: Detailed experimental characterization of multi-material joints, corrosion analysis of resulting joints, evaluation of assembly and repair using novel non-destructive tools, and evaluation of damage-induced behavior of joints and resulting failure modes.

C. Design, Testing and Applications:

- Task #4: Development of design tools and databases using robust, experimentally validated simulations at the nano-, micro- and macro- (large) scale structural simulations.
- Task #5: Experimental Evaluation of large-scale industrial multi-material joints in: a) in-plane mode (lap-joints), b) out-of-plane mode (T-/Pi- joints) and c) torsional mode (super charger rotor). Also evaluate repair and re-assembly for aforementioned joints.
- Task #6: Experimental validation /proof-of-concept on an industrial joint and dissemination of results.

Results and Discussion:

1. Design of Experiments

The incorporation of nanoparticles in adhesives introduces multi-functionality to the resulting system with enhancements in multiple properties including mechanical (stiffness, strength), fracture (delamination resistance, energy absorption), thermal and moisture diffusion properties along with value added properties such as electromagnetic, MW coupling, etc., On the other hand incorporation of nanoparticles increase the design space for the development and design of the resulting materials and components. Hence a strategic selection of experiments to explore and obtain 'performance bounds/limits' of resulting materials is essential. In this study, GnP are embedded in the thermoplastic adhesive to investigate its thermal response while they are subjected to external MW radiations, while inheriting the enhancements in mechanical properties. Hence, there is a need to understand the influence of GnP concentration on both mechanical properties and on microwave coupling + thermal behavior at both material level and at the component (joints) level.

As mentioned earlier, a detailed characterization of mechanical and thermal properties is essential as it enables

identification of "performance limits" of various properties, exploiting the full benefits / synergy in multiple properties (e.g., stiffness-toughness balance) offered by these novel materials while allowing optimal activation of adhesives. [2] Figure V-54 illustrates the work-flow adopted to achieve these goals within the project. The acronyms used in Figure V-54 are defined as follows: finite element methods (FEM), American Society for Testing and Materials (ASTM), DMA dynamic mechanical analysis (DMA), differential scanning calorimetry (DSC), Fourier Transform Infrared (FTIR), scanning electron microscopy (SEM), and atomic force microscopy (AFM).

2. Processing of bulk 'pristine' and 'GnP modified' adhesives:

In this work, the thermoplastic material selected was nylon-6. The choice of thermoplastic depends on the desired application, and instead of studying multiple thermoplastics a single adhesive was selected. The overall approach and the results from this work can be directly extended to other thermoplastics. In this work, prior to the melt extrusion process, the nylon-6 pellets were exposed to 70°C for four hours to eliminate any presence of moisture. Then, melt extrusion of pristine and GnP-modified nylon-6 was carried out in a DSM® Micro 15 cubic centimeters (cc) Compounder, (vertical, co-rotating, twin-screws micro-extruder) operating at 260°C for 3 min at a screw speed of 100 revolutions per minute (rpm). The melted material was then directly transferred in to a DACA® Micro-injector with the barrier temperature ($T_{barrier}$)=260°C and the mold temperature (T_{mold})=100°C. The injection pressure applied for injection molding of tensile, impact, flexural coupons and discs was around 0.97 megapascals (MPa). The melt extrusion and injection molding systems are shown in Figure V-55. The resulting injection molded samples were used for experimental testing and the discs were used for adhesive film production.
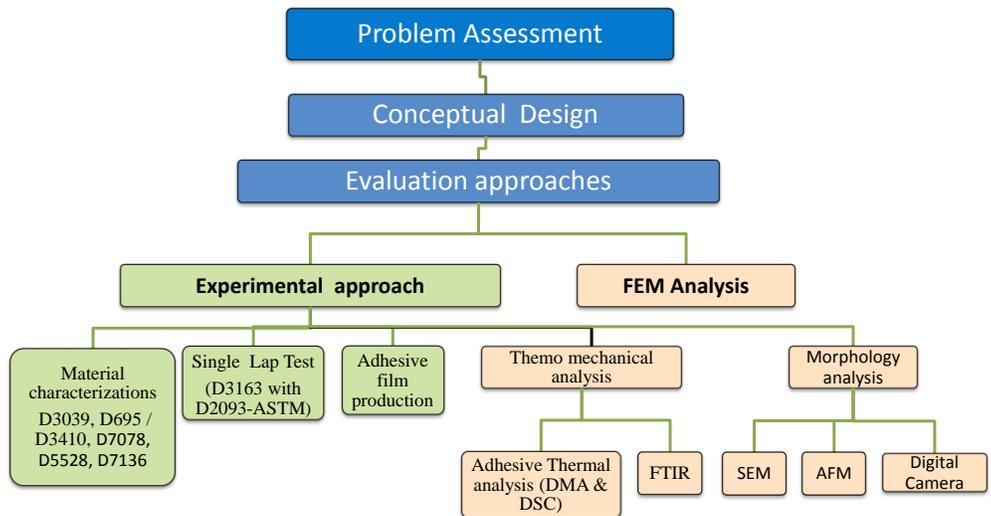
Figure V-54: Work-flow adopted to develop active adhesives.
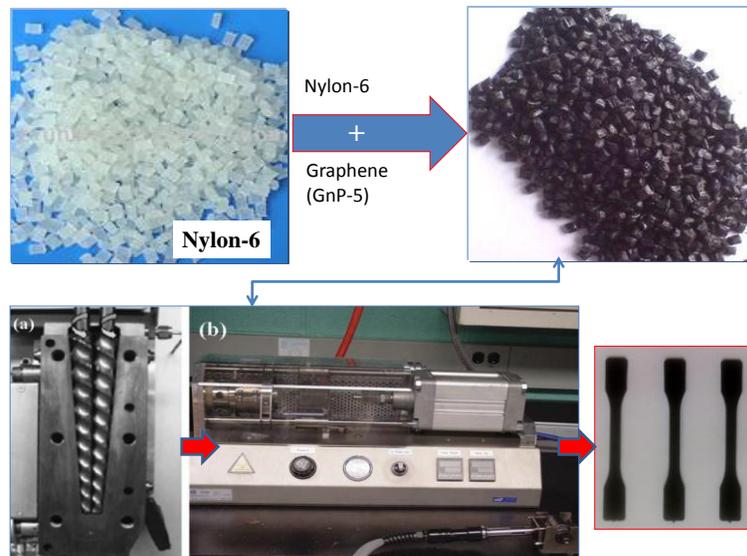
Figure V-55: Manufacturing process of pristine and GnP-modified nylon-6 coupons.

3. Manufacturing process of adhesive films ('pristine' and 'GnP reinforced') films:

The discs developed from the injection molded specimens were placed between stainless steel plates covered by a high-temperature resistant polyimide film, Kapton® (from DuPont®) to enable ease of adhesive film removal. To control/maintain the adhesive film thickness, 0.09 millimeter (mm) thick Al spacers were placed between the top and bottom plates. To eliminate/reduce entrapped air, the entire setup was covered by a vacuum bag and subjected to vacuum pressure of 1 atmosphere (atm). While maintaining the vacuum pressure, the plates were heated at a rate of 5 degrees Centigrade per minute (°C/min) for up to 260°C, followed by an isothermal process for 5 min. In order to obtain the desired film thickness, successive pressures of 30, 60, and 90 MPa were applied on the plates with a time interval of 3-5 min. One of the challenging problems during film production was inconsistent film thickness. The applied pressure caused the plates to deflect and consequently the central portion of the adhesive film was reduced. To minimize the deflection, additional spacers were also placed at the center, as shown in Figure V-56.

4. Material characterization of 'pristine' and 'GnP-modified nylon-6:

Tensile and flexural tests were performed using a universal testing system (UTS) electro-mechanical equipment. All tests were performed at room temperature and the results reported here are the average of a minimum of five specimens per case. The tensile tests were performed according to ASTM D638. A 1000 pound (lb) (454 kilogram (kg)) standard load cell attached to the UTS frame and external laser extensometer were used to measure applied force and resulting longitudinal strain, respectively. On the other hand, flexural tests (three-point bending mode) were performed according to the ASTM D770-10 on the same machine with a load cell of 100 lb. (45.4 kg). The dimensions of the samples for flexural tests were 62.7 mm ×12.24 mm×3.2 mm. The span length was set at 50.8 mm. The crosshead speed was calculated based on specimen geometry, according to ASTM standard, and was set at 0.05 inches per minute (in/min) A linear variable differential transformer (LVDT) was used to measure the deflection in flexural tests. Impact resistance tests (Izod type) were carried out according to ASTM D256 standard test. The dimensions of the samples for impact resistance tests were 62.7 mm x 10.72 mm×3.91 mm cross-sectional area at the mid-notch.
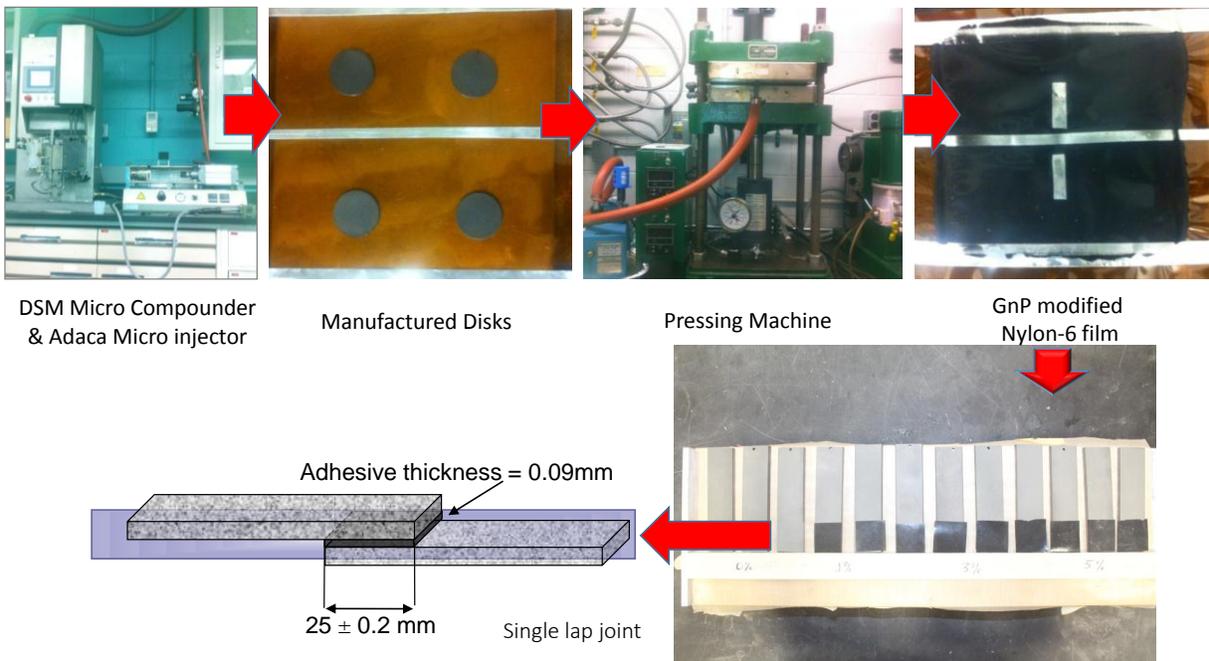
Figure V-56: Processing of 'pristine' and 'GnP-modified' nylon-6 films.

In order to achieve the desired crosshead velocities as specified by ASTM D638, three testing speeds, namely, 0.05, 0.50, and 5.00 (in/min) were adopted to evaluate the tensile strengths of pristine and GnP-modified nylon-6. Figure V-57a provides the tensile strengths of pristine and GnP-modified nylon-6. The tensile strength of pristine nylon-6 was observed to reduce with increasing GnP content. At crosshead speeds of 0.05 in/min and corresponding to 5 wt% GnP content, the tensile strength of nylon-6 reduced by ~19%. As the crosshead speed was increased to 0.50 and 5.00 in/min, the degree of reduction showed slight improvement in the order of ~17% and 15%, respectively. It is evident from Figure V-57b that the GnP-modified nylon-6 is more responsive to strain rate than pristine nylon-6. At 5.00 in/min, 3 wt% of GnP-modified nylon-6 exhibited better tensile strengths relative to other material configuration in this study. The reduction in tensile strengths due to addition of GnP was by 'design' and was expected. The GnP used was non-functionalized and the tests were performed to obtain the baseline/control data prior to exploring the benefits of chemical functionalization. On the other hand, the study on effect of strain rate on the adhesives and the improvements observed in GnP modified adhesive shows promise in use of such adhesives for high-strain rate automotive applications, such as crash components etc., Nevertheless, the work is in progress to evaluate the effect of GnP functionalization and to fully explore this benefit before any strong conclusions could be derived.

Figure V-58 provides the flexural strength and modulus of pristine and GnP-modified nylon-6. The flexural strength of GnP-

modified nylon-6 increases significantly as the GnP content increases. For example, for 5 wt.% GnP, the flexural strength of the adhesive improved by more than 10% relative to pristine nylon-6. Similarly, the flexural modulus of GnP-modified nylon-6 also increases significantly with increase in GnP content. For example, for 5 wt% GnP in nylon, the flexural modulus improved by more than 30% relative to pristine nylon-6.
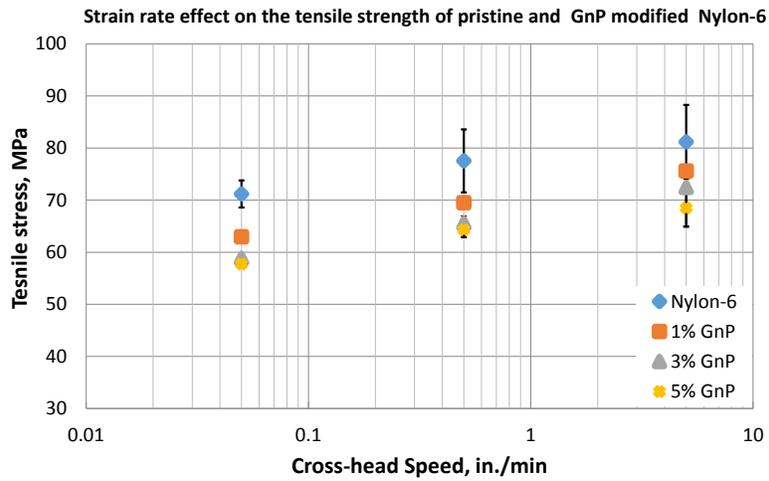
a)
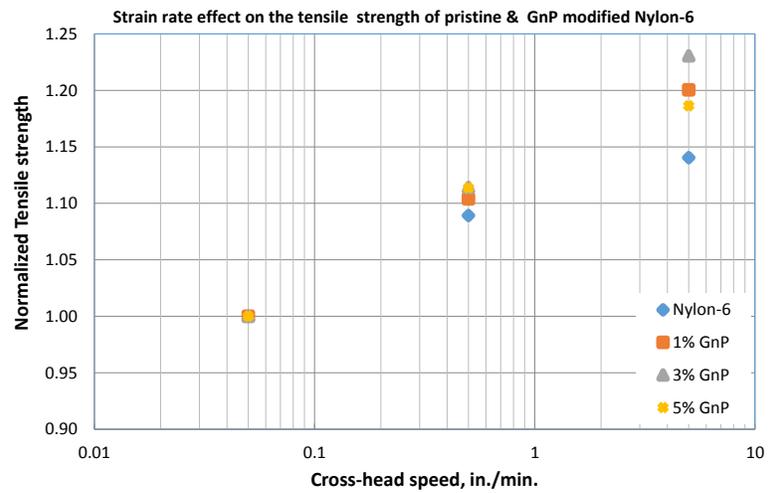
b)

Figure V-57: Strain rate effect on pristine and GnP modified nylon-6: a) tensile strength, b) normalized tensile strength.

a)

Comparison of the Flexural Modulus of pristine and GnP modified Nylon-6

b)
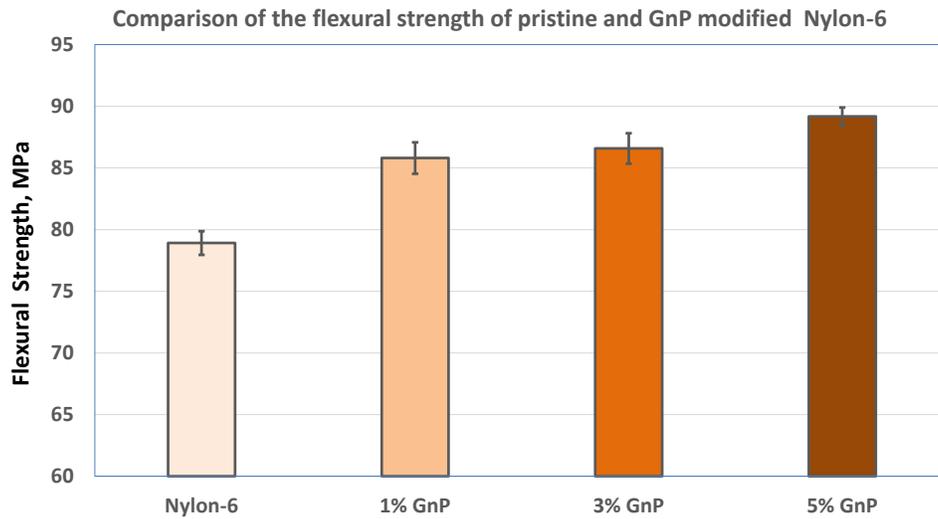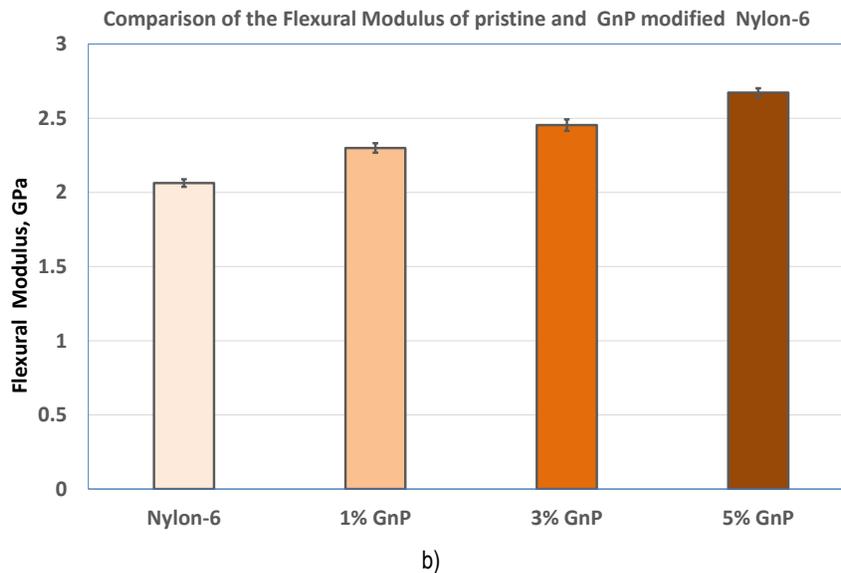
Figure V-58: Comparison of flexural properties of pristine and GnP modified nylon-6: a) Strength, b) Modulus.

Figure V-59 provides the impact strengths of pristine and GnP-modified nylon-6. Similar to tensile strengths, the impact strength of nylon-6 was observed to reduce with increasing GnP content. This phenomenon can be explained by the fact that the inclusion of rigid filler in a relatively tough polymer has detrimental effect on the impact strength. Similar to the discussion on tensile strengths, improved chemical functionalization can address this issue and possibly improve or at least maintain the toughness similar to pristine nylon-6.

5. Single Lap-Joints with pristine and GnP modified nylon-6:

Initially, the baseline, or 'control' specimens, corresponding to single lap joints of Al (Al 6061, phosphoric acid anodized) substrates with pristine adhesive were manufactured, followed by dissimilar material (Al-steel) single lap adhesive joints using both pristine and GnP-modified nylon-6. Next, single lap-joints with GFRP (glass-fiber reinforced composite, plain-weave S-glass reinforced with SC-15® from Applied Poleramics Inc.) adherends were developed. The low temperature resistance of SC-15® resin created problems during melting of nylon-6 and hence high temperature-resistant GFRP substrates with SC-122® resin (Applied Poleramics Inc.) were developed, and resulting multi-material joints have been recently manufactured. The experimental characterization of these high-temperature GFRP joints is in progress and will be provided in the next report. The need for high temperature adherends is only for thermal heating of the adhesives along with adherends. During targeted heating of adhesives only using MW radiations, high temperature adherends need not be used.

Comparison of the impact energy of pristine and GnP modified Nylon-6
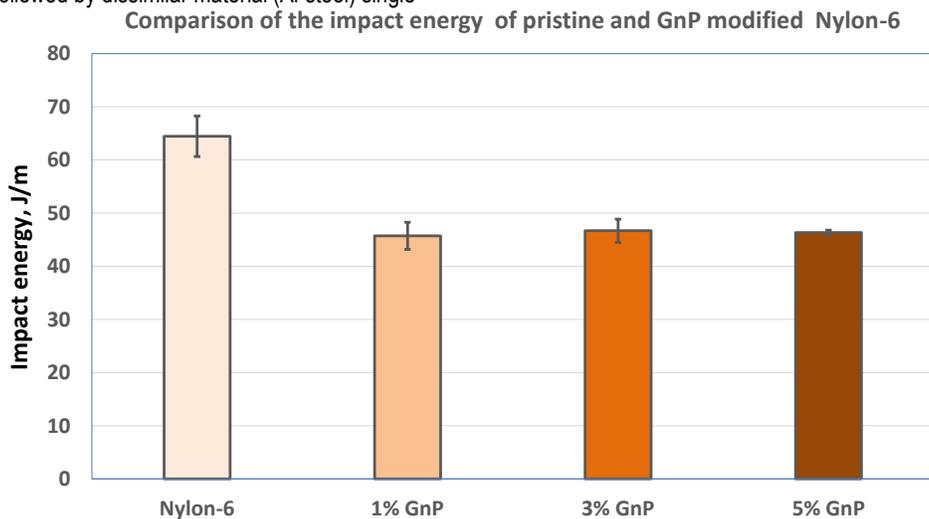
Figure V-59: Comparison of the impact energy in joules per meter (J/m) of pristine and GnP modified nylon-6.

Shear Strength of pristine and GnP modified Nylon-6
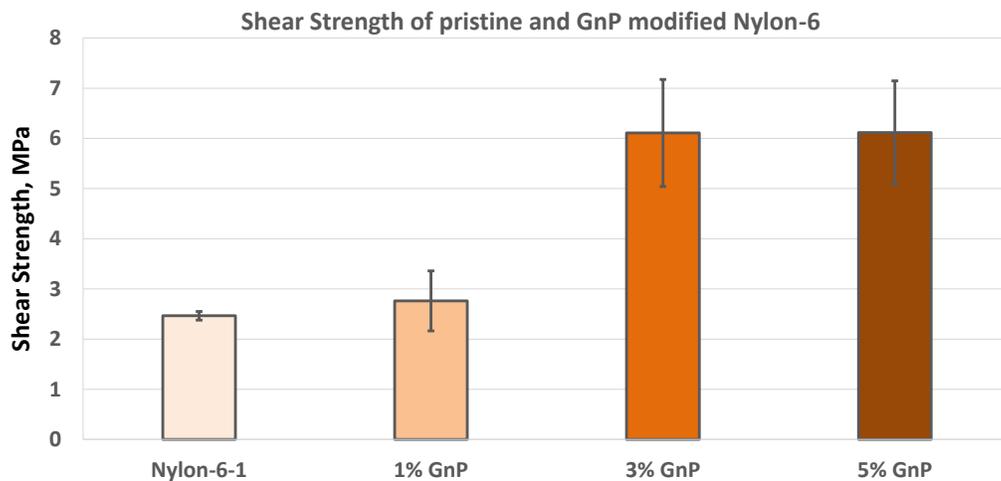
Figure V-60: Comparison of shear strengths of pristine and GnP-modified nylon-6.

Figure V-60 provides the lap-shear test results of single lap joints of dissimilar materials (steel-Al). The inclusion of GnP in pristine adhesive film was observed to significantly improve the shear strength of resulting joints. It appears that there was no significant increase in shear strengths beyond 3 wt% GnP. Nevertheless, additional experimental tests using standard statistical methods [3] are essential prior to making strong conclusions. Statistically significant (sample number (n) > 6) experimental tests for various combinations of adherends are in progress and will be reported in the upcoming report

6. Failure surface morphology analysis using scanning electron microscopy (SEM):

The morphology of fracture surfaces of pristine and GnP-modified nylon-6 based single lap joints were observed with a SEM. The SEM samples were coated with a thin layer (3-4 nanometer (nm)) of platinum prior to examinations. The following summarizes the outcomes from SEM observations shown in Figure V-61:

- For a given GnP modified nylon-6, the SEM images showed clusters of GnPs with less than tens of micrometers of diameter, indicating a poor interfacial adhesion in the material,
- SEM observation showed that the agglomeration of GnPs is more pronounced when the concentration increases.
- SEM observations revealed that the fracture surfaces of GnPs are smooth.

These observations are consistent with the experimental reduction in tensile and impact strengths. As mentioned earlier, the GnP used was 'as-received' and not chemically functionalized to be compatible with the host polymer. Chemical functionalization would improve bonding between the GnP and host polymer, improve dispersion of GnP, eliminate clustering, improve exfoliation and overall improve the mechanical behavior or resulting adhesives and joints.
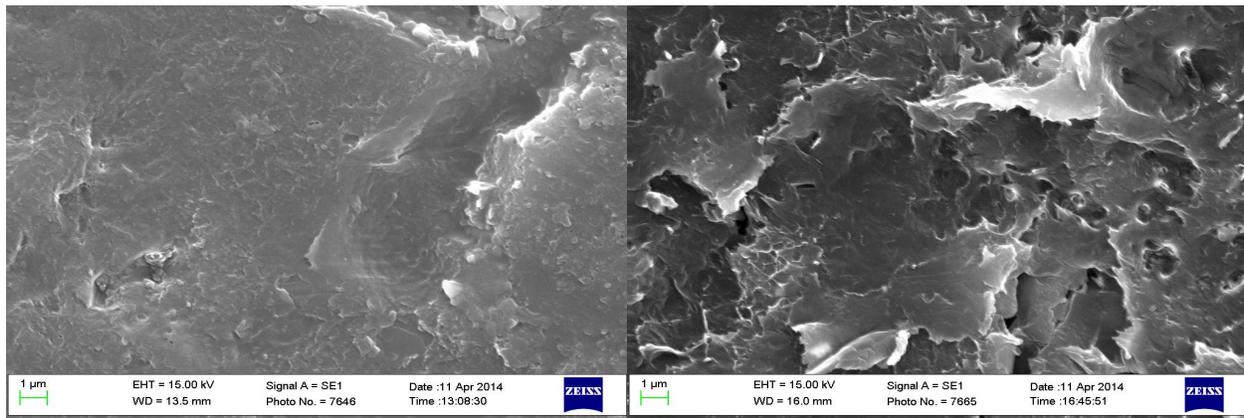
0 wt.% GnP

3 wt.% GnP

1 wt.% GnP   5 wt.% GnP
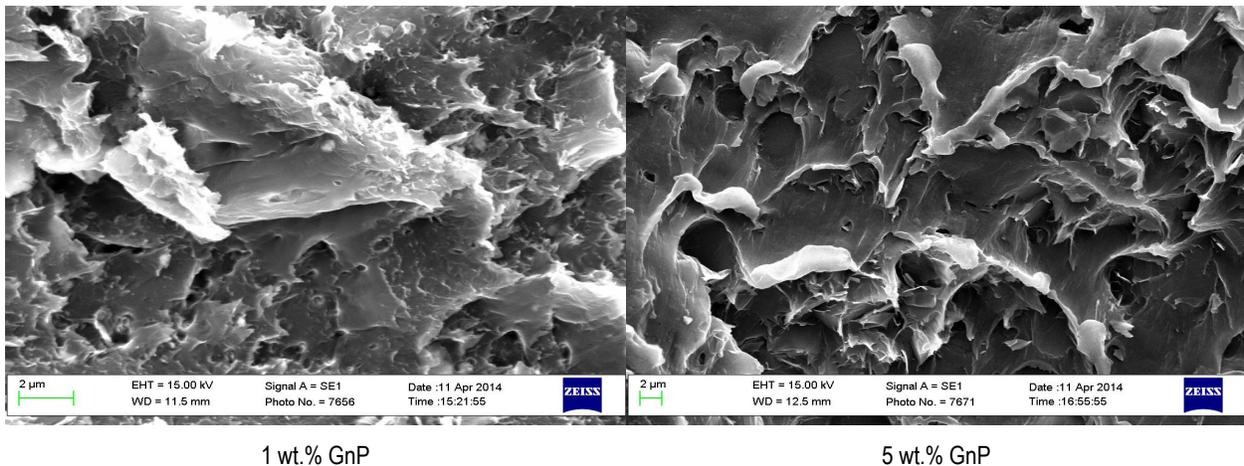
Figure V-61: Fracture surface observations, all magnifications at 5000X.

7. Nano-scale Simulations and Homogenization:

Nanoscale modeling allows the possibility of understanding and designing materials considering the nanoscale and upwards. One of the main advantages of a computational approach as the one taken in this project is that it eliminates costly trial and error experiments, and provides extrapolation of key experimental data with confidence and in a rational manner. [4] Further, computational analysis provides confidence that the new materials developed possess the desired properties. Most importantly, accurate nanoscale simulations provide quantitative evaluation of mechanisms that improve or detriment the macroscale properties.

Considerable work on characterization of graphene/polymer nanocomposites for mechanical, thermal and electrical properties exists, but work on fracture/damage resistance is limited. Additionally, the functionalization (for example, coating GnP with rubber) can further improve the toughness and resistance to fracture. While the use the rubber coated graphene is promising, its influence on resulting joints is not fully understood. Furthermore, the development of design tools for structural joints requires that the nanoscale properties are fully

and accurately transferred to the macro/structural scale. Nanoscale simulations in the form of unit cell homogenization, allow obtaining effective properties of the tailorable adhesive. The unit cell, or representative volume element (RVE) can either be in 2-dimensional (2D) or 3-dimensional (3D).

Figure V-62 and Figure V-63 show sample 2D and 3D RVEs respectively containing 2.5 wt% of GnP. While work on thermoplastic development and characterization is in progress, experimental results on vinyl ester (VE) composites with varying graphene contents was readily available in our group. Additionally, the effect of carboxyl terminated butadiene acrylonitrile (CTBN) functionalization on resulting modulus was also available. Nanoscale simulations were developed to compare the predictions with these experimental results. The use of thermoplastic adhesive instead of vinyl-ester is a direct, simple extension, in the form input of material properties. This will be continued as the database of experimental characterization results of GnP reinforced nylon gets populated.

Figure V-62: 2D Representative Volume Element (RVE).
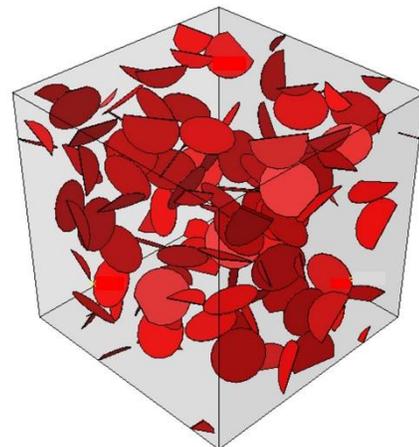
Figure V-63: 3D (RVE).
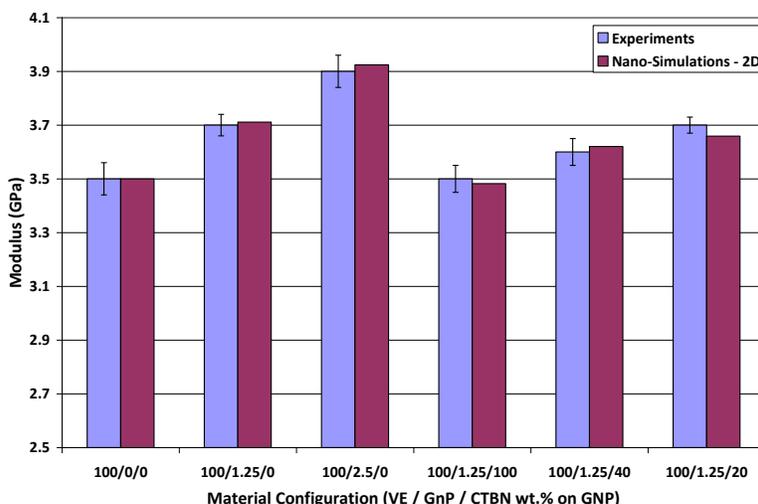
Figure V-64: Comparison of Experimental Modulus (E_{11}) with Numerical Predictions.

The material properties used for the simulations in Figure V-62 and Figure V-63 are: matrix: Young's Modulus E=3.5 GPa, Poisson's ratio (ν)=0.35, graphene, E=200 GPa (back calculated using rule of mixtures from experimental data), ν =0.16, rubber coating: E= 1.0 GPa, ν =0.4. All analyses were performed using Digimat® (MSC software). The 3D simulations were performed in ABAQUS® while the random particle generations was done in Digimat®. Figure V-64 shows the comparison of experimental results with numerical predictions. Overall good agreement in experimental and numerical predictions were observed.

Technology Transfer Path

The deliverables (procedures and results) of this project will be transferred to the industries through the collaboration with EATON. EATON is an industrial partner as a part of this project. Additionally, the results and findings will be shared with U.S. Army Tank Automotive Research Development and Engineering Center (TARDEC) to facilitate applications on ground vehicles.

Conclusion

An efficient joining technique that can inherit the advantages of both the bonded (light-weight, elimination of holes and associated stress concentrations) and bolted (ease of repair and re-assembly) techniques while being acceptable to available industrial and assembly line processes is of immediate interest for a wide range of applications. This project deals with the development of 'active adhesives' for dissimilar material joining that would allow reversible bonding of joints through 'targeted heating' of the adhesives. This would allow for inheriting all the benefits of bonded joints along with ease of re-assembly/dis-assembly, in-situ repair and recovery of micro-cracks or damage over the service life of the joint.

The 'active adhesives' were developed by incorporating electrically conductive GnP in a thermoplastic adhesive. The percolated network of graphene particles (at less than 2 wt%) can couple with microwave radiations via non-contact methods, thereby increasing the adhesive temperature beyond the required processing temperature. This would allow the adhesive to melt and flow over adherends, and upon curing can lead to a structural bond. Conversely, the microwave/graphene coupling can be used to dis-assemble and repair the joints and resulting components.

During the past year considerable progress was made to develop active adhesive technology for multi-material joints in lightweight structures. The mechanical properties (tensile, strain rate effects on tensile, and impact), thermo-mechanical behavior and processing parameters of both pristine and GnP modified nylon-6 adhesives were experimentally characterized. Additionally, dissimilar material lap-joints with combinations of adherends including Al, steel and composites were manufactured using both pristine and GnP modified nylon-6 adhesives. Experimental lap-shear tests on resulting joints were also performed. Furthermore, a cost-effective, out-of-autoclave liquid molding process was used to manufacture composite adherends with high temperature resistance to achieve the adhesive processing temperatures without affecting or degrading the adherent properties. In parallel, numerical simulations at the nano-scale to obtain effective/homogenized properties of the active adhesives were developed. Experimentally validated numerical simulations for structural lap-joints are also being developed, with the aim that the experimentally validated simulations would allow to extrapolate the material and structural behavior outside the experimental matrix studied in this work.

Experimental characterization of both pristine and GnP modified adhesive showed improvement in tensile and flexural modulus. Reduction in tensile strengths and impact strengths were observed. This reduction was expected as the GnP used was 'as-received' and not chemically functionalized to be

compatible with the host polymer. This was done by 'design' to obtain the lower bound of performance prior to chemical functionalization. In spite of the lack of functionalization, at the structural/joint-level, the lap-shear strengths significantly improved with increasing GnP content.

Overall, the progress and results from this work show great promise in use of GnP reinforced thermoplastics as 'active' adhesives for dissimilar material joining. Incorporation of novel non-destructive evaluation tools in experimental characterization and use of such accurate measurements in numerical simulations can provide an excellent tool for 'rational' development of design tools and elimination of 'trial-and-error' approach. Additional work on optimizing the GnP processing parameters including chemical functionalization, detailed experimental characterization of both adhesives and joints, study of activation, dis-assembly and in-situ repair would allow to fully understand and exploit the benefits offered by these novel active adhesives for a wide range of applications.

Presentations/Publications/Patents

1. Haq M. (August 2014) "Active, Tailorable Adhesives for Dissimilar Material Bonding, Repair and Assembly" Presented to U.S. Council for Automotive Research, Southfield, MI.

2. Koricho EG, Haq, M, Khomenko A, Drzal LT. (November 2014) "Thermo-mechanical properties and strain-rate dependency of graphene reinforced thermoplastic materials and joints". Manuscript submitted to "*Composites Science and Technology*" (unpublished as of the date of this report).

References

1. Verna, E.; Koricho, E.G.; Cannavaro, I.; Brunella, V.; Belingardi, G.; Roncato, D.; Martorana, B.; Lambertini, V.; Neamtu, V.S.; Ciobanu, R. (2013). "Adhesive joining technologies activated by electro-magnetic external trims." *International Journal of Adhesion and Adhesives* (46); pp. 21-25.

2. Rafael, C.S.; Recardo, L.A.; Antònio, F.A.; Marco, A. (November 2007). "Mechanical characterization of glass/epoxy composite material with nanoclay." *Proceedings of COBEM, 19th International Congress of Mechanical Engineering*, Brasilia, DF, pp. 1-8.

3. Weibull, W. J. (1951). "A statistical distribution function of wide applicability." *Journal of Applied Mechanics* (18); pp. 293-297.

4. Haq, M.; Liu, W.; Patterson, E.A.; Drzal, L.T. (June 2011) "A Computational Approach to enhance the understanding of Novel, Hybrid Graphene/Rubber Nanocomposites." *Engineering Mechanics Institute (EMI) Annual Conference*; Boston, Massachusetts.

Adrian S. Sabau, Principle Investigator
Oak Ridge National Laboratory
1 Bethel Valley Road
Oak Ridge, TN 37831
Phone: (865) 241-5145
E-mail: sabaua@ornl.gov

C. David Warren, Principle Investigator
Oak Ridge National Laboratory
1 Bethel Valley Road
Oak Ridge, TN 37831
Phone: (865) 574-9693
E-mail: warrencd@ornl.gov

Will Joost, Technology Area Development Manager
U.S. Department of Energy
1000 Independence Avenue, SW
Washington, DC 20585
Phone: (202) 287-6020; Fax: (202) 856-2476
E-mail: William.Joost@ee.doe.gov

Contractor: Oak Ridge National Laboratory
Contract No.: DE-AC05-00OR22725

Abstract/Executive Summary

The project objective is to demonstrate a breakthrough laser structuring technology for joining carbon fiber polymer composites (CFPC) and aluminum (Al) components. The innovations include the texturing of both the Al surface and the CFPC surface and engineering "rough" surfaces on Al and CFPC prior to an adhesive bonding operation. 3M Company (3M) formulated the adhesives; Plasan Carbon Composites, Inc. (Plasan), provided the composite; and Cosma, Inc. (Cosma), provided the Al. All three companies are partners on this project.

In this first year of the project, the effort focused on assessing the effect of laser processing on the surfaces of the Al and CFPC materials. High-resolution optical profiler images revealed that the surface roughness increased from 226 nanometer (nm) for the as-received surface to 392 nm for the laser interference structuring surface. 3D Keyence optical microscope scanning depth profiles for the CFPC surfaces showed that the carbon fibers were exposed on both the top surface and the side surfaces. Following the surface assessment, joint specimens were made at 3M and Oak Ridge National Laboratory (ORNL). ORNL measured the shear lap strengths of baseline joint specimens.

A dramatic increase in the lap shear strength compared to the baseline data was observed for the laser processed specimens, demonstrating the proof of concept for the use of laser structuring and/or laser ablation technology for surface preparation of both CFPC and Al coupons prior to adhesive joining.

Accomplishments

- Materials that are commonly used in the automotive industry were selected for this project based on a review of industrial practices conducted at Cosma, Plasan and 3M to ensure a straightforward pathway to dissemination and application of the joining technology that is being developed in this project.
- ORNL measured the single-lap shear strength for baseline specimens.
- Diffuse reflectivity data over a range of wavelengths were obtained for the CFPC and for bare carbon fiber. The data indicated that the optical properties of the CFPC itself do not vary strongly with the wavelength over the range of wavelengths available, while the resin affects the optical properties of the CFPC at wavelengths higher than 280 nm.
- After 13 baseline specimens were joined at 3M using procedures for joining the Al and CFPC specified by 3M, ORNL tested the joint specimens and measured the baseline lap shear strengths.
- Laser structuring of Al 5182 specimens was successfully performed. High-resolution optical profiler images revealed that the surface roughness increased from 226 nm for the as-received surface to 392 nm for the laser interference structured surface.
- Laser ablation of the CFPC was performed with no apparent damage to the carbon fiber. The 3D Keyence optical microscope profiles of laser-ablated specimens showed that the resin rich, composite surface layer had been removed and carbon fibers had been exposed on both the top surface and the side surfaces, creating an ideal bonding surface for the adhesive.
- The increases in the measured lap shear strength compared to the cleaned only baseline and the abraded and cleaned baseline were estimated to be between 560 and 750% and 20 and 54%, respectively.

Future Directions

- Evaluate the variability in the lap shear strength of a single-lap joint.
- Identify optimum operating parameters for the laser-structuring of Al and laser ablation for CFPCs.

- Present lap shear strength data for range, mean, and standard deviation for Al-CF joints that are obtained with the following surface preparations for each adhesive: (a) ethanol cleaned, (b) abraded and ethanol cleaned, and (c) laser treated. A minimum of six specimens will be used per each condition.
- Identify optimum adhesives based on results for lap shear strength of single-lap joints produced with all 3M three adhesives used in this work.

Technology Assessment

- Target: Achieve 20% improvement over baseline samples prepared without laser structuring in dynamic super lap shear strength of a double lap shear joint produced by using Al and CFPCs, both with laser structured surfaces.
- Gap: Conventional adhesive joining techniques for CFPCs and Al use extensive surface preparation techniques such as grit blasting and solvent wiping followed by abrading with ScotchBrite.
- Gap: Conventional adhesive joining techniques for CFPCs and Al exhibit significant process variability.

✧   ✧   ✧   ✧   ✧

Introduction

The proposed technology will enable the increased use of both Al and carbon fiber composites in primary automotive structures. Body structure makes up a significant fraction of the weight of a vehicle and therefore represents a significant opportunity to reduce the weight of a vehicle. According to multiple analyses by the United States Council for Automotive Research, the U.S. Department of Energy, and ORNL, Al alloys have the potential to reduce component weight by 30–60%, and carbon fiber composites have the potential to reduce component weight by 40–70%.

To date, CFPC and Al 5000, 6000, or 7000 series components are joined by simply overwrapping the CFPC over the Al or using specially formulated adhesives coupled with extensive surface preparation techniques. Traditional industrial techniques used to prepare Al surfaces for bonding include grit blasting, solvent wiping followed by abrading, and anodizing. The results from grit blasting and abrasion techniques are inconsistent; a more controlled process would be an improvement. In addition, these processes are empirical, employ several steps, and are labor-intensive surface preparation methods that are incompatible with the degree of automation required in automotive applications.

By using a laser structuring technique [1] prior to the adhesive bonding operation, the untreated smooth adhesive/composite interface of the Al and CFPC was replaced by a rough fiber-reinforced interface, which was expected to increase the bond strength of the CFPC/adhesive interface. Cosma will specify the joint configurations for development of this technology, focusing on carbon fiber/aluminum joints that they believe will be needed for future

automotive component designs. The loading conditions and environmental stressors (i.e., corrosion conditions) will be those typically used for validation of those component subsystems.

Approach

The untreated, smooth adhesive/composite interface between the Al and the CFPC was proposed to be replaced by a rough fiber-reinforced interface, which was expected to increase the bond strength of the CFPC/adhesive interface. The rougher surface would be created by using a laser structuring technique before the adhesive bonding operation.

Cosma supplied Al 5182 samples that were 1.5 mm gauge, 100 mm width, and 300 mm long. Larger sized samples will be provided as needed. Plasan supplied CFPC specimens with T700S carbon fiber and T83 resin (epoxy); the samples were 12 in. × 12 in., 4 plies thick, and 0/90 plaques. Three adhesives were selected for this project based on their compatibility with the Al alloy and the CFPC. The selection process took place at 3M. These adhesives were selected: DP460 (an epoxy), DP620 (a polyurethane), and DP810 (a low-odor acrylic).

A 10 hertz (Hz), Q-switched neodymium-doped yttrium aluminum garnet (Nd:YAG) laser (Quanta-Ray PRO 230, Spectra Physics) was used in this study. With only 10 nanoseconds (ns), the laser pulse duration is very short, creating an extremely high power above 100 megawatt (MW), resulting in greater than 1012 degrees Kelvin per second (^{0}K/s) heating rates. The beam diameter was 8 mm. The fundamental emission with the wavelength of 1064 nm was transformed to 355 nm and 266 nm using nonlinear crystals. The maximum laser energy per pulse was 0.15 joules (J) at 355 nm and 0.038 J at 266 nm. Patterns can be dot-, line-, and ring-shaped [2 - 6]. A mechanical shutter selected the number of pulses was selected by a mechanical shutter. In some experiments, the laser pulse fluence was increased by using two identical focal lenses in each path of the split beam to focus laser beams from its original size of 8 mm to smaller sizes. Features of the structured surface morphology include:

- size: 1–500 nm
- density: 20–2,000/m^2
- undulation spacing: 0.5–50 mm
- structured area of 0.27 cm^2/shot
- scanning speed: 10,000 lines at a time; 79 million dots at a time; up to 162 cm^2/min.

CFPCs were laser processed using both the one-beam (i.e., without the power interference) and two-beam laser interference setup; Al specimens were processed using the laser interference setup. After laser structuring, the Al and CFPC were joined using the adhesives supplied by 3M. 3M also recommended the procedures for joining the Al and the CFPC. Finally, ORNL tested different joint specimens to obtain the baseline shear lap strength.

Results and Discussion

Cosma, Plasan and 3M reviewed industrial needs to ensure that the materials used in this project would ensure a straightforward pathway to dissemination of the joining technology developed in this project. These materials were selected:

- Al 5182;
- A CFPC of prepreg T83 resin (epoxy) and T700S carbon fiber in a 0/90 layup; and
- Three adhesives: DP460 (an epoxy), DP620 (a polyurethane), and DP810 (a low-odor acrylic).

The 5xxx Al alloy series is being used in inner vehicle body structure and it does not age like Al 6xxx series. Plasan has several parts in production using this T700S/T83 CFPC. Using this CFPC material would reduce the mass in more components.

Optical Properties

Optical measurements were performed on several samples in order to select laser wavelengths that would be appropriate for processing CFPC. Specifically, the absorption properties of the resin were sought. The desired laser ablation wavelengths for the CFPC were those at which the resin would exhibit high absorption while absorption by the carbon fiber is minimized. The following optical measurements were conducted: (1) normal-incidence generalized ellipsometry, (2) diffuse reflection, and (3) spectroscopic ellipsometry.

The following samples were studied:

- carbon fiber composite panel (which is the CFPC, including resin and fiber);
- carbon fiber modified such that the resin content would be reduced or eliminated (stretched with and without sizing); and
- a carbon fiber sample mounted in an epoxy specimen mold, but epoxy was not allowed to surround the fiber tows.

Diffuse reflectivity data, which is shown in Figure V-65, indicate that the optical properties of the carbon fiber itself do not vary strongly in the range of the wavelengths studied. Studies of the CFPC showed fairly consistent absorption

above 280–300 nm, but a significant absorption (the converse of diffusivity) below 280 nm. Based on this reflectivity data alone, for an effective ablation of the resin, a laser wavelength of 266 nm be is recommended. However, the variation of the maximum laser power with the wavelength should be taken into consideration.

Baseline Metrics

After the baseline specimens were joined at 3M Corp., ORNL tested different joint specimens to obtain the baseline shear lap strength in pounds per square inch (psi) (Figure V-66). The best results were observed using the DP460NS adhesive, specifically for the cross-ply CFPC joined with Al which is the primary focus of this project.

Surface Morphology of Al and CFPC Surfaces after Laser Processing

Laser structuring of Al 5182 specimens was successfully attained. Also, laser ablation of CFPC was attained with no obvious damage to the carbon fiber themselves. Both CFPC and Al specimens were laser structured using the interference technique in the as-received condition (i.e., without any additional surface preparation steps). A Wyko™ 9100 vertical scanning interferometer was used to measure the height of the specimen surfaces. Figure V-67 and Figure V-68 show the profilometry data and the analyzed surfaces of the as-received surfaces and of the surfaces structured using the laser interference technique, respectively. High-resolution optical profiler images revealed that the surface roughness increased from 226 nm for the as-received surface to 392 nm for laser interference structuring surface.

Optical micrographs and 3D Keyence optical microscope scanning depth profiles for the CFPCs are shown in Figure V-69 and Figure V-70 for the as-received condition and for the laser-ablated condition. The 3D Keyence microscope profile of the laser-ablated specimen shows that the carbon fibers are directly exposed on both the top surface and on side surfaces, creating an ideal bonding surface for the adhesive.
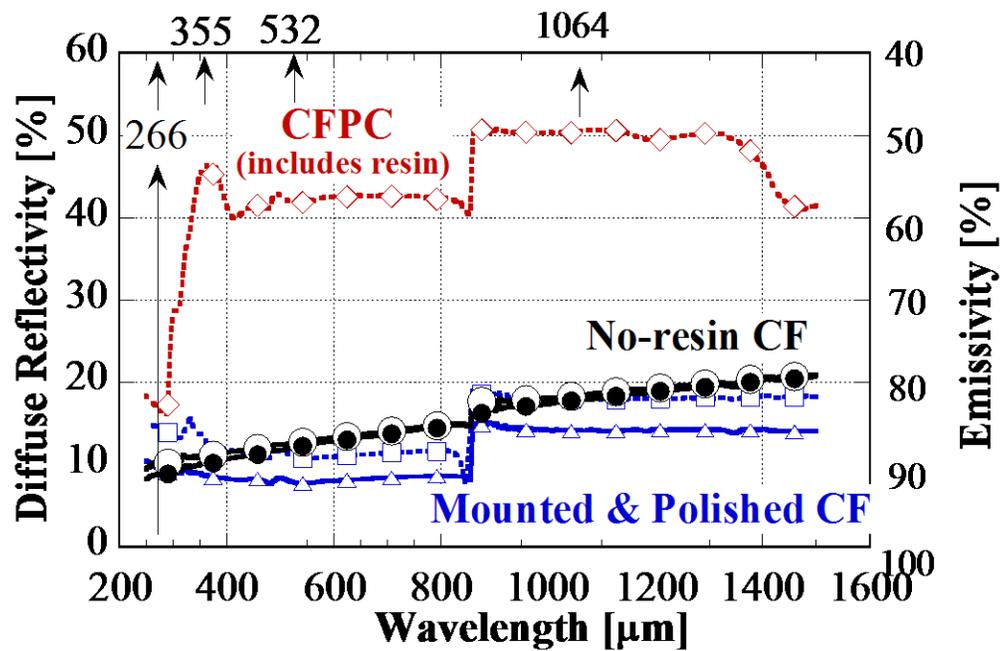
Figure V-65: Diffuse reflectivity data for the CFPC samples considered showing variations in the percentages of diffuse reflectivity and emissivity for over several wavelengths in microns (µm).
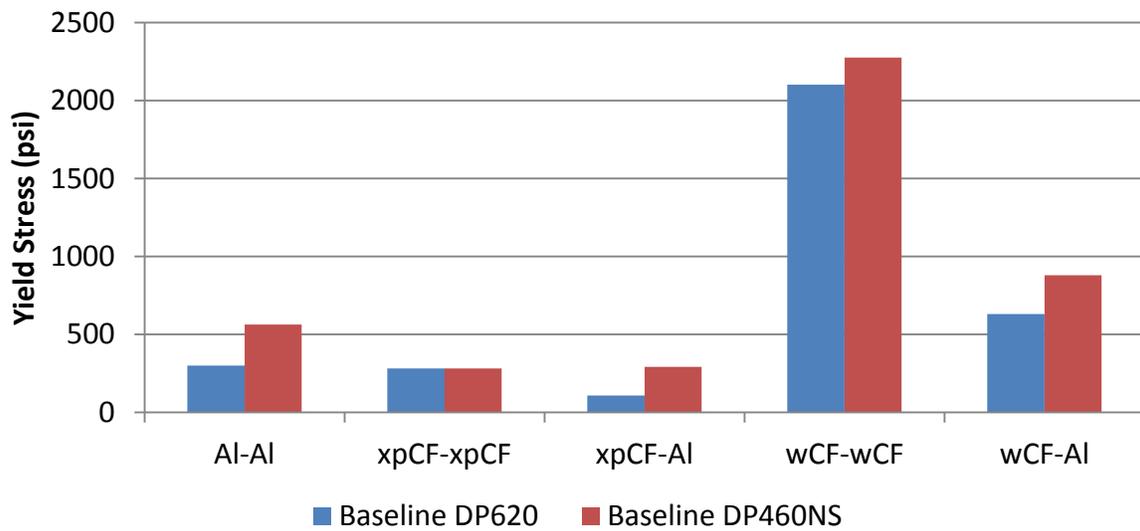
Figure V-66: Baseline single-lap shear results for DP620 and DP460 adhesives. (xpCF—cross-ply carbon fiber composite; wCF—woven carbon fiber composite).
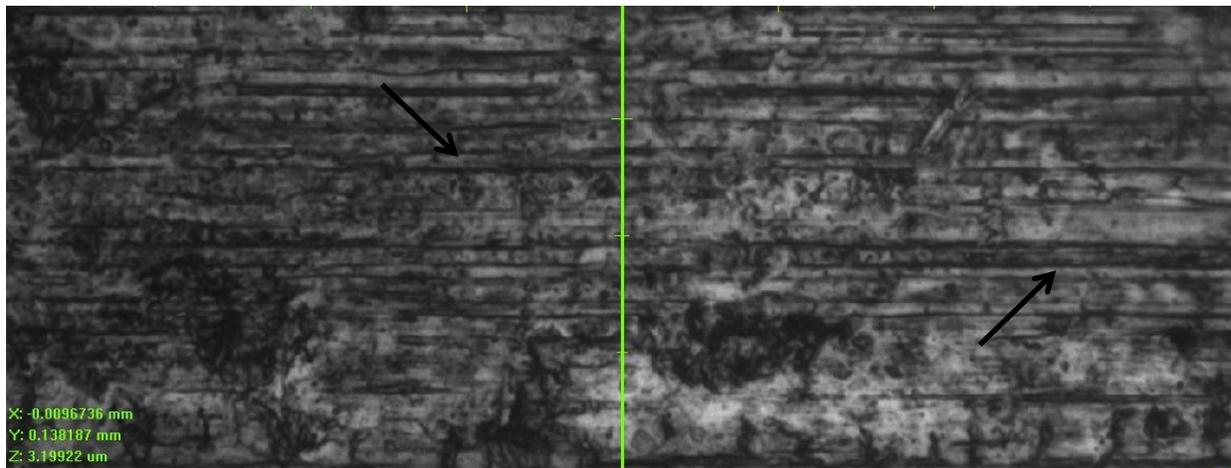
(a)
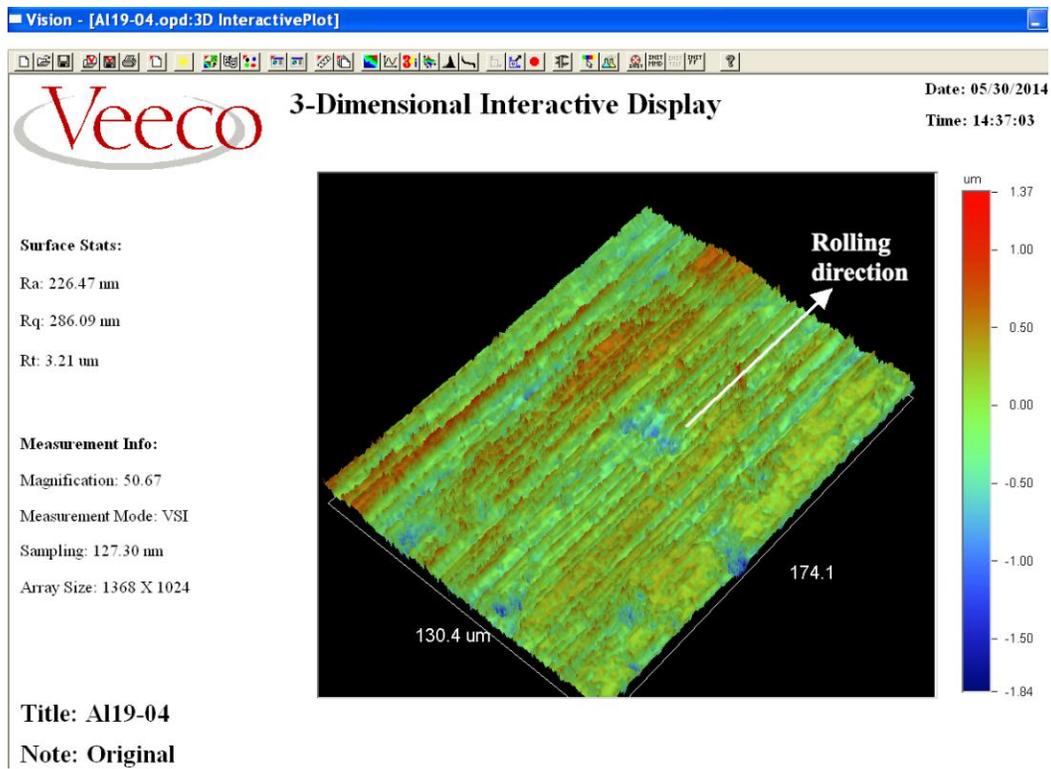
(b)

Figure V-67: Profilometry data for an as-received, unprocessed Al specimen: (a) optical micrograph showing the analyzed region (horizontal striations are due to rolling) and (b) profilometry data indicating the rolling direction.
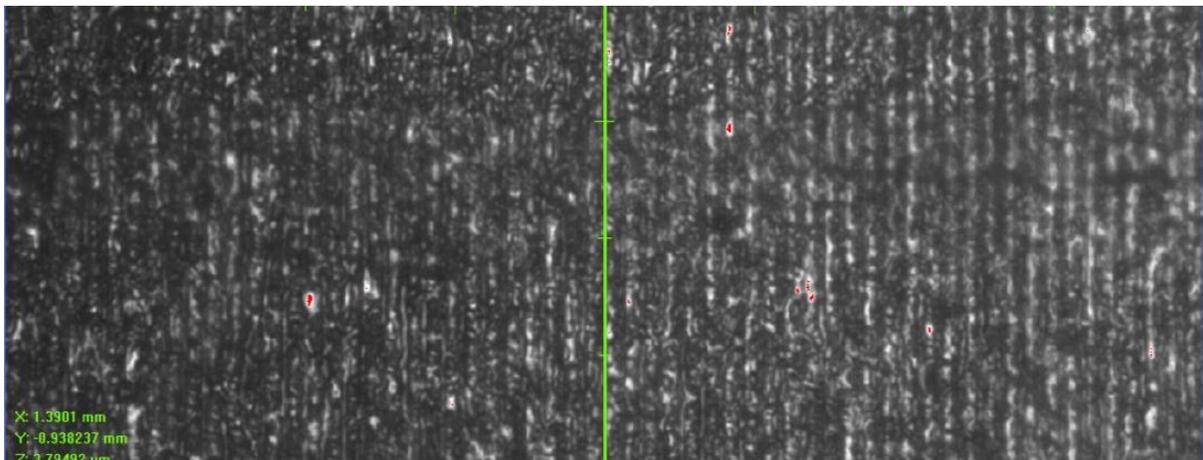
(a)
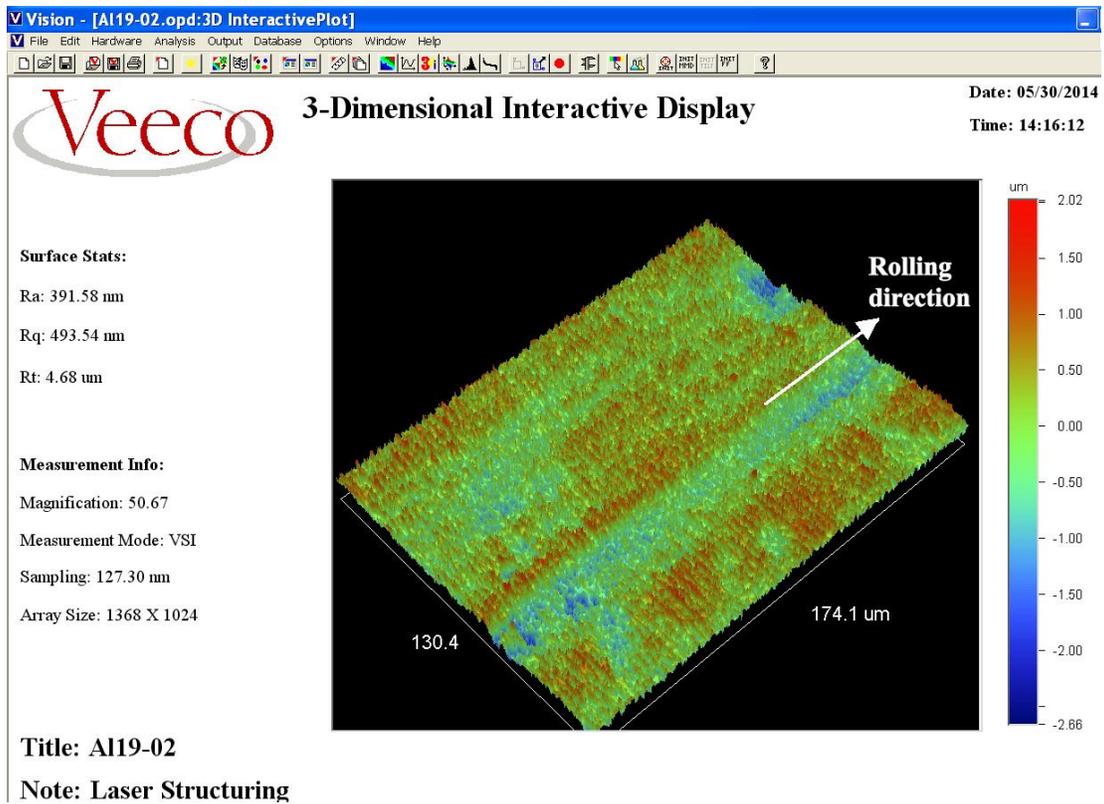
(b)

Figure V-68: Profilometry data for a laser-structured Al specimen: (a) optical micrograph showing laser-induced striations (the rolling direction is perpendicular to the laser-induced striations) and (b) profilometry data also showing laser-induced striations perpendicular to the rolling direction.
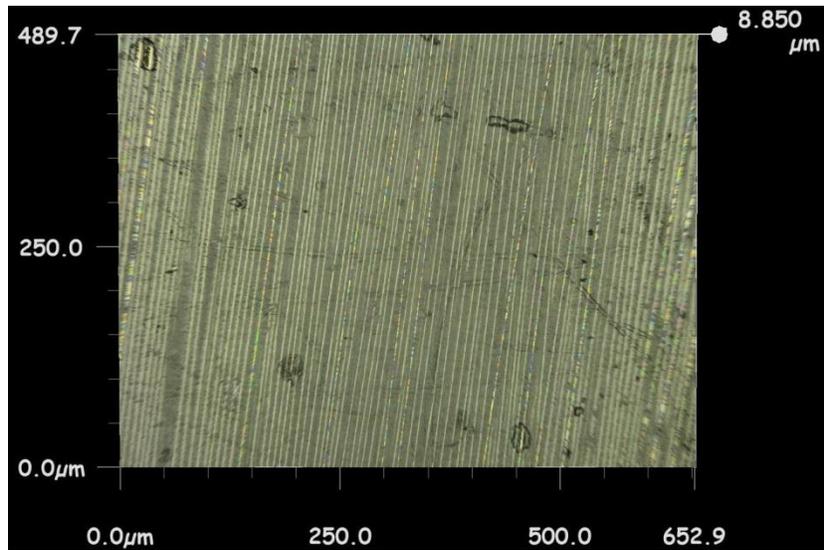
(a)
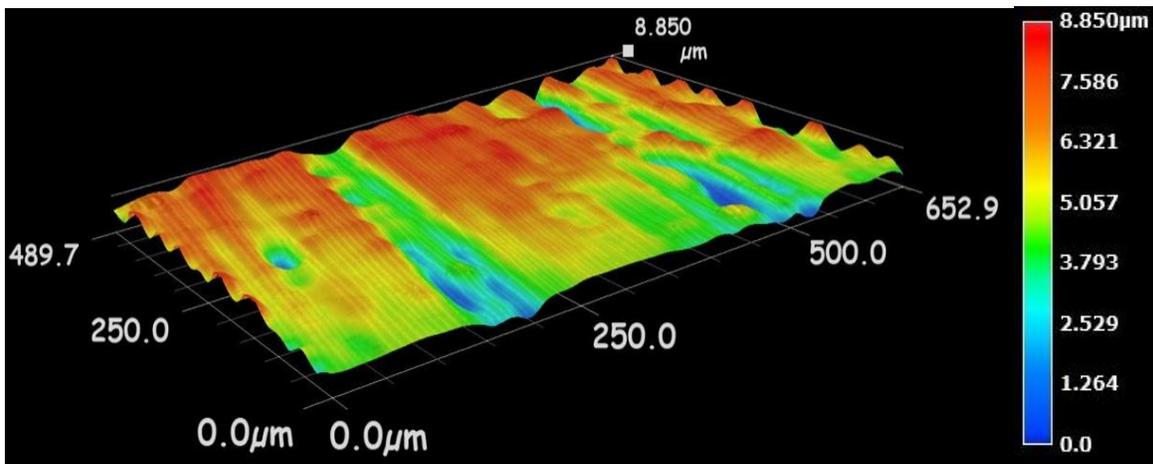
(b)

Figure V-69: Data for CFPC specimen in the as-received condition: (a) micrographs and (b) 3D scanning depth profile showing that the surface roughness is mostly less than 8.85 µm.

(a)

(b)
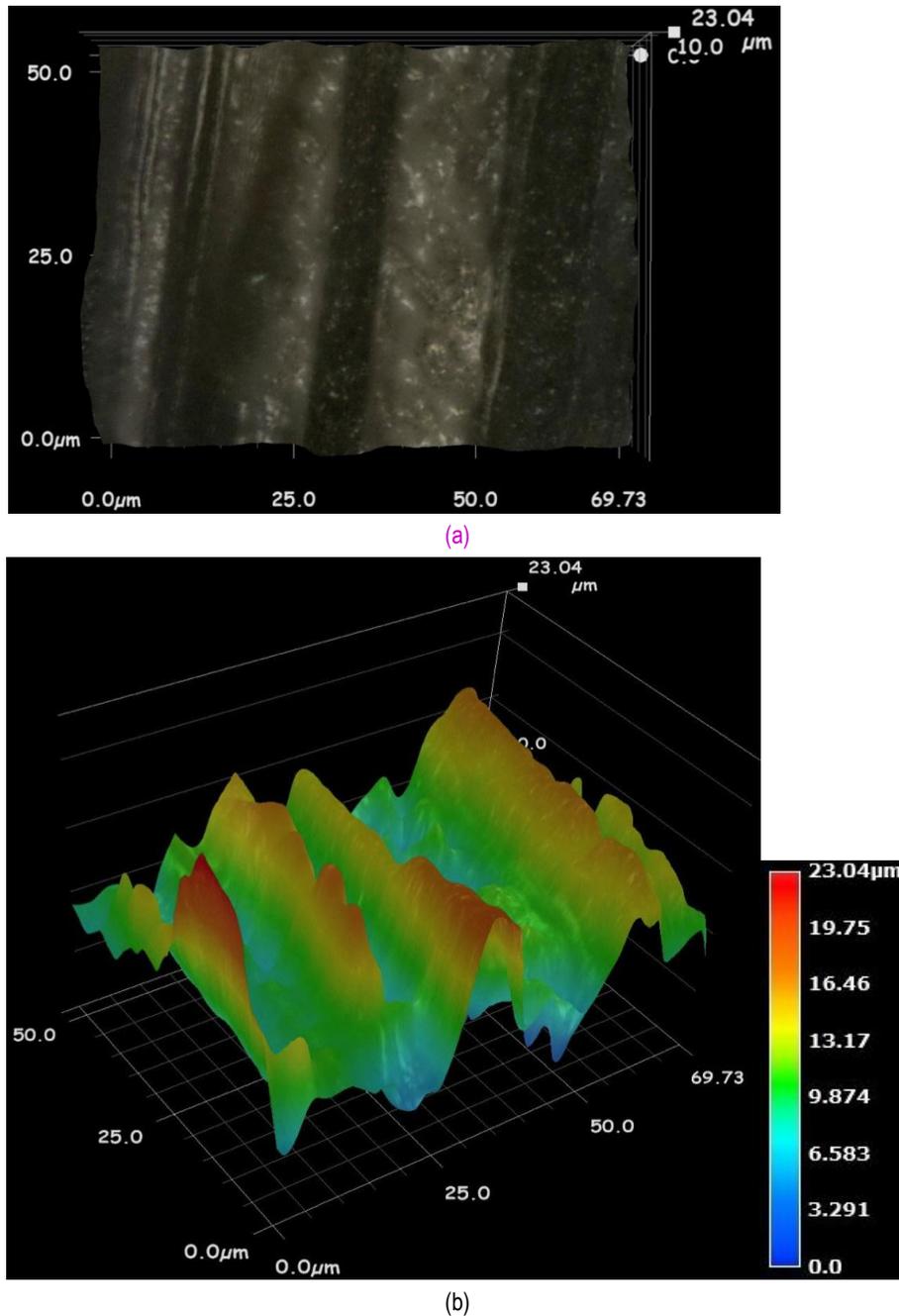
Figure V-70: Surface analysis for a laser-ablated Plasan CFPC specimen: (a) micrographs and (b) 3D scanning depth profile showing that the ablated thickness is 23 μm.

Several joint specimens were made, as shown in Table V-8, in order to assess the effect of the laser-structured surface preparation over conventional surface preparations. After they were laser structured, ten CFPC coupons were joined with either cleaned Al coupons or with cleaned laser-structured Al coupons. All the Al coupons that were joined with laser-structured CFPC coupons were only cleaned with ethanol (i.e., they were not abraded).

Table V-9 shows the results from the mechanical testing of the lap shear strength; the increase in the lap shear strength with respect to the "cleaned only" baseline and "abraded and cleaned" baseline was estimated to be between 560–750% and 20–54%, respectively for CFPC ablated and laser structured Al.

Table V-8: Joint specimens made to assess the effect of laser-structured surface preparation over conventional surface preparation.

Joint specimens	Preparation of CFPC	Preparation of Al
6	laser structured (not cleaned)	ethanol cleaned only (not abraded)
4	laser structured (not cleaned)	laser structured (not cleaned)
6—baseline	ethanol cleaned only (not abraded)	only cleaned (not abraded)
6—baseline	abraded and ethanol cleaned	abraded and ethanol cleaned

Table V-9: Increase in lap shear strength of laser-processed material joints with respect to "cleaned only" baseline and "abraded and cleaned" baseline.

CFPC	Al	Increase in lap shear strength with respect to "**cleaned only**" (%)	Increase in lap shear strength with respect to "**abraded and cleaned**" (%)
CFPC ablated	cleaned only (not laser processed)	643–753	34–54
CFPC ablated	laser structured	563–706	20–46

Technology Transfer Path

Two tier I suppliers (Cosma and Plasan) that are U.S.-based and participants in this project will have the ability to commercialize this technology. This technology is attractive because the use of lighter weight, adhesively joined materials in automotive applications would reduce gas consumption and production of greenhouse gasses. Enabling the joining of these lightweight substrates in the process being developed in this work would give credibility to incorporating them in a larger structure for automotive testing. Issues related to the process scale-up will be addressed by the industrial partners. Several steps toward commercialization are included:

- Cosma, Plasan and 3M identified materials that are commonly used in the automotive industry and reviewed industrial needs to ensure that the materials used in this project would ensure a straightforward pathway to dissemination of the joining technology developed in this project.
- 3M Company selected the adhesives based on the commercialization plans of two tier I suppliers, Cosma (Al structures) and Plasan (carbon fiber composites structures).

Conclusion

Laser structuring of the Al surface was demonstrated. High-resolution optical profiler images revealed that the surface roughness increased from 226 nm for the as-received surface to 392 nm for the laser interference structuring surface.

Laser ablation of the carbon fiber composite was demonstrated. Optical micrographs and 3D Keyence microscope scanning depth profiles for the CFPCs show that the carbon fibers are directly exposed on both the top surface and on the side surfaces, creating an ideal bonding surface for adhesives. A wide range of adhesive compounds was selected, allowing the study of adhesive effect on joint quality and maximizing the chances of success. ORNL measured the shear lap strengths of baseline joint specimens.

A dramatic increase in the lap shear strength compared to the baseline data was observed for the laser-processed specimens, demonstrating the proof of concept for the use of laser structuring and/or ablation technology for surface preparation of both CFPC and Al coupons prior to adhesive joining.

Presentations/Publications/Patents

1. Sabau, A. S.; Chen, J.; Jones, J. F.; Hackett, A.; Jellison, G. D.; Daniel, C.; Warren, C. D.; Rehkopf, J. D. (March 2015) "Surface Modification of Carbon Fiber Polymer Composites After Laser Structuring". To be presented by invitation at the 2015 TMS Annual Meeting and Exhibition, Orlando, FL.
2. Chen, J.; Sabau, A. S., Jones, J. F.; Hackett, A.; Daniel, C.; Warren, C. D. (March 2015) "Aluminum Surface Texturing by Means of Laser Interference Metallurgy". In preparation to be submitted for presentation to the 2015 TMS Annual Meeting and Exhibition, Orlando, FL.

References

1. Daniel, C.; Mücklich, F.; Liu, Z. (2010) "Periodical micro-nano-structuring of metallic surfaces by interfering laser beams." *Appl. Surf. Sci.*, *208–209*, pp. 317–321.

2. Daniel, C.; Mücklich, F. (2004) "Quantification of periodical surface structures by white light interferometry." *Prakt. Metallogr.*, (*41*:6), pp. 277–285.

3. Mücklich, F.; Daniel, C.; Lasagni, A.; Yu, F. (2004) "Direct Surface Patterning Induced by Interfering Laser Beams." *Mat. Res. Soc. Symp. Proc.*, Vol. EXS-2, M11.1.

4. Mücklich, F.; Lasagni, A.; Daniel, C. (2005) "Laser Interference Metallurgy—Periodic Surface Patterning and Formation of Intermetallics." *Intermetallics*, (13:3–4), pp. 437–442.

5. Mücklich, F.; Lasagni, A.; Daniel, C. (2006) "Laser Interference Metallurgy—using interference as a tool for micro/nano structuring." *Int. J. Mater. Res.*, (97:10), pp. 1337–1344.

6. Daniel, C. (2006) "Biomimetic structures for mechanical applications by interfering laser beams—more than only holographic gratings." *J. Mater. Res.*, (21), pp. 2098–2105.

V.6 Collision Welding of Dissimilar Materials by Vaporizing Foil Actuator–The Ohio State University

Glenn Daehn, Principal Investigator
Ohio State University
141 Fontana Labs
116 W 19th
Columbus, OH
Phone: (614) 292-6779
E-mail: daehn.1@osu.edu

Anupam Vivek, Co-Principal Investigator
Ohio State University
348 McQuigg Labs
105 W Woodruff Avenue
Columbus, OH
Phone: (608) 332-4892
E-mail: vivek.4@osu.edu

Adrienne Riggi, Project Officer
National Energy Technology Laboratory
3610 Collins Ferry Road
P.O. Box 880
Morgantown, WV 26507-0880
Phone: 304-285-5223
Adrienne.riggi@netl.doe.gov

William Joost, Technology Area Development Manager
U.S. Department of Energy
1000 Independence Avenue, S.W.
Washington, DC 20585
Phone: (202) 287-6020; Fax: (202) 856-2476
E-mail: william.joost@ee.doe.gov

Contractor: The Ohio State University
Contract No.: DE-EE0006451

Abstract/Executive Summary

The feasibility of using Vaporizing Foil Actuator Welding (VFAW) technique for welding dissimilar material combinations of aluminum, steel, and magnesium alloys has been tested. Seventeen material systems were screened using VFAW in a couple of different configurations. By launching flyer plates into target plates that have different angle grooves in them, optimal welding parameters could be obtained. Some issues that were encountered during the application of this configuration are introduced. Welding to flat targets was found to be a more viable screening test, and 11 material systems were tested using this method. Effective welding of aluminum to high strength and galvannealed steel, and aluminum to magnesium was accomplished.

Metallography and mechanical testing (peel and lap shear mode) were conducted on each of the welded samples. A wavy interface consisting of intermittent regions of intermetallic compounds was revealed. Most of the samples were very strong in lap shear, and failure generally occurred in base material. During peel testing, some systems failed in the base metal. For the cases where the weld interface splits apart, maximum peel strengths ranged from 6 newtons per millimeter (N/mm) to 33 N/mm. Methods for creating lap and spot welds were also developed. Based on the FY 2014 work, six material systems have been selected for more intensive study during FY 2015.

Accomplishments

- Screened 17 dissimilar metal combinations consisting of magnesium, steel, and aluminum alloys for welding using VFAW. More than 10 combinations were successfully welded.
- Down selected six material systems based on their weldability and expected resistance to corrosion. (FY 2014)
- Created approximately 90 welded samples and subjected samples to mechanical testing and microanalysis. (FY 2014)
- Welded high strength steels, such as dual phase (DP) 780 and Boron-quenched steel to aluminum alloy (AA) 6061 T4. Upon peel and lap shear testing, failure occurred in base metal rather than in the weld. (FY 2014)
- Collision welding to galvannealed steel was accomplished for the first time. Welded galvannealed steel JAC 270F to aluminum 6061 T4, and mechanical testing resulted in failure in parent aluminum. (FY 2014)
- Successfully welded wrought as well as cast magnesium alloys to AA 6061-T4. Additionally, wrought magnesium sheet was also welded directly to uncoated JAC 270F steel. (FY 2014)
- Demonstrated the effectiveness of use of interlayers for creating strong bonds with pairs that are relatively difficult to weld. (FY 2014)
- Performed welding in lap, as well as spot configurations. (FY 2014)

Future Directions

- Based on the information gained (from FY 2014) on ideal conditions for weld creation for each of the 6 selected material system, develop prototype coupons and subject them to mechanical testing pre- and post-corrosion treatment.
- Half of the prototype coupons are going to be e-coated by Honda Research. These samples will be mechanically tested after corrosion treatment.

- Characterize joining induced defects and understand the failure mechanisms for the samples that fail within the weld.
- Develop an automated system for creating VFA welds with minimal manual involvement. This will increase repeatability and reduce experimental cycle time.
- Broaden the application of VFAW to different configurations.

Technology Assessment

- Target: Reduce the VFAW process time to 1 cycle/minute and increase reproducibility in weld quality.
- Gap: Currently material handling, process assembly, and system firing are all manual. These factors introduce variability at every step of the process. While demonstrating basic feasibility of the technique for welding dissimilar metals was the main focus of FY 2014, industrial adaptation would require reduced cycle times and better reliability.
- Target: Create prototype dissimilar material welds that retain at least 80% of their strength after being subjected to a G85-02 type modified salt spray (fog) test.
- Gap: Due to disparate reduction potentials of aluminum, magnesium, and steel, galvanic corrosion is a major problem in their joining. This issue will be addressed in FY 2015 by implementing common mitigation strategies including sealing, e-coating, and insertion of intermediate layers.

✧   ✧   ✧   ✧   ✧

Introduction

This project aims to meet the challenge of effectively welding starkly dissimilar materials, namely, steel, aluminum, and magnesium for creating multi-material automotive body structures. The primary issue we are addressing in the phase I of this project is the formation of unwanted, brittle intermetallic compounds (IMCs) at the weld interface. Corrosion due to disparate electrochemical potentials is also a major issue with dissimilar material joining. Corrosion mitigation by using intermediate layers, e-coating, and sealing, will be pursued during FY 2015. Traditional fusion-based welding between dissimilar combination of aluminum, steel, or magnesium always leads to formation of IMCs, which are brittle. Upon mechanical testing, failure in such weld samples tends to happen within the weld. For instance, Al-Fe welds made by resistance spot welding often contain IMCs and are not tough enough to be applied in the body in white. Solid-state welding techniques, like friction stir and collision welding, offer a method that avoids or reduces the formation of IMCs.

In this project, a novel method for collision welding, developed at Ohio State University (OSU), is being used. Usually, collision welding relies on the use of high explosives to provide the driving force. However, explosive welding [1] is limited to large scale applications. Besides, there are stringent regulations with respect to transport, storage, and handling of explosives that make it difficult to apply in mass production

industries, such as the automotive industry. Magnetic pulse welding [2] can be used for welding at smaller scales; however, actuator longevity at high pressures and operating cycle frequencies have often restricted the application of this technique.

The new technique [3] has been utilized here. A schematic for the VFAW assembly is shown in Figure V-71. The main driver of these experiments is a 0.0762 mm thick aluminum foil, which is a consumable, replaced after every experiment. When a high, short-duration current pulse, driven by a capacitor discharge, is passed through the foil, the foil vaporizes rapidly due to Joule heating. This phenomenon, also known as electrically exploding foils [4], creates a high pressure region around the foil, which, in this case, has a thick steel block on one side and the flyer sheet on the other. Therefore, the flyer sheet gets driven to high velocities toward the target plate. Standoff sheets between the flyer sheet and target plate provide the distance over which the flyer is accelerated. Additionally, the height of the standoff sheets and the horizontal distance between them help create an oblique collision, which is necessary for weld creation. Between the two metals to be welded, the flyer is chosen based on density, strength, and ductility of the joining members. Ideally, the flyer materials should be one that is lighter, less strong, and more ductile between the two metals. However, in some cases where all three criteria cannot be met simultaneously, the more ductile material is chosen. Flyer sheet thickness ranges from 0.5 mm to 1.5 mm. As for target plates, because they are stationary, they can be as thick as needed.

Approach

Fifteen different combinations of dissimilar materials were to be screened in order to select five of them for intensive characterization in the second phase. The starting sets of alloys tested include:

- Steel: JAC270F (thickness = 0.6mm), DP780 (1mm), high-strength, low alloy (HSLA) 656a (6mm), HSLA 588a (6mm), Boron Quenched Steel (2mm), Aluminum: 6061 T6 (0.8mm and 0.9mm), 6061 T4 (0.8mm and 0.9mm), 5052 (0.8mm), and
- Magnesium: AM60B (3mm), AZ31B (0.8mm)
- Aluminum was one of the flyer materials when used as a joining member. During the welding of steel and magnesium, steel was chosen as the flyer plate. In most of the cases, OSU worked with uncoated material. However, welding of galvannealed JAC270F with AA6061 T4 was also done without removing the coating. For each type of flyer, velocity was measured with high temporal resolution by using photonic Doppler velocimetry (PDV). Arcing through work pieces or the backing blocks tends to reduce the efficiency of the process. Therefore, current and voltage were measured in order to ensure that the electric current did not arc through a path other than the foil actuator. Two types of experimental configurations shown in Figure V-71 were implemented for screening: grooved target and flat target welding.

Two types of experimental configurations were implemented for screening: grooved target and flat target welding.
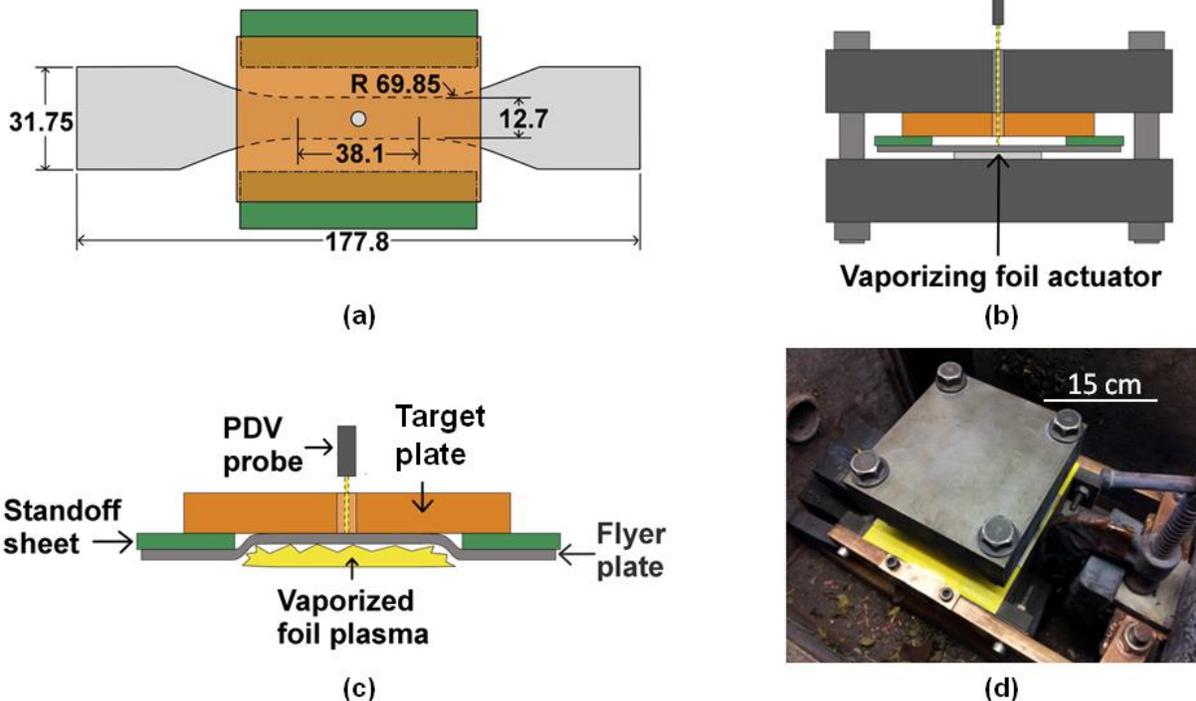
Figure V-71: Vaporizing foil actuator welding (VFAW) set up: (a) top view of the foil actuator, flyer sheet, standoff, and target stack, (b) side view of the stack along with the positioning of the photonic Doppler velocimeter (PDV) probe, (c) formation of weld after foil actuator's vaporization, (d) VFAW set up inside the experimental chamber.

Grooved Target

Six grooves of angles ranging from 8° to 28° were machined into target plates using electro-discharge machining. These were impacted with aluminum flyer sheets launched by the vaporizing foil actuator operating at varying input energy levels (ranging from 4 kilojoules (kJ) to 10 kJ). With high-resolution measurement of velocity using PDV and microscopic observation of the welded interfaces, a complete welding process window could be created [5]. Assessment of the weld quality was based purely on optical observation, as the samples do not lend well to mechanical testing. The optimal collision parameters determined from such experiments were intended to be utilized to create prototype welds in the second phase. However, some issues were encountered with this method, which rendered it not as useful a screening method as initially envisioned. In order to make this method work, certain variations, such as introducing a vacuum between the joining members, using compliant intermediate layers, and slotting the bottom of the grooves, were implemented.

Flat Target

This is the more commonly used configuration of VFAW where a flat target plate is used and the angle of collision is created by the standoff distance, which was typically 1.6mm. The part of the flyer sheet directly above the foil actuator is launched flat while the rest of the flyer sheet follows and collapses onto the target plate. Welding takes place in the regions of oblique collapse, where the collision angle and velocity, which are continuously varying, are within the welding process window. Generally, a weld is created above the perimeter of the former position of the active narrow section of the foil actuator. For each material combination tested using this method, the standoff distance was kept at 1.6 mm, and the flyer impact velocity was varied by changing the input energy (between 6 kJ and 12 kJ). Experiments were repeated three times at an intermediate energy level for each set. The samples were sectioned as shown in Figure V-722 and subjected to mechanical testing and metallography. Mechanical testing was conducted in lap shear as well as peel mode as illustrated in Figure V-73.
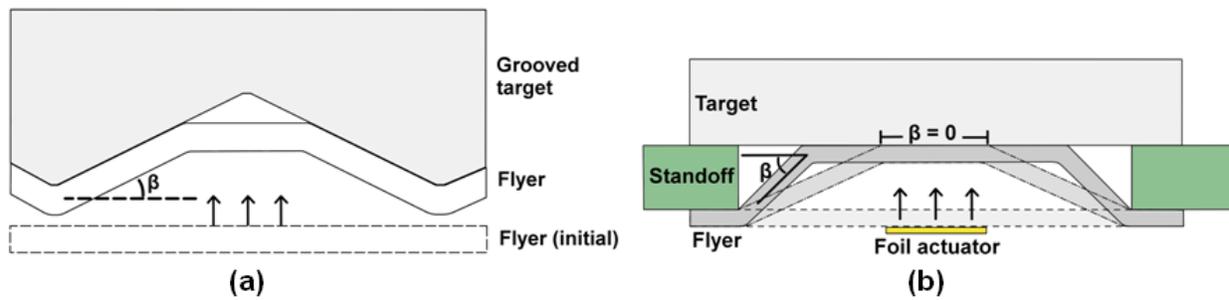
Figure V-72: Schematics of flyer collapse onto (a) grooved target, (b) flat target. It should be noted that the view in (a) is along the width direction of the foil actuator while (b) is a view along the length direction of the foil actuator. β is the dynamic collision angle.
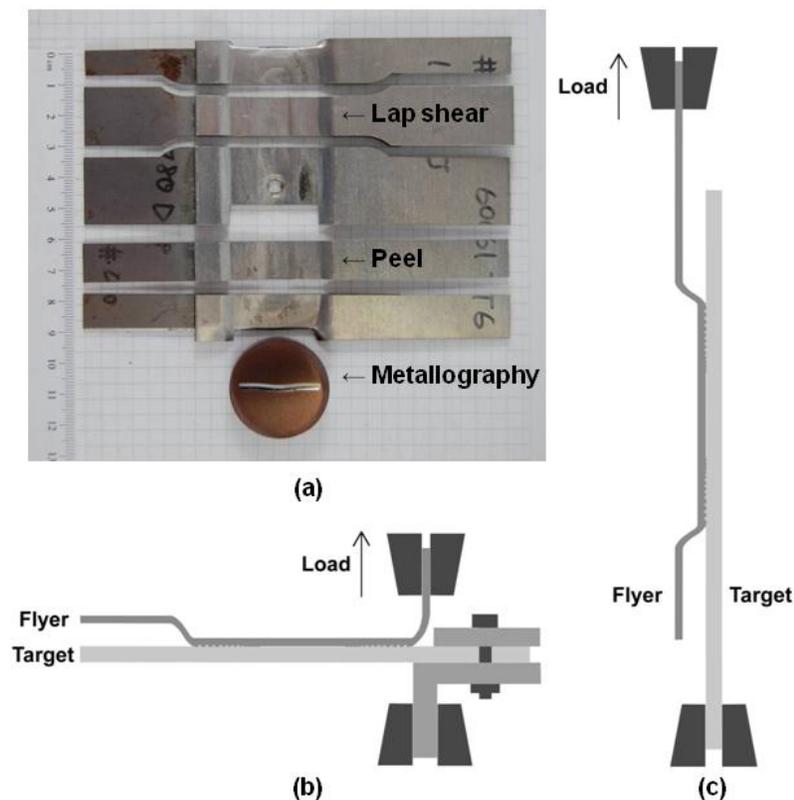
Figure V-73: (a) Sectioned sample for mechanical testing, (b) peel testing setup, (c) lap shear testing setup.

Results and Discussion

Velocity Measurement

Velocity-distance curves for each type of flyer launched during this study are shown in Figure V-74. Figure V-74 shows that the flyer velocity increases with input energy, and the shot-to-shot repeatability is good. In fact, the three traces of the 0.6mm-thick JAC270F flyer obtained at 8 kJ input energy overlap almost perfectly. Although not shown here, increasing the input energy does not always result in a proportional increase in flyer impact velocity. At very high input energy

levels, the electromagnetic interactions between the foil actuator, the backing block, and the flyer plate could substantially deform the flyer plate before foil vaporization, thereby reducing the driving pressure. In any event, driving pressure and impact velocities achieved using this technique are significantly greater than those obtained by magnetic pulse welding, which operates at a similar size scale as VFAW. Because of the ability to reach similar velocities as during explosive welding, VFAW offers the capability to effectively weld a wide range of difficult-to-weld material combinations.
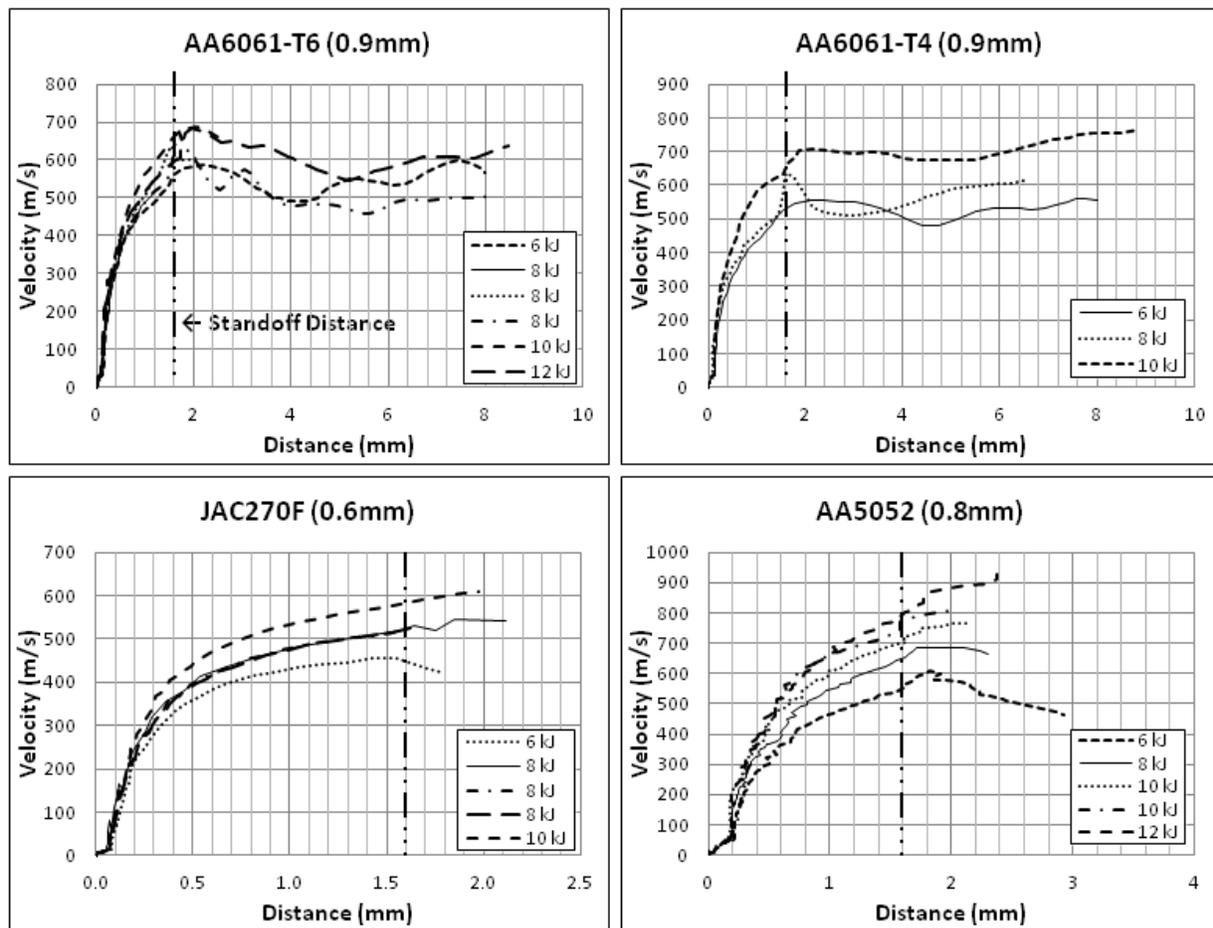
Figure V-74: Velocity vs Distance curves for each flyer material.

Grooved Target

This method was used with six material systems. Figure V-75 shows the variation of interface structure for AM60B/AA6061-T4 weld. Significant differences in amplitude and frequency of the interfacial waves could be observed. Quite a few of the welded sections, especially ones obtained at lower energies, came apart during sample sectioning. The minimum velocity required to obtain a sample with welds that remained intact after the experiment was 640 meters per second (m/s).

Figure V-76 shows typical cross-sections of aluminum/magnesium and aluminum/steel grooved target weldments. While most of the aluminum/magnesium samples came out welded, generally, the aluminum/steel samples had an air-gap between the target and flyer plates. Peeled surfaces of the

aluminum/steel samples depicted significant melting at the interface. Air-rebound, shock heating, and staggered timing of welding in different grooves could have contributed to these weak weldments. Countermeasures, such as introducing a vacuum between flyer and target plates, using an intermediate layer to distribute the energy over two interfaces, and using a slotted target for allowing exit of the compressed air and jetted materials, were implemented. As shown in Figure V-76, these modifications enabled successful welding in the grooved targets. However, they also complicated the simple screening method that was initially envisioned. Also, some material systems welded with flat targets but not with grooved targets. Therefore, after the end of the second quarter, flat target welding was preferred for conducting the screening tests.

Collision velocity, energy / Collision angle	488m/s 4kJ	640 m/s, 6 kJ	660m/s, 7 kJ	787 m/s, 8 kJ	822 m/s, 10 kJ
8°	No weld		**1 mm** Peeled while cutting		
12°	No weld		Peeled while cutting		
16°	No weld		Peeled while cutting		
20°	No weld	Peeled while cutting			
24°	No weld	Peeled while cutting			
28°	No weld	Peeled while cutting			

Figure V-75: AA6061-T4 Flyers (0.8mm thick) impacted with AM60B grooved targets.
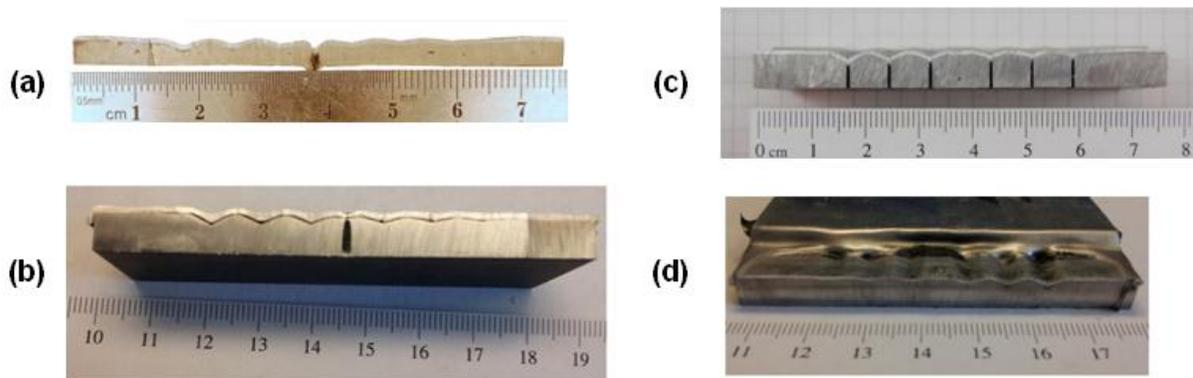
Figure V-76: Grooved target welds with material combinations and experimental conditions: (a) AA6061-T4/AM60B, no vacuum, (b) AA6061-T4/HSLA 656a, no vacuum, (c) AA6061-T4/HSLA656a, slotted target, no vacuum, (d) AA6061-T4HSLA 656, AISI 1018 steel interlayer.

Flat Target

This configuration was implemented for 11 disparate material systems. All of them, barring JAC270F/AM60B, welded successfully. The interfacial morphology of some of those welds is shown in Figure V-77. All the interfaces were wavy, and IMCs (depicted by intermediate contrast), if any, were intermittent in most cases. Some voids could also be seen in the joints made with AZ31B sheets. OSU successfully welded AM60B magnesium alloy to JAC270F steel with an AA3003 aluminum alloy interlayer in between. Figure V-77 also shows, however, that a region where all the layers are continuously welded could not be obtained. By varying the standoff height and input energy, OSU will be continuing the work to join this three-layer system because the interlayer serves the dual purpose of improving weldability and mitigating corrosion between iron and magnesium Besides, welding of galvannealed steel to ultra-high strength steel was accomplished.

Figure V-78 illustrates a typical set of mechanical testing data obtained from peel and lap shear testing of AA6061-T4/JAC270F welded samples. In peel, failure occurred through the weld interface; whereas in lap shear, failure occurred in the JAC270F sheet in a ductile manner. Note that the site of failure in peel testing is in the weld; whereas, the site of failure in lap shear testing occurs where iron (Fe) exists. Table V-10 gives the maximum peel and lap shear loads normalized by sample width. Failure in the base metal occurred more frequently during lap shear testing as compared to peel testing. Lap shear testing could not be conducted on some of the weldments due to initial shape of the samples. Nevertheless, the peel strength of those samples was generally very good, if tested in lap shear mode with failures occurring in the parent materials outside the welded region.

Based on the screening tests conducted in FY 2014 and their relevance to the automotive industry, OSU down selected the following material systems for intensive characterization of failure mechanisms, joining induced defects, and corrosion testing in FY 2015:

- DP780/AA6061-T4
- JAC270F/6061-T4
- AM60B/AA6061-T4
- AZ31B/AA5052
- Boron steel (1.5 gigapascal (GPa))/AA6061T4
- AM60B/AA3003/JAC270F (uncoated).
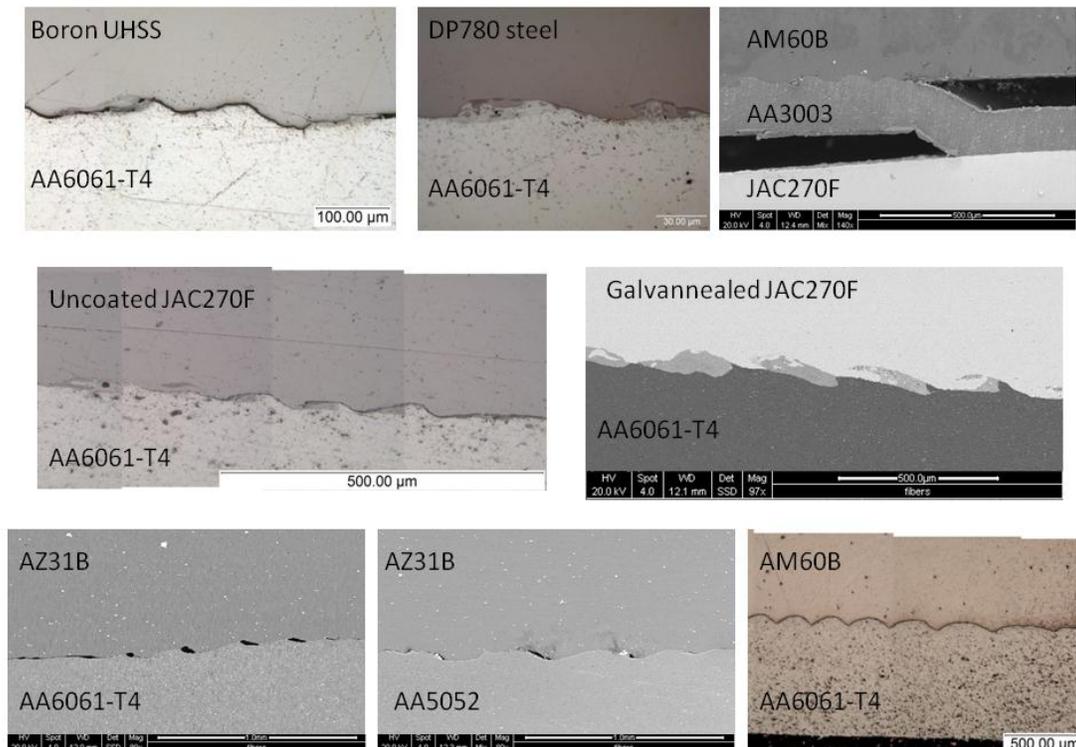
Figure V-77: Scanning electron and optical microscope images of the wavy welded interfaces between dissimilar materials (Note: UHSS is ultra-high strength steel).
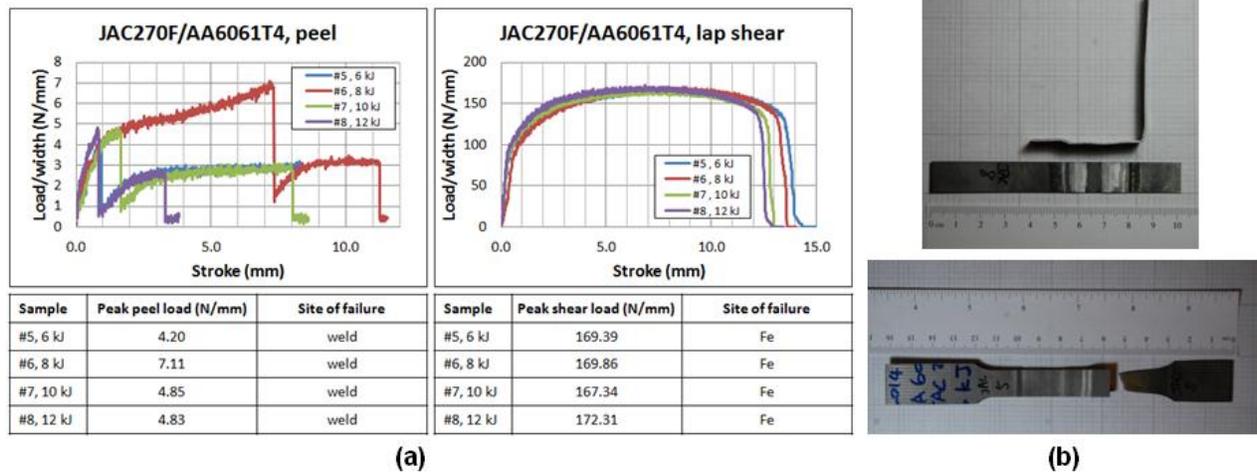
Figure V-78: Mechanical testing data for JAC270F (uncoated)/AA6061-T4 welds: (a) test data, (b) tested samples.

Table V-10: Peel and lap shear strengths of material systems welded in flat-flat configuration.

Material System	Peel		Shear	
	Peak load normalized by width (N/mm)	Location of failure	Peak load normalized by width (N/mm)	Location of failure
DP780/AA6061-T6	12.3	Weld	303.9	Al
DP780/AA6061-T4	33.3	Al	187.4	Al
HSLA 588a/AA6061-T4	39.8	Al	--	--
JAC270F/AA6061T4	>18.6	Weld	98.9	Al
AM60B/AA6061T4	32.5	Weld	--	--
AM60B/AA3003/JAC270F	14.9	Weld	--	--
AZ31B/AA6061T4	8.4	Weld	151.3	Al
AZ31B/JAC270F (uncoated)	--	(split during sectioning)	--	--
AZ31B/AA5052	6.0	Weld	119.7	Mg
JAC270F (uncoated)/AA6061T4	7.1	Weld	169.9	Fe
Boron steel (1.5 GPa)/AA6061T4	48.6	Al	--	--

Technology Transfer Path

While screening tests were the focus for FY 2014, some work was also done to develop methods for creating welds that resemble typical lap and spot welds more closely. The resulting samples from VFAW based lap welding and spot welding are shown in Figure V-79. Additionally, in order to increase cycle frequency and reproducibility of this process, OSU will design an automated system as illustrated in Figure V-79(c). The six-foot tall system with automated material handling and firing systems will be built during FY 2015.

In addition to discussions with Honda Research and Alcoa on material selection and corrosion inhibition strategies, OSU developed a close working relationship with Johnson Controls Inc. (JCI), which is looking to integrate VFAW into their manufacturing process to enable creation of multimaterial, lightweight automotive seating structures.
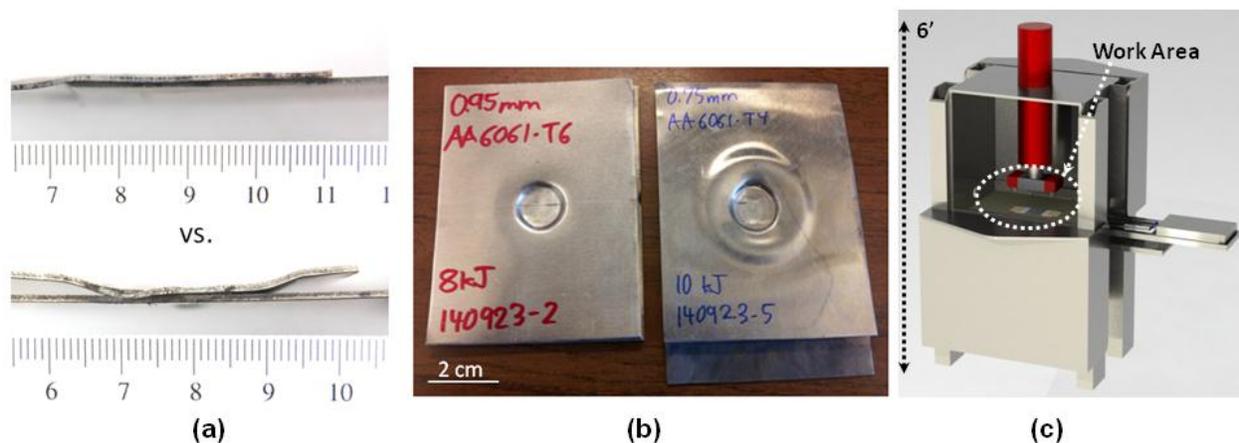
Figure V-79: Efforts toward technology transfer: (a) lap weld without overhangs, (b) spot weld, (c) a schematic of the automated VFAW system.

Conclusion

During FY 2014, VFAW was utilized for screening 17 dissimilar material systems. Two types of screening configurations, grooved target and flat target, were implemented. While grooved target method was found to be not as robust as initially planned, successful welding was accomplished with almost all the material combinations subjected to flat target welding. Welded interfaces had a wavy morphology, and IMCs, if any, were distributed intermittently along the interface. It is encouraging to be able to effectively weld automotive grade aluminum to high strength steel, as well as galvannealed steel. Mechanical testing of the welded samples yielded varied results. Welds were stronger in lap shear mode than in peel mode; in some cases, samples would fail across the weld interface during peel testing but fail outside the weld during lap shear testing. Aluminum/steel welds were generally strong in peel mode, and during testing of some of the combinations, failure even occurred in base metal. With aluminum/magnesium samples, maximum peel strengths as high as 32.5 N/mm and as low as 6 N/mm were obtained. We have selected six systems for making a larger number of prototype welds in FY 2015 in order to study their failure mechanisms and develop corrosion inhibition strategies for them. We have also developed processes for creating lap and spot welds, which will enable faster industrial adaptation of the VFAW technique. With the automated system under development, a future objective will be to create many welds per hour and obtain statistically viable data on the process.

Presentations/Publications/Patents

1. Vivek, A., Hansen, S., Benzing, J., He, M., & Daehn, G.S., (2014) "Impact Welding of Aluminum to Copper and Stainless Steel by Vaporizing Foil Actuator: Effect of Heat Treatment Cycles on Mechanical Properties and Microstructure." *Metallurgical and Materials Transactions A*, pp.1-11.

2. Vivek, A., Daehn, G.S., Liu, B.C., et al., (2014), "Impulse Manufacturing: Multi-material Joining.", presented at *Global Lightweight Vehicle Manufacturing Congress 2014, May 28-29, 2014, Detroit, MI*. http://www.global-lightweight-vehicle-manufacturing-2014.com/

3. Liu, B.C., Vivek, A., Daehn, G.S., (forthcoming 2015). "Use of Vaporizing Foil Actuator for Impact Welding of Aluminum Alloy Sheets with Steel and Magnesium Alloys." *TMS Light Metal*.

4. Vivek, A., Daehn, G.S., (2014),"Welding in Lap and Spot Configurations with Vaporizing Foil Actuator". Provisional patent application, *The Ohio State University*.

References

1. Findik, F., "Recent developments in explosive welding." *Materials & Design, (32*:3), 2011; pp. 1081-1093.

2. Psyk, V., Risch, D., Kinsey, B. L., Tekkaya, A. E., & Kleiner, M., "Electromagnetic forming—A review." *Journal of Materials Processing Technology*, (*211*:5), 2011; pp. 787-829.

3. Vivek, A., Hansen, S. R., Liu, B. C., & Daehn, G. S." Vaporizing foil actuator: a tool for collision welding." *Journal of Materials Processing Technology* (213:12), 2013:pp 2304-2311.

4. Chace, W. and Moore, H., 1959, *Exploding Wires*, 4 vols. Plenum Press.

5. Vivek, A., Liu, B. C., Hansen, S. R., & Daehn, G. S. "Accessing collision welding process window for titanium/copper welds with vaporizing foil actuators and grooved targets." *Journal of Materials Processing Technology*, (214:8), 2014; pp. 1583-1589.

V.7 Vehicle Lightweighting – 40% and 45% Weight Savings Analysis: Technical Cost Modeling for Vehicle Lightweighting – IBIS Associates, Inc.

Anthony Mascarin, Principle Investigator
1601 Trapelo Road, Suite 163
Altham, MA 02451
Phone: (781) 290-0400
E-mail: tony.mascarin.ibis@gmail.com

James Francfort, Project Manager
Idaho National Laboratory
2525 Fremont Avenue
Idaho Falls, ID 83415
Phone: 208-526-6787
E-mail: james.francfort@inl.gov

Carol Schutte, Technology Area Development Manager
U.S. Department of Energy
1000 Independence Avenue, SW
Washington, DC 20585
Phone: (202) 586-1022
E-mail: carol.schutte@ee.doe.gov

Ed Owens, Technology Area Development Manager
U.S. Department of Energy
1000 Independence Avenue, SW
Washington, DC 20585-0340
Phone: (202) 586-4830; Fax: (202) 856-2476
E-mail: Edwin.Owens@ee.doe.gov

Contractor: IBIS Associates, Inc.
Contract No.: ID14517

Abstract/Executive Summary

The U.S. Department of Energy's (DOE's) Vehicle Technologies Office (VTO) commissioned this study to model and assess the technical feasibility and manufacturing economics of alternative design and production strategies for a series of lightweight vehicle design concepts. The strategic targets were a 40% and a 45% overall vehicle weight reduction relative to a standard North American midsize passenger sedan at an effective price of $3.42 per pound (lb) saved. The baseline vehicle was representative of a typical midsize passenger car. System- and component-level mass/cost breakdowns and lightweighting strategies from several engineering and cost study sources were used. This

effort's goal was to determine the technical viability of 40% and 45% weight reduction, and the economic conditions required to meet the stated mass reduction and price target. The target baseline was a mainstream vehicle; however, the analysis also explored what is potentially possible with current and developmental lightweight strategies without the constraints of previously-invested capital, material/supply relationships, platform commonality, market preferences of ever-increasing power and luxury, and other business pressures. The analysis' ultimate purpose was to assess the technical viability and cost effectiveness of achieving aggressive weight reduction. This foundation dictated several important underlying assumptions that must be considered in context with the resulting cost comparisons:

- Full detail of functionally equivalent, crashworthy designs is not available for many of the proposed advanced concepts. The analysis results are therefore speculative and most likely represent a best possible case scenario.
- Costing was performed in regard to fully implemented, high-volume processes, with automation and expected learning curve improvements, not as current developmental or low-volume introductory practices.
- The economic comparison was made in terms of the original equipment manufacturers' (OEM) direct manufacturing cost per vehicle. Most subsystems, therefore, included the margins of one or more supplier levels that would be included in the OEM purchase cost. Those systems manufactured by the OEM include costs of tooling, production capital, energy, direct and indirect manufacturing labor, and material. Engineering; selling, general, and administrative costs; profit; and dealer margins were not included at this level.

Through the use of established technologies, state-of-the-art designs, and some level of power and luxury downsizing (if accepted by the market), mass reduction on the order of 30% can be achieved with a moderate price premium and relatively low technical risk.

Four design concept scenarios that closely follow the major industry design directions were evaluated, including: 1) Optimized Steel, 2) Aluminum-Intensive, 3) Multi-Material, and 4) Carbon Fiber Composite-Intensive. Four intermediate stages for each scenario were evaluated to understand the incremental costs along the paths to these targets. The analysis indicates that a 37 - 45% reduction in a standard midsized vehicle is within reach IF carbon fiber composite materials and manufacturing processes are available, and IF customers will accept a reduction in vehicle features and content, as demonstrated with Multi-Materials and Carbon

Fiber Composite – Intensive vehicle scenarios. The analysis also concluded:

- Achieving this level of mass reduction at the target price of $3.42 per pound saved is only possible with significant improvements in carbon fiber processing technologies and a reduction in the carbon fiber price itself.
- Achieving 40% mass reduction will require a significant amount of advanced lightweighting involving both moderate technical risk for high-volume production (magnesium) and high-technical-risk processes (automated and rapid-cycle-time composite forming). The price premium will remain very high until high-volume, low-cost carbon fiber is available.
- Mass reduction of 45% or more will require not only extensive use of lightweight materials such as carbon fiber and magnesium but also next-generation electrical and interior systems. The goal could be more readily achieved if there were significant changes in market expectations of performance, comfort, and features.

Continued exploration of lightweighting technologies will identify the best course forward in terms of optimizing the amount of mass reduced relative to the price premium.

Accomplishments

- Completed a comprehensive compilation of industry knowledge of vehicle mass reduction techniques and approaches from a literature review of relevant previous work, interviews (researchers, vehicle manufacturers, and supplier engineers/designers), published vehicle specification data, and IBIS Associates, Inc. (IBIS) databases and previous cost analyses. (FY 2013)
- Developed a Technical Cost Model to analytically evaluate the weight reduction performance and cost effectiveness of four weight reduction scenarios down to the component level. From this analysis, determined the technology paths for reaching the vehicle weight reduction targets of 40% and 45%. The cost-effectiveness of each option was determined and technology gaps for realistically meeting these goals were defined. (FY 2013)
- Determined that through the use of established technologies, state-of-the-art designs, and some level of power and luxury downsizing, if accepted by the market, mass reduction on the order of 30% can be achieved with a moderate price premium and relatively low technical risk. (FY 2013)
- A significant amount of advanced lightweighting would be required for 40% mass reduction. The lightweighting would include both high-volume production (magnesium), which involves moderate technical risk, and automated and rapid cycle time composite forming, which involves high technical risk. The cost premium will remain very high until high-volume, low-cost carbon fiber is available. Achieving this will require a 90% reduction in direct processing costs and the price of carbon fiber would have to drop by 52% from $12.50/lb in the baseline analysis to $6.00/lb. (FY 2013)

- Determined that achieving a weight reduction of 45% or more will require extensive use of lightweight materials, such as carbon fiber and magnesium, but also next-generation electrical and interior systems. To achieve this, the carbon fiber price would have to be further reduced by 30% to $4.20/lb because of the greater amount of carbon composites used and the expensive strategies needed to achieve additional weight savings. (FY 2013)

Future Directions

- Future analysis will target developing a meaningful lightweighting solution cost spectrum.
- Develop an understanding of the most cost-effective approach(s) to a given level of mass savings over a broad range of weight reduction targets up to 40%.
- Analysis and assessment of cost reduction potential for critical advanced lightweighting technologies including carbon fiber processing, raw carbon fiber materials, glass fiber composites, and magnesium processing cost reduction.
- Explore key processing variables for the proposed manufacturing concepts and help define the technology development goals that are critical to cost-effective lightweighting strategies.

Technology Assessment

- Target: Achieving the target 40% and 45% mass reduction at the target price of $3.42 per pound saved
- Gap: Reaching 40% and 45% weight reduction targets are reliant on carbon fiber component costs. Reaching the targets require increasingly more significant improvements in: 1) carbon fiber processing technologies, and 2) carbon fiber price also has to be significantly reduced (52% and 66%).

❖   ❖   ❖   ❖   ❖

Introduction

The project's purpose was to develop a technical cost model to assess the manufacturing economics of alternative design and production strategies for a series of lightweight vehicle concepts being developed in the industry. The project goal was to understand the technical viability of meeting 40% and 45% weight reduction targets relative to a standard North American midsize passenger sedan, as well as the economic conditions required to meet a $3.42/lb saved price target. This figure was determined using a simple payback model, which calculated weight reduction's effect on fuel consumption throughout the entire (15-year, 150,000 mile) vehicle life. The U.S. Energy Information Administration Annual Energy Outlook 2011 High Oil Price case (projected fuel price data out to 2025) was used to estimate fuel price. [1]

Although the target baseline is a mainstream passenger vehicle, the analysis explored what is potentially possible with

V.7. Vehicle Lightweighting – 40% and 45% Weight Savings Analysis:
Technical Cost Modeling for Vehicle Lightweighting – IBIS Associates, Inc.

Mascarin–IBIS

current and developmental lightweight strategies without the constraints of previously invested capital, material supply relationships, platform commonality, market preferences of ever-increasing power and luxury, and other business pressures. The ultimate purpose of the analysis was to assess the technical viability of achieving aggressive weight reduction.

This foundation dictated several important assumptions (summarized below) underlying the economic analysis that were considered in context with the resulting cost comparisons.

Full detail of functionally-equivalent, crashworthy designs are not available for many proposed advanced concepts. The analysis results are therefore speculative and most likely represent a best-possible-case scenario. Real-world application of these concepts may involve additional processing, performance, comfort, safety, and corrosion measures that are not fully understood at this time.

Costing was performed in regard to fully implemented, high-volume processes, with automation and expected learning curve improvements, not as current developmental or low-volume introductory practices.

Economic comparison was made in terms of the OEMs' direct manufacturing cost per vehicle. Most subsystems, therefore, included the margins of one or more supplier levels that would be included in the OEM purchase cost. Those systems manufactured by the OEM, such as engines and body structures, did include costs of tooling, production capital, energy, direct and indirect manufacturing labor, and material. [2] [3] Engineering; selling, general, and administrative costs; profit; and dealer margins were not included at this level.

Approach

The focus of the current lightweighting analysis program is a standard North American midsize passenger sedan (e.g., Chevrolet Malibu, Chrysler 200, Ford Fusion, and Honda Accord). The baseline vehicle is intended to be a generic representation of this vehicle class and is based on an amalgam of the specifications of these cars with a target mass matching the Environmental Protection Agency (EPA) test mass for a 2012 midsize vehicle. The mass was 3,603 lb, which includes 300 lb added occupant/cargo equivalent on top of a 3,304 lb curb weight. Descriptive information on current component designs for the baseline vehicle was provided by DOE and the Ford/Vehma Multi-Material Lightweight Vehicle (MMLV) team. [4] This information served as a starting point from which to collect additional data and develop a generic midsize vehicle description from available public information.

A compilation of knowledge was performed including a literature review of relevant previous work, interviews, published vehicle specification data, and IBIS databases and previous cost analyses. Previous published studies included: Ford/Vehma Fusion breakdown data [5], Ford/Vehma MMLV Mach 1 and 2 data [6], Lotus Phase 1 lightweighting [7], FEV,

Inc. (FEV) light-duty mass reduction cost analysis [8], Aluminum Association Body-in-White (BIW) studies [9 - 11], Honda study and report on an National Highway Traffic Safety Administration (NHTSA) study [12], and United States Council for Automotive Research (USCAR) United States Automotive Materials Partnership LLC's Automotive Composites Consortium (ACC) lightweighting studies. [13 – 15]

The study results from the two most robust total vehicle lightweighting exercises with published material found to date: the EPA-sponsored FEV report [8] and the DOE-sponsored Ford/Vehma MMLV program [5] [6] were analyzed and compared to determine the mass savings and cost performance. The analysis was done down to the system level using the following categories: 1) body (body-in-white and panels, bumpers, body hardware, glazings, and exterior trim), 2) powertrain (engine lightweight materials and downsizing, fuel storage, transmission, driveline and axles, cradle, and exhaust), 3) chassis (suspension, brakes, wheels, tires, and steering), 4) interior (instrument panel, trim, and seating and restraints)

Using the published literature study, industry interview, third-party lightweighting study analysis results, four vehicle lightweighting scenarios were developed that the research team felt had the potential to achieve the target 40% mass reduction relative to a conventional midsize passenger car. Each scenario, built around a common body structure architecture, was addressed in the developer concept model. The four scenarios were:

Optimized Steel – This scenario was built around the body structure developed by Lotus Engineering and refined by FEV/EDAG for the EPA study [8] [11]. The body structure utilized high-strength steels and part count reduction to reduce mass. Additionally, FEV-projected savings for the body, powertrain, chassis, interior, and electrical system were included in this scenario.

Aluminum-Intensive – This scenario was assessed based on application of the mass savings of a nearly all-aluminum body structure to the baseline vehicle [9 - 11]. In addition to the body-in-white, the cradle, bumpers, and wheels were also aluminum. Secondary powertrain and chassis weight savings were also taken into account.

Multi-Material – This scenario applied the savings for each of the mass reduction technologies known to have been applied in the Ford/Vehma MMLV Mach 1. [5] [6]

Carbon Fiber Composite-Intensive – This scenario started with the multi-material scenario and applied carbon fiber for all body, panels, bumpers, and suspension components. This scenario is less robust in terms of providing a functionally equivalent design to a mass-produced midsize passenger vehicle than the other scenarios. However, carbon fiber composites potentially offer the greatest level of weight savings, making its assessment important in evaluating the feasibility of achieving the DOE's most aggressive mass reduction targets. [16]

Results and Discussion

Each concept was assessed and compared to each other first in terms of mass reduction performance and then in terms of direct manufacturing cost. The 40% vehicle mass reduction target effort was followed by a similar effort to determine the technical feasibility of cost-effectively achieving a 45% vehicle mass reduction. While traditional vehicle lightweighting designs start with weight targets in mind and focus on a holistic redesign of the vehicle, this study utilized a 4 stage progression for performing this exercise. This methodology was utilized as a way to better assimilate all the data from several independent studies [17] [18] previously performed to explicitly quantify 1) weight savings contribution of specific lightweighting strategies and, 2) the associated costs of each, both within the framework of an aggregate vehicle concept. It is not intended to suggest that the intermediate "stages" would be a design endpoint for a concept or represent the actual sequence of technology adoption by manufacturers. In Stage 1, the body-in-white and panel mass were reduced. Stage 2 added the powertrain and chassis weight savings strategies. Stage 3 further applied reduced-weight interior systems (e.g., instrument panel, trim, door modules, and seating). In Stage 4, the concept offering the greatest weight reduction for each system is applied and additional secondary mass reductions were taken into account. In addition, where appropriate, powertrain and chassis systems were downsized according to the reduced overall vehicle mass to maintain the same overall vehicle performance. Figure V-80 shows an example of the

mass savings potential at the component level for the Stage 4 Multi-Material scenario compared to the baseline case. Identical analyses were done for all four scenarios. Figure V-81 summarizes the predicted total vehicle with system-level mass breakdown for each evaluated scenario.

The vehicle mass and manufacturing costs breakdown follows the same subsystem list as established in earlier DOE cost analyses. Technical cost models of the manufacturing and assembly processes were then employed where reported costs or projections for a given component in the data collection were not available. Technical cost modeling performed by IBIS addresses process costs by performing dynamic economic simulations of manufacturing processes. In this approach, the process starts with a user-defined manufacturing scenario in terms of component geometry, production volume, and accounting assumptions. The models then assess equipment, tooling, and building capital requirements based on definitions of individual components and process parameters. Variable costs in terms of material, labor, and energy are calculated based on component geometry, scrap [19] [20] and yield losses, process rates, and equipment usage. Manufacturing overhead labor, maintenance cost, and the interest cost of investments and working capital are also included. This dynamic approach is particularly useful for exploring cost sensitivities, such as production rate and yield, as well as for understanding the equipment and tooling implications of material and design differences and for making projections of conceptual or developmental processes.
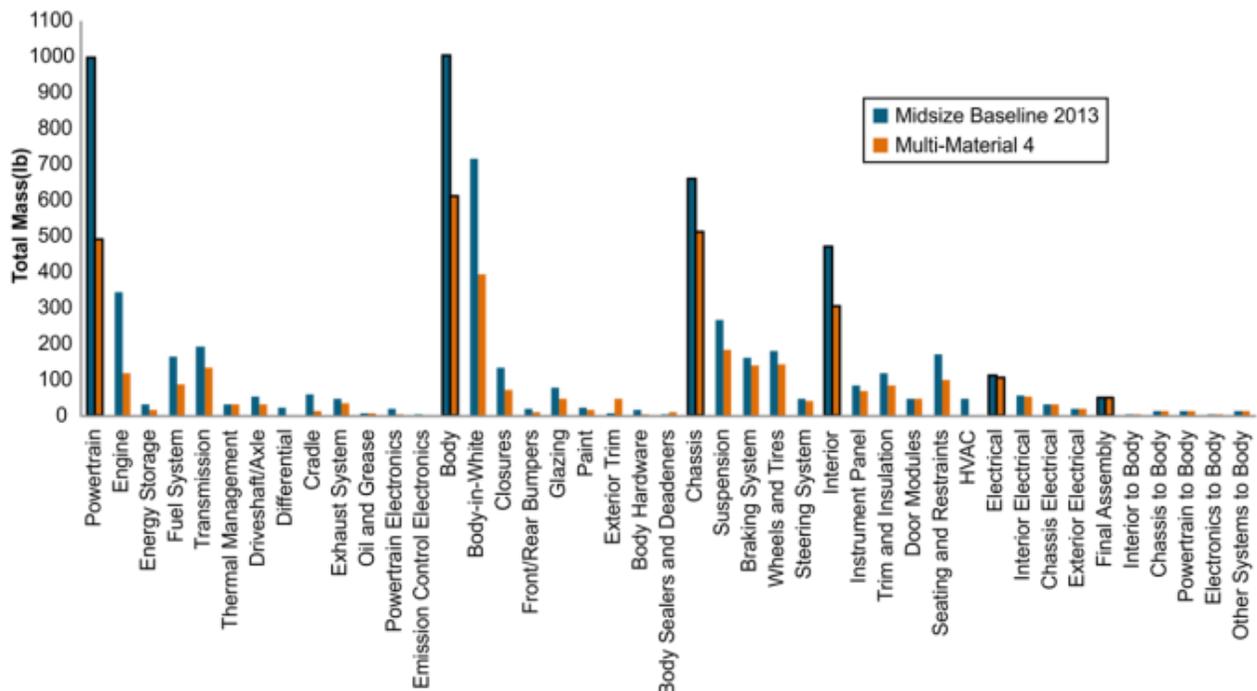
Figure V-80: Baseline to Stage 4 Mass Reduction.

V.7. Vehicle Lightweighting – 40% and 45% Weight Savings Analysis:
Technical Cost Modeling for Vehicle Lightweighting – IBIS Associates, Inc.

Mascarin–IBIS
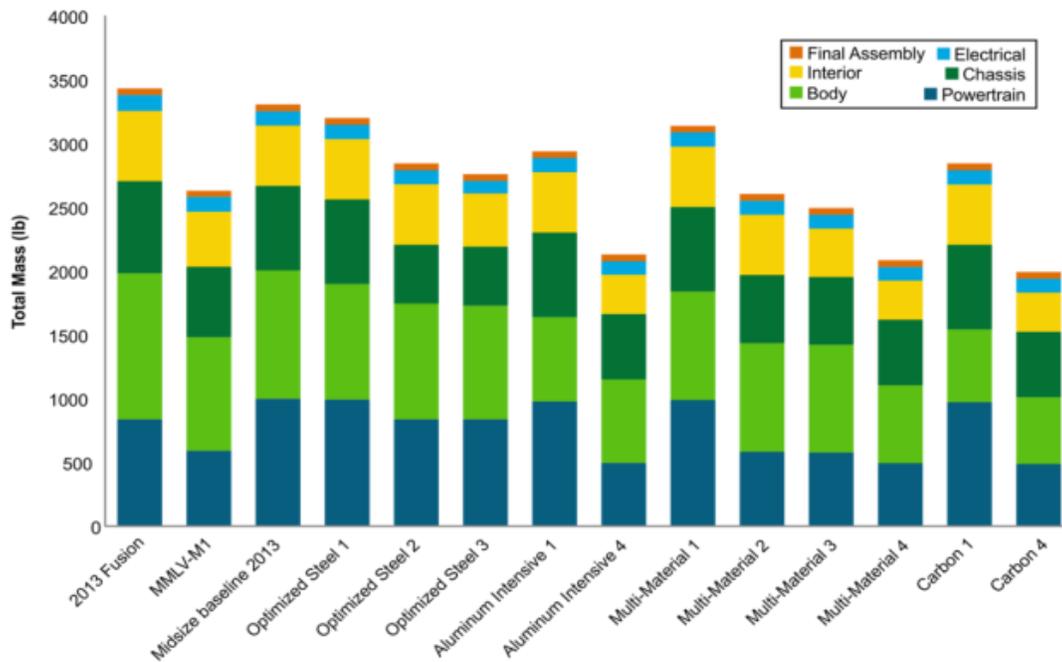
Figure V-81: Scenario Mass Comparison with System-Level Breakdown.

Vehicle production was addressed under five system groups and more than 30 subsystems, plus assembly operations. In total more than 60 mass and cost line items were addressed. Individual case studies were conducted for each scenario and lightweighting stage using the vehicle lightweighting technical cost model to perform a holistic vehicle analysis of mass and cost. Each case was compared to the vehicle baseline to determine the overall mass reduction and total vehicle cost, and therefore the cost of weight savings. Two scenarios for carbon fiber were developed using, respectively, current (Figure V-82) and projected (Figure V-83) carbon processing costs.
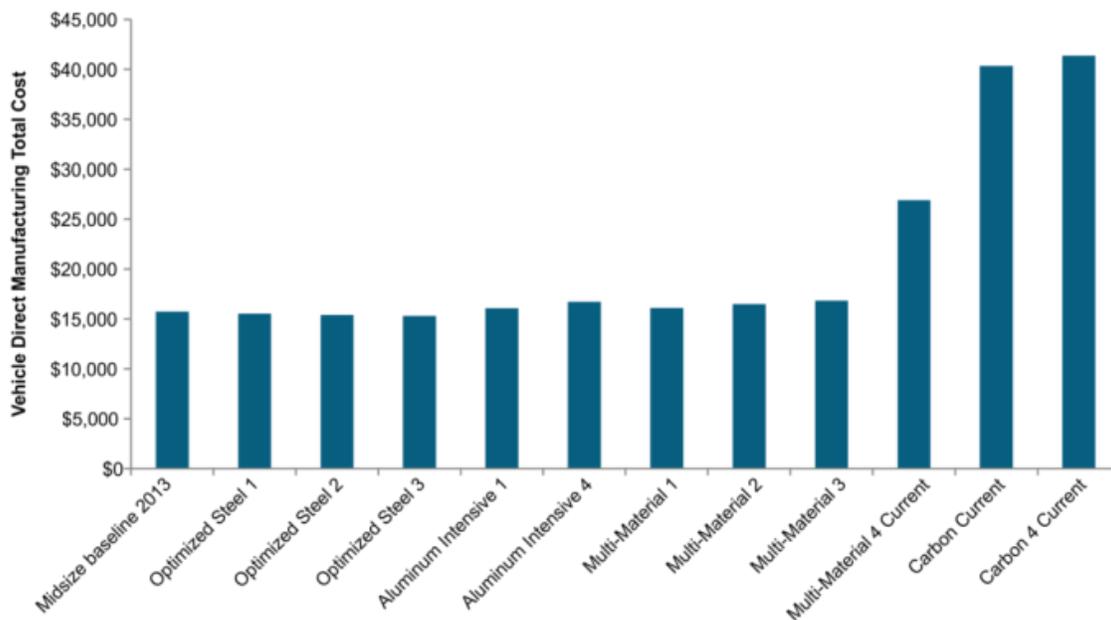
Figure V-82: Scenario Cost Comparison (current carbon processing cost).
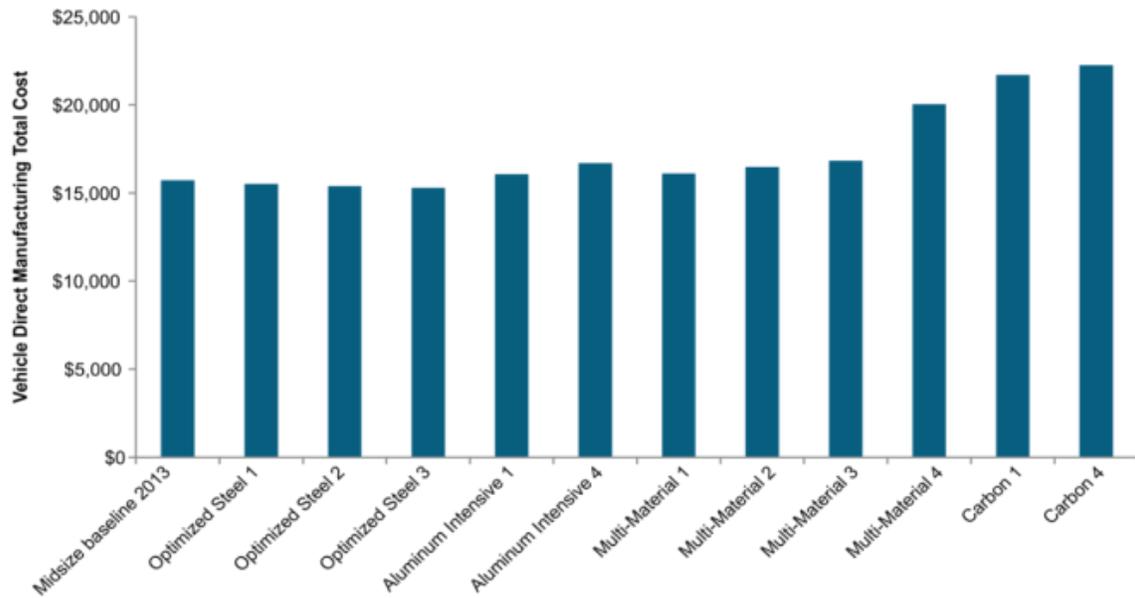
Figure V-83: Scenario Cost Comparison (projected carbon processing cost).

Only the Carbon Fiber Composite-Intensive Stage 4 scenario had the potential to meet the 40% mass reduction target, so this was the only option that was examined further (Figure V-84). The bulk of the mass reduction is from the carbon fiber BIW (~400 lb) and the downsized engine and suspension system (225 lb) that this enables. The direct

manufacturing cost (Figure V-85) and resulting cost effectiveness of the mass savings were also determined (Figure V-86). Positive value results represent a cost premium, while negative value results represent a cost savings.
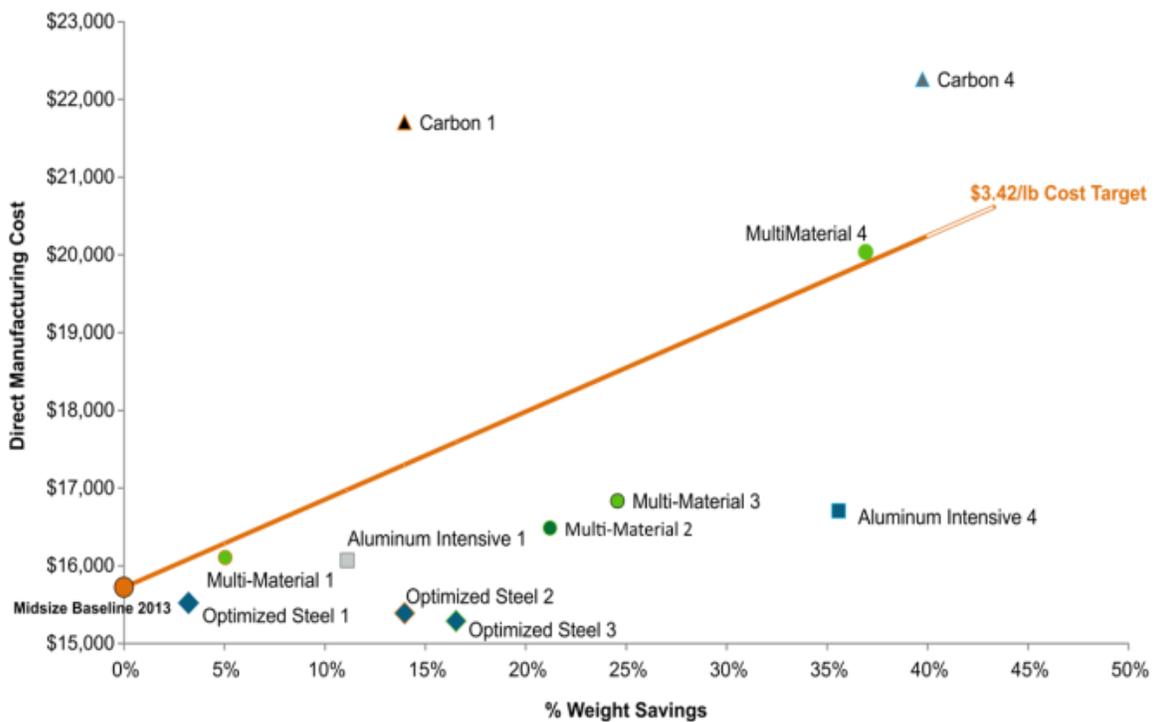
Figure V-84: Mass Reduction Relative to Vehicle Cost.

V.7. Vehicle Lightweighting – 40% and 45% Weight Savings Analysis:
Technical Cost Modeling for Vehicle Lightweighting – IBIS Associates, Inc.

Mascarin–IBIS
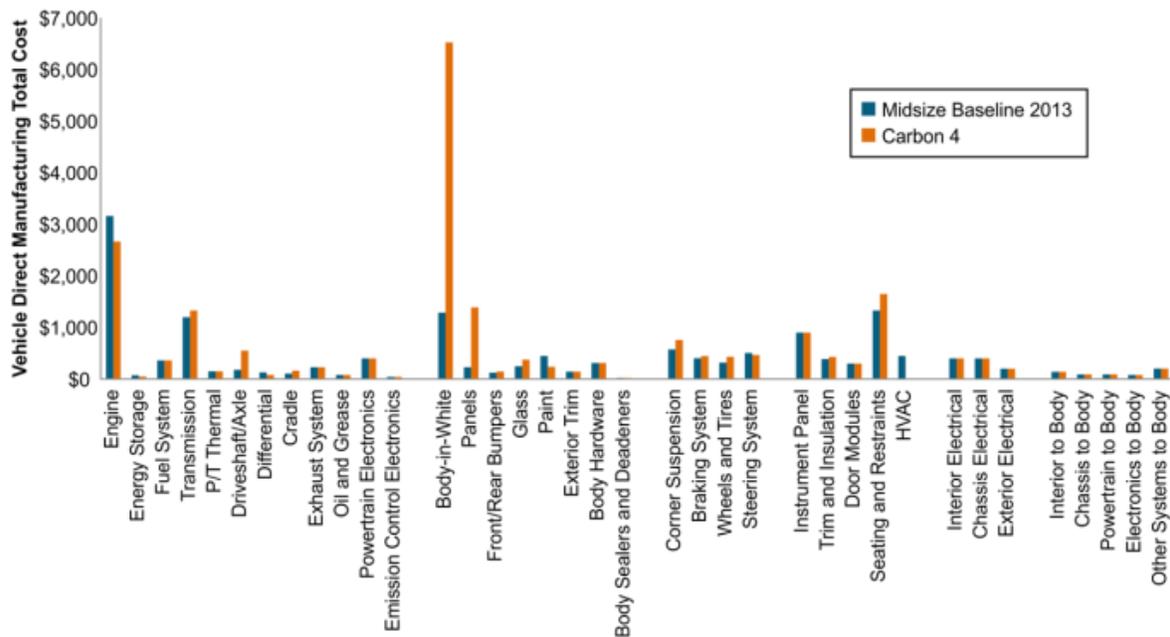
Figure V-85: Carbon Fiber Composite-Intensive Scenario Stage 4 – Direct Manufacturing Cost Relative to Baseline by System.
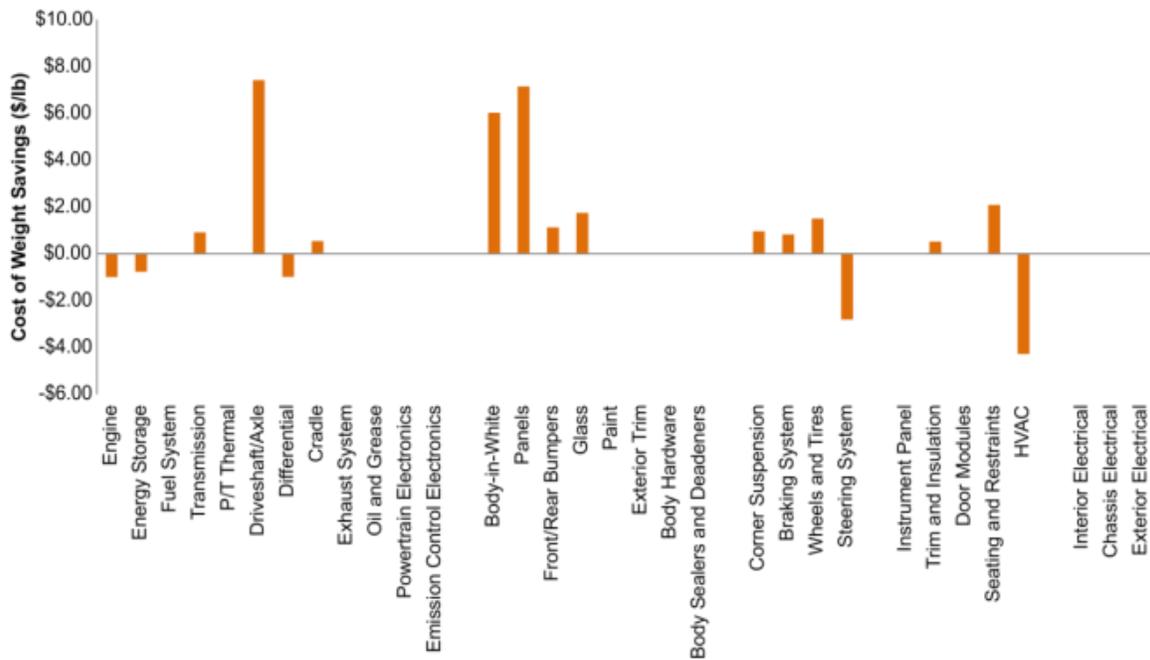
Figure V-86: Carbon Fiber Composite-Intensive Scenario Stage 4 – Direct Manufacturing Cost of Mass Reduction by System.

To meet the target $3.42 per pound saved, the $6,528 body-in-white cost would have to be further reduced to $4,281 (a 34% decrease). The most likely path for this further reduction would be from a reduction in the carbon fiber price itself. [21] [22] The analysis showed that carbon fiber price would have to drop from $12.50/lb in the baseline analysis to $6.00/lb.

The second project phase was to assess the technical feasibility and cost effectiveness of reaching a 45% weight reduction relative to the baseline vehicle. The Carbon Fiber

Intensive vehicle scenario, Stage 4 (i.e., "Carbon 4"), served as the starting point to explore additional mass and cost-saving strategies to further reduce the vehicle mass by an additional 165 lb to reach the 1,817 lb vehicle weight target. Meeting this mass reduction at the $3.42-per-pound-saved price target would result in a direct manufactured vehicle cost of only $20,809; well below the cost of the less aggressive 40% mass reduction target results, even under optimal projected process economics at current market conditions. The analysis pursued an approach similar to that for the 40% reduction targets in terms of identifying potential strategies for further weight savings and then assessing material pricing conditions required to achieve the cost-of-weight-savings target. To achieve the more aggressive 45% reduced weight goal, additional speculative technologies were considered, including: magnesium (extruded bumpers, body hardware, brake calipers, steering wheel and column housing, and the instrument panel beam), carbon fiber wheels, long fiber polypropylene composite door modules, carbon ceramic brake disks, lightweight tires, lithium-ion starter batteries, and an in-vehicle network to replace the conventional wiring harness. The largest weight savings came from the chassis, body, and the downsized powertrain.

The carbon fiber BIW is the largest contributor to the weight savings and vehicle cost. The BIW, panels, and wheels are all based on carbon fiber usage and are all disproportionately expensive relative to the baseline compared to other subsystems employing other weight-saving strategies. Reaching the target price for 45% weight savings ($20,829) requires that the Stage 5 Carbon Fiber Composite-Intensive scenario reduce overall vehicle cost by nearly $4,400. The analysis showed that carbon fiber price would have to drop further from $12.50/lb in the baseline analysis to $4.20/lb to meet the $3.42/lb target price of the weight savings.

Technology Transfer Path

The analysis performed for, and the conclusions drawn from, this study inform the U.S. DOE Vehicle Technologies Office's Lightweight Materials Program of the opportunities, barriers, and technical gaps for applying significant lightweighting to mainstream light-duty vehicles. The technical and economic conclusions are intended to guide the DOE's definition for future vehicle lightweighting goals to retarget them to enable the largest, most cost-effective fleetwide petroleum fuel savings that is possible.

Conclusion

From examining the broad picture of multiple technologies covering a broad range of potential weight savings, cost premiums, and technology readiness, the following conclusions were drawn.

- Achieving 40-45% mass reduction at the target price of $3.42 per pound saved is only possible with significant

improvements in processing technologies and a reduction in the carbon fiber price itself.

- A significant amount of advanced lightweighting would be required for 40% mass reduction. The lightweighting would include both high-volume production (magnesium), which involves moderate technical risk, and automated and rapid cycle time composite forming, which involves high technical risk. The cost premium will remain very high until high-volume, low-cost carbon fiber is available.

- Mass reduction of 45% or more will require not only extensive use of lightweight materials, such as carbon fiber and magnesium, but also next-generation electrical and interior systems. The goal could be more readily achieved if there were significant changes in market expectations of performance, comfort, and features.

- Through the use of established technologies, state-of-the-art designs, and some level of power and luxury downsizing, if accepted by the market, mass reduction on the order of 30% can be achieved with a moderate price premium and relatively low technical risk.

References

1. U.S. Energy Information Administration Annual Energy, U.S. Annual Energy Outlook 2011. 2011.

2. Edmunds.Com. [Online] December 2013. http://www.edmunds.com.

3. Wards Automotive 2013 Yearbook. s.l. : Wards Auto, 2013.

4. Department of Energy Vehicle Technologies Office, Draft Midsize 2013 Baseline for Ford/Vehma MMLV Program. s.l. , 2013.

5. Skszek, T. and Conklin, J. *Multi-Material Lightweight Prototype Vehicles Demonstration.* s.l. : U.S. Department of Energy, National Energy Technology Laboratory, 2013. Progress Report on Award DE-EE0005574.

6. Skszek, T. and Zaluzec, M., *Demonstration Project for a Multi-Material Lightweight Prototype Vehicle - Vehma International of America, Inc.*. s.l. : U.S. Department of Energy, 2012. DOE VTO April 2012.

7. Lotus Engineering Inc*. An Assessment of Mass Reduction Opportunities for a 2017-2020 Model Year Vehicle Program.* s.l. : International Council on Clean Transportation, 2010.

8. FEV. *Light-Duty Vehicle Mass Reduction and Cost Analysis - Midsize Crossover Utility Vehicle.* Washington, DC : U.S. Environmental Protection Agency, 2012. EPA-420-R-12-026.

9. IBIS Associates, Inc. *Advantages of Automotive Aluminum and Advanced Powertrains.* s.l. : The Aluminum Association, 2008.

10. Summe, Todd; "Aluminum Vehicle Structure - Manufacturing and Lifecycle Cost Analysis." The Aluminum Association, 2005.

V.7. Vehicle Lightweighting – 40% and 45% Weight Savings Analysis:
Technical Cost Modeling for Vehicle Lightweighting – IBIS Associates, Inc.

Mascarin–IBIS

11. EDAG**.** *Venza Aluminum BIW Concept Study.* s.l. : The Aluminum Association, April 2013.

12. NHTSA. Corporate Average Fuel Economy for MY 2012-MY2016 Passenger Cars and Light Trucks Final Regulatory Impact Analysis. Washington, DC : s.n., 2010.

13. Honda. *Honda's Study and Report on the Study Commissioned by NHTSA: 'Mass Reduction for Light-Duty Vehicles for Model Years 2017--2025,' DTNH22-11-C-00193.* s.l. : NHTSA Mass-Size-Safety Workshop, 2013. Public Presentation.

14. United States Automotive Materials Partnership LLC**.** *Final Report Compilation: Cooperative Agreement DE-FC26-02OR22910 Projects from January 1, 2002 through January 31, 2011.* Southfield, MI : USAMP, April 2011.

15. United States Automotive Materials Partnership. *Magnesium Vision 2020: A North American Automotive Strategic Vision for Magnesium.* s.l. : United States Council for Automotive Research, 2006.

16. Vehicle Technologies Office. *Workshop Report: Light Duty Vehicles Material Technical Requirements and Gaps.* s.l. : U.S. Department of Energy, August 2012.

17. IBIS Associates, Inc. Technical Cost Model Analysis for a Structural Composite Underbody, Supporting USCAR – ACC Composite Underbody Program. s.l. : United States Consortium for Automotive Research, 2010.

18. IBIS Associates, Inc. Internal Proprietary Data. Concord, Massachusetts : s.n., 2014.

19. Vehicle Survivability and Travel Mileage Schedules. Washington, DC : NHTSA, 2006.

20. Transportation Energy Databook. Table 3.12 : Oak Ridge National Laboratory, 2014.

21. Warren, C. David**.** *Lightweighting Composites and Lower Cost Carbon Fiber.* s.l. : U.S. Department of Energy, Oak Ridge National Laboratory, March 2013.

22. Berger, Ludwig**.** Cheaper carbon fibre will slash auto making costs-manufacturer. *www.reuters.com.* [Online] March 28, 2014. quoting SGL's Hubert Jaeger. http://www.reuters.com/article/2014/03/28/sgl-fibres-idUSL5N0MP2RP20140328.

V 8.   Safety Data and Analysis – Lawrence Berkeley National Laboratory

Tom Wenzel, Principal Investigator
Lawrence Berkeley National Laboratory
1 Cyclotron Road, 90R4000
Berkeley, CA 94720
Phone: (510) 486-5753
E-mail: TPWenzel@lbl.gov

Carol Schutte, Technology Area Development Manager
U.S. Department of Energy
1000 Independence Avenue, SW
Washington, DC 20585
Phone: (202) 586-1022
E-mail: carol.schutte@ee.doe.gov

Ed Owens, Technology Area Development Manager
U.S. Department of Energy
1000 Independence Avenue, SW
Washington, DC 20585-0340
Phone: (202) 586-4830; Fax: (202) 856-2476
E-mail: Edwin.Owens@ee.doe.gov

Contractor: Lawrence Berkeley National Laboratory (LBNL)
Contract No.: DE-AC02-05CH11231

Abstract/Executive Summary

In FY 2014 LBNL compiled its previous analyses into a report on the sensitivity of light-duty vehicle crash frequency per vehicle mile of travel (VMT) to additional vehicle and driver variables. In addition LBNL conducted an analysis of the sensitivity of the 2012 results on the relationship between mass reduction and societal fatality risk per VMT to the definition of "lighter" vs. "heavier" vehicles. We participated in monthly conference calls of the inter-agency team studying the historical relationship of vehicle mass and risk using recent data. Coordination with the team was necessary to prepare for an update of the 2012 study to cover model year 2003 to 2010 vehicles between calendar years 2005 and 2011, to be included in the mid-term review of the 2017-25 fuel economy/carbon dioxide (CO_2) emission standards. Finally, trends in vehicle miles of travel, both at the state level, using national data, and for individual vehicles and households, using odometer readings and vehicle registration data over several years in California and Texas, were analyzed to begin estimating what effect recent changes in gasoline prices and economic conditions have had on vehicle miles of travel. This analysis will include examination of trends in police-reported crashes over time in 18 states to better understand what

vehicles and drivers may have reduced their travel in response to changing fuel prices and economic conditions.

Accomplishments

- Participated in monthly discussions by the interagency working group (Department of Energy (DOE), National Highway Traffic Safety Administration (NHTSA), and the Environmental Protection Agency (EPA)) on upcoming research on the relationship between vehicle weight/size and safety, in support of federal agency rulemakings on fuel economy/greenhouse gas emission standards for new light-duty vehicles.
- Compiled previous research into a draft report on the sensitivity of the estimated effect of mass reduction on crash frequency to several additional vehicle and driver characteristics. The additional variables included handling and braking capability by vehicle model from Consumer Reports road tests; initial vehicle purchase price and vehicle manufacturer; average household income and "bad driver" rating by vehicle model; and whether the driver was using alcohol or drugs or was properly restrained.
- Conducted a new analysis of the sensitivity of the 2012 estimates of the effect of mass reduction on societal fatality risk to the definition of "light" vs. "heavy" cars and light trucks. The analysis found that the estimated effect of mass reduction on societal fatality risk per VMT did not consistently decrease as vehicle weight increased. A draft report was prepared and circulated to the interagency team.
- Used national data to analyze trends in state-level vehicle registrations, gasoline use, and miles of travel to better understand the leveling off of national VMT growth beginning in 2004.
- Began analyzing seven years of vehicle odometer and registration data from California and Texas to assess how changing gasoline prices and economic conditions have influenced consumer vehicle purchase decisions and vehicle use, by household.

Future Directions

- Continue participating with the interagency working group on the statistical analysis of the relationship between vehicle mass or footprint and societal fatality risk per VMT, crash frequency per VMT, and societal fatality risk per crash. The working group will update the 2012 analysis to calendar years 2005 to 2011 for the midterm review of the 2017 to 2025 standards.
- Complete the analysis of annual vehicle odometer data from the Texas vehicle emission inspection program to

understand the extent to which driving activity recently changed in response to the economic downturn and changing gas prices. The reduction in driving likely contributed to the large decline in fatalities in recent years.

✧   ✧   ✧   ✧   ✧

Introduction

Reducing vehicle mass is perhaps the easiest and least-costly method to reduce fuel consumption and greenhouse gas emissions from light-duty vehicles. However, the extent to which government regulations should encourage manufacturers to reduce vehicle mass depends on what effect, if any, light-weighting vehicles is expected to have on societal safety. As part of an interagency analysis effort between NHTSA, EPA, and DOE, LBNL has been examining the relationship between vehicle mass and size and U.S. societal fatality and casualty risk, using historical data on recent vehicle designs. This research effort informs the agencies on the extent to which vehicle mass can be reduced in order to meet fuel economy and greenhouse gas emissions standards, without compromising the safety of road users.

In FY 2014 LBNL published two draft reports. The first examined the sensitivity of the relationship between vehicle mass/size and crash frequency to several additional variables that capture differences by vehicle model and their drivers [1]. The second tested the sensitivity of the relationship between vehicle mass/size and societal risk per VMT to the definition of "lighter" vs. "heavier" cars and light trucks [2].

Results and Discussion

The approach taken, results, and conclusions from each of the additional analyses LBNL conducted are discussed separately below.

1. Sensitivity of crash frequency model to additional variables

LBNL first examined the results of three vehicle braking and handling tests conducted by Consumer Reports: 1) the maximum speed achieved during the avoidance maneuver test, 2) acceleration time from 45 to 60 miles per hour (mph), and 3) dry braking distance. When these three test results are added to the LBNL baseline regression model of the number of crashes per mile of vehicle travel in cars, none of the three handling/braking variables are associated to have the expected effect on crash frequency. In other words, an increase in maximum maneuver speed, a decrease in the time to reach 60 miles per hour, or a decrease in braking distance on dry pavement in cars, either separately or combined, is associated with an <u>increase</u> in the likelihood of a crash, of any type or with a stationary object.

Adding one or all of the three handling/braking variables has relatively little effect on the estimated relationship between mass or footprint reduction in cars and crash frequency in all types of crashes, as shown in

Table V-11. However, the beneficial effect of mass reduction in heavier-than-average cars on crash frequency with stationary objects only is expected to increase, from a 0.17% reduction in crash frequency in the baseline model to as much as a 1.34% reduction in crash frequency when all three variables are included, as indicated in Table V-12.

Table V-11: Estimated effect of mass or footprint reduction on 13-state crash frequency (crashes per VMT), under alternative regression model specifications, *all crashes.*

Variable	NHTSA baseline model (crashes per VMT)	1. Using only vehicles with CR test results	2. Including MANEUVER (max speed on avoidance maneuver test)	3. Including ACC45TO60 (sec to accelerate from 45 to 60 mph)	4. Including DRYBRAKE (stopping distance in feet on dry surface)	5. Including MANEUVER, ACC45TO60, and DRYBRAKE
UNDRWT00	1.97%*	1.95%*	1.80%*	2.14%*	1.94%*	2.03%*
OVERWT00	1.34%*	1.20%*	0.99%*	1.10%*	1.12%*	0.97%*
FOOTPRNT	0.85%*	0.96%*	0.93%*	1.14%*	0.97%*	1.12%*
MANEUVER	—	—	0.82%*	—	—	0.42%*
ACC45TO60	—	—	—	-1.80%*	—	-1.58%*
DRYBRAKE	—	—	—	—	-0.12%*	-0.06%*

* statistically significant at the 95% level.

Note: All re-weight the estimated coefficients from nine regression models by crash type by the number of fatalities by type of crash after assuming full penetration of ESC technology (NHTSA baseline model). Estimates converted from odds to probabilities.

Table V-12: Estimated effect of mass or footprint reduction on 13-state crash frequency (crashes per VMT), under alternative regression model specifications, *crashes with stationary objects only.*

Variable	NHTSA baseline model (crashes per VMT)	1. Using only vehicles with CR test results	2. Including MANEUVER (max speed on avoidance maneuver test)	3. Including ACC45TO60 (sec to accelerate from 45 to 60 mph)	4. Including DRYBRAKE (stopping distance in feet on dry surface)	5. Including MANEUVER, ACC45TO60, and DRYBRAKE
UNDRWT00	1.18%*	1.27%*	0.80%*	1.60%*	1.22%*	1.19%*
OVERWT00	-0.17%*	-0.60%*	-1.27%*	-0.79%*	-0.89%*	-1.34%*
FOOTPRNT	2.52%*	2.82%*	2.74%*	3.12%*	2.88%*	3.02%*
MANEUVER	—	—	2.65%*	—	—	1.63%*
ACC45TO60	—	—	—	-3.03%*	—	-2.20%*
DRYBRAKE	—	—	—	—	-0.43%*	-0.27%*

* statistically significant at the 95% level.

Note: All re-weight the estimated coefficients from nine regression models by crash type by the number of fatalities by type of crash after assuming full penetration of ESC technology (NHTSA baseline model). Estimates converted from odds to probabilities.

Because Consumer Reports test results could be matched to vehicle models representing only 40% of all cars, 22% of all CUVs and minivans, and essentially none of all light trucks, adding the braking/handling test results can only provide limited insight into how a vehicle's braking and handling characteristics affect the frequency it is involved in crashes and was not used in the sensitivity regression analyses discussed below.

LBNL next estimated the effect of adding five additional variables to the regression models in order to test the sensitivity of the relationship between mass or footprint reduction and crash frequency. Figure V-87 compares the relationship between each of the five variables and crash frequency. Figure V-88 compares the effect adding each variable individually, or adding all five variables, has on the estimated effect of mass reduction on crash frequency for cars.

Alternative Model 1 includes the initial purchase price, in thousands of dollars, by vehicle model, as derived from the Polk vehicle identification number (VIN) decoder; this information was available for about 97% of the vehicles in the state crash databases. Table V-13 indicates that average initial purchase price varies from just over $19,000 for two-door cars to over $30,000 for large pickups and all-wheel drive cars. As shown in Figure V-87, crash frequency is slightly reduced for every additional $1,000 in the initial purchase price of a particular vehicle model.

Alternative Model 2 includes the average income of households that own a particular model of vehicle. The data are derived from California vehicle registration data, based on the median income in the zip code in which individual vehicles are registered, averaged over all vehicles of a given model. This information was available for about 97% of the vehicles in the state crash databases. Table V-13 indicates that average

household income ranges from just under $49,000 for pickups to over $58,000 for all-wheel drive cars (police cars, which are owned by government agencies located in predominantly urban zip codes, have an average "household" income of only $40,000). Figure V-87 suggests that crash frequency also decreases slightly for each $1,000 increase in household income.

Alternative Model 3 includes dummy variables for 15 vehicle makes; the relationship between vehicle make and crash frequency is not shown in Figure V-87.

The average "bad driver" rating by vehicle model is added to alternative Model 4. In its 2003 report NHTSA created a "bad driver" rating variable based on whether alcohol or drugs were involved in the current crash, whether the driver had a valid license or was accused of reckless driving in the current crash, or whether the driver had a moving violation within the last three years. Table V-13 indicates that sporty cars have the highest average bad driver rating, 0.80, followed by 2-door cars (0.66), while minivans and police cars have an average bad driver rating of less than 0.30. In terms of individual vehicle models, the bad driver rating varies from 0.16 for Honda Odyssey to 1.08 for Lexus IS-300 and Acura CL. We assigned the average bad driver rating to each vehicle model in the state crash cases, and included the variable in the regression models (the NHTSA and LBNL 2012 reports excluded Fatality Analysis Reporting System (FARS) cases where drivers were suspected of alcohol or drug use, or were otherwise "bad" drivers). We only included the bad driver rating for vehicle models that had at least 50 individual vehicles in the FARS data, which accounted for about 95% of all the vehicles in the crash data an induced exposure data. Figure V-87 suggests, surprisingly, that car crash frequency increases as bad driver rating increases; however, increasing

bad driver ratings are associated with an expected reduction
in crash frequency in light trucks and CUVs/minivans.
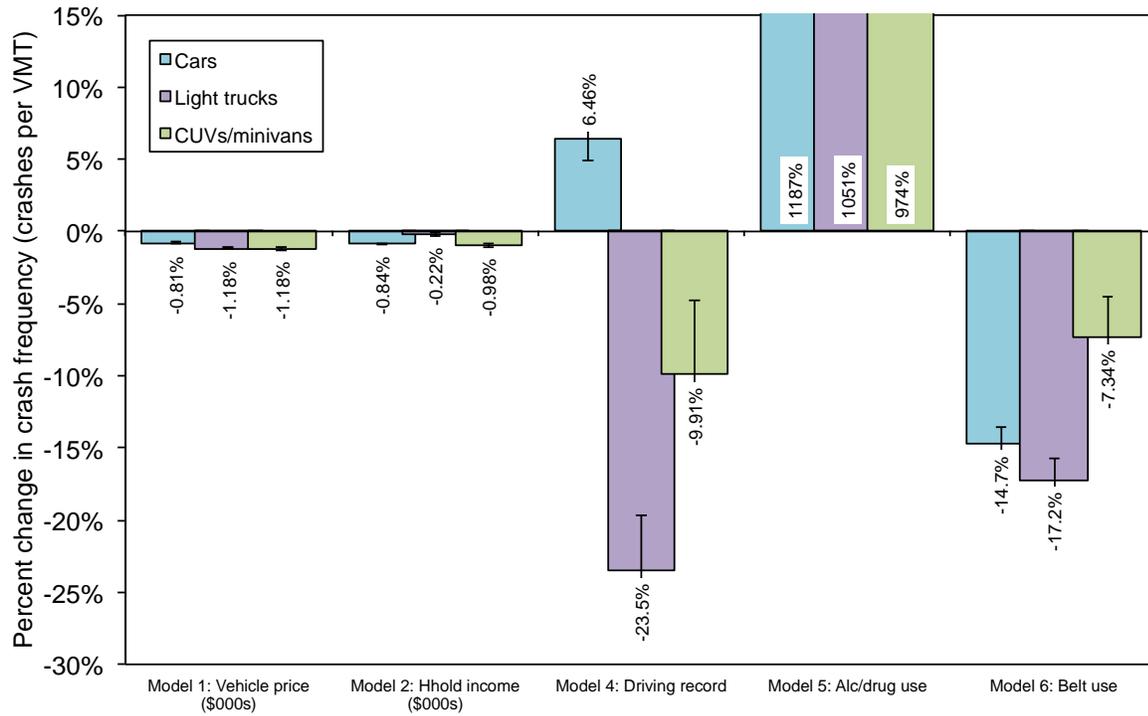
Figure V-87: Estimated effect of individually adding five additional variables on the change in crash frequency estimated in baseline model, by vehicle type.
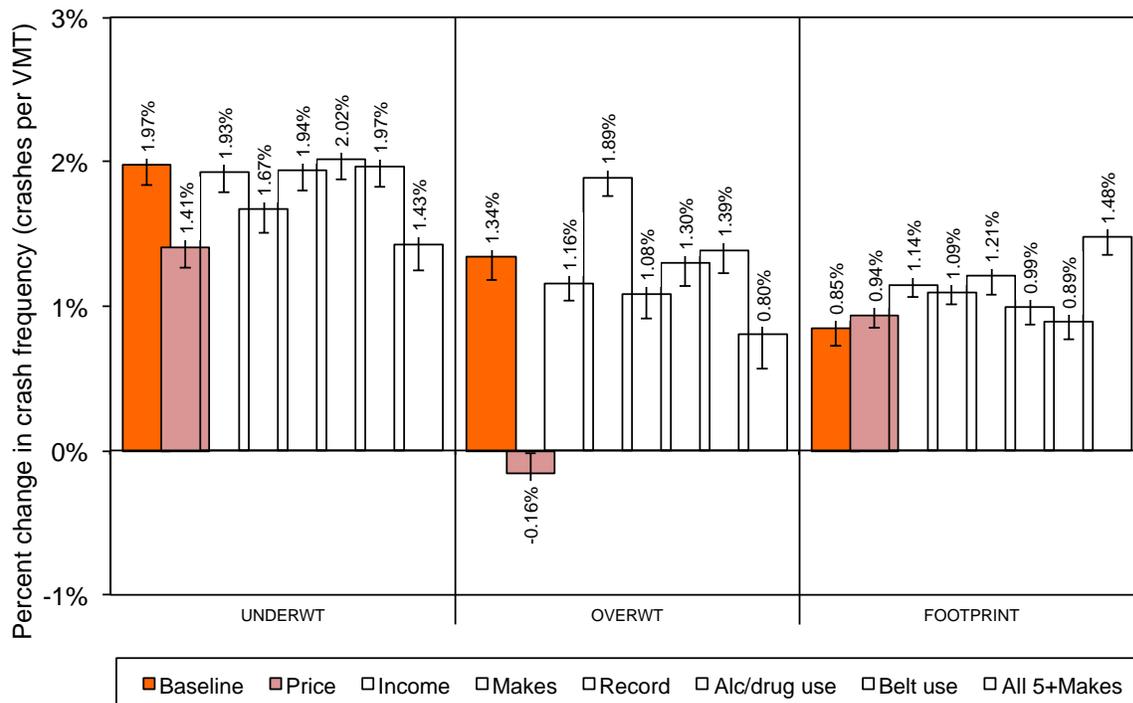

Figure V-88: Estimated effect of adding five additional variables on the estimated change in mass or footprint reduction on crash frequency, cars.

Table V-13: Average vehicle and driver characteristics, by vehicle type.

Vehicle type	Average initial purchase price	Average household income	Average bad driver rating	Percent drivers using alcohol or drugs	Percent drivers not using restraints
2-dr cars	$19,181	$49,748	0.66	3.88%	3.64%
4-dr cars	$20,174	$49,249	0.49	2.41%	2.61%
Sporty cars	$24,870	$51,406	0.80	5.65%	4.18%
Police cars	$25,070	$40,441	0.26	0.53%	4.02%
AWD* cars	$30,229	$58,517	0.52	2.79%	1.72%
Sm pickups	$24,321	$48,045	0.56	4.51%	4.19%
Lg pickups	$30,854	$48,561	0.49	3.91%	4.61%
SUVs**	$29,710	$51,515	0.48	2.83%	2.60%
CUVs***	$25,100	$54,574	0.36	1.83%	1.79%
Minivans	$25,555	$50,464	0.25	1.09%	1.75%
Full vans	$24,003	$49,517	0.37	1.44%	2.48%
All	$23,352	$50,033	0.49	2.76%	2.83%

Note: NHTSA baseline regression model and alternative models exclude the vehicle types shown in red.

*AWD is all-wheel drive

**SUV is truck-based sport utility vehicle

***CUV is car-based crossover utility vehicle

Alternative Models 5 and 6 account for whether the drivers in the state crash data cases were suspected of using alcohol or drugs, or were not wearing safety restraints, respectively, at the time of the crash. These data were reported for about 96% of the crash cases, and about 94% of the induced exposure crash cases used to estimate vehicle miles of travel. There are very few case vehicles whose driver was suspected of using alcohol or drugs or was not wearing a safety restraint. Only 2.76% of drivers in all crashes, and only 88 of over 127,000 drivers in the induced exposure cases (0.07%), were suspected of using alcohol or drugs, and only 2.83% of drivers in all crashes, and only 722 of over 134,000 drivers in the induced exposure cases (0.53%), were not wearing their restraints. Table V-13 indicates that suspected alcohol/drug use was highest in small pickups (4.51%) and lowest in police cars (0.53%) and minivans (1.09%); drivers in sporty cars, police cars, and pickups were most likely not to use restraints (over 4%), while drivers in minivans, CUVs, and all-wheel drive cars were least likely not to use restraints (under 2%). Figure V-87 suggests that crash frequency increases dramatically if the driver was using alcohol or drugs, and decreases substantially if the driver was properly using his or her restraint.

Figure V-88 shows the estimated effect of adding the five additional variables shown in Figure V-87, individually and cumulatively, on the estimated effect of mass or footprint reduction on crash frequency, for cars. The last columns in the figure ("All 5 + Makes") represent the estimated effect of Model 7, which includes all five of the additional variables

(initial vehicle purchase price, average household income, average bad driver rating, driver alcohol/drug use, and driver restraint use), plus 15 vehicle makes, in one regression model. Including all of the variables reduces the number of crash cases by about 15%. Because of the large number of control variables added to the model (20 additional variables, for a total of 63), alternative Model 7 excludes control variables that are not statistically-significant. While including all of the additional variables in Model 7 reduces the estimated effect of mass or footprint reduction on crash frequency in cars in many cases, in all but one case the sign of the coefficient does not change from the sign in the NHTSA baseline model.

Including these variables, either individually or including all in the same regression model, does not change the general results of the baseline NHTSA regression model: that mass reduction is associated with an increase in crash frequency in all three types of vehicles, while footprint reduction is associated with an increase in crash frequency in cars and light trucks, but with a decrease in crash frequency in CUVs/minivans. The variable with the biggest effect is initial vehicle purchase price, which dramatically reduces the estimated increase in crash frequency in heavier-than-average cars (and in heavier-than-average light trucks, and all CUVs/minivans). These results suggest that other, more subtle, differences in vehicles and their drivers account for the unexpected finding that lighter vehicles have higher crash frequencies than heavier vehicles, for all three types of vehicles.

2. Sensitivity of fatality risk model to different definition of "lighter" vs. "heavier" cars and light trucks

In the 2012 report in support of the recent fuel economy/greenhouse gas emission standards [3], NHTSA used logistic regression models to estimate the effect of a 100-lb reduction in vehicle mass, or a 1-square foot reduction in vehicle footprint, on societal fatality risk per vehicle miles of travel. Estimated coefficients were generated from 27 regression models, one each for three vehicle types (passenger cars; light duty trucks, i.e. pickups and SUVs; and car-based vehicles regulated as light-duty trucks, i.e. crossover utility vehicles, or CUVs, and minivans). For each vehicle type, a separate regression model was run for nine crash types. The estimated coefficients from each of the 27 regressions were re-weighted by the expected number of fatalities in each type of crash after full adoption of electronic stability control technology (ESC).

In the baseline model, NHTSA used a two-piece linear variable for car and light truck mass, with the flex point for each vehicle type based on the median curb weight of each vehicle type (3,106 lbs for cars, 4,594 lbs for light trucks. Because there were not enough fatalities involving case CUVs and minivans, a single variable for CUV/minivan weight was used). Of the five vehicle types (lighter- and heavier-than-average cars and light trucks, and CUVs/minivans), the estimated coefficients were statistically significant for only one, lighter-than-average cars. This report examines whether using different groupings of vehicle weight results in a greater number of vehicle types with a statistically-significant estimate of the effect of mass reduction on societal fatality risk per VMT.

LBNL tested the sensitivity of the results from the NHTSA baseline regression model, which used a single flex point at the median vehicle weight, to eight alternative weight groupings:

- Alternative 1: one flex point, weight divided into quartiles;
- Alternative 2: one flex point, weight divided into sestiles;
- Alternative 3: one flex point, weight divided into octiles;
- Alternative 4: two flex points at the 25th and 75th weight percentile, weight divided into quartiles;
- Alternative 5: one flex point at the 75th percentile;
- Alternative 6: one flex point at the 25th percentile;
- Alternative 7: 2-dr cars treated separately from 4-dr cars, and small pickups/SUVs treated separately from large pickups;
- Alternative 8: use the "crossover" weight rather than the median weight.

For the revised LBS100 values, LBNL used the same method NHTSA used for driver age groups: i.e. for the lightest vehicles, LBS100 values were calculated for all of the UNDRWT variables, while for the heaviest vehicles values were calculated for all of the OVERWT variables. For example, under Alternative 3, which used a separate weight variable for eight octiles of vehicle weight, a 2,478 lb car has the following values shown in Table V-14.

Table V-14: LBS100 values for a 2,478-lb car, using eight weight groups.

Variable	Weight group	LBS100 Value
UNDRWT8A	< 2,559 lbs	-0.81
UNDRWT8B	2,559 to 2,676 lbs	-1.17
UNDRWT8C	2,676 to 2,944 lbs	-2.68
UNDRWT8D	2,944 to 3,106 lbs	-1.62

The sum of these values for the four UNDRWT variables is -6.28 which relates to the difference between the curb weight of the subject vehicle (2,478 lbs) and the median curb weight for cars (3,106 lbs). Figure V-89 and Figure V-90 show the estimated effect of mass reduction in the NHTSA baseline model (shown in orange) and alternative Models 1 through 6, for cars and light trucks, respectively. For simplicity, all of the results shown are for a single regression model across all crash types, and do not reweight the coefficients by crash type to account for full adoption of ESC technology. If mass reduction is consistently associated with an increase in risk, one would expect that the lightest and heaviest vehicles in alternative Models 1 (dark blue), 2 (dark green), and 3 (red), would have larger estimated effects of mass reduction than the vehicles closer to the median mass. However, this is not the case. The estimated effect of mass reduction tends to be smallest, and usually not statistically-significant, in the lightest and heaviest vehicles, both for cars in Figure V-91 and light trucks in Figure V-92.

Model 4 uses the same weight groups as Model 1, but rather than calculating LBS100 for individual based on the median weight of all vehicles for lighter-than-average vehicles, the model calculates LBS100 based on the median mass of the lightest 50% of vehicles (2,676 lbs for cars, 4,023 lbs for light trucks), and for heavier-than-average vehicles LBS100 is based on the median mass of the heaviest 50% of vehicles (3,367 lbs for cars, 5,200 lbs for light trucks). Figure V-89 and Figure V-90 indicate that Model 4 (shown in purple) estimates that mass reduction in the lightest and heaviest cars is associated with a nearly 3% reduction in fatality risk per VMT, but no significant change in risk for cars closer to the median weight for cars. This result is unexpected; if decreased mass is consistently associated with increasing risk, we would expect the lightest cars to be associated with the largest increase in risk.

Model 5 uses only two weight groups, but sets the flex point for LBS100 at the 75th percentile weight for each type of vehicle. In this case, 75% of cars and trucks are included in the lighter vehicle group, while only 25% of vehicles are included in the heavier group. As indicated in Figure V-89, Model 5 (shown in light blue) estimates, as expected, that mass reduction in the lightest 75% of cars is associated with an increase in risk, while mass reduction in the heaviest 25% of cars is associated with a decrease in risk. Figure V-90 indicates that Model 5 also estimates in the expected direction for light trucks, with the estimated increase in risk for the lightest 75% of light trucks higher than in the baseline model, and now statistically-significant, while the estimated decrease in risk for the heaviest 25% of light trucks is much more beneficial than in the baseline model (a 1.17% reduction, rather than a 0.42% reduction in risk).
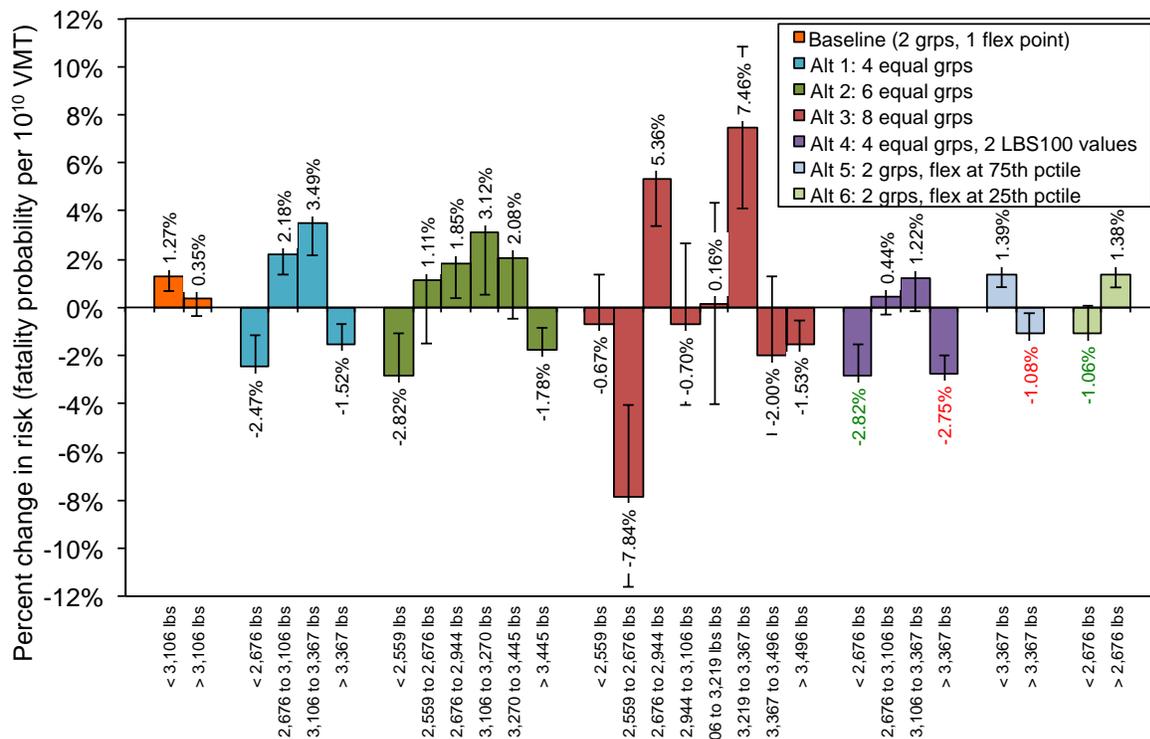
Figure V-89: Estimated effect of car mass reduction on U.S. societal fatality risk per VMT, baseline model and six alternative weight groups.
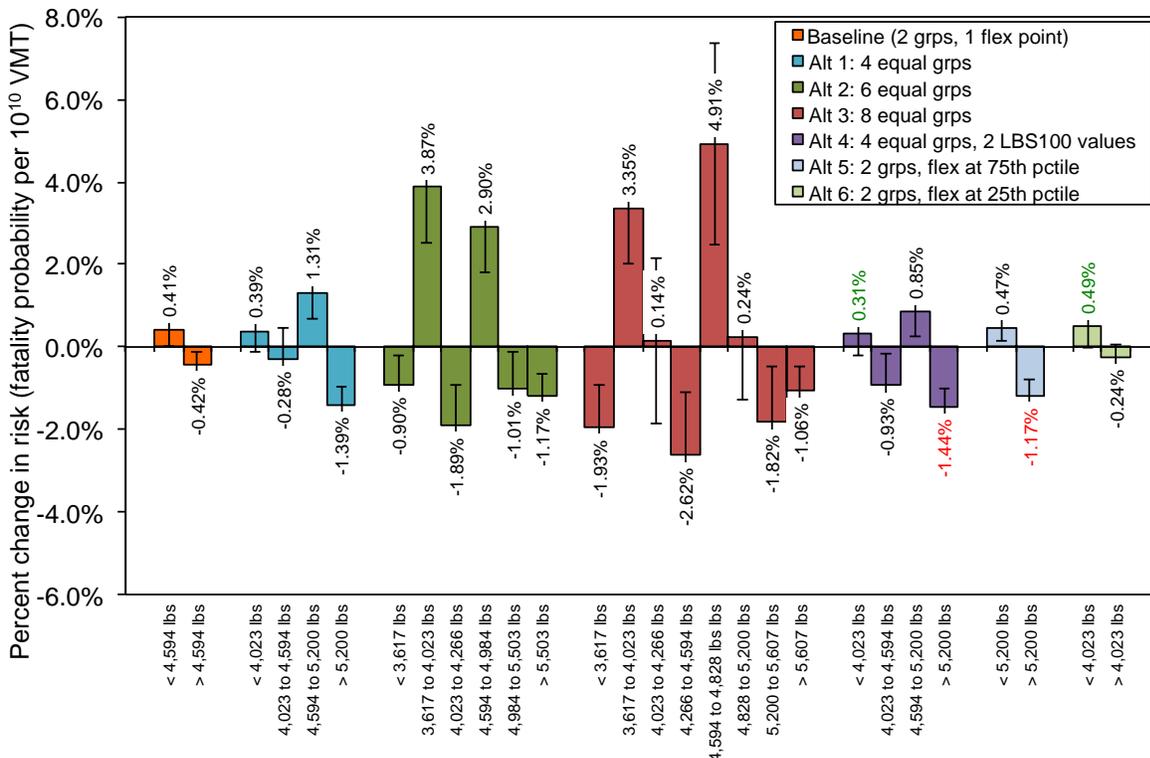

Figure V-90: Estimated effect of light truck mass reduction on U.S. societal fatality risk per VMT, baseline model and six alternative weight groups.

Model 6 in Figure V-89 is the opposite of Model 5, with the flex point set at the 25th percentile weight. The estimates of Model 6 (shown in light green) are in the unexpected direction, with mass reduction in the lightest 25% of cars associated with a large reduction in risk, and mass reduction in the heaviest 75% of cars associated with a large increase in risk. For light trucks, the estimated effect of mass reduction on risk in Model 6 is similar to that in the baseline model.

In Model 7 the relationship between mass reduction and risk in two-door cars is modeled separately from that in four-door cars, and the relationship in small trucks and SUVs is modeled separately from that in large pickups. Figure V-91 compares the baseline estimates with those of two-door and four-door cars, while Figure V-92 compares the baseline estimates with those of small pickups/SUVs and large pickups. In Figure V-91, Model 7 estimates that mass reduction is associated with a larger increase in risk in lighter-than-average four-door cars than in heavier-than-average four-door cars, as in the baseline model. However, Model 7 estimates an unexpected result for two-door cars: mass reduction in lighter-than-average two-door cars is associated with a reduction in risk, while mass reduction in heavier-than-average two-door cars is associated with a large increase in risk.

As shown in Figure V-92, Model 7 estimates the same relationship for small pickups/SUVs as for all light-trucks combined in the baseline model. Mass reduction in lighter-than-average trucks is associated with a slight increase in risk, while mass reduction in heavier-than-average trucks is associated with a slight decrease in risk. However, the relationship for small pickups/SUVs is smaller than in the baseline model. Model 7 shows an unexpected result when large pickups are modeled separately from small pickups/SUVS. In this case, mass reduction in lighter-than-average large pickups is associated with a large, statistically-significant reduction in risk, while mass reduction in heavier-than-average large pickups is associated with an increase in risk. This unexpected result is similar to that obtained by Model 7 for two-door cars, shown in Figure V-91.

LBNL next estimated the weight at which the effect of mass reduction on risk on average is estimated to become a benefit rather than a detriment (i.e. changes from an increase in risk to a reduction in risk). This estimated "crossover" weight is 3,888 lbs for cars and 4,710 lbs for light trucks. Figure V-93 shows the estimated effect of mass reduction on societal

fatality risk per VMT after replacing the median curb weight for cars and light trucks with these crossover weights. The figure indicates that using the crossover weights estimates that mass reduction in heavier cars is associated with a large decrease in fatality risk, and reduces somewhat the estimated increase in risk for lighter cars. In addition, when using the crossover weights all four estimates become statistically-significant. The crossover weight for cars is the 90th percentile of weight for cars, while the crossover weight for light trucks is only the 60th percentile weight for light trucks.

One possible explanation for the inconsistent trend in fatality risk over four, six and eight mass groups is that there are other differences among vehicles, drivers, or crash characteristics across the weight groups that are not controlled for by the independent variables in the logistic regression model. Table V-15 shows the average values of vehicle, driver and crash characteristics across the eight weight groups. For cars, the weight group with the highest reduction in risk associated with mass reduction in Figure V-89 is shown in green in each table, while the weight group with the highest increase in risk associated with mass reduction is shown in red in each table.

Both weight and footprint increase as the car weight group increases; however, the curb weight of the car's crash partner is very consistent across the different weight groups. The fraction of two-door cars decreases as car weight increases, while the fraction of cars equipped with side airbags, ABS, and ESC increases as car weight increases. The fraction of cars that are luxury cars is highest for the heaviest cars. The trends by manufacturer country of origin are not consistent, although lighter cars tend to be dominated by Japanese models while heavier cars tend to be dominated by U.S. models. Regarding driver characteristics, the heaviest vehicles tend to have the highest fraction of male drivers and old drivers, and the lowest fraction of young drivers; there is no consistent trend between the fraction of bad drivers, those that use safety restraints, and those that use alcohol or drugs as vehicle mass increases. The crash circumstances are also fairly similar across the different weight groups.
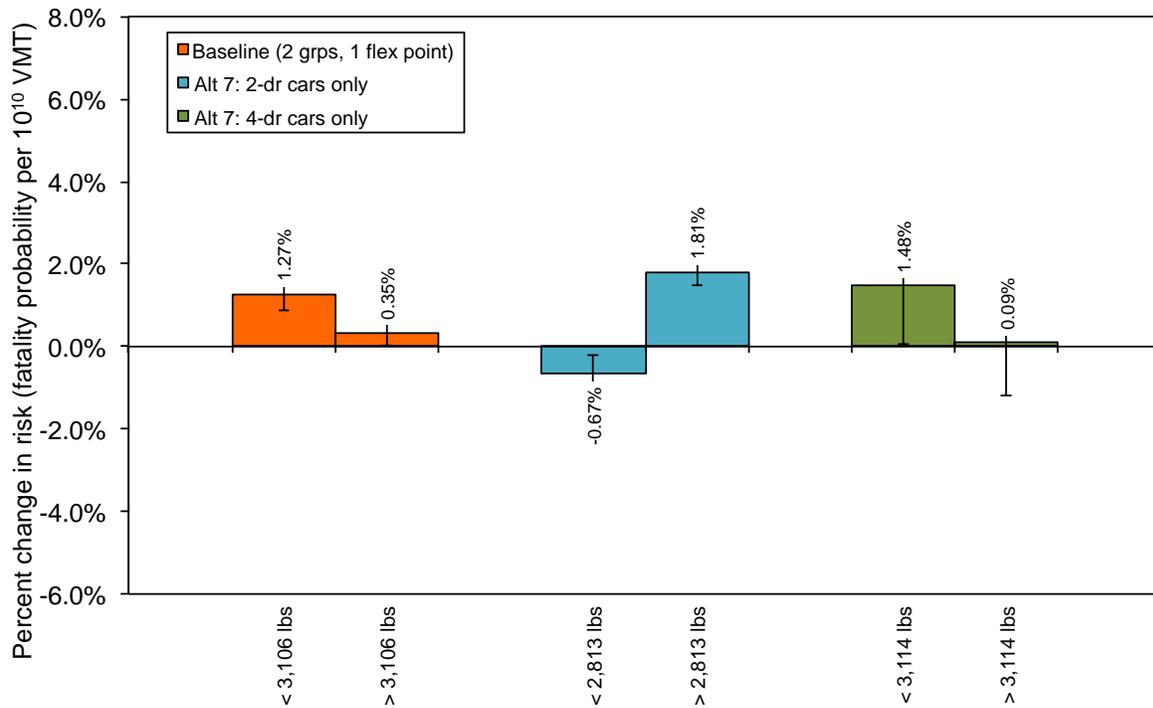
Figure V-91: Estimated effect of car mass reduction on U.S. societal fatality risk per VMT, baseline model and treating 2-door cars separately from 4-door cars.
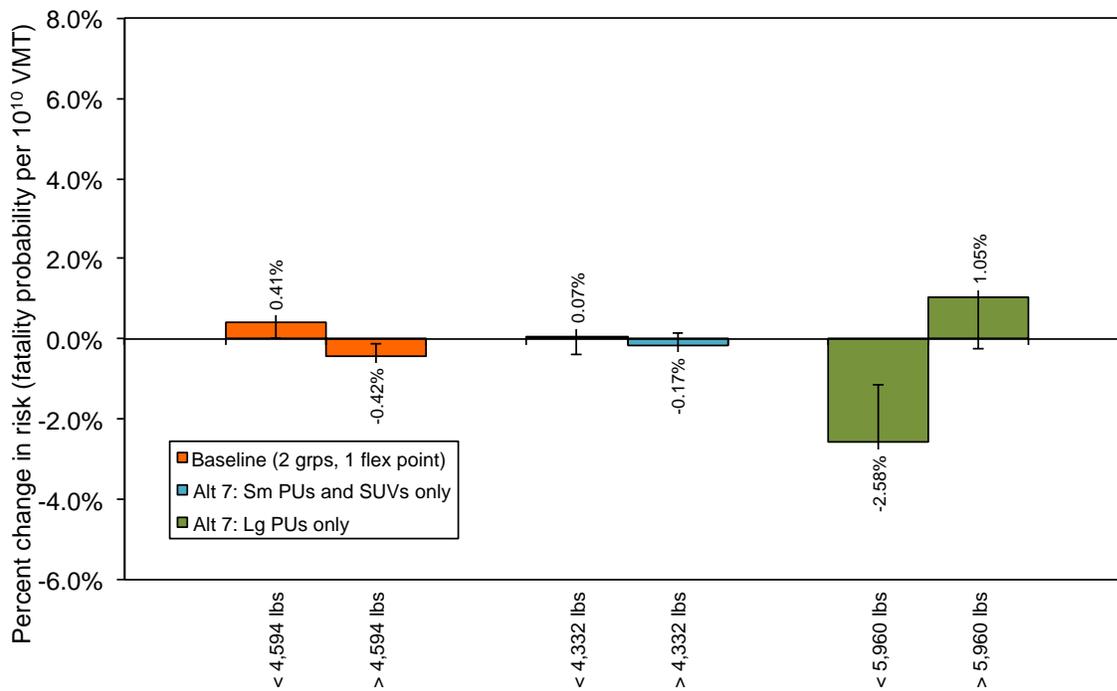

Figure V-92: Estimated effect of light truck mass reduction on U.S. societal fatality risk per VMT, baseline model and treating small pickups and SUVs separately from large pickups.
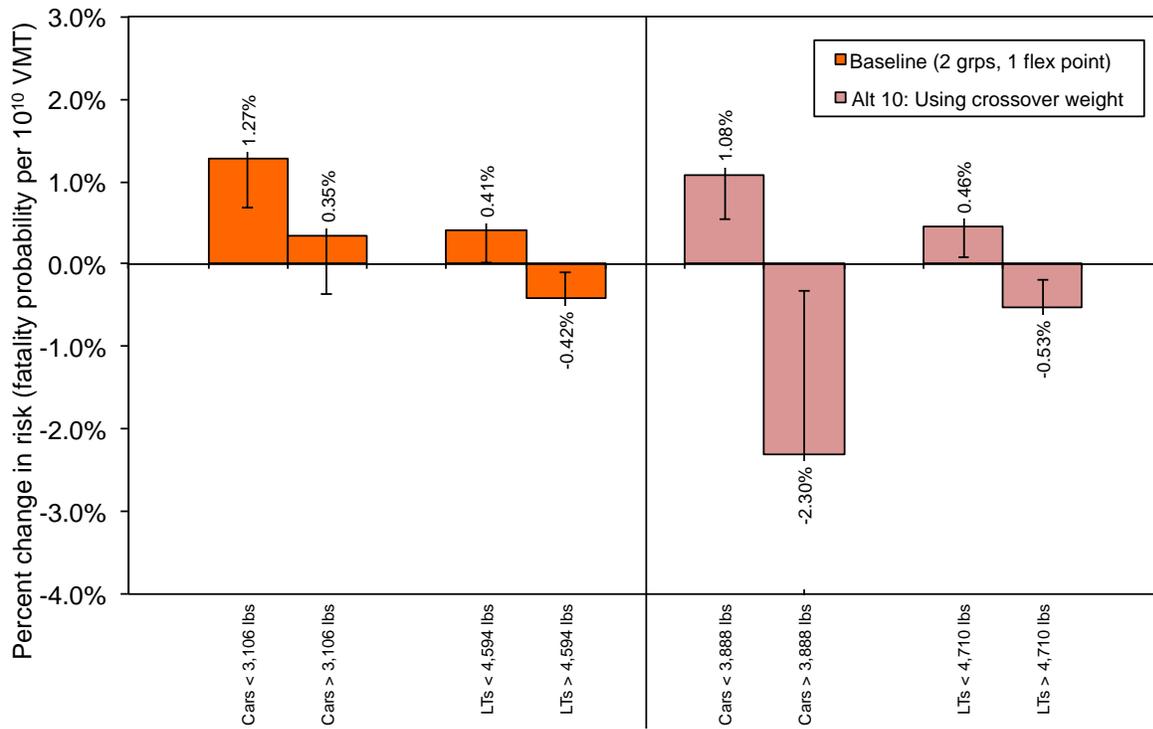
Figure V-93: Estimated effect of mass reduction on U.S. societal fatality risk per VMT, baseline model and alternative using crossover curb weights.

Table V-15: Average car, driver, and crash characteristics by eight weight groups.

Characteristic	<2,559 lbs	2,559 to 2,676 lbs	2,676 to 2,944 lbs	2,944 to 3,106 lbs	3,106 to 3,219 lbs	3,219 to 3,367 lbs	3,367 to 3,496 lbs	>3,496 lbs
				Eight weight groups				
Curb weight	2,434	2,619	2,770	3,037	3,167	3,304	3,429	3,734
Partner curb wt.	3,685	3,708	3,737	3,618	3,595	3,621	3,591	3,616
Footprint	39.91	41.44	41.76	43.61	44.72	45.53	46.47	48.58
2-door cars	28%	22%	21%	18%	12%	5%	16%	5%
Side airbags	5%	6%	41%	25%	28%	42%	33%	69%
ABS	22%	35%	41%	63%	47%	72%	80%	89%
ESC	2%	1%	1%	2%	5%	14%	12%	36%
US mfr	33%	60%	38%	38%	38%	29%	55%	68%
Japan mfr	53%	35%	30%	49%	49%	60%	25%	24%
European mfr	0%	0%	6%	11%	11%	3%	13%	6%
Korean mfr	13%	3%	22%	2%	2%	5%	7%	0%
Other mfr	2%	2%	3%	0%	0%	2%	0%	1%
Luxury brand	0%	1%	3%	1%	1%	0%	5%	12%
Low-risk models	44%	52%	41%	74%	80%	78%	66%	52%
High-risk models	23%	42%	51%	21%	17%	16%	27%	28%
Male driver	37%	36%	38%	38%	38%	43%	43%	52%
Young driver	49%	51%	47%	43%	38%	29%	29%	16%
Old driver	3.8%	3.8%	3.8%	4.4%	4.5%	7.6%	7.8%	15.8%
Bad driver	1.3%	1.6%	1.4%	1.4%	1.2%	1.1%	1.4%	1.1%
Restraint use	73%	70%	72%	72%	73%	76%	73%	78%
Alcohol/drug use	39%	39%	41%	39%	39%	37%	39%	34%
At night	20%	20%	20%	19%	18%	17%	17%	16%
Rural county	21%	25%	22%	22%	22%	23%	26%	23%
High-speed road	16%	17%	17%	17%	17%	17%	18%	18%
High fatality state	43%	45%	43%	44%	45%	43%	43%	43%

In summary, the average characteristics of vehicles, drivers, and crash circumstances by weight group do not appear to explain the lack of a consistent trend of decreasing fatality risk as mass increases.

Conclusion

In FY14 LBNL conducted several analyses to better understand the relationship between decreasing vehicle weight or footprint and increasing crash frequency. Including several new variables that were thought to influence crash frequency to the regression model did not change the result of the baseline model that lighter or smaller vehicles have higher crash frequency. LBNL also tested whether changing the definition of "light" vs. "heavy" vehicles would change the results of the baseline 2012 regression model. Using more categories of vehicle weight, rather than less or greater than the median weight, did not achieve the expected results. The estimated effect of mass reduction on societal fatality risk per VMT did not

consistently decrease as vehicle weight increased. When the weight "flexpoint" was optimized to reduce fatality risk, LBNL was able to obtain a large, statistically-significant increase in risk from mass reduction in lighter cars, and a similar decrease in risk from mass reduction in heavier cars; however, the flexpoint necessary to achieve this statistical result was at the 90th percentile weight for cars, and would dramatically reduce the sample size of "heavy" cars if used. Finally LBNL began analyzing state-level vehicle registrations, gasoline use, and miles of travel, to better understand the leveling off of national VMT growth beginning in 2004 and seven years of vehicle odometer and registration data from California and Texas, to assess how changing gasoline prices and economic conditions have influenced consumer vehicle purchase decisions and vehicle use by household. These analyses may be used to adjust the VMT weights used in the updated fatality risk analysis for the midterm review of the fuel economy/greenhouse gas emission standards, to be conducted in FY15.

Presentations/Publications/Patents

None

References

1. Wenzel, Tom (February 2014). Sensitivity of Light-Duty Vehicle Crash Frequency per Vehicle Mile of Travel to Additional Vehicle and Driver Variables. Draft report prepared for the Office of Energy Efficiency and Renewable Energy, US Department of Energy; Lawrence Berkeley National Laboratory (internal only)

2. Wenzel, Tom (July 2014). Effect of Using Different Vehicle Weight Groups on the Estimated Effect of Mass Reduction on U.S. Societal Fatality Risk per Vehicle Miles of Travel. Draft report prepared for the Office of Energy Efficiency and Renewable Energy, US Department of Energy; Lawrence Berkeley National Laboratory.

3. Kahane, C.J. (August 2012). *Relationships Between Fatality Risk, Mass, and Footprint in Model Year 2000-2007 Passenger Cars and LTVs*. National Center for Statistics and Analysis, National Highway Traffic Safety Administration, Final Report, DOT HS 811 665.